Sami Khomsi · François M. Roure ·
Mansour Al Garni ·
Ammar Amin   *Editors*

Arabian Plate and Surroundings: Geology, Sedimentary Basins and Georesources

Springer

Regional Geology Reviews

The Geology of series seeks to systematically present the geology of each country, region and continent on Earth. Each book aims to provide the reader with the state-of-the-art understanding of a regions geology with subsequent updated editions appearing every 5 to 10 years and accompanied by an online "must read" reference list, which will be updated each year. The books should form the basis of understanding that students, researchers and professional geologists require when beginning investigations in a particular area and are encouraged to include as much information as possible such as: Maps and Cross-sections, Past and current models, Geophysical investigations, Geochemical Datasets, Economic Geology, Geotourism (Geoparks etc), Geo-environmental/ecological concerns, etc.

More information about this series at http://www.springer.com/series/8643

Sami Khomsi • François M. Roure •
Mansour Al Garni • Ammar Amin
Editors

Arabian Plate and Surroundings: Geology, Sedimentary Basins and Georesources

Springer

Editors
Sami Khomsi
Faculty of Earth Sciences
King Abdulaziz University
Jeddah, Saudi Arabia

François M. Roure
Géosciences
IFP Energies Nouvelles
Rueil-Malmaison Cedex, France

Mansour Al Garni
Geophysics
King Abdulaziz University
Jeddah, Saudi Arabia

Ammar Amin
Faculty of Earth Sciences
King Abdulaziz University
Jeddah, Saudi Arabia

Preface

This book focuses on the Arabian Plate and its surroundings, including some key areas from Saudi Arabia, Lebanon in the east, to Egypt and Tunisia in Northern side of the African plate. It comprises a set of 10 papers combined into three different themes, dealing successively with the (I) Sedimentary basins, petroleum resources and reservoirs in the Arabian plate, (II) Geophysics and structural styles, (III) Hydrology, hydrogeology and water resources of the Arabian plate in the Kingdom of Saudi Arabia.

Part I: Sedimentary Basins, Petroleum Resources and Reservoirs in the Arabian Plate

Part I is made up of a very comprehensive set of three original papers.

The first paper by N. AL-Ghamdi and M. Pope deals with the Stratigraphic architectures, facies anatomies of the Lower Cretaceous Biyadh and Shu'aiba formations, and their implications on platform evolution and global correlation in Saudi Arabia, providing an updated data base on the sedimentary facies variations of the lower Cretaceous reservoirs in the eastern province.

The second paper by Gabor Tari et al., with an in-depth review of The Lower Cretaceous Chouf Sandstone of Lebanon which is a regional reservoir level in the Levant, northern Arabian plate, Lebanon. The authors discuss a model of a wide-rift style extensional episode for northern Lebanon during the Early Cretaceous (Valanginian to Barremian), which provided the accommodation space for the deposition of the Chouf Sandstone Formation. They present also some future exploration concepts.

The third paper by M. Bédir and M. Issaoui deals with a comprehensive view of the Seismic tectono-stratigraphy and hydrocarbon prospectivity of the deep marine Oligo-Miocene siliciclastic reservoirs lowstands in the Northern Levant Basin based on detailed interpretations of seismic sections and subsurface data in the offshore Lebanon.

The fourth paper by S. Rohais and R. Delphine is dealing with Source-to-sink analysis of the Plio-Pleistocene deposits in the Suez rift (Egypt). The authors present a study of the Plio-Pleistocene deposits in the Suez rift (Egypt) using stratigraphic records and quantitative geomorphology analysis. They constrain relief evolution in a rift setting from a high-resolution database at basin-scale including, digital elevation model, outcrops and subsurface data. They present five main stages ranging from rift initiation to tectonic quiescence (Oligo-Miocene) as well as a post-rift stage (Plio-Pleistocene).

Part II: Geophysics and Structural Styles

This part is mad up of three chapters.

The first paper by Gharbi et al., deals with The Southern Atlas front in southern Tunisia: Regional-scale geometry and structural evolution. It is based on presentation and discussions

of balanced cross section in the Southern Atlas front in the southern Atlas of Tunisia, including some insights from outcropping structures.

The second paper by H. Harbi is a review on the use of U-Pb zircon geochronology and geochemistry for some plutonic rocks from the Afif terrane of Saudi Arabia along the Arabian Shield. The author integrates the analyses in a big regional view and discusses the implications of the results for the crustal evolution in the Arabian shield.

The third paper by Al Garni et al. is about aeromagnetic data investigation of Al-Shamiyya area, northeast of Makkah quadrangle, Saudi Arabia. The authors integrate aeromagnetic data interpretations to underline and interpret the structural lineaments and framework in Al Shamiyya terranes, a key area and part of the Arabian shield.

Part III: Hydrology, Hydrogeology and Water Resources

The first paper by S. Bajabaa deals with groundwater contamination in the Wadi Haliy area, southwestern Arabian Shield, Saudi Arabia. The author shows a set of important analyses and interpretations in term of water pollution by heavy metals in an area with huge needs for good water resources in the Arabian shield.

The second paper by N. S. Al-Amri, and A. M. Subyani, treats the analysis of rainfall, missing data, frequency and PMP in Al-Madinah area, Western Saudi Arabia. The authors discuss deeply the estimation of rainfall variability, especially in arid regions, and major elements for flood prediction and water resources development design works. Such approach presents a major challenge to water resources management in arid regions due to the extreme random and erratic nature of rainfall events, which is further compounded by climate change impact.

The third paper by H. A. Saleem, M. O. Alharbi and A. M. Subyani discusses and presents the hydrochemical assessment of groundwater within the lower Wadi Ranyah, Western Saudi Arabia, using multivariate statistical technique. In fact, Wadi Ranyah is located in an arid region of the western mountains of Saudi Arabia, which is a highly potential resource for both surface and groundwater. This shallow aquifer is highly demanding and it is subjected to intense exploitation due to the influence of human activities.

Jeddah, Saudi Arabia   Sami Khomsi
Rueil-Malmaison Cedex, France   François M. Roure
Jeddah, Saudi Arabia   Mansour Al Garni
Jeddah, Saudi Arabia   Ammar Amin

Contents

Part I

Sedimentary Basins, Petroleum Resources and Reservoirs in the Arabian Plate

High-Resolution Stratigraphic Architectures, Facies Anatomies of the Lower Cretaceous Biyadh and Shuʾaiba Formations, and Their Implications on Platform Evolution and Global Correlation

Nasser AL-Ghamdi and Mike Pope

Abstract

The Early Cretaceous Biyadh and Shuʾaiba formations form giant carbonate reservoirs with complex architectures and heterogeneous reservoir characteristics. This paper presents an integrated research where, core data, wireline logs, biostratigraphy and stable isotope data are integrated to constrain the stratigraphic architectures for reservoir characterization. The study also provides a new regional and global correlation that has significant implications on the evaluation of paleo climate and glacio-eustatic controls of the Lower Cretaceous systems. The Biyadh Formation consists of a composite sequence and four high-frequency sequences. S1 and S2 formed the TST with chalky mudstone facies that shallow up to skeletal grainstone of S3 and S4. The Shuʾaiba Formation consists of a 2nd-order sequence, comprised of four 3rd-order sequences and ten high-frequency sequences. S1–S3 record the initial TST followed by the regional MFS (K70) and the deposition of an extensive *Lithocodium*/coral facies. S4–S6 marks the onset of rudist buildup that changed laterally to fore-bank, slope and basinal settings with basinward clinoform geometry, followed by HST of shallow lagonnal milliolids packstone facies of S7 and S8. S9 and S10 occured on the platform edge recording progradational systems formed during a major forced regression in the Late Aptian. They composed of a lowstand wedge of argillaceous mudstone that shallow upward to grainy marginal facies. A refined position of K70 and K80 and their relation with the global sea-level changes and perturbations in the Earth system have been proposed. Evidences of glacial events during the Aptian are recorded within the Shuʾaiba sequences alternating with warming events associated with nannoconids crisis and Oceanic Anoxic Event (OAE 1a). The stratigraphic record in this study and their global correlation suggests that the Barremian stage was dominated by warm greenhouse interval, followed by rapid climate change of possibly more transitional interval in the Aptian associated with glacial events.

1.1 Introduction

The Lower Cretaceous Shuʾaiba Formation is one of the main oil producers in the United Arab Emirates, Oman, Qatar and Saudi Arabia (Alsharhan and Nairn 1986; Alsharhan 1995; Hughes 2000; Borgomano et al. 2002; van Buchem et al. 2002; Immenhauser et al. 2004; van Buchem et al. 2010; AL-Ghamdi and Read 2010). The Lower Cretaceous Barremian and Aptian successions of Biyadh and Shuʾaiba Formations (Figs. 1.1 and 1.2), are NE-trending carbonate rudist build-up with average thickness of 600 ft (183 m) located in a remote area within the Empty Quarter. The Shuʾaiba carbonate build-up in the study area formed on the edge of a shallow ramp bordering the adjacent intra-shelf basin (Fig. 1.1). The Shuʾaiba Formation has complex facies architecture with heterogeneous reservoir quality, due to the development of rudist banks, syn-depositional faulting and later diagenetic overprinting. Sequences within the build-up are difficult to map, likely because of growth faulting, depositional topography, rapid facies changes and stacking and shingling of rudist banks. The Shuʾaiba reservoir in the study area has been producing for 14 years and a high-resolution sequence stratigraphic framework is essential to build a secondary development plan for this giant oil field.

Early description for the Shuʾaiba Formation was conducted by Ziegler (1976). The first geological model for reservoir modeling was produced by Aktas and Hughes (2000). However, the descriptive framework was mainly in terms of depositional setting rather than rock types.

N. AL-Ghamdi (✉)
Saudi Aramco, Dhahran, Saudi Arabia
e-mail: NASSER.GHAMDI.3@ARAMCO.COM

M. Pope
Texas A&M University, Kingsville, USA

Fig. 1.1 Aptian paleogeographic map for the Arabian Plate showing the location of study area and the intrashelf basins. Modern plate boundaries are shown with red lines
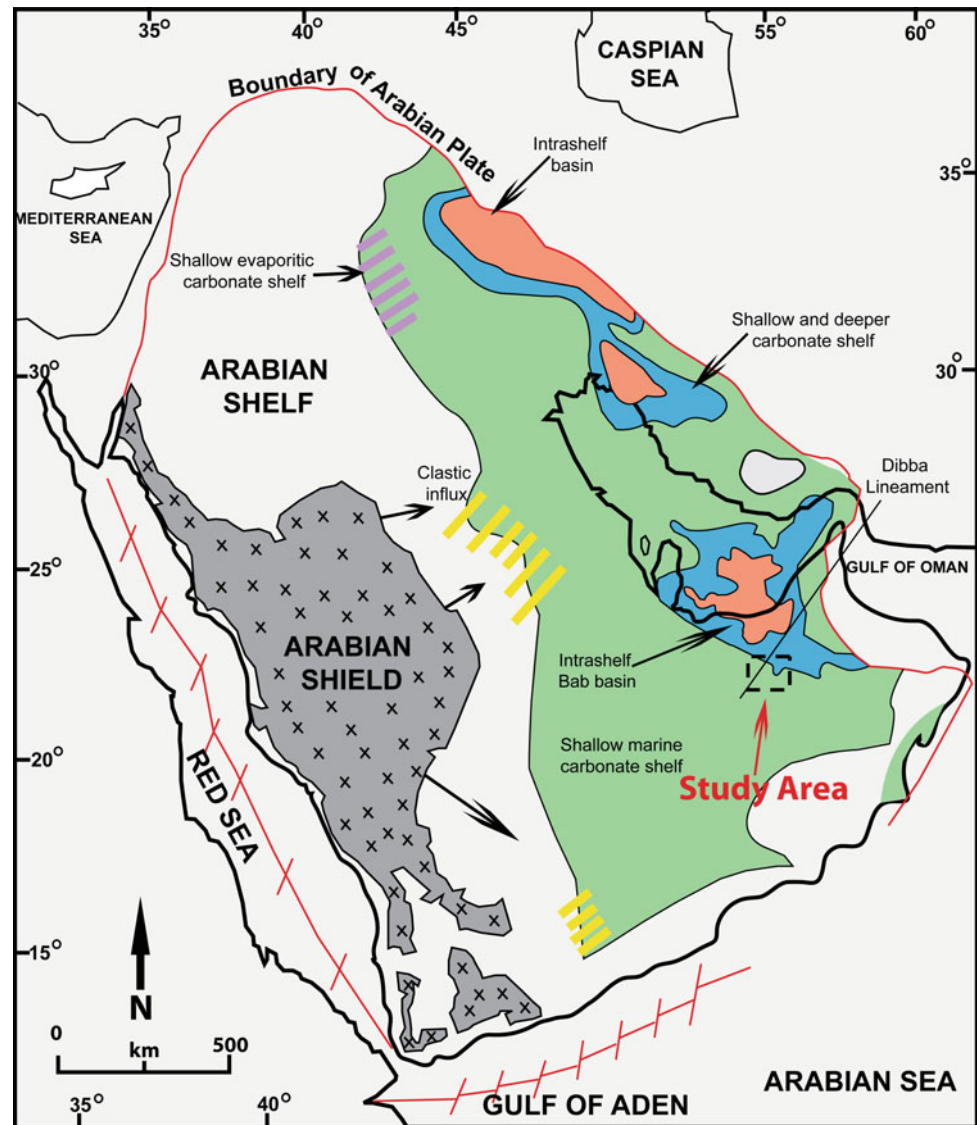
A detailed description of biofacies and their environments was provided by Hughes (2000). A higher resolution stratigraphic model and detailed description, including the first clinoform geometries on the platform margin was outlined by AL-Ghamdi and Read (2010). However, this model was only based on 14 wells, limited stable isotope and biostratigraphic data. This study presents a new high-resolution rock-based, sequence-stratigraphic model, refining the 2-D reservoir facies anatomy using 55 cored-wells, gamma ray logs and extensive isotope data (26 wells). This detailed framework will be integrated with petrophysical and engineering data to build new 3-D reservoir and simulation models and it should provide insights for new horizontal drilling locations and secondary and tertiary hydrocarbon recovery.

The Aptian stage provide one of most prominent time in geological history that records dramatic changes in biota and environmental conditions associated with the perturbation of global carbon cycles (Föllmi et al. 1994; Jenkyns 2003; Weissert and Erba 2004). The Lower Cretaceous Barremian and Aptian record global high sea-level changes, that greatly influenced the stratigraphic records (Matthews and Frohlich 2002; Immenhauser and Matthews 2004; Al-Husseini and Matthews 2010; Droste 2010). High-resolution orbital cyclostratigraphy of the Aptian suggests that the main driving mechanism are the ∼400 and ∼100 ky eccentricity orbital cycles (Al-Husseini and Matthews 2010; Huang et al. 2010). The high-resolution rock-based stratigraphic framework in this study will be tied to and compared with global sea-level charts (Rohl and Ogg 1998; Hardenbol et al. 1998; Haq and Schutter 2008), the standard carbon isotope curve (Föllmi et al. 2006) and cyclostratigraphy (Al-Husseini and Matthews 2010) to evaluate the influence of global sea-level changes on the evolution of the Shu'aiba platform. This
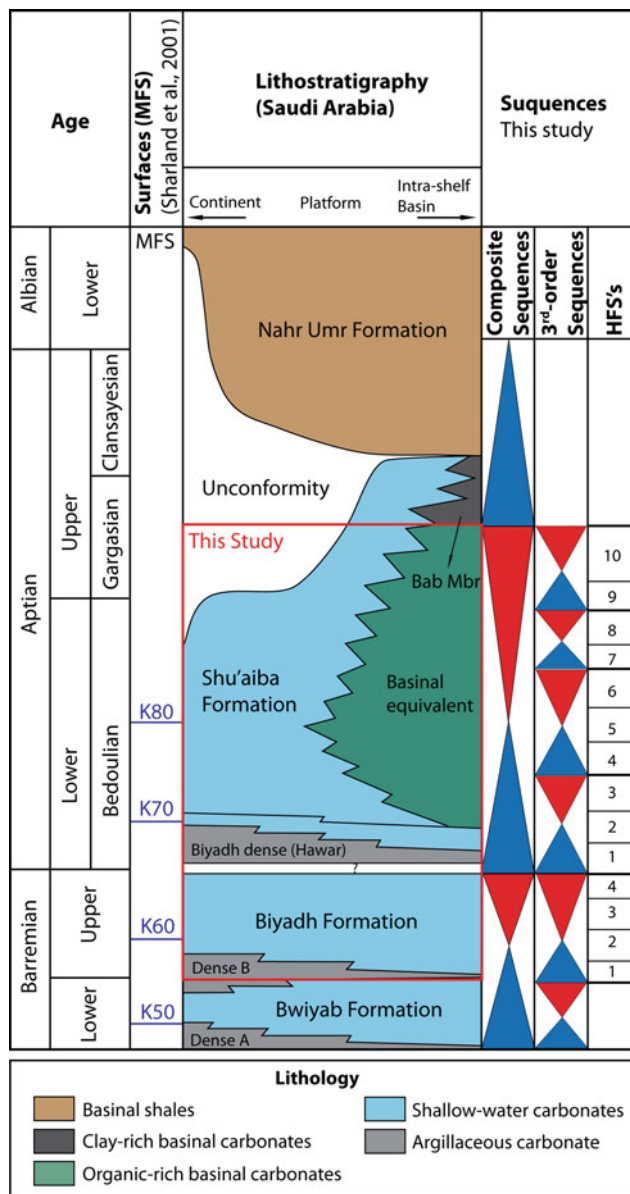
Fig. 1.2 Barremian to Aptian chronostratigraphy of the study area, showing the general sequence stratigraphy. Modified from van Buchem et al. (2010)

global correlation is the key to understand and evaluate the regional stratigraphic framework and hierarchy of the Early Cretaceous Arabian Plate presented in van Buchem et al. (2010). It also help refine our understanding of global climate during the Early Cretaceous Barremian and Aptian, because it was suggested that the Aptian may record a time of global cooling interval, within the prevailing Cretaceous greenhouse system, possibly associated with glaciation in the poles (Weissert and Lini (1991); Frakes et al. 1995; Frakes 1999; Stoll and Scharge (2000); Alley and Frakes 2003; AL-Ghamdi and Read 2010). The global correlation will help improve our understanding of the

Biyadh and Shu'aiba stratigraphic architecture, thus providing a better chronostratigraphic model for reservoir development and possible exploration potential in the area and around the world.

1.2 Geological Setting

The present Arabian Plate (Fig. 1.1) is bordered to the north by a convergent margin with the Eurasian Plate, forming the fold and thrust belt of the Taurus and Zagros Mountains. To the west and southwest, are the divergent rift zones in the Gulf of Aden and Red Sea. The northwestern margin is bounded by strike-slip faults in the Gulf of Aqaba and the Dead Sea region. The Arabian Shield, a block of Precambrian basement, in the western part of the Arabian Peninsula, periodically provided siliciclastic sediments to the Arabian shelf, that formed on the eastern Arabian Peninsula. The Arabian shelf thus consists of both siliciclastic and carbonates rocks and started as an intra-cratonic phase from Proterozoic to Middle Permian, followed by a passive margin phase in the Mesozoic. This culminated in the active margin phase in the Cenozoic that persists to the present-day (Harris et al. 1984; Christian 1997; Sharland et al. 2001).

The Early Cretaceous is marked by rifting of the Indian, Australian and Antarctic plates away from the African and Arabian plates. The Arabian Plate separated from Africa and moved toward the Neo-TethysOcean and developed passive margins on its north, northeast, and southeast margins. The eastern margin of the Arabian Plate faced the open Neo-TethysOcean, and lay several degrees south of the equator. Early Cretaceous intra-shelf basins were created by infra-Cambrian Hormuz salt movement (Sharland et al. 2001; Ziegler 2001). Rudist banks, such as those in the Shaybah region, were deposited on the margins of these intra-shelf basins during the Aptian. The intra-shelf basins were separated from the open Neo-TethysOcean by a narrow carbonate barrier system (Christian 1997; Sharland et al. 2001; Ziegler 2001; Greselle and Pittet 2005).

The Shu'aiba Formation described in this field study is located on a northeast-trending, doubly plunging anticline, and is divided by zone of EW-trending faults into northern and southern blocks (Fig. 1.3). The regional structure was mainly affected by northeast-trending faulting parallel to the Dibba Lineament, and sub-parallel to the trend of Shaybah field. The field is located on a basement uplift that appears to have influenced the growth of the build-up, implying syn-sedimentary tectonics (AL-Ghamdi and Read 2010). This syn-depositional faulting influenced the stratigraphic framework, the thickness and facies distribution of the Shu'aiba successions. The field was divided into two depositional blocks by an E-NE-trending growth fault zone; each block has its own distinctive facies architecture and

Fig. 1.3 Base map and facies distribution at S6 of Shu'aiba platform showing three cross-section traverses (A–A', B–B' and C–C') and 55 cored-wells used in this study
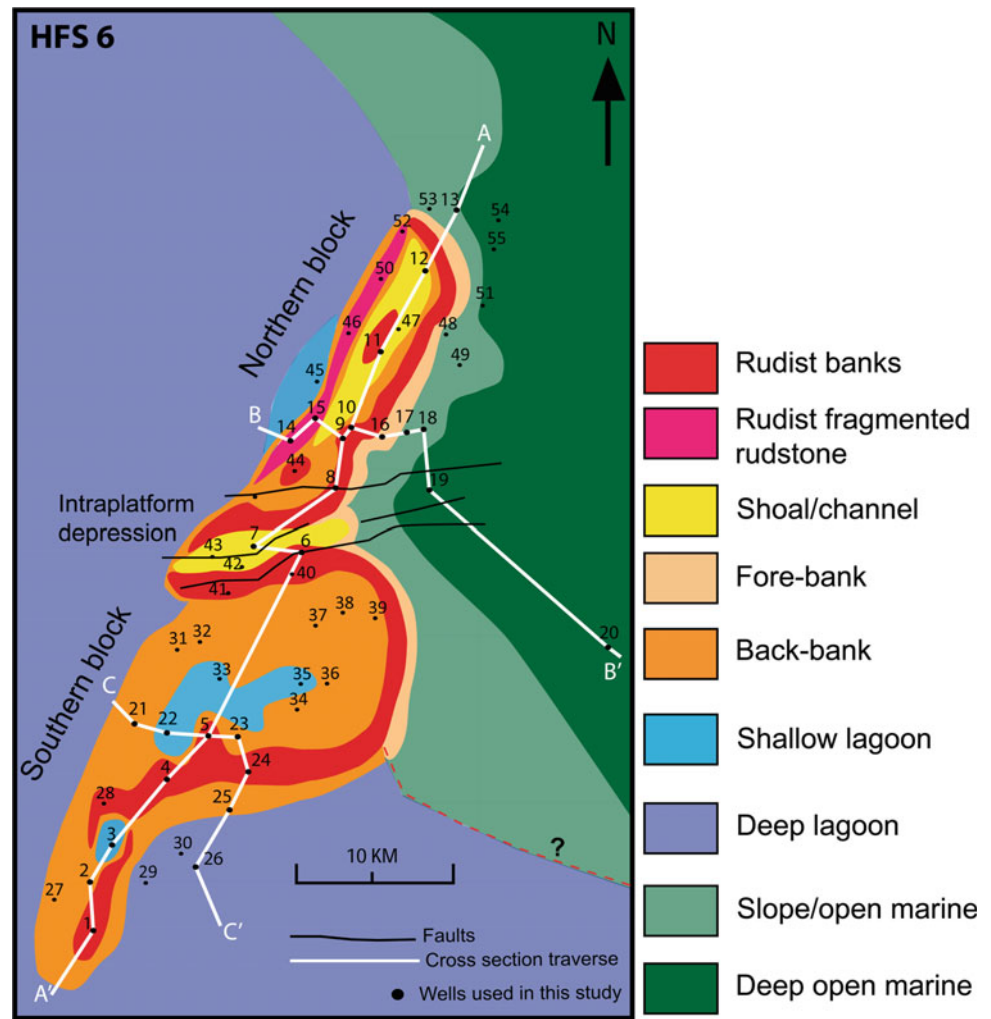
sequence-stratigraphic development. The present-day Shaybah structure was developed during the Cenomanian in response to intra-oceanic compressional tectonics in the Neo-Tethys region, and was truncated by pre-Aruma erosion (Middle Turonian unconformity) related to uplift of ophiolitic nappes in Oman (Aktas and Hughes 2000).

1.3 Methodology and Data Sets

Fifty five cored wells, averaging 450 ft (140 m) each, totaling 16,142 ft (4,920 m) of cores, penetrating the Shu'aiba Formation were logged bed-by-bed and examined using a binocular microscope. Three Wells (12, 11 and 9) penetrate deeper into the Barremian Biyadh Formation, providing the first opportunity to describe and evaluate this succession. Core descriptions included gross lithology (shale, limestone and dolomite), rock type, grain-size, shape and sorting, vertical succession of lithologies, location of bounding surfaces, types of biotic constituents and pore

system distribution. Microfacies analysis were examined using thin sections during the core logging to confirm the types of constituents (including foraminifera) and diagenetic modifications of grains and matrix. Stable carbon and oxygen isotope data from 26 wells also were collected and calibrated with core descriptions to constrain the age model of the Shu'aiba Formation especially in the slope and open marine settings where the Lower/Upper Aptian boundary occurred.

A generalized type core description of the entire study interval (Fig. 1.4) calibrated to its gamma ray log provides the basis for a 1-D interpretation of lithofacies and sequence stratigraphy. Sequence boundaries, maximum flooding surfaces and various scales of sequences and parasequences were picked on the logged sections (Fig. 1.4). Sequence boundaries were picked at significant erosional surfaces above successions of parasequences that progressively shallowed and or thinned up-section. Maximum flooding surfaces (MFS) or units (MFU) were placed at the base of the deepest water facies within a sequence and at the tops of
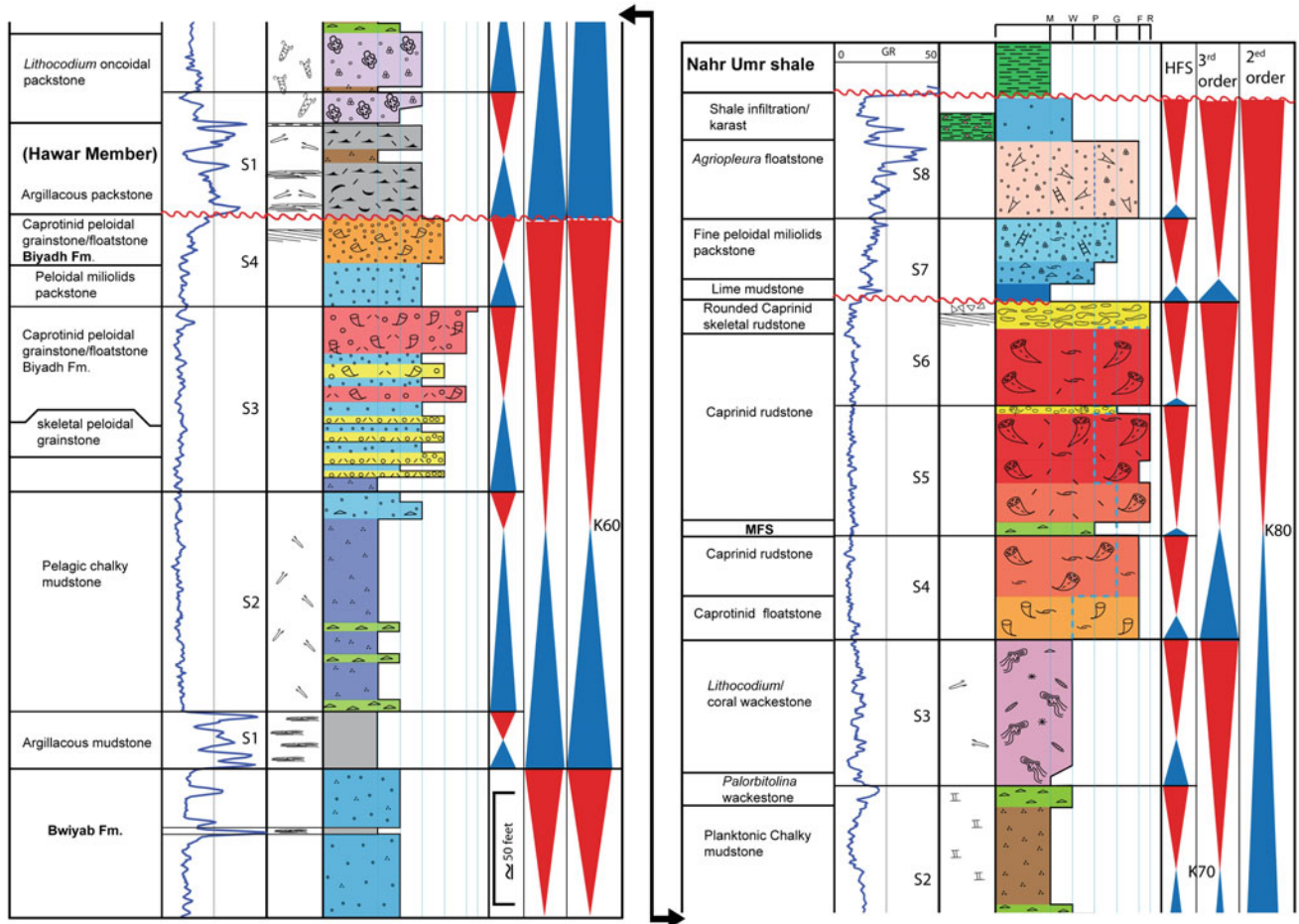
Fig. 1.4 Type composite core description showing general lithofacies description, sequence stratigraphy and gamma ray logs within the marginal setting

upward deepening trends of parasequence sets. Where possible, parasequence boundaries and maximum flooding surfaces were traced across the build-ups, to generate a depositional model. Facies cross-sections within this sequence-stratigraphic framework were made by interpolating between cored wells using Walther's law within the conceptual ramp depositional model.

In order to correlate the sequences, the base of the Shu'aiba Formation (the top of Hawar unit) was used as a datum for the cross-sections because it has distinctive high gamma-ray response in all wells associated with a thin stylolitic shale layer. The northern and southern blocks were correlated using the top Shu'aiba unconformity to bridge the medial fault zone. Seismic data were examined to constrain the sequence picks along the margin of the build-up where clinoform development was likely (e.g. Yose et al. 2010); however, it proved of limited value, due to the absence of a clear reflector at the top of the Shu'aiba Formation, and the occurrence of multiple artificial reflections within this unit.

1.4 Facies Description

The lithofacies of the Shu'aiba Formation were previously described and interpreted by AL-Ghamdi and Read (2010); using 14 cored wells. A detail biofacies and depositional environment study was conducted by Hughes (2000). This paper presents more updated lithofacies descriptions using cores and petrographic analysis from 55 cored-wells located across the entire field (Fig. 1.3). This extensive data set resulted in newly recognized facies (e.g. shoal facies complex and the upper Aptian facies; Figs. 1.5, 1.6, 1.7 and 1.8) and also helped refine the interpretation of depositional environments and produces more accurate facies maps and depositional cross-sections of the Biyadh and Shu'aiba Formations. The detail facies descriptions are summarized in Tables 1.1 and 1.2 and the facies are illustrated in Figs. 1.5, 1.6, 1.7 and 1.8. Figures 1.9, 1.10, 1.11, 1.12 and 1.13 illustrates the position of each lithofacies within a low angle ramp model. These depositional models especially, Fig. 1.12

Fig. 1.5 Core sample photographs of typical facies in Biyadh Formation. **a** Argillaceous black, dense mudstone, overlain by sharp contact and white carbonate of Biyadh Formation. **b** Clean chalky mudstone facies within the Lower part of Biyadh Formation, representing the maximum flooding unit (K60). **c** Sharp erosional contact at top of cycle within HFS 3 of Biyadh Formation, separating subtidal wackestone facies, from the peloidal grainstone facies. **d** Oncoidal coral skeletal grainstone facies in HFS 3 of Biyadh Formation. **e** *Glassomyophorus* rudist floatstone facies from HFS 4 of Biyadh Formation, overlain by sharp contact (cycle top) and skeletal peloidal grainstone facies. **f** *Glassomyophorus* rudist floatstone facies, capped by a scalloped surface and major sequence boundary (SB1) at the top of the Biyadh Formation, overlain by dark-gray argillaceous *Palorbitolina* packstone of Hawar unit. Arrows indicate karst fill from Hawar unit infiltrated into the rudist facies of Biyadh Formation
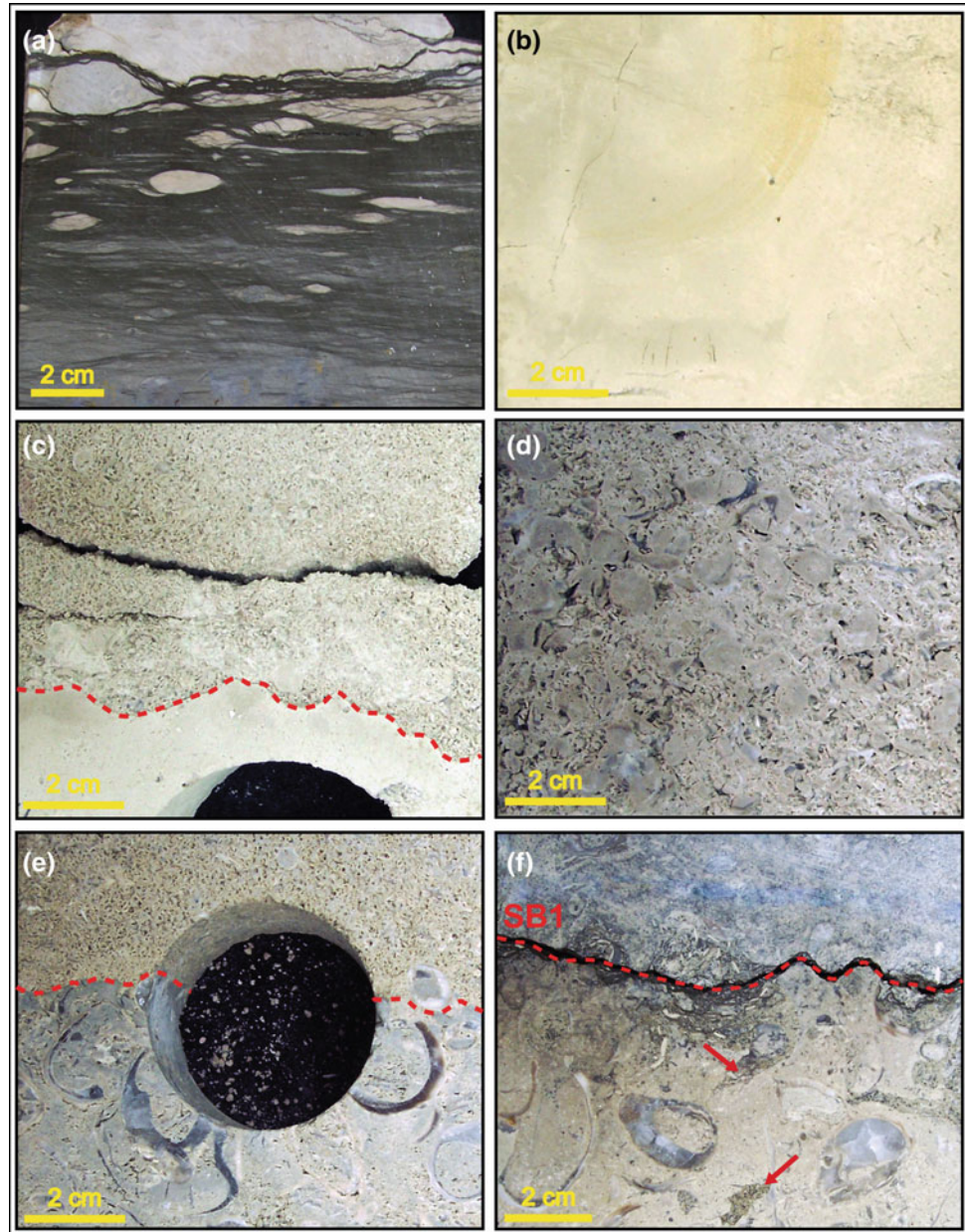
show lateral facies transition from inner ramp/lagoon, back-bank, bank-crest, fore-bank, slope to basin settings in the Far East. Seventeen significant lithofacies were determined in this study on the basis of fossil assemblages, rock type, texture and sediment constituents. These lithofacies were grouped into four major facies associations (lagoonal facies, shelf marginal facies, Open marine/slope facies and basinal facies) that are linked to major depositional environments (Tables 1.1 and 1.2). However, smaller-scale lithofacies also were recognized and interpreted, such as platy coral versus branching coral or rudist in situ floatstone versus rudist in situ rudstone facies. These facies with subtle differences in their characteristics or their environments were lumped with other similar facies to simplify the stratigraphic cross sections and to make facies distribution less complicated in the 3-D reservoir modeling. In addition, these 17 lithofacies also were sub-divided on the basis of their significant petrophysical properties and hence their impact on reservoir performance. The following is a brief summary of these four major facies associations:

1. Inner ramp/lagoonal facies association (Table 1.1). This facies association occurs mainly in the upper part of Biyadh Formation and in the upper part of the Shu'aiba Formation. These facies were deposited in moderate-to-low energy inner ramp/lagoonal setting with a
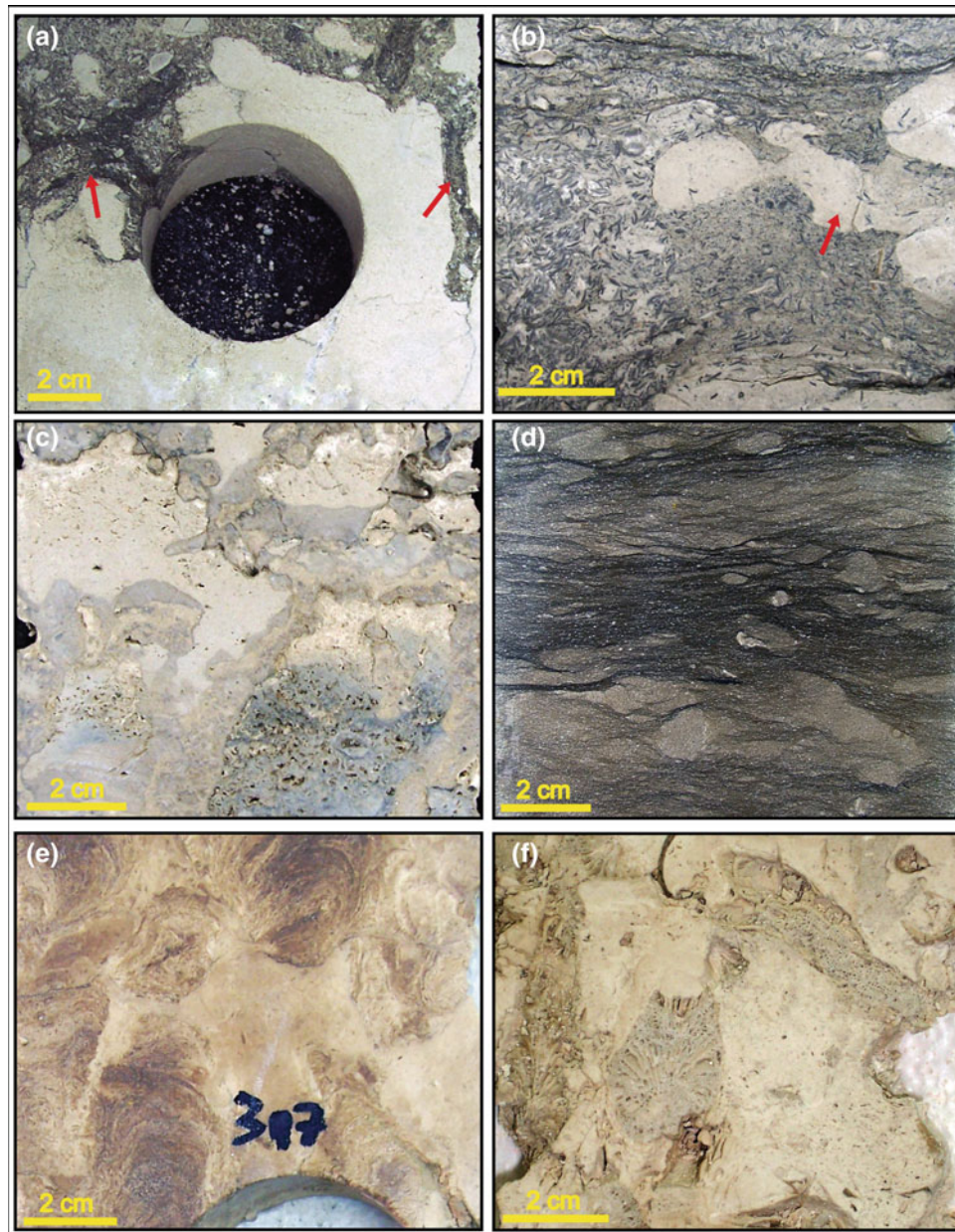
Fig. 1.6 Core sample photographs of typical deep subtidal and *Lithocodium* facies in Shu'aiba Formation. **a** Karst fill (arrows) from Hawar unit infiltrated into the rudist facies of Biyadh Formation at SB1. **b** Dark gray *Palorbitolina* packstone of Hawar "dense" unit. Burrowing and bioturbation occurred on the right hand side (arrow). **c** Bioturbated on coidal *Lithocodium* miliolid packstone facies at basal Shu'aiba Formation (shallow subtidal, upper ramp environment). **d** Black, wispy-laminated mudstone/wackestone facies (deep lagoon/deep restricted environments). **e** *Lithocodium* aggregatum wackestone/boundstone facies, columnar-laminated morphology (open-marine algal platform). **f** Platy coral floatstone includes extensive leaching (open-marine algal platform)
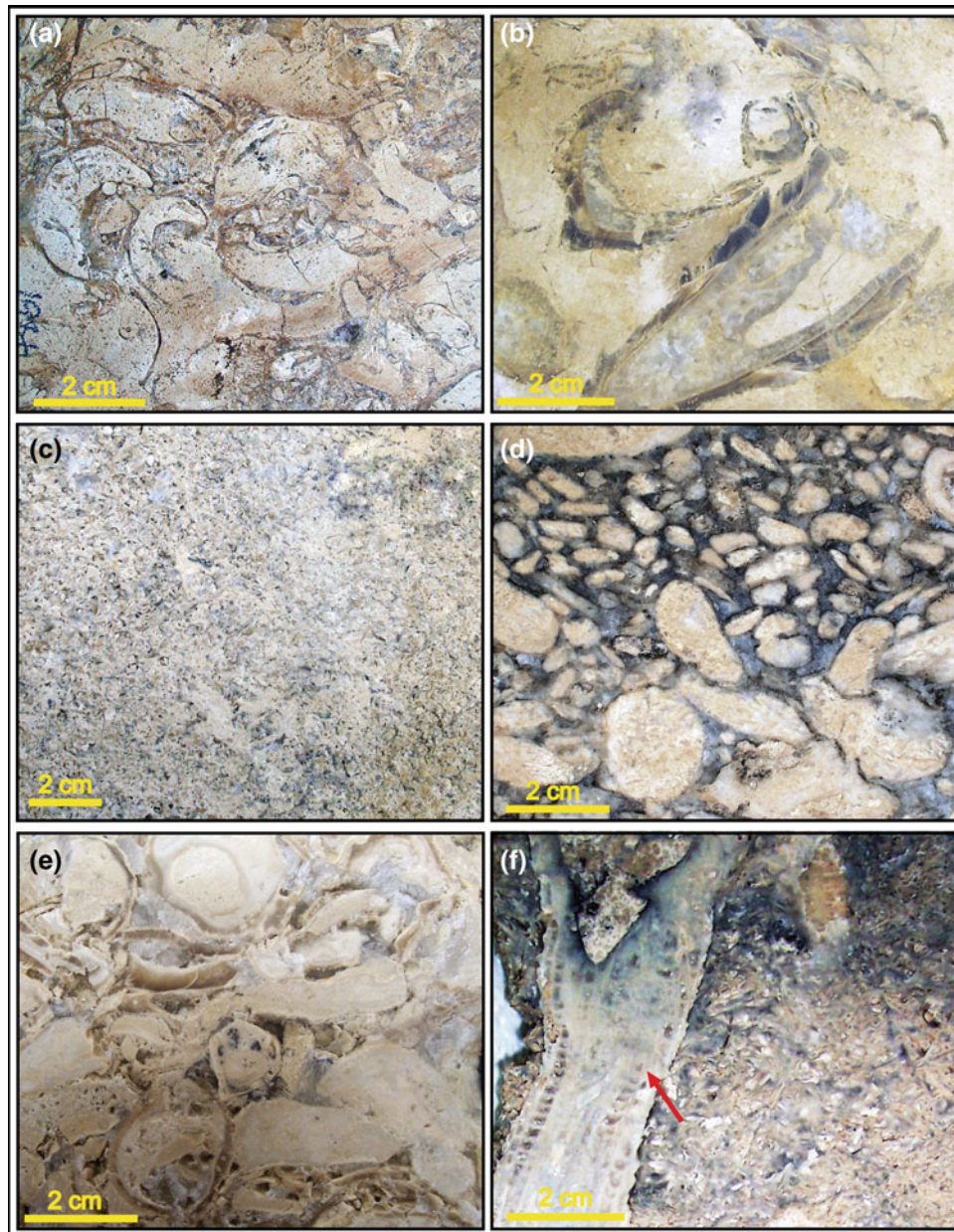
Fig. 1.7 Core sample photographs of typical rudist facies in Shu'aiba Formation. **a** Caprotinid *Glassomyophorus* floatstone (back-bank). **b** *Agriopleura* floatstone (shallow lagoon/inner ramp). **c** Skeletal debris grainstone (shoal/channel). **d** Well rounded, cemented *Offneria* rudstone (high-energy beach/shoal). **e** Caprinidrudist debris *Offneria* rudstone (high-energy bank-crest/shoal). **f** In-situ (life position) caprinid *Offneria* floatstone (bank-crest). Arrow points out to live-position *Offneria*rudist

maximum of 10–15 m water depth in a moderate to low energy (Hughes 2000; AL-Ghamdi and Read 2010). These lithofacies include: peloidal milliolid packstone/wackestone, *Agriopleura* floatstone and deep lagoonal mudstone/wackestone facies. However, the deeper lagoonal facies were deposited in restricted deeper water environments, or in restricted ponds within the platform interior.

2. Shelf marginal rudist buildup facies association (Table 1.1). This facies association formed mainly within the middle part of the Shu'aiba Formation forming thick and massive rudist buildups. It also formed in the uppermost part of the Biyadh Formation. Lithofacies includes; in situ and rudist facies (mainly *Offneria* type) within bank-crest, reworked rudist debris rudstone/grainstone, Caprotinid rudist floatstone
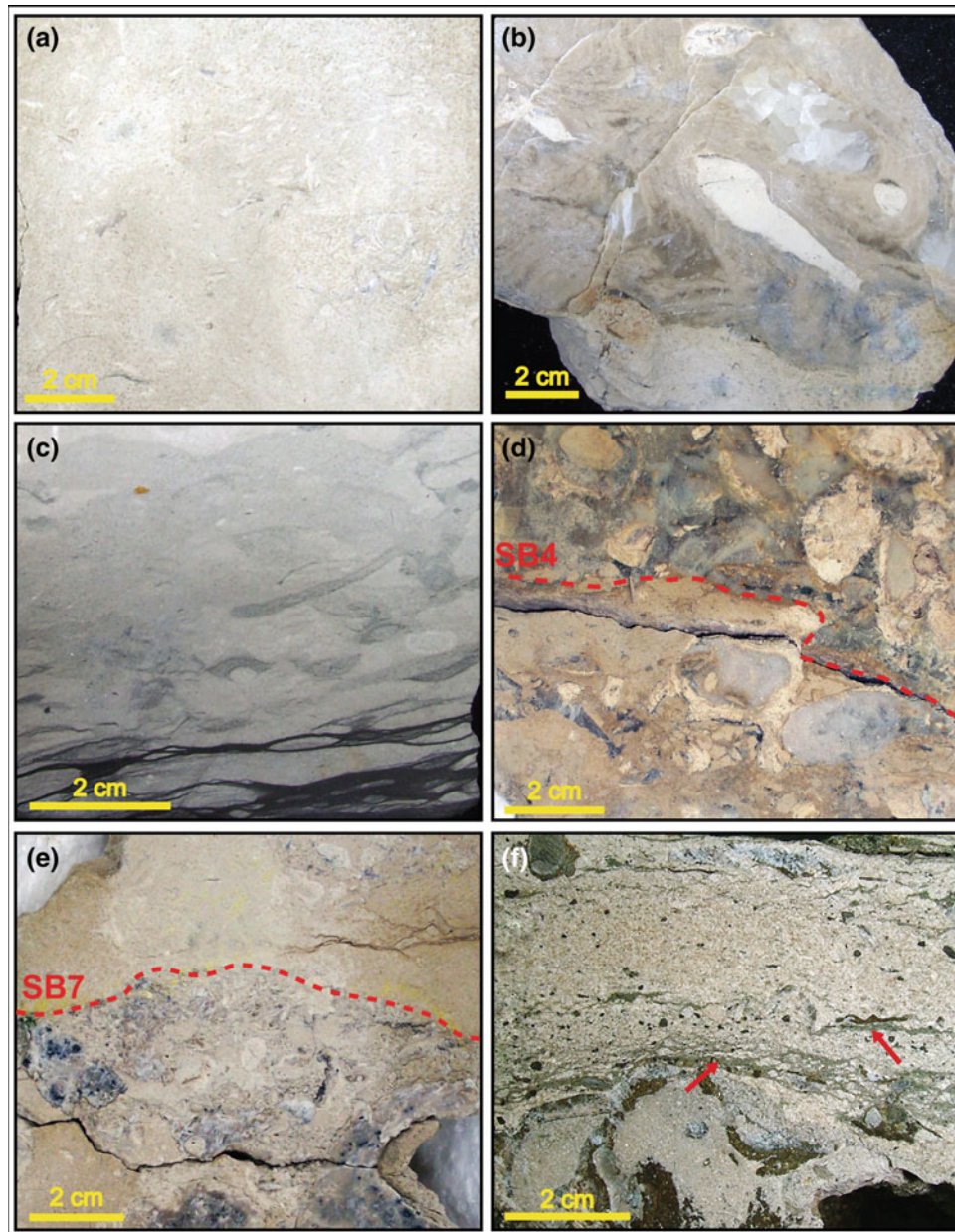
Fig. 1.8 Core sample photographs of typical deep ramp facies and sequence boundaries in Shu'aiba Formation. **a** *Palorbitolina* wackestone (deep open-marine). **b** Massive stromatoporoid boundstone, (Upper Aptian marginal setting). **c** Dark wispy-stylolite argillaceous mudstone (Upper Aptian Boundary). **d** Sequence boundary 3 (SB3), separating *Lithocodium* facies below from the overlying rudist facies. **e** Sequence boundary 7 (SB7) at top of the rudist buildups, marking the termination of the Lower Aptian Caprinid rudist associated with subaerial exposure surface. **f** NahrUmr green shale (arrows) infiltrated into the upper part of Shu'aiba during karstfication associated with the major late Aptian unconformity

(back-bank) and skeletal grainstone/packstone of fore-bank/shallow slope.

3. Open marine algal platform facies association (Table 1.2). This facies association includes the algal platform of *Lithocodium*/coral facies, oncoidal *Lithocodium* packstone facies, argillaceous packstone of Hawar unit and the *Palorbitolina* wackestone. These units are generally characterized by mud-dominated matrix and high diversity of associated biota, including foraminifera. These facies were deposited in a relatively deep open marine setting within the lower part of the Shu'aiba Formation. The exception of these lithofacies is the

Table 1.1 Summary of Lithofacies in shelf margin settings

Facies association	Facies	Colour code	Description	Sed. structure	Matrix (in rudstone/floatstone)	Fossils	Energy	Pore type	Depth (estimated)	Environments
Inner ramp/lagoon	Very fine skeletal peloidal packstone/grainstone	[blue]	Very fine-fine-medium grained, moderately-well sorted rounded, abundant skeletal grains, common peloids, rare pelletal grains, intergranular cement	Low angle cross beds		Abundant miliolids, textularids, *Vercorsella areneta*, *Debarina hahounerensis*, high-trochoid *Palorbitolina* common dasyclad alga (*Salpingoporella*), rare *Lithocodium*, common (*Agriopleura*)	Low/moderate	Common MO and micro porosity	5–10 m	Shallow lagoon
	Agriopleura packstone/floatston	[pink]	Pebble-gravel size rudists, elongate V-shape and U-shape		Very fine-fine skeletal peloidal packstone/grainstone	Abundant—common *Agriopleura*, common iliolids, low-trochoid *Palorbitolina*	Low/moderate	Common MO and micro porosity	5–15 m	Shallow-moderately deep lagoon
	Lime mudstone/wackestone	[purple]	Silty to very fine grains, abundant mud,argillaceous, chert	Abundant bioturbation large burrows, microstylolites, nodular bedding		Abundant miliolids and benthonic forams (*Textularia, Vercorsella, Debarina*) common *Palorbitolina*, common to rare *Lithocodium*, locally planktic forams	Very low	Micro porosity rare MO	25–35 m	Deep lagoon
Shelf margin	Well rounded rudist debris rudstone/grainstone	[yellow]	Granule—pebble to coarse sand, well rounded, well sorted, mud-free, may occur as well cemented below sequence boundary or very porous shoal debris/channel	Cross beds	Grainstone	Abundant caprinid rudist debris of (*Offheria murgensis*)	Very high	Abundant VG and MO	<5 m	Beach/shoal or channel
	Rudist-fragmente packstone/grainstone	[yellow]	Fine-coarse skeletal grains, angular-moderately rounded, moderately sorted, fine-coarse equent calcite cements	Cross beds		Mainly caprinid skeletal depris of *Offheria*, rare caprotinid depris, common coral and echinodenns, common benthonic foraminifera	Moderately high	Common VG, MO, less common micro porosity	5–15 m	Shallow- fore-bank
	In situ caprinid rudstone/floatstone	[red]	Pebble-gravel size rudists, angular—moderately rounded, poorly sorted, *in situ* rudist (unbroken)		Packstone-wackestone, mudstone (locally)	Large *in situ* caprinid rudist (*offneria*)	High/locally moderately low	Abundant VG and MO Common micro porosity	5–10 m	Bank-crest (in situ)
	Caprinid skeletal-fragment floatstone/rudstone	[orange]	Pebble-very coarse grains, poorly-moderately sorted, rudist and bivalve skeletal debris		Grainstone/packstone, mudstone (locally)	Abundant caprinid rudist (*Offheria*) less common caprotinid (*Glassomyophorus*) Abundant caprotinid rudist	High	Abundant VG and MO	5–10 m	Bank-crest/proximal bank- edge/shoal

(continued)

Table 1.1 (continued)

Facies association	Facies	Colour code	Description	Sed. structure	Matrix (in rudstone/floatstone)	Fossils	Energy	Pore type	Depth (estimated)	Environments
	Caprotinid floatstone		Coarse-sand to pebble-size grains, poorly sorted		Wackestone/mud-rich packstone	(*Glossomyophorus costatus*), common *Palorbitolina*, less common (*Agriopleura*) less common *Lithocodium*	Low/moderate	Common MO and micro-porosity, rare VG	5–30 m	back bank, relatively deep, transgressive rudist
	Fine-medium skeletal packstone		Medium sand size, moderately-well rounded, well sorted, common peloids, common fine-medium intergranular equant calcite cements			Skeletal debris of mainly *Ofheria*, bivalve, oyster, common foraminifera include; *Textularia and Palorbitolina*	Moderate	Abundant MO	20–30 m	Deep fore-bank/shallow slope

Palorbitolina argillaceous packstone of the Hawar unit that was deposited in a more restricted shallow marine subtidal environment (van Buchem et al. 2002, 2010).

4. Deep open marine basinal facies association (Table 1.2). This facies association is the deepest water facies within the Shu'aiba and Biyadh formations. Lithofacies include chalky pelagic mudstone within the deep open-marine settings occurred far east toward the basin, planktonic *Hedbergella* mudstone within the lower part of the Shu'aiba Formation representing a major flooding unit (K70) and the argillaceous intrashelf basin that formed far to the east within the Bab basin.

1.5 Sequence Stratigraphy

1.5.1 Introduction

The sequence stratigraphic framework presented here builds on the rock-based stratigraphic framework of AL-Ghamdi and Read (2010), using more core data, stable isotope chemostratigraphy and available biostratigraphic data. This study also presents the first stratigraphic framework for the Biyadh Formation in Saudi Arabia with new core data (Figs. 1.4 and 1.15). The stratigraphic frameworks of the Biyadh and Shu'aiba formations in this study are compared with the regional Lower Cretaceous 2nd- and 3rd-order sequence stratigraphic model of van Buchem et al. (2010). However, some differences occurred between the frameworks presented here and van Buchem et al. (2010), such as the location of the major MFS of Shu'aiba sequence and the hierarchy of the Shu'aiba Formation. This study presents a more detailed high-resolution stratigraphic framework on the order of 400 ky (HFS's) and higher-scale parasequences that control the reservoir facies anatomy and hence, reservoir quality. The type core description with associated gamma ray logs, interpreted sequences are shown in Fig. 1.4, summarizing the sequence stratigraphic framework of the Biyadh and Shu'aiba Formations. Integrated carbon isotope data, gamma ray and sequence stratigraphy were integrated to better define the age model of the Shu'aiba Formation, particulary defining the Lower/Upper Aptian boundaries on the platform edges (Fig. 1.14). Four detailed stratigraphic cross sections (Figs. 1.15, 1.16, 1.17 and 1.18) were constructed; one in Biyadh Formation (Fig. 1.15), two west-east dip trending sections in Shu'aiba Formation (Figs. 1.16 and 1.17) and one north-south strike trending section in Shu'aiba Formation (Fig. 1.18).

The stratigraphic successions of Biyadh and Shu'aiba Formations are part of one large scale second order super sequence with a duration of about 17 My. This super

Table 1.2 Summary of Lithofacies in open marine and basinal settings

Facies association	Facies	Colour code	Description	Sed. structure	Matrix (in rudstone/floatstone)	Fossils	Energy	Pore type	Depth (estimated)	Environments
Open marine and slope	Coral packstone/floatstone		Pebble-coarse grains, elongate-rounded shape,moderately sorted		Mudsotne/wackestone	Abundant branching or platy coral, some massive coral heads,debris of echinoderm, bivalve, common *Lithocodium*, rare *Palorbitolina*	Low/moderate	Abundant MO and VG, common micoporosity	10–30 m	Open marine/lagoon
	Lithocodium oncoid miliolid packstone		Fine-medium sand size, poorly sorted, peloids, pebble size *Lithocodium* lumps, oncoid, lime mud	Highly bioturbated, large irregular burrows		*Abundant miliolids, Textularia,* common *Lithocodium* lumps, (NO *Palorbitolina*)	Moderatly high energy	Common MO and micoporosity	10–15 m	Shallow carbonate platform
	Lithocodium aggregatum wackestone/bindstone		Encrusting *Lithocodium,* fine- medium sand-size, poorly sorted	Abundant-common burrows, wispy mcrostylolites	Chalky mudstone/wackestone	Abundant *Lithocodium aggregatum,* common, coral, echinoderm debris, skeletal fragments of bivalve, abundant/common (*Textularia, Vercorsella arenata,Debarina hahounerensis*), *Palorbitolina,* miliolids. Rare planktic forams	Moderate-low	Abundant micro porosity	20–35 m	Open marine algal platform/lagoon
	Palorbitolina wackestone		Chalky-fine grians, common, moderately friable	common burrow and microstylolites		Abundant low-trochoid *Palorbitolina* abundant/common; (*Textularia, Vercorsella, Debarina*) common miliolids, rare/common planktic forams,common *Lithocodium* common echinoderm debris, common *Gastropodes*	Low	Abundant micro porosity	<25–30 m	Open marine
	Dark argillaceous *Palorbitolina* packstone		Dark gray, granule size *Palorbitolina,* Fine-medium sand size, dense, poorly sorted peloids, common glauconite and pyrite, highly argillaceous and organic matters, reddish oxidized materials	Abundant burrows and bioturbations, hard grounds, normal-graded scour fills,wispy micostylolites		Abundant low-trochoid *Palorbitolina,* high diversity of benthonic foraminifera, common textularids, common echinoderm and bivalve debris	Low	Dense, rare micro porosity	10–25 m	Condensed section, relatively shallow marine

Table 1.2 (continued)

Facies association	Facies	Colour code	Description	Sed. structure	Matrix (in rudstone/floatstone)	Fossils	Energy	Pore type	Depth (estimated)	Environments
Deep margin/basin	Chalky pelagic wackestone/mudstone	[green]	Fine-medium sand size, moderately-well rounded, well sorted, common peloids, common fine-medium intergranular equant calcite cements	Common burrows		Skeletal debris of rudist, bivalve, oyster, common foraminifera include; *Textularia and Palorbitolina*	Low	Microporosity, MO	25–30 m	Deep slope, open marine
	Planktonic lime mudstone	[brown]	White-light gray, clay size, chalky, very friable, structureless, semi-pelagic	Common burrows		Abundant planktic foraminifera (*Hedbergella*), abundant/common *Palorbitolina*, textularids, *Rotalids, Lenticulina*	Very low	Abundant micro porosity	40–50 m	Deep open marine, deepest water facies
	Shaly lime mudstone/shale (intrashelf basin)	[dark]	Black-dark gray, mudy-silty grains, highly argillaceous, highly organic, common siliciclastic (quartz)				Very low		50–70 m	very deep open marine intrashelf basin

sequence is bounded at the base by the Late Valanginian unconformity and is capped by the Late Aptian unconformity (Sharland et al. 2001). The Biyadh Formation occurs within the TST, while the Shu'aiba Formation occurs within the HST of the super sequence.

1.5.2 Biyadh and Shu'aiba Sequence Stratigraphy

The following are brief descriptions of each sequence within the Biyadh and the Shu'aiba Formations, focusing on the high-frequency sequences (HFS type sequence). The term "sequence, or S" refers here to the high-frequency sequences that range in duration from 400 ky to 1 My at maximum, whereas the longer-term 3rd-order sequences and smaller-scale parasequences will be specified when mentioned.

1.6 Late Barremian Sequence

The Late Barremian Biyadh Formation is penetrated in three wells beneath the Shu'aiba Formation (Wells 11, 12 and 9). It is equivalent to the Arabian Plate Barremian 2 sequence of the Barremian supersequence of van Buchem et al. (2010). The Late Barremian succession is composed of one 3rd-order composite sequence and four high-frequency sequences (Fig. 1.15). S1 starts with a TST of black argillaceous dense mudstone (Fig. 1.5a) at the base of Biyadh Formation characterized by its high gamma ray values representing the initial TST of the composite sequence. This dense unit is similar in sedimentology and log characteristics to the Hawar unit at the base of the Shu'aiba Formation, but it does not contain abundant *Palorbitolina*. Due to the limited core materials in this interval, it is not clear if this argillaceous unit is dominated by *Palorbitolina* deposited in a shallow restricted environment similar to the Hawar unit or if this is deeper basinal facies without *Palorbitolina*. Abundant *Palorbitolina* occur in equivalent units in the region (van Buchem et al. 2010).

S2 contains a thick bioturbated marly lime mudstone facies representing the late TST with the maximum flooding interval of the 3rd-order composite sequence. This is a deep shelf or open marine facies of uniform thickness that is interbedded with thin *Palorbitolina* wackestone units. The MFS of S2 occurs in the middle part of the sequence containing abundant deep chalky mudstone (Fig. 1.5b). This MFS also is the major MFS for the late Barremian composite sequence, corresponding to MFS K60 of Sharland et al. (2001). This high frequency sequence is capped by shallow skeletal packstone facies with common gastropods and *Textularid* foraminifera.

Late Barremian Biyadh Formation, low angle homoclinal ramp
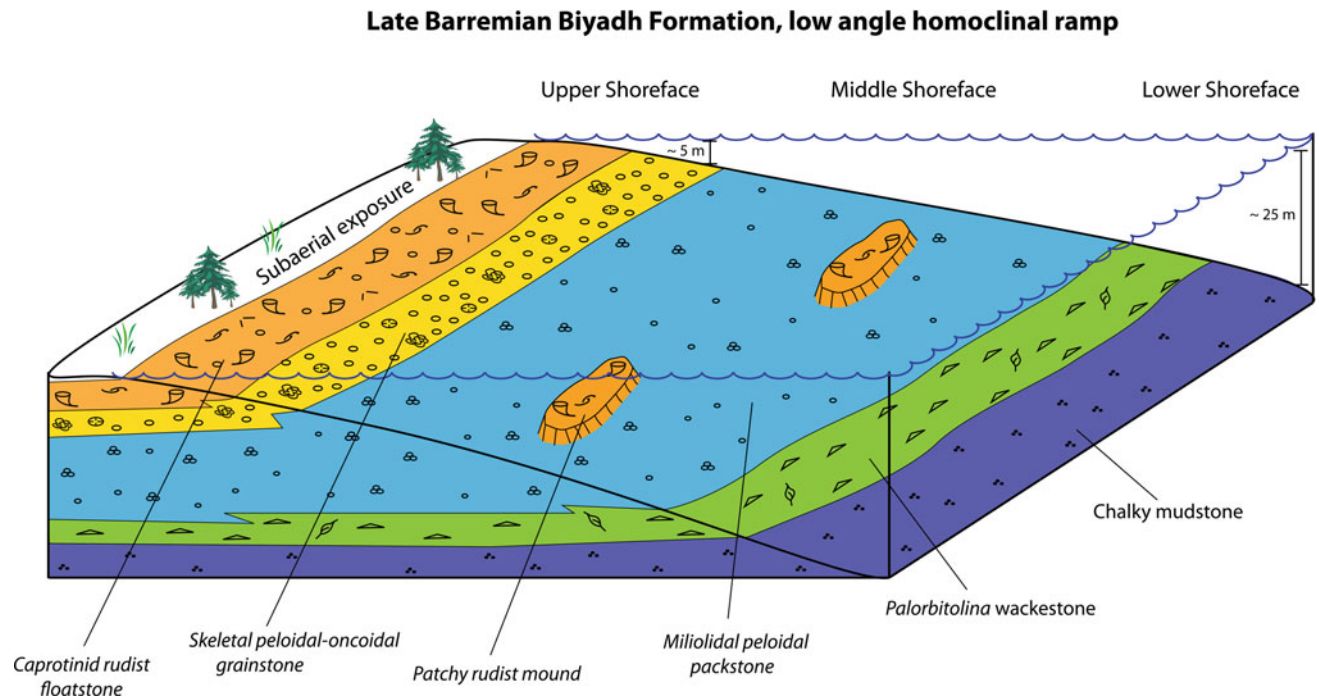
Fig. 1.9 Depositional model of Late Barremian Biyadh Formation shows the position of each facies on a low angle homoclinal ramp platform

Fig. 1.10 Depositional model for the Hawar unit showing restricted shallow subtidal/tidal flat environment (condensed unit)

Early Aptian Hawar unit, restricted shallow subtidal
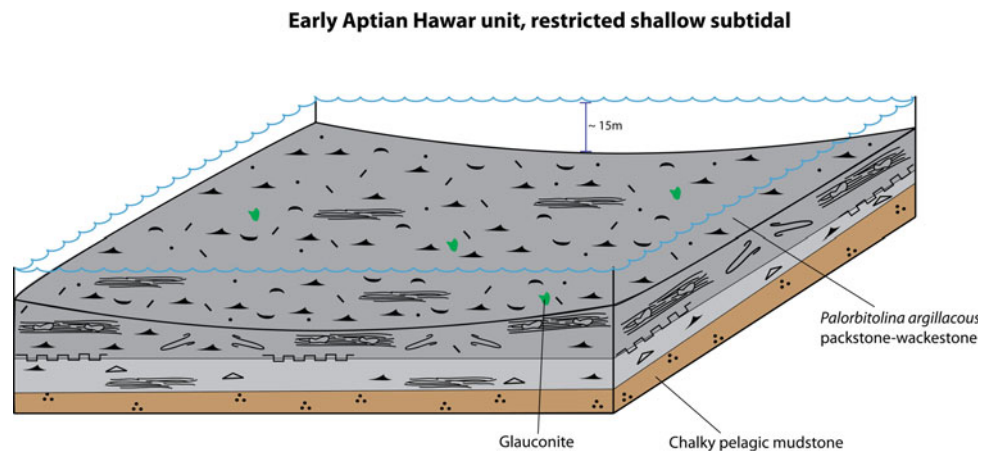
Sequences 3 and 4 record changes in facies and depositional environment from deeper open marine pelagic mudstone to shallow subtidal rudist caprotinid facies. These sequences start with initial flooding unit ~10 ft (3 m) of lower shoreface mudstone that gradually shallows upward to peloidal/oncoidal grainstone/packstone facies associated with branching corals. These sequences are capped by thick upper shoreface rudist barrier facies composed mainly of caprotinid *Glassomyophorus* rudist floatstone. In addition, these S3 and S4 are characterized by meter- to decimeter scale parasequences, possibly fifth-order cycles or higher (Fig. 1.15). These small-scale parasequences have sharp, erosional, irregular surfaces at their base with clean coarse grainstone facies composed of *Palorbitolina*, peloids, oncoidal and skeletal fragments deposited during flooding events (Fig. 1.5c, d). These grainstone facies deepen upward to fine skeletal packstone/wackestone facies and are capped by another sharp and irregular contact overlain by the next parasequence. The correlation between different wells suggests that these parasequences can extend for long distances (up to ~5 km), and can be mapped on their log characteristics (Fig. 1.15). These small-scale parasequences are unique in the Barremian Biyadh Formation and do not occur in the Shu'aiba Formation.

Early Aptian *Lithocodium* algal platform
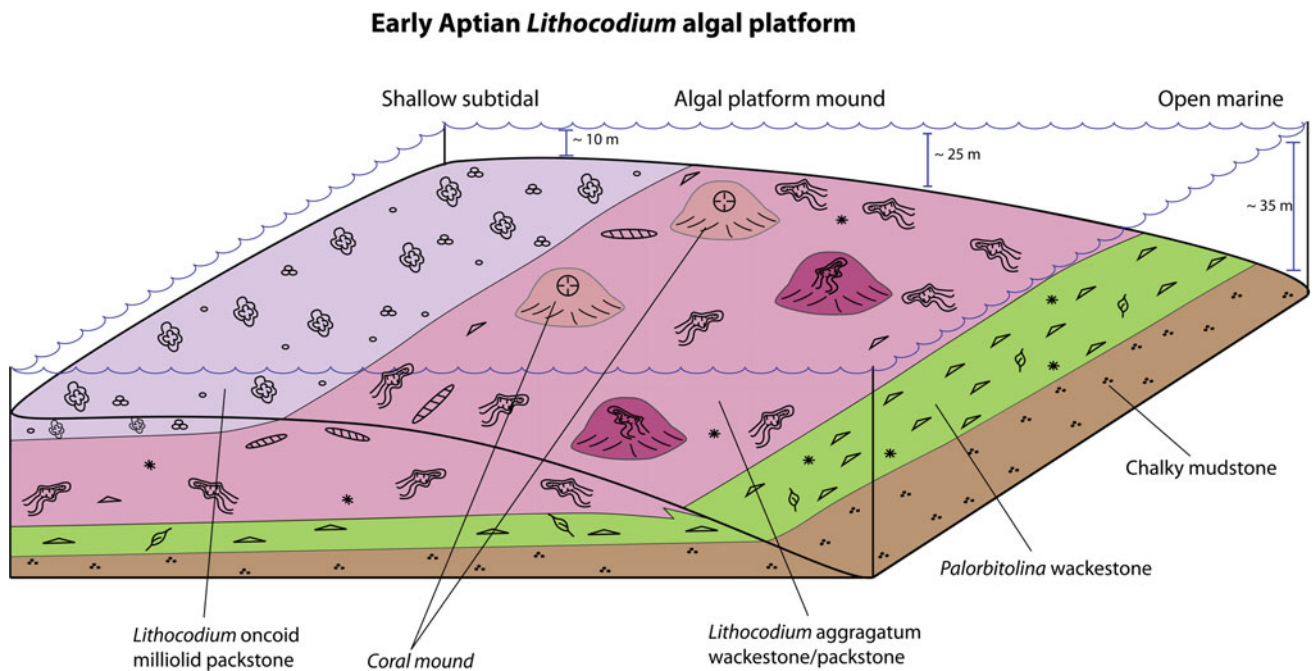
Fig. 1.11 Depositional model for the *Lithocodium* algal platform of Lower Shu'aiba Formation, HFS's 2 and 3

Early Aptian rudist builup marginal platform, S4-S6 (Shu'aiba Formation)
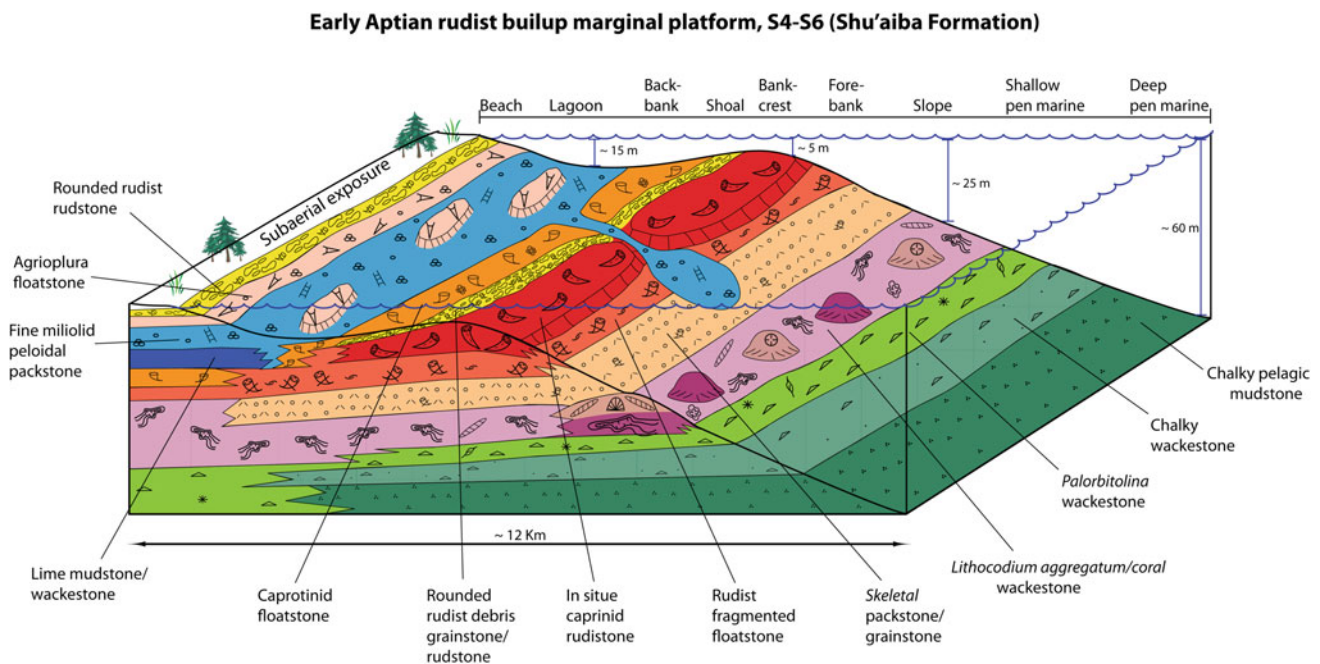
Fig. 1.12 Depositional model for HFS's 4–6 within the rudist buildups, showing the position of each facies in a barrier-bank low angle ramp

The upper part of Late Barremian sequence is dominated by the *Glassomyophorus* and *Agriopleura* floatstone associated with clean peloidal miliolid grainstone matrix (Fig. 1.5e). These rudists do not form colonial rudstone buildups as in the Shu'aiba Formation; they form a uniform barrier bank facies possibly developed in the shallow upper shoreface or beach environment (Fig. 1.9) that can be traced field wide. No Caprinid *Offneria* rudist occurred in the Barremian Biyadh Formation.

Late Aptian shelf edge prograding platform (S9-S10)
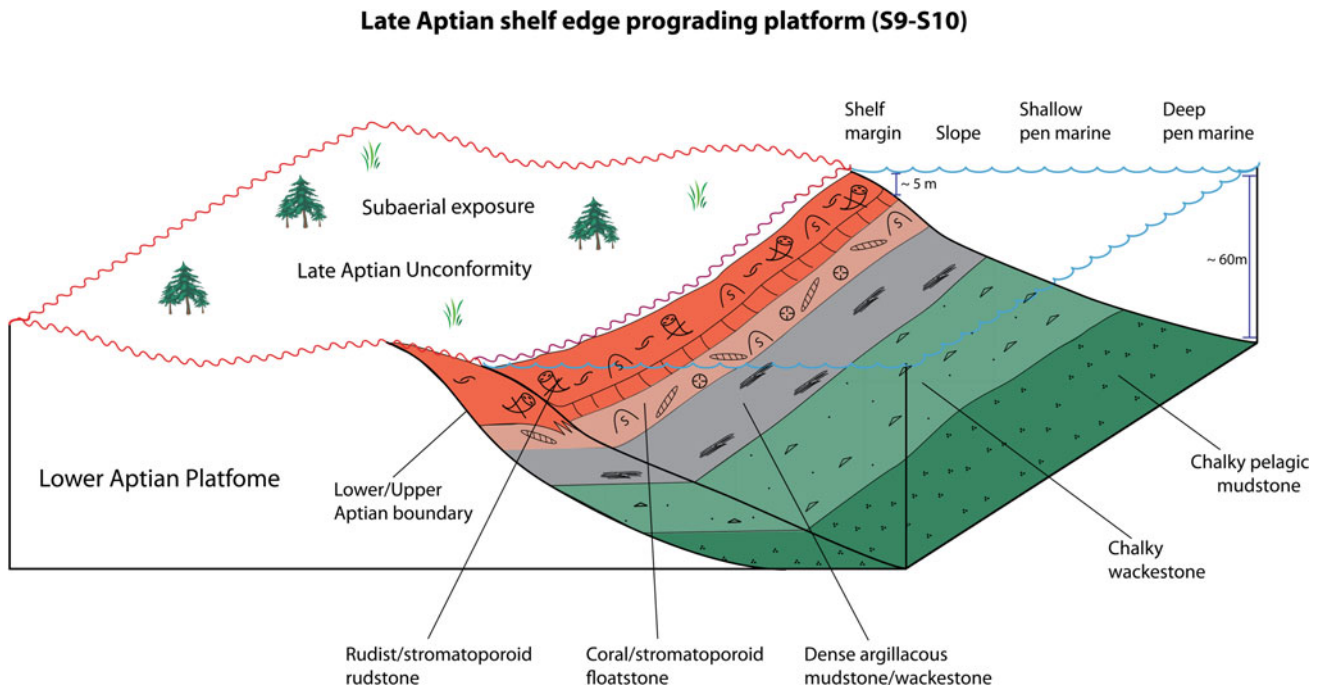
Fig. 1.13 Depositional model for the Upper Aptian HFS's 9 and 10 showing the shelf marginal edge within the prograding sequences. The pre-existing Early Aptian platform was subaerially exposed during this time
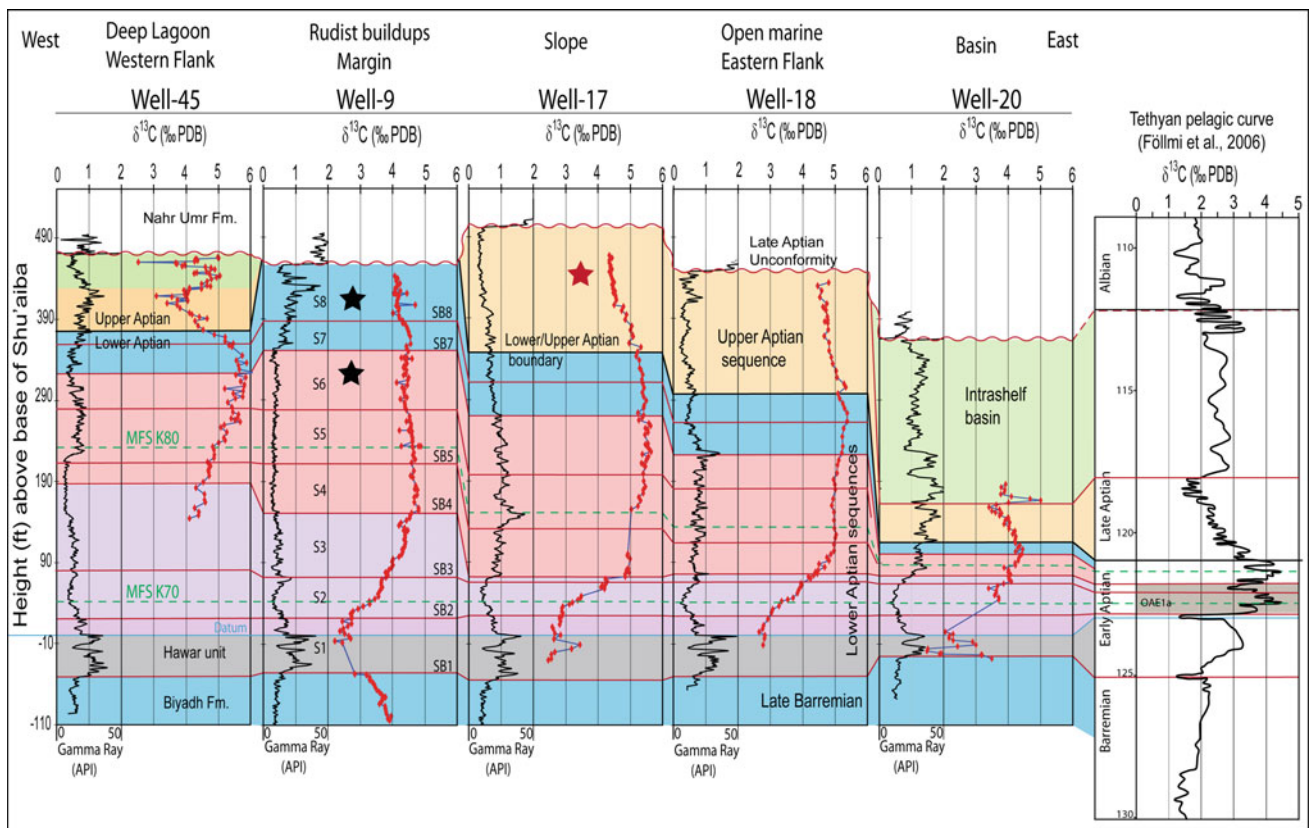
Fig. 1.14 West-East type chronostratigraphic cross section of the Shu'aiba Formation correlating gamma ray logs and $\delta^{13}C$ isotope curves. The carbon isotopes are correlated with the Tethyan pelagic curve of Föllmi et al. (2006). Major sequence boundaries are shown in red. The purple shaded zone is the *Lithocodium* algal platform facies that corresponds to major global positive excursion in the early Aptian that is related to Oceanic Anoxic Event 1a. Upper Aptian prograding sequences are shown in orange and green. Red star indicates late Aptian rudist *Horiopleura* of the Polyconitidae family, while black stars indicate early Aptian rudist Caprinid *Offneria* below SB6 and Caprotinid *Agriopleura* above SB6
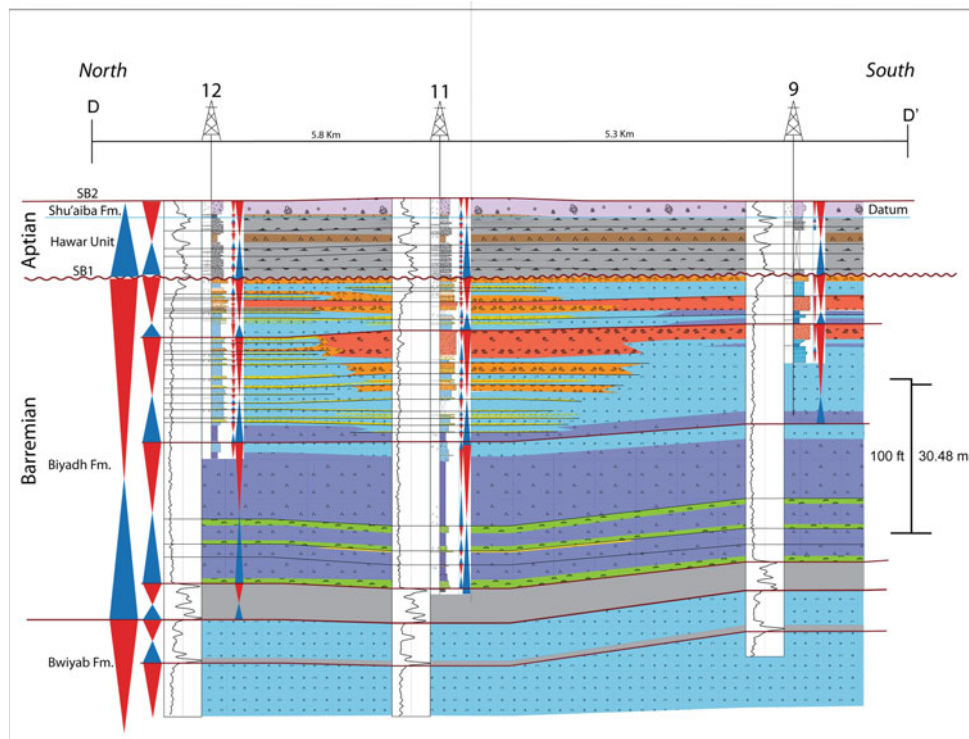
Fig. 1.15 Detail N-S stratigraphic cross section (D–D′) of Biyadh Formation and Hawar Member on the Northern block. This cross section illustrates the layer-cake stratigraphy of these units along with high scale parasequences. See Fig. 1.3 for location
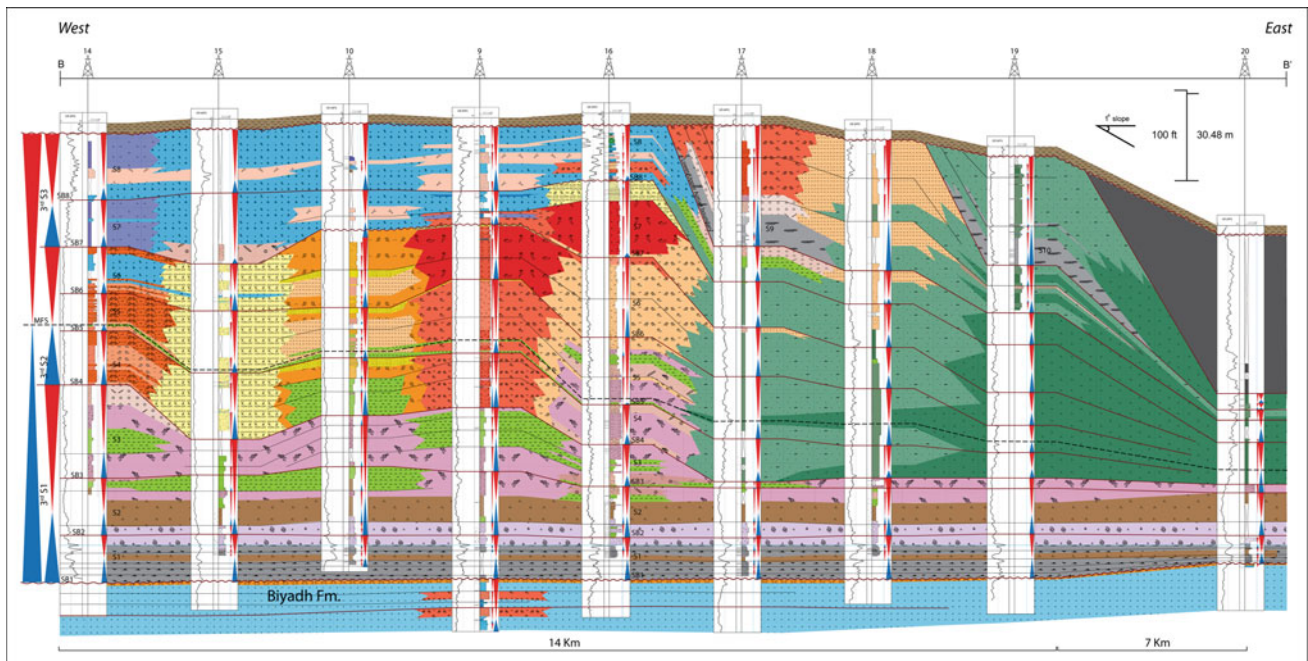
Fig. 1.16 Detail W-E dip oriented stratigraphic cross section of Shu'aiba Formation on the Northern block. The prograding Upper Aptian sequences produced clinoform geometries on the eastern platform edge. Note the lateral facies changes across the platform to basin transition. Ramp crest commonly grew more than surrounding area leading to differential accommodation. See Fig. 1.3 for location
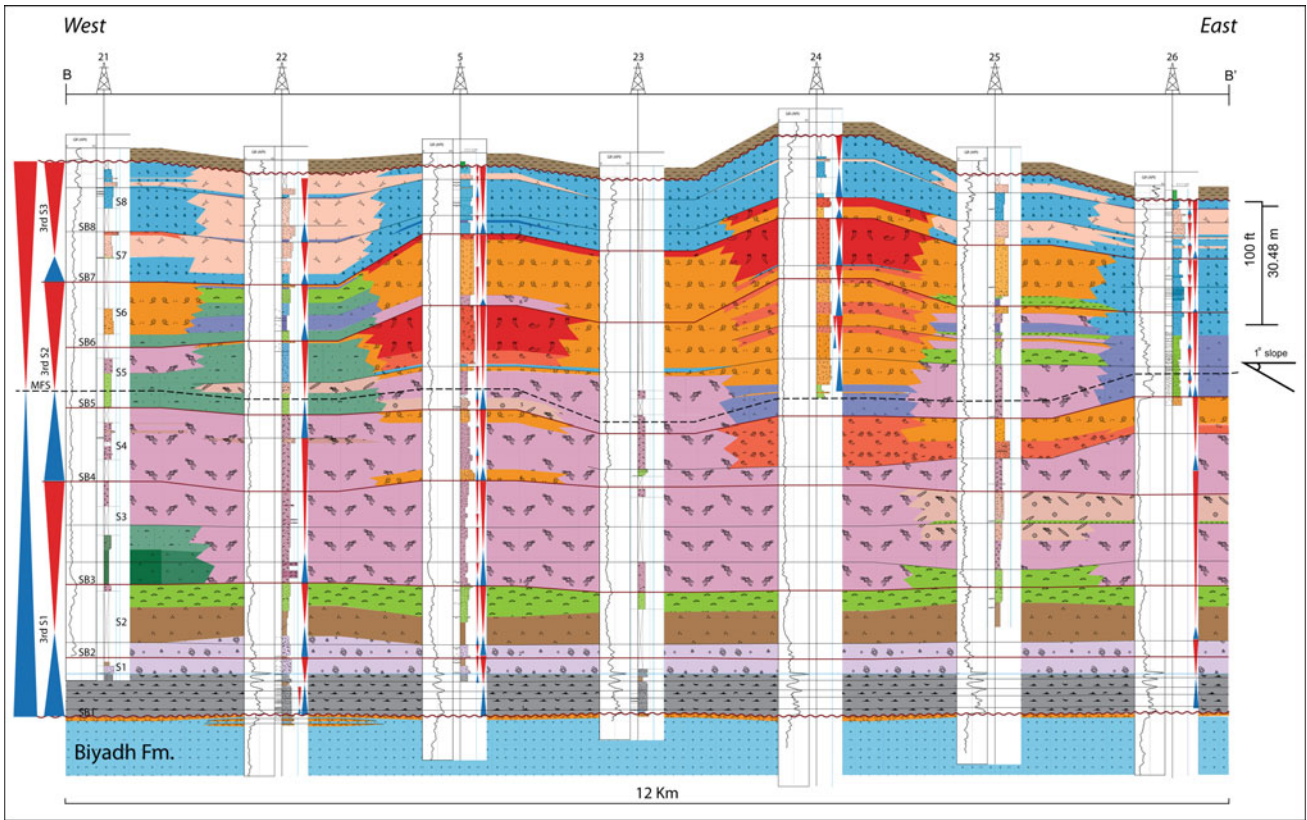
Fig. 1.17 Detail W-E stratigraphic cross section of Shu'aiba Formation on the Southern block. This cross section shows thicker *Lithocodium* facies and less stratigraphic complexity than the northern block. See Fig. 1.3 for location
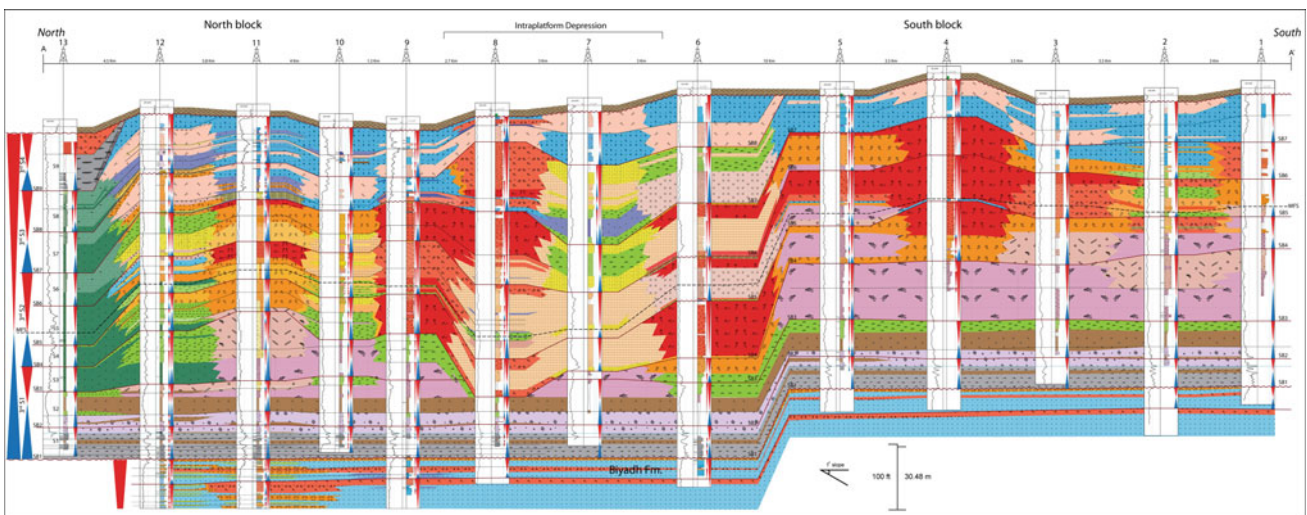
Fig. 1.18 Detail N-S stratigraphic cross section of Shu'aiba Formation from Southern and Northern blocks across the intraplatform depression. Note how the intraplatform depression is dominated by skeletal debris packstone surrounding by rudist buildups. See Fig. 1.3 for location

1.7   Lower Aptian Sequence 1 (S1)

This sequence overlies the regional sequence boundary and exposure surface of sequence boundary 1 (SB1) that separates the underlying Late Barremian Biyadh Formation and the overlying Early Aptian Hawar unit of the Shu'aiba Formation (Fig. 1.5f). This boundary represents a subaerial exposure surface that is mapped regionally (van Buchem et al. 2010; Droste 2010). This boundary also is significant because it corresponds to one of the major global depletion of carbon isotope values during the Early Cretaceous (Fig. 1.14). The Hawar unit, previously known as "Biyadh dense unit" in Saudi Arabia was lithostratigraphically separated from the Shu'aiba Formation and grouped with the Barremian Biyadh Formation (Ziegler 1976; Aktas and Hughes 2000; Hughes 2000). However, this unit should not be tied to the Biyadh Formation, because it is genetically related to the composite sequence of the Shu'aiba Formation as the TST of sequence 1 and has unique lithological and petrophysical characteristics, acting as a seal between the Shu'aiba and Biyadh formations (Witt and Gokdag 1994; van Buchem et al. 2002). Therefore, this unit is considered here as a separate unit rather than a unit within the Biyadh Formation as interpreted previously.

S1 began with the deposition of a dark-colored argillaceous *Palorbitolina* packstone facies of the base at the Hawar unit. This unit is characterized by abundant black *Palorbitolina*, glauconite, pyrite, reddish oxidized material and marine-cemented hardgrounds (Fig. 1.6a, b). This facies records the regional initial transgression (TS) following platform exposure at the end of the Barremian. This transgression was deposited in relatively shallow water ranging from ∼10–20 m water depth (Fig. 1.10), based on its associated fauna and grainy texture, despite the abundant argillaceous content. Shallow tidal flat facies with subaerial exposure surfaces were documented in a coeval sequence from Oman outcrops (van Buchem et al. 2002, 2010). This TS unit has a sheet-like geometry with nearly uniform thickness that is correlated regionally (Fig. 1.16). Moreover, this regional transgression coincides with a global depletion in carbon isotope signature (Fig. 1.14) and it is correlated globally (AL-Ghamdi and Pope 2014). The MFS of this sequence is a clean, pelagic chalky mudstone facies (brown facies), characterized by low *Palorbitolina* abundance, and lower gamma ray values. This suggests that as water deepened across the platform, fewer or no *Palorbitolina* were deposited, resulting in a clean skeletal facies of predominatly planktonic and pelagic foraminifera. At the top of Hawar unit, gamma ray values record the highest value in all the Shu'aiba Formation associated with deposition of a thin (few centimeters thick) black argillaceous mudstone. This marker is regionally correlated and used here as a datum for all stratigraphic correlations (Fig. 1.16). This sequence is capped by a sharp contact and abrupt change in facies from the dark argillaceous *Palorbitolina* packstone of the Hawar unit to the shallow subtidal, low density white-oncoidal *Lithocodium*/peloidal packstone of basal Shu'aiba Formation. This oncoidal *Lithocodium* facies has a uniform thickness across the platform and records the onset of the porous Shu'aiba successions and it represents the HST of S1 (Fig. 1.6c).

Five high-frequencies, decimeter-scale parasequences were identified and mapped throughout the field within the transgressive Hawar unit. These parasequences begin with highly argillaceous bioturbated *Palorbitolina* packstone marking a flooding surface and they deepen upward to lighter-colored, less argillaceous wackestone capped by a marine cemented hardground or firmground surface.

1.8   Lower Aptian Sequence 2 (S2)

This sequence begins with a thin flood unit of lime mudstone above SB2 (Figs. 1.16, 1.17 and 1.18) occurs within the oncoidal *Lithocodium* facies of S1. AL-Ghamdi and Read (2010) picked SB2 higher, at the top of oncoidal *Lithocodium* facies at the base of the pelagic chalky *Hedbergella* mudstone unit that is here interpreted to be the maximum flooding unit (MFU) of S2 rather than both the flooding surface and MFU. This flooding surface is thin but it extends throughout the field and also can be picked on the basis of its thin, high gamma ray value. The TST of this sequence is the oncoidal *Lithocodium/Bacinella* packstone facies that deepen upward to the extensive sheet-like deep planktonic *Hedbergella* chalky lime mudstone. This facies is one of the deepest water facies in the Early Aptian Shu'aiba succession and was interpreted to be the MFU of the Shu'aiba composite sequence (AL-Ghamdi and Read 2010). However, it is interpreted here only as the MFU of S2; equivalent to the regional MFS K70 of Davies et al. (2002). This facies has the lowest gamma ray values in the entire Shu'aiba Formation, due to its clean matrix with no argillaceous or clay materials. This facies grades upward to *Palorbitolina* wackestone with local *Lithocodium aggregatum*, which represent the HST of sequence 2 and is capped by a relatively higher energy facies of *Lithocodium/Palorbitolina* packstone. The top of this facies is a significant time marker associated with high gamma ray signal that is correlatable across the field. This gamma ray marker represents the termination of the sheet-like uniform layers associated with a low angle carbonate ramp, and the onset of a transitional carbonate platform with extensive algal *Lithocodium aggregatum/coral* mounds on the margin passing into an intrashelf basin on the eastern side (Fig. 1.16).

1.9 Lower Aptian Sequence 3 (S3)

The base of sequence 3 (SB3) is picked above the *Palorbitolina* packstone associated with of high gamma ray time marker (Figs. 1.16, 1.17 and 1.18). S3 records a change in platform setting from uniform homogeneous strata to more heterogeneous and mounded like strata with more prounounced lateral changes of depositional settings. This sequence is distinguished by its extensive *Lithocodium aggregatum* wackestone/boundstone interbedded with platy coral floatstone (Fig. 1.6e). The coral facies have a more grainy texture relative to the *Lithocodium* facies, and are interpreted as parasequence caps (Fig. 1.6f). However, *Lithocodium aggregatum* facies is the dominant facies in this sequence, forming a mound-like topographic high on the middle of the field that builds clinoforms toward the eastern basinal setting (Fig. 1.16). The southern block has a thicker *Lithocodium aggregatum* unit compared to the northern block with columnar growth morphology that extends into the overlying S4 (e.g. Wells 21, 22 and 25) (Fig. 1.17). The extensive *Lithocodium* facies shows subtle shallowing upward to *Palorbitolina* wackestone or platy coral floatstone representing the HST of this sequence. This sequence has thicker strata with backstepping geometries on the platform (Fig. 1.16) and thinner strata on the eastern side associated with clinforms geometry toward the basinal settings where deeper wackestone/mudstone facies were deposited (e.g. well 13 on the north, well 17 on the eastern flank).

1.10 Lower Aptian Sequences 4-6 (S4–S6)

SB4 is picked at the base of the first occurrence of the rudist buildup facies or its coeval detrital skeletal wackestone facies (Figs. 1.16 and 1.18). SB4 records a major change in depositional environment with an abrupt change in facies from the algal dominated facies (*Lithocodium*/coral platform) to the shallow water rudist floatstone/rudstone facies on the margin and fine skeletal wackestone on the slope and open marine settings. Carbon isotopes record a significant chronostratigraphic marker in all depositional settings at SB4 with an almost constant value of ∼4.5‰ representing an abrupt change in the carbon cycle related to abrupt change in global climate associated with a recovery of carbonate production and the development of rudist buildup facies (Fig. 1.14); (Föllmi et al. 2006; Jenkyns 2003; AL-Ghamdi and Pope 2014). Sequences 4–6 are equivalent to the 3rd-order Early Aptian sequence 3 of van Buchum et al. (2002, 2010), which represent the main rudist buildups of the Shu'aiba Formation. S4–S6 form one large 3rd-order shallowing upward sequence capped by subaerial exposure surface of SB6, but this larger 3rd-order sequence is here

divided into three HFS's on the basis of the detail core descriptions and stacking patterns. During the deposition of these sequences, a syn-depositional fault system was reactivated creating the intraplatform depression that divided the Shu'aiba platform into northern and southern blocks (Fig. 1.18). These two blocks records different depositional histories, sequence geometries and diagenetic histories (AL-Ghamdi and Read 2010; Aktas and Hughes 2000).

On the northern-block marginal setting, the TST of S4 is dominated by the caprotinid type rudist *Glassomyophorus costatus* floatstone (Fig. 1.7a), that deepens slightly upward to the MFS of thin skeletal packstone and then shallows upward into the HST of rudist rudstone at the top of S4. On the eastern flank, lateral facies change occur with equivalent interbedded platy coral floatstone and *Lithocodium* boundstone (e.g. well 16), changing laterally to open marine wackestone and then to deep basinal mudstone facies farthest to the east. On the southern block, S4 has only a thin transgressive caprotinid rudist facies that deepen upward to extensive *Lithocodium aggregatum* facies and then shallow upward into thin caprotinid rudist floatstone (Fig. 1.17). Caprinid rudists do not occur in the southern block in this sequence.

Sequence 5 records major deepening indicated by the presence of *Palorbitolina* wackestone within the rudist buildups (e.g. wells 14, 10, and 2) (Figs. 1.16, 1.17 and 1.18). On the flanks, major deepening is recorded by extensive black mudstone facies (e.g. wells 21 and 26), representing the regional maximum flooding unit of the large scale Shu'aiba composite sequence (Fig. 1.6d). This composite MFS is different than the composite Shu'aiba MFS picked previously (AL-Ghamdi and Read 2010) in the lower chalky mudstone facies and is also different than the MFS picked by van Buchum et al. (2010) at the uppermost part of "AP 2 sequence" near the contact between the *Lithocodium* facies and the rudist buildups. Regional stratigraphic correlation suggests that this MFS is most likely equivalent to the K80 MFS of Sharland et al. (2001) and Davies et al. (2002), but higher resolution biostratigraphy is required to accurately determine the age of this surface.

On the northern block, the intraplatform depression of S5 is dominated by skeletal peloidal grainstone that was shed from the surrounding rudist buildups (Fig. 1.18). This intraplatform depression formed a channel-like body with high-energy currents winnowing the sediments and forming clean grainstone facies (Wells 7 and 8); (Fig. 1.7c). The northern block platform interior (e.g. wells 10, 12 and 11); (Fig. 1.18) is more likely a shoal or back-shoal setting dominated by high-energy environments rather than a restricted back bank as previously interpreted (Aktas and Hughes 2000; Hughes 2000; AL-Ghamdi and Read 2010). This skeletal grainstone facies is similar to the grainstone in

the intraplatform depression, however, the location of the grainstone in the intraplatform depression was controlled by syn-depositional faulting rather than a depositional shoal setting. S5 on the southern block also records massive in situ rudist buildups, but they are not as abundant as on the northern block. Restricted ponds or a low-energy lagoonal platform interior of *Palorbitolina* wackestone/mudstone facies was deposited locally between these rudists (e.g. Wells 25, 22 and 2). This makes the southern block a low reservoir quality compare to the northern block.

Sequence 6 represents an overall shallowing upward trend within the rudist buildups in all wells, with the development of thick, massive shallow water rudist facies. Also, the lagoonal and platform interior settings have thin rudist units within this sequence. S6 begins with a thin flood of wackestone or *Glassomyophorus* rudist floatstone stacked on the previous rudists buildup of sequences 4 and 5. The rudist buildups of S6 are different from those of S4 and S5, being dominated by in situ recumbent caprinid rudist *Offneria murgensis* recording high-energy bank-crest settings with colonized rudist barriers (Fig. 1.7e, f). Sequence 6 is capped by a thin (~1 m) unit of well-rounded, well-sorted rudist rudstone facies that likely developed in a high-energy beach environment and represent

the shallowest water facies in the Shu'aiba successions (Fig. 1.7d). This facies is very well cemented, possibly due to the influence of meteoric waters during the exposure of this platform and may act as a reservoir baffle or even barrier zone. A red clay soil content that infiltrates down between the rudist fragments (Fig. 1.8e) indicating a subaerial exposure surface developed on top of this facies (wells 4, 9 and 46). Oxygen isotope values at this sequence boundary shows 1.5–2‰ depletion, suggesting meteoric diagenesis (AL-Ghamdi and Pope 2014). Sequence 6 has pronounced lateral facies changes with clinoform geometries from rudist rudstone at the margin to skeletal packstone and wackestone on the slope and in open marine settings with a correlative conformity surface (Fig. 1.19). On the southern block, sequence 6 records overall upward shallowing rudist buildups facies, but the high-energy beach facies on top of the rudists are absent. The absence of this high-energy facies on the southern block suggests that the northern block was influenced by higher energy wave that formed the beach deposits but these were not formed or preserved on the southern block. On southern block, sequence 6 also records the termination of the *Offneria* rudist buildups, whereas the northern blocks contains rudist buildups in the overlying sequences.
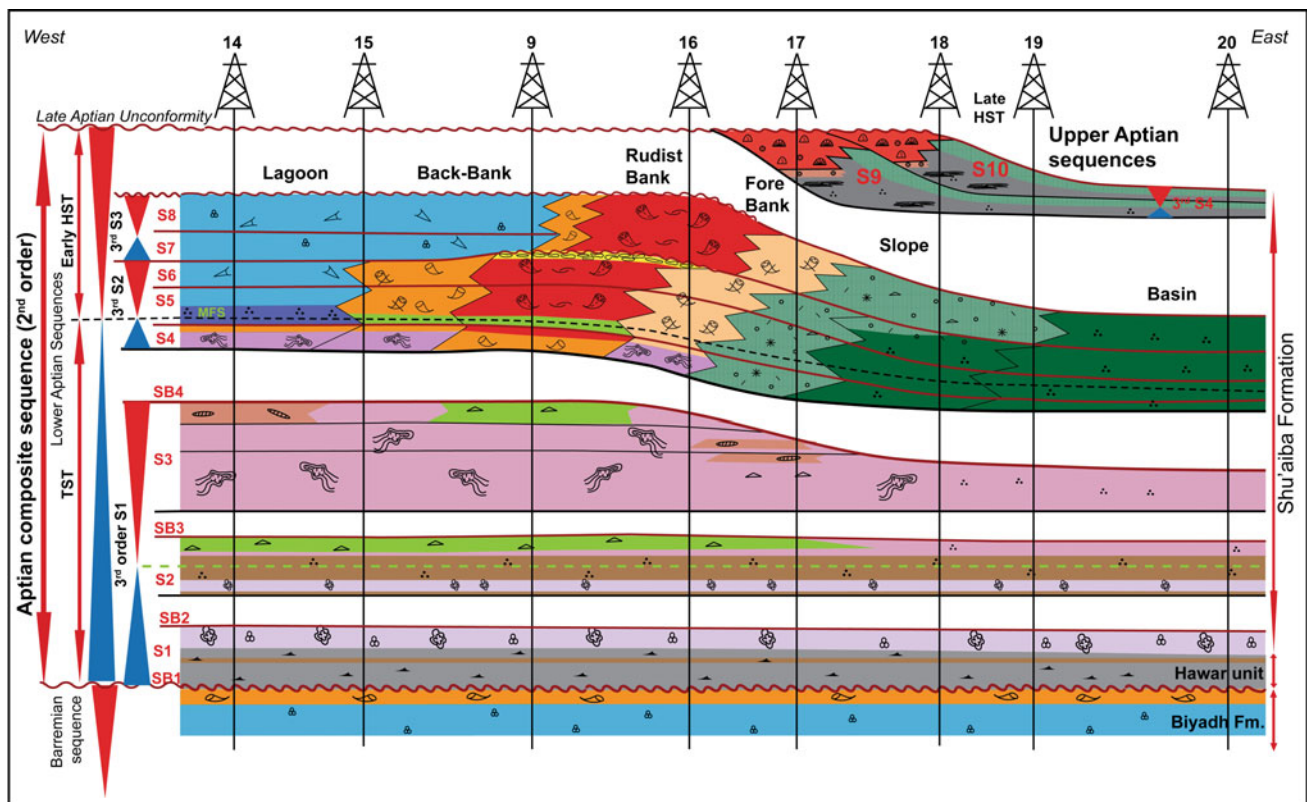
Fig. 1.19 Schematic stratigraphic profiles of the Shu'aiba Formation showing the evolution of the Shu'aiba platform within the depositional profiles and the Shu'aiba stratigraphic hierarchy

1.11 Lower Aptian Sequence 7(S7)

On the southern block, sequence 7 represents the end of Aptian sequences and it is capped by the Late Aptian unconformity at top of the Shu'aiba Formation (Fig. 1.17). S7 begins with a thin transgressive unit of deep lagoonal mudstone that shallows upward to shallow lagoonal peloidal milliolid packstone facies. The only rudists occurring in this sequence is the elongate caprotinid *Agriopleura or Pachytraga* that form local patchy mounds (Fig. 1.7b). The upper part of this sequence gradually deepens to mudstone facies contains infiltrated shale from the Nhr-Umr Formation beneath the top unconformity. The deepening trend from shallow miliolidal packstone to wackestone/mudstone below the top of the Shu'aiba Formation occurs in most wells. On the northern block, S7 begins with a mudstone flooding surface including rip up clasts and reworked rudist fragments and deepens upward to deep lagoonal mudstone. This mudstone is overlain by the miliolidal packstone facies with local *Agriopleura* floatstone facies. However, thick massive rudist buildups of *Offneria* rudist rudstone still developed local patchy rudist buildups, commonly stacked on rudist buildups that formed in sequence 6 (Wells 8, 12 and 16); (Fig. 1.18). This rudist units do not form continuous barrier banks, but they are patchy mounds surrounded the lagoonal facies with a prograding shingled geometry. These patchy rudist buildups are capped by high energy rounded-rudist rudstone formed in a beach environment that was subaerially exposed similar to the facies that cap sequence 6. The top of sequence 7 records the termination of the in situ rudist buildups within the Shu'aiba Formation and the demise of the caprinid *Offneria* rudist species (Hughes 2000).

1.12 Lower Aptian Sequence 8 (S8)

This sequence only occurs on the northern block, due to the influence of the syn-depositional subsidence that moved the northern block down and provided accommodation space on the northern block when the south block was exposed and eroded by the Late Aptian unconformity (AL-Ghamdi and Read 2010; Fig. 1.18). This sequence is the last phase of sedimentation on the Shu'aiba Formation platform margin. However, more sequences are still developed on the eastern platform edges. S8 is dominated by shallow lagoonal peloidal miliolid packstone/wackestone facies interbedded with thin, deeper lagoonal mudstone facies. *Agriopleura* floatstone facies occur as local patchy rudist mounds or as the caps to shallowing upward successions, but no colonized rudist occurred in this sequence. This sequence records a deepening trend of mudstone facies below the Late Aptian unconformity similar to S7 on the southern block. This

unconformity formed karst that locally penetrates deeper than 30 ft (10 m) into the top of the Shu'aiba Formation (e.g. wells 16 and 52; Fig. 1.8f).

1.13 Upper Aptian Sequences 9 and 10 (S9 and S10)

Sequences 9 and 10 are Upper Aptian sequences identified for the first time in this study. They formed only on the northern block as shelf edge prograding sequences, during which the interior of the Shu'aiba platform was subaerially exposed and eroded (Figs. 1.17 and 1.19a). These sequences are equivalent to sequences Apt4a and Apt4b of van Buchum et al. (2010). The Lower/Upper Aptian boundary is a conformable surface and was picked initially on the basis of carbon isotope values (Fig. 1.14) and coincides with an abrupt change in facies from fine skeletal and detrital packstone of the Lower Aptian slope of S8 to dark dense argillaceous mudstone facies of S9 (Fig. 1.8c). In addition, nannofossil data from well 19 confirms the Late Aptian age of these sequences with the first occurrence of the nanno-fossil *Lithraphidites houghtonii* (AL-Ghamdi and Pope 2014). Thus, biostratigraphy integrated with core description and chemostratigraphy constrain the age of these prograding sequences (AL-Ghamdi and Pope 2014). The argillaceous mudstone averages about 20–30 ft thick (6–9 m) and shallows upward into grainy coral floatstone facies overlain by massive reefal facies containing mixed stromatoporoid and rudist rudstone (Fig. 1.8b). The argillaceous mudstone facies occurring at the base of these sequences possibly represent a lowstand prograding wedge, similar to what has been interpreted by van Buchem et al. (2010) and Yose et al. (2010). The Late Aptian rudists mainly are *Horiopleura* species of the Polyconitidae family (Skelton 2008; Saudi Aramco internal report), quite different type than the lower Aptian caprinid and caprotinid rudists. The range of *Horiopleura* rudists extends from the Aptian to the lower Albian (Skeleton and Masse 2000). These shelf edge sequences prograde toward the intrashelf basin with clinoform geometries and laterally change facies to open marine skeletal packstone/wackestone and finally to deep pelagic basinal mudstone. At least nine high-frequency sequences were described from seismic in the coeval Bu-Hasa field, and they prograde >10 km from the shelf edge toward the basin (Pierson et al. 2010). It is possible that more prograding sequences formed far to the east in the study area, but more data (e.g. seismic data) is necessary to confirm this interpretation. The Upper Aptian prograding sequences also occurred in the far northern edge of the platform where wells 53, 13 and 54 have similar depositional settings to the eastern flank with similar facies and similar stacking

patterns. Upper Aptian sequences also formed on the northwestern flank as shown in the carbon isotope curve in well 45 (Fig. 1.14), but differ from the eastern flank in that they do not have shallow water rudist facies or slope and open marine settings, instead the Upper Aptian here records restricted lagoonal environments.

Finally, the Bab intrashelf basin occurs on the far eastern side in well 20, and is thought to be the latest Upper Aptian or early Lower Albian (van Bucum et al. 2010). It is the last stage of basin infill and is dominated by organic-rich lime mudstone interbedded with sandstone.

1.13.1 Parasequences

Parasequences are an important component of the stratigraphic framework and reservoir characterization as they control the reservoir properties and hence the simulation model and its fluid flow behavior (Kerans and Tinker 1997). Therefore, higher-scale parasequences of the Biyadh and Shu'aiba Formations were identified and mapped to better characterize their reservoirs and to provide a higher-resolution genetic layering scheme for the 3-D reservoir model. Also, their stacking pattern, thickness and magnitude will provide better understanding on the driving mechanism of the stratigraphic records and the effect of climate within a global or regional scale.

1.14 Parasequences in Biyadh Formation

There are 34 parasequences identified in Biyadh Formation, most of them can be traced between wells and throughout the field (Fig. 1.15). Of these 34 parasequences, four formed in S1; five in S2; 13 formed in S3 and 12 formed in S4. Parasequences in S1 occurred within the argillaceous dense unit at basal Biyadh Formation. No cores penetrate the entire interval of this unit, but four meter-scale ($\sim$5 ft thick, 1.5 m) cycles can be mapped throughout the area on gamma ray logs. As similar to Hawar unit, the higher gamma ray values of this unit indicate highly argillaceous mudstone representing flooding surface that change upward to more clean, deeper and less argillaceous mudstone. Parasequences within S2 are thicker $\sim$15 ft (4.5 m) cycles, that begin with a *Palorbitolina* wackestone and deepen upwards to chalky mudstone facies. Major changes in parasequences pattern occurred at S3 where many more (13) small scale $\sim$2–5 ft (0.6–1.5 m) cycles are delineated within the shallow upward S3. These cycles are characterized by a sharp erosional contact at the base overlain by oncoidal peloid grainstone facies or rudist floatstone representing a flooding surface that shallow upward to less grainy packstone/wackestone facies (Fig. 1.5c). Most of these cycles can be correlated between

the wells and may have some impact on reservoir quality distribution (Fig. 1.15).

1.15 Parasequences in Shu'aiba Formation

The Shu'aiba Formation contains at least 37 parasequences within the Early and Late Aptian sequences, 31 parasequences formed in the Lower Aptian back-bank or platform interior settings and at least 6 additional parasequences formed in the Upper Aptian prograding wedges on the flanks. Of the 31 parasequences; seven formed in S1 (including 6 in Hawar unit), whereas S2–S10 include 3–4 parasequences each. Parasequences within S1 and S2 are sheet-like units and are calibrated to gamma-ray logs, thus they can be mapped throughout the field. Parasequences in S3 within the *Lithocodium*/coral mounds have slightly different geometries due to the development of *Lithocodium* mounds on the platform margin and clinoform prograding toward the basin. Therefore, more parasequences are recorded on the platform margin than the slope or open-marine settings. Associated fauna were used to pick some these parasequences, where the relatively deeper water *Lithocodium* facies is interbedded with the relatively shallower coral facies.

Generally, the in situ rudist buildups within the bank-crest at S4–S6 are poorly cyclic and do not record higher-order parasequences, due to their nature as reefal buildups geometry with massive framework and higher sedimentation rate. However, parasequences are better developed on the back-bank, shoal or fore-bank settings. Interbedded of different type of rudists, such as the deeper water *Glassomyophorus* rudist and the shallow water *Offneria* rudist within these sequence are used as an evidences of cycle changes. These parasequences S4–S6 are locally continued and are rarely mappable over the rudist buildups. In addition, these parasequences cannot be mapped over the open marine settings, due to the unchanged and uniform lithofacies deposited in coeval open marine and basinal settings.

The upper part of the Shu'aiba Formation (S7–S8) has seven parasequences at maximum that can be mapped locally. These parasequences have deep lagoonal mudstone at the base that shallows upward into peloidal miliolid packstone or *Agriopleura* floatstone facies. Exposure surfaces formed locally at the top of these parasequences.

Parasequences in the Upper Aptian sequences 9 and 10 are characterized by a basal dense argillaceous mudstone that changes upward into coral/stromatoporoid floatstone or skeletal packstone facies. These parasequences show clinoform geometries and can be mapped locally, with a top lap geometry against the Upper Shu'aiba Unconformity.

1.16 Discussion

1.16.1 Barremian Versus Aptian Sequence Stratigraphy

Although there are some similarity in the facies associations between the Late Barremian Biyadh Formation and the Aptian Shu'aiba Formation, there are many differences between the two units with regards to their depositional settings and facies architecture. First, the entire Biyadh Formation is composed of one large scale 3rd-order shallowing up sequence recording a single long-term sea level rise and fall. Conversely, the Shu'aiba Formation records a large scale composite sequence/or 2nd-order sequence, built by four 3rd-order sequences, built by 10 high frequency sequences. The Biyadh Formation was deposited on a shallow subtidal ramp with relatively thin rudist banks at the upper shoreface environments (Fig. 1.9). The Shu'aiba depositional platform evolved from, restricted subtidal, algal dominated ramp to marginal rudist barrier bank (Figs. 1.10, 1.11, 1.12 and 1.13). The shallow subtidal ramp of the Biyadh Formation formed sheet-like layers at all scales (3rd-order sequences to parasequences) because there were no tectonic rim developed during this time, therefore, there was no major lateral changes in depositional setting and no intrashelf basinal architecture developed at this time. This is indicated by the uniform sheet-like strata of all the large and small scale parasequences within the Biyadh Formation, they are layer-cake strata and do not have the shingle or clinoform geometries like the overlying Shu'aiba Formation (Fig. 1.15). The rudist facies in Biyadh Formation also correlate as a layer cake unit and are dominated by the elongate caprotinid *Glassomyophorus and Agriopleura species* with no evidence of the high-energy reefal caprinid rudist of *Offneria* species.

In addition, the average thickness of the Biyadh sequence is about 220 ft (67 m) whereas the average thickness of the Shu'aiba Formation is about 450 ft (137 m). This is due to the absence of extensive *Lithocodium* aggregatum algal mounds and a colonized rudist buildups in the Biyadh Formation.

1.16.2 Shu'aiba Formation Hierarchy and Platform Evolution

The Shu'aiba Formation, including Hawar unit and the Late Aptian sequences is about 530 ft (160 m) thick and is composed one large scale composite 2nd-order sequence (spanning ~7 My) comprised of four 3rd-order sequences (~1–2 My each) and 10 high frequency sequences (~400 ky–1 My; Fig. 1.19a). Previous study of AL-Ghamdi and Read (2010), interpreted 7 HFS's in the Shu'aiba platform within the Early Aptian, but did not interpret any 3rd-order sequences, due to the lack of biostratigraphic markers and poor age control within the Shu'aiba platform. This study used much more data than previous study and is also incorporating much more carbon isotope data that helps constrain the ages beyond the resolution of biostratigraphy (Fig. 1.14). Thus, eight HFS's (S1–S8) were identified and mapped on the Early Aptian Shu'aiba platform, plus two more HFS's (S9 and S10) are mapped on the Late Aptian platform edge, compared to seven HFS's in AL-Ghamdi and Read (2010). The extra sequence in the Early Aptian in this paper is S3 that is a significant chronostratigraphic marker, in addition to its association with a notable change in platform geometry and basin configuration. Thus interpreted as an individual HFS rather than parasequence.

On the basis of stacking patterns, stratigraphic geometry, facies association and carbon isotope curves, the ten HFS's in the Shu'aiba Formation can be grouped into four 3rd-order sequences with possible duration of ~1–2 My each. These 3rd-order sequences are abbreviated as 3rd-order S1, 3rd-order S2, 3rd-order S3 3rd-order S4 to differentiate them from the HFS's S1–S10. The first 3rd-order S1 consists of S1, S2 and S3 that are characterized by a transgressive phase associated with sea-level rise, mud-dominated facies, and open marine algal platform environments, with *Lithocodium*/coral and *Palorbitolina* facies. This 3rd-order sequence represents a global diminish of carbonate production with the absence of rudist buildups that were replaced by extensive *Lithocodium aggregatum* and coral facies (Huck et al. 2012). The second 3rd-order sequence (3rd-order S2) is composed of sequences S4, S5 and S6, associated with the development of massive rudist buildup facies. This sequence is dominated by aggrading geometries and relative sea-level still stand with high sedimentation rates representing the early HST of the Shu'aiba 2nd-order composite sequence. The 3rd-order S2 also records an individual shallowing upward sequence where the base is dominated by transgressive *Glassomyophorus* rudist facies that shallow upward into a high-energy *Offneria* rudist facies that is capped by rounded rudist debris rudstone facies formed in a beach environment followed by subaerial exposure of the platform. 3rd-S2 here is equivalent to "Apt3" in van Buchem et al. (2010) and Yose et al. (2010).

3rd-order sequence 3 is composed of S7 and S8 and it overlies the SB7 exposure surface that records the termination of the colonized *Offneria* rudist buildups on the southern block. This 3rd-order sequence represents the last stage of deposition on the platform margin with shallow lagoonal miliolids peloidal packstone facies interfingering with local *Agriopleura* rudists. The stratigraphic geometry of this

sequence is dominated by late HST of the Shu'aiba composite sequence with slight progradation of the rudist and shallow lagoonal facies toward the basin. This sequence was extensively eroded and karstified during the Late Aptian unconformity that formed during a global sea-level fall (estimated of ∼30 m sea-level drop), possibly due to polar glaciation (Al-Husseini and Matthews 2010). The fourth 3rd-order sequence (3rd-order S4) is composed of the Upper Aptian (S9 and S10) that prograde from the shelf edge into the intrashelf basin. This sequence was only deposited on the northern platform edge during a forced regression and major sea-level fall in the Late Aptian. Core descriptions integrated with carbon isotope data confirm two prograding sequences formed on the flanks of the Shu'aiba platform, however, more prograding sequences may exist farther east toward the basin (Fig. 1.14). Yose et al. (2010) and Pierson et al. (2010) were able to identify nine prograding sequences on the U.A.E giant field A, using seismic data.

1.16.3 Maximum Flooding Surfaces

The regional maximum flooding surfaces of the Early Cretaceous Biyadh and Shu'aiba Formations have been debated, especially the maximum flooding surfaces K70 and K80. Sharland et al. (2001) defined three major flooding surfaces within the study interval; (K60) in the Late Barremian Biyadh Formation, and (K70 and K80) in the Early Aptian Shu'aiba Formation. Sharland et al. (2001) placed K60 within the unit at the base of the Biyadh Formation, placed K70 at the top of the Hawar dense unit corresponding to the highest gamma ray signal at the contact between Hawar unit and basal Shu'aiba Formation, and placed K80 higher in the Shu'aiba section coeval to the tar unit of intrashelf Bab Member.

K60 in this paper was placed higher in the section within the mudstone facies of S2 at the base of the Biyadh Formation (coeval to Khariab Formation in the U.A.E). It is similar to the placement of K60 in van Buchem et al. (2010) but different than the K60 of Sharland et al. 2001 that was picked within the dense unit underneath (Fig. 1.15).

Davies et al. (2002) on his updated study, refined the location of K70 and placed it higher in the section within lower part of the Shu'aiba Formation, corresponding to the chalky *Hedbergella* planktonic mudstone facies that also was interpreted to be the deepest water facies of the Shu'aiba Formation (AL-Ghamdi and Read 2010). In addition, K70 was interpreted to be the MFS of the entire Early Cretaceous supersequence (Sharland et al. 2001; Davies et al. 2002; AL-Ghamdi and Read 2010). The Hawar unit, was previously interpreted as a deep, open platform with planktonic foraminifera associated with the predominant argillaceous

Palorbitolina packstone facies (Hughes 2000). AL-Ghamdi and Read (2010) interpreted the Hawar dense unit as deposited in relatively deep water environments, but with lack of planktonic foraminifera, thus K70 maximum flooding surface was placed higher in the section within the clean chalky planktonic mudstone facies that interpreted to represent the deepest water facies of the Shu'aiba Formation. However, evidence of mud cracks and possible exposure surfaces within the coeval Hawar unit, especially in the outcrop of Jabal Akhdar (Oman), suggests that the Hawar unit may deposit in tidal flat or shallow restricted environments rather than a deep open marine setting and representing the early TST rather than the maximum flooding surface (van Buchem et al. 2002, 2010; Pittet et al. 2002; Stronhmenger et al. 2006).

van Buchem et al. (2010) however did not recognize K70 as a major surface, they only recognized the K80 as the major MFS of the entire Lower Cretaceous super sequence. Moreover, van Buchem et al. (2010), Droste (2010) and others, picked K80 on the basis of the general stratigraphic trend near the contact from the lower Shu'aiba transgressive phase dominated by *Lithocodium/Bacinella* facies to the middle Shu'aiba rudist buildups regressive phase. However, there is no discrete surface that can be identified for this MFS event and gamma ray logs also do not have a significant increase associated with this surface in the region. We agree that the MFS K80 is probably the major MFS for the Shu'aiba composite sequence rather than K70, but we do not agree that it is located at the contact between the *Lithocodium/Bacinella* facies and the rudist buildups facies. This contact is a major sequence boundary (SB 4 in this study and base of Apt3 in van Buchem et al. 2010), marked by a sharp contact and abrupt change in facies (Fig. 1.8d), depositional environment, and also change in the global carbon isotope values, thus it cannot be a sequence boundary and maximum flooding surface at the same time. K80 in this study is placed on a clear physical surface in cores, that is higher in the section than the K80 of van Buchem et al. (2010), within the rudist buildups facies of S5 associated with a major flooding surface and deep water facies recorded in cores associated with higher gamma ray signals, especially on the flanks of the field (Figs. 1.16, 1.17, 1.18 and 1.19). This is a major drowning event within S5 that occurred across the entire field and also occurred within the in situ rudist bank-crest setting, where deeper water *Palorbitolina* mudstone/wackestone was deposited within the rudist buildups indicating major platform drowning event (e.g. wells 14, 9, 10 and 12). On the platform edge, major deepening is recorded with the deposition of a thick succession of deeper water, black-laminated mudstone facies. Placing K80 at this surface makes S1–S4 the TST of the entire Shu'aiba composite sequence with general aggrading

and backsteeping geometries. S5–S8 then become the early HST with aggrading and slight prograding geometries toward the basin. S9–S10 is the late HST with strong, downstepping and progradational geometries (Fig. 1.19). In addition, the rudist buildups in S4, beneath the K80 are mainly dominated by the relatively deep water transgressive caprotinid *Glassomyophorus* rudist, but above K80 the caprinid *Offneria* rudists are the predominant rudist type. Therefore, K80 here is the turnover surface (MFS) between the large scale TST and HST of the Shu'aiba composite sequence.

Although K80 is considered the major MFS of the Shu'aiba composite sequence, K70 is still an important flooding unit and it is picked here as the MFS of the HFS S2 and the MFS of the 3rd-order sequence 1. K70 also is an important surface, because it is associated with the onset of the major carbon isotope positive excursion of the Early Cretaceous just beneath the *Lithocodium/Bacinella* facies, coeval to widespread black shale deposited during the global OAE 1a (Immenhauser et al. 2005). It is not clear why this MFS (K70) and its associated facies, the deep planktonic chalky mudstone unit (brown color in the cross sections) was not clearly defined and mapped in the region. This MFS was described as a secondary higher-order flooding event with limited correlation potential (e.g. van Buchem et al. 2010).

1.16.4 Anatomy of the Shu'aiba Formation Platform

A series of facies maps (Fig. 1.20a–g) were generated for each HFS (S3–S10) to illustrate the evolution of Shu'aiba platform and to track the changes in its depositional anatomy to determine its influence on reservoir quality. These facies maps are crucial for constructing a 3-D geocellular model and also for predicting reservoir quality and guiding new drilling programs. They also are important to understand the influence of third order sea-level changes during the Aptian on the Shu'aiba platform and the effect of syn-depositional faulting on facies development. The facies maps were constructed using the 55 cored wells at the top of each sequence representing the HST of each sequence. S1 and S2 were not included in the facies maps, because their facies are sheet-like strata across the region without any lateral facies changes.
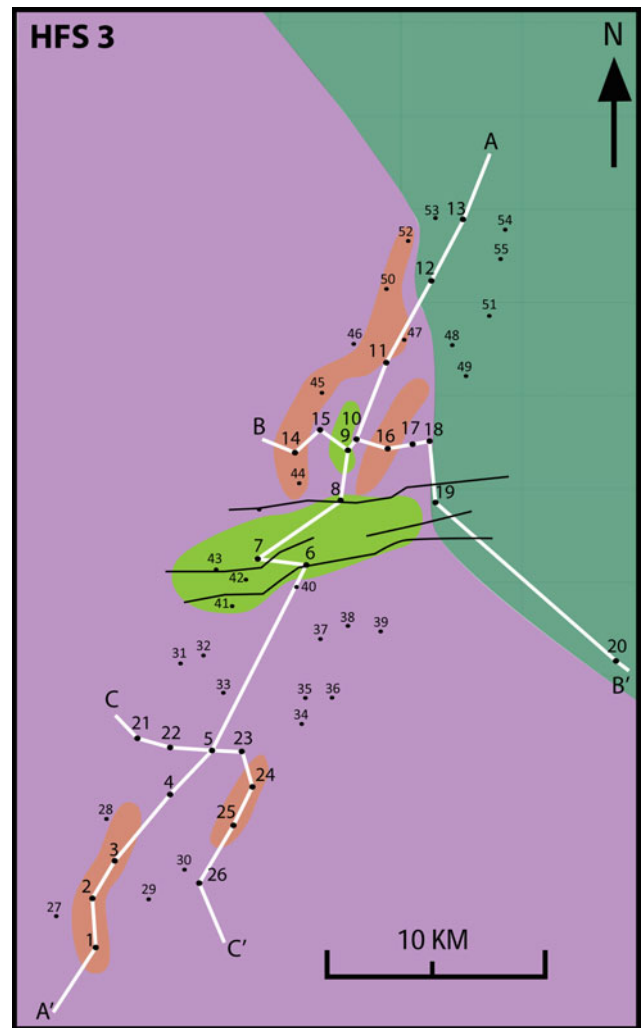
Fig. 1.20 **a** Facies map at top of HFS 3. This facies is dominated by *Lithocodium* facies. Intraplatform depression is dominated by *Palorbitolina* wackestone facies (green). Coral facies form local mounds on the flanks. **b** Facies map at top of HFS 4. This map shows the initiation of the rudist buildups. The southern block still develops extensive *Lithocodium* on the western margin. **c** Facies map at top of HFS 5. Rudist buildups rimmed the northern block, while the western side of the southern block is open to deep lagoonal facies. **d** Facies map at top of HFS 6. Extensive and continuous rudists buildups formed around the field. **e** Facies map at top of HFS 7. The platform is dominated by inner ramp lagoonal facies, but rudist buildups still forming in the eastern margin. **f** Facies map at top of HFS 8. The southern block is subaerially exposed and the northern block is dominated by inner ramp shallow lagoonal facies. **g** Facies map of the Upper Aptian sequences 9 and 10. The whole platform was subaerially exposed except the north and eastern margins of the northern block, where prograding sequences occurred
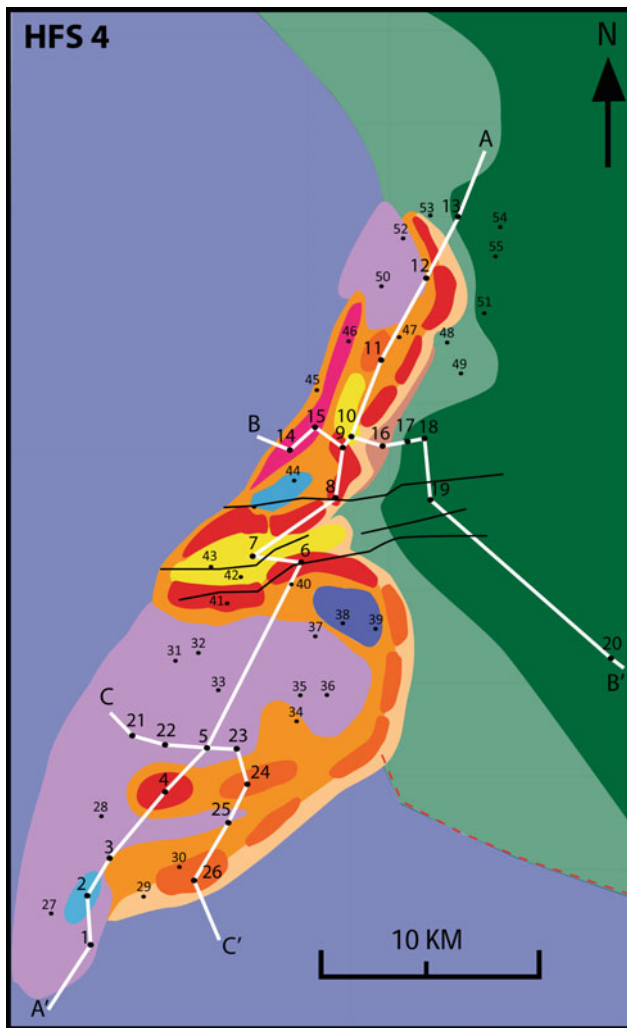
Fig. 1.20 (continued)
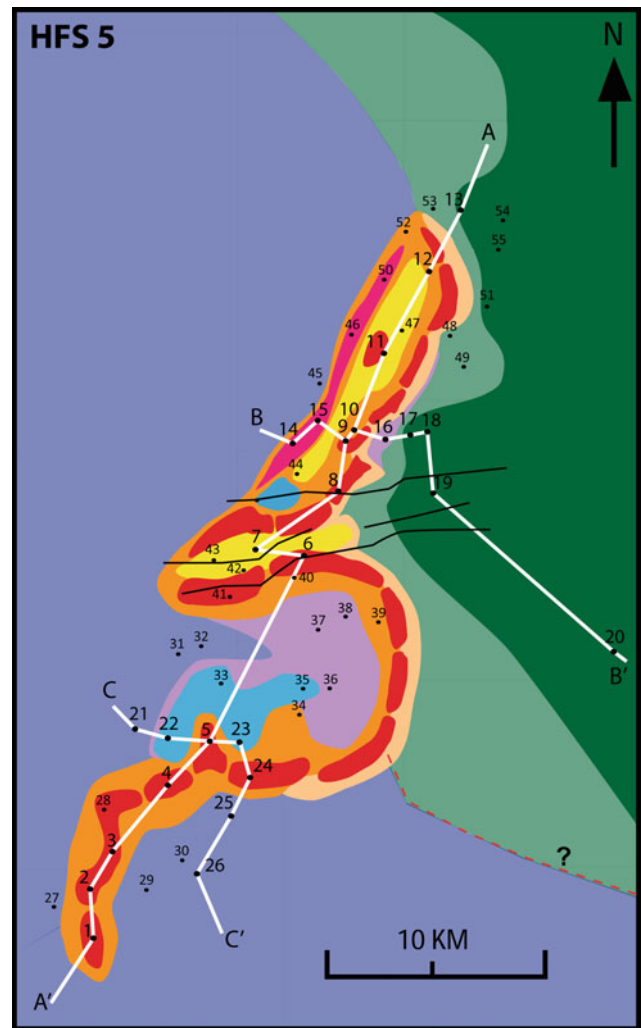
Fig. 1.20 (continued)

1.17   Facies Anatomy of HFS 3 (S3)

Sequence 3 is dominated by the development of *Lithocodium*/coral algal mounds with subtle lateral facies changes to *Palorbitolina* wackestone (Fig. 1.20a). In this sequence, the Shu'aiba platform is dominated by the *Lithocodium* facies associated with global sea-level rise that flooded epicontinental basins around the world during the development of Oceanic Anoxic Event 1a. This *Lithocodium* facies is coeval to black shale and the global OAE 1a elsewhere (Immenhauser et al. 2005). The *Lithocodium* facies in this sequence develop a thick and extensive algal mound on the margin that thins toward the eastern side of the basin and changes to deep, open marine facies. Patchy coral mounds of mixed platy and massive corals developed locally to the north and south. These coral facies may extend for several kilometers and providing high reservoir quality due to the

abundance of intergranular and moldic porosity within the corals (Fig. 1.6f). These coral mounds developed on top of the *Lithocodium* facies as topographically higher coral mounds were suitable place for the rudist buildups to initiate in the following sequences, such as the elongate coral unit on the north that is overlain by the high-energy rudist facies that has the highest reservoir quality in all wells. The intraplatform depression between the northern and southern blocks was dominated by *Palorbitolina* wackestone facies without significant *Lithocodium* or coral developed due to sediment starvation and its topographic low position. Therefore, S3 thins dramatically in this zone or pinches out altogether (Wells 7 and 8) (Fig. 1.18). This change in the facies at the intraplatform depression suggests that the syn-depositional fault systems initiate early in this sequence, because previous sequences were uniform beneath this depression area (AL-Ghamdi and Read 2010).
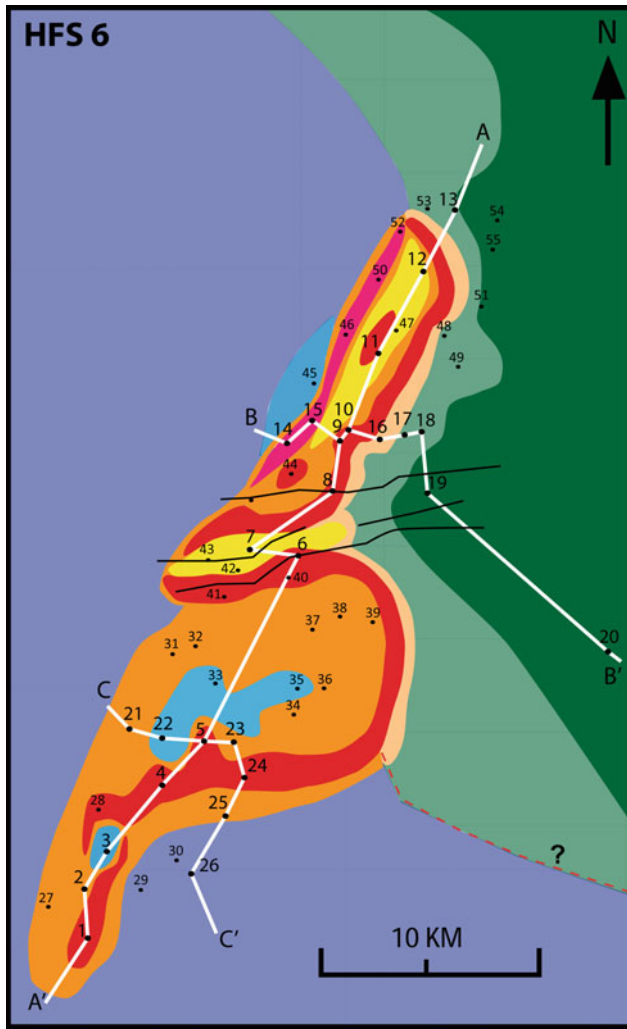
Fig. 1.20 (continued)
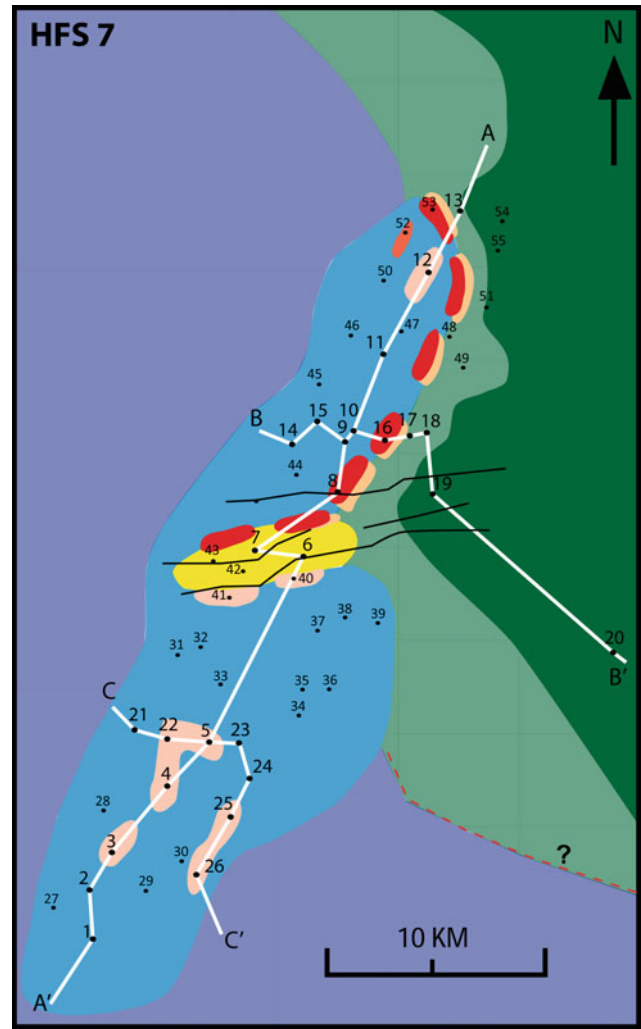
Fig. 1.20 (continued)

1.18 Facies Anatomy of HFS 4 (S4)

Sequence 4 formed at the base of the 3rd-order S2, recording the onset of the rudist buildups along the north and south margins of the platform (Fig. 1.20b). The south margin rudist facies passes eastward into an open marine *Lithocodium* algal platform or lagoonal facies, whereas the northern block developed more extensive rudist buildups that transitioned into a fragmented rudist shoal except along the northeastern flanks (Wells 50 and 52) where the *Lithocodium* facies persisted, suggesting an open environment to deeper water facies off the margin. The rudist buildups in this sequence are dominated by mixed *Glassomyophorus* and *Offneria* rudists in the northern and mainly *Glassomyophoru*s rudists on the southern block, suggesting the northern block was influenced by higher energy waves than the southern block. The rudist buildups on the eastern

flanks were interpreted as the windward margin whereas the western flank was the leeward margin (AL-Ghamdi and Read 2010). However, the western flank rudist facies (pink) is dominated by fragmented rudists rudstone in a grainy matrix with abundant moldic and vuggy porosity and was deposited under a higher energy environment than the eastern flank (red) (Fig. 1.7e). Conversely, the eastern flank rudist facies, is dominated by in situ rudist rudstone/floatstone with muddy matrix filling and infiltrating the rudists with moderate to good porosity. Rudist buildups in this sequence formed north-south oriented buildups, with discontinuous elongated barriers possibly separated by tidal channels (Fig. 1.12). These discontinuous rudist buildups was conceptually interpreted on the basis of discontinuous barrier banks (or reefs) in modern carbonates platforms such as the Great Pearl Bank barrier of the Arabian Gulf (Hughes 1997) and the Great Barrier Banks of Australia (J.F Read, personnel com.). The intraplatform depression is dominated
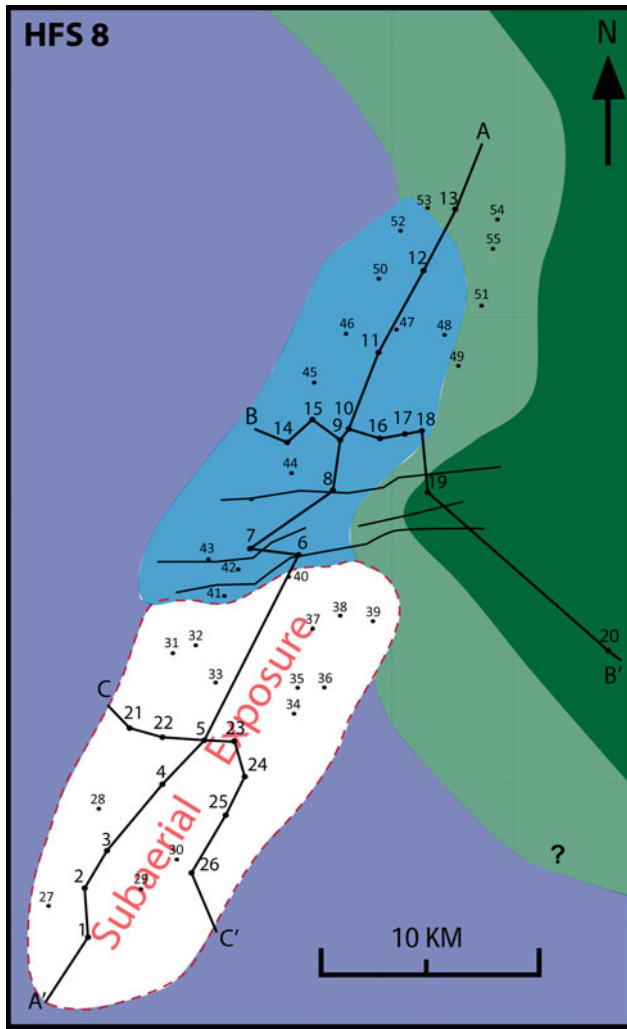
Fig. 1.20 (continued)

Fig. 1.20 (continued)

by detrital grainstone facies developed in an elongated W-E trending trough with high-energy currents in a channel-like geometry. This detrital grainstones were sourced from the surrounding rudist buildups that developed on the topographically high W-E trending rim created by fault systems, possibly along deep seated basement faults as suggested by seismic data. The platform interior in the northern block is generally dominated by the back-bank *Glassomyophorus* rudist floatstone with no evidence of deep lagoonal ponds or restricted lagoons as previously thought (Hughes 2000). The southern block, however has deeper back-bank or lagoonal settings dominated by *Lithocodium aggregatum* facies as shown on the western flank (Fig. 1.20b).
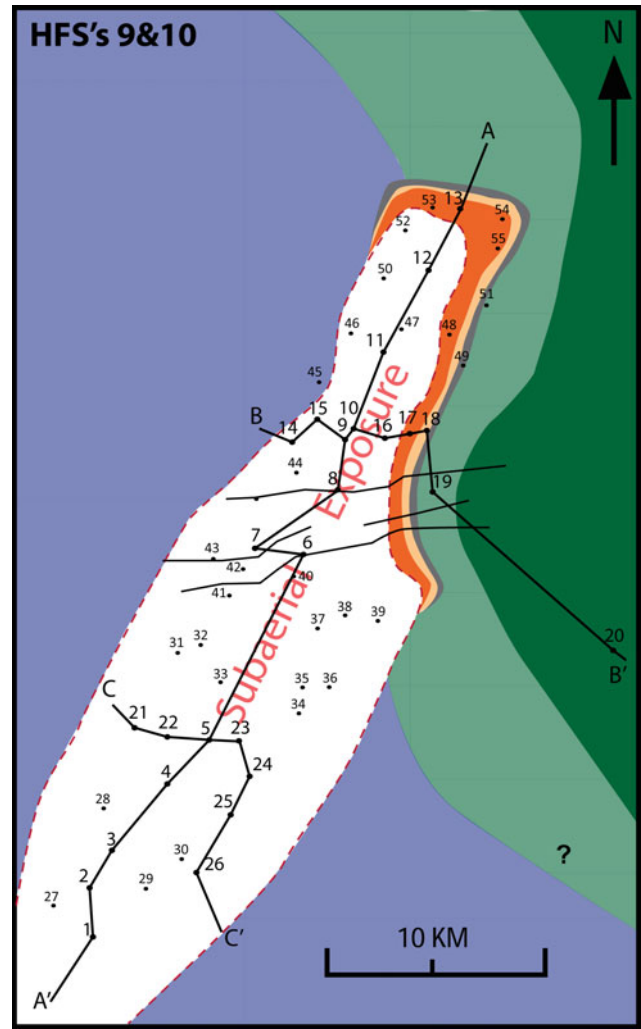
1.19 Facies Anatomy of HFS 5 (S5)

The rudist buildups in this sequence continued to develop a stacked sequence above the previous platform margins, but the buildups extend further around the platform (Fig. 1.20c). For instance, rudist buildups were established above the *Lithocodium* facies of S4 on the far south and possibly attached to the previous rudist buildups on the central part at Well 4 with an elongated north-south trend. The northern block has similar rudist trends as the previous sequence, but they also extended into Wells 50 and 52 forming a amore continuous rim around the platform over *Lithocodium* facies

in S4. A major change in facies in the northern block is the development of a high-energy grainstone shoal (Fig. 1.7c), in the platform interior (yellow zone, Fig. 1.20c) as an elongated north-south trending zone. This high energy grainstone in the platform interior was deposited in a shoal or shallow back-bank settings and surrounded by in situ rudist buildups on both sides. The southern block, however does not have such high energy shoal facies, instead, the platform interior is dominated by low energy lagoonal wackestone or *Lithocodium*/coral facies (e.g. Wells 33, 23 and 35). The deep lagoonal facies marks a widespread deepening event that were clearly recorded on the flanks wells (e.g. wells 21, 26, 30 and 45) associated with the regional maximum flooding unit (MFU, K80) of the Shu'aiba 2nd-order composite sequence, coeval to the K80 of Sharland et al. (2001). This MFU is also recorded within the rudist buildup barrier as a thin unit of *Palorbitolina* wackestone facies.

1.20   Facies Anatomy of HFS 6 (S6)

Sequence 6 has well established rudist barrier banks around the field and records the shallowest water facies of the Shu'aiba Formation associated with subaerial exposure surface (Fig. 1.20d). Rudist buildups are mainly dominated by the high-energy, recumbent *Offneria* rudists (Fig. 1.7f), that formed more continuous in situ rudist barriers. Therefore, the rudist facies predominate across the entire platform, either as a rim of barrier banks, or back-bank, or fore-bank fragmented rudist rudstone. The platform interior on the northern block is dominated by high-energy grainstone as well as by a new established local rudist buildups in the central part of the platform (Well 11 and 44). The platform interior in the southern block also is dominated by moderately deep back-bank rudist facies, except where deep restricted ponds in the central part of the platform interior (Wells 22, 12 and 3). The northeastern flanks is dominated by fine skeletal wackestone/mudstone deposited in slope and open marine settings as in previous sequences, but subtle shallowing occurs in this stage to more detrital skeletal packstone. The rudist buildups in this sequence are capped by thin, well-rounded, well-cemented rudist rudstone facies of high-energy beach environments (Fig. 1.7d), followed by an exposure surface, marking the termination of rudist buildups in the southern block and the end of the 3rd-order sequence 2.

1.21   Facies Anatomy of HFS 7 (S7)

Sequence 7 is dominated by extensive shallow lagoonal/inner ramp environments with fine skeletal peloidal milliolid packstone/wackestone facies on both north and south blocks (Fig. 1.20e). However, the northern block still developed rudist barrier banks on the eastern side, backed by shallow lagoonal sediments. These rudist buildups have similar trends to previous rudist buildups, but are slightly shifted basinward representing slight progradation of the platform margin settings. These rudists are possibly discontinues separated by tidal channels. The intraplatform depression still contains fragmented rudist skeletal grainstone, therefore a rudist buildups likely formed around the trough to source this grainstone facies. The southern block is entirely dominated by the shallow lagoonal sediments excepts where *Agriopleura* rudist floatstone that developed local mounds.

1.22   Facies Anatomy of HFS 8 (S8)

Sequence 8 only occurs on the northern block, while the southern block was subearially exposed (Fig. 1.20f). The northern block is dominated by shallow lagoonal facies that prograded basinward. The intraplatform channel was buried by the shallow lagoonal facies. Rudist buildups did not form during this sequence.

1.23   Facies Anatomy of HFS's 9 and 10 (S9 and S10)

Sequences 9 and 10 are Upper Aptian sequences formed only on the northern lock platform edges as a prograding sequences into the basin during a long-term sea level fall (Fig. 1.20g). Facies anatomy of these sequences include shallow water rudist/stromatoporoid/coral marginal facies formed marginal setting on the eastern and around the far northern part of the field. An upper Aptian wedge along the western flank (Well 45) consists solely of shallow lgoonal facies, with no rudist or shallow marginal facies occurred in this wedge. The shallow water marginal facies on the eastern flank passes laterally into slope and deep open marine facies. Moreover, these Upper Aptian sequences begin with a flooding even of an argillaceous mudstone at their base interpreted as low-stand wedges. This argillaceous mudstone
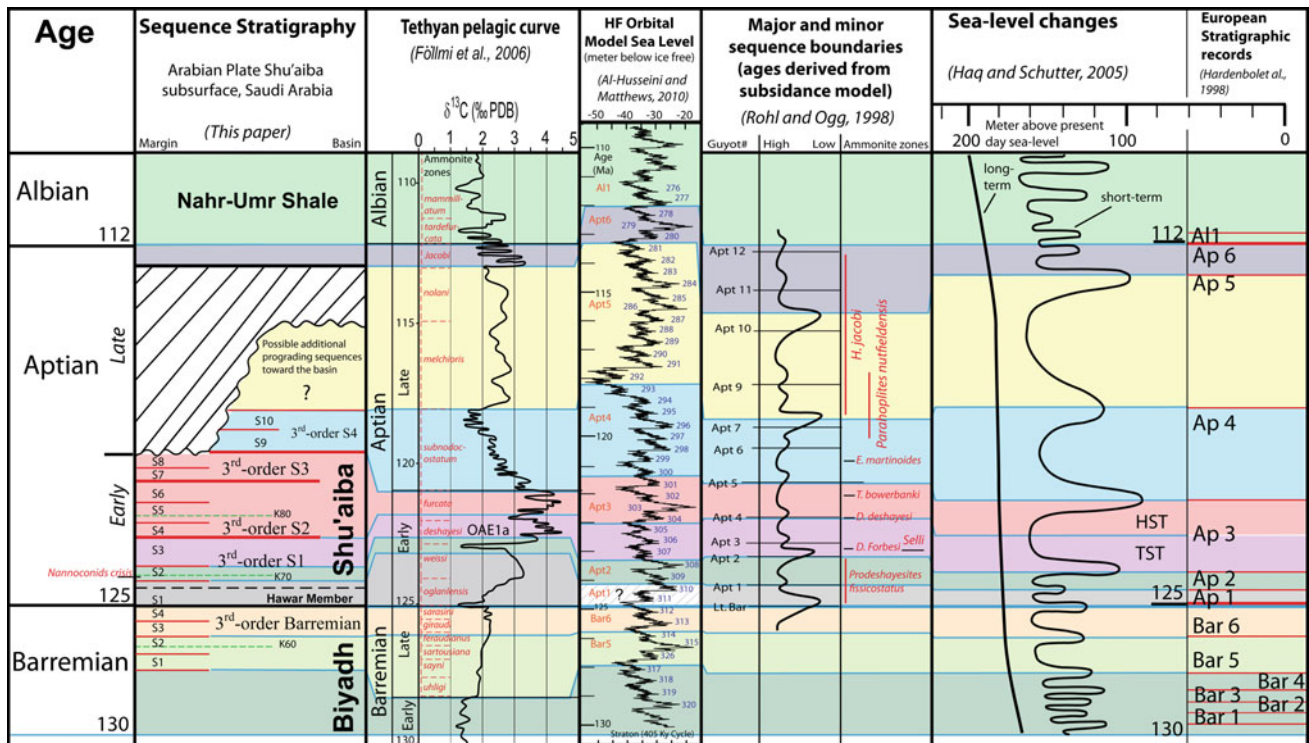
Fig. 1.21 Composite global correlation between the Arabian Plate Biyadh and Shu'aiba formations and the global stratigraphic records. The colors used for each sequence were arbitrary to highlight the sequence. Supplementary figure. Legend, symbols and color codes of lithofacies used in the above cross sections

is interpreted as a continuous N-S elongate wedge that may act as a reservoir barrier to fluid flow movement. The interpretation of this mudstone as a low-stand wedge may imply a separation in the reservoir units, however, pressure data is required to substantiate this interpretation.

1.23.1 Global Correlation

The Lower Cretaceous Barremian and Aptian successions of the subsurface Biyadh and Shu'aiba Formations record major subaerial sequence boundaries and dramatic facies changes associated with growth and demise of carbonate platforms that can be linked to global changes in sea-level, ocean chemistry, and Milankovitch orbital forcing. To evaluate this relationship, the stratigraphic framework of the Biyadh and Shu'aiba Formations presented in this paper were calibrated to biostratigraphy and stable isotope chemostratigraphy and correlated to: (1) the global sea-level curve of Haq and Schutter (2008); (2) the sequence stratigraphic records from European sections (Hardenbol et al. 1998); (3) the high-resolution sea-level changes recorded in Pacific guyots (Rohl and Ogg 1998); (4) the high-resolution orbital model sea-level (Al-Hussaini and Matthews 2010) and (5) the global carbon isotope curve of the Tethyan

pelagic records (Föllmi et al. 2006) (Fig. 1.21). This correlation suggests that the 3rd-order sequences of the Biyadh and Shu'aiba Formations formed in response to global sea-level changes and to rapid Earth's climate changes. Also, most HFS's can be correlated globally, but are less pronounced than the 3rd-order sequences. The high-resolution orbital forcing model of Al-Husseini and Matthews (2010) is controlled by the 405 ky eccentricity cycles (called stratons), driven mainly by glacio-eustaty. Some of these stratons are correlated directly to some HFS's in this study, especially the HFS's in the Biyadh and the lower part of the Shu'aiba Formations. The following is a brief discussion of each sequence with their correlated sea-level and chemostratigraphic curves and the significant and implications of their global correlations.

1.23.2 3rd-Order Barremian Sequence (Biyadh Formation)

The 3rd-order composite sequence of the Biyadh Formation is composed of four HFS's (S1-S4) and is coeval to Ap Bar2 of van Buchem et al. (2010). The correlation suggests that S1 and S2, which are the TST of this sequence, are correlated with Bar 5 in Hardenbol et al. (1998) and formed

during one sea-level rise and fall of Haq and Schutter (2008) and correlates to stratons 326-314 of the orbital sea-level model (Al-Husseini and Matthews 2010). The extreme spike of the orbital model at straton 315, represents the maximum sea-level rise and is correlated with the MFS of the Biyadh 3rd-order composite sequence corresponding to the deepest water facies in Biyadh Formation, which is the chalky mudstone facies at the middle of Biyadh S2. This MFS is well correlated with the 3rd-order regional MFS (K60) of Sharland et al. (2001) and van Buchem et al. (2010). The coeval Tethys carbon isotope curve of this sequence shows subtle change with an overall minor gradual increase from 1.5‰ at the base of S1 to 2.2‰ at the top of S2 (Fig. 1.21).

The HST of the 3rd-order Biyadh sequence is composed of two HFS's (S3 and S4) and they are correlated to the global Bar 6 of Hardenbol et al. (1998), and formed during one global sea-level rise and fall of Haq and Schutter (2008). S3 and S4 are well correlated with stratons 313 and 312 of Al-Husseini and Matthews (2010), suggesting that each of these HFS's is an ~400 ky cycle. This correlation suggests that the Biyadh 3rd-order composite sequence can be separated into two smaller scale 3rd-orders sequences, each on the order of ~1–1.5 My duration, where the mud dominated- TST sequences S1 and S2 of the Biyadh Formation comprise one sequence coeval to Bar 5, and the grain-dominated- HST sequences S3 and S4 comprise another sequence coeval subtle change with an overall minor gradual increase from 1.5‰ at the base of S1 to 2.2‰ at the top of S2 (Fig. 1.21).

The HST of the 3rd-order Biyadh sequence is composed of two HFS's (S3 and S4) and they are correlated to the global Bar 6 of Hardenbol et al. (1998), and formed during one global sea-level rise and fall of Haq and Schutter (2008). S3 and S4 are well correlated with stratons 313 and 312 of Al-Husseini and Matthews (2010), suggesting that each of these HFS's is an ~400 ky cycle. This correlation suggests that the Biyadh 3rd-order composite sequence can be separated into two smaller scale 3rd-orders sequences, each on the order of ~1–1.5 My duration, where the mud dominated- TST sequences S1 and S2 of the Biyadh Formation comprise one sequence coeval to Bar 5, and the grain-dominated- HST sequences S3 and S4 comprise another sequence coeval to Bar 6. S3 and S4 contains many small-scale parasequences (13 parasequences for each sequence). Since S3 and S4 are ~400 ky in duration; each parasequence appears to be fifth-order cycles spanning ~40 ky duration and may be related to obliquity orbital forces.

1.23.3 3rd-Order Early Aptian Shu'aiba Sequence 1

The Early Aptian 3rd-order sequence 1 is composed of three sequences (S1, S2 and S3) and occurred in the lower part of the Shu'aiba Formation and includes the Hawar unit. This sequence is coeval to the Ap Apt1 and 2 of van Buchem et al. (2010). SB1 is a major sequence boundary that separates the Barremian Biyadh Formation from the Aptian Hawar unit and Shu'aiba Formations and it is linked to the Barremian-Aptian boundary (~125 My) and correlates with the global sequence boundary at the base of Apt 1 in Hardenbol et al. (1998) and Rohl and Ogg (1998). This boundary represents a major high magnitude sea-level fall possibly on the order of tens of meters that can be traced worldwide (Hillgartner et al. 2003; Droste 2010; Al-Husseini and Matthews 2010). This boundary is associated with a negative carbon isotope excursion that also is correlated worldwide and is used in this correlation as a datum for the global correlation (Fig. 1.27). This boundary also reflects major rapid change in global climate from cooling and sea-level fall during the Late Barremian to global warming and sea-level rise during the overlain Early Aptian (Jenkyns 2003; Weissert and Erba 2004). The major negative carbon isotope excursion in the earliest Early Aptian is related to dissociation of methane hydrates, possibly triggered by an increase in volcanism on the Ontong-Java Plateau (dated ~125–119 Ma) with large amount of CO_2 released to the atmosphere causing a greenhouse warm climate and coincident warming of bottom waters on continental shelves that resulted in global warming and sea-level rise in the earliest Early Aptian (Larson and Erba 1999; Weissert and Erba 2004; Föllmi et al. 1994, 2006; Jahren et al. 2001; Jenkyns 2003). The Barremian-Aptian boundary in the Shu'aiba Formation is overlain by S1 with the deposition of the argillaceous Hawar unit. S1 is correlated with Apt1 in Hardenbol et al. (1998) and Apt1 in Rohl and Ogg (1998), associated with global sea-level rise in the earliest Aptian (Fig. 1.14). The Early Aptian stratons 311 and 310 are correlated with Apt1 and thus seem to be correlated with the Hawar unit in the Shu'aiba Formation. However, Al-Husseini and Matthews (2010) correlated these stratons with lowstand wedge sequences only present in the Oman Ocean margin that onlap onto the SB1 sequence boundary (Droste 2010). Stratons 311 and 310 were interpreted to be coeval to the subaerial exposure of SB1 and thus the Hawar unit is correlated to stratons 309 and 308. This correlation may work as a regional interpretation within the Arbian Plate sequence

stratigraphic framework, but when stratons 309 and 308 are correlated globally to Apt1 of Hardenbol et al. (1998), there will be a problem with correlating the rest of the sequences with the sea-level curve and global isotope signature. For instance, if stratons 309 and 308 are linked to the Hawar unit and correlated with the global Apt 2 instead of Apt1, that will make stratons 304-301 equivalent to Ap3 of Hardenbol et al. (1998), and correlative to the global OAE1a event as interpreted by Al-Husseini and Matthews (2010). That correlation suggests that the rudist dominated (3rd-order sequence 2) in this study, or the equivalent AP Apt 3 of van Buchem et al. (2010) correlates with the OAE1a (Selli unit) in the standard isotope curve of Föllmi et al. (2006). The OAE1a should correlate to the *Lithocodium* dominated interval of the Shu'aiba Formation which is S3 (within the 3rd-order sequence 1) in this study or Ap Apt 2 of van Buchem et al. (2010). The carbon isotope records of Shu'aiba Formation integrated with biostratigraphy (Fig. 1.14) strongly suggest that the Hawar unit is correlated with the first negative excursion above the Barremian-Aptian boundary and hence is correlated to Apt 1 and the sea-level rise above the boundary.

S2 of the Shu'aiba Formation records a major deepening event associated with the deposition of chalky *Hedbergella* mudstone, which is the deepest water facies of the Shu'aiba platform. This flooding event is coeval to K70 of Davies et al. (2002) and it correlates to the onset of the major positive enrichment of carbon isotope values, just beneath OAE1a. MFS K70 is possibly correlated to the highest sea-level rise of straton 308 of Al-Husseini and Matthews (2010) and to the sea-level rise of Ap 2 of Hardenbol et al. (1998). S2 here with its deeper facies and K70 likely correlates with the Early Aptian nannoconid crisis defined from the Tethyan pelagic sediments. The nannoconid crisis was caused by a reduction in calcification, due to the high atmospheric CO_2 just before the OAE 1a, and is associated with a global warming event and sea-level rise (Luciani et al. 2006).

The Shu'aiba S3 is dominated by an extensive *Lithocodium aggregatum* wackestone and is correlated to the maximum carbon isotope enrichment and to the OAE 1a. S3 possibly correlates to stratons 307-305 and to the TST of the Ap3 of Hardenbol et al. (1998). This correlation differs from the correlation of Al-Husseini and Matthews (2010) that correlate stratons 304-301 to the OAE1a and to the Ap Apt3

of van Buchem et al. (2010). This latter correlation contradicts the biostratigraphic zonation, therefore, the correlation provided here is suggested as an update for correlating the Arabian Plate stratigraphic records to the global records.

1.23.4 3rd-Order Early Aptian Shu'aiba Sequence 2

This 3rd-order sequence is a rudist bearing unit composed of three sequences (S4,S5 and S6) that formed in the middle part of the Shu'aiba Formation and it is coeval to the Ap Apt3 of van Buchem et al. (2010). This sequence correlates with the upper part (HST) of Ap 3 of Hardenbol et al. (1998), deposited during the HST of the global sea-level curve of Haq and Schutter (2008). It also correlates to the Apt 4 sequence in the Pacific Guyot of Rohl and Ogg (1998). This sequence possibly correlates with stratons 304-301 where the maximum sea-level rise occurred within straton 303 coeval to the proposed MFS of the Shu'aiba composite sequence presented here, and corresponding to the regional K80 of Sharland et al. (2001). This MFS occurs within S5 and is well recorded in all wells of the study area. The carbon isotope curve of the Tethys pelagic record of Föllmi et al. (2006) correlated to this unit shows enrichment values at the *furcata* ammonite zone corresponding to the maximum sea-level rise. This enrichment of carbon isotope values should not be confused with the lower major enrichment that correlates to the *deshayesi* ammonite unit related to the global OAE1a. The carbon isotope values of the Shu'aiba platform record within this sequence range from 4.5 to 5‰ with more uniform values corresponding to the development of the extensive rudist buildups (Fig. 1.14). Al-Husseini and Matthews (2010), however, correlated stratons 304–301 to Apt 3 of Hardenbol et al. (1998) and to Ap Apt3 of van Buchem et al. (2010), but correlated these stratons to the lower major carbon isotope enrichment of the *deshayesi* ammonite unit associated with the OAE1a. However, this interpretation contradicts with the stratigraphic framework, facies and chemostratigraphy presented here, because both the 3rd-order sequence 2 in this paper and the Ap Apt3 of van Buchem et al. (2010) are rudist-dominated sequences that developed above the OAE1a. The 3rd-order sequence 2 represents a recovery of carbonate productivity after the demise of carbonate

buildups in the lower Hawar unit, the nannoconid crisis and the *Lithocodium aggregatum* interval that acts as a substitute to the rudist buildups during the carbon perturbation intervals and OAE1a in the Early Aptian (Immenhauser et al. 2005).

1.23.5 3rd-Order Early Aptian Shu'aiba Sequence 3

This 3rd-order sequence consists of S7 and S8 and it is part of the HST of the Shu'aiba composite sequence. This sequence appears to be a regional, rather than a global individual sequence, but when combined with 3rd-order S2, it correlates with the late HST of the global Ap3 of Hardenbol et al. (1998). In the marginal setting, the top of this sequence records a prominent sea-level fall that correlate with the global sea-level fall at the top of Ap3.

1.23.6 3rd-Order Late Aptian Shu'aiba Sequence 4

Late Aptian Shu'aiba sequence 4 formed only on the platform edge as a progradational wedge composed of S9 and S10, representing a forced regression system and is coeval to the Ap Apt4 of van Buchem et al. (2010). It also correlates with Ap4 of Hardenbol et al. (1998) and with Apt5 in Rohl and Ogg (1998). The orbital model shows eight stratons (300–293) correlate to this sequence, suggesting that more progradational sequences may occur basinward in the study area, similar to the nine prograding sequences interpreted from seismic data in nearby fields (Pierson et al. 2010; Yose et al. 2010). The stratigraphic record from the Pacific Guyots shows a maximum of two or three sequences correlated to the eight prograding sequences in the Arabian Plate. This suggests that these prograding sequences might be correlated regionally rather than globally, reflecting more local relative sea-level changes. The carbon isotope curve shows gradual upward depletion in this sequence indicated a cooling interval may have followed the major positive enrichment associated with the OAE 1a.

The global sequence Ap5 of Hardenbol et al. (1998) correlates to Apt9, Apt10 in the Pacific Guyots and to stratons 292–281. This sequence does not form in the Shu'aiba study interval here but may occur in the far eastern part of the Shu'aiba platform as small scale prograding wedges. The orbital cycles in Ap5 suggest a substantial glacio-eustatic lowstand on the order of ∼30 m sea-level drop (Al-Husseini and Matthews 2010). This sea-level drop culminates to the top of Ap5 of Hardenbol et al. (1998) where the largest sea-level drop of the Aptian stage occurred (Haq and Schutter 2008). The Pacific guyot also records a

major sea-level drop just above Apt10 that correlates to the global sea-level curve. The Late Aptian unconformity at the top of the Shu'aiba Formation formed during this major sea-level drop, producing a major subaerial unconformity and karst features. The base of the Nahr-Umr Formation represents the latest Aptian transgression (Al-Husseini and Matthews 2010) and correlates to Apt 6 of Hardenbol et al. (1998), Apt 12 of the Pacific guyots and the global sea-level curve of Haq and Schutter (2008). Nahr-Umr shale formed above the top Shu'aiba unconformity and record a widespread sea-level rise, possibly representing the meltdown of the Late Aptian glaciations (Al-Husseini and Matthews 2010); and corresponding to an abrupt positive enrichment in the carbon isotope curve just beneath the Aptian/Albian boundary.

1.23.7 Implication and Significance of Global Correlations

The global correlation presented above suggests that the Biyadh and Shu'aiba Formations records a strong influence of the 3rd-order global sea-level changes associated with changes in carbon isotope signature, ocean chemistry and global climate on the development of Biyadh and Shu'aiba platforms. This correlation suggests major differences in the sea-level magnitude are associated with changes in stratigraphic accumulation between the Barremian and the Aptian stages (Fig. 1.21). The Barremian stage has lower amplitude sea-level fluctuations with relatively thinner sequences compare to the Aptian stage that has higher amplitude sea-level fluctuations associated with thicker sequences and more pronounced condensed sections. Also, the Barremian stage is dominated by a small-scale parasequences (decimeter scale), whereas the Aptian stage is dominated by larger-scale parasequences (meter scale), except the Hawar unit. The Barremian parasequences of the Biyadh Formation have an average duration of 30–40 ky, whereas the Aptian parasequences have an average duration of 100 ky. This suggests that the glacio-eustatic control of the eccentricity orbital cycles were not the main driving mechanism for both the Barremian and Aptian stages. The parasequences of the Barremian Biyadh Formation possibly reflect obliquity cycles, whereas the parasequences of the Aptian Shu'aiba Formation may reflect small-scale eccentricity. Therefore, the Barremian stage may have recorded a warmer global climate, compared to the Aptian that records cooling and warming intervals with possible glaciations recorded during the base (SB1), middle (SB7) and upper part of the Aptian. Thus, the Aptian stage is not a uniform greenhouse period. Instead, it is more transitional time interrupted by glacial events as suggested by stratigraphic records, sea-level fluctuations and isotope data.

1.24 Conclusions

A detailed high-resolution rock-based stratigraphic framework of the Lower Cretaceous (Barremian and Aptian) Biyadh and Shu'aiba Formations provides an updated stratigraphic and depositional framework for these units. This framework are developed from 55 cored wells, biostratigraphy and 26 carbon isotope curves, covering the entire Shu'aiba platform in one the most prolific giant carbonate reservoirs in the Middle East. The Late Barremian Biyadh Formation is composed of one 3rd-order composite sequence (~3 My), comprised of four high-frequency sequences (S1–S4). S1 and S2 are the TST of the Barremian composite sequence and K60 is the composite MFS, occurring within S2. These sequences are composed predominantly of relatively deep subtidal mud-dominated *Palorbitolina* chalky wackestone/mudstone facies. S3 and S4 are the HST of the Barremian composite sequence and are composed of high-energy shallow water subtidal with Caprotinid rudist and peloidal grainstone facies. This sequence is capped by a regional subaerial boundary (SB1) recording a global sea level fall.

The entire Shu'aiba Formation formed a 2nd-order composite sequence (~7 My duration) composed of four 3rd-order sequences (~1–2 My) and ten HFS's (S1–S10; each ~405 ky–1 My duration). S1 records the initial TST with the deposition of Hawar unit, followed by S2 that records the deepest water facies and the regional MFS (K70). S3 is the late TST of the Shu'aiba composite sequence and is characterized by the deposition of extensive *Lithocodium aggregatum*/coral facies associated with the onset of differentiated platform-to-basin settings with slight clinoform and backstepping geometries. The 3rd-order sequence 2, consisting of S4-S6, records the onset of a well-established platform-margin setting containing rudist buildup facies that changed toward the platform interior into lagoonal facies and transitioned basinward into fore-bank, slope and basinal settings with pronounced clinoform geometries. This sequence has a transgressive lag at its base dominated by *Glossomyophorus* rudists that deepen upward to the regional composite MFS (K80). This is followed by the higher energy bank-crest of in situ caprinid rudist rudstone facies that is capped by well-rounded rudist fragments deposited in beach environments followed by the development of exposure surface (SB 7). S7 and S8 are dominated by shallow lagoonal peloidal miliolid packstone facies associated with local *Agriopleura* floatstone, representing the HST of the Shu'aiba composite sequence.

The newly identified Upper Aptian sequences S9 and S10 are recorded on the northern-block within prograding platform edge and slope settings that formed during a major forced regression. These sequences were identified on the basis of chemostratigraphic analysis calibrated with biostratigraphy. These sequences form a lowstand wedge of argillaceous wackestone facies that may act as a possible reservoir baffle zone, changing upward to high energy marginal facies of mixed rudist and stromatoporoid/coral facies. Regional correlation suggests that more prograding sequences likely formed basinward.

High-resolution maps of facies distribution were generated to define the depositional anatomy and reservoir facies distribution. These maps are crucial when integrated with petrophysical parameters to determine the 3-D reservoir model, and help predict the uncertainty between the wells, thus enhancing the 3-D reservoir characterization. The Shu'aiba platform is divided into northern and southern blocks, each with their own distinctive facies distribution and depositional anatomies. The northern block records higher energy facies with grainstone shoals/channels developed in the platform interior, whereas the southern block has thicker *Lithocodium aggregatum* algal platform facies with relatively lower energy environments. The southern block has deeper lagoonal environments within the platform interior.

A refined global correlation between the Arabian Plate and global stratigraphic records and global sea-level curves was generated on the basis of this study. This correlation strongly suggests a direct influence of the 3rd-order sea-level fluctuations in the Biyadh and Shu'aiba Formations. The Shu'aiba Formation records the perturbations of global carbon cycles associated with the nannoconids crisis and OAE1a. The global nannoconids crisis appears to be correlated with the deep chalky mudstone facies associated with the MFS in S2, that is coeval to the regional MFU (K70). The OAE1a with its distinctive carbon isotope values is coeval to the *Lithocodium aggregatum* facies of S3 and correlated to the TST of global sequence AP3. This correlation also suggests that Aptian HFS's were mainly controlled by glacio-eustatic sea-level changes and the long term eccentricity cycles (~405 ky) were the main driving mechanism. The Barremian sequences record low magnitude sea-level changes with relatively thinner sequences compared to the Aptian. Moreover, the Barremian parasequences likely reflect obliquity (~40 ky), whereas the Aptian parasequences are likely controlled by small scale eccentricity (~100 ky) cycles. The Shu'aiba Formation records major subaerial hiatus reflecting glacial intervals, interrupted by major flooding units reflecting global warming intervals. These changes in the stratigraphic records and sea-level magnitude between the Barremian and Aptian suggest a

prevailed greenhouse period during the Barremian, changed rapidly into a transitional climate period in the Aptian interrupted by glacial events.

References

Aktas G, Hughes GW (2000) Stratigraphic framework of Shu'aiba Formation, Shaybah Field, Saudi Arabia: a basis for reservoir development of an Aptian carbonate ramp complex. In: 4th Middle East Geosciences Conference, GEO 2000, Abstracts. GeoArabia, vol 5, no 1, p 11

Al-Husseini MI, Matthews RK (2010) Tuning Late Barremian–Aptian Arabian Plate and global sequences with orbital periods. In van Buchem FSP et al. (eds) Barremian–Aptian stratigraphy and Hydrocarbon habitat of the Eastern Arabian Plate: Manama, Bahrain, Gulf Petro Link, GeoArabia Special Publication 4, vol 1, pp 199–228

Alley NF, Frakes LA (2003) First known Cretaceous glaciation: living stone Tillite member of the Cadna-owie Formation, South Australia. Aust J Earth Sci 50:139–144

Alsharhan AS (1995) Facies variation, diagenesis, and exploration potential of theCretaceous rudist-bearing carbonate of the Arabian Gulf. AAPG Bulletin 79(4):531–550

AL-Ghamdi NM, Read JF (2010) Facies-based sequence-stratigraphic framework of the Lower Cretaceous rudist platform, Shu'aiba Formation, Saudi Arabia. In van Buchem et al (eds) Barremian–Aptian stratigraphy and hydrocarbon habitat of the Eastern Arabian Plate, vol 4, pp 367–410. GeoArabia Special Publication

AL-Ghamdi NM, Pope M (2014) Integrated high-resolution chemostratigraphy and facies-based stratigraphic architecture of the Lower Cretaceous (Aptian), Shu'aiba Formation, Saudi Arabia. AAPG Bulletin 98(8):1521–1549

Alsharhan AS, Nairn AEM (1986) A review of the Cretaceous Formations in the Arabian Peninsula and Gulf: Part I. Lower Cretaceous (Thamama Group) Stratigraphic and Paleogeography. Journal of Petroleum Geology 9:365–392

Borgomano J, Masse JP, AlMaskiry S (2002) The Lower Aptian Shuaiba carbonate outcrops in Jebel Akhdar, northern Oman: Impact on static modelling for Shuaiba petroleum reservoirs. AAPG Bull 86:1513–1529

Christian L (1997) Cretaceous subsurface geology of the Middle East region. GeoArabia 2(3):239–255

Davies RB, Casey DM, Horbury AD, Sharland PR, Simmons MD (2002) Early to mid-Cretaceous mixed carbonate-clastic shelfal systems: examples, issues and models from the Arabian Plate. GeoArabia 7:541–598

Droste HJ (2010) Sequence-stratigraphic framework of the Aptian Shu'aiba Formation in the Sultanate of Oman. In van Buchem FSP, Al-Husseini MI, Maurer F, Droste HJ (eds) Barremian-Aptianstratigraphy and hydrocarbon habitat of the Eastern Arabian Plate. GeoArabia Special Publication 4, Gulf PetroLink, Bahrain, vol 1, pp 229–283

Föllmi KB, Weissert H, Bispin M, Funk H (1994) Phospho genesis, carbonisotope stratigraphy, and carbonate platform evolution along the Lower Cretaceous northern Tethyan margin. Geological Society of America Bulletin 106:729–746

Föllmi KB, Godet A, Bodin S, Linder P (2006) Interactions between environmental change and shallow water carbonate buildup along the northern Tethyan margin and their impact on the Early Cretaceous carbon isotope record. Paleoceanography 21 ((PA4211)):1–16

Frakes LA (1999) Estimating the global thermal state from Cretaceous sea surface and continental temperature data. In Barrera E, Johnson CC (eds) Evolution of the Cretaceous ocean-climate system geological society of America. Special paper 332, pp 49–57

Frakes LA, Alley NF, Deynoux M (1995) Early Cretaceous ice rafting and climate zonation in Australia. Int Geol Rev 37:567–583

Greselle B, Pittet B (2005) Fringing carbonate platform at the Arabian Plate margin in northern Oman during the Late Aptian Middle Albian: Evidence for high-amplitude sea-level changes. Sed Geol 175:367–390

Hardenbol J, Thierry J, Farley MB, Jacquin T, de Graciansky PC Vail P (1998) Mesozoic and Cenozoic sequence chronostratigraphic framework of European basins. In Graciansky PC et al. (eds) Mesozoic and Cenozoic sequence stratigraphy of European Basins. SEPM Special Publication vol 60, pp 3–13, charts 1–8

Haq BU, Al-Qahtani AM (2005) Phanerozoic cycles of sea-level change on the Arabian Platform. GeoArabia 10(2):127–160

Haq BU, Shutter SR (2008) A chronology of Paleozoic sea-level changes. Science 322:64–68

Harris PM, Frost SH, Seiglie GA, Schneidermann N (1984) Regional unconformities and depositional cycles, Cretaceous of the Arabian Peninsula. Am Assoc Pet Geol Bull 36:67–80

Hillgartner H, van Buchem FSP, Gaumet F, Razin P, Pittet B, Grotsch J, Droste H (2003) The Barremian-Aptian evolution of the eastern Arabian carbonate platform margin (northern Oman). J Sediment Res 73:756–773

Huang C, Hinnov L, Fischer AG, Grippo A, Herbert T (2010) Astronomical tuning of the Aptian Stage from Italian reference sections. Geology 38:899–902

Huck S, Heimhofer U, Immenhauser A (2012) Early Aptian algal bloom in a neritic proto–North Atlantic setting: Harbinger of global change related to OAE 1a? Geol Soc Am Bull 133:637–660

Hughes GW (1997) The great pearl bank barrier of the Arabian Gulf as a possible Shu'aiba Analogue. GeoArabia 2(3):279–303

Hughes GW (2000) Bioecostratigraphy of the Shu'aiba Formation, Shaybah field, Saudi Arabia. GeoArabia 5(4):545–578

Immenhauser A, Matthews RK (2004) Albiansea-level cycles in Oman: The 'Rosetta Stone' approach. GeoArabia 9(3):11

Immenhauser A, Hillgärtner H, Sattler U, Bertotti G, Schoepfer P, Homewood P, Vahrenkamp V, Steuber T, Masse J-P, Droste HJ, Tall-vanKoppen JJ, vanderKooij B, vanBentum E, Verwer K, Hoogerduijn-Strating E, Swinkels W, Peters J, Immenhauser-Potthast I, AlMaskery S (2004) Barremian-lower Aptian Qishn Formation, Haushi-Huqf area, Oman: a new outcrop analogue for the Kharaib/Shu'aiba reservoirs. GeoArabia 9:153–194

Immenhauser A, Hillgartner H, vanVentum E (2005) Microbial-foraminiferal episodes in the Early Aptian of the southern Tethyan margin: ecological significance and possible relation to oceanic anoxic event 1a. Sedimentology 52:77–99

Jahren AH, Arens NC, Sarmiento G, Guerrero J, Amundson R (2001) Terrestrial record of methane hydrate dissociation in the Early Cretaceous. Geology 29(2):159–162

Jenkyns HC (2003) Evidence for rapid climate in the Mesozoic-Palaeogene green house world. Phil Trans Royal Society, London A361:1885–1916

Kerans C, Tinker S (1997) Sequence stratigraphy and characterization of carbonate reservoirs. SEPM Short Course Notes No. 40, 130 p

Larson RL, Erba E (1999) Onset of the mid-Cretaceous green house in the Barremian-Aptian: igneous events and the biological, sedimentary and geochemical responses. Paleoeanography 14:663–678

Luciani V, Cobianchi M, Lupi C (2006) Regional record of a global oceanic anoxic event: OAE1a on the Apuila platform margin, Gargano Promontory, Southern Italy. Cretac Res 27:754–772

Matthews RK, Frohlich C (2002) Maximum flooding surfaces and sequence boundaries: comparisons between observations and orbital forcing in the Cretaceous and Jurassic (65–190 Ma). GeoArabia 7 (3):502–538

Pierson BJ, Eberli GP, Al-Mehsin KM, Al-Menhali S, Warrlich GMD, Droste HJ, Maurer F, Whitworth J, Drysdale D (2010) Seismic stratigraphy and depositional history of the Upper Shu'aiba (LateAptian) in the UAE and Oman. In van Buchem FSP, Al-Husseini MI, Maurer F, Droste HJ (eds) Barremian-Aptian stratigraphy and hydrocarbon habitat of the eastern Arabian Plate. GeoArabia Special Publication 4, Gulf PetroLink, Bahrain

Pittet B, van Buchem FSP, Hillgärtner H, Grotsch P, Razin J, Droste H (2002) Ecological succession, paleo-environmental change, and depositional sequences of Barremian Aptian shallow-water carbon atesin northern Oman. Sedimentology 49:555–581

Rohl U, Ogg JG (1998) Aptian-Albian eustatic sea levels. In GF Camoin, PJ Davies (eds) Reefs and carbonate platforms in the Pacific and Indian Oceans. International Association of Sedimentologists, Special Publication 25, pp 77–92

Sharland PR, Archer R, Casey DM, Davies RB, Hall SH, Heward AP, Horbury AD, Simmons MD (2001) Arabian Plate sequence stratigraphy. GeoArabia, Special Publication 2, PetroLink, Bahrain, p 371

Sharland PR, Casey DM, Davies RB, Simmons MD, Sutcliffe OE (2004) Arabian Plate sequence stratigraphy. GeoArabia 9:199–214

Skeleton PW, Masse J-P (2000) Synoptic guide to the Lower Cretaceous rudist bivalves of Arabia. Soc Econ Paleontol Mineral 69:85–95

Stoll HM, Scharge DP (2000) High resolution stable isotope records from the Upper Cretaceous of Italy and Spain: glacial episodes in a greenhouse planet? Geological Society of America Bulletin 112:308–319

Strohmenger CJ, Weber LJ, Ghani A, Al-Mehsin K, Al-Jeelani O, Al-Mansoori A, Al-Dayyani T, Vaughan L, Khan SA, Mitchell JC (2006) High-resolution sequence stratigraphy and reservoir characterization of upper Thamama (Lower Cretaceous) reservoir of a giant AbuDhabi oilfield, United Arab Emirates. In Harris PM, Weber LJ (eds) Giant hydrocarbon reservoir of the world: From rockstore servoir characterization and modeling 2006. AAPG, Memoir 88/SEPM Special Publication, pp 141–173

van Buchem FSP, Pittet P, Hillgartner H, Grotsch J, Mansouri AI, Billing IM, Droste HHJ, Oterdoom WH, Van Steenwinke M (2002) High-resolution sequence stratigraphic architecture of Barremian/Aptian carbonates innorthern Oman and the United Arab Emirates (Kharaib and Shuaiba formations). GeoArabia 7:461–500

van Buchem FSP, Al-Husseini MI, Maurer F, Droste HJ, Yose LA (2010) Sequence-stratigraphic synthesis of the Barremian-Aptian of the Eastern Arabian Plate and implications for the petroleum habitat. In vanBuchem FSP, Al-Husseini MI, Maurer F, Drost HJ (eds) Barremian-Aptian stratigraphy and hydrocarbon habitat of the eastern Arabian Plate. GeoArabia Special Publication 4, Gulf Petro Link, Bahrain vol 1, pp 9–48

Weissert H, Lini A (1991) Ice age interludes during the time of Cretaceous greenhouse climate? In Muller DW, Mckenzie JA, and Weissert H (eds) Controversies in modern geology. Academic Press, London, pp 173–191

Weissert H, Erba E (2004) Volcanism, CO2andpalaeoclimate: a LateJurassic-Early Cretaceous carbon and oxygen isotope record. J Geol Soc London 161:695–702

Witt W, Gokdag H (1994) Orbitolinid biostratigraphy of the Shu'aiba Formation (Aptian), Oman–implications for reservoir development. In Simmons MD (ed) Micropalaeontology and Hydrocarbon Exploration in the Middle East. British Micropalaeontological Society Publication Series, Chapman and Hall, Cambridge, pp 221–242

Yose LA, Strohmenger CJ, Al-Hosani I, Bloch G, Al-Mehairi Y (2010) Sequence-stratigraphic evolution of an Aptian carbonate platform (Shu'aiba Formation) eastern Arabian Plate, onshore AbuDhabi, United Arab Emirates. In van Buchem FSP, Al-Husseini MI, Maurer F, Droste HJ (eds) Barremian-Aptian stratigraphy and hydrocarbon habitat of the Eastern Arabian Plate. GeoArabia Special Publication 4, Gulf Petrolink, Bahrain, vol 2, pp 309–340

Ziegler MA (1976) Rocks and fabrics in the lower Cretaceous Shu'aiba Formation of the Shaybah field and in eastern Saudi Arabia. Internal report, Saudi Aramco

Ziegler MA (2001) Late Permian to Holocene paleofacies evolution of the Arabian Plate and its hydrocarbon occurrences. GeoArabia 6(3):445–504

The Lower Cretaceous Chouf Sandstone of Lebanon: A Regional Reservoir Level in the Levant?

Gabor Tari, Chloe Asmar, David Schneider, Fadi H. Nader,
Bernhard Grasemann, Jonathan Church, Andras Zamolyi,
Mohammad Fallah, Harald Bauer, and Georg Hatzenbichler

Abstract

The lowermost unit of the Cretaceous succession onshore Lebanon is a widespread prominent sandstone formation traditionally known as the "Grès de Base". The formation commonly consists of sandstones with some claystones, shales, lignites and locally volcanic rocks. Based on outcrop samples taken in the central and northern parts of Mount Lebanon the petrographical composition of the typical Chouf Sandstone is dominated by monocrystalline quartz (85–95%) indicating a well-sorted sandstone. Sedimentological observations suggest that the Chouf Formation deposited in fluvial, coastal plain and deltaic environments. The Barremian Chouf Sandstone is variable in thickness, ranging from a few metres to more than 700 m. Some abrupt lateral isopach variations are interpreted to be the result of deposition in individual extensional mini-basins located in a much larger overall basin extending into neighbouring Syria, Jordan and Israel/Palestine. Due to the lack of subsurface information, the isopach values were estimated from remote sensing observations of the Chouf outcrop geometries in NW Lebanon. Assuming a syn-rift origin for this formation, the thickness measurements were interpreted in the context of numerous half-grabens with the master normal faults trending WNW-ESE. The petrography of the Chouf Sandstone exposed at the surface suggests a potentially moderate to good reservoir in the subsurface as well. U–Pb detrital zircon geochronology of eight Chouf rock samples collected in NW Lebanon confirms this interpretation in agreement with earlier findings on age equivalent sandstones, some 400 km to the south. The good reservoir potential of these regional Neocomian to Barremian sandstones is mostly due to their recycled nature from quartz-rich Cambrian-Ordovician sandstones. Age-equivalent sandstones are proven reservoirs in the broader region, therefore the Chouf play could be a viable petroleum exploration target in both offshore and onshore Lebanon.

2.1 Introduction

Unlike other segments of the Eastern Mediterranean, offshore Lebanon remains undrilled to date even though academic and petroleum exploration industry efforts targeting the deepwater basin have been intensified during the last few years (e.g. Nader 2011; Hawie et al. 2013; Bou Daher et al. 2016; Ghalayini et al. 2018).

The area of study described in this paper is located in the northern part of onshore Lebanon between Beirut and Tripoli (Fig. 2.1). The main goals of this work were (a) to better define the potential petroleum reservoir character of the Lower Cretaceous siliciclastic sequence outcropping in Lebanon, (b) to better understand the regional provenance of the very distinct Chouf Sandstone Formation in relation to its correlative formations in the adjacent regions of Syria, Jordan and Israel/Palestine and (c) to further contribute to the existing geodynamic models suggesting a period of rifting for the origin of these regionally widespread sandstones.

The siliciclastic Chouf Formation, earlier regarded as Neocomian (e.g. Walley 1983) but now considered as Barremian (Granier et al. 2015, 2016), is one of the most distinctive geologic units in Lebanon sandwiched between the dominantly carbonate successions of the Mesozoic (Fig. 2.2). Early geologic mapping efforts (e.g. Heybroek

G. Tari (✉) · C. Asmar · J. Church · A. Zamolyi · M. Fallah
OMV Exploration & Production, Vienna, Austria
e-mail: Gabor.Tari@omv.com

D. Schneider
Department of Earth and Environmental Sciences,
University of Ottawa, Ottawa, Canada

F. H. Nader
Department of Geology, IFP Energies Nouvelles, Paris, France

B. Grasemann · H. Bauer · G. Hatzenbichler
Department of Geodynamics and Sedimentology,
University of Vienna, Vienna, Austria

Fig. 2.1 Geologic map of Lebanon compiled from 1:200,000 scale geologic maps (Dubertret 1955, 1975)
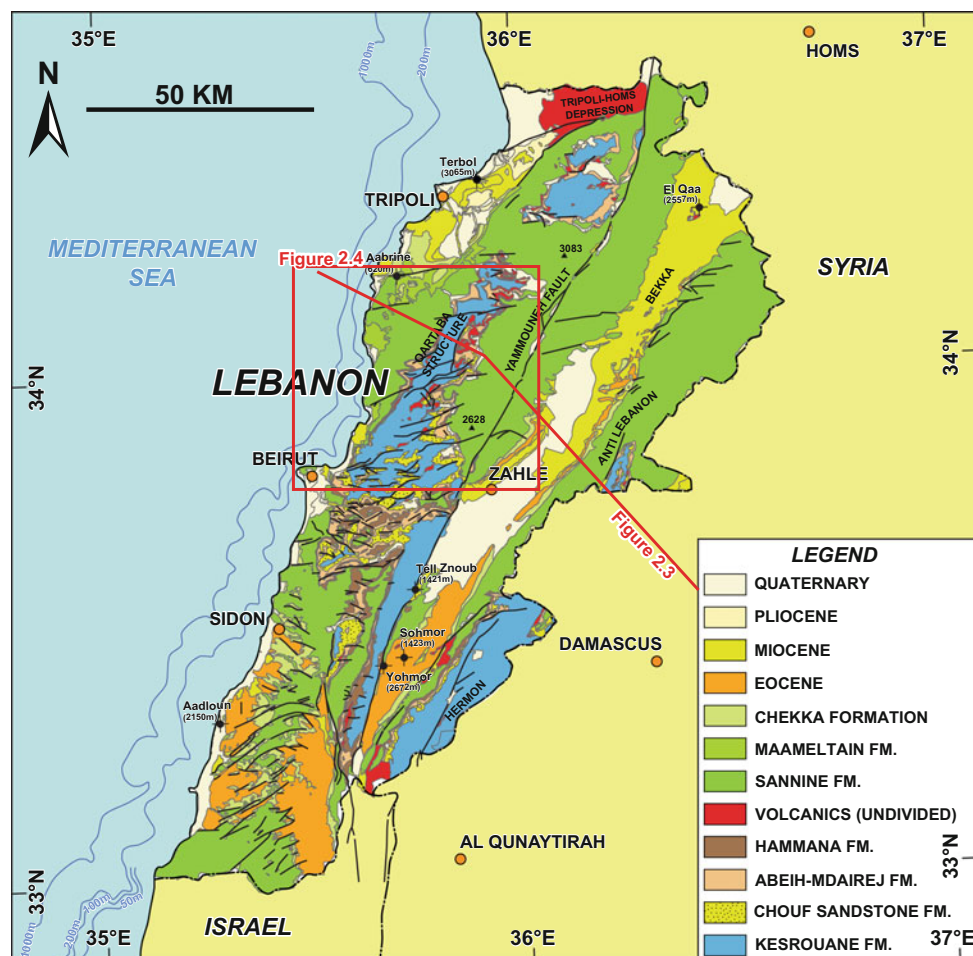
and Dubertret 1945; Dubertet 1963, 1966) established its dominant lithologic composition as a fluvial, limnic, estuarine and deltaic sedimentary succession corresponding to gradual subsidence in this part of the Levant during Valanginian to Barremian times (Fig. 2.2).

Age-equivalent Lower Cretaceous sandstones are proven reservoirs in offshore Egypt, north of the Sinai (e.g. Yousef et al. 2010) and onshore Israel (e.g. Gardosh et al. 2011). Whereas there are some wells which penetrated the Chouf onshore Lebanon (Beydoun 1977a, 1981) the potential petroleum reservoir characteristics of this formation have not been studied in detail, even though the Chouf sequence clearly extends into offshore Lebanon where it could be considered as an exploration target (Nader 2011; Ghalayini et al. 2018). Therefore our work has been specifically focusing on the petrography and the provenance of the Chouf Sandstone.

In addition to confirming the reservoir porosity and permeability values reported from the Helez Field in Israel (Gilboa et al. 1990) using samples collected on the surface in Lebanon, heavy mineral analysis has also been conducted. This work was done to assess the degree of recycling and

preservation of heavy minerals from a pre-existing sandstone succession as the source. Additionally, for the very first time in Lebanon, U–Pb dating of detrital zircons was done to test the provenance hypotheses outlined for age-equivalent sandstone units in Israel/Palestine and Jordan (Kolodner et al. 2009).

Lateral thickness variations within the Chouf Sandstone (ranging between 0 and 700 m) were already noticed by Heybroek (1942), Dubertret (1955) which could be best interpreted in terms syn-depositional extensional grabens. If correct, the Chouf Formation, with its fluvial, deltaic to neritic sandstones, appears to be a syn-rift unit, as proposed by some (e.g. Homberg et al. 2010; Hatzenbichler et al. 2013). Based on field observations, similar thickness variations in the underlying Upper Jurassic formations have already been interpreted as the result of syn-rift normal faulting (Collin et al. 2010). Due to the lack of sufficient subsurface well data (Beydoun 1977a, b, 1981) and the availability of only a few reflection seismic profiles onshore Lebanon (Nader et al. 2016), we used a combination of field and remote sensing data to construct an isopach map. To explain the observed map-view variations in the Chouf thickness, we built on the microtectonic

PERIOD	STAGE/EPOCH	LITHOLOGY AND WEATHERING PROFILE	STRATIGRAPHIC UNIT AND FACIES	DEPOSITIONAL/TECTONIC ENVIRONMENT	LEGEND
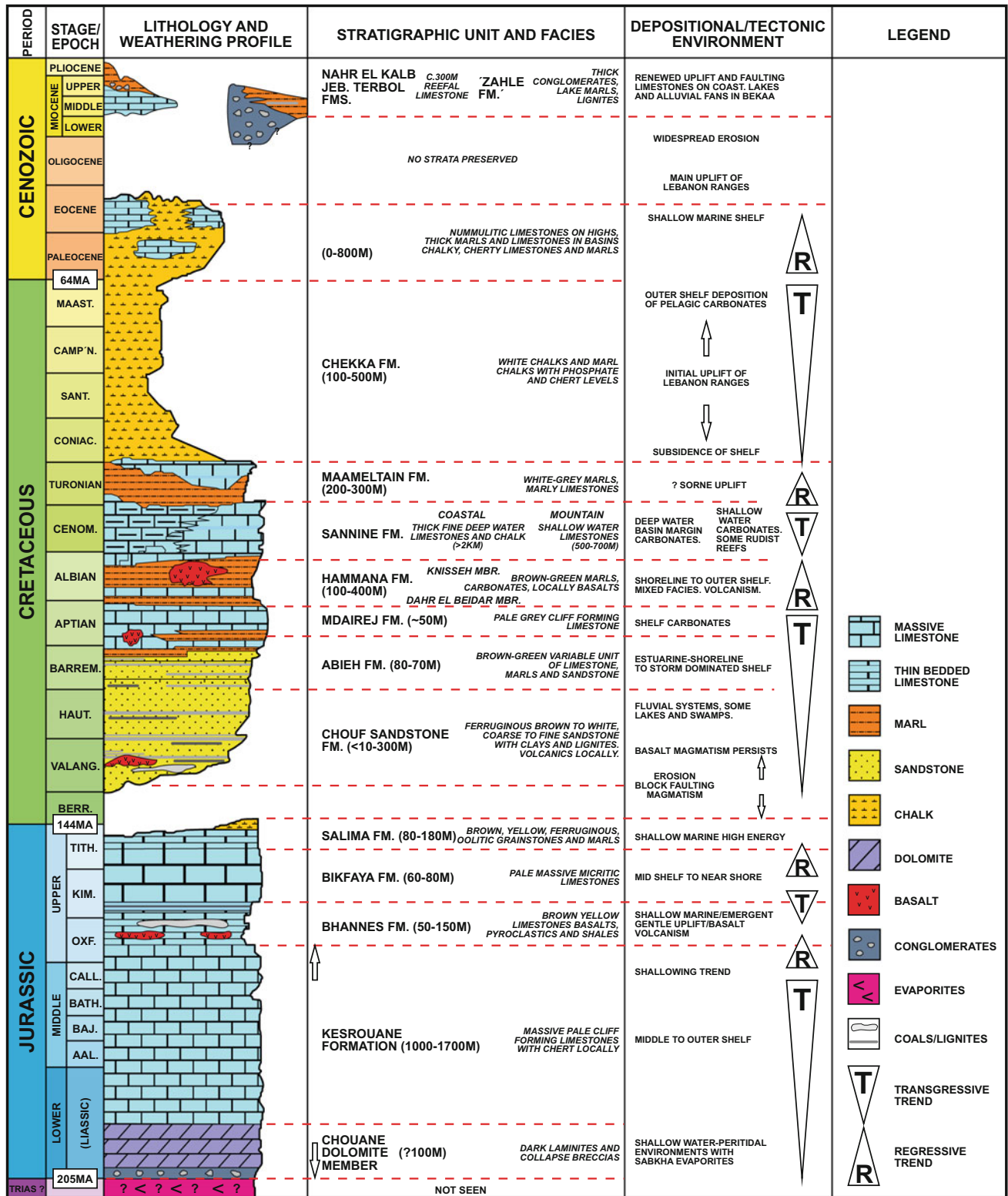
Fig. 2.2 Stratigraphy of onshore Lebanon based upon outcrop geology. Modified from Walley (1998)

measurements of Homberg et al. (2010) and assumed WNW-ESE trending, individual Early Cretaceous sub-basins during the deposition of the Chouf Sandstone. If our speculative map pattern of fault-controlled extensional mini-basins can be extrapolated into the nearby area of offshore Lebanon, some prospective targets of thick Chouf Sandstone reservoirs might be expected.

Finally, we propose a model of a low-strain, wide-rift style extensional episode for central and northern Lebanon during the Early Cretaceous which superimposed perpendicularly on the pre-existing NNE-SSW trending margin of the Levant Basin.

2.2 Data Base and Methods Used in This Study

One of the main sources for the geologic data in this study is the outcrop rock samples we have collected during two geologic field work campaigns in 2012 and 2013 in central and northern Lebanon. Specifically to the Chouf Sandstone Formation, it was sampled in seven locations and numerous outcrops have been sampled (Fig. 2.1). These NNE-SSW trending outcrop belts along the flank of large antiforms are pre-determined by the post-Neocomian development of the region, but most importantly by the Miocene to Recent updoming and erosion (Fig. 2.3) due to the sinistral transpression along the Yammoûneh Fault Zone as the northerly continuation of the Levant (or Dead Sea) fault system (e.g. Walley 1988; Däeron 2007).

The petrography and mineral composition of the Chouf rock samples were studied in detail by Bauer (2014) by thin section, X-ray diffraction (XRD) and heavy mineral analysis. In addition, U–Pb detrital zircon geochronology of eight Chouf Sandstone samples was completed by two different laboratories: at the University of Toronto and at the

University of Arizona. The standard methods of laser ablation and inductively coupled plasma mass spectrometry (LA-ICP-MS) U–Pb detrital zircon geochronology were followed in both laboratories (cf. Vermeesch 2004; Gehrels and Pecha 2014). See Supplementary Material for details about laboratory protocols. In Toronto, a combined 105 single grain analyses were performed from seven samples due to the small sample size and relative yields of zircon from each rock. In Arizona, a 103 single grain analysis was performed on one tuffitic Chouf Sandstone sample which provided sufficient numbers of zircons. The results reported are <10% discordant. Imaging of the zircons was conducted via scanning electron microscopy back-scatter emission and cathodoluminescence methods.

In order to test the syn-rift nature of the Chouf Sandstone, modern high-resolution QuickBird Digital Elevation Model (DEM) satellite data sets (with 0.75 m horizontal and 4 m vertical resolution) were used to derive thickness data points for the Chouf Sandstone in NW Lebanon (Hatzenbichler et al. 2013; Asmar et al. 2013). One important reason to use high-resolution satellite data for onshore Lebanon is the general lack of structural measurements, such as dip/strike, on the existing 1:50,000 and 1:200,000 scale vintage geologic maps (Dubertret 1955, 1966). In lieu of these basic data, the "Three-Point Method" was applied. The workflow of this method is based on the selection of three points representing the three corners of a triangle placed on the same common geologic surface, such as a marker bed. The dip/strike measurements were carried out using ArcGIS analysing Quickbird satellite images and DEM data. To solve the three-point problem the two of the three corner points of the selected triangle with the biggest difference in elevation are connected to form a dip line. The location of the third point is interpolated onto the dip line by solely using the point's elevation. Connecting this interpolated point with the third point then provides the strike line. The
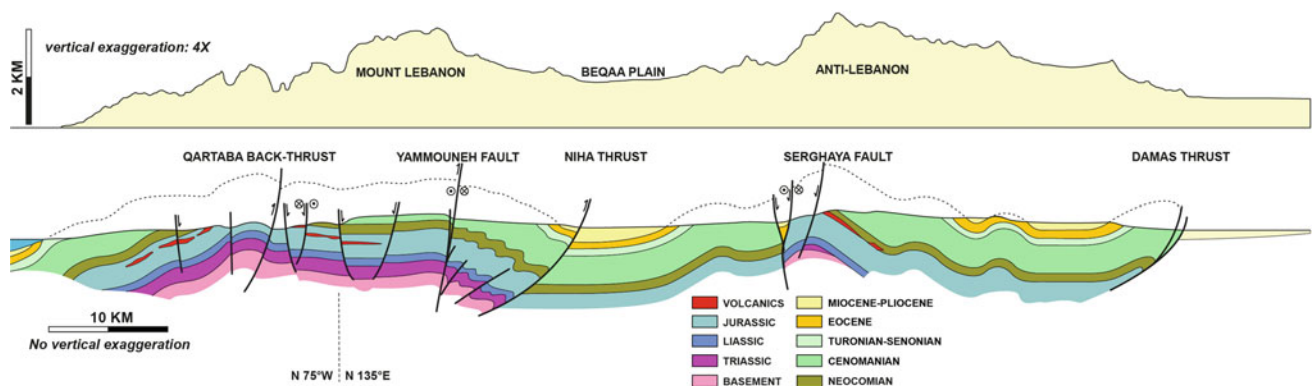
Fig. 2.3 Regional structural transect across Lebanon and adjacent Syria, adapted from Daëron (2005). The depicted amount of missing section above the Mount Lebanon area is conceptual and it is only loosely constrained by zircon (U–Th)/He cooling ages (Asmar et al. 2014a) suggesting that Lower Cretaceous clastics were never buried sufficiently deep enough to reset the helium systematics

dip value is derived by measuring the perpendicular distance between the strike line and the lowermost point. The method was streamlined by using a MatLab platform and exporting the results into an ArcGIS toolbox (Asmar et al. 2014a, b).

In the case of the Chouf Sandstone bedding surfaces were used. The identification of the bedding planes is not as easy in sandstones as in carbonate sequences as they are more prone to erosion and do not always form hogbacks (cuestas). Using this method, it was not only possible to determine the dip/strike values remotely, but also the true stratigraphic thickness of the Chouf Sandstone was derived in 47 locations in northern and central Lebanon (Table 2.1). It is to be noted, however, that after ground truthing the results in a few selected places in the study area, the error bars of the remote sensing measurements was established, i.e. up to 29° for the dip direction and up 25° for the dip angle values (Bauer 2014).

2.3   Stratigraphy and Structure of Lebanon

The stratigraphic column of onshore Lebanon (Fig. 2.2) is primarily based on a compilation of geological outcrops throughout the country (e.g. Dubertret 1955, 1975; Beydoun 1975; Walley 1998). The combined thickness of the exposed post-Triassic strata is approximately 6.5 km, however, this maximum thickness is not likely to be present in any one location. The majority of the original field work was completed by Dubertret and his group of co-workers between 1929–1961 who managed to map the Lebanese geology and largely defined its stratigraphy. However, due to lateral facies changes the stratigraphic nomenclature varies across his 1:50,000 and 1:200,000 scale geological map sheets.

The exposed stratigraphic column of onshore Lebanon can be largely divided into three sequences: Jurassic, Cretaceous to Eocene and Miocene to Quaternary. The entire Jurassic, the middle part of the Cretaceous and the Middle Miocene are dominated by neritic carbonate successions, whereas in the Upper Cretaceous and the Lower Paleogene chalk is the most common lithology (Fig. 2.2). In onshore Lebanon it is only the Lower Cretaceous sequence which is dominated by siliciclastics. The three clastic formations in this sequence, the Salima, Chouf and Abieh formations, will be reviewed in details in the next chapter.

Many aspects of the structural evolution of Lebanon remain relatively poorly constrained. Interpretation of the geological structures of Lebanon within a coherent structural-tectonic scheme was offered by Quennel (1984), Butler et al. (1998), Walley (1998, 2001), Homberg et al. (2009, 2010) and Nader (2011, 2014).

For example, the growth history of the large onshore Lebanese anticlines (Fig. 2.3) is still controversial. Whereas similar large features can be dated using the recently acquired speculative 2D and 3D reflection seismic data offshore (e.g. Ghalayini et al. 2014), the age of the major folding episode(s) onshore remains questionable as the Cenozoic and Upper Cretaceous cover has been eroded due to the neotectonic uplift (Figs. 2.1 and 2.3). Regardless, the age of folding episodes are thought to be either Late Cretaceous and Eocene (Walley 1998), Early and Late Miocene (Homberg et al. 2009, 2010), pre-Messinian (Butler 1998) or even Pliocene (Quennel 1984).

An examination of the tectonic structures and mechanical analysis of the meso-scale brittle deformation (Homberg et al. 2010) indicate that Lebanon has experienced four major tectonic events since the Late Mesozoic. The first was an Early Cretaceous extensional phase oriented N-S to NNE-SSW. It produced WSW-ENE to WNW-ESE normal faults with offsets up to several hundreds of metres and led to the development of an approximately WNW-ESE-trending basin system. For our present study of the Neocomian Chouf Sandstone Formation, this is the critical structural period.

A second extensional period occurred during Eocene time and persisted perhaps until the Oligocene. The Early Neogene period marked a dramatic change in the structural evolution of Lebanon after which strike-slip and reverse faulting and folding dominated. During Early Miocene times, an E-W compressional period produced moderate folding and faulting. A second, but much more pronounced folding episode occurred during the Late Miocene time due to a NNW-SSE compressional event (Homberg et al. 2010). Obviously, from a hydrocarbon trap formation standpoint, this last deformational period is the most important one, both onshore and offshore Lebanon.

It has been also suggested that the prominent fold trains in Lebanon, including the Quartaba Anticline (Fig. 2.3) are part of the Syrian Arc structures, which form an arcuate folded belt extending from the Western Desert of Egypt through Sinai into the Palmyride Basin of Syria (e.g. Chaimov et al. 1992; Moustafa and Khalil 1995; Guiraud and Bosworth 1997; Walley 1998, 2001).

The amount of eroded section above the large Syrian Arc anticlines (Fig. 2.3) is very important for hydrocarbon generation modelling. Equally critical is the proper understanding of the timing of the regional uplift and exhumation as its inception ended any hydrocarbon generation at depth. The charge timing risk may be quantified from the temporal overlap between the formation of the anticlines (as traps) and the regional uplift and erosion (cessation of charge). Whereas the timing is still a matter of debate, a preliminary zircon (U–Th)/He thermochronology study of the Chouf

Table 2.1 Coordinates of the points where the three-points method was used to estimate the true stratigraphic thickness of the Chouf Formation. The thickness values are given in meters

Thickness (m)	Lat long (WGS84)	
769.50	33° 58′ 30.037″N	35° 47′ 17.179″E
172.70	33° 50′ 39.466″N	35° 46′ 16.783″E
195.00	33° 42′ 21.994″N	35° 30′ 7.026″E
281.30	33° 56′ 32.172″N	35° 50′ 20.948″E
120.00	34° 1′ 3.652″N	35° 48′ 14.04″E
18.60	34° 16′ 4.49″N	35° 57′ 17.211″E
32.00	34° 14′ 38.245″N	35° 57′ 14.431″E
102.20	34° 13′ 52.184″N	36° 0′ 25.654″E
83.30	34° 15′ 14.502″N	36° 0′ 29.75″E
33.40	34° 15′ 20.897″N	35° 59′ 1.163″E
32.20	34º 5′ 21.857″N	35° 45′ 59.925″E
70.50	34° 1′ 8.036″N	35° 41′ 36.618″E
52.50	34° 0′ 42.731″N	35° 41′ 44.007″E
138.60	34° 7′ 12.416″N	35° 47′ 14.148″E
41.20	34° 9′ 5.866″N	35° 48′ 23.792″E
43.10	34° 13′ 14.881″N	35° 50′ 31.727″E
16.70	34° 13′ 16.961″N	35° 54′ 20.603″E
230.60	34° 14′ 40.845″N	35° 54′ 36.722″E
31.00	34° 12′ 21.77″N	35° 56′ 53.145″E
338.20	34° 9′ 42.698″N	35° 52′ 13.795″E
110.00	34° 5′ 49.085″N	35° 52′ 3.22″E
120.00	34° 3′ 42.935″N	35° 50′ 53.778″E
105.00	33° 59′ 21.002″N	35° 40′ 3.99″E
218.40	33° 54′ 22.979″N	35° 47′ 36.029″E
193.70	33° 51′ 51.218″N	35° 49′ 24.978″E
310.00	33° 46′ 19.248″N	35° 34′ 45.31″E
190.00	33° 44′ 0.297″N	35° 33′ 28.864″E
210.00	33° 42′ 17.662″N	35° 32′ 9.407″E
260.00	33° 46′ 12.391″N	35° 38′ 41.92″E
280.00	33° 51′ 59.526″N	35° 42′ 15.209″E
430.30	33° 51′ 7.056″N	35° 41′ 14.759″E
230.80	33° 51′ 3.474″N	35° 35′ 39.255″E
383.00	33° 50′ 29.136″N	35° 37′ 5.831″E
220.00	33° 54′ 16.52″N	35° 43′ 16.189″E
533.00	33° 57′ 33.019″N	35° 46′ 47.883″E
196.70	34° 1′ 34.571″N	35° 46′ 33.118″E
84.00	33° 58′ 16.656″N	35° 38′ 50.386″E
225.20	33° 57′ 10.302″N	35° 38′ 17.67″E
443.30	33° 55′ 47.299″N	35° 36′ 4.252″E
747.00	33° 31′ 4.346″N	35° 37′ 22.099″E
368.60	33° 32′ 29.304″N	35° 37′ 24.284″E
166.20	33° 35′ 14.492″N	35° 38′ 9.585″E

(continued)

Table 2.1 (continued)

Thickness (m)	Lat long (WGS84)	
394.60	33° 32′ 0.435″N	35° 33′ 6.333″E
208.00	33° 38′ 14.472″N	35° 39′ 49.008″E
105.00	33° 39′ 12.444″N	35° 40′ 13.462″E
59.50	33° 42′ 11.718″N	35° 41′ 21.756″E
660.00	33° 20′ 33.743″N	35° 28′ 35.26″E

Sandstone provided Late Ordovician to Early Silurian ages, indicating that the Lower Cretaceous clastics were never been buried deep enough (i.e. 200 °C) to reset the helium systematics (Asmar et al. 2014a).

2.4 Detailed Lithostratigraphic Description of the Immediate Pre- and Post-Chouf Formations

Beneath the Lower Cretaceous Chouf Formation the Uppermost Jurassic stratigraphy has a threefold division (Fig. 2.2) in our study area in NW Lebanon (Fig. 2.4). The sequence is subdivided into a lower volcanic unit (Bhannès), a middle massively-bedded limestone unit (Bikfaya) and a thinly-bedded carbonate unit (Salima). In places it is evident that a pre-Chouf Sandstone extensional faulting and localized unconformities of Late Jurassic to Neocomian age has removed some of the upper beds (Collin et al. 2010).

Dubertret's Salima Limestone (Dubertret 1955, 1975) is a very variable sequence of brown-yellow ferruginous oolitic limestones, often burrowed and cross-bedded, alternating with brown marls. The unit is thinly bedded (although some massive units occur, especially at the top) and therefore it tends to correlate with relatively recessive topography in the field. Thicknesses vary depending on the extent of the pre-Chouf Formation erosion, and range from a few metres to approximately 180 m at Salima, at the *locus typicus*. However, locally the Salima Formation can be totally absent. The Salima Formation is considered as Tithonian in age (Walley 1983, 1988, 1997) although its stratigraphic top may extend up into the Berriasian-Valanginian as it was proposed by some (Clark and Boudagher-Fadel 2001; Ferry et al. 2007; Granier et al. 2015, 2016).

Besides the age of the Salima Formation, there are some uncertainities about the nature of the contact between the Salima and the overlying Chouf Formation. In most places there is a unconformity and evidence for subaerial erosion (Fig. 2.5) before the deposition of the overlying Chouf Sandstone (Fig. 2.2). However, in the Metn and Kesrouane areas there could be a more subtle lithologic transition to the Chouf Formation as the uppermost few metres of the Salima Formation is a quartz-rich ferruginous grainstone. This could represent a

phase of mixed carbonate and siliciclastic deposition in the area as the result of the overall end Jurassic regression.

Our own analysis of the Salima Formation was based on an outcrop sample purposefully collected at the very top of the formation. Based on petrographic analysis, the sample is a ferrigeneous dolomite with abundant clasts of iron oxide-rich concretions (Fig. 2.5b). The dolomite also contains iron oxide ooids and irregularly distributed, poorly-sorted and very altered quartz grains. We interpreted this sample of the Salima Formation, containing also abundant volcanic fragments and chert, as corresponding to a weathering surface or a paleo-soil horizon. This isolated finding suggests the presence of an unconformity and a hiatus between the Salima and Chouf formations (see also Granier et al. 2015, 2016).

On top of the Chouf Formation, there is no major unconformity (Fig. 2.2) at the base of the overlying Abeih Formation. The boundary is well defined, as the overlying Abeih Formation is abundant in oysters, dated as Barremian, and it also contains pisolites (Walley 1983).

Recent work by Maksoud et al. (2014) and Granier et al. (2015, 2016) shows that the Abeih Formation is actually Aptian (Bedoulian) in age. Formerly the *Couches à gastropoda*, the Abeih Formation varies between fossiliferous limestones, marls and sandstones with a general upwards trend of terrigenous clastics passing into carbonates. Besides gastropods and bivalves, various orbitolinid foraminifers are present in the central Mount Lebanon area and some amber may also occur. In northern Lebanon, the Abeih Formation is a distinctive sequence of cross-bedded, ochre brown ferruginous sandy grainstones with green clays. The majority of the Abeih Formation facies in central Lebanon appears to be lagoonal, deltaic, estuarine and littoral, whereas in northern Lebanon the depositional environment appears to be shallow water within the storm dominated shelf. Occasional limestone beds seem to represent storm events leading to re-deposition of material in a shelf or lagoon setting. Locally, the Abeih Formation also contains basalts and pyroclastic material (Fig. 2.2).

The thickness of the Abeih Formation is about 170 m in the Chouf area, but it is commonly less than half of this amount. In the Chouf region the base of the Abeih Formation is widely represented by a pisolitic paleo-soil horizon. The top of the Abeih Formation is identified as the base of the massive cliff-forming limestones belonging to the Mdairej Formation. The age range of the formation was considered as Barremian to earliest Aptian (Fig. 2.2). Overall, the depositional environment of the Abeih

Fig. 2.4 The geology of central part of NW Lebanon showing the location of the Chouf Sandstone outcrop samples analyzed in this study. For location see Fig. 2.1
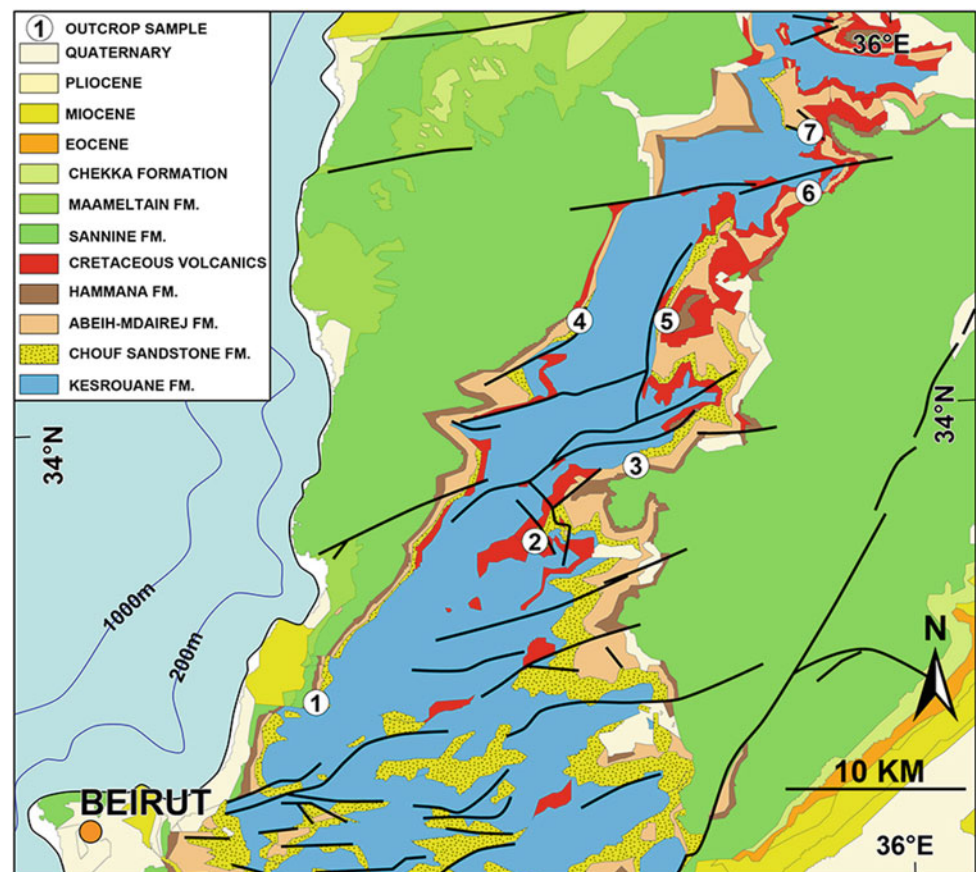
Fig. 2.5 **a** Outcrop photograph of the topmost part of the Salima Formation and
b micro-photograph of the Salima Formation (Lat/Lon: 34° 07′ 12.00″N, 35° 46′ 47.25″E). The dolomite with abundant clasts of iron-oxide rich concretions, partly also iron oxide ooids, irregulary distributed poorly sorted quartz grains, totally altered, weathered volcanic fragments and chert. These observations are intepreted in terms of a weathering surface and possibly even a paleosoil horizon
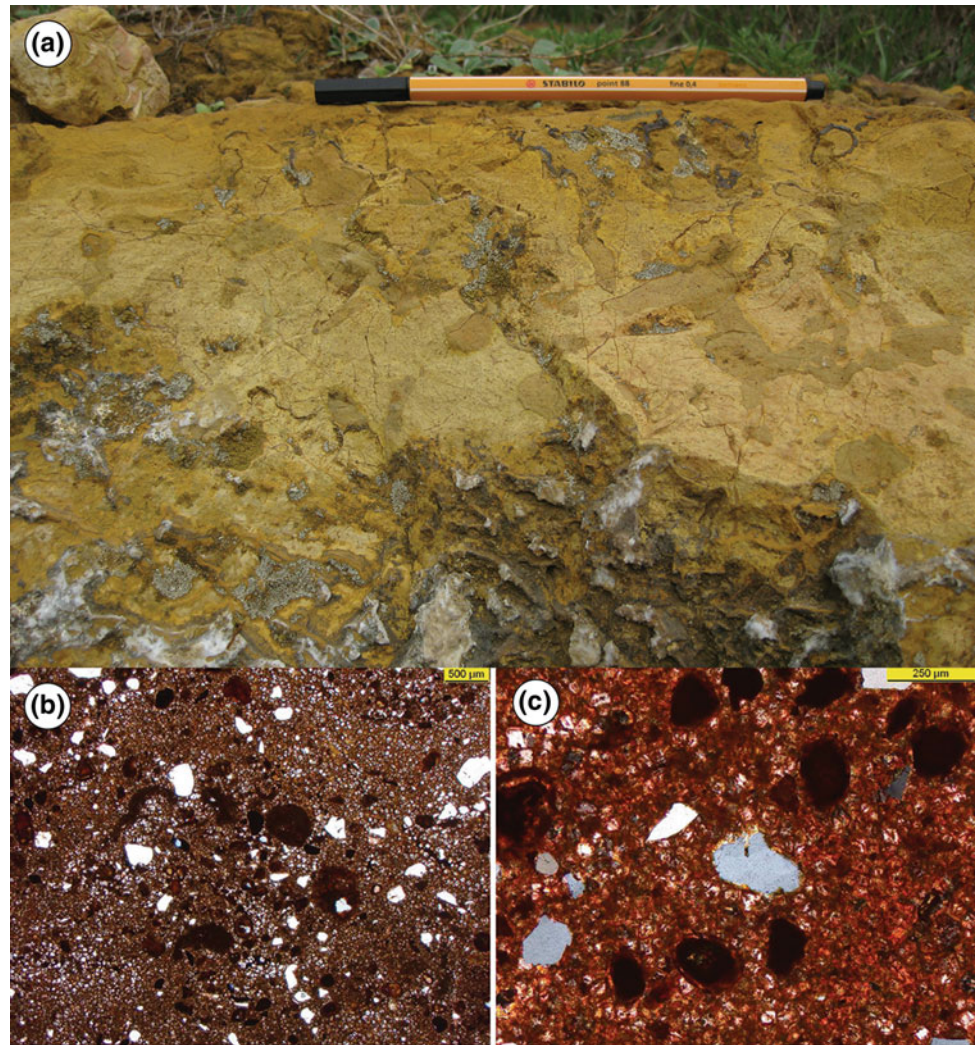
Formation is transitional between the aeolian, fluvial, limnic Chouf and the overlying shallow marine Mdairej Formation.

2.5 Chouf Sandstone Formation: Lithology, Sedimentology and Provenance

The lowermost unit of the Cretaceous is the prominent sandstone traditionally known as the Grès de Base or 'C1' of the Dubertret map sheets (Dubertret 1955, 1966). The surface distribution of the Chouf follows the NNE-SSW trending outcrop belts along the flanks of major antiforms (Figs. 2.3 and 2.4).

Besides overview papers describing the overall Mesozoic stratigraphy of onshore Lebanon (Dubertret 1955, 1975; Saint-Marc 1970, 1980; Beydoun 1977a, 1996; Walley 1983, 1997; Nader 2011, 2014; Ghalayini et al. 2018), quite a few studies dealt with the Chouf Formation specifically, such as Ukla (1970), Tixier (1972), Bellos (2008) and

recently Bauer (2014). Lithologically, the formation is very heterogeneous, but it typically contains ferruginous brown, yellow to white sandstone, frequently cross-bedded, with interbedded clays, shales and lignites (Fig. 2.6). Basalts can also be found within the Chouf Sandstone Formation and also reddish or greenish blue clayey beds which are weathered volcanic tuffs or tuffits. The volcanics tend to occur at the base of the Chouf succession. Locally, woody or coaly fragments, often with pyrite, marcasite and occasionally amber can be found (Maksoud et al. 2017). A detailed sedimentological analysis of the Chouf Formation in the Jezzine region in southern Lebanon (Bellos 2008) identified six different lithofacies: arenites, muddy quartz-rich sandstones, clayey-muddy quartz-rich sandstones, graywacke, clay and limestones.

The age range of the Chouf Sandstone Formation (Fig. 2.2) remains poorly constrained (e.g. Walley 2001). However, regional lithologic equivalents of the Chouf Sandstone in Israel/Palestine (Cohen 1976; Shimron and

Fig. 2.6 Outcrop photograph of the Chouf Sandstone Formation at a temporary building site with sandstones inbedded with clays, shales and lignitic beds (34° 0′54.54″N; 35°45′33.62″E), Chris Walley is for scale
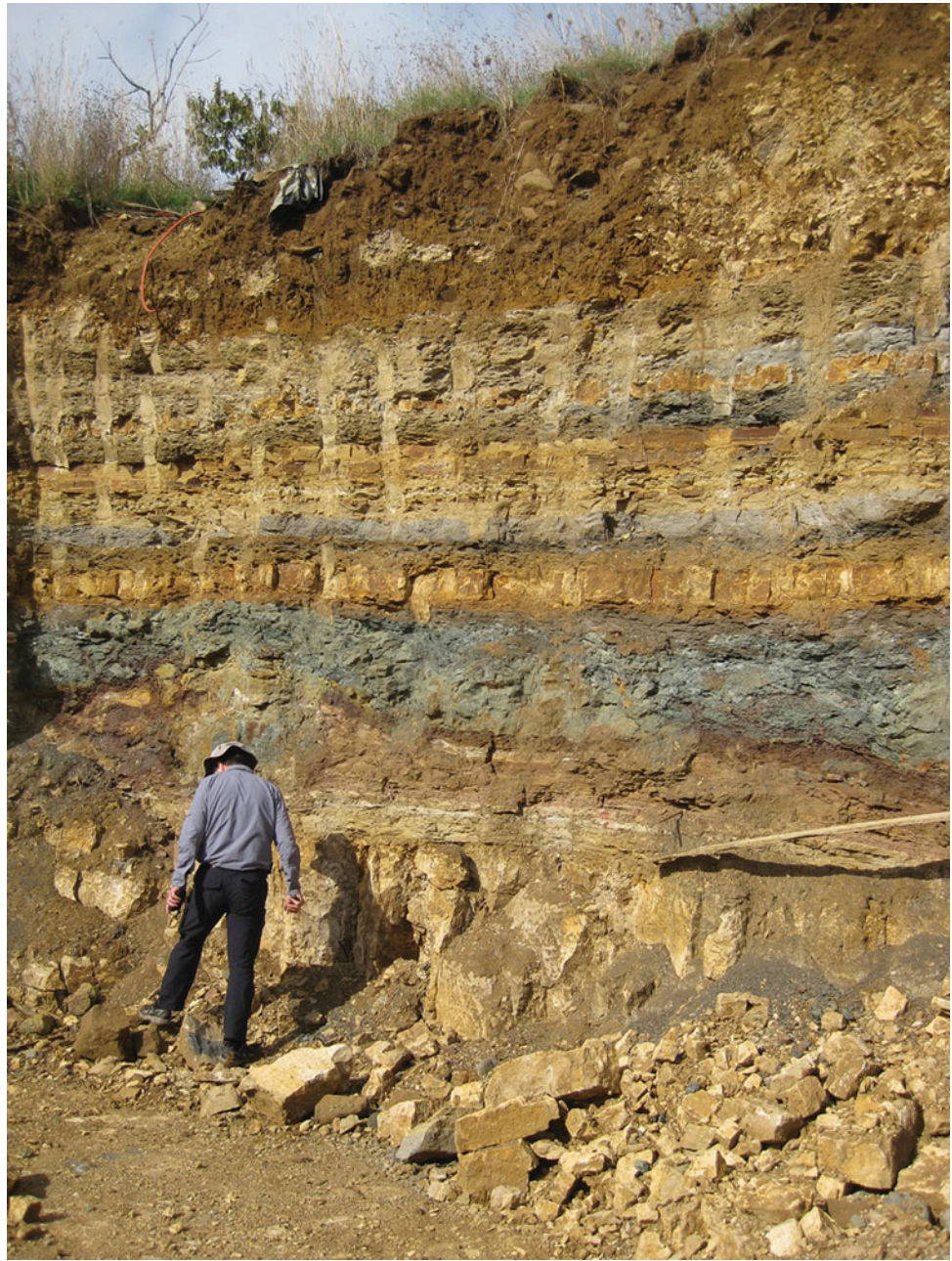
Lang 1989; Kolodner et al. 2009), Jordan (Amireh 1991, 1992, 1994, 1997; Lüning et al. 2014), Syria (Ponikarov et al. 1969; Chaimov et al. 1992; Barrier et al. 2014) and Egypt (Bachman et al. 2010) indicate that even if the initial deposition of the Chouf started during the Berriasian or Valanginian, most of the Chouf sequence is Barremian in age (Granier et al. 2015, 2016). The Chouf Sandstone is presumed to have been deposited under a fluvial, limnic to deltaic and littoral environment. In general, the formation appears to be fluvial at the base and in the east and deltaic at the top and in the west. Locally, even aeolian facies has been described (e.g. Bellos 2008). The Chouf Sandstone thins

northwards reflecting the fact that its clastic provenance area was located to the southeast, in the Arab-Nubian High region of the Arabian Plate.

In this study we have sampled the Chouf Sandstone at seven locations (Table 2.2) in central Lebanon (Fig. 2.4). As the Chouf Sandstone is almost the only prominent siliciclastic unit in Lebanon, it is heavily utilized for building sand and therefore many of our samples were collected in quarries (Fig. 2.7a). With a potential petroleum reservoir in mind, we purposefully sampled the sandstone units within the Chouf Formation and avoided the other lithologies within the succession. Petrographic and XRD analyses

Table 2.2 Coordinates of the Chouf Formation samples in NW Lebanon

Sample	Stop	Lat long degrees (WGS84)	
1	S2/01	33° 56′ 50.16″N	35° 38′ 10.39″E
2	S4/02	34° 1′ 14.45″N	35° 45′ 56.16″E
3	S7/04	34° 3′ 27.45″N	35° 49′ 20.39″E
4	S14/05	34° 7′ 33.14″N	35° 47′ 40.65″E
5	S18/06	34° 7′ 39.20″N	35° 50′ 47.69″E
6	S23/07	34° 11′ 20.61″N	35° 55′ 59.53″E
7	S26/08	34° 13′ 20.01″N	35° 55′ 55.90″E

Fig. 2.7 a Outcrop photograph of the Chouf Sandstone Formation with thick cross-bedded massive sandstone beds (Lat/Lon: 34° 01′ 14.61″N, 35° 45′ 55.20″E) and **b** thin-section photo of the Chouf from the same outcrop. Note the dominance and rounded nature of quartz grains in this mature quartz arenite. The quartz grains are well sorted, weakly cemented by ferruginuos clay minerals and minor quartz cement. This sandstone would be a good reservoir rock with its 24% thin-section porosity
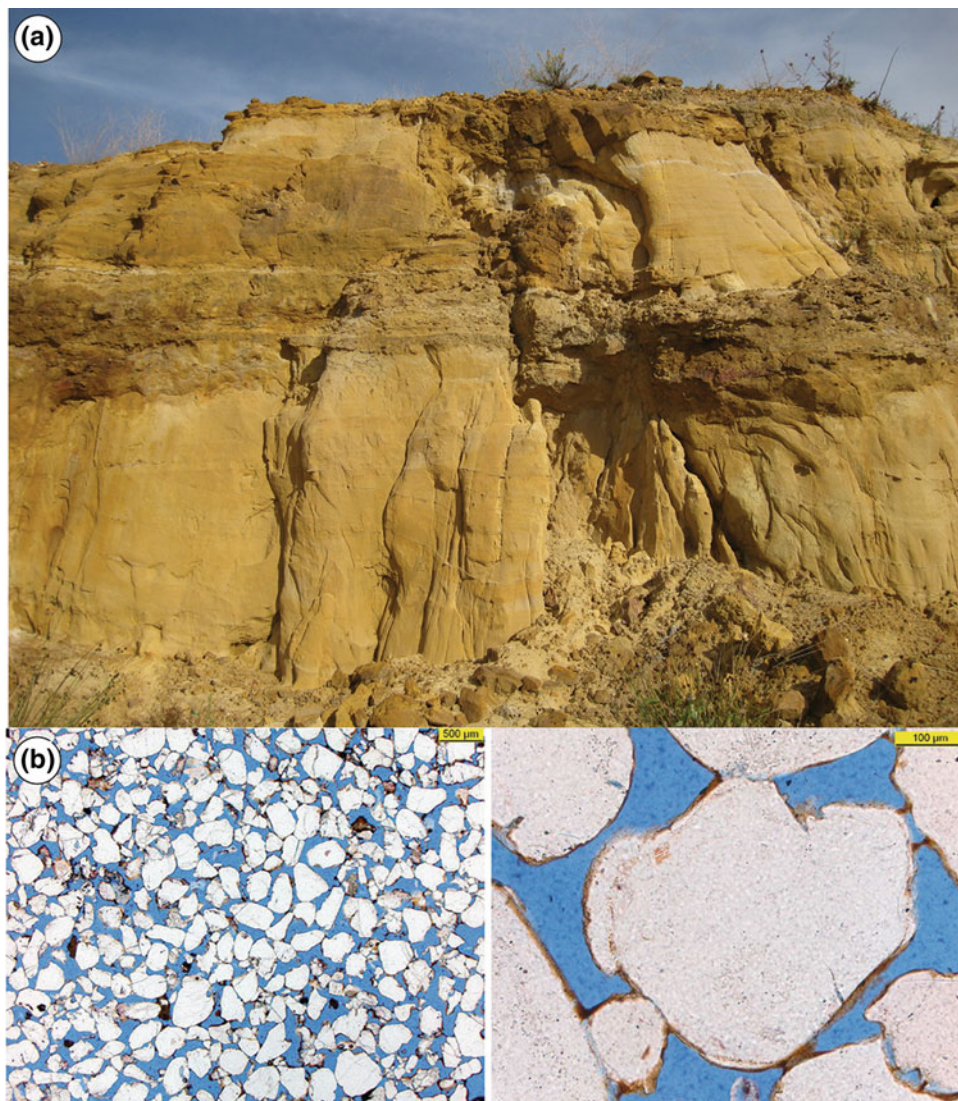
showed that the Chouf Sandstone is weakly cemented by ferruginous clay minerals and 90–95% of the composition is mono-crystalline quartz indicating clean, well-sorted sandstone (Figs. 2.7b and 2.8a). Poly-crystalline quartz, feldspar, and clay clasts are present only in all samples. The cement is quartz and ferruginous clay coating the mineral rims (Fig. 2.7b). The average porosity of the sandstone samples based on thin section analysis was around 24%.

As to the heavy mineral composition of the Chouf Sandstone, all samples showed very similar results (Bauer

Fig. 2.8 **a** Petrographical composition of Chouf Sandstone (Lat/Lon: 34° 01′ 14.61″N, 35° 45′ 55.20″E). The porosity based on the thin section is estimated as 24%, **b** heavy mineral spectra from five Chouf field samples. Adapted from Bauer (2014)
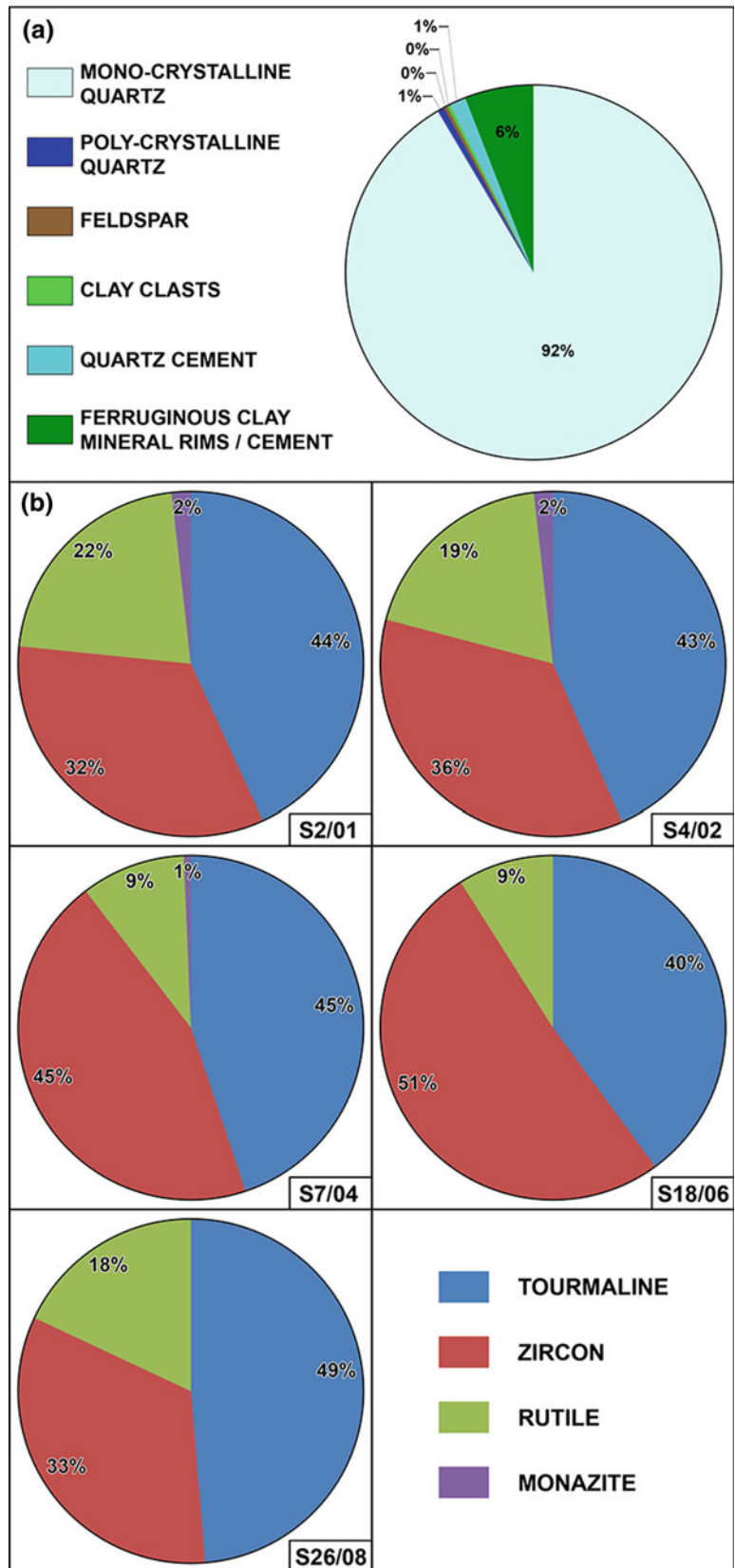
Fig. 2.9 Photograph of the Chouf sandstone facies overlying weathered volcanic units which might be equivalent to the Tayasir volcanics in the southern Levant (Lat/Lon: 34° 16′ 05.53″N, 35° 57′ 09.74″E)

2014). Tourmaline and zircon dominated all the samples with 40–50% and 30–50%, respectively (Fig. 2.8b). Rutile was also found in every sample, in the range of 10–20%. Monazite was identified in small amounts (1–2%) in the southern samples (Fig. 2.4). Minor amounts of titanite and garnet were also present. Interestingly, apatite was not found in the heavy mineral spectrum at all which likely points to the strongly recycled nature of these sandstones.

Extrusive volcanic sequences can be found within the Chouf Formation especially around its base (Fig. 2.9). Since most of these volcanics seem to be quite weathered we have not attempted to date them via $^{40}Ar/^{39}Ar$ or K–Ar methods as Segev (2009) did in northern Israel on the Tayasir volcanics (Valaniginian to Hauterivian). Instead, we have selected an intra-Chouf bluish green clayey unit which appeared to be a tuffitic bed (Fig. 2.10a) in order to possibly provide a datable volcanic marker horizon. Based on the thin section analysis of this sample (Fig. 2.10b), it turned out to be a glauconitic, sandy limestone/dolomite. The subtle stratification and the mixture of elements in a very mature sandstone (well-rounded metamorphic quartz, rutile and frequent bone fragments), with the subsequent dolomitization of the entire rock, is interpreted as a tuffit deposited in a subaqueous setting. The presence of glauconite suggests a shallow water environment. As some of the zircons were observed as inclusions in quartz grains of probably volcanic origin, U–Pb dates from these zircons (Fig. 2.11) could potentially provide the age of the Early Cretaceous volcanism.

2.6 Geochronological Data from the Chouf Formation

For the first time in Lebanon, LA-ICP-MS U–Pb geochronology was performed on zircons extracted from eight Chouf Sandstone samples from seven outcrop locations (Fig. 2.4). These detrital zircon results are shown here in two groups corresponding to the measurements made at the University of Toronto (Table 2.3) and at the University of Arizona (Table 2.4), respectively (Figs. 2.12, 2.13 and 2.14 and Supplementary Material). The results are statistically identical given the sample details, i.e. 105 zircons from seven locations combined (Figs. 2.12 and 2.13a) and 103 zircons from one location (Fig. 2.13b). With the exception of a few Archean outliers, the U–Pb ages fall into three broad populations: (i) a few small Paleoproterozoic populations (1600–2600 Ma), (ii) a Neoproterozoic Grenvillian population (750–1000 Ma), and (iii) a Pan-African population (575–650 Ma). Only one single zircon is slightly younger then the Pan-African population, yielding a $^{206}Pb/^{238}U$ age of 491 ± 5 Ma (i.e. Late Cambrian). Typically, a conservative method for determining maximum depositional age determinations (MDA; Dickinson and Gehrels 2009) involves calculating the youngest mode of ages, containing three or more U–Pb age determinations within 2 S.E. analytical error. However, in our study the single and isolated age of ca. 490 Ma is interpreted as the age of primary deposition in an Early Paleozoic (Cambrian to Ordovician) basin. These

Fig. 2.10 a Prominent bluish-green tuffit bed within the Chouf Formation, off-set by a circa 10 meters normal fault (Lat/Lon: 34° 3′ 27.45″N, 35°49′ 20.39″E), b micro-photograph of Chouf Sandstone Formation from the tuffit and c the same with crossed Nicols

detrital zircons were then redeposited into the ca. 120–135 Ma Chouf sands during the Early Cretaceous rifting in the area (e.g. Homberg et al. 2010). Unfortunately, with regard to the dating of the intra-Chouf tuffitic bed (Fig. 2.10a) and discovering volcanic zircons originating from the coeval magmatism in the broader area (Lang and Steinitz 1989; Abdel-Rahman 2002; Segev 2009), none of the 103 zircons analyzed provided an Early Cretaceous age (Fig. 2.13b).

The detrital zircon spectra of the Lebanese Lower Cretacous samples can be compared to that of the age-equivalent unit in southern Israel (Fig. 2.15a) published by Kolodner et al. (2009). The match of these spectra (Fig. 2.14) is remarkable even though the locations of the corresponding samples are separated by 400 km in a N-S direction. Moreover, as already noted by Kolodner et al. (2009), the overall age signal in the Lower Cretaceous clastics is very

similar to the detrital zircon age spectra previously obtained from the Cambrian–Ordovician sections of Israel and Jordan (Kolodner et al. 2006). Thus, the most probable provenance of the Lower Cretaceous sandstones in Lebanon, Jordan and Israel is a relatively proximal Palaeozoic, most probably Upper Cambrian to Ordovician sandstone succession exposed to the southeast. "Mass-produced" Cambro-Ordovician quartz-rich sandstones (Avigad et al. 2003, 2005; Weissbrod 2005) are indeed very widespread in North Africa and NE Arabia as a consequence of the erosional weathering of very large Pan-African terranes after the cessation of the East African Orogeny. The post-orogenic "molasse"-type Cambro-Ordovician siliciclastics were subsequently recycled, perhaps repeatedly, in the following 400 Myr until the Early Cretaceous (Kolodner et al. 2009), apparently with no major change in their provenance area in NE Arabia. A regional-scale Hercynian unconformity

Fig. 2.11 Zircon crystals separated from the tuffitic Chouf Formation shown on Fig. 2.10 (63–125 µm heavy mineral fraction). These zircons were dated by the U–Pb method (see Fig. 2.13b)
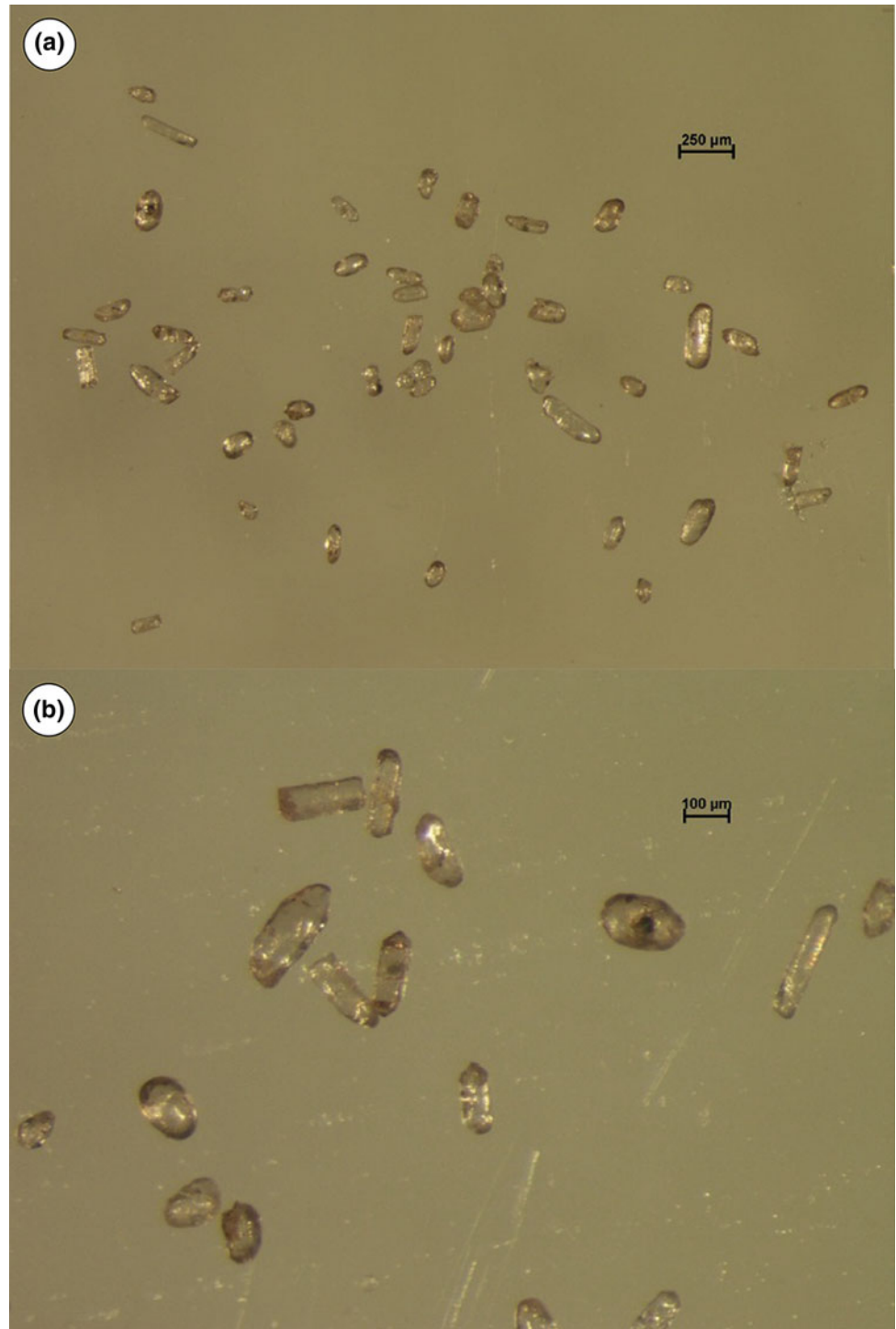
subcrop map (Wood 2015) also underlines the possible presence of Cambrian and Ordovician units at depth in our study area in NW Lebanon as the primary source of recycled sandstones of the Chouf Formation (Fig. 2.15).

As a very important consequence for hydrocarbon exploration, this recycling process was largely responsible for the overall good reservoir properties of the Chouf Sandstone and its age equivalent formations in the broader region.

Table 2.3 U-Pb isotopic data for zircon from Chouf Sandstone, University of Toronto analyses

Analysis	U (ppm)	Th/U	207Pb*/206Pb*	±	207Pb*/235U*	±	206Pb*/238U*	±	RhoXY	Apparent ages (Ma)						
										206Pb*/238U*	± (Ma)	207Pb*/235U*	± (Ma)	207Pb*/206Pb*	± (Ma)	Conc (%)
S14105-12	125	0.508	0.07335	0.00142	1.67218	0.03963	0.16637	0.00210	0.533	992.1	11.6	998.0	15.0	1011.1	40.2	98.0
S14105-14	43	1.257	0.06670	0.00264	1.12824	0.04753	0.12343	0.00167	0.321	750.2	9.6	766.9	22.5	815.8	81.3	91.5
S14105-15	185	0.221	0.06054	0.00146	0.81243	0.02238	0.09791	0.00120	0.446	602.1	7.1	603.8	12.5	610.1	52.5	98.6
S14105-16	86	0.510	0.06632	0.00194	0.93381	0.02967	0.10290	0.00116	0.353	631.4	6.8	669.6	15.5	800.5	61.1	77.8
S14105-17	207	0.567	0.06943	0.00107	1.46216	0.02751	0.15416	0.00149	0.514	924.2	8.3	914.9	11.3	892.5	33.0	103.8
S14105-19	37	0.278	0.06518	0.00351	0.95337	0.05344	0.10726	0.00158	0.263	656.8	9.2	679.9	27.4	756.9	110.2	86.1
S14105-20	393	0.191	0.11957	0.00082	5.69131	0.07333	0.34906	0.00340	0.757	1930.1	16.3	1930.0	11.1	1930.0	15.1	100.0
S14105-21	123	0.140	0.06199	0.00151	0.87798	0.02376	0.10369	0.00112	0.397	636.0	6.5	639.9	12.8	653.6	52.5	97.2
S14105-22crks	271	0.306	0.06630	0.00092	1.19763	0.02130	0.13202	0.00130	0.552	799.4	7.4	799.5	9.8	799.8	30.8	99.9
S14105-23	229	0.198	0.06390	0.00112	0.92702	0.01923	0.10617	0.00104	0.474	650.5	6.1	666.1	10.1	719.1	38.4	90.0
S14105-24	163	0.480	0.07355	0.00128	1.59777	0.03323	0.15946	0.00164	0.495	953.8	9.1	969.3	12.9	1004.7	36.3	94.5
S14105-26	81	0.844	0.06016	0.00196	0.76329	0.02668	0.09341	0.00107	0.328	575.7	6.3	575.9	15.3	576.7	70.3	99.8
S14105-7	46	0.505	0.06509	0.00286	1.14564	0.05287	0.12901	0.00173	0.291	782.2	9.9	775.2	24.8	755.0	90.6	103.8
S14105-8	81	0.447	0.10595	0.00169	3.59864	0.07047	0.24862	0.00258	0.529	1431.3	13.3	1549.2	15.5	1714.0	30.3	81.6
S14105-9	216	0.211	0.06218	0.00116	0.77364	0.01718	0.09094	0.00099	0.488	561.1	5.8	581.9	9.8	663.7	41.0	83.9
S18106-1	96	0.395	0.06362	0.00197	1.18482	0.03956	0.13766	0.00156	0.340	831.4	8.9	793.6	18.3	688.6	65.7	122.1
S18106-10	267	0.107	0.06497	0.00108	0.92930	0.01921	0.10489	0.00115	0.532	643.0	6.7	667.3	10.1	750.1	36.6	85.0
S18106-13	93	0.356	0.07508	0.00159	1.51045	0.03796	0.14755	0.00177	0.479	887.2	10.0	934.6	15.3	1048.1	43.9	83.6
S18106-14crks	677	0.342	0.06249	0.00068	0.90053	0.01512	0.10559	0.00118	0.667	647.1	6.9	652.0	8.1	669.2	26.7	96.5
S18106-17	380	0.066	0.12374	0.00082	5.73956	0.07601	0.33944	0.00344	0.765	1884.0	16.5	1937.3	11.4	1994.9	15.1	93.6
S18106-2	183	0.781	0.05646	0.00175	0.60327	0.01989	0.07911	0.00080	0.308	490.8	4.8	479.3	12.5	424.6	68.6	116.2
S18106-20	37	0.258	0.24252	0.00267	19.35111	0.34332	0.58323	0.00733	0.708	2961.9	29.8	3059.5	17.1	3124.2	19.8	93.5
S18106-21	18	0.193	0.07761	0.00501	1.15646	0.07825	0.10894	0.00212	0.287	666.6	12.3	780.3	36.3	1120.9	124.2	57.4
S18106-23	153	0.137	0.06084	0.00123	0.87453	0.02041	0.10523	0.00111	0.453	645.0	6.5	638.0	11.0	613.4	44.4	105.4
S18106-26crks	16	0.480	0.07567	0.00394	1.65831	0.09137	0.16065	0.00279	0.315	960.4	15.5	992.7	34.4	1064.9	101.8	89.4
S18106-3	182	0.340	0.06481	0.00173	0.84996	0.02514	0.09725	0.00109	0.378	598.3	6.4	624.6	13.7	721.2	57.1	82.2
S18106-4	97	0.970	0.06698	0.00211	1.09736	0.03743	0.12130	0.00142	0.343	738.0	8.2	752.1	18.0	794.1	65.9	92.5
S18106-5crks	76	0.338	0.15934	0.00184	9.32096	0.14975	0.43169	0.00421	0.607	2313.3	18.9	2370.1	14.7	2419.3	21.6	94.8
S18106-7	49	0.333	0.06095	0.00300	0.81982	0.04203	0.09893	0.00131	0.258	608.2	7.7	607.9	23.2	607.2	103.7	100.2
S18106-8	96	0.227	0.12199	0.00162	4.77528	0.08678	0.28704	0.00314	0.602	1626.7	15.7	1780.6	15.2	1966.0	25.7	80.5

(continued)

Table 2.3 (continued)

Analysis	U (ppm)	Th/U	Isotope ratios							Apparent ages (Ma)						Conc (%)
			207Pb*/206Pb*	±	207Pb*/235U*	±	206Pb*/238U*	±	RhoXY	206Pb*/238U*	± (Ma)	207Pb*/235U*	± (Ma)	207Pb*/206Pb*	± (Ma)	
S2107-11	141	0.152	0.08080	0.00112	2.31052	0.04120	0.20774	0.00211	0.571	1216.8	11.3	1215.5	12.6	1213.3	28.6	100.3
S2107-12	106	0.637	0.05950	0.00168	0.76072	0.02365	0.09313	0.00115	0.396	574.0	6.8	574.4	13.6	576.0	60.9	99.6
S2107-13	134	0.756	0.07700	0.00117	1.76967	0.03520	0.16782	0.00195	0.585	1000.1	10.8	1034.4	12.9	1107.6	32.0	89.5
S2107-17	85	0.480	0.06722	0.00163	1.15932	0.03160	0.12619	0.00140	0.408	766.1	8.0	781.6	14.8	826.3	51.2	92.3
S2107-18	61	0.313	0.07256	0.00181	1.56904	0.04425	0.15813	0.00192	0.430	946.4	10.7	958.0	17.4	985.0	51.0	95.8
S2107-19	179	0.579	0.06719	0.00106	1.19485	0.02341	0.12995	0.00134	0.527	787.6	7.7	798.2	10.8	828.1	34.4	94.8
S2107-23	27	0.739	0.07205	0.00359	1.43871	0.07504	0.14600	0.00210	0.276	878.5	11.8	905.2	30.8	970.8	99.1	89.8
S2107-24	204	0.219	0.06081	0.00123	0.76552	0.01789	0.09216	0.00096	0.444	568.3	5.6	577.2	10.3	612.3	44.7	92.5
S2107-25	137	0.565	0.07394	0.00118	1.70912	0.03436	0.16941	0.00179	0.527	1008.9	9.9	1012.0	12.8	1018.7	34.3	99.0
S2107-2crks	52	0.489	0.07879	0.00193	1.80276	0.05031	0.16889	0.00206	0.437	1006.0	11.3	1046.5	18.1	1131.9	49.3	88.0
S2107-4crks	171	0.330	0.06804	0.00123	1.23209	0.02556	0.13361	0.00120	0.434	808.4	6.8	815.3	11.6	834.1	38.5	96.7
S2107-5	182	0.338	0.06375	0.00151	0.84123	0.02195	0.09732	0.00095	0.374	598.7	5.6	619.8	12.0	697.8	50.8	85.1
S2107-6	82	0.400	0.06768	0.00164	1.22735	0.03336	0.13311	0.00153	0.424	805.6	8.7	813.1	15.1	833.8	50.5	96.4
S2107-7	49	0.397	0.06737	0.00191	1.30262	0.04029	0.14131	0.00162	0.371	852.1	9.2	846.9	17.6	833.3	58.8	102.4
S2107-8	161	0.311	0.05964	0.00142	0.69337	0.01845	0.08461	0.00093	0.412	523.6	5.5	534.8	11.0	583.1	51.8	89.4
S23107-10.1	75	0.350	0.06497	0.00240	0.81029	0.03212	0.09191	0.00121	0.333	566.8	7.2	602.6	17.9	739.6	77.2	75.6
S23107-11	19	0.558	0.07833	0.00318	1.67539	0.07508	0.15756	0.00288	0.407	943.2	16.0	999.2	28.2	1124.3	79.5	82.7
S23107-12	53	0.488	0.06153	0.00227	0.84876	0.03378	0.10150	0.00142	0.351	623.2	8.3	624.0	18.4	626.9	78.4	99.4
S23107-13	20	0.274	0.07122	0.00516	0.98271	0.07399	0.10142	0.00201	0.263	622.7	11.7	695.0	37.3	936.5	142.3	64.9
S23107-14	110	0.305	0.07474	0.00135	1.73617	0.03851	0.17058	0.00203	0.536	1015.3	11.2	1022.0	14.2	1036.5	37.4	97.8
S23107-15	113	0.241	0.06561	0.00141	1.13127	0.02743	0.12666	0.00132	0.431	768.8	7.6	768.4	13.0	767.1	45.5	100.2
S23107-16	237	0.227	0.07393	0.00093	1.64636	0.02747	0.16363	0.00159	0.583	976.9	8.8	988.2	10.5	1013.2	27.3	96.1
S23107-18c	97	0.391	0.06430	0.00199	0.84028	0.02785	0.09654	0.00104	0.326	594.1	6.1	619.3	15.3	712.5	65.3	82.6
S23107-18r	28	0.277	0.07076	0.00395	0.92840	0.05378	0.09668	0.00143	0.255	594.9	8.4	666.8	28.0	918.0	111.2	63.2
S23107-19c	759	0.015	0.11147	0.00086	3.21198	0.04273	0.21342	0.00201	0.707	1247.0	10.7	1460.1	13.7	1785.3	17.1	66.9
S23107-21	124	0.422	0.13748	0.00126	7.28708	0.11178	0.39197	0.00432	0.718	2131.9	20.0	2147.2	10.3	2161.9	18.6	98.4
S23107-23	102	0.338	0.07167	0.00167	1.55705	0.04116	0.15998	0.00185	0.438	956.7	10.3	953.3	16.2	945.5	48.0	101.3
S23107-24	123	0.068	0.06137	0.00197	0.75465	0.02604	0.09016	0.00104	0.333	556.5	6.1	570.9	15.0	628.9	68.7	88.0
S23107-4	27	0.363	0.07513	0.00466	1.22012	0.07982	0.11878	0.00242	0.311	723.5	13.9	809.8	35.9	1055.1	120.4	66.8
S23107-5	85	0.346	0.07516	0.00239	1.60772	0.05526	0.15692	0.00190	0.353	939.6	10.6	973.2	21.3	1049.8	63.5	88.7

(continued)

Table 2.3 (continued)

Analysis	U (ppm)	Th/U	207Pb*/206Pb*	±	207Pb*/235U*	±	206Pb*/238U*	±	RhoXY	Apparent ages (Ma)						Conc (%)
										206Pb*/238U*	± (Ma)	207Pb*/235U*	± (Ma)	207Pb*/206Pb*	± (Ma)	
S23107-9	71	0.844	0.07355	0.00231	1.68710	0.05891	0.16880	0.00241	0.409	1005.5	13.3	1003.7	22.1	999.7	63.5	100.6
S26108-11	176	0.325	0.17710	0.00146	10.88844	0.16455	0.45475	0.00515	0.750	2416.4	22.8	2513.6	14.0	2593.2	16.6	91.8
S26108-12	389	0.526	0.07619	0.00077	1.72315	0.02700	0.16750	0.00181	0.690	998.3	10.0	1017.2	10.1	1058.0	22.7	93.9
S26108-13	250	0.232	0.07457	0.00095	1.71093	0.03132	0.17014	0.00201	0.646	1012.9	11.1	1012.6	11.7	1012.0	28.1	100.1
S26108-21	148	0.529	0.11984	0.00122	5.57634	0.08907	0.34406	0.00374	0.680	1906.2	17.9	1912.5	13.7	1919.3	20.9	99.2
S26108-22	78	0.473	0.11293	0.00152	4.99969	0.08743	0.32595	0.00331	0.580	1818.7	16.1	1819.3	14.7	1819.9	25.7	99.9
S26108-24	416	0.014	0.11930	0.00076	5.41245	0.06619	0.33256	0.00308	0.757	1850.8	14.9	1886.8	10.5	1926.7	14.3	95.5
S26108-26r	250	0.016	0.06115	0.00094	0.84302	0.01561	0.10055	0.00092	0.494	617.6	5.4	620.8	8.6	632.5	34.3	97.5
S26108-28	192	0.622	0.12252	0.00104	5.67613	0.07575	0.33770	0.00317	0.703	1875.6	15.3	1927.7	11.5	1984.3	16.8	93.7
S26108-29	105	0.219	0.05980	0.00151	0.79989	0.02231	0.09744	0.00106	0.389	599.4	6.2	596.8	12.5	586.7	54.8	102.3
S26108-4	114	0.188	0.06456	0.00146	0.96430	0.02462	0.10955	0.00111	0.397	670.2	6.5	685.5	12.7	736.3	48.9	90.5
S26108-5	178	0.570	0.07401	0.00106	1.68560	0.02979	0.16696	0.00151	0.513	995.3	8.4	1003.1	11.2	1020.1	30.5	97.4
S26108-6	124	0.422	0.12929	0.00134	6.31460	0.09695	0.35789	0.00362	0.659	1972.2	17.2	2020.5	13.4	2070.2	20.3	94.5
S26108-7	68	0.441	0.07355	0.00186	1.59107	0.04472	0.15878	0.00179	0.402	950.0	10.0	966.7	17.4	1005.0	51.4	94.1
S26108-8	91	0.622	0.07377	0.00170	1.69075	0.04397	0.16859	0.00187	0.427	1004.3	10.3	1005.0	16.5	1006.6	47.1	99.8
S26108-9	120	0.664	0.06386	0.00174	0.81702	0.02473	0.09431	0.00112	0.391	581.0	6.6	606.4	13.8	702.6	58.3	81.9
S4102-10	179	0.107	0.06186	0.00140	0.82110	0.02107	0.09738	0.00106	0.423	599.0	6.2	608.7	11.7	644.7	49.2	92.6
S4102-11	140	0.208	0.06920	0.00121	1.46011	0.03192	0.15485	0.00186	0.548	928.1	10.4	914.1	13.1	880.4	37.4	105.8
S4102-12	121	0.531	0.06182	0.00172	0.78216	0.02377	0.09273	0.00104	0.368	571.7	6.1	586.7	13.5	645.4	59.6	88.1
S4102-14	100	0.413	0.06252	0.00218	0.89267	0.03341	0.10453	0.00130	0.332	640.9	7.6	647.8	17.8	671.9	73.8	95.2
S4102-16	111	0.855	0.07352	0.00188	1.49720	0.04411	0.14880	0.00201	0.459	894.3	11.3	929.2	17.8	1013.2	52.2	87.4
S4102-18	531	0.114	0.06365	0.00085	1.06235	0.01852	0.12187	0.00120	0.565	741.3	6.9	735.0	9.1	715.8	30.3	103.8
S4102-19	79	0.832	0.07472	0.00205	1.54877	0.04746	0.15123	0.00184	0.396	907.8	10.3	950.0	18.8	1049.0	55.8	85.6
S4102-2	321	0.207	0.17654	0.00110	10.25663	0.12642	0.42447	0.00412	0.788	2280.7	18.6	2458.2	11.4	2608.4	12.6	85.1
S4102-22	117	0.373	0.17410	0.00187	10.62627	0.17231	0.44568	0.00461	0.638	2376.0	20.6	2491.0	15.0	2586.1	20.8	90.3
S4102-24	232	0.689	0.06436	0.00156	0.85812	0.02318	0.09753	0.00104	0.395	599.9	6.1	629.1	12.6	735.5	51.7	80.7
S4102-27	61	0.510	0.05964	0.00331	0.77815	0.04507	0.09559	0.00152	0.275	588.5	8.9	584.4	25.5	568.6	116.9	103.7
S4102-3	44	1.520	0.06697	0.00312	1.27229	0.06178	0.13879	0.00181	0.269	837.8	10.3	833.4	27.3	821.7	94.8	102.1
S4102-4	77	0.258	0.05816	0.00232	0.75907	0.03212	0.09533	0.00126	0.312	587.0	7.4	573.5	18.4	520.3	85.9	113.4
S4102-8	407	0.100	0.06254	0.00093	0.90005	0.01690	0.10527	0.00110	0.559	645.2	6.4	651.8	9.0	674.5	33.0	95.4

(continued)

Table 2.3 (continued)

Analysis	U (ppm)	Th/U	Isotope ratios							Apparent ages (Ma)						Conc (%)
			207Pb*/206Pb*	±	207Pb*/235U*	±	206Pb*/238U*	±	RhoXY	206Pb*/238U*	± (Ma)	207Pb*/235U*	± (Ma)	207Pb*/206Pb*	± (Ma)	
S4102-9	298	0.330	0.06415	0.00101	0.94908	0.01826	0.10838	0.00109	0.523	663.3	6.3	677.6	9.5	725.4	34.4	91.0
S7104-10	97	0.162	0.06805	0.00197	1.04522	0.03371	0.11190	0.00148	0.410	683.8	8.6	726.5	16.6	860.8	59.9	78.3
S7104-11	146	0.311	0.07554	0.00132	1.77558	0.03825	0.17216	0.00196	0.528	1024.0	10.8	1036.6	13.9	1063.2	36.4	96.0
S7104-12	185	0.297	0.07059	0.00125	1.28909	0.02806	0.13427	0.00158	0.541	812.2	9.0	840.9	12.4	917.5	37.2	87.8
S7104-14	54	0.453	0.06686	0.00298	1.07453	0.05082	0.11860	0.00181	0.323	722.5	10.5	741.0	24.6	797.1	91.2	90.1
S7104-16	22	0.454	0.08945	0.00668	1.26955	0.09899	0.10498	0.00228	0.279	643.5	13.3	832.2	43.4	1376.2	137.6	44.1
S7104-17	441	0.188	0.06135	0.00095	0.85667	0.01619	0.10312	0.00101	0.518	632.7	5.9	628.3	8.8	612.7	34.6	103.4
S7104-18	296	0.094	0.12870	0.00115	6.57562	0.09438	0.37668	0.00362	0.669	2060.8	16.9	2056.1	12.6	2051.4	18.8	100.5
S7104-20	112	0.285	0.06587	0.00212	1.11184	0.03861	0.12377	0.00145	0.337	752.2	8.3	759.1	18.4	779.2	67.3	96.3
S7104-22	25	4.378	0.13351	0.00345	6.98072	0.21320	0.38200	0.00593	0.508	2085.6	27.6	2109.0	26.9	2131.8	45.4	97.5
S7104-24	363	0.218	0.06236	0.00093	0.96784	0.01864	0.11297	0.00126	0.577	690.0	7.3	687.4	9.6	678.7	33.3	101.7
S7104-5	212	0.115	0.06150	0.00136	0.81541	0.02048	0.09701	0.00106	0.435	596.9	6.2	605.5	11.4	637.9	48.0	93.3
S7104-6	242	0.309	0.06144	0.00154	0.84057	0.02326	0.09982	0.00107	0.386	613.3	6.2	619.5	12.8	641.9	54.0	95.3
S7104-7	108	0.619	0.06332	0.00203	0.92448	0.03216	0.10621	0.00132	0.358	650.7	7.7	664.7	16.9	712.6	67.6	90.9
S7104-8	66	0.339	0.06206	0.00245	0.90164	0.03808	0.10552	0.00151	0.339	646.7	8.8	652.6	20.2	673.1	82.8	95.9
S7104-9	95	0.212	0.07050	0.00179	1.36604	0.04061	0.14095	0.00207	0.495	850.0	11.7	874.5	17.3	936.9	52.2	90.1

Table 2.4 U-Pb isotopic data for zircon from Chouf Sandstone, University of Arizona analyses

Analysis	U (ppm)	206Pb*/204Pb*	U/Th	206Pb*/207Pb*	±(%)	207Pb*/235U*	±(%)	206Pb*/238U*	±(%) corr.	error corr.	Apparent ages (Ma)						
											206Pb*/238U*	±(Ma)	207Pb*/235U*	±(Ma)	206Pb*/207Pb*	±(Ma)	Conc(%)
S7-03-55	482	171433	3.5	16.6715	2.0	0.6939	3.6	0.0839	2.9	0.82	519.4	14.7	535.2	14.8	602.9	43.7	86.1
S7-03-41	553	175693	1.1	17.3771	2.0	0.6943	3.6	0.0875	3.1	0.84	540.7	15.9	535.4	15.1	512.5	43.1	105.5
S7-03-42	323	97672	2.2	17.1773	1.9	0.7040	3.2	0.0877	2.6	0.80	542.0	13.5	541.2	13.6	537.9	42.5	100.7
S7-03-60	957	112910	8.2	16.9321	1.8	0.7260	3.0	0.0891	2.4	0.80	550.5	12.8	554.2	12.9	569.3	39.1	96.7
S7-03-23	509	59754	1.7	17.3302	2.2	0.7263	3.6	0.0913	2.8	0.79	563.1	15.3	554.4	15.3	518.5	48.0	108.6
S7-03-17	44	37945	2.1	16.5968	4.0	0.7610	5.6	0.0916	3.9	0.69	565.0	20.9	574.6	24.6	612.6	87.5	92.2
S7-03-86	105	39312	1.1	16.3168	2.7	0.7897	4.9	0.0935	4.1	0.84	575.9	22.4	591.0	21.8	649.3	56.9	88.7
S7-03-71	456	99034	0.8	16.1423	1.9	0.8020	3.3	0.0939	2.7	0.82	578.6	14.9	598.0	14.8	672.4	39.6	86.0
S7-03-77	205	47180	1.8	15.8885	2.1	0.8191	3.8	0.0944	3.2	0.84	581.5	17.8	607.6	17.5	706.2	44.9	82.3
S7-03-45	137	60715	2.3	17.3741	2.0	0.7491	3.5	0.0944	2.9	0.81	581.5	15.9	567.7	15.3	512.9	44.7	113.4
S7-03-107	306	134122	1.7	16.8018	1.6	0.7854	2.8	0.0957	2.2	0.80	589.2	12.5	588.6	12.3	586.1	35.6	100.5
S7-03-72	616	69144	4.6	16.6235	2.6	0.7995	3.6	0.0964	2.5	0.69	593.2	13.9	596.5	16.1	609.2	56.1	97.4
S7-03-54	171	169174	3.0	16.3820	2.6	0.8148	4.0	0.0968	3.0	0.75	595.7	17.1	605.2	18.2	640.8	56.4	93.0
S7-03-84	80	56001	1.5	16.2321	2.6	0.8231	5.7	0.0969	5.0	0.88	596.2	28.5	609.8	25.9	660.5	56.5	90.3
S7-03-7	70	31538	2.0	16.9545	2.6	0.7913	3.7	0.0973	2.7	0.73	598.6	15.5	591.9	16.7	566.4	55.6	105.7
S7-03-88	96	93917	3.2	17.2682	2.6	0.7783	3.7	0.0975	2.6	0.72	599.6	15.1	584.5	16.4	526.4	56.3	113.9
S7-03-35	35	8482	19.4	17.0655	2.7	0.7897	4.3	0.0977	3.4	0.77	601.1	19.3	591.0	19.4	552.2	59.9	108.9
S7-03-74	277	43116	2.8	17.0618	2.3	0.7932	4.3	0.0981	3.6	0.85	603.6	20.9	593.0	19.2	552.7	49.4	109.2
S7-03-49	325	42439	2.7	16.1217	2.6	0.8425	5.1	0.0985	4.4	0.86	605.6	25.4	620.5	23.7	675.1	55.3	89.7
S7-03-79	162	66555	2.1	16.8845	2.5	0.8059	4.0	0.0987	3.1	0.78	606.8	18.2	600.2	18.2	575.4	54.4	105.5
S7-03-20	32	33347	6.3	15.9267	3.5	0.8546	4.7	0.0987	3.1	0.66	606.9	18.2	627.2	22.2	701.0	75.5	86.6
S7-03-105	138	43270	4.0	16.9149	2.8	0.8051	4.2	0.0988	3.1	0.73	607.2	17.8	599.7	18.9	571.5	61.5	106.3
S7-03-33	47	118947	0.9	15.3860	5.6	0.8890	6.4	0.0992	3.0	0.47	609.7	17.3	645.8	30.4	774.1	118.2	78.8
S7-03-109	88	45397	1.2	15.8281	2.9	0.8688	4.6	0.0997	3.5	0.77	612.8	20.7	634.9	21.6	714.3	61.7	85.8
S7-03-31	205	171200	3.5	16.5764	2.1	0.8327	3.5	0.1001	2.9	0.81	615.1	16.8	615.1	16.3	615.3	44.9	100.0
S7-03-26	155	18268	2.4	16.4536	2.5	0.8428	3.9	0.1006	3.0	0.77	617.8	17.6	620.7	18.1	631.4	53.9	97.8
S7-03-9	155	38050	3.7	16.2717	1.6	0.8585	3.3	0.1013	2.9	0.87	622.1	17.1	629.3	15.6	655.2	35.4	94.9
S7-03-99	347	77339	2.8	16.7894	2.3	0.8377	4.3	0.1020	3.7	0.85	626.2	22.0	617.9	20.1	587.7	49.6	106.6
S7-03-11	274	133923	3.5	15.3115	2.3	0.9291	4.1	0.1032	3.4	0.83	633.0	20.5	667.2	20.0	784.3	47.7	80.7
S7-03-83	139	34260	1.6	16.8589	2.2	0.8440	3.2	0.1032	2.3	0.73	633.1	14.1	621.3	14.9	578.7	48.0	109.4

(continued)

Table 2.4 (continued)

Analysis	U (ppm)	206Pb*/204Pb*	U/Th	Isotope ratios							Apparent ages (Ma)						Conc (%)
				206Pb*/207Pb*	±(%)	207Pb*/235U*	±(%)	206Pb*/238U*	±(%) corr.	error corr.	206Pb*/238U*	±(Ma)	207Pb*/235U*	±(Ma)	206Pb*/207Pb*	±(Ma)	
S7-03-95	425	213325	52.3	16.0941	2.4	0.8880	3.5	0.1036	2.5	0.72	635.8	15.2	645.3	16.6	678.7	51.7	93.7
S7-03-63	251	171680	2.3	16.1882	2.2	0.8844	3.0	0.1038	2.0	0.67	636.9	12.0	643.4	14.2	666.3	47.4	95.6
S7-03-92	292	124631	3.5	16.2911	2.2	0.8801	4.3	0.1040	3.6	0.85	637.8	22.1	641.1	20.3	652.7	47.9	97.7
S7-03-10	229	216200	15.7	16.1692	2.3	0.9067	4.0	0.1063	3.3	0.81	651.4	20.3	655.3	19.4	668.8	50.0	97.4
S7-03-37	50	35189	1.4	16.1602	2.8	0.9079	4.5	0.1064	3.5	0.78	651.8	21.9	655.9	21.9	670.0	60.6	97.3
S7-03-15	190	29057	0.8	15.9599	2.6	0.9195	5.0	0.1064	4.2	0.85	652.0	26.2	662.1	24.2	696.6	55.9	93.6
S7-03-32	158	33018	1.4	16.2730	2.2	0.9061	3.9	0.1069	3.1	0.81	655.0	19.5	655.0	18.6	655.1	48.0	100.0
S7-03-90	22	41950	2.9	15.3058	2.7	0.9701	6.0	0.1077	5.4	0.90	659.3	33.9	688.5	30.2	785.1	56.4	84.0
S7-03-106	137	41512	3.6	16.4463	2.6	0.9040	4.1	0.1078	3.2	0.77	660.1	19.8	653.9	19.8	632.3	56.9	104.4
S7-03-14	193	26034	1.5	16.0844	1.9	0.9245	3.3	0.1078	2.7	0.81	660.2	16.7	664.7	16.0	680.0	41.1	97.1
S7-03-24	185	151225	2.0	16.3680	1.6	0.9094	2.8	0.1080	2.3	0.83	660.9	14.3	656.7	13.3	642.6	33.4	102.8
S7-03-73	112	26796	1.1	16.1759	2.1	0.9205	3.4	0.1080	2.7	0.79	661.1	16.7	662.6	16.4	667.9	44.4	99.0
S7-03-13	215	185927	1.3	16.3825	2.2	0.9114	3.7	0.1083	2.9	0.79	662.8	18.2	657.8	17.7	640.7	47.9	103.4
S7-03-52	57	23471	1.9	16.2304	3.2	0.9340	5.2	0.1099	4.1	0.78	672.4	25.9	669.7	25.4	660.7	68.8	101.8
S7-03-18	96	45995	3.8	16.0622	2.1	0.9444	3.4	0.1100	2.7	0.80	672.9	17.5	675.2	17.0	683.0	44.4	98.5
S7-03-48	68	19080	1.9	16.3221	2.4	0.9295	3.7	0.1100	2.8	0.76	672.9	18.1	667.4	18.3	648.6	52.0	103.8
S7-03-101	158	30896	5.2	15.5514	2.4	0.9832	3.5	0.1109	2.6	0.73	678.0	16.4	695.3	17.6	751.6	50.4	90.2
S7-03-104	51	29480	2.2	14.8075	3.3	1.0437	4.0	0.1121	2.3	0.56	684.8	14.6	725.7	20.8	854.3	69.0	80.2
S7-03-75	181	54763	2.6	15.9762	2.0	0.9711	3.5	0.1125	2.9	0.82	687.4	18.6	689.0	17.5	694.4	42.9	99.0
S7-03-38	88	66708	2.8	15.6906	2.4	0.9928	4.6	0.1130	3.9	0.85	690.0	25.6	700.1	23.3	732.8	51.6	94.2
S7-03-1	179	29136	3.2	16.4010	2.0	0.9569	2.9	0.1138	2.1	0.73	694.9	14.1	681.7	14.6	638.3	43.2	108.9
S7-03-85	306	118167	4.9	16.0715	2.3	0.9855	4.1	0.1149	3.3	0.82	701.0	22.0	696.4	20.4	681.7	50.0	102.8
S7-03-102	129	114072	2.3	15.1716	2.8	1.0944	3.8	0.1204	2.5	0.67	733.0	17.5	750.7	20.0	803.6	59.0	91.2
S7-03-70	893	144470	2.7	15.5355	2.0	1.0955	3.0	0.1234	2.2	0.74	750.3	15.7	751.2	15.8	753.7	42.2	99.5
S7-03-96	60	46129	1.9	14.8264	2.8	1.1637	3.7	0.1251	2.4	0.65	760.0	17.0	783.7	20.0	851.6	57.8	89.2
S7-03-69	316	80826	10.8	14.9760	1.9	1.1826	4.2	0.1284	3.8	0.89	779.0	27.6	792.5	23.1	830.7	39.2	93.8
S7-03-29	147	26934	1.4	15.1569	2.8	1.1776	4.4	0.1294	3.5	0.78	784.7	25.6	790.2	24.3	805.6	57.7	97.4
S7-03-64	275	101502	3.4	15.4674	2.2	1.1613	3.8	0.1303	3.0	0.80	789.4	22.5	782.6	20.5	763.0	47.1	103.5
S7-03-16	82	24519	2.1	14.7473	2.2	1.2593	4.9	0.1347	4.3	0.89	814.6	33.2	827.6	27.7	862.7	46.7	94.4
S7-03-66	274	70026	1.4	15.0391	1.7	1.2495	3.3	0.1363	2.8	0.85	823.6	21.6	823.2	18.4	822.0	35.4	100.2

(continued)

Table 2.4 (continued)

Analysis	U (ppm)	206Pb*/204Pb*	U/Th	Isotope ratios							Apparent ages (Ma)						Conc (%)
				206Pb*/207Pb*	±(%)	207Pb*/235U*	±(%)	206Pb*/238U*	±(%) corr.	error	206Pb*/238U*	±(Ma)	207Pb*/235U*	±(Ma)	206Pb*/207Pb*	±(Ma)	
S7-03-110	207	105344	1.3	14.9246	2.6	1.2665	4.4	0.1371	3.6	0.81	828.2	27.9	830.8	25.1	837.9	53.8	98.8
S7-03-51	70	43176	2.3	14.4009	3.5	1.5354	5.1	0.1604	3.6	0.72	958.8	32.5	944.7	31.1	911.8	72.1	105.2
S7-03-5	121	40961	1.5	14.2684	2.8	1.5223	3.8	0.1575	2.5	0.67	943.1	22.2	939.4	23.1	930.8	57.2	101.3
S7-03-80	535	144764	1.7	14.0407	1.4	1.4944	6.4	0.1522	6.2	0.97	913.1	52.7	928.1	38.7	963.8	29.3	94.7
S7-03-28	379	49316	1.2	14.0006	1.8	1.5164	3.2	0.1540	2.7	0.83	923.3	22.9	937.0	19.5	969.6	35.9	95.2
S7-03-62	126	36452	1.8	13.9561	2.0	1.5099	3.9	0.1528	3.4	0.86	916.8	28.9	934.4	24.1	976.1	41.4	93.9
S7-03-67	132	193181	1.0	13.7998	1.6	1.6823	2.5	0.1684	1.9	0.77	1003.2	18.0	1001.9	16.1	999.0	32.7	100.4
S7-03-44	97	40701	1.1	13.7487	2.1	1.6281	3.9	0.1623	3.3	0.85	969.8	30.0	981.1	24.8	1006.5	42.6	96.4
S7-03-98	253	97051	2.1	13.7483	2.2	1.6908	4.3	0.1686	3.7	0.86	1004.4	34.2	1005.1	27.4	1006.6	44.6	99.8
S7-03-94	490	90139	1.4	13.7109	2.0	1.5874	3.7	0.1579	3.1	0.85	944.8	27.2	965.3	22.8	1012.1	39.7	93.4
S7-03-22	202	30005	0.7	13.6407	1.6	1.7003	3.1	0.1682	2.6	0.85	1002.2	24.3	1008.6	19.7	1022.5	33.1	98.0
S7-03-39	261	105533	1.6	13.6102	2.0	1.7383	3.8	0.1716	3.2	0.84	1020.8	30.2	1022.8	24.5	1027.0	41.2	99.4
S7-03-12	611	175380	3.7	13.2305	2.1	1.6706	3.2	0.1603	2.4	0.75	958.5	21.6	997.4	20.5	1084.0	42.5	88.4
S7-03-50	135	64352	2.3	13.0198	2.1	1.7580	3.6	0.1660	2.9	0.81	990.1	26.6	1030.1	23.2	1116.2	42.3	88.7
S7-03-25	482	150790	1.3	12.0740	2.2	2.2847	4.2	0.2001	3.7	0.86	1175.7	39.3	1207.6	30.0	1265.1	42.1	92.9
S7-03-19	198	51559	1.2	9.2393	2.0	4.6753	4.5	0.3133	4.1	0.90	1756.9	62.5	1762.8	38.0	1769.9	36.7	99.3
S7-03-91	273	100615	0.8	8.7964	1.9	5.1185	3.9	0.3265	3.4	0.87	1821.6	53.4	1839.2	32.9	1859.1	34.5	98.0
S7-03-68	185	69187	3.2	8.6334	2.1	5.4779	4.9	0.3430	4.5	0.91	1901.1	73.5	1897.1	42.3	1892.8	37.3	100.4
S7-03-53	178	61410	3.0	8.4663	2.5	5.3822	4.8	0.3305	4.1	0.85	1840.7	65.8	1882.0	41.3	1927.9	45.2	95.5
S7-03-40	169	186786	3.8	8.4489	2.5	5.1498	4.1	0.3156	3.2	0.78	1768.0	49.2	1844.4	34.5	1931.6	45.1	91.5
S7-03-108	216	102128	4.2	8.3969	2.3	5.6089	6.7	0.3416	6.3	0.94	1894.3	103.0	1917.5	57.7	1942.6	41.3	97.5
S7-03-21	162	1510515	1.4	8.3415	1.3	5.6049	2.5	0.3391	2.2	0.87	1882.3	36.0	1916.9	21.9	1954.4	22.6	96.3
S7-03-57	300	207481	5.8	8.2079	2.1	5.9255	3.5	0.3527	2.8	0.80	1947.7	46.3	1965.0	30.0	1983.2	37.1	98.2
S7-03-65	53	36031	2.5	7.8096	2.4	6.3795	4.0	0.3613	3.2	0.80	1988.5	54.7	2029.4	35.3	2071.3	42.9	96.0
S7-03-6	479	63662	17.4	7.3044	2.3	6.7862	3.7	0.3595	2.9	0.78	1979.8	49.3	2083.9	32.9	2188.4	40.7	90.5
S7-03-76	358	222417	2.4	7.2059	1.4	6.6163	3.4	0.3458	3.1	0.91	1914.4	50.8	2061.5	29.7	2212.0	24.3	86.5
S7-03-30	306	73686	1.2	6.6698	1.7	8.3150	4.3	0.4022	4.0	0.92	2179.3	74.0	2266.0	39.4	2345.1	29.2	92.9
S7-03-61	364	96679	1.6	6.5765	2.3	8.7132	3.5	0.4156	2.6	0.75	2240.5	49.9	2308.5	32.1	2369.2	40.0	94.6
S7-03-46	477	84616	1.3	6.5650	1.4	7.2316	3.7	0.3443	3.4	0.92	1907.4	55.6	2140.4	32.7	2372.1	24.4	80.4
S7-03-100	165	169878	5.5	6.3501	1.6	9.2139	3.0	0.4244	2.5	0.85	2280.2	48.0	2359.5	27.0	2428.7	26.6	93.9
S7-03-56	258	87681	1.2	6.2914	1.6	9.8701	3.2	0.4504	2.8	0.88	2396.9	57.0	2422.7	29.9	2444.5	26.3	98.1

(continued)

Table 2.4 (continued)

| Analysis	U (ppm)	206Pb*/204Pb*	U/Th	206Pb*/207Pb*	± (%)	207Pb*/235U*	± (%)	206Pb*/238U*	± (%) corr.	error	206Pb*/238U*	± (Ma)	207Pb*/235U*	± (Ma)	206Pb*/207Pb*	± (Ma)	Conc (%)
				Isotope ratios							Apparent ages (Ma)						
S7-03- 3	445	475551	1.3	6.1739	1.9	10.3948	3.9	0.4655	3.4	0.87	2463.6	69.1	2470.6	35.9	2476.3	32.2	99.5
S7-03- 34	104	191516	0.9	6.1680	1.9	10.2440	6.5	0.4583	6.3	0.96	2431.9	127.1	2457.1	60.6	2478.0	31.6	98.1
S7-03- 87	66	147402	1.0	6.1374	2.0	10.0400	4.1	0.4469	3.6	0.88	2381.5	71.3	2438.5	37.7	2486.3	32.9	95.8
S7-03- 43	372	95211	1.7	6.0486	2.1	9.8923	2.9	0.4340	1.9	0.68	2323.5	37.9	2424.8	26.4	2510.9	35.4	92.5
S7-03- 82	414	565821	0.5	5.9019	2.2	10.4608	3.3	0.4478	2.5	0.76	2385.3	50.5	2476.5	31.0	2552.1	36.6	93.5
S7-03- 93	153	114183	1.1	5.8635	2.1	10.8852	5.7	0.4629	5.3	0.93	2452.4	107.3	2513.4	52.7	2563.0	34.9	95.7
S7-03- 47	204	111152	1.1	5.6565	1.8	11.5463	3.5	0.4737	3.0	0.86	2499.7	62.2	2568.3	32.7	2622.9	29.9	95.3
S7-03- 97	265	60962	2.6	5.6148	2.2	11.0368	3.3	0.4494	2.4	0.74	2392.8	48.3	2526.2	30.5	2635.3	36.6	90.8
S7-03- 81	255	245746	1.7	5.6107	1.9	10.7686	4.2	0.4382	3.8	0.90	2342.6	74.2	2503.4	39.2	2636.5	31.2	88.9
S7-03- 78	136	223342	1.4	5.5348	1.5	12.2403	3.2	0.4913	2.8	0.88	2576.5	60.1	2623.0	30.2	2659.1	25.5	96.9
S7-03- 36	114	252567	2.0	5.1248	2.1	13.2145	3.5	0.4912	2.8	0.80	2575.7	58.7	2695.1	32.7	2785.9	34.3	92.5
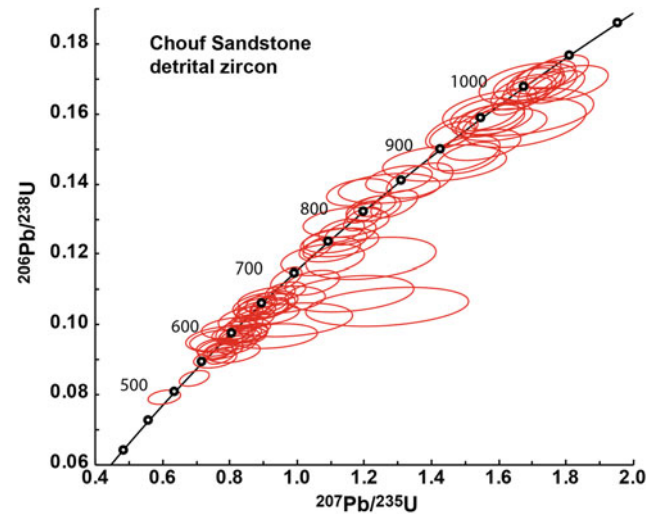
Fig. 2.12 Concordia diagram of U-Pb zircon ages of seven Chouf Sandstone samples (n: 105) showing data between 500 and 1100 Ma. For the location of the samples see Table 2.2 and Fig. 2.4

2.7 The Isopach Map of the Chouf Formation: Is It the Chouf Formation a Syn-rift Unit?

Several studies addressed the isopach variations of the Chouf Sandstone in Lebanon (Kanaan 1966; Ukla 1970; Walley 1998). Onshore isopach maps proposed for the Chouf Formation (supported by well data) reveal that this unit is absent in northern Lebanon (e.g. missing in the Terbol-1 well, Fig. 2.1) and the formation thickens southwards, towards central and southern Lebanon (Adloun-1 well: 170 m of carbonates, marls, silts and sandstones) reaching more than 300 m measured in outcrops in the Jezzine area, about 20 km south of Beirut (Dubertret 1975). This thickness variation has been attributed to a NW-SE Late Jurassic-Early Cretaceous extensional phase in the southern Palmyride Basin that extended into central and southern Lebanon (Robertson and Dixon 1984; Chaimov et al. 1992; Walley 1998).

The Early Cretaceous rifting phase in Lebanon, described by Homberg et al. (2009, 2010), started during the Valanginian and ended by the beginning of the Cenomanian. The normal faults corresponding to this extensional period have a typical strike direction between WNW-ESE to WSW-ENE with a mean dip of 60° (Fig. 2.1). At least one of these outcrop-scale normal faults offsetting Lower Cretaceous clastics was shown to have a syn-depositional growth fault character. On a larger scale, the map-view length of these faults ranges from several kilometers to several tens of kilometers with a corresponding offsets up to several hundred meters. The corresponding extensional stress field was directed NNE-SSW with minor local variations. Homberg
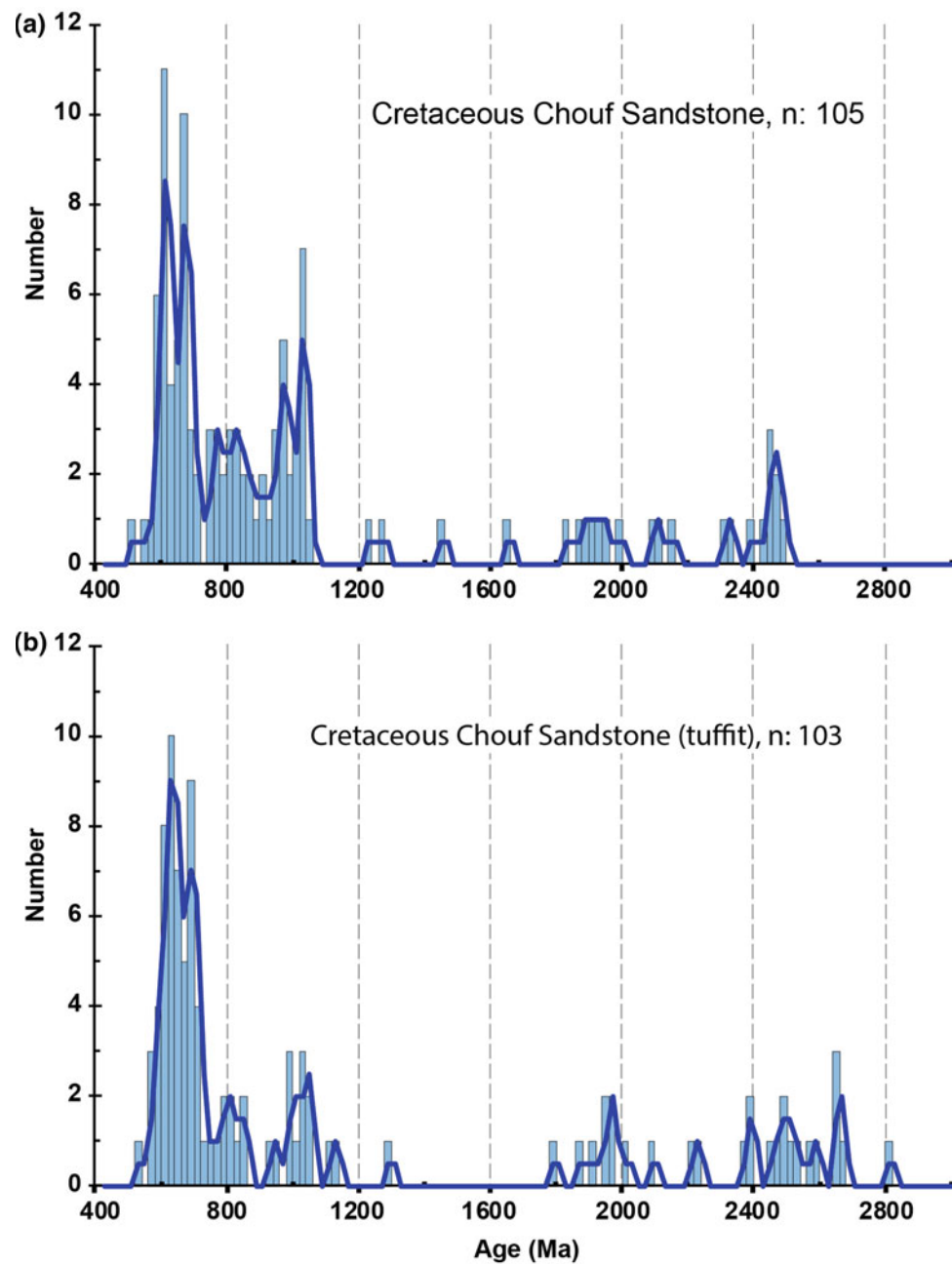
Fig. 2.13 Detrital zircon spectra of the Chouf Sandstone **a** taken from seven localities shown in Fig. 2.4, n: 105, and **b** taken from the tuffit sample shown in Fig. 2.10, n: 103. Data are ^{238}U/^{206}Pb ages

et al. (2009, 2010) also suggested that the thickness variations in the Lower Cretaceous sedimentary sequences, reported by many, reflect deposition in fault-controlled grabens located within an overall WNW-ESE trending basin.

During our field work in central and northern Lebanon we did find numerous brittle faults with WNW-ESE trends offsetting the Chouf Formation (e.g. Fig. 2.10a), but we could not find evidence for syn-depositional normal faults. Therefore, in order to test the syn-rift nature of the Chouf

Sandstone, we attempted to refine and quantify the isopach variations mentioned by many (e.g. Dubertret 1955) within the Lower Cretaceous sequence. Instead of detailed and time-consuming field work, burdened by some accessibility issues, we relied on remote sensing data sets, such as modern high-resolution satellite data sets (with ∼0.75 m horizontal and 4 m vertical resolution) to derive true stratigraphic thickness data points, as described earlier, for the Chouf Sandstone in Lebanon (Table 2.1).
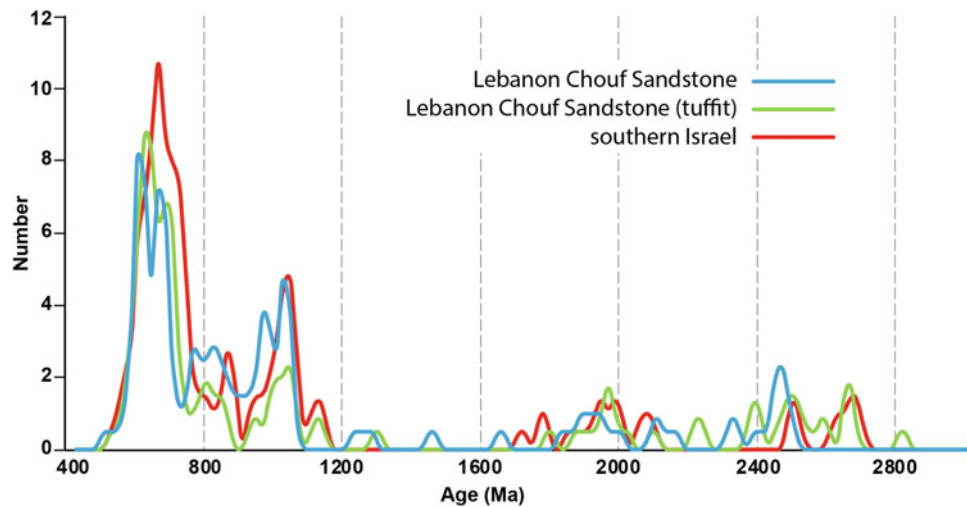
Fig. 2.14 Comparison of the combined Chouf Sandstone detrital zircon spectrum (this work) with that of the age-equivalent unit in southern Israel (Kolodner et al. 2009). The match of these spectra is very good even though the locations of the corresponding samples are about 400 km apart. Blue is the spectrum out of the seven samples (Fig. 2.13a), green is the spectrum from the tuffit sample (Fig. 2.13b) and red is the spectrum of detrital zircons from southern Israel. Data are $^{238}U/^{206}Pb$ ages

The challenge of compiling a reasonable isopach map, in the overall absence of subsurface data points, is that the Chouf outcrops are patchy and scattered (Fig. 2.1) due to the post-depositional erosion of large parts of this formation (Fig. 2.3). Therefore our hand-contouring of the Chouf isopach data points (Table 2.1) is admittedly a conceptual attempt only to show a speculative map-view pattern with several WNW-ESE trending half-grabens in our study area (Fig. 2.16). Whereas our input Chouf isopach data points may have a significant error, on the order of 20–30% due to the uncertainities associated with use of the three-points method described earlier, the presence of a few mini-basins with relatively thick (300–700 m) sedimentary fill is clear. It is also to be noted that the separation of the lithologically somewhat similar Chouf and Abieh formations (Fig. 2.2) is obviously more problematic using remote sensing data than by direct observations on the field.

Regardless, based on our data sets we see enough evidence in central and northern Lebanon to assume the deposition of the Chouf Sandstone in a "wide-rift" setting (sensu Buck 1991), whereas the low-strain extension was distributed across a few hundred kilometres-wide region with numerous fault-controlled mini-basins. In our opinion, the syn-rift basin fill character of the Chouf Sandstone Formation is a reasonable interpretation, in agreement with previous workers (Homberg et al. 2009, 2010; Hatzenbichler et al. 2013; Bauer 2014). We also assume that this wide rift basin complex extends farther to the west, towards offshore Lebanon, and also towards the east beneath the Bekaa Basin. This assumption has important implications for hydrocarbon exploration.

2.8 The Chouf Petroleum Play and Its Regional Proven Analogues

Given its near-surface presence, the Chouf Sandstone Formation is not a viable reservoir target for most part of onshore Lebanon (Alsharhan and Nairn 1997; Renouard 1955; Beydoun 1988; Beydoun and Dunnington 1975; 1981; Nader 2011; Nader and Swennen 2004; 2014; Ghalayini et al. 2018; Klitzch and Squyres 1990). However, this sequence is located at sufficient depth (>1 km) near the coastline and beneath the Lebanese shelf and also beneath the Bekaa Plain (Nader et al. 2016). Moreover, there are useful and proven analogues for a Lower Cretaceous clastic play in Israel and Egypt which underline the potential of this particular play.

The most relevant play analogue is the Helez Field in Israel (Shenhav 1971; Cohen 1976; Gilboa et al. 1990; Gardosh et al. 2006, 2011; Gardosh and Tannenbaum 2014). The Helez Field, a complex of three fields: Helez, Brur and Kokhav, is located some 55 km south of Tel Aviv and it was discovered in 1955.

The field complex has a combination trap with structural and stratigraphic elements along a NNE-SSW trending structure down a hinge zone (or "shelf break" of Garfunkel and Derin 1983). Landward from the hinge zone, Lower Cretaceous platform sediments were deposited over a gently inclined Jurassic erosional surface, whereas a deeper water shaly facies was formed on the basinward-side. The gross reservoir succession of the Valanginian to Barremian Helez Formation has been subdivided into several members with
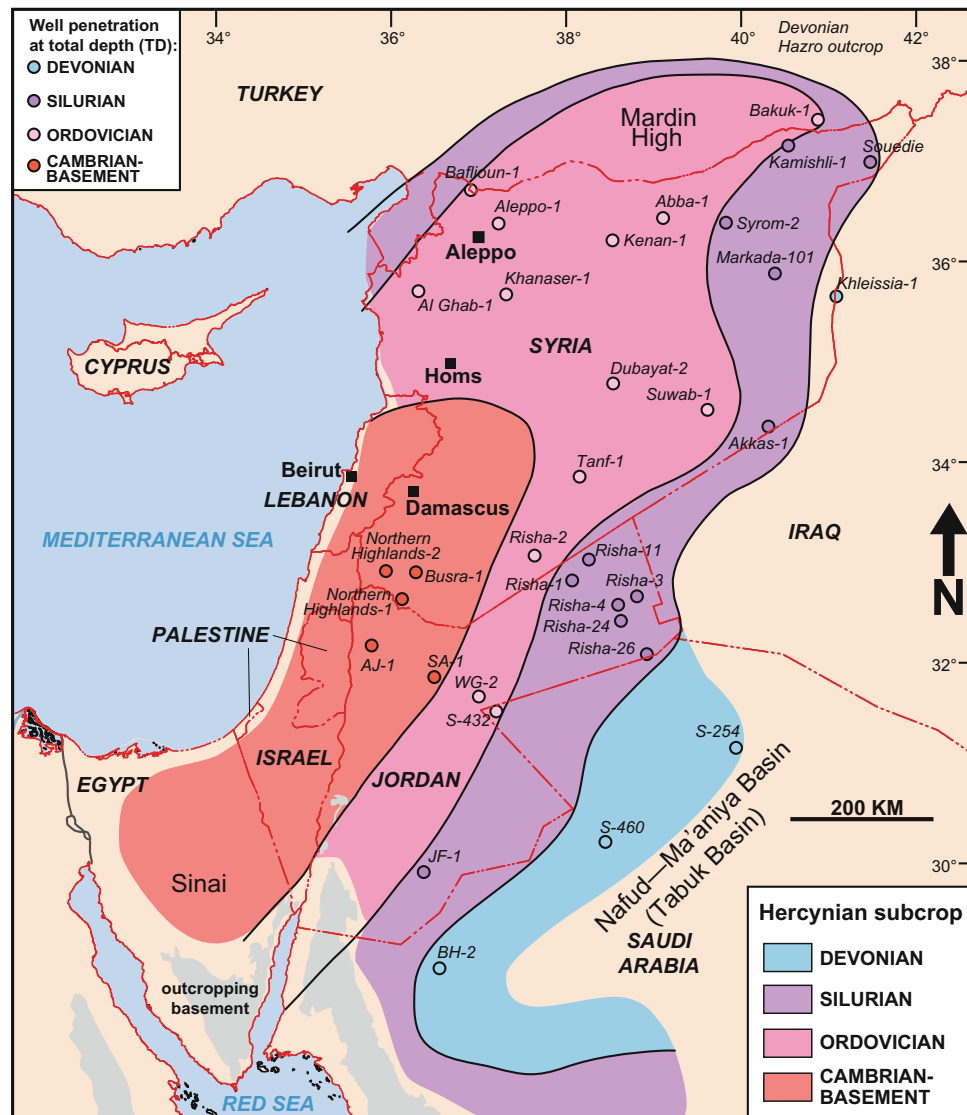
Fig. 2.15 Regional-scale subcrop map of the Hercynian unconformity highlighting the presence of Cambrian and Ordovician units in our study area in Lebanon as the primary source of recycled sandstones of the Chouf Formation. Modified after Reches et al. (1981) and Wood (2015)

well-correlatable sandstone, dolomite and shale lithologic units. The various members within the very heterogeneous Helez Formation provide very poor to good reservoirs with a relatively small net-to-gross reservoir ratio. Shenhav (1971) and Gilboa et al. (1990) reported three main Helez sandstone types, corresponding to (a) open marine, (b) coastal/estuarine and (c) aeolian depositional environments, with average porosity and permeability values ranging between 16–32% and 30–200 md, respectively. As to the source of oil in the Helez Field, the Middle Jurassic open-marine spiculitic Barnea Limestone was identified by Bein and Sofer (1987) suggesting that the hydrocarbon-generating kitchen for the oil accumulation was located basinward at 4500–5000 m depth.

Similar Jurassic units were found onshore Lebanon and analyzed by Bou Daher et al. (2016) and Barabasch et al. (2018).

A somewhat less relevant play analogue is provided by the oil discovery of the Mango-1 well, in easternmost offshore Egypt (Yousef et al. 2010; EGAS 2012). The Mango-1 well was drilled in 1985 and tested/flowed light oil at a rate of 10,000 BOPD and 4.5 MMSCFG/d from Lower Cretaceous sandstones (EGAS 2012). A 332 m gross sandstone sequence, with seven reservoir quality sandstone bodies (with average porosities of 16–26%) have been drilled in the well. Two sand bodies have been found to be oil-bearing and were tested at the rate of 10,000 BOPD and 4.5 MMSCFG/d. As to the play analogy, even though the tested oil-bearing

Fig. 2.16 Conceptual interpretation of the Chouf isopach data points, assuming that WNW-ESE trending normal faults (Homberg et al. 2009, 2010) are responsible for the pronounced lateral thickness changes. The Chouf isopach values shown in metres were derived by remote sensing methods, see text. Note the speculative nature of the map as most of the Chouf sequence has been eroded away in the central part of the study area as the background geologic map shows (cf. Fig. 2.4). The same map-view faulting pattern, however, could be expected in offshore Lebanon to the west and also beneath the Bekaa Plain to the east (Fig. 2.1)
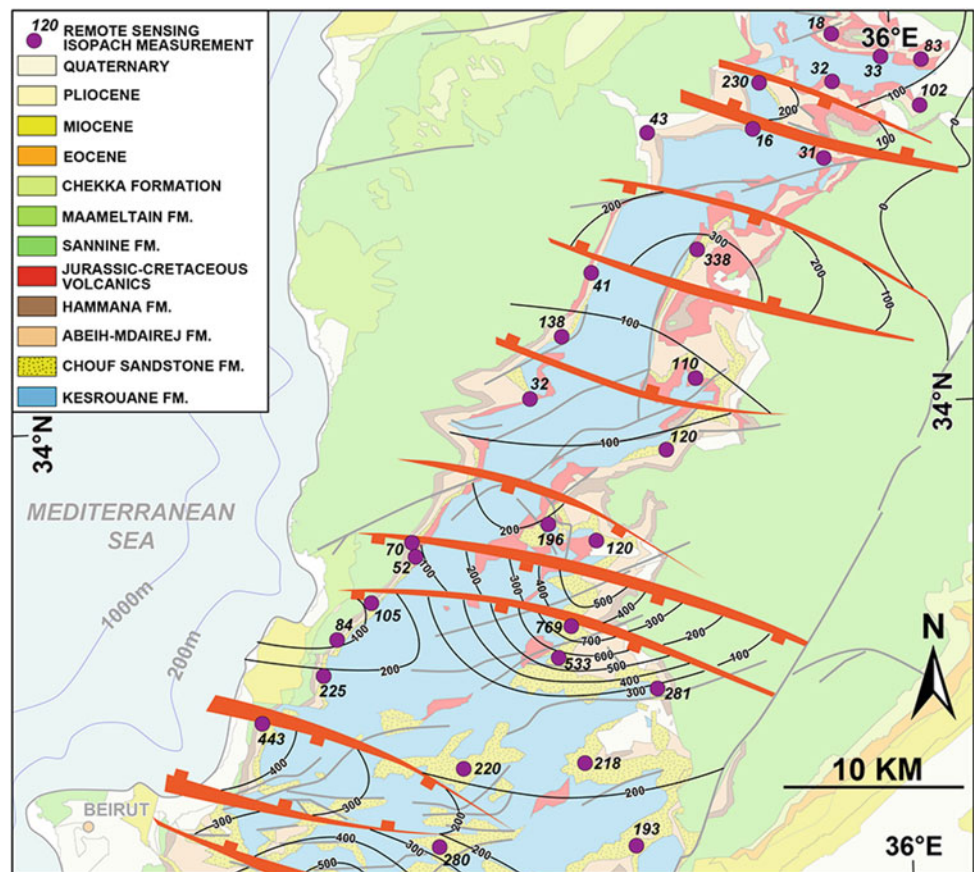
sandstones were Lower Cretaceous, they were younger than the Chouf Sandstone, i.e. Aptian-Albian in age. Moreover, the Mango sandstones were deposited in deep water sub-marine fan delta and channelized system that have been deposited in an outer shale slope environment (EGAS 2012).

The reservoir of the Chouf play offshore Lebanon is the Chouf Sandstone Formation, the main focus of the present paper. The Chouf is a very heterogeneous succession with some non-reservoir facies lithologies such as claystones and shales (e.g. Figure 2.5). However, the sandstone units of the Chouf Formation have moderate to good reservoir properties (Fig. 2.7b), similarly to the age equivalent Helez Formation discussed above (Gilboa et al. 1990).

The most obvious source for this play is the sequence of Jurassic carbonates which should, given their more basin-ward position, have higher TOCs offshore than onshore (Ghalayini et al. 2018). Deeper source intervals, like the Triassic Amanus Shale could also contribute. The hydro-carbons then would have migrated up-dip from a kitchen area which is located in the present-day deepwater basin, using unconformity surfaces, like the top Jurassic one, and fault conduits. The traps are likely to be associated extensional rotated fault blocks along the hinge zone of the deepwater basin margin (Nader 2011, 2014). Besides structural trap-ping, stratigraphic trapping mechanisms could also be con-sidered. Ghalayini et al. (2018) showed a potential example of this where a potential flat-spot was observed on seismic data within an assumed Lower Cretaceous clastic wedge offshore Lebanon. Whereas stratigraphic traps have a riskier exploration profile, the advantage of these clastic wedges with an up-dip pinch-out is that they likely extend along the entire margin offshore Lebanon (Ghalayini et al. 2018). Finally, the immediate top seal for an intra-Chouf reservoir is provided by the impermeable argillaceous limestone and shale units of the overlying Abeih Formation (Fig. 2.2).

A drawback of the Chouf play in offshore Lebanon is that it can be chased only in a relatively narrow (20–40 km wide) fairway along the margin (Fig. 2.1) as its reservoir target is located beyond economically drillable depth basinward (> 6–7 km).

2.9   Geodynamic Context of the Syn-rift Lower Cretaceous Clastics in the Broader Region

To better understand the broader context of the wide-rift style Neocomian to Barremian extension we have described in NW Lebanon, two other topics are considered here: (a) volcanism and (b) regional-scale structural evolution during the Lower Cretaceous.

Laws and Wilson (1997) provided an overview about the Early Triassic-Cretaceous rifting and magmatism along the western edge of the Arabian Peninsula from Egypt in the south to Syria in the north. Specifically, the Late Jurassic-Early Cretaceous volcanism throughout the Levant region is clearly rift-related according to most authors (e.g. Shimron and Lang 1989; Mouty et al. 1992; Laws and Wilson 1997; Abdel-Rahman 2002; Segev 2009) based on their geochemical signature such as major and trace element (including rare earth element) and Sr–Nd isotopic compositions. This observation also supports the syn-rift scenario proposed for the Chouf Sandstone.

The timing and kinematics of the opening of the offshore Levant Basin are long debated topics. A WNW-ESE direction of opening during the Triassic and Jurassic was proposed by many (e.g. Garfunkel and Derin 1983; Robertson 1998; Walley 1998; Ben-Avraham et al. 2002; Gardosh et al. 2010). This model is primarily based on the NNE-SSW trending structural fabric of pre-Late Permian, Early to Middle Triassic, and Early to Middle Jurassic grabens onshore and offshore in the Levant (e.g. Roberts and Peace 2007; Gardosh et al. 2006, 2010, 2011). Recent crustal-scale and basin modelling studies of the northern Levant Basin also assumed a Triassic to Early Jurassic rifting period (Inati et al. 2016, 2018; Barabasch et al. 2018).

Importantly, there are no well penetrations of the critical Cretaceous, Jurassic to Triassic sequences in the deepwater part of the entire Levant Basin to date, which would confirm the inferred age of the syn-tectonic basin fill. Therefore, the timing of the opening of the offshore Levant Basin remains enigmatic and the lack of well-control leaves room for alternative models. Segev et al. (2018) proposed a very different opening model where the Levant Basin opened during the Cretaceous, roughly 100 Myr later than the prevailing models favoured so far. The corresponding drastic change in the thermal evolution of the entire offshore Levant Basin, however, has not been addressed so far by these authors.

Regardless of the age, the dominant NNE-SSW trending structural fabric of the offshore Levant is perpendicular to the Early Cretaceous WNW-ESE trending meso-scale faults documented by Homberg et al. (2009, 2010) or the similarly trending syn-depositional grabens during the Late Jurassic (i.e. Kimmeridgian, Collin et al. 2010) documented onshore

Lebanon. The markedly different orientations of the prevailing extensional stress fields require a geodynamic scenario involving the entire Levant region.

The two contrasting models of the timing of the Levant Basin opening put the Early Cretaceous low-strain extensional period during the deposition of the Chouf Formation into two very different geodynamic contexts. If the Levant basin opened as an oceanic basin by Middle Jurassic times (e.g. Garfunkel and Derin 1983), then the Early Cretaceous extensional period was just a superimposed rifting attempt.

Alternatively, if the Levant Basin opened as an oceanic domain during the Late Cretaceous (Segev et al. 2018), then the Valanginian to Barremian extensional period in our study area in NW Lebanon was the initial wide-rift style period before the Aptian-Albian break-up of the margin with the subsequent seafloor spreading during the Cenomanian-Turonian. In our view, this scenario is at odds with recent modelling work done for the northern Levant Basin (Inati et al. 2016, 2018; Barabasch et al. 2018).

We also note another challenge for putting the extensional basin system responsible for the deposition of the Chouf sequence in a clear geodynamic context. Whereas we described a WNW-ESE trending basin system earlier (Fig. 2.16), regional isopach maps of the Chouf Formation either define a N-S trend (e.g. Kanaan 1966; Ukla 1970) or a NE-SW trend (e.g. Wood 2001; Hawie et al. 2013). Therefore there is a discrepancy between the regional-scale isopach patterns versus the WNW-ESE to WSW-ENE trending fault pattern Homberg et al. (2009, 2010) described in NW Lebanon.

We suggest that there might be several reasons for this apparent discrepancy: (a) the regional isopach maps are still poorly constrained with sufficient amount of subsurface data; (b) there is no clear subdivision and precise stratigraphic correlation of the Lower Cretaceous formations across the country borders in the region and (c) the pre-existing Palmyra basin system (e.g. Ghalayini et al. 2017) might have also had an influence on the source-to-sink depositional patterns. Clearly, more work needs to be done in order to define the regional extent of the Valanginian to Barremian (but not Aptian-Albian!) wide-rift style basin system we have interpreted in NW Lebanon.

2.10   Conclusions

We propose a model of a wide-rift style extensional episode for northern Lebanon during the Early Cretaceous (Valanginian to Barremian), which provided the accommodation space for the deposition of the Chouf Sandstone Formation. We speculate that the laterally frequently changing isopach pattern and the lithologically very heterogeneous nature of

the Chouf is the result of deposition in syn-sedimentary half-grabens trending perpendicular to the Levant margin.

Based on U–Pb zircon geochronology, the Chouf has an identical detrital zircon spectrum compared to the age equivalent siliciclastics in southern Israel, some 400 km to the south. This spectrum and the petrography of the Chouf suggest its recycling from Cambrian to Ordovician quartz-rich sandstones.

Despite the significant amount of non-reservoir lithofacies within the Chouf Formation such as shales, lignites, volcanics, etc., its sandstone units have the clear potential to be moderate to good reservoirs in a petroleum systems context. There are also proven reservoir analogues in the broader Levant for what we term the Chouf play in Lebanon. This play remains untested in offshore Lebanon.

References

Abdel-Rahman AM (2002) Mesozoic volcanism in the Middle East: geochemical, isotopic and petro-genetic evolution of extension-related alkali basalts from central Lebanon. Geol Magaz 139:621–640

Alsharhan AS, Nairn AEM (1997) Sedimentary basins and petroleum geology of the Middle East. Elsevier Science, Amsterdam, p 843p

Amireh BS (1991) Mineral composition of the Cambrian—Cretaceous Nubian series of Jordan: provenance, tectonic setting and climatological implications. Sed Geol 71:99–119

Amireh BS (1992) Sedimentology and mineral composition of the Kurnub Sandstone in Wadi Qseib, SW Jordan. Sed Geol 78:267–283

Amireh BS (1994) Heavy and clay minerals as tools in solving stratigraphic problems: a case study from the Disi Sandstone (Early Ordovician) and the Kurnub Sandstone (Early Cretaceous) of Jordan. N Jb Geol Paläont Mh H 4:205–222

Amireh BS (1997) Sedimentology and palaeogeography of the regressive-transgressive Kurnub Group (Early Cretaceous) of Jordan. Sed Geol 112:69–88

Asmar C, Grasemann B, Nader F, Tari G (2013) The Qartaba Anticline (central Mount Lebanon): Implications for the tectonic evolution of onshore Lebanon. In: EGU General Assembly Conference Abstracts, p 15

Asmar C, Schneider DA, Grasemann B, Nader FH, Tari G (2014a). The Lower Cretaceous Chouf Sandstone of Lebanon: Tracking Caledonian tectonism in a Tethyan sediment. In: EGU General Assembly Conference Abstracts, p 16

Asmar C, Grasemann B, Tari G (2014b) The Qartaba Structure (Mount Lebanon): structural study and modeling. In: EGU General Assembly Conference Abstracts, p 16

Avigad D, Kolodner K, McWilliams M, Persing H, Weissbrod T (2003) Origin of northern Gondwana Cambrian sandstone revealed by detrital zircon SHRIMP dating. Geology 31:227–230

Avigad D, Sandler A, Kolodner K, Stern RJ, McWilliams M, Miller N, Beyth M (2005) Mass-production of Cambro-Ordovician quartz-rich sandstone as a consequence of chemical weathering of Pan-African terranes: Environmental implications. Earth Planet Sci Lett 240:818–826

Barabasch J, Ducros M, Hawie N, Bou Daher S, Nader FH, Littke R (2018) Integrated 3D forward stratigraphic and petroleum system modeling of the Levant Basin, Eastern Mediterranean. In: Basin Research, in press

Barrier É, Machhour L, Blaizot M (2014) Petroleum systems of Syria in Marlow L, Kendall C, Yose L (eds). AAPG Memoir 106:335–378

Bauer H (2014) Tectonic evolution of the Northern Mount Lebanon region with particular reference to the Lower Cretaceous Chouf Formation (Lebanon), MSc thesis, University of Vienna, 153 p

Bein A, Sofer Z (1987) Origin of oils in Helez region, Israel—implications for exploration in the eastern Mediterranean. Am Assoc Petrol Geol Bull 71:65–75

Bellos GS (2008) Sedimentology and diagenesis of some Neocomian-Barremian rocks (Chouf Formation), Southern Lebanon. Master's Thesis, American University of Beirut, Beirut, Lebanon, 277 p

Beydoun ZR (1977a) Petroleum prospects of Lebanon: re-evaluation. Am Asso Petrol Geol Bull 61(1):43–64

Beydoun ZR (1977b) The levantine countries: the geology of Syria and Lebanon (maritime regions). In: Nairn AEM, Kanes WH, Stehli FG (eds) the ocean basins and margins, vol 4A—the Eastern Mediterranean. Plenum Press, New York, pp 319–353

Beydoun ZR (1981) Some open questions relating to the petroleum prospects of Lebanon. J Pet Geol 3(3):303–314

Beydoun ZR (1988) The Middle East: regional geology and petroleum resources. Scientific Press Ltd, London, p 296

Beydoun ZR, Dunnington HV (1975) The petroleum geology and resources of the Middle East. Scientific Press, Beaconsfield, England, p 100

Beydoun ZR, As-Saruri ML, Baraba' RS (1996) Sedimentary basins of the Republic of Yemen: their structural evolution and geological characteristics. Revue de l' Institute Francais du Petrole, 51, 763–775

Bou Daher S, Ducros M, Michel P, Hawie N, Nader FH, Littke R (2016) 3D thermal history and maturity modelling of the Levant Basin and its eastern margin, offshore–onshore Lebanon. Arab J Geosci 9(6):440

Buck WR (1991) Modes of continental lithospheric extension. J Geophys Res Solid Earth 96(B12):20161–20178

Butler RWH, Spencer S, Griffiths HM (1998) The structural response to evolving plate kinematics during transpression: evolution of the Lebanese restraining bend of the Dead Sea Transform. In: Holdsworth RE, Strachan RA, Dewey JF (eds) Continental Transpressional and Transtensional Tectonics, vol 135. Geological Society London, Special Publications, pp 81–106

Chaimov TA, Barazangi M, Al-Saad D, Sawaf T, Gebran ALI (1992) Mesozoic and Cenozoic deformation inferred from seismic stratigraphy in the southwestern intracontinental Palmyride fold-thrust belt Syria. Geol Soc Am Bull 104:704–715

Clark GN, Boudagher-Fadel MK (2001) The larger benthic foraminifera and stratigraphy of the Upper Jurassic/Lower Cretaceous of Central Lebanon. Revue de micropaleontologie 44:215–232

Cohen Z (1976) Early Cretaceous buried canyon: influence on accumulation of hydrocarbons in the Helez oil field, Israel. AAPG Bulletin 60:108–114

Collin PY, Mancinelli A, Chiocchini M, Mroueh M, Hamdam W, Higazi F (2010) Middle and Upper Jurassic stratigraphy and

sedimentary evolution of Lebanon (Levantine margin). Palaeoenvironmental and geodynamic implications. In: Homberg C, Bachmann M (eds) Evolution of the Levant Margin and Western Arabia Platform since the Mesozoic, vol 341. Geological Society, London, Special Publications, pp 227–244

Daëron M (2005) Rôle, cinématique et comportement sismique á long terme de la faille de Yammoûneh. Unpublished Ph.D. thesis, Institut de Physique du Globe de Paris. 179 p

Dickinson WR, Gehrels GE (2009) Use of U–Pb ages of detrital zircons to infer maximum depositional ages of strata: a test against a Colorado plateau Mesozoic database. Earth Planet Sci Lett 288:115–125

Dubertret L (1955) Carte Géologique du Liban au 1/200,000. Note Explicative

Dubertret L (1963) Liban, Syrie: chaine des grands massifs côtiers et confins à l'est. In: Dubertret L (ed) Lexique Stratigraphique International III, Asie, CNRS Paris, Fasc. 9–103, 155 p

Dubertret L (1966) Liban, Syrie et bordure des pays voisins. Première partie. Tableau stratigraphique avec carte géologique au millionième. Notes et Mém. Moyen Orient 8:251–358

Dubertret L (1975) Introduction à la carte géologique a 1/50000 du Liban. Notes et Mém. Moyen-Orient 23:345–403

EGAS (2012) Bid-round Technical Report, Block 6, N. El Arish offshore. http://www.egas.com.eg/BidRound2012/block006.pdf. Last accessed on 15 Sept 2018

Ferry S, Merran Y, Grosheny D, Mroueh M (2007) The Cretaceous of Lebanon in the Middle East (Levant) In: Bulot LG, Ferry S, Grosheny D (eds) Relations between the northern and southern margins of the Tethys Ocean during the Cretaceous Period: Notebooks on Geology, Brest, Memoir 2007/2, pp 38–42

Gardosh M, Tannenbaum E (2014) Petroleum systems of Israel. In: Marlow L, Kendall C, Yose L (eds) Petroleum systems of the Tethyan region. AAPG Memoir, pp 106, 179–216

Gardosh M, Druckman Y, Buchbinder B, Rybakov M (2006) The Levant Basin Offshore Israel: stratigraphy, structure, tectonic evolution and implications for hydrocarbon exploration. Geophysical Institute of Israel, pp 1–119

Gardosh MA, Garfunkel Z, Druckman Y, Buchbinder B (2010) Tethyan rifting in the Levant region and its role in Early Mesozoic crustal evolution. In: Homberg C, Bachmann M (eds) Evolution of the Levant Margin and Western Arabia Platform since the Mesozoic, Geological Society, London, Special Publications, vol 341, pp 9–36

Gardosh MA, Weimer P, Flexer A (2011) The sequence stratigraphy of Mesozoic successions in the Levant margin southwestern Israel: a model for the evolution of southern Tethys margins. AAPG Bull 95:1763–1793

Garfunkel Z, Derin B (1983) Permian-early Mesozoic tectonism and continental margin formation in Israel and its implication for the history of the Eastern Mediterranean. In: Dixon JE, Robertson RHF (eds) The geological evolution of the Eastern Mediterranean: Geological Society London Spec. Publication 12, pp 187–202

Gehrels G, Pecha M (2014) Detrital zircon U–Pb geochronology and Hf isotope geochemistry of Paleozoic and Triassic passive margin strata of western North America. Geosphere 10(1):49–65

Ghalayini R, Daniel J-M, Homberg C, Nader FH, Comstock JE (2014) Impact of Cenozoic strike-slip tectonics on the evolution of the northern Levant Basin (offshore Lebanon). Tectonics 33(11):2121–2142

Ghalayini R, Daniel J, Homberg C, Nader FH, Darnault R, Mengus J, Barrier E (2017) The effect of the Palmyra trough and Mesozoic structures on the Levant margin and on the evolution of the Levant Restraining bend. In: Roure F, Amin A, Khomsi S, Al-Garni MAM (eds) Lithosphere dynamics and sedimentary basins of the Arabian plate and surrounding areas, Springer, pp 149–172

Ghalayini R, Nader FH, Bou Daher S, Hawie N, Chbat WE (2018) Petroleum systems of Lebanon: an update and review. J Pet Geol 41 (2):189–214

Gilboa Y, Fligelman H, Derin B (1990) Helez-Brur-Kokhav Field, Israel, Southern Coastal Plain. AAPG Treatise in Geology, Structural Traps IV: Tectonic and Nontectonic Fold Traps, pp 319–345

Granier B, Azar D, Maksoud S, Gèze R, Habchi R (2015) New fossiliferous sites with Barremian Charophyta in the "Grès du Liban" auct. (Lebanon), with a critical perspective regarding the nature of Munieria Deecke, 1883. Carnets Geol 15:199–229

Granier B, Toland C, Gèze R, Azar D, Maksoud S (2016) Some steps toward a new story for the Jurassic-Cretaceous transition in Mount Lebanon. Carnets Geol. 16:247–269

Guiraud R, Bosworth W (1997) Senonian basin inversion and rejuvenation of rifting in Africa and Arabia: synthesis and implications to plate-scale tectonics. Tectonophysics 282:39–82

Hatzenbichler G, Bauer H, Grasemann B, Tari G, Nader FH, Church J, Schneider D (2013) The lower cretaceous chouf sandstone of Lebanon: is it a syn-rift clastic sequence? EGU General Assembly Conference Abstracts, 15, 9816

Hawie N, Gorini C, Deschamps R, Nader FH, Montadert L, Grajeon D, Baudin F (2013) Tectono-stratigraphic evolution of the northern Levant Basin (offshore Lebanon). Mar Pet Geol 48:392–410

Heybroek F (1942) La géologie d'une partie du Liban Sud. Leidsche Geol Meded 12:251–470

Heybroek M, Dubertret L (1945) Cartes géologiques du liban au 1:50 000e. Feuille de Jezzine (avec notice explicative). République Libanaise, Ministére des Travaux Publics, Beyrouth

Homberg C, Barrier E, Mroueh M, Hamdan W, Higazi F (2009) Basin tectonics during Early Cretaceous in the Levant margin, Lebanon. J Geodynam 47:218–223

Homberg C, Barrier E, Mroueh M, Müller C, Hamdan W, Higazi F (2010) Tectonic evolution of the central Levant margin (Lebanon) since Mesozoic. In: Homberg C, Bachmann M (eds) Evolution of the Levant Margin and Western Arabia Platform since the Mesozoic. Geological Society, London. Special Publication, vol 341, pp 245–268

Inati L, Zeyen H, Nader FH, Adelinet M, Sursock A, Rahhal ME, Roure F (2016) Lithospheric architecture of the Levant Basin (Eastern Mediterranean region): a 2D modeling approach. Tectonophysics 693:143–156

Inati L, Lecomte JC, Zeyen H, Nader FH, Adelinet M, Rahhal ME, Sursock A (2018) Crustal configuration in the northern Levant basin based on seismic interpretation and numerical modeling. Mar Pet Geol 93:182–204

Kanaan F (1966) Sedimentary structures and thickness and facies variation in the basal cretaceous sandstones of central lebanon. Master's thesis, American University of Beirut, Faculty of Arts and Sciences, Department of Geology

Klitzch E, Squyres C (1990) Paleozoic and Mesozoic geological history of northeastern Africa based upon new interpretation of Nubian strata. Am Assoc Petrol Geol Bull 74:1203–1211

Kolodner K, Avigad D, Mcwilliams M, Wooden JL, Weissbrod T, Feinstein S (2006) Provenance of north Gondwana Cambrian-Ordovician sandstone: U-Pb SHRIMP dating of detrital zircons from Israel and Jordan. Geol Mag 143:367–391

Kolodner K, Avigad D, Ireland TR, Garfunkel Z (2009) Origin of Lower Cretaceous ('Nubian') sandstones of North-east Africa and Arabia from detrital zircon U–Pb SHRIMP dating. Sedimentology 56(7):2010–2023

Lang B, Steinitz G (1989) K-Ar dating of Mesozoic magmatic rocks in Israel: a review. Israel J Earth Sci 38:89–103

Laws ED, Wilson M (1997) Tectonics and magmatism associated with Mesozoic passive continental margin development in the Middle East. J Geol Soc (London) 154:459–464

Lüning S, Kuss J (2014) Petroleum geology of Jordan. In: L. Marlow, C. Kendall, L. Yose (eds) Petroleum systems of the Tethyan region. AAPG Memoir 106: 217–239

Maksoud S, Granier B, Azar D, Gèze R, Paicheler JC, Moreno-Bedmar JA (2014) Revision of "Falaise de BLANCHE" (Lower Cretaceous) in Lebanon, with the definition of a Jezzinian Regional Stage. Carnets de Géologie 14(18):401–427

Maksoud S, Azar D, Granier B, Gèze R (2017) New data on the age of the Lower Cretaceous amber outcrops of Lebanon. Palaeoworld 26 (2):331–338

Moustafa AR, Khalil SM (1995) Rejuvenation of the Tethyan passive continental margin of northern Sinai: deformation style and age (Gebel Yelleq area). Tectonophysics 241:225–238

Mouty M, Delaloye M, Fontignie D, Piskin O, Wagner JJ (1992) The volcanic activity in Syria and Lebanon between Jurassic and Actual. Schweiz Miner Petrogr Mitt 72:91–105

Nader FH (2011) The petroleum prospectivity of Lebanon: an overview. J Pet Geol 34(2):135–156

Nader FH (2014) The geology of Lebanon. Scientific Press Ltd., Beaconsfield, Bucks, UK, p 108

Nader FH, Swennen R (2004) Petroleum prospects of Lebanon: some remarks from sedimentological and diagenetic studies of Jurassic carbonates. Mar Pet Geol 21:427–441

Nader FH, Browning-Stamp P, Lecomte JC (2016) Geological interpretation of 2D seismic reflection profiles onshore Lebanon: implications for petroleum exploration. J Pet Geol 39(4):333–356

Ponikarov VP, Kazmin VG, Kozlov VV, Krasheninnikov VA, Kikhailov IA, Razvalyaev AV, Sulidi-Kondratoev ED, Uflyand AK, Faradzhev VA (1969) Syria, p 215. http://refhub.elsevier.com/S0264-8172(13)00215-8/sref82

Quennel AM (1984) The western Arabia rift system. In: Dixon JE, Robertson AHF (eds) The geological evolution of the Eastern Mediterranean. Blackwell, Oxford, pp 775–788

Reches ZE, Hoexter DF, Hirsch F (1981) The structure of a monocline in the Syrian Arc system, middle east-surface and subsurface analysis. J Pet Geol 3:413–426

Renouard G (1955) Oil prospects of Lebanon bull. Am Assoc Petrol Geol Bull 39(11):2125–2169

Roberts G, Peace D (2007) Hydrocarbon plays and prospectively of the Levantine Basin, offshore Lebanon and Syria from modern seismic data. GeoArabia 12:99–124

Saint-Marc P (1970) Contribution a la Connaissance du Crétacé Basal au Liban: Rev. Micropaleontol 12:224–233

Saint-Marc P (1980) Le passage Jurassique-Crétacé et le. Crétacé inférieur de la region de Ghazir (Liban central). Géologie Méditerranéenne 7:237–245

Segev A (2009) Ar-40/Ar-39 and K-Ar geochronology of Berriasian-Hauterivian and Cenomanian tectonomagmatic events in northern Israel: implications for regional stratigraphy. Cretac Res 30:810–828

Segev A, Sass E, Schattner U (2018) Age and structure of the Levant basin, Eastern Mediterranean. Earth Sci Rev 182:233–250

Shenhav H (1971) Lower Cretaceous sandstone reservoirs, Israel: petrography, porosity, permeability. AAPG Bull 55:2194–2224

Shimron AF, Lang B (1989) Cretaceous magmatism along the southeastern flanks of Mount Hermon. Israel J Earth Sci 38: 125–142

Tixier B (1972) Le "Grès de Base" Crétacé du Liban: Étude Stratigraphique et Sédimentologique. Notes et Mémoires sur le MoyenOrient. 12:187–215

Ukla S (1970) Subsurface geology and well correlation in north and central Lebanon: Master's Thesis. American University of Beirut, Beirut, Lebanon, p 125

Vermeesch P (2004) How many grains are needed for a provenance study? Earth Planet Sci Lett 224:441–451

Walley CD (1983) A revision of the Lower Cretaceous stratigraphy of Lebanon. Geol Rundsch 72:377–388

Walley CD (1988) A braided strike-slip model for the northern continuation of the Dead Sea Fault and its implications for Levantine tectonics. Tectonophysics 145:63–72

Walley CD (1997) The lithostratigraphy of Lebanon: a review. Lebanese Science Bulletin 10:81–107

Walley CD (1998) Some outstanding issues in the geology of Lebanon and their importance in the tectonic evolution of the Levantine Region. Tectonophysics 298(1):37–62

Walley CD (2001) The Lebanon passive margin and the evolution of the Levantine Neo-Tethys. In: Ziegler PA, Cavazza W, Robertson AHF, Crasquin Soleau S (eds) Peri-Tethys Memoir 6: Peri-Tethan Rift/Wrench Basins and Passive Margins, Mémoires du Muséum national d'histoire naturelle 186:407–439

Weissbrod T (2005) The Palaeozoic of Israel and its Environs. In: Hall JK, Krasheninnikov VA, Hirsch F, Benjamini C, Flexer A (eds) Geological Framework of the Levant. Volume II: The Levantine Basin and Israel, pp 283–316

Wood BGM (2015) Rethinking post-Hercynian basin development: Eastern Mediterranean region. GeoArabia 20(3):175–224

Yousef M, Moustafa AR, Shann M (2010) Structural setting and tectonic evolution of offshore north Sinai, Egypt. In: Homberg C, Bachmann M (eds) Evolution of the Levant Margin and Western Arabia Platform since the Mesozoic, Geological Society, London, Special Publications, vol 341, pp 65–84

Seismic Tectono-Stratigraphy and Hydrocarbon Implications of Lowstand Deep Marine Oligo-Miocene Siliciclastic Reservoirs in the Northern Levant Basin

3

Mourad Bédir and Mohamed Naceur Aissaoui

Abstract

The recent discoveries of commercial gas fields in the Miocene sandstones structural/stratigraphic traps along the southern sector of the Levant Basin drove the interest of the industrial and scientific community. For that, basin tectonic structuring and seismic sequence stratigraphy study of Oligo-Miocene Siliciclastic deposits interval horizons have been undertaken to follow and precise stratigraphic traps. This work based on the analysis and interpretations of new regional E-W and N-S 2D seismic lines calibrated to wells data and lithostratigraphic outcrops had highlighted the basin configuration and sequence deposits infill nature and distribution of Oligocene and Miocene lowstand Siliciclastic reservoirs around the north Levant basin. Oligo-Miocene infilling horizons of the basin is controlled by deep-seated inherited and reactivated faults mainly oriented WNW-ESE and NE-SW. Based on their ages and seismic sequence stratigraphy concepts, they are interpreted as organized in 3 s order sequences composed by 5 Oligocene, 4 Lower Miocene, and 5 to 7 Middle-Upper Miocene third order seismic sequences system tracts. Early lowstand horizons are interpreted as presenting a downlap prograding sigmoid, oblique and mounded slope fans system tracts and basin floor mounds of large turbidites sheets and lobes overlain by late lowstand incised channels, canyons and levees and transgressive onlaps and toplaps. These system tracts are deformed and structured by Tertiary faults and Anticlines and synclines folds. Reservoir fair maps domains of the different lowstand system tracts highlight three main depositional sectors: slope, toe of slope and basin floor. They are vertically and laterally superposed and shifted. These clastic deposits present progradational configurations of slope fans as well as sheeted configurations channels, canyons and levees and basin floor lobes. The documented analogues in the Lebanon, Cyprus and Palestine continental coast outcrops are reported as deposits of gravity slides and slumps, turbidites, debris flows, mass flows, sandstones, and conglomerates alternated by hemipelagic marls. Hydrocarbon structural and stratigraphic trap types are discussed according the highlighted reservoir sequence structuring and system tract distribution.

3.1 Introduction

The northern Levant basin in eastern Mediterranean sea in the lebanon-Syrean-Cyprus offshore (Fig. 3.1) is essentially an exploration frontier zone that has been known during recent last years by hydrocarbon Gas discoveries in its southern part in Nile Delta in Egypt, and the near offshore areas of Palestine (Roberts and David 2007; Nader 2011; Plummer et al. 2013).

The Neogene plays are represented by Miocene sandstones turbidites as it was discovered firstly in Dalit 1 and Tamar 1 (Gardosh et al. 2008), succeeded by Leviathan 1 with gross mean reserves of 16 TCF of biogenic gas and Aphrodite 1 discoveries. The source rocks are assured by Jurassic, Cretaceous and Tertiary hemipelagic rich organic marls and mud (Roberts and David 2007; Nader 2011; Plummer et al. 2013). Thermogenic source rocks are still to be proven in the basin (Figs. 3.2 and 3.3).

Seismic profiles has shown a gas chimney features from Tertiary horizons as well as a Mesozoic Reef build ups (Roberts and David 2007).

Despite the hydrocarbon potential of Oligocene sandstone reservoirs, they are not yet studied and explored. In addition

M. Bédir (✉)
Georesource Laboratory, Centre of Water Researches and Technologies, University of Carthage, Borj Cedria—Technopark, B.P 273 8020 Soliman, Tunisia
e-mail: bedmour@yahoo.fr

M. N. Aissaoui
Freelance Consultant, Madrid, Spain
e-mail: nasser.aissaoui@yahoo.fr

Fig. 3.1 Location map of study area and seismic lines of Fig. 3.11, showing the major structural elements bounding the Levant basin. The major gas fields are colored in red (in Hawie 2013)
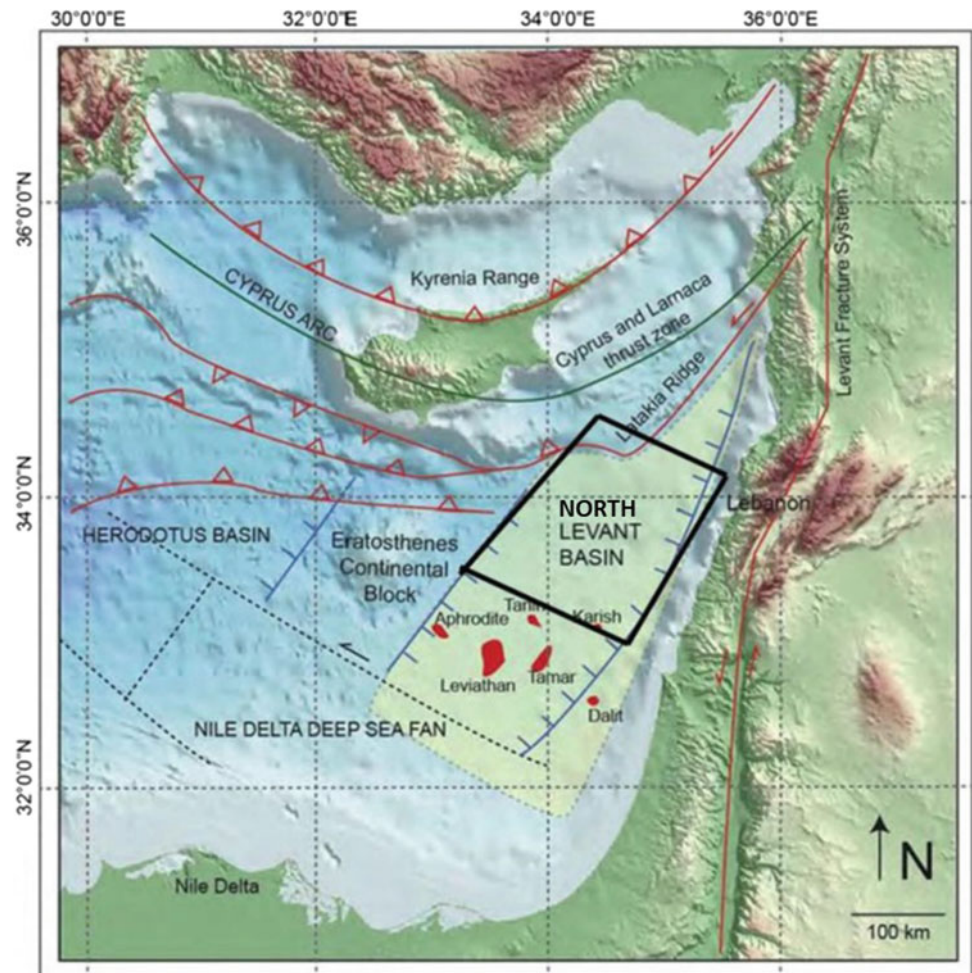
to the Neogene play, several gas and oil accumulations are present in the area as well as in Mesozoic as Cenozoic carbonate and sandstones reservoirs (Figs. 3.2 and 3.3).

Studies of structural and lithostratigraphic Mesozoic and Cenozoic deposits has been extensively documented in surrounding continental outcrops of Lebanon, Palestine, Syria, Egypt and Cyrus (Brew et al. 2001; Hardenberg and Robertson 2007; Gardosh et al. 2008; Bowman 2011; Nader 2011; Hawie et al. 2013).

With the acquisition of the 2D seismic data using new PGS geostreamer technique in 2008, data quality for all horizons is optimised with good resolution until to the deeper reflectors. The latter will permits to better interpret structural and seismic stratigraphy of horizons to highlight their tectonic structuring, sequence system tracts organization and lowstand paleogeographic distribution. This study will focus on the Oligocene and Miocene horizons reservoirs.

Secondly, hydrocarbon structural and stratigraphic trap types will be discussed according the sequence reservoir deposit system tract architecture and distribution as well as their tectonic structuring.

Eight selected 2D regional seismic reflection sections have been analyzed and interpreted. Depositional sedimentary environments distribution is proposed for Oligocene and Miocene systems tracts and time isochron and isopach maps are used to support this framework around the study area.

3.2 Deep Water Clastics Hydrocarbon Importance

The deep water clastic reservoirs target is a new Hydrocarbon world challenge in unexplored frontier areas around the world as the Levant basin.

Most deep-water resources have been discovered in Cenozoic-age with almost 90% of the resources found within deepwater sandstone turbidites (Weimer et al. 2007). These deposits produce hydrocarbons from lobes, sheets, channel fills, and thin beds in levee–overbank settings
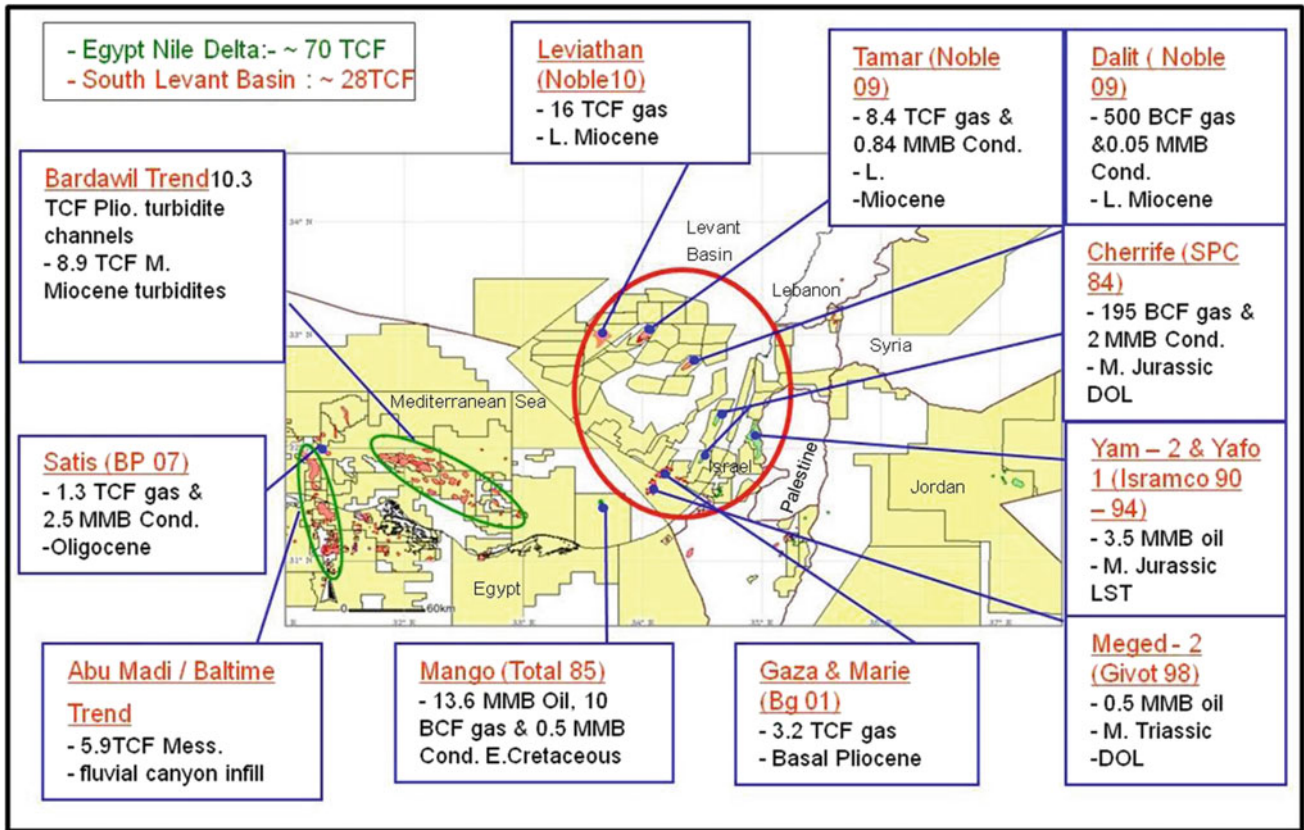
Fig. 3.2 East Mediterranean Hydrocarbon reserves repartition discovered in Mesozoic and Cenozoic deposits
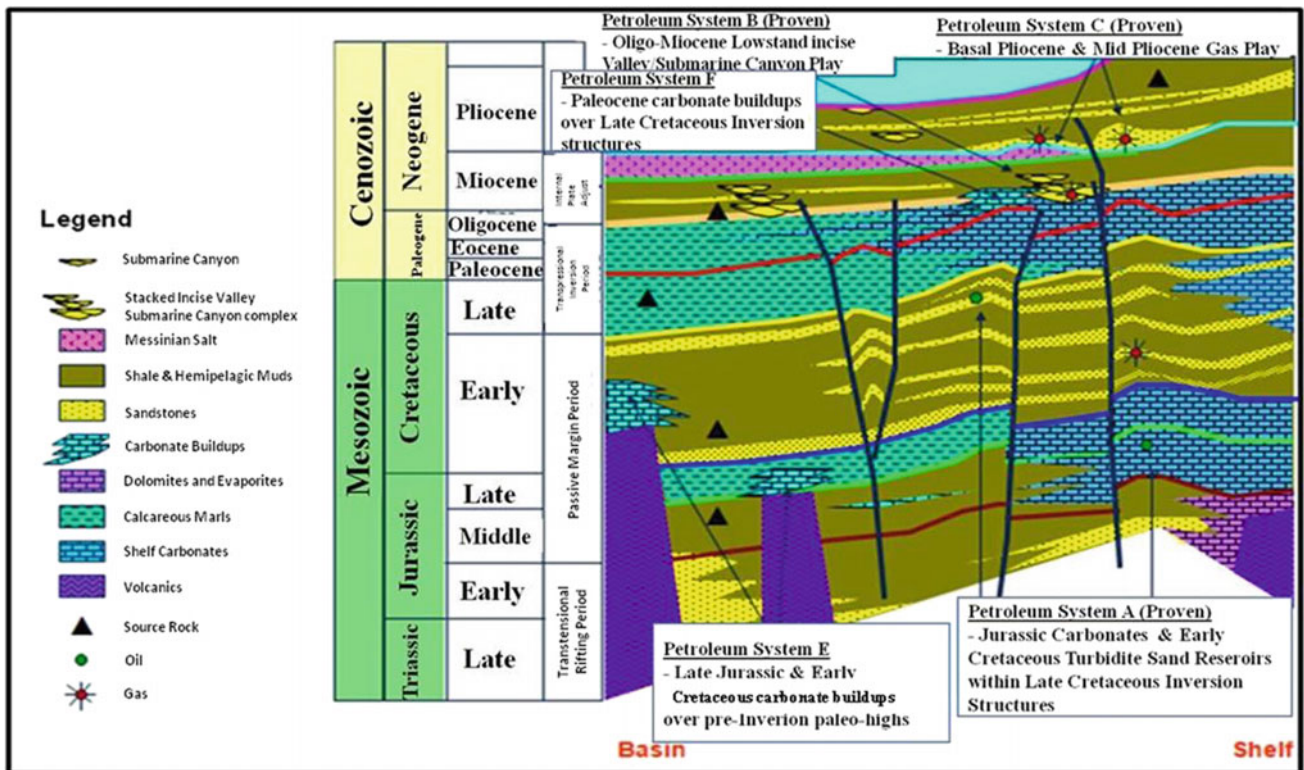
Fig. 3.3 Eastern Mediterranean general stratigraphic column and Meso-Cenozoic Hydrocarbon play systems and gas and oil fields (Ben-Gai and Druckman 2013, modified)

(Chapin et al. 1994; Mahaffie 1994; Richards and Bowman 1998). Reservoir characteristics of continuity and connectivity present poor to excellent quality in deep-water sands.

High net-to-gross slope fans and basin-floor sheet and channel-fill sands provide excellent reservoirs. Porosity and permeability in deep-water reservoirs can be excellent (>30% porosity and hundreds darcy's of permeability).

Trap types reservoirs are classified according to the basin types (Worral et al. 2001): as mobile substrates (salt, shale) fed by large rivers, mobile substrates fed by small rivers and non mobile substrates fed by small rivers, About 75% of the discoveries in deep water occur in the first two types of basins (Weimer et al. 2007).

Traps in mobile substrates are generally structural to combined structural/stratigraphic. Significant proportion (∼65%) of resources is from fields that have a stratigraphic component to their trap.

Deep-water fold belts are a common structural style in association with mobile substrates. These fold belts have been recognized in many lower slopes and ultra-deepwater basins worldwide. Structural trapping is dominant in these features (Weimer et al. 2007).

Stratigraphic traps occur in a variety of styles. Several discoveries have been made during the past few years in (1) stratigraphic onlap traps, (2) updip pinchout associated with homoclinal dip and (3) channelized fill of submarine canyons and submarine canyon truncation traps (Weimer et al. 2007).

3.3 Geotectonic Setting and Basin Evolution

The Levant Basin is bounded to the northeast by Cyprus and Larnaca thrust zone, to the west by the Eratosthenes Seamount and to the south, by the Leviathan Ridge and the Nile Delta Cone (Figs. 3.1 and 3.4). To the north, it is bordered by the Latakia basin and to the eastern side, it is limited by the coastal margin faults of N-S Dead Sea transform fault and the Palmyrides fold belt (Robertson 1998a, b; Rybakov and Segev 2004; Hawie et al. 2013, 2014; Plummer et al. 2013).

Geophysical seismic and gravity studies (Rybakov and Segev 2004; Tapponier et al. 2004; Gardosh et al. 2008; Eppelbaum and Katz 2011) show that the Levant basin contains up to 15,000 m of Mesozoic and Cenozoic layers (Fig. 3.6). The basin have been affected by compression and extension due to plate motions. Along the western Lebanon offshore margin, NE-SW and N-S-trending faults follow the direction of Dead Sea sinistral Transform (Robertson 1998a, b; Rybakov and Segev 2004; Tapponier et al. 2004;
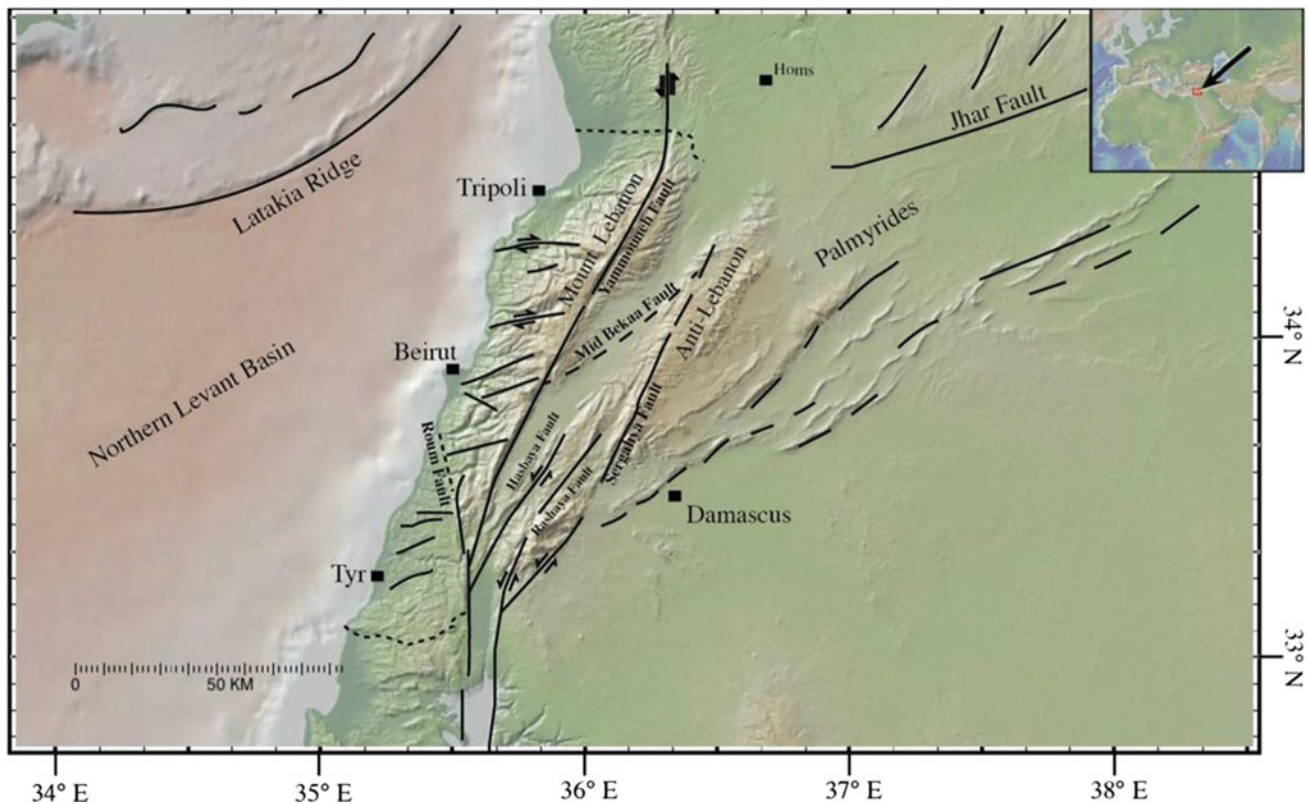
Fig. 3.4 Structural map of Lebanon and the Palmyrides showing the major strike slip flower faults trends and structures (in Hawei 2013)

Robertson and Mountrakis 2006; Hawie et al. 2013; 2014) (Fig. 3.4). The latter fault delimitates Arabian plate and the Levant basin.

Extensional events have been documented in the latest Paleozoic, in Middle and Late Triassic and in Early Jurassic (Freund et al. 1975; Garfunkel and Derin 1984; Robertson 1998a, b; Garfunkel 1998; Robertson and Mountrakis 2006; Gardosh and Druckman 2006; Tapponier et al. 2004; Hawie et al. 2013, 2014; Montadert et al. 2014).

These events are marked by normal faults with several kilometers of throw. These stages are accompanied by magmatic activity and formation of NE-SW oriented graben and horsts.

The main tectonic structuring stages of the Levant basin consist on Mesozoic rifting and Cenozoic convergence phases (Fig. 3.6). Rifting phase is related to the breakup of the Gondwana plate and the formation of the Neotethys Ocean system. This rifting event is also recognized and well documented in the central Mediterranean north African Atlassic margin plate (Bédir et al. 1992; Bédir 1995; Bédir et al. 2000 and 2001; Bouaziz et al. 2002; Melki et al. 2010).

Basement structures associated with the Early Mesozoic extension are found in the deep parts of Levant basin as Leviathan Ridge and the Eratosthenes high (Figs. 3.5, 3.6 and 3.7) (Robertson and Mountrakis 2006; Gardosh and Druckman 2006; Gardosh et al. 2008; Plummer et al. 2013; Hawie et al. 2013, 2014). The rifting mechanism in the Levant area reached an early magmatic stage. Although

magmatic intrusions and stretching of the crust took place, no indications for sea-floor spreading and emplacement of new oceanic crust are found (Gardosh and Druckman 2006). The eastern continental margin of the central Levant is characterized by a sharp continental-oceanic crustal transition, exhibited on the bathymetry as a steep continental slope (Figs. 3.5 and 3.6).

The post-rift phase is associated with cooling and subsidence that was probably more intense within the basin than on the margins (Robertson and Mountrakis 2006; Plummer et al. 2013). The Late Jurassic to Middle Cretaceous section records a gradual formation of a passive-margin profile and the subsequent development of a deep-marine basin bordered by a shallow-marine shelf (Fig. 3.5) (Bein and Gvirtzman 1977; Garfunkel 1998).

The passive-margin stage is characterized by recurring cycles of marine transgressions and regressions associated with relative sea-level changes (Flexer et al. 1986; Gardosh 2002). The latter are marked by marine onlaps, unconformity surfaces, stacking of carbonate platforms, on the basin's margin, and mass transported deposition in the basin (Hawie 2013).

In Late Cretaceous to Paleogene times, the region experienced compressions due to the convergence of the African and Eurasian plates (Fig. 3.7). This led to the inversion of the previously formed NE-SW trending grabens and to strike-slip faulting due to differential plate motion (Figs. 3.5 and 3.6). The same compressions and inversions are
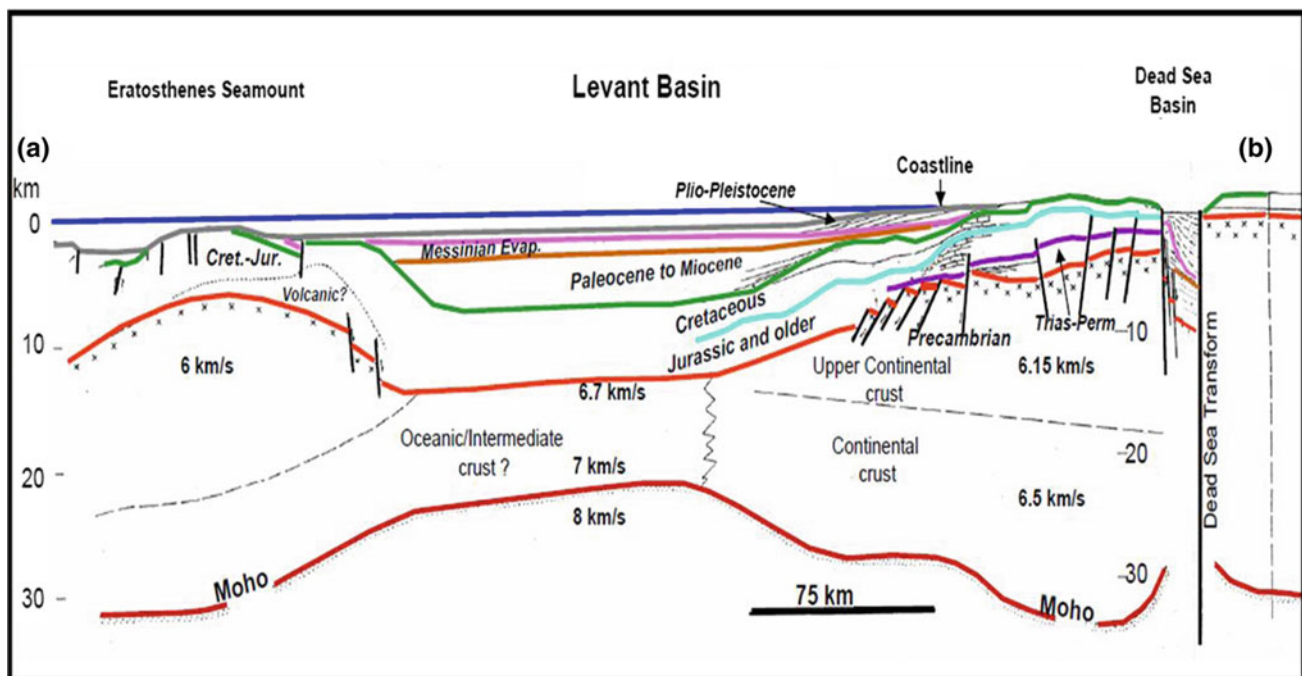
Fig. 3.5 East-West regional geoseismic cross section of Levant basin showing continental and seamount borders, continental and oceanic crust and Phanerozoic series infill (Gardosh et al. 2008)

Fig. 3.6 Triassic-Jurassic tectonic rifting and Tertiary compressional stages and associated structuring of Levant basin (Tapponnier et al. 2004)

Fig. 3.7 E-W and N-S regional cross sections showing onshore & offshore relationship structuring of subduction ridges of Cyprus, Latakia and Levant foreland basins (Plummer et al. 2013)

documented in the central Mediterranean north African Atlassic margin by Bédir et al. (1987, 1992), Bédir (1995), Bouaziz et al. (2002); Khomsi et al. (2006, 2009, 2016).

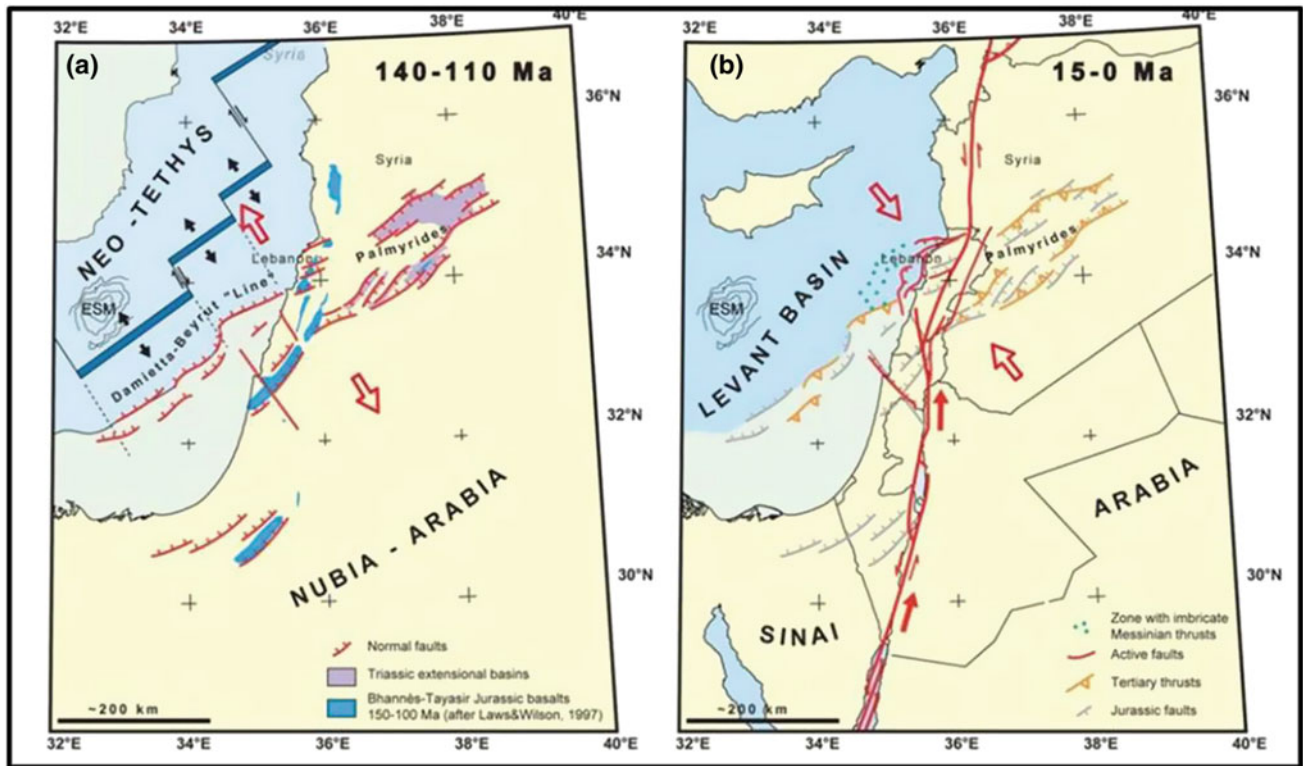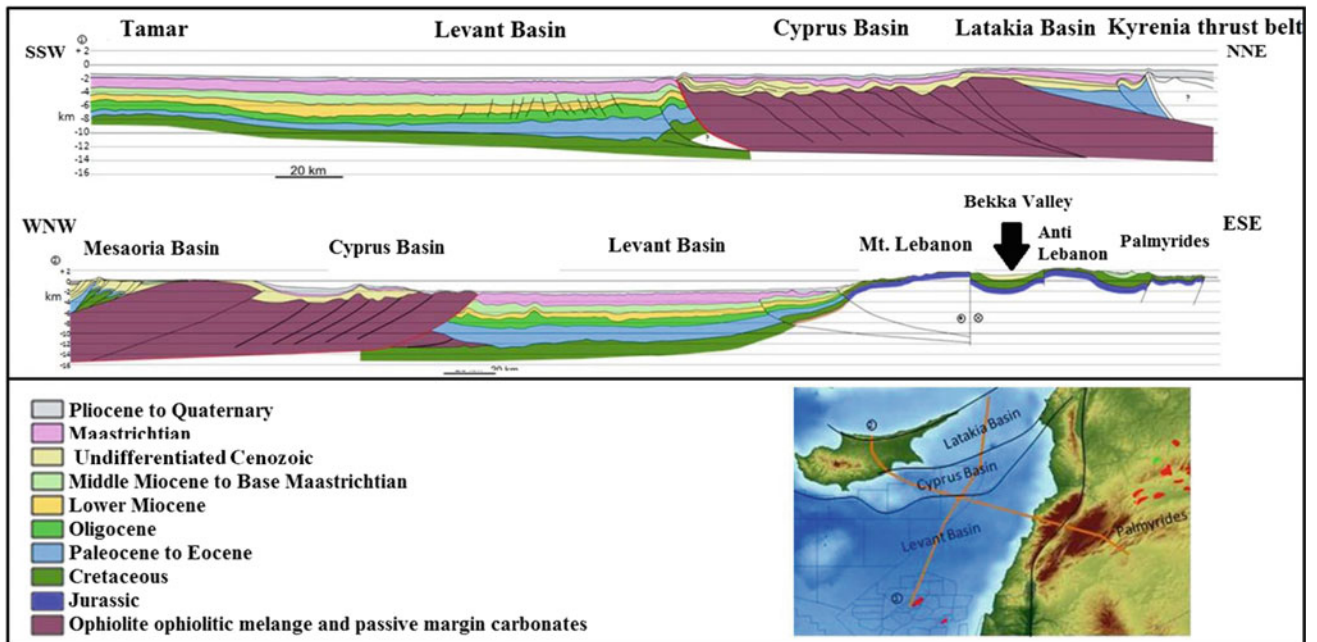Tertiary compressive events induced central basin subsiding area surrounded by uplifted shelves and slopes in eastern, western, northern and southern borders (Fig. 3.7), corresponding respectively to the continental Syrian Arc fold belt, submarine Cyprus Arc, Eratosthenes Seamount and Leviathan ridge (Robertson 1998a, b; Plummer et al. 2013; Hawie et al. 2013, 2014). Deep seated inherited sub-vertical NE-SW and NW-SE strike slip faults guide and control Mesozoic and Cenozoic basin deposits.

These compressional events are manifested by large-scale contractional deformation of Cyprus Arc and the Syrian Arc fold belt (Krenkel 1924; Picard 1959; Hawie et al. 2013, 2014). Syrian Arc folds are extending from the Western Desert of Egypt, through Palestine to Lebanon and Syria. Based on surface studies, Walley (2001) suggested two main folding phases: Late Cretaceous and Early Tertiary. The subsurface and outcrop studies of the Levant Basin and surroundings confirmed this suggestion (Gardosh and Druckman 2006; Bar et al. 2008; Gardosh et al. 2008). Briais et al. (2009), Hawie et al. (2013, 2014) and Plummer et al. (2013) had reported seismic evidence for Neogene active shortening in offshore of Lebanon.

At the end of Miocene, the Mediterranean Sea became isolated from the Atlantic Ocean, which led to the deposition of up to 1500 m of evaporates in the Levant Basin (Hsu et al. 1973a, b; Neev et al. 1976; Ryan 1978; Cohen 1988; Druckman et al. 1995; Gradmann et al. 2015). This event lasted about 1.5 million years is known as the "Messinian Salinity Crisis" (Butler et al. 1999; Lofi et al. 2008, 2011; Gorini et al. 2015). The crisis was followed by inundation of the basin with oceanic waters and Pliocene to recent sedimentation.

The present-day Levant basin can be described as a foreland basin of the African Plate convergence. To the north, the thrust belt caused by the Africa-Eurasia plate collision is materialized in the Cyprus Arc and Larnaca/Latakia Ridge system. North of this thrust belt, several 'piggy-back' basins can be recognized, such as the Latakia Trough, Iskenderun, Adana and Cilicia basins (Fig. 3.7).

3.4 Regional Tertiary Stratigraphy and Depositional Environments

The knowledge of the stratigraphy and the deposit environments of onshore Oligo-Miocene around the offshore study area of Levant basin is very important for the seismic stratigraphy and system tract calibration and interpretation for depositional reconstructions in absence of close petroleum wells calibrations in this frontier area.

For this purpose, synthesis of Oligo-Miocene regional stratigraphy around the offshore study area is presented from several published works. The data has been selected from eastern continental border outcrops of Levant basin of Palestine, Lebanon, Syrian Arc, Turkey and offshore Cyprus and Eratosthenes.

3.5 Eocene

In the eastern continental and southern offshore areas of the Levant of the basin; in Palestine, Syria, Lebanon and North Sinai and Nile Delta, Lower and Middle Eocene facies are predominantly pelagic containing shallower neritic levels of nummulitic (Brew et al. 2001; Roberts and David 2007; Gardosh et al. 2008; Hawie 2013). This assemblage of deep and shallow carbonate deposits suggest a mass transport origin in a deeper basinal setting (Buchbinder et al. 1988; Hawie 2013), beginning in latest Early Eocene times (Benjamini 1993). Canyon incisions and eroded surfaces are documented in Syrian-Lebanon, Palestine outcrops and in the southern offshore Nile Delta (Figs. 3.8, 3.9 and 3.10).

In proximal areas an unconformity was found between the Middle Eocene chalky Formation and the hemi-pelagic marls ones. It was denominated the "Upper Clastic Division" of Ball and Ball (1953). Occasional mass transported conglomerates are found especially in distal areas. Upper Eocene deposits are locally truncated by the major unconformity of Early Oligocene (Dolson et al. 2000; Hawie 2013).

In Lebanon and Syrian outcrops (Hawie 2013) and in the petroleum wells, as well as in Cyprus (Roberts and David 2007) and Nile Delta in Egypt, Eocene deposits exhibits limestones and hemipelagic mudstones but Upper Eocene presents siliciclastics sandstones and channels (Figs. 3.9 and 3.10).

3.6 Oligocene

In the eastern and southern continental area, a major unconformity is reported between Late Eocene and Early Oligocene deposits There, a regional unconformity surface developed at the top of Eocene carbonates (Figs. 3.8, 3.9 and 3.10); in the Negev and the Judea Mountains (Picard 1951; Garfunkel and Horowitz 1966; Gardosh et al. 2008; Steinberg et al. 2011) and in the Palmyride Arc zone (Brew et al. 2001) and Lebanon (Hawie 2013).

The same unconformity level is well documented in the northern red sea and the gulf of Suez (Dolson et al. 2000) (Fig. 3.10). Zilberman (2000, 2001) named this unconformity "the upper erosion surface" and pointed out that it

Fig. 3.8 Tertiary lithostratigraphy Formations and deposits of southeastern Lebanon-Palestine Levant margin (Gardosh et al. 2008, modified)
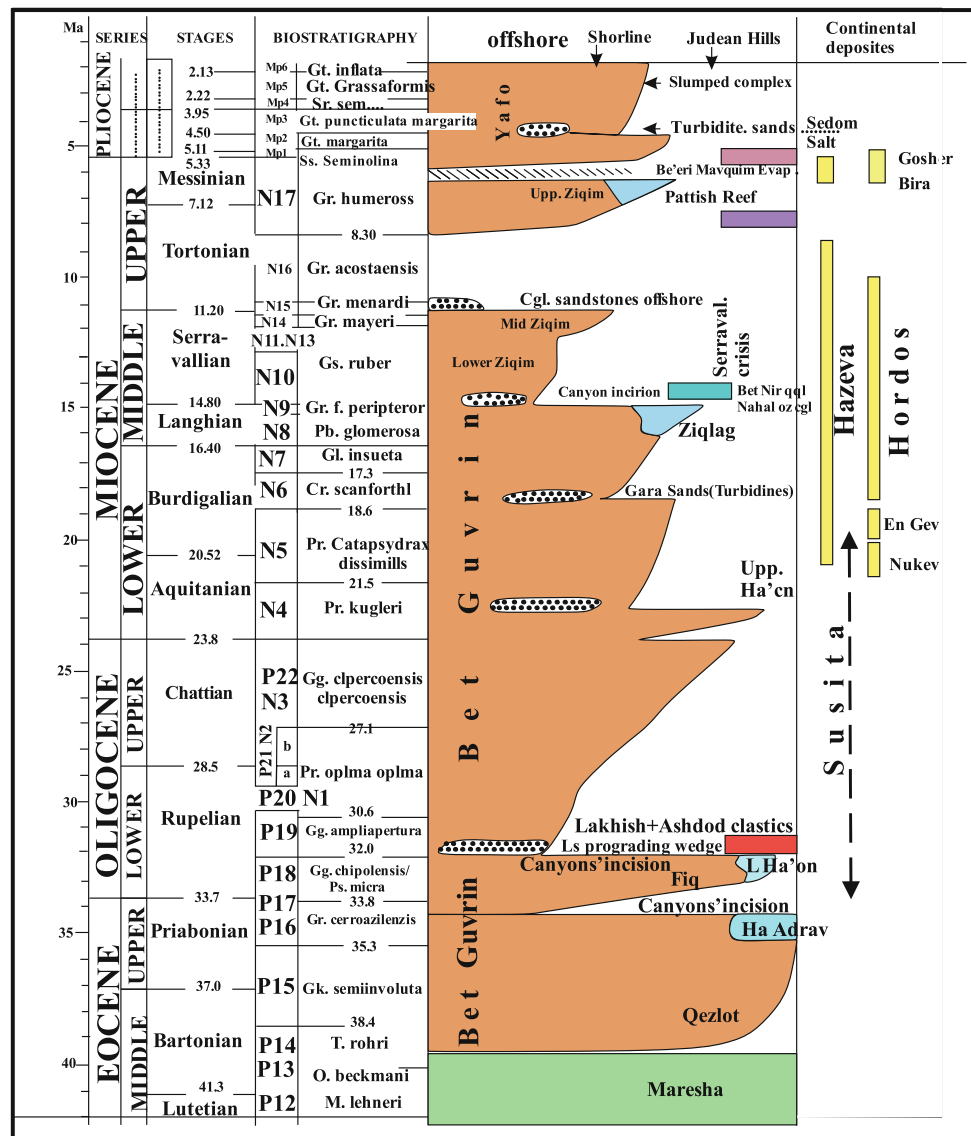
postdates Upper Eocene deposits and predates Miocene continental deposits of the Hazeva Group (Figs. 3.8 and 3.9). Whereas in the southern offshore Nile Delta and North Sinai zones; Oligocene deposits are composed by marls and sandstone turbidites (Dolson et al. 2001).

In the Hanna-1 borehole, which is located at the distal part of the Ashdod Canyon (Gardosh et al. 2008; Steinberg et al. 2011; Plummer et al., 2013), the base of the canyon fill was dated as Lower Oligocene Rupelian age (Micro-Strat Inc 2003). Well log correlation from coastal to offshore basin area show a lateral lithologic variation of Oligocene marls and carbonates from proximal zone to a calciturbidites and conglomerates levels occurrence in distal zone of the margin (Figs. 3.8, 3.9 and 3.10).

Patchy argellious limestones and marls outcrops of lowermost Oligocene are sparsely spread from the Golan to the Northern Negev and Palmyrides. They are more common in wells along the Mediterranean coastal plain and offshore areas, where they are included in the lower part of the Bet Guvrin Formation in Palestine (Fig. 3.8). These sediments consist of deep-water pelagic marly chalks, and their aerial distribution largely follows the distribution of the Upper Eocene deposits, except for their absence in the Southern Negev (Buchbinder et al. 2005).

Upper Oligocene deposits have a limited inland distribution due to their strong erosion and infilling to the Levant basin. However, sediments penetrate more inland to the Lower Shefela region (Lakhish Formation) (Roberts and David 2007; Gardosh et al. 2008; Steinberg et al. 2011), characterized by slumped blocks, debris flows and occasional sandy calcareous turbidites (Lakhish area). These mass transported sediments are covered by a few meters of
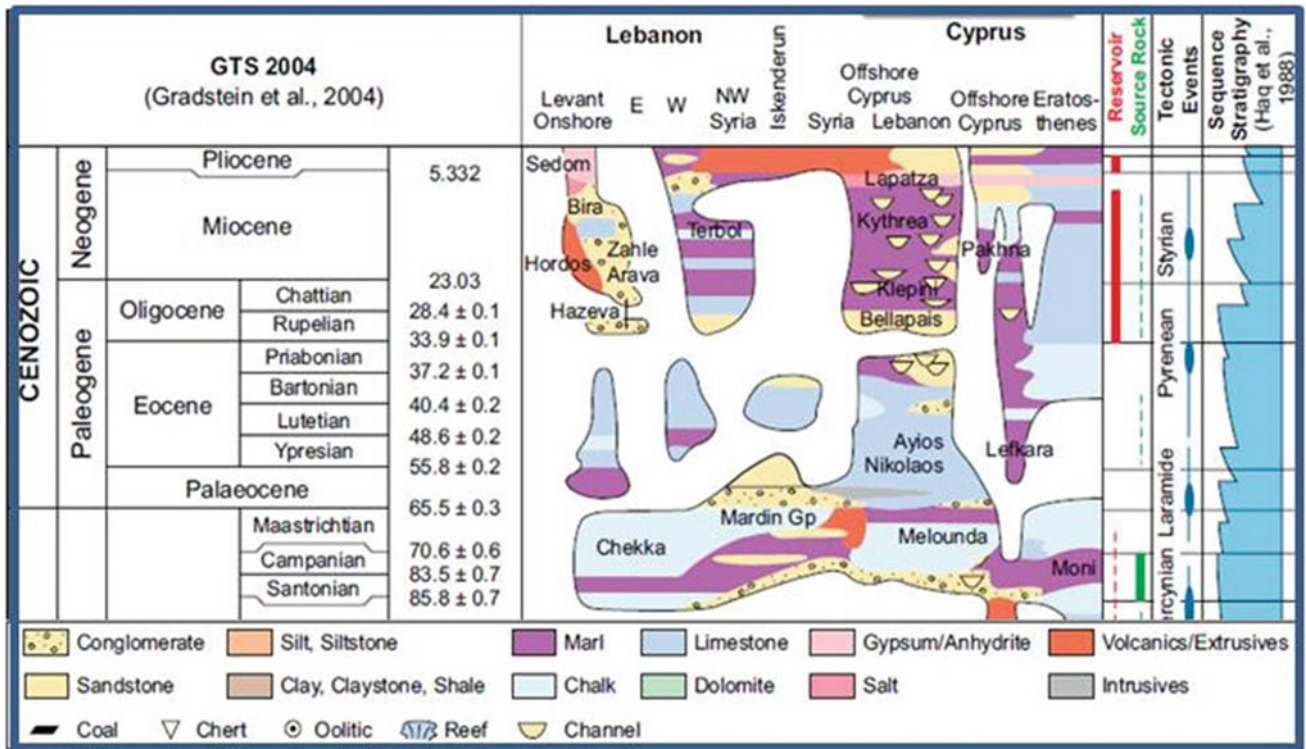
Fig. 3.9 Regional Tertiary lithostratigraphic chart, associated reservoirs and source rocks, tectonic events and eustatic cycles of western offshore of Cyprus, Erathostenes sea mount and eastern continental margin of Lebanon and Syria (Roberts and David 2007)
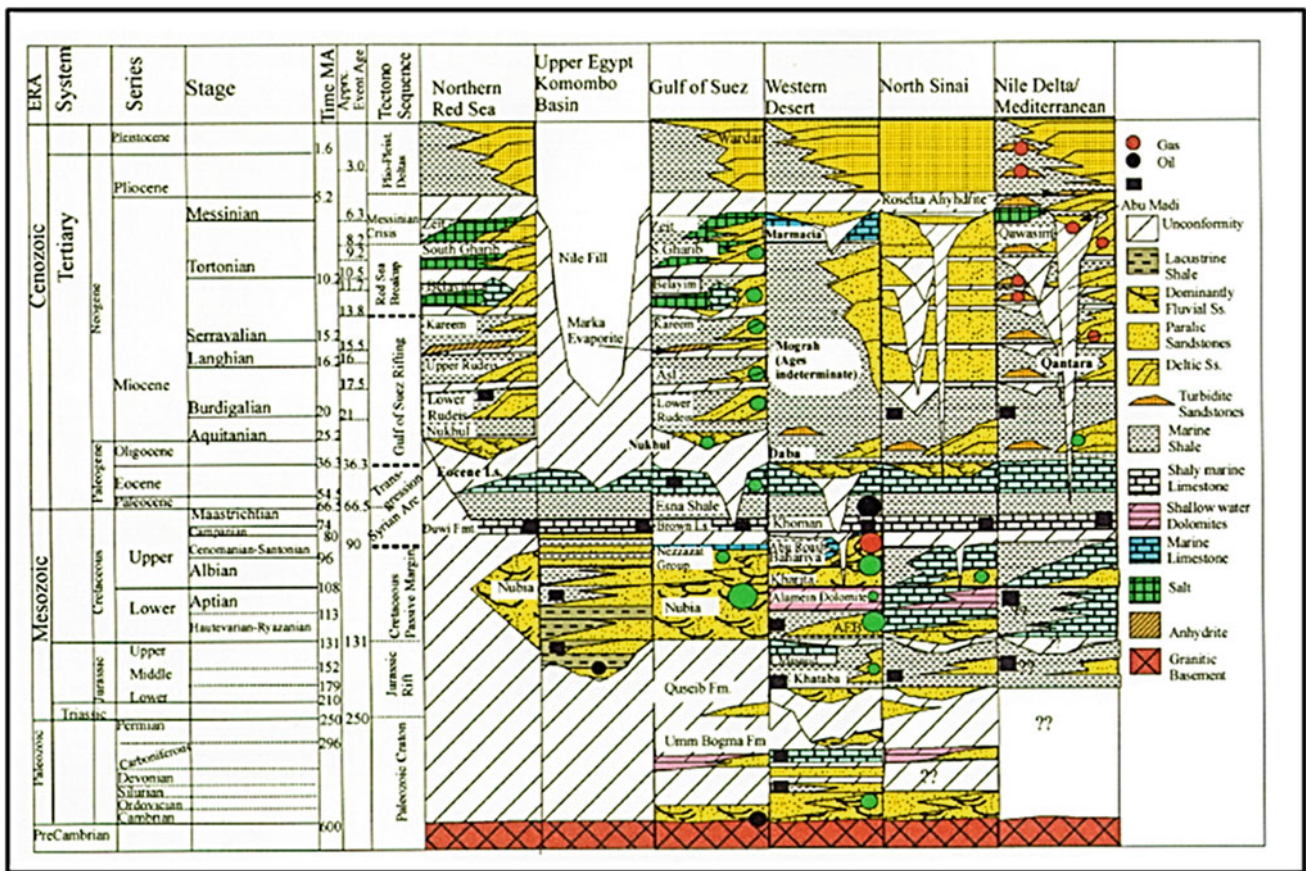
Fig. 3.10 Lithotratigraphic correlation chart from continental North Sinai and Western desert to offshore Nile in Egypt showing Mesozoic and Cenozoic lateral deposits changes and major tectono-stratigraphic unconformities and Hydrocarbon occurrences (Dolson et al. 2000)

in situ large-foraminiferal limestone representing a lowstand prograding wedge (Buchbinder et al. 2005). More than 300 m of sand and conglomerates of this phase were penetrated in the Ashdod wells in the Palestine coastal Plain (Gardosh et al. 2008).

To the northern border of Levant basin, near the Taurus fold belt, Satur et al. (2007) has detailed in the outcrops of Adana Neogene basin in eastern Turkey, an Oligo-Miocene deep sea fan lobes deposits and turbidites of clastic Cingoz Formation. This turbiditic system presents two feeders directions of supply; one from the East and the other from the West.

3.7 Lower Miocene (Aquitanian-Burdigalian)

In the eastern Palestine margin, Early Miocene cycle begin by onlap of the upper Ha'on Member of Ben Guvrin Formation (Susita Formation) (Fig. 3.8). It reached the Golan area across the Rift Valley (Buchbinder et al. 2005). However, their hemi-pelagic sediments were largely eroded from the hilly backbone of the country. The facies is ubiquitously pelagic or hemi-pelagic (Bet Guvrin type), except in the most proximal outcrops in the Golan Heights (Gardosh et al. 2008).

Burdigalian sediments are limited to the Coastal Plain and offshore area. Canyon incision was renewed and mass transported deposits occasionally accumulated, as documented by the Gaza sands turbidites (Martinotti 1973). Also in the well correlations along Ashdod canyon Axis, in offshore Gaza, in Hannah 1 well, Burdigalian level contain sandstones (Gardosh et al. 2008).

In the Well log correlations of Syrian Latakia coastal area (Brew et al. 2001), marl and limestone levels of Lower Miocene present lateral variations from proximal area of marls and limestones to sandstones deposits of Fars Formation to the distal area.

In the North Sinai and offshore Nile Delta, Aquitanian-Burdigalian deposits are in environmental continuity with Oligocene marine shales and turbiditic sandstone (Fig. 3.10).

3.8 Middle Miocene (Langhian-Serravallian)

Langhian deposits show a development of a carbonate platform and hemi-pelagic deposits of Ziqlag Formation (Fig. 3.8) unconformably lying the western flank of the Judean anticline (Buchbinder and Zilberman 1997; Buchbinder et al. 1993).

Bet Guvrin facies in Palestine and Jebrine Formation in Palmyrides (in Brew et al. 2001) show a thick (250 m) succession of conglomerate, consisting of limestone, chalk and chert pebbles apparently derived from Cretaceous to Tertiary Formations. These deposits have been also encountered in the Nahal Oz-1 borehole in the Afiq Canyon (Druckman et al. 1995; Gardosh et al. 2008).

Serravallian sediments, represented by Ziqlag Formation (Fig. 3.8), terminate abruptly when the sea level dropped and erosion and canyon incision resumed, leaving behind their products: conglomerates and overbank deposits (Bet Nir conglomerate) Buchbinder et al. 1986).

In well logs of Syrian Latakia coastal area, Lower Miocene contain sandstone deposits to the distal area whereas Middle Miocene Serravallian deposits are composed from proximal to distal zones by more frequent siltstones and sandstones beds intercalated in limestones and marl levels (Brew et al. 2001). Small onlap episodes of limited landward penetration are indicated by the Middle Formation.

In the southern offshore Nile Delta, Langhian and Serravallian deposits are composed by marine shales, fluvial and deltaic sandstones and turbiditic sandstones intercalated by several erosional unconformities and hiatuses reflecting the strong siliciclastic sedimentary dynamics that is one of the important feeder for the north Levant basin (Fig. 3.10).

3.9 Upper Miocene (Tortonian-Messinian)

Sediments of this cycle are relatively common in the Palestine outcrops (Buchbinder and Zilberman 1997) and especially in wells in the eastern coastal Plain and offshore. The deposits are represented by basinal hemi-pelagic marly sedimentation, capped by coral and algal reefs of the Pattish Formation in proximal platform position (Figs. 3.8 and 3.9).

However, in the offshore extension of the Afiq Canyon l, hemi-pelagic muds are found, interbedded with mass transported sands and conglomerates of chert pebbles (Gardosh et al. 2008). The forced regression of this cycle is represented by the lower part of the Mavqiim anhydrites (Fig. 3.8).

The Messinian evaporites are found throughout the Mediterranean region (Hsu et al., 1973a, b; Neev et al. 1976; Ryan 1978). The deposition of offshore Mavqiim evaporites and continental Sedom Salt (Gradmann et al. 2015; Gardosh et al. 2008) (Figs. 3.8, 3.9 and 3.10) which are composed mainly of halite and some anhydrite, followed a major sea-level drop associated with the closure and desiccation of the Mediterranean Sea (Hsu et al. 1973a, b, 1978; Gvirtzman and Buchbinder 1978 Ryan 1978; Cohen 1988; Druckman et al. 1995; Butler et al. 1999; Gradmann et al. 2015; Lofi et al. 2008, 2011; Gorini et al. 2015). The area of evaporate accumulation extended throughout the Levant basin to about 20–40 km west of the present-day coastline (Gardosh and Druckman 2006; Bertoni and Cartwright 2007).

The Messinian evaporites most likely filled a preexisting topographic depression (Tibor et al. 1992). However, during short highstand onlap episodes, the brine covered the slope

and penetrated through deep canyons further inland. Remnants of the Messinian evaporates in the form of a few tens of meters of thick halite and anhydrite beds were encountered in various wells in the eastern coastal areas of Levantine basin (Druckman et al. 1995; Cohen 1988).

Whereas in the southern offshore of the Nile Delta, Messinian deposits re in continuity with Serravallian-Tortonian ones with fluvial and deltaic sandstones and turbidites intercalated by marine shales (Fig. 3.10).

3.10   Datasets and Methods

The 2D seismic grid of the study area has been acquired in 2008 using new PGS geostreamer technique which consists on measuring both the pressure wave field using hydrophones, and the vertical component of the particle velocity using motion sensors on two recording sensors. By combining the data from the two sensors the energy can be separated into up- and down-going parts.

By considering only the up-going wave field, the ghost reflexion is removed, thus optimise the data quality, not just for one seismic horizon but for all horizons from shallow to deeper ones.

Seismic data and analyses have been interpreted by Geoframe charisma software and time seismic and depth mapping by CPS3. Seismic processing of sections is under normal polarity and zero phase amplitude which means that the reflection coefficient of positive acoustic impedance of lithologic contrast is represented by negative amplitude and vice versa and it is situated in the medium amplitude. Seismic reflection positive amplitude polarity is represented in red color whereas negative one is in blue.

Regional seismic sections oriented E-W (A, A', B, C, D, E) and N-S (F, G, H, I) have been selected to identify and highlight seismic sequence boundaries and system tract horizons distribution of Oligocene and Miocene from West to East and South to North in the northern Offshore Levant basin (Fig. 3.11).

These seismic sections present good resolution for second and third order seismic stratigraphy interpretations but some deformed and faulted areas present bad resolution. These lines extend vertically to eight seconds of two way time wave travel. The length average extends from 50 to 160 km (Fig. 3.11).

In the study area, Extracted Constant interval velocity from layer computed from stacking velocity of Line C shows that Oligocene reflectors velocity is about 2900 m/s and those of Lower to Middle-Upper Miocene reflectors are about 2600 m/s (Fig. 3.12). The average interval thickness between Oligocene horizons is about 60–70 m whereas for those of Lower and Middle-Upper Miocene they are about of 50 m.

Fig. 3.11 North Levant basin study area location map of used PGS 2 D selected seismic lines and petroleum wells
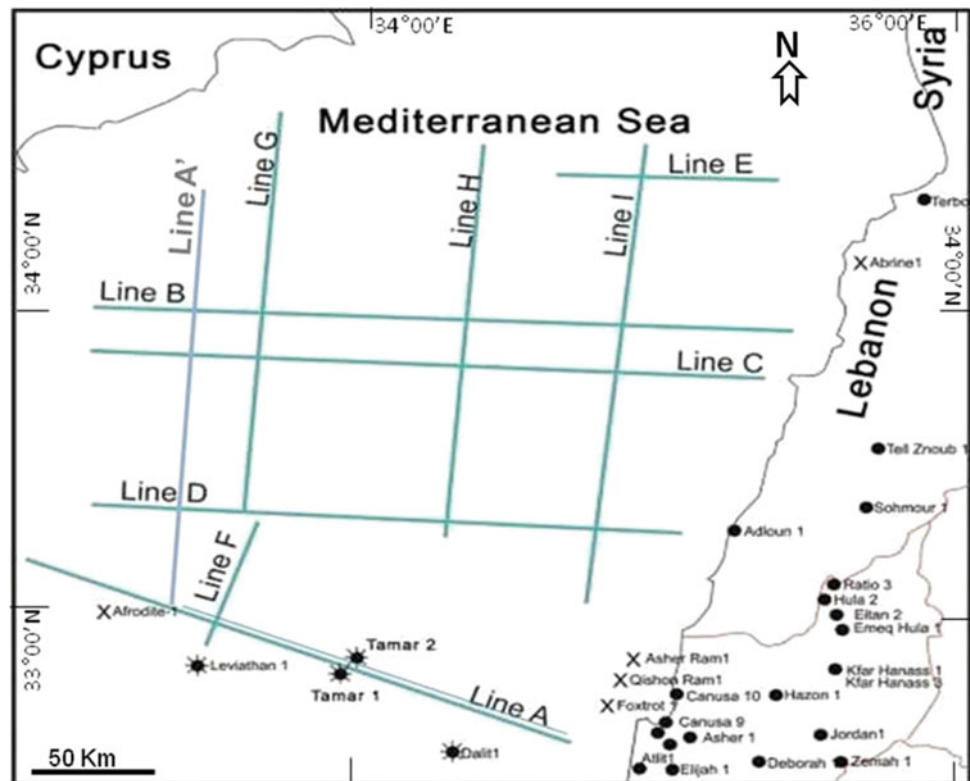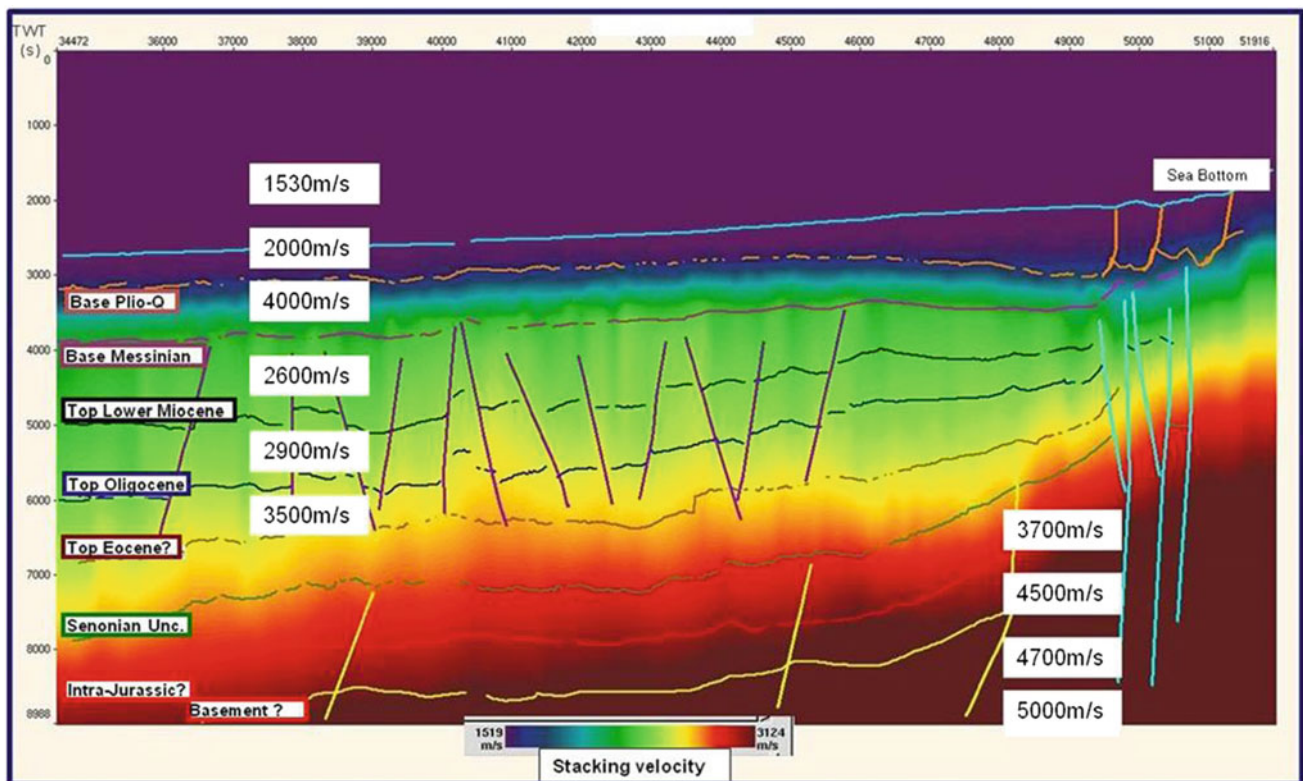
Fig. 3.12 Extracted constant interval velocity from layers computed from stacking of southern seismic line C (see Fig. 3.11 for line C location)

Despite the absence of petroleum wells in this study frontier zone area, calibration of seismic horizons had been established from the southern petroleum wells of Hannah 1, Yam 2, Yam-Yafo 1, Tamar 1 and Leviathan 1, located few kilometers southwest of the study area. This calibration has been established by seismic lines link of A and A' (Figs. 3.11 and 3.13).

Seismic horizon interpretation representing regional extension of the unconformities and seismic character along seismic section A and those of the study area (Fig. 3.13) has facilitated the correlation between southern and northern offshore areas (Gardosh et al. 2008).

The main seismic markers concerning Tertiary horizons representing unconformity surfaces are those of Top Eocene, Base Oligocene, Top Oligocene, Top Lower Miocene, Top Upper Middle Miocene, Base Messinian salt and Base Pliocene (Fig. 3.13).

Seismic and sequence stratigraphic analyses and interpretations are based on horizon reflection terminations and external and internal patterns geometries and configurations which are indicative of depositional system tracts types and sedimentary environments between platform to basinward, according theoretical sequence deposit system tracts and

boundaries of Memory 26 of the American Association of Petroleum Geology Bulletin (Vail et al. 1977; Mitchum et al. 1977; Rybakov and Segev 2004) and sequence seismic stratigraphy concepts especially in Siliciclastic environments (Vail et al. 1987; Van Wagoner et al. 1988; Homewood et al. 2002; Galloway 1989; Vail et al. 1991; Catuneanu 2002, 2003). Interest will be focused on lowstand sequence horizons for the potential sandstone reservoir distribution target.

Depositional sedimentary lowstand system tracts environment maps of Oligocene and Miocene are reconstructed and established from seismic stratigraphic analyses and interpretations.

As the studied Oligo-Miocene deposits are from deep marine Siliciclastic environments varying from shelf continental margin to deep marine basin and constitute a reservoir targets, we have used several deep marine clastic sequence stratigraphy systems around the world known by their hydrocarbon reservoir characteristics (Chapin et al. 1994; Mahaffie 1994; Gardner and Sonnenfeld 1999; Bédir et al. 1996; Richards and Bowman 1998; Worral et al. 2001; Catuneanu 2002; Sharnugam 2003; Catuneanu 2006; Gardner et al. 2003; Weimer et al. 2007; Bouma et al. 2007; Bédir et al. 2016).
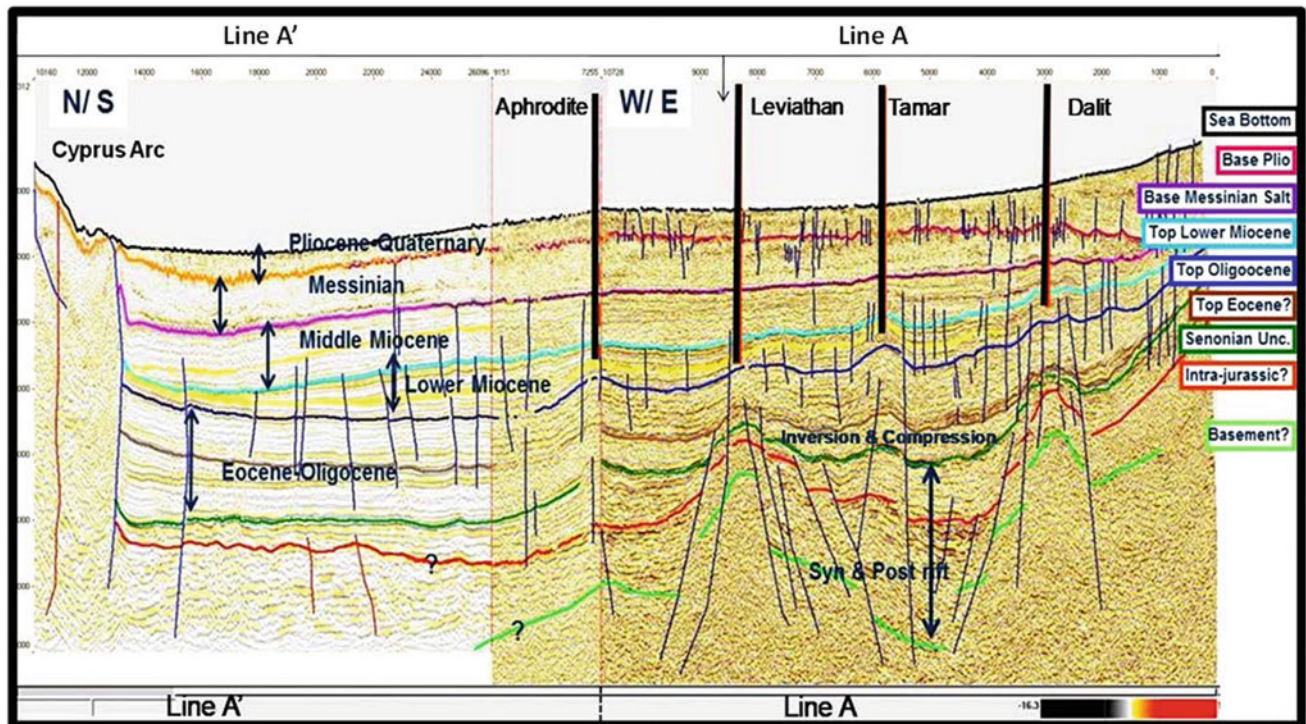
Fig. 3.13 WNW-ESE and N-S structural seismic calibration link lines A and A' of Mesozoic and Cenozoic horizons showing southern central Leviathan ridge and northern subsiding basin exhibiting Mesozoic rifting and Cenozoic compression inversion throw deep-rooted sub-vertical faults and space lateral migrations of subsidence axis (vertical dark arrows)

3.11   Seismic Lines Analyses

3.11.1   E-W Central Area Lines B, C and D

3.11.1.1   Seismic Tectonics

Seismic analyses by picking horizons and seismic stratigraphy of the central study area through lines B and C have led to highlight the Oligo-Miocene basin and horizon structuring and configuration.

E-W Seismic line B and C extend for about 150 km, from Eratosthenes seamount to the west to Lebanese coastal and continental shelf to the east (Figs. 3.14 and 3.15). These lines are near each other, they present globally the same basin configuration. However seismic resolution and attributes of Oligocene and Miocene horizons show some differences in the recognition of terminations and internal and external patterns.

Structurally, the central part of line B (Fig. 3.14), C (Fig. 3.15) and D (Fig. 3.16), exhibits an Oligo-Miocene horizons thickening which represents the subsiding area of Levant basin. Towards the basin flank/wedges of the sections, Lower Miocene horizons thins and pinches out with angular discontinuities, indicating uplifted and resistant domains. These borders are bounded by deep-seated sub-vertical Strike Slip normal and reverse faults. Faults seem to be inherited from the Triassic-Jurassic stage rifting of the basin and reactivated during the different tectonic events of Mesozoic rifting and Tertiary compressive orogenies of Levant basin as documented in the first part of this work, by several regional studies (Robertson 1998a; Robertson and Mountrakis 2006; Hawie et al. 2013 and 2014).

Basin inversion with axis subsidence migration between Eastern and Western sides are visible from Eocene-Oligocene and Lower Miocene horizons packages marked by lateral thickening, thinning and pinch outs of Lower and Middle Upper Miocene. The western side of the line shows tilting of the basin to the West during Oligocene (Figs. 3.14, 3.15 and 3.16).

In the central part and borders of the sections a set of normal faults are reactivated in reverse movements and folding affecting Oligocene and Miocene horizons, some of them has acted as syn-sedimentary faults.

Top depth Oligocene and Miocene structural time maps highlight an NW-SE directions of these faults in central depression of northern Levant basin, whereas eastern and western northern Cyprus and Latakie arc and southern
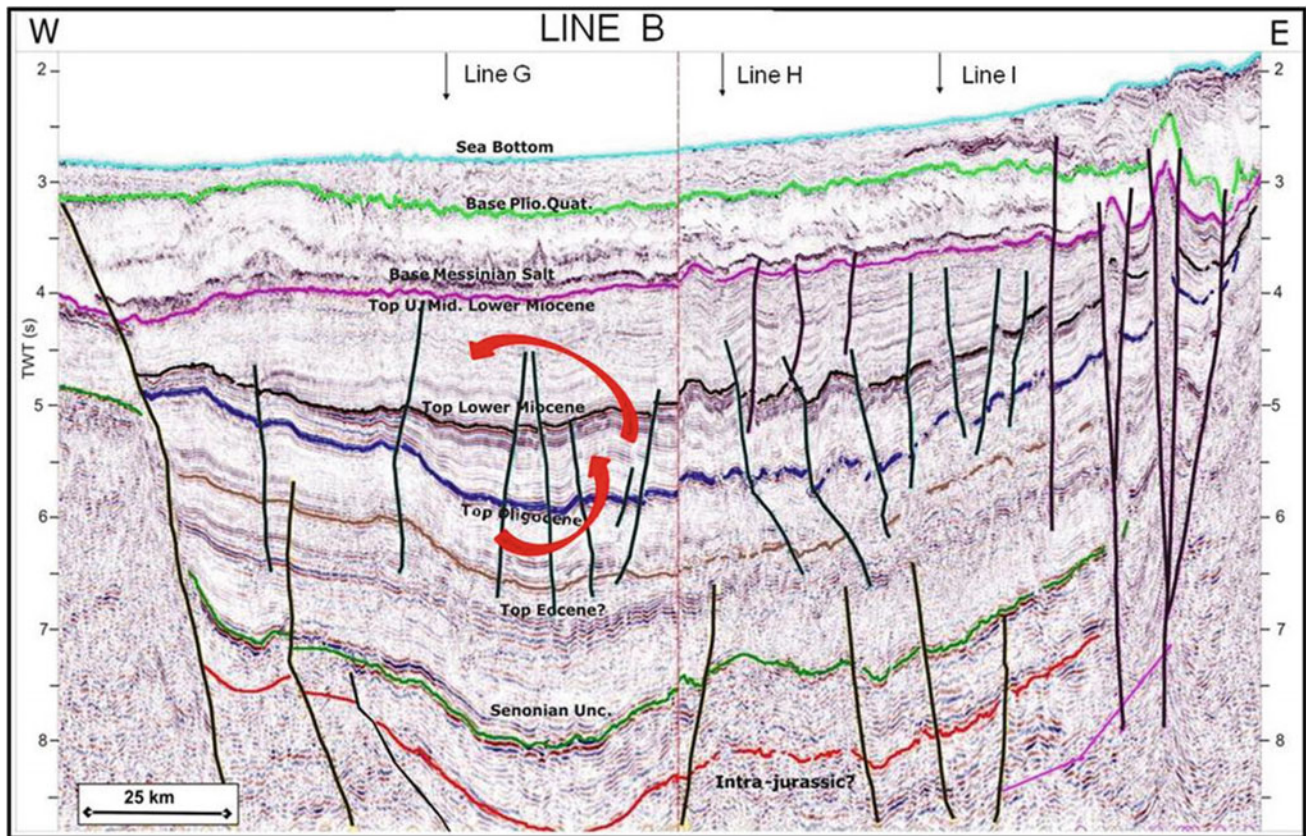
Fig. 3.14 Central E-W uninterpreted structural seismic line B showing deep-seated and syn-sedimentary sub-vertical strike slip normal and reverse faults, Oligocene and Miocene unconformities and eastern and western space lateral axis subsidence migration and inversion (red arrows)

Leviathan ridge highs represent border wedges limited by NE-SW and N-S faults (Figs. 3.17 and 3.18). Deep central depression surrounded by the basin borders is well highlighted by these depth maps.

3.11.2 Seismic Sequence Stratigraphy

3.11.2.1 Oligocene

Early Oligocene horizons overlie Eocene-Cretaceous ones by a strong erosive unconformity (Figs. 3.19, 3.20 and 3.21). Under top Eocene horizons, important incised canyon configurations have been highlighted (Bédir and Aissaoui 2017). They may be corresponding to Upper Eocene clastic deep marine outcrop deposits of eastern coastal border of the basin. Stratigraphic synthesis in the first part of this report have documented strong erosional unconformity and conglomeratic deposits in Upper Eocene outcropping sediments related to the global eustatic fall in this period.

Oligocene horizons are subdivided into 5 third order seismic sequences (OL1 to OL5) limited at the base by downlap terminations and to the top by toplap and onlap terminations (Figs. 3.19, 3.20 and 3.21). Each sequence started by progradational horizons of fall stage early lowstand deposits located essentially on the flanks of the western basin border. External geometrical patterns of these progradational horizons are ranged from mounded and sigmoidal to oblique. In sequences OL2, OL3, OL4 and OL5, above the progradational horizons, and laterally follow an important erosive surfaces and incised canyons of lowstand stage (Figs. 3.14, 3.15 and 3.16). These canyons are present from upper to lower slope. They present single storey type. Their width range from 5 to 10 km and their average in axis thickness is about 300–600 m according the average seismic interval velocity of 2900 m/s.

These are generally located along faults suggesting a guide role of the latter in the trend of canyons pathways (Bédir and Aissaoui 2017). According the structural map of top Oligocene (Fig. 3.17). These faults are directed NW-SE
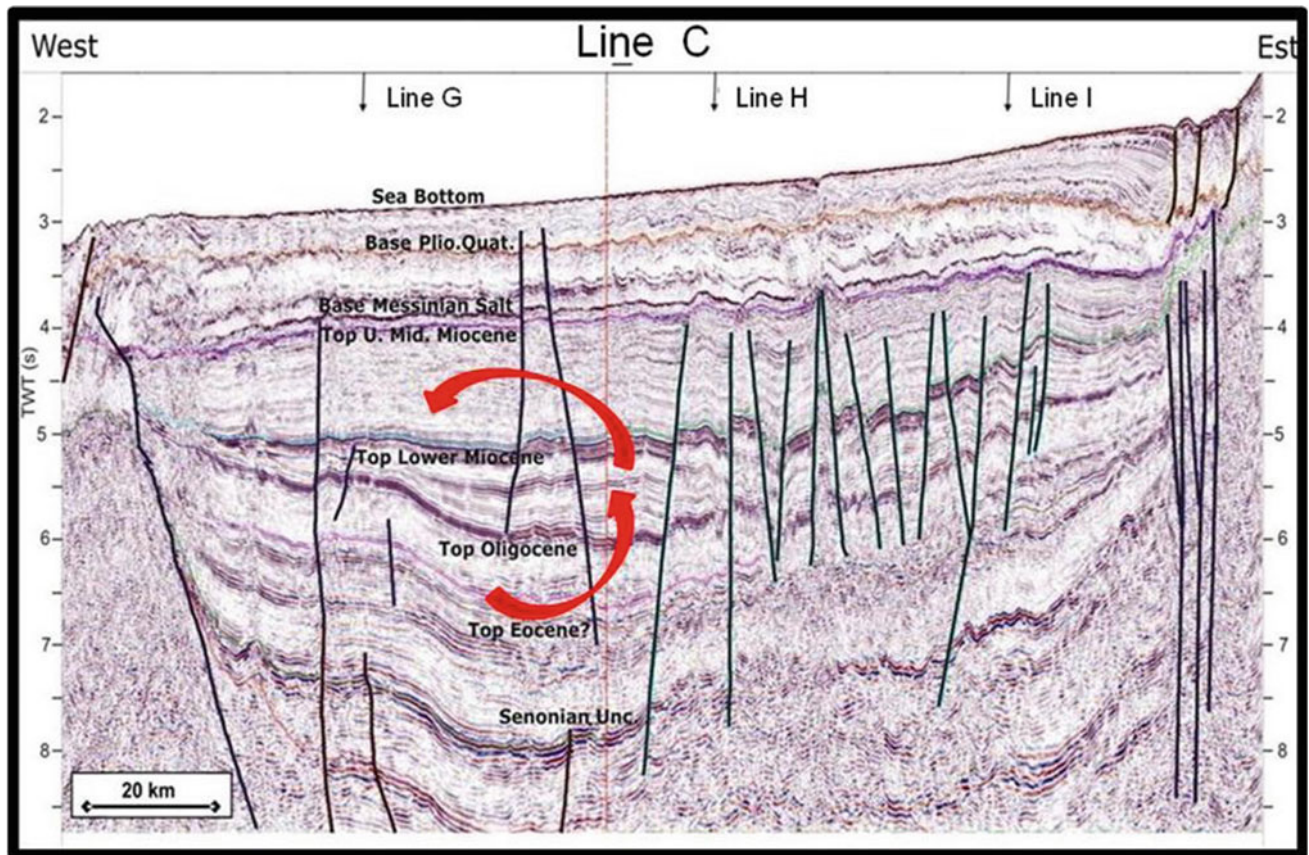
Fig. 3.15 Central E-W uninterpreted structural seismic line C showing deep-seated and syn-sedimentary sub-vertical normal and reverse faults, Oligocene and Miocene unconformities eastern and western lateral subsidence migration and inversion (red arrows)

in the central part of the basin and NE-SW and N-S to its eastern, western and northern borders, so canyon pathways and conduits seem to be oriented along the footwalls of these faults.

The infilling deposits reflectors inside the canyons are from different types; chaotic, complex and prograded (Mitchum et al. 1977). The infilling geometry presents eastern dip downlap terminations to the western side of the basin and western ones to the eastern side. The latter could imply eastern and western feeders of canyons.

Upper sequences terminate by canyons and channels infill configurations sealed by toplap and onlap surfaces representing the transgressive and maximum flooding surface overlain by highstand horizon (Figs. 3.19, 3.20 and 3.21). On these seismic lines, it appears that the western basin border represents in Oligocene time a slight paleo-slope occupied by progradational system tracts and intensive incised canyons in the lower slope. The vertical and lateral distributions of canyons from the lower sequences to the upper ones show a lateral migrations (Bédir and Aissaoui 2017). These results are new arguments for the presence of these canyons to the western basin slope.

In the central part of the seismic lines, mound and sheet horizons configuration appears as turbiditic fan bodies (Figs. 3.19, 3.20 and 3.21).

To the western border and lower slope basin, seismic acoustic characters are marked by discontinuous reflectors with low to middle amplitude for progradational and canyon features whereas more continuous and middle to high amplitude reflectors characterize toplap and onlap upper sequence limit boundaries.

3.11.3 Lower Miocene

Lower Miocene section extending from Aquitanian to Burdigalian age present important configuration change according to the Oligocene horizons; seismic horizons package show thickening in the centre of the basin and strong reductions and pinch outs towards the western and eastern edges that are more individualized than the Oligocene structuring (Figs. 3.19, 3.20 and 3.21). Lower Miocene basal horizons overly unconformably late Oligocene ones by an angular surface in the western and eastern basin slope
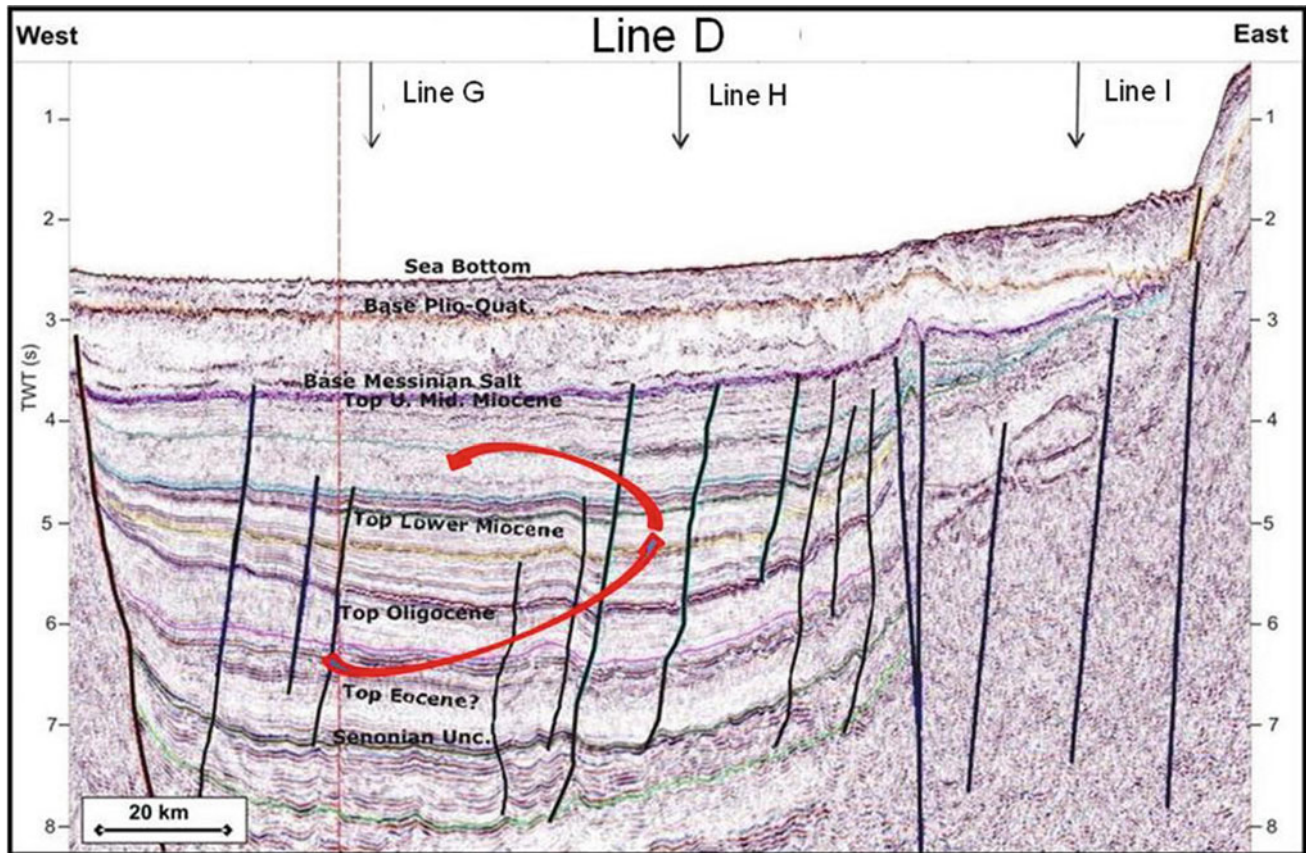
Fig. 3.16 Central E-W uninterpreted structural seismic line D showing deep-Seated sub-vertical strike slip normal and reverse faults, Oligocene and Miocene unconformities, eastern and western lateral axis subsidence migration and inversion (black arrows)

flanks. This unconformity seems to be due to the Upper Oligocene event that uplifted the two border slopes and subsided the central part of the basin.

Lower Miocene horizons present 4 third order seismic sequences M1 to M4, limited at the base by downlap terminations and to the top by toplap and onlap features (Figs. 3.19, 3.20 and 3.21). The base of sequences shows a progradational sigmoidal, oblique and shingled offlaps and mounds of fall stage lowstand deposits situated on the flanks of the western and eastern basin slopes and mounded and sheet configurations to the centre of the basin (Bédir and Aissaoui 2017).

Upper sequences are characterized by storey incised canyons and channels located in central part of the basin. They are covered by toplap and onlap surfaces representing the transgressive and maximum flooding surface overlain by highstand horizon. The reflectors inside these canyons show prograded and onlap fill. Their average width is about 3–7 km and in axis thickness is between 100 and 180 m.

As it was the case of the Oligocene canyons, Lower Miocene ones are in majority the footwalls of faults that are mapped in the structural map in the central basin area as NW-SE direction and NE-SW and N-S along eastern and western shelf margins (Fig. 3.18).

In the central part of the seismic lines, sheet and mound configurations suggest a fan lobes and deep sea fan deposits. Their average width is about 3 km and axis thickness about 100–150 m.

From the western Cyprus arc high basin edge of the slope, seismic reflectors show lateral variation of continuity, amplitude and frequency whereas more continuous and middle to high amplitude characterize toplap and onlap sequence limit boundaries.

To the eastern continental basin slope, despite intensive folding deformations and faults, progradational horizon configurations can be detected as mounded and oblique structures.

3.11.4 Middle-Upper Miocene

Middle Upper Miocene horizons range from Langhian to Serravallian and Tortonian deposits overlain by the base of Messinian salt. It constitutes a new horizons package that

Fig. 3.17 Top Oligocene structural depth map showing NW-SE faults in the central basin and NE-SW and N-S ones in the western and eastern shelf borders of the northern Levant basin (CI: 100 m)
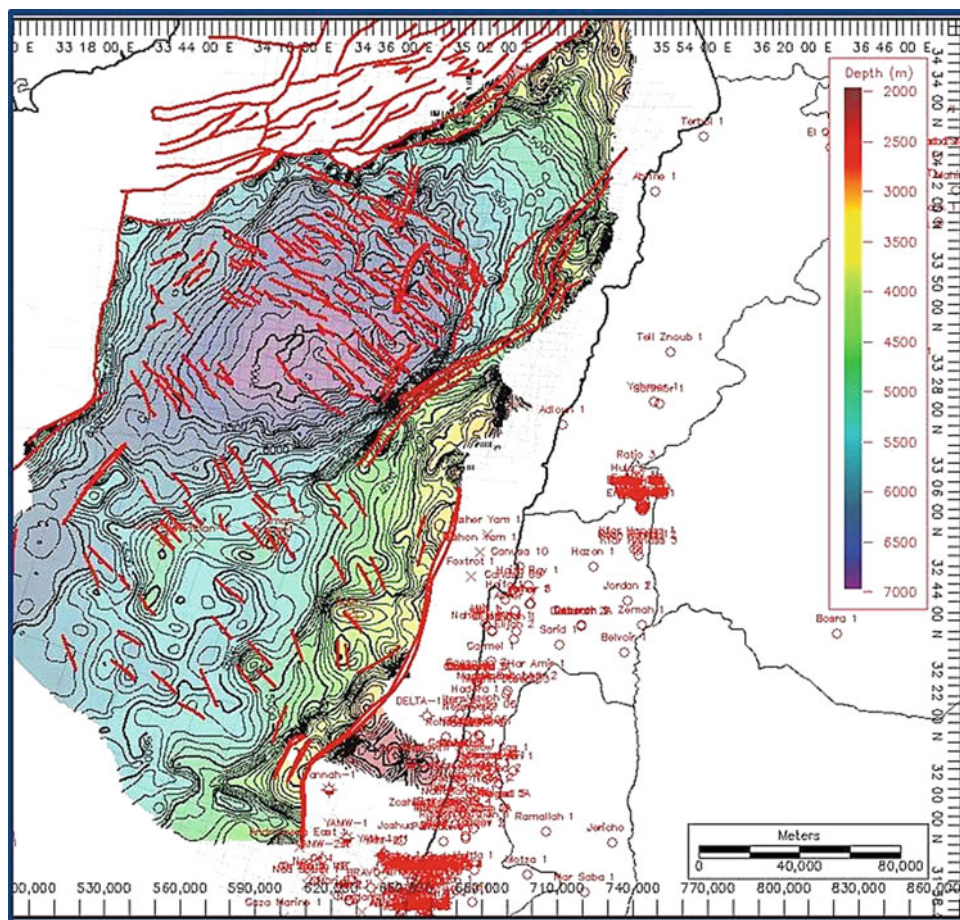
contrast with Lower Miocene ones by more transparent seismic facies and newly appearance of incised canyons and channels (Figs. 3.19, 3.20 and 3.21).

Third order sequence subdivisions of Middle to Upper Miocene show 5 to 7 sequences (M5 to M9) limited by toplap/onlap gradational and retrogradational horizons.

In fact, basal Middle Miocene blue horizons represents langhian deposits that overly unconformably lower Miocene lowstand horizons of sequence M4 according a progressive retrogradational onlap parallel horizons towards the western and eastern basin edge high slopes (Figs. 3.19, 3.20 and 3.21).

Nevertheless, they represent a transgressive and highstand system tract cycle of sequence M4 in the global eustatic chart (Haq et al. 1987; Vail et al. 1991); these transgressive deposits are related to the transgressive and highstand sea level rise of Langhian which are well documented regionally around central and western Mediterranean and known in North African margin by the grainstone bioclastic shelf transgressive carbonates of Ain Ghrab Formation and highstand planctonic Mahmoud Formation shales

(Bismuth 1984; Ben Ismail 1984; Bédir et al. 1996; Bédir et al. 2016).

Seismic characteristics of this transgressive and highstand horizons are marked here by a general parallel and continuous seismic horizon marker with middle to high amplitude reflectors (Figs. 3.19, 3.20 and 3.21) which suggests a uniform depositional environment of alternation of low and moderate energy related to marls, mudstones and carbonates as documented in Israeli-Palestine outcrops and wells of the eastern coast (Gardosh et al. 2008).

To the western basin slope, at the base of these system tracts, we can note some sigmoidal progradational horizons on the slope and channelized reflectors towards the basin (Figs. 3.19, 3.20 and 3.21). It could be a transgressive progradational system tract of this Langhian highstand deposits as mentioned in the base of the related eustatic global chart cycle (Haq et al. 1987; Vail et al. 1991).

This is also has been found in central Lebanon outcrops where Langhian deposits present basin compact mudstone carbonates at the base and proximal slope slumped
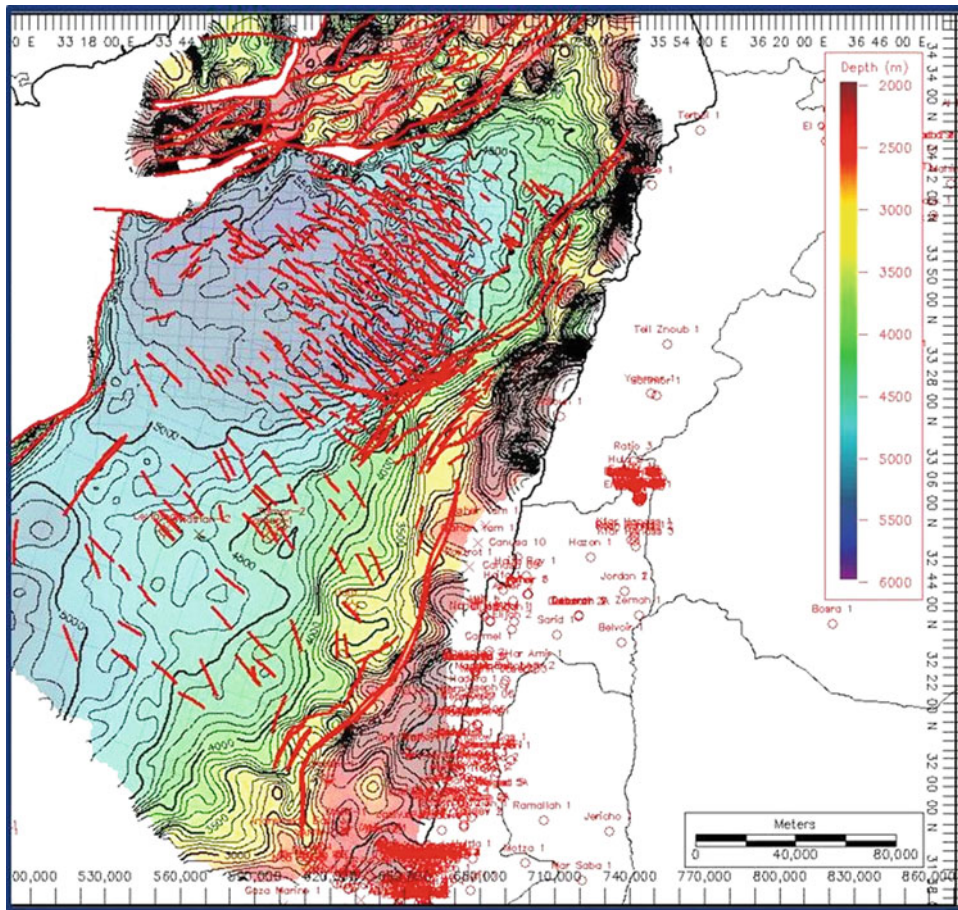
Fig. 3.18 Top Lower Middle Miocene structural depth map showing NW-SE faults in the eastern basin and NE-SW and N-S ones in the western and eastern shelf borders in the northern Levant basin with southeastern migration subsidence (CI: 100 m)
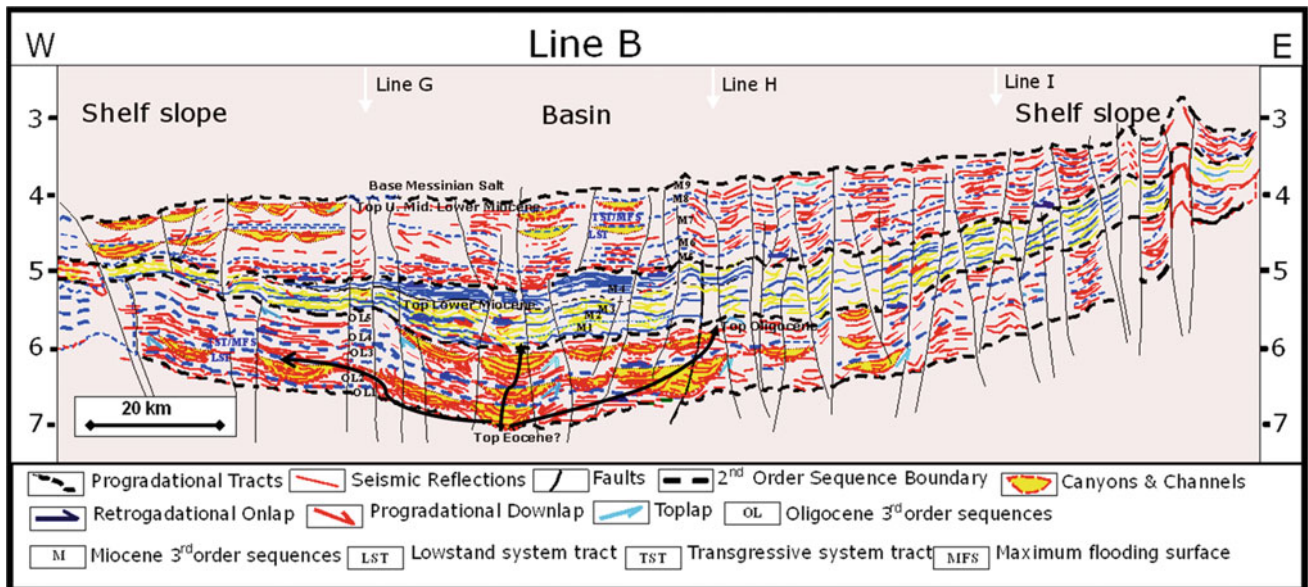
Fig. 3.19 Central E-W geo-seismic sequence stratigraphic section of line B showing Oligocene and Miocene seismic horizons configurations with Lowstand prograding Downlaps, Transgressive retrograding tst/mfs and Highstand aggrading Onlap/Toplap system tracts, storey and multistory canyons and channels space lateral migrations (black arrows)
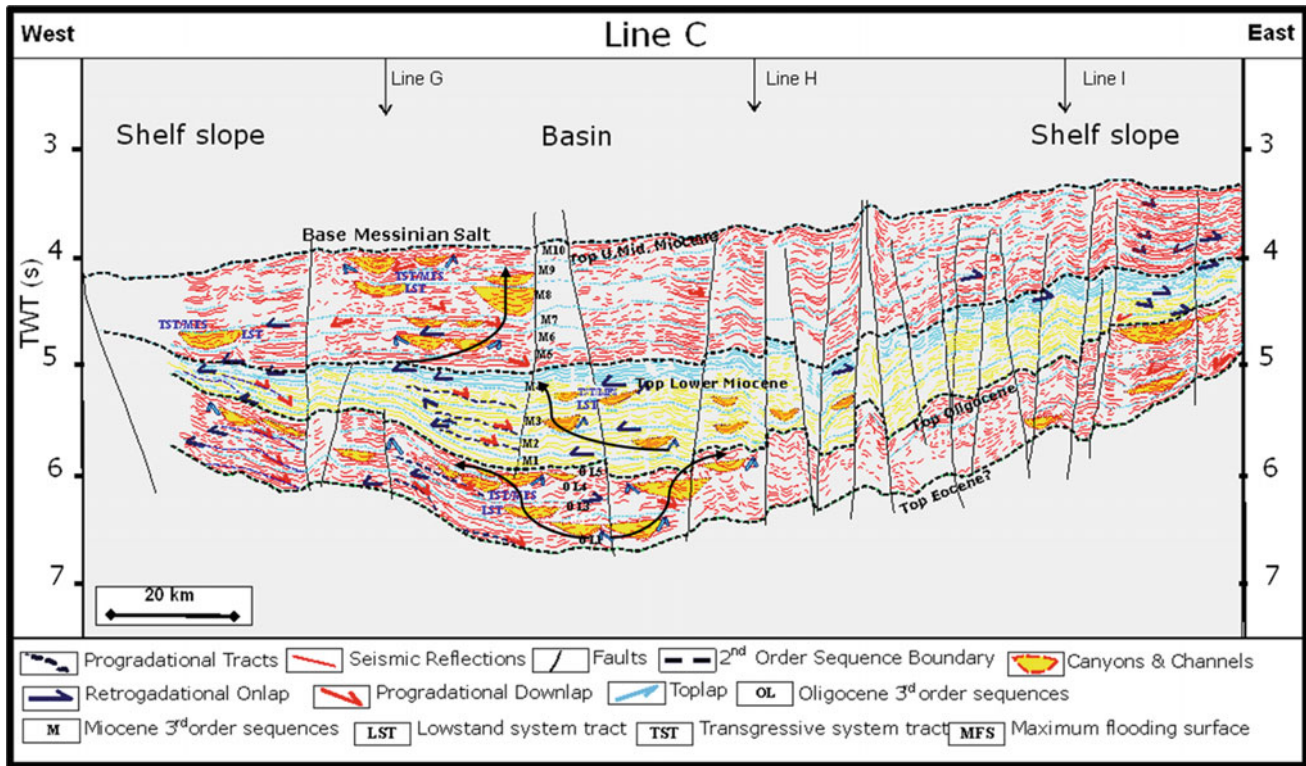
Fig. 3.20 Central E-W Geo-Seismic sequence stratigraphic section of Line C showing Oligocene and Miocene seismic horizons configurations with Lowstand prograding Downlaps, Transgressive Retrograding TST/MFS and Highstand aggrading Onlap/Toplap system tracts, storey and multistory canyons and channels space lateral migrations (black arrows)

sediments and turbidites with large incisions at the top of the deposits (Hawie 2013).

Middle to Upper Miocene Serravallian horizons, of sequence M5 overlay M4 reflectors by an erosive basal surface unconformity. The first basal horizons of this sequence present downlap progradational configurations from the western basin edge slope to the center of the basin. Onlap retrogradational reflector terminations are well visible towards the western slope flank.

Sequences begin by a progradational horizons of early fall stage lowstand deposits presenting oblique and mounded bodies and ending by channel and storey canyons structures to the western side of the basin. The deposits reflectors inside the canyons are predominantly of prograded, complex and onlap fill types (Mitchum et al. 1977).

Based on seismic average interval velocity of Miocene horizons, the thickness in axis of these canyons and channels is about 150–200 m, the average width ranges from 3 to 5 km and can reach 10 km in some cases.

Sequences M7 and M8 show predominately transparent seismic facies to the western part of the seismic line and downlap mounded configuration at the base and channels to the top suggesting a fan lobes and deep sea fan deposits as it was shown and documented in the same basin by seismic horizon amplitude analysis by Hawie (2013), where Late

Miocene NE-SW trending channels and fan lobes has been highlighted in the eastern border of the basin (Fig. 3.22), with feeder and distributaries. This corroborates with the present seismic stratigraphy analysis.

Sequences M8 and M9 present basal mounded horizons ending to the top by important incised canyon configurations to the central and western part of the sections (Figs. 3.19, 3.20 and 3.21).

The location of incised canyons seems to be guided by deep-seated faults footwalls that are oriented NW-SE in this central part of the basin according to the Top Lower Middle Miocene time structural map (Fig. 3.18) as it was the case for Oligocene sequences (Fig. 3.17).

3.11.5 WNW-ESE Southern Area Line A

3.11.5.1 Seismic Tectonics

The line A extends nearly 160 km from WNW to ESE (Figs. 3.11 and 3.23). The western and eastern limits of the line present clear slope and high areas corresponding respectively to the Eratosthenes sea mount and continental shelf of Palestine, Syria and Lebanon. Seismic horizons are strongly folded from Upper Cretaceous to Upper Miocene. Folds are flanked by deep-seated sub-vertical strike slip
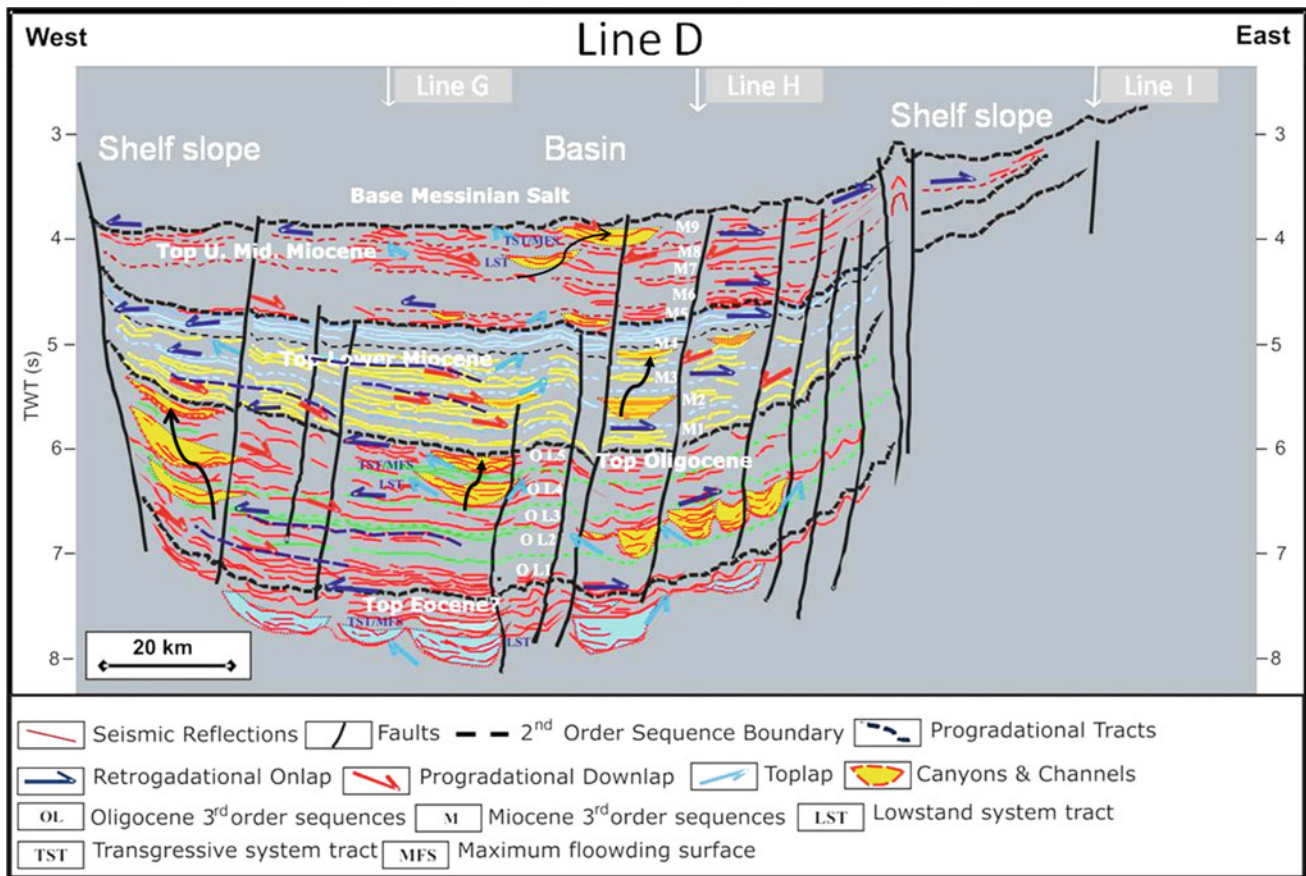
Fig. 3.21 Central E-W Geo-Seismic Sequence Stratigraphic Section of Line D Showing Eocene, Oligocene and Miocene Seismic Horizons Configurations with Lowstand prograding Downlaps, Transgressive Retrograding TST/MFS and Highstand aggrading Onlap/Toplap system tracts and storey canyons and channels Space lateral migrations (black arrows)

faults. This structuring indicates that successive tectonic compressional events happened at Upper Cretaceous, Upper Eocene, Upper Oligocene, Lower Miocene and Upper Miocene (Fig. 3.23). These tectonic events are well printed by important angular unconformities visible in the western and eastern basin wedges as well as in the central basin folds. This southern area of the study summarizes the successive events that created the Syrian and Cyprus arcs from Upper Cretaceous to Upper Neogene.

Seismic horizons of Oligocene, Lower Miocene and Middle-Upper Miocene presents more thickening to the western side of the line and strong thinning towards the eastern and western edges of the basin as well as around the central fold flanks due to the syn-sedimentary folding and associated synclines (Fig. 3.23). Pinch outs are well defined in Oligocene and Lower Miocene.

Seismic horizons of all the studied series present strong thinning towards the two borders of the basin as well as in the central fold flanks due to the synsedimentary folding and

associated synclines (Fig. 3.23). Pinch outs are well individualized in Oligocene and Lower Miocene.

3.11.6 Seismic Sequence Stratigraphy

3.11.6.1 Oligocene
Early Oligocene horizons overlay Eocene-Cretaceous reflectors by a strong erosive toplap unconformity clearly exhibited towards the eastern margin slope (Fig. 3.24).

Despite the disturbance of reflectors by tectonic deformations, some parts of the line allowed to recognize sequence boundaries and terminations showing a subdivision into 5 third order Seismic Sequences (OL1 to OL5) limited at the base by downlap terminations and to the top by toplaps and onlaps (Fig. 3.24).

Progradational downlap horizons of early lowstand deposits can be identified at the base of sequences on the lower slope flanks of the eastern and western basin borders
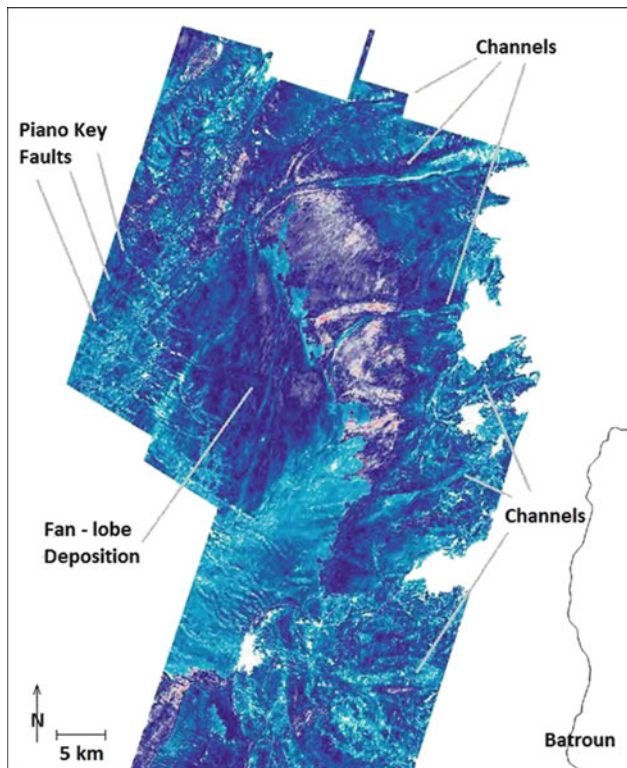
Fig. 3.22 Late Miocene fan system with feeder and distributaries on the amplitude map with low amplitudes shown in blue, higher amplitudes in light blue and highest amplitudes in red color. NE-SW trending channels and fan lobes are clearly visible (Hawie 2013)

as well as in the central basin zone (Fig. 3.24). These features present mounded and oblique geometries well visible in OL1 sequence in the central gutter synclines of folds.

Oligocene horizons present discontinuous reflectors and laterally variable amplitude ranging from low to high along the section. Transparent facies between reflections suggest homogeneous density mud material dominance in some parts of the basin (Fig. 3.24). The latter indicates variable middle to high hydrodynamic energy of sedimentary deposition. As identified on central area E-W lines, these features suggest existence to the western basin area of turbiditic deep sea fan deposits during Oligocene as in the precedent E-W seismic lines B (Fig. 3.14), C (Fig. 3.15) and D (Fig. 3.16). Canyon faults relationship is also found here in this southern line (Fig. 3.24).

This southern area exhibits intensive and frequent erosive surfaces of incised storey canyons of lowstand stage present in all Oligocene sequences (Fig. 3.24). They are distributed from upper western and eastern slopes to the central basin. Their interior reflectors present complex, prograded, onlap and chaotic fill types.

From lower sequence OL 1 to upper sequence OL 5, incised canyons exhibit clear lateral migrations from the

center of the basin to the western slope as well as to the eastern slope (Fig. 3.24).

Width canyons vary from 3 to 10 km and the average thickness ranges approximately from 100 to 350 m.

3.11.7 Lower Miocene

Lower Miocene basal horizons overlay unconformably late Oligocene horizons by an angular surface to the western and eastern basin wedges (Fig. 3.24).

Seismic horizons show thickness variations along this line due to the existence of syn-sedimentary anticline and syncline structures where horizons and sequences exhibits reductions around folds and thickening in the syncline gutters attested by angular onlaps (Fig. 3.24). Towards the eastern and western high borders of the basin strong thinning of sequences is well identified.

Lower Miocene horizons are subdivided in 4 third order seismic sequences M1 to M4, limited at the base by downlap terminations and to the top by toplap and onlap aggradational and retrogradational configurations (Fig. 3.24).

The base of sequences show a progradational configurations of sigmoidal, oblique and shingled offlaps, mounds and sheet towards the syncline gutters located on the flanks slopes and the centre of the basin (Fig. 3.24). Seismic reflections show incised channels and canyons from sequences M1 to M4 distributed along the line from West to Est. These canyons are smaller than those of Oligocene ones.

They show reflection infill of complex, prograded and onlap fill types. Average width of canyons bodies is about 3 to 4 km and axis thickness between 100 and 150 m.

Basal Middle Miocene (blue horizons) overlays unconformably lowstand reflectors of sequence M4 according to a progressive gradational/retrogradational onlap parallel horizons towards the western and eastern basin edge high slopes and also on the flanks of central intra-basin folds (Fig. 3.24).

Lowstand Miocene seismic reflectors present lateral variation of continuity, amplitude and frequency giving more transparent facies picture that contrast with more continuous reflectors and middle to high amplitude of condensed section of toplap and onlap sequence limit boundaries (Fig. 3.24).

3.11.8 Middle-Upper Miocene

Middle Upper Miocene horizons show more general transparent seismic facies than Lower Miocene ones (Fig. 3.24). Third order sequence subdivisions present 5 sequences (M5 to M9) limited by downlap progradation of lowstand system tracts at the base and toplap/onlap aggradational and
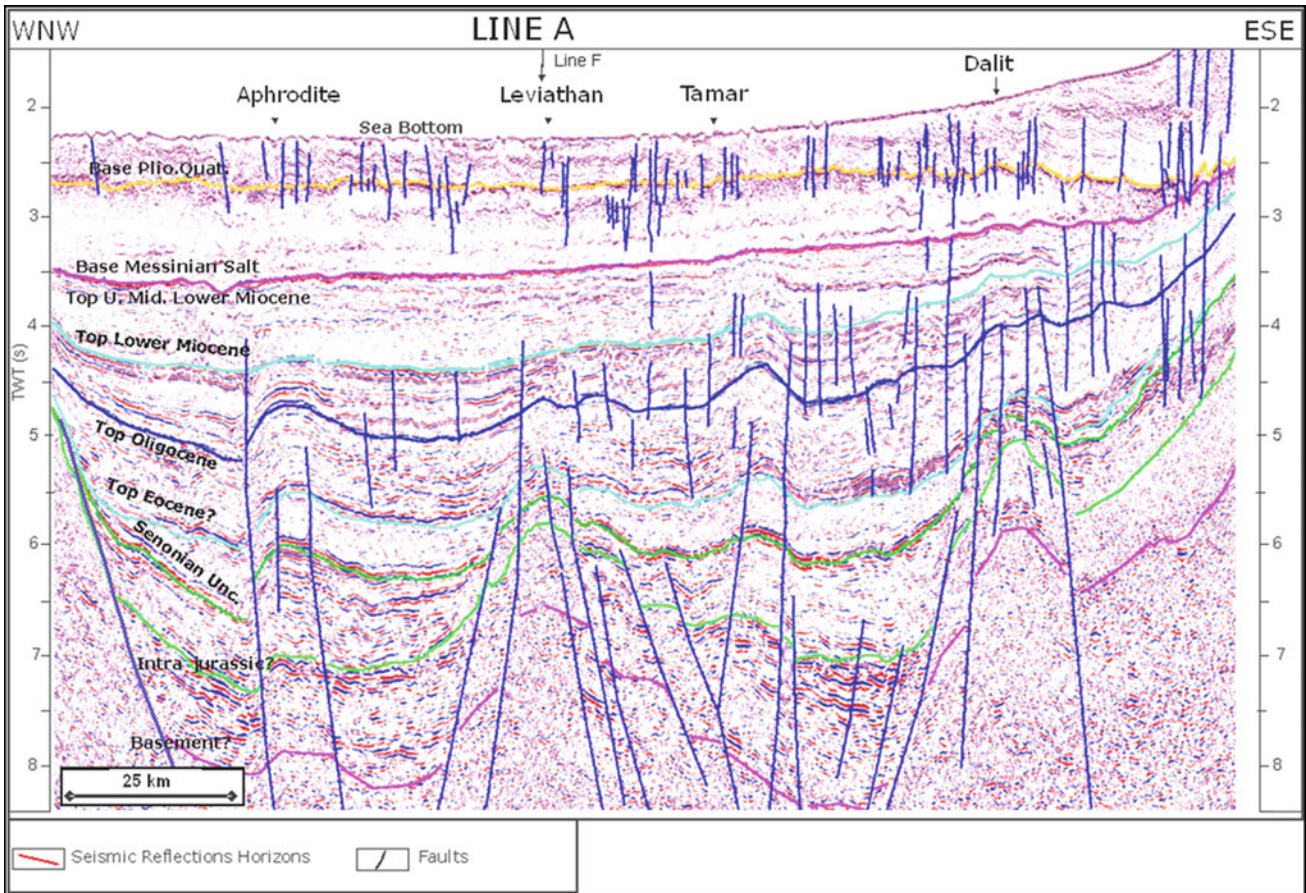
Fig. 3.23 Southern WNW-ESE uninterpreted structural seismic line A across Aphrodite, Leviathan, Tamar and Dalit Gas fields structures, showing Mesozoic rifting and Late Cretaceous-Tertiary compression inversions and folding with sub-vertical deep-seated transtensive and transpressive faults
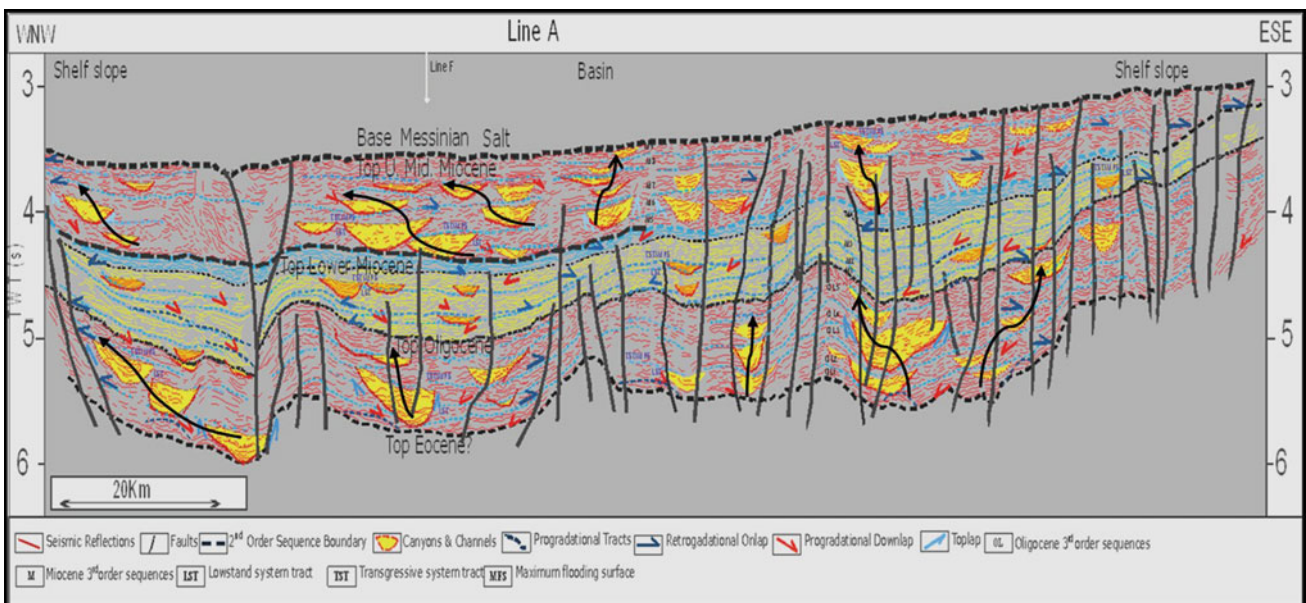
Fig. 3.24 Southern WNW-ESE Geo-seismic sequence stratigraphic section of line A showing Oligocene and Miocene seismic horizons configurations with Lowstand prograding Downlaps, Transgressive retrograding TST/MFS and Highstand aggrading Onlap/Toplap system tracts and storey/multistory canyons and channels space lateral migrations (black arrows)

retrogradational of transgressive and highstand system tracts at the top.

Upper sequences terminate by important storey incised canyons that cut lower sequence horizons and also sequence boundary limits (Fig. 3.24). These canyons extend from West to East and from the sequence M5 to sequence M9. They show space lateral migrations towards the West and towards the East. The infilling reflectors of canyons show complex, prograded and chaotic types fill.

Seismic horizons of sequence M5 overlay M6 reflectors by basal sigmoid and shingled downlap progradational configurations on the slope borders and in the central basinal zone. Nevertheless, they present discontinuous reflectors with low amplitude indicating middle to high energy of fan deposits of silicoclastics sandstone and shale lobes (Fig. 3.24).

Sequences M5 and M7 show predominately transparent seismic facies to the central and western part of the seismic line that indicates a predominant homogeneous facies whereas to the Eastern border of the basin reflections become of high amplitudes and good continuity due to the reduction of sequences and condensed sections of transgressive and maximum flooding surface unconformities on the shelf margin (Fig. 3.24).

Incised canyon bodies have an average thickness in axis from 180 to 350 m and width from 3 to 10 km.

3.11.9 E-W Northern Area Line E

3.11.9.1 Seismic Tectonics

Line E is located in the north-eastern part of the study area and has about 50 km length. It is the shortest line of the selected sections and represents the narrowest part of the basin to the North (Figs. 3.11 and 3.25).

Western side of the line show strong fold anticline and thrusting of the Cyprus arc printing a tectonic inversion of the western border slope of the basin. Central part of the line exhibits foreland basin in Oligocene and Miocene horizons that are structured in folded synclines. Intensive deformations affect Oligocene and Miocene horizons represented by a central and eastern folds bounded by reverse faults (Fig. 3.25).

Folds in central part of the basin are bounded by deep-seated flower faults suggesting transpressional movements and attested by angular unconformities (Fig. 3.25) as it was documented in the other E-W seismic lines of central and southern basin study area. The central and lateral folding of the basin created syn-sedimentary synclines attested by the distribution of seismic sequences pinch outs and onlap terminations.

Thinning of seismic sequence horizons of Oligocene, Lower Miocene and Middle-Upper Miocene is observed
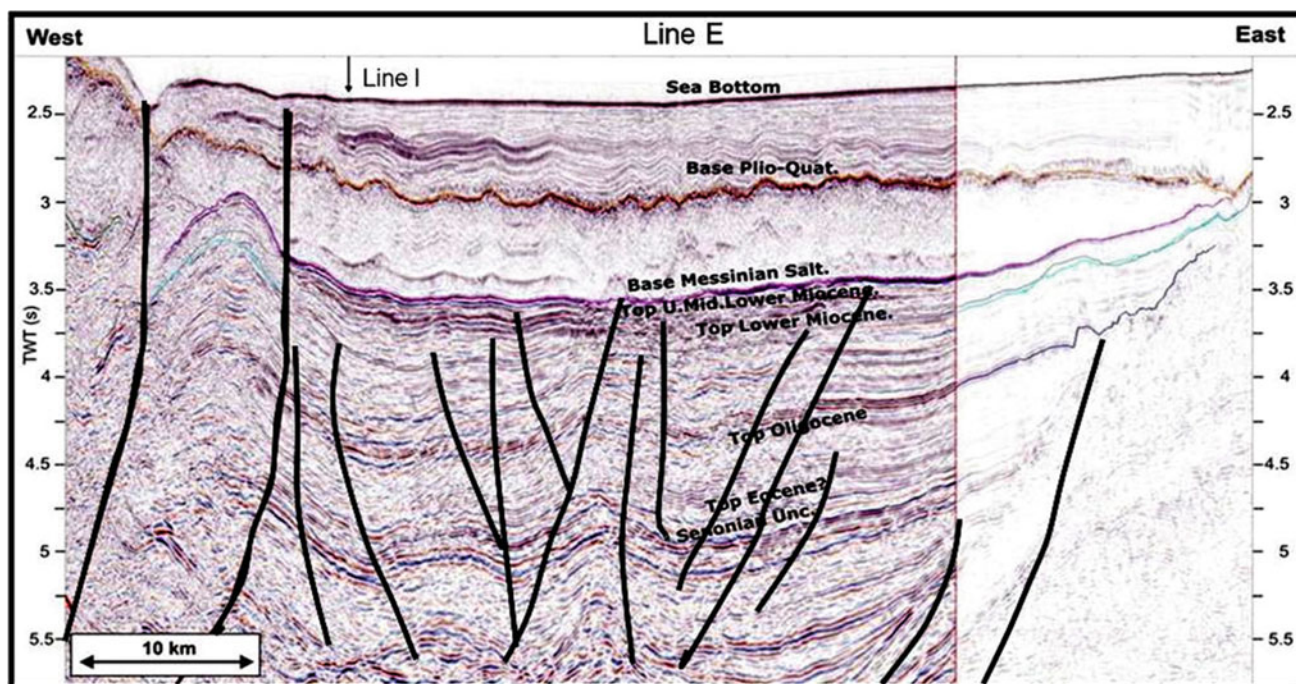
Fig. 3.25 Northern E-W uninterpreted structural seismic line E showing Cyprus-Latakia compression arcs, deep-seated sub-vertical and flower structures strike slip faults, Oligocene and Miocene horizon folding

toward the western Cyprus Arc border. More important reduction to the eastern slope margin occurred (Fig. 3.25).

3.11.10 Seismic Sequence Stratigraphy

3.11.10.1 Oligocene

Early Oligocene horizons overlay Eocene-Cretaceous reflectors by an erosive toplap unconformity. Oligocene horizons present progressive onlaps on the eastern flank of the basin. Acoustic parameters of horizons show discontinuous reflectors and laterally variable amplitude ranging from low to high (Fig. 3.26).

Recognition of sequence boundaries and terminations in tectonic deformations and faults context is a difficult exercise. Nevertheless, subdivision into 5 third order seismic Sequences (OL1 to OL5) has been tentatively identified by basal downlap, toplap and onlap terminations (Fig. 3.26).

Seismic sequences begin at the base by progradational downlap horizons of early lowstand deposits on the lower slope flanks as well as in the central basin zone and by onlap retrogradational terminations on the high flanks of slopes. These features present sigmoidal, shingled and mounded geometries (Fig. 3.26).

These geometries indicate high hydrodynamic energy of sedimentary deposition. As identified on the other E-W lines, these features suggest existence to the northern area of the Levant basin of high energy turbiditic deep sea fan deposits during Oligocene (Fig. 3.26). Directions of downlap progradational bodies and onlaps indicate western, eastern and probably northern clastic source origin.

The northern area of the basin exhibits intensive erosive surfaces of multistorey and stacked incised canyons of lowstand stage present from base to upper Oligocene sequences. They are located on the two syncline faulted gutters of the central fold. These canyons cut the upper sequence toplap horizons boundaries of Oligocene and Lower Miocene (Fig. 3.26). It's the only area from selected lines that show so remarkable incised canyons superposition from Oligocene to Lower Miocene. This fact suggests a northern and/or northeastern feeder of the infill supplies.

In addition, we should remember the existence of deep sea fan turbidites and conglomerates deposits of Cingoz and Kici Oligo-Miocene Formation outcropping in eastern Turkey (Satur et al. 2007; Boulton et al. 2007; Plummer et al.); which is located to the northern part of seismic line E. This turbiditic system presents two feeders; one from the East and another from the West.

It is clearly stated here that canyons are guided by tectonism as it was the case in the central and southern E-W seismic sections. These canyons present bigger sizes due probably to their proximity to continental feeders. Width varies from 3 to 10 km and the average in axis infill thickness is approximately 250–1500 m. The infilling deposits reflectors inside the canyons show complex and prograded types exhibiting shingled and sigmoid downlap oblique
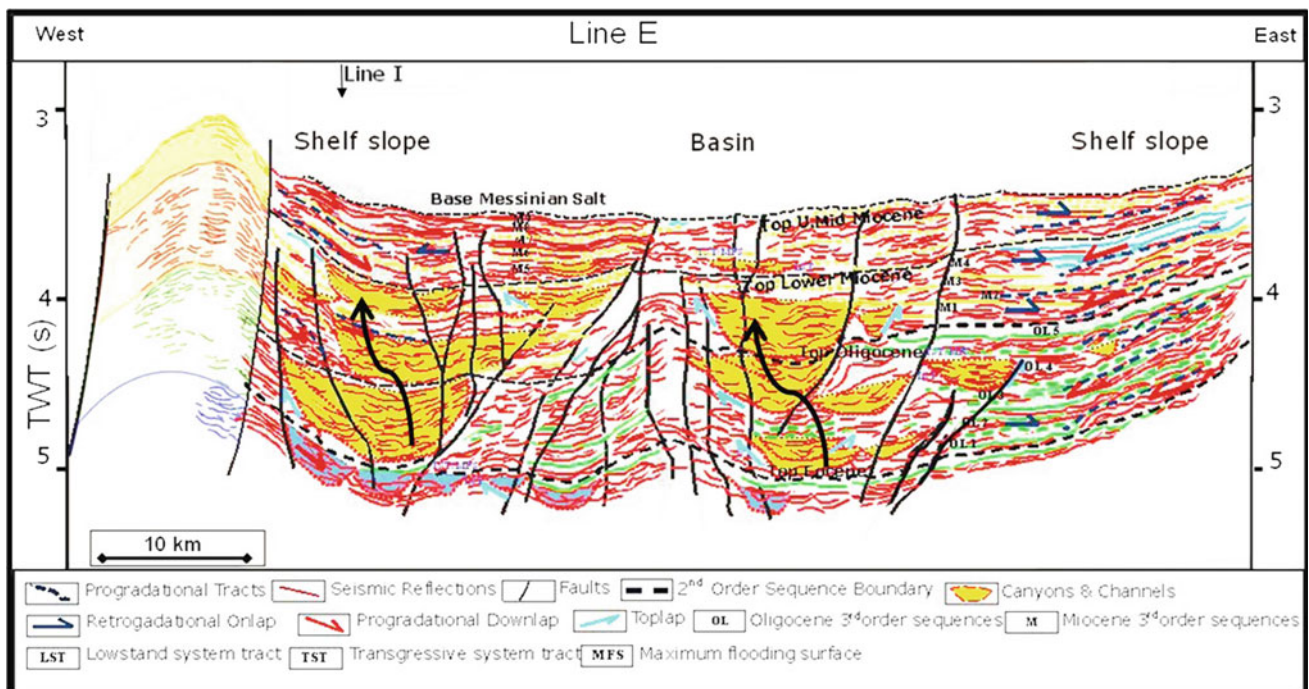
Fig. 3.26 Northern E-W Geo-Seismic sequence stratigraphic section of line E showing Eocene, Oligocene and Miocene seismic horizons configurations with Lowstand prograding Downlaps, Transgressive retrograding TST/MFS and Highstand aggrading Onlap/Toplap system tracts and storey/multistory canyons and channels space lateral migrations (yellow arrows)

terminations (Fig. 3.26) which indicate a variable low to high hydrodynamic energy during sediment depositions.

3.11.11 Lower Miocene

Lower Miocene basal horizons overlay unconformably late Oligocene horizons by an angular surface in the western and eastern basin wedges (Fig. 3.26).

Seismic horizons package show thickness variations along this line due to the existence of synsedimentary anticline and syncline structures where horizons and sequences exhibits reductions around folds and thickening in the syncline gutters attested by onlaps. Towards the eastern and western high borders flanks of the basin occurs strong thinning of sequences with progressive onlaps. In the western flank of the central fold Lower Miocene horizons infill a syncline gutter (Fig. 3.26).

As in the others E-W seismic lines, Lower Miocene horizons can be subdivided in 4 third order seismic sequences M1 to M4, limited at the base by downlap terminations and to the top by toplap and onlap gradational and retrogradational configurations (Fig. 3.26).

The base of sequences show a progradational configurations of sigmoidal, oblique and shingled offlaps and mounds towards the western and eastern border of the basin and in the central fold flanks (Fig. 3.26). Seismic reflections shows incised channels and canyons from sequences M1 to M4 distributed along the line from West to Est. These canyons are in continuity of the Oligocene ones.

Upper sequences are characterized by channels of late lowstand stage toplapped by toplap and onlap surfaces. Average width of canyons bodies is about 3–10 km and axis thickness about 500–800 m.

Seismic reflectors show lateral variation of continuity, amplitude and frequency and more transparent facies in the central part of the line whereas more continuous reflectors of middle to high amplitude appear on the high zone border edge of the basin marked by condensed toplap and onlap sequence limit boundaries (Fig. 3.26).

First Middle Miocene (blue horizons) of transgressive and highstand deposits of sequence M4 are here absent in the western side of the basin due to the strike position of this line on the onlap termination of these reflectors in N-S section I. In contrary, they appear in the eastern flank slope of the line and disappear to the center of the basin due probably to the strong erosion of sequence M4.

3.11.12 Middle-Upper Miocene

In this line, sequences present thickness reduction. Nevertheless, 4 to 5 third order sequences (M5 to M9) has been

recognized (Fig. 3.26). Each sequence ends vertically by channel configurations.

First Middle Miocene transgressive horizons that represent the top of M4 are present only in the eastern part of the line because this line crossed the high onlap termination of these reflectors.

Progradational bodies of sequences present sigmoid, shingled and mounded configurations on the slope borders as well as in the basin zone (Fig. 3.26).

Reflectors of sequence M5 and M6 present discontinuity and variable amplitudes with more transparent seismic facies and more thickness than sequence M7 to M9. The latter show important thinning, more continuity and high amplitudes (Fig. 3.26).

3.11.13 Western Area N-S Lines F and G

3.11.13.1 Seismic Tectonics

After the analysis and interpretation of E-W seismic lines, it is important to follow the basin configuration and seismic reflection patterns along N-S strike position to match the interpretation of E-W sections. Logically all the seismic sequence subdivisions and internal and external reflection patterns are the same in the two directions. Nevertheless, some changes of lateral evolution and distribution along N-S direction present new results for mapping and constructing the system tract distribution around the study area. Three seismic N-S lines will be presented.

This section is composed by two lines F and G (Figs. 3.11 and 3.27), linking the South to the North and intersect the E-W line A calibrated by Tamar 1 and Leviathan 1 gas fields (Fig. 3.12).

Along this composed line, the basin is limited to the North by a slope which is the high Cyprus Arc domain and to the South by the Leviathan ridge. From North to South, Oligocene and Miocene horizons show thickness variations with inversion basin structuring and subsidence migration between Senonian-Eocene and Oligocene and Lower Miocene and between Lower and Middle to Upper Miocene (Fig. 3.27). Basin block has been strongly tilted along N-S direction and northern border was uplifted by the compressional thrusting of Cyprus arc during Miocene time.

Deep-seated sub-vertical strike slip faults bordered the northern and southern highs of the slopes and intra-basinal fault network affects Mesozoic and Cenozoic horizons. These faults are ancient normal faults of Mesozoic rift stage reactivated in reverse and thrust movements during Tertiary times creating the folding of Mesozoic and Tertiary horizons (Fig. 3.27).

On E-W lines, the inversion and tilting of the basin block has been also detected. Tilting is generally occurred to the
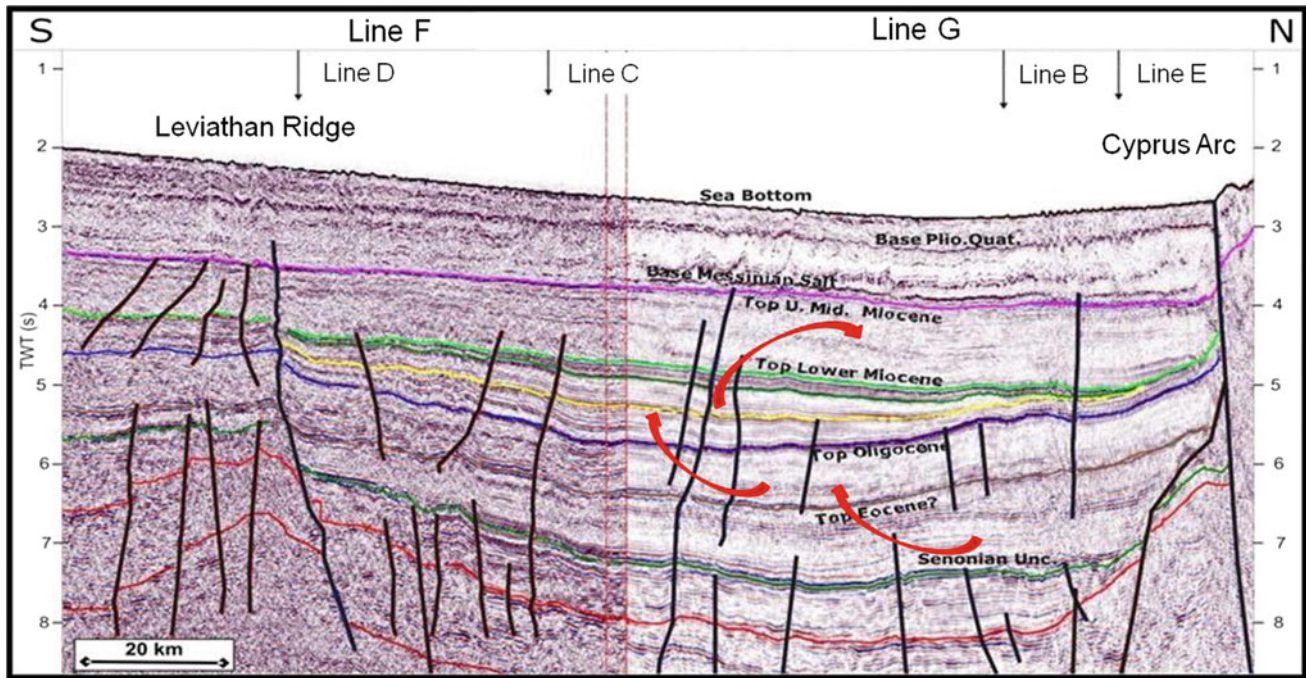
Fig. 3.27 Eastern N-S uninterpreted structural seismic linked lines F and G showing deep-seated and syn-sedimentary sub-vertical strike slip normal and reverse faults, Oligocene and Miocene unconformities, southern and northern lateral axis subsidence migration and inversions (red arrows)

western side of the basin whereas eastern border played as high zone till Oligocene with pinch outs in Miocene.

3.11.14 Seismic Sequence Stratigraphy

3.11.14.1 Oligocene

Early Oligocene horizons overlay Top Eocene ones by a strong erosive and angular unconformity in toplap which is well documented in the southern border of the basin (Fig. 3.28).

Oligocene horizons are subdivided to 5 third order seismic sequences (OL1 to OL5) limited at the base by downlap terminations and to the top by toplap and onlaps towards the slope border flanks of the basin (Fig. 3.28).

Sequences show progradational horizons at the base of early lowstand deposits visible on the southern flank of the basin border. External and internal patterns of these progradational horizons are sigmoid and oblique (Fig. 3.28).

Upper sequences terminate by canyons and channels configurations toplapped by toplap and onlap surfaces of transgressive and Maximum flooding surface overlain by highstand horizons.

From sequences OL1 to OL5, above the progradational patterns and laterally, occurred erosive surfaces of incised canyons of late lowstand stage infilling. These canyons are distributed along the seismic line as a storey type (Fig. 3.28).

Their internal reflection infilling horizons present complex, prograded, mounded and onlap fill types (Mitchum et al. 1977). From lower sequences to upper ones and from southern and northern positions, they exhibit North to South and South to North directions of oblique downlap reflectors.

Canyon position is also bounded by footwalls of faults (Fig. 3.28) as it is the case along E-W lines. The question is: what are the directions of these faults? If we refer to the structural map of Top Oligocene, these faults are mapped as WNW-ESE faults and could be visible in the two directions of seismic lines but with different angle of striking. Nevertheless, there are also some N-S and NE-SW faults seen in the map.

These vertical and lateral distributions of canyons from the lower sequence OL1 to OL5 show a lateral migration from the northern to southern part of the basin (Fig. 3.28). The latter indicates the sinuosity and the space-temporal evolution of the canyon progression in the basin.

The canyons width range from 3 to 10 km with major sizes of 8–10 km reaching sometimes 15 km. The average axis thickness infill is about 150–300 m (Fig. 3.28).

Seismic acoustic characters are marked by discontinuous reflectors with variable low to middle-high amplitude and low frequency. The most continuous reflectors exhibiting higher amplitudes are seen on the toplap horizons of transgressive system tracts and in some progradational reflectors (Fig. 3.28).
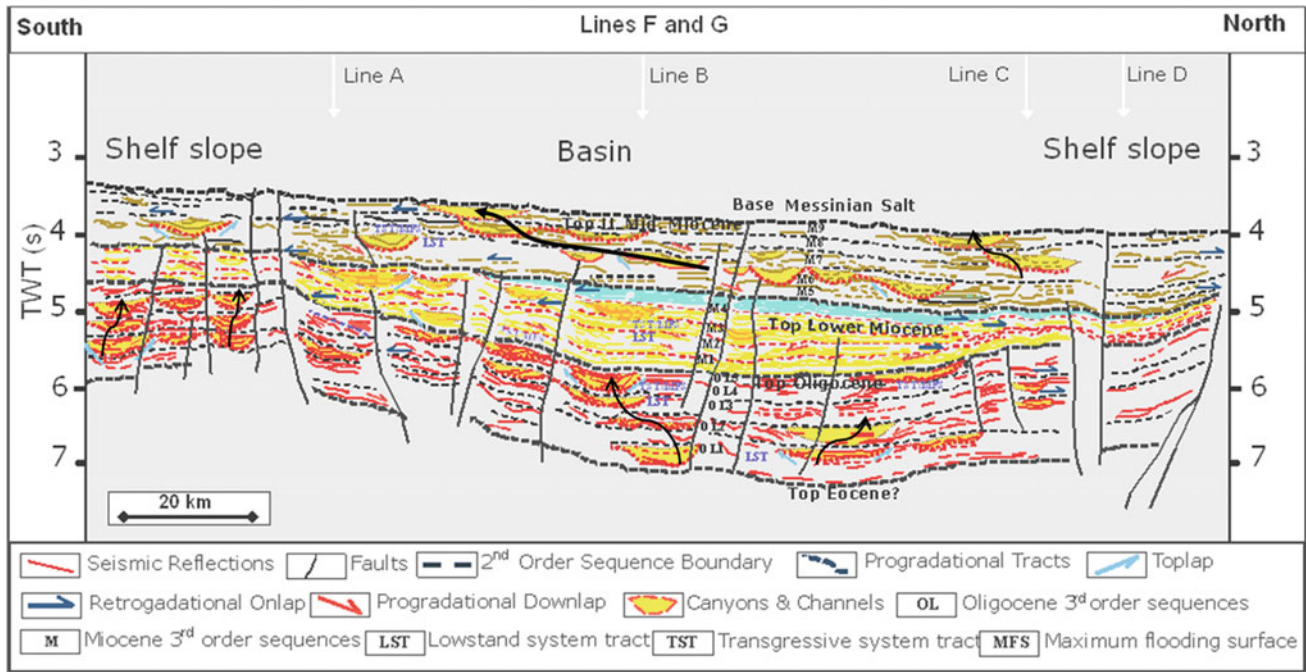
Fig. 3.28 Eastern N-S Geo-Seismic sequence stratigraphic section of lines F and G showing Oligocene and Miocene seismic horizons configurations with Lowstand prograding Downlaps, Transgressive retrograding TST/MFS and Highstand aggrading Onlap/Toplap system tracts and storey/multistory canyons and channels space lateral migrations (black arrows)

3.11.15 Lower Miocene

Seismic horizons package show thickening in the centre of the basin and strong reductions and pinch outs towards the northern Cyprus Arc folds and southern Leviathan ridge border slopes highs that are more defined than Oligocene time (Fig. 3.28).

Lower Miocene basal horizons overlay unconformably late Oligocene horizons by an angular surface of toplap. The unconformity and reduction number of horizons are consequences of an Upper Oligocene inversion event that elevate the two border slopes and subside the central part of the basin as rim syncline.

Lower Miocene horizons present the same 4 third order seismic sequences M1 to M4, limited at the base by downlap reflectors and to the top by toplap and onlap terminations (Fig. 3.28).

The base of sequences shows a progradational sigmoidal, oblique and shingled reflectors of early lowstand deposits situated on the flanks of the northern and southern basin wedges slopes and mounded and sheet configurations to the centre of the basin (Fig. 3.28).

Upper sequences of M1 to M4 present channels and storey incised canyons mainly in sequences M3 and M4 covered by toplap and onlap transgressive surfaces (Fig. 3.28).

In the central part of the seismic line, sheet and mound configurations indicate a deep sea fan deposits. Their average width is about 3 km and in axis thickness about 100–150 m.

Seismic reflectors present middle to good continuity and middle to high amplitudes. Frequency of horizons is low to high whereas more continuous and high amplitude reflectors characterize toplap limit sequence boundaries.

Basal Middle Miocene Langhian deposits (blue horizons) overlay unconformably lowstand horizons of sequence M4 representing its transgressive and highstand deposits according a progressive retrogradational onlap parallel horizons towards the northern and southern basin wedge high slopes (Fig. 3.28).

3.11.16 Middle-Upper Miocene

Middle Upper Miocene horizons show thickening towards the northern side of the basin. Horizon packages parameters contrast with Lower Miocene ones by more transparent seismic facies and appearance of incised canyons and channels (Fig. 3.28).

Third order sequence subdivisions show 5 to 7 sequences (M5 to M9) limited by toplap/onlap gradational and retrogradational horizons.

Middle to Upper Miocene Serravallian horizons of basal sequence M5 overlay Langhian reflectors of M4 sequence according the basal toplap erosive unconformity, visible on

the two slope flanks of northern and southern borders of the basin.

The base sequences present progradational horizons of sigmoid and mounded bodies (Fig. 3.28). Onlap reflectors are present on high flanks of the northern and southern slope wedges.

Top sequences of show incised channels from sequence M6 to M9. They exhibit space-lateral migration from northern to southern parts of the basin. Infilling deposits configurations inside the canyons show mainly prograded and onlap fill types.

Acoustic reflectors parameters exhibit general transparent facies, discontinuity and high frequency. The average thickness in axis is about 130–250 m whereas the width ranges from 3 to 10 km.

3.11.17 N-S Central Area Line H

3.11.17.1 Seismic Tectonics

This N-S line is running along the central part of the basin study area (Figs. 3.11 and 3.29). Oligocene and Miocene horizons are more strongly faulted and deformed than the western line H.

According to the line H, the basin is limited to the North by a slope which suggest a back higher area of Cyprus Arc folds and to the South by the Leviathan ridge. From North to South, Oligocene and Miocene horizons present thickness

variations with inversion basin structuring and migration axis subsidence between Eocene-Oligocene and Lower Miocene as well as between Lower and Middle to Upper Miocene (Fig. 3.29).

Basin block has been strongly tilted along N-S direction and northern border was uplifted by the compressional thrusting of Cyprus arc.

Deep-seated sub-vertical strike slip faults bound the northern and southern highs of the slopes as well as and intra-basinal Mesozoic and Cenozoic horizons. These faults has been reactivated in reverse movements inducing the folding of Mesozoic and Tertiary horizons (Fig. 3.29).

3.11.18 Seismic Sequence Stratigraphy

3.11.18.1 Oligocene

Despite the intensive deformations and faulting of horizons in this line, we tentatively tried to highlight the configurations and patterns of reflectors.

Early Oligocene horizons overlie Top Eocene ones by an erosive toplap unconformity (Fig. 3.30) which is well exposed in the central and southern of the basin. Under this unconformity, important incised canyon configurations are present as it was documented in the E-W and N-S previous studied lines. Thus Upper Eocene horizons exhibit important incised canyons related to the important sea level fall of late Eocene (Haq et al. 1987; Vail et al. 1991).
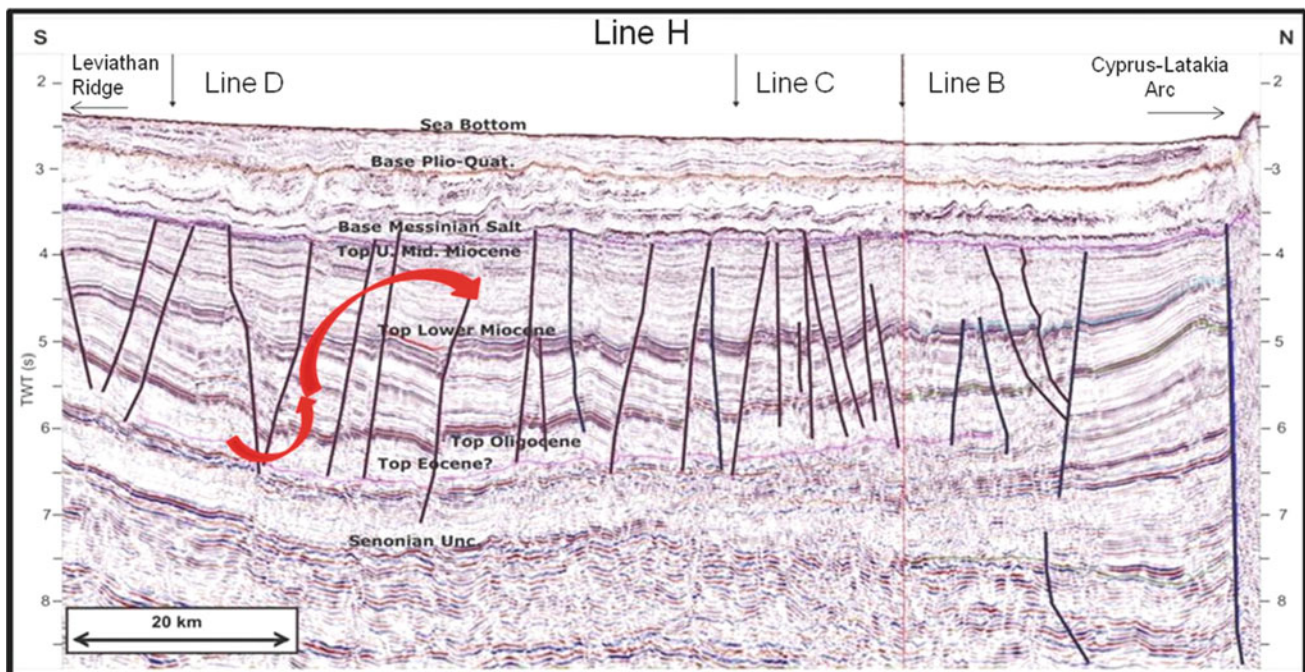
Fig. 3.29 Central N-S uninterpreted structural seismic line H showing syn-sedimentary sub-vertical normal and reverse faults, Oligocene and Miocene unconformities and northern lateral axis subsidence migration and inversion (red arrows)
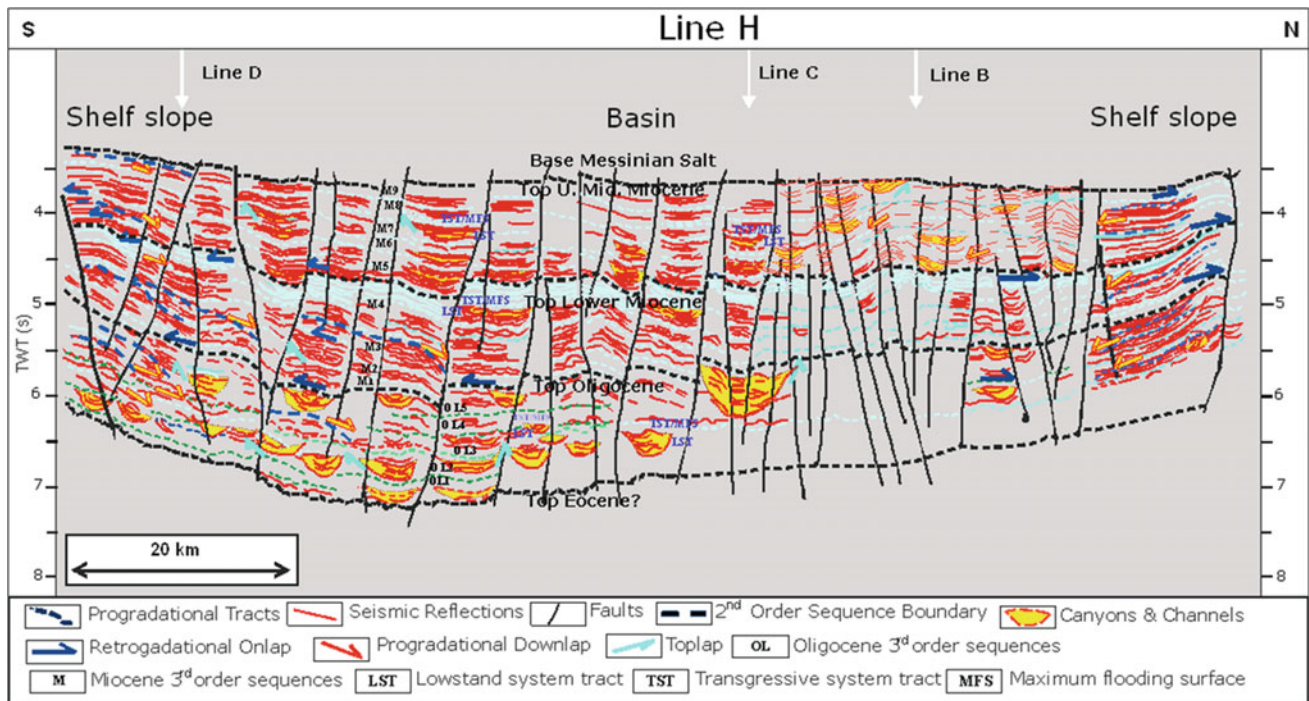
Fig. 3.30 Central N-S Geo-Seismic sequence stratigraphic section of line H showing Oligocene and Miocene seismic horizons configurations with Lowstand prograding Downlap, Transgressive retrograding TSt/MFS and Highstand aggrading Onlap/Toplap system tracts and storey canyons and channels with space lateral migrations (black arrows)

Oligocene horizons are subdivided to 5 third order Seismic Sequences (OL1 to OL5) limited at the base by downlap terminations and to the top by toplaps and onlaps towards the slope border flanks of the basin (Fig. 3.30).

Sequences show basal progradational horizons identified on the northern and southern flanks of the slope basin borders. External and internal corresponding patterns are sigmoid, oblique and mounded.

Incised canyons are distributed from sequence OL1 to OL5 along the line with importance of size and frequency from the centre to the lower southern slope of the basin.

Along this central N-S line, canyon position is also bounded by faults. The infilling horizons of the canyons show predominately onlap configurations: This is identified for the first time in comparison to the previous interpreted E-W and N-S lines. It can reflect a depositional significance in terms of infilling mechanism in distal position in the centre of the basin.

Vertical and lateral distribution of canyons from the lower sequence OL1 to upper one OL5, show a lateral migration from the centre to the southern lower slope of the basin and from the southern slope to the center of the basin (Fig. 3.30). This migration indicates the sinuosity and the space-temporal evolution of the canyon progressions.

Their width ranges from 3 to 5 km with single case in the central part of the basin that measure 10 km. The average in axis thickness infill is about 150–350 m, occasionally reaching 600 m (Fig. 3.30).

Seismic acoustic characters are greatly disturbed by faults and deformation of reflectors. Nevertheless, in general discontinuous reflectors with low to middle-high amplitude and low frequency are defined. These acoustic parameters are similar to those of the Oligocene horizons of the previous studied lines in this central area of the basin.

3.11.19 Lower Miocene

Seismic horizons show thickening in the centre of the basin and strong reduction and pinch outs towards the northern and southern border slopes (Fig. 3.30).

Lower Miocene basal horizons overlay unconformably late Oligocene horizons by a toplap angular surface. Horizons package is subdivided in 4 third order seismic sequences M1 to M4, limited at the base by downlap reflectors and to the top by toplap and onlap terminations.

The base of sequences show a progradational sigmoidal, oblique and shingled bodies located on the flanks of the northern and southern basin wedges slopes. They are thicker and more developed on the southern slope (Fig. 3.30).

Only upper sequence of M4 present channels and incised canyons toplapped by Langhian transgressive horizons.

Intensive deformations and faults do not allow to well identify these channels and canyons which should be present because they are already seen in the E-W direction on the intersection with lines C (Fig. 3.15) and D (Fig. 3.16).

In the central part of the seismic line, internal sequence horizons present continuous parallel configurations with low to middle amplitude and low frequency reflecting sheets of deep sea fan deposits in the central part of the basin. They are extended along the entire basin floor. Toplap seismic reflectors of sequence boundaries show good continuity and high amplitudes.

Basal Middle Miocene (blue horizons) overlies unconformably M4 lowstand reflectors and channels according to the same progressive retrogradational onlap parallel horizons towards the northern and southern basin wedge high slopes (Fig. 3.30).

3.11.20   Middle-Upper Miocene

Middle Upper Miocene horizons exhibit general transparent seismic facies than Lower Miocene. Incised canyons and channels are present (Fig. 3.30).

Third order sequence subdivisions show 5 to 7 sequences (M5 to M9) limited by toplap/onlap gradational and retrogradational horizons.

Middle to Upper Miocene Serravallian horizons of basal sequence M5 overlay langhian reflectors of M4 sequence according to the basal toplap erosive unconformity (Fig. 3.30). Above this surface, onlap terminations are well identified on the two high borders slopes.

Downlap terminations are detected at the base of sequences, corresponding to the progradational system tracts of the sequence M5. The latter shows sigmoid and mounded reflection patterns.

The summit of sequences show incised channels and canyons infill. They exhibit space-lateral migration to northern and southern parts of the basin (Fig. 3.30).

Infilling deposit configurations are of prograded and onlap fill types. The average thickness in axis is about 200–350 m, the width ranges from 2 to 5 km.

Acoustic reflectors parameters exhibit general transparent facies and high frequency in contrast to the underlined Lower Miocene horizons. They are more continuous on the flanks of slope borders and more discontinuous to the centre of the basin.

3.11.21   N-S Eastern Area Line I

3.11.21.1   Seismic Tectonics

This N-S line I is located to the eastern side of the study area (Figs. 3.11 and 3.31). The block basin is limited to the North by a high where Oligocene and Miocene horizon packages present thickness reductions and pinch outs. To the Southern border of the basin, this reduction is more accentuated due to the high angle slope ridge of southeastern continental shelf.

As in the previous N-S presented lines, tectonic inversion affected the basin between Eocene-Oligocene and Lower Miocene as well as between Lower and Middle to Upper Miocene (Fig. 3.31). Basin block has been strongly tilted along N-S direction and northern border was uplifted by the compressional thrusting.

Tectonic deformations affect intensively Tertiary horizons. Deep-seated sub-vertical faults bound the northern and southern highs of the slopes as well as central-basin Mesozoic and Cenozoic horizons. The border faults represent the rifting ancient normal faults of Triassic-Jurassic, removed in compressional movements inducing the folding of Mesozoic and Tertiary horizons in the borders and inside the basin (Fig. 3.31).

3.11.22   Seismic Sequence Stratigraphy

3.11.22.1   Oligocene

Early Oligocene horizons overlay Top Eocene ones by a strong erosive toplap unconformity (Fig. 3.32) which shows important multistory incised canyons configurations, particularly to the southern high slope of the basin which corresponds to the continental shelf of southeastern coastal margin of Syrian Arc.

To the southern high ridge of the basin, Upper Eocene horizons show progradation features towards the basin slope overlain by important incised canyons probably corresponding to Upper Eocene clastic deep marine deposits as it was highlighted in the E-W and N-S lines (Fig. 3.32).

Oligocene horizons are subdivided into 5 third order Seismic Sequences (OL1 to OL5) limited at the base by downlap terminations and to the top by toplaps and onlaps towards the slope border flanks (Fig. 3.32).

Sequences show basal progradational horizons identified on the southern flank of the slope basin border exhibiting external and internal patterns of sigmoid, oblique and some mounded configurations.

Incised canyons are distributed from sequence OL1 to OL5 from the centre to the southern and northern slope of the basin (Fig. 3.32). Along this central N-S line, canyon positions are also bounded by faults. The infilling horizons of the canyons show complex, prograded and chaotic types.

Vertical and lateral distributions of canyons from the lower sequence OL1 to upper sequence OL5 show a stacked and storey types with lateral migration from the centre to the northern and to the southern lower slope basin. The canyons' width ranges from 2 to 10 km and the average in axis thickness is about 100–300 m.
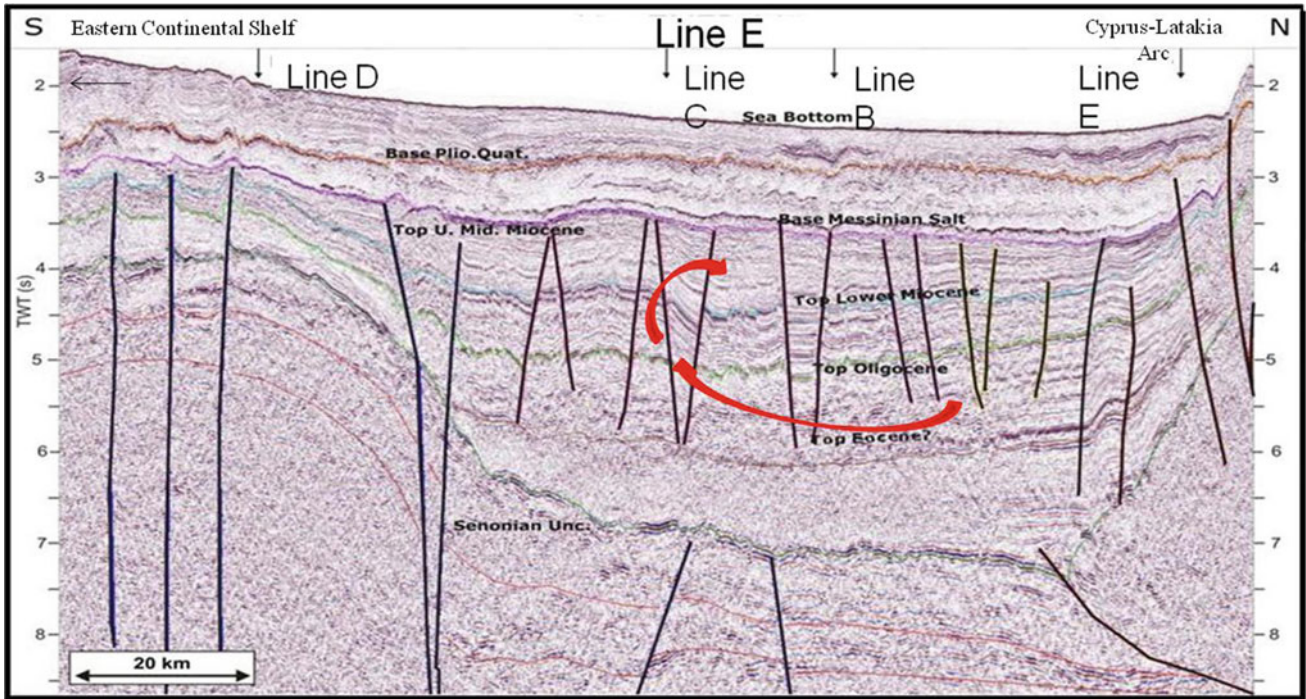
Fig. 3.31 Eastern N-S uninterpreted structural seismic line I showing deep-seated and syn-sedimentary sub-vertical strike slip normal and reverse faults, Oligocene and Miocene unconformities, southern and northern lateral axis subsidence migration and inversion (red arrows)
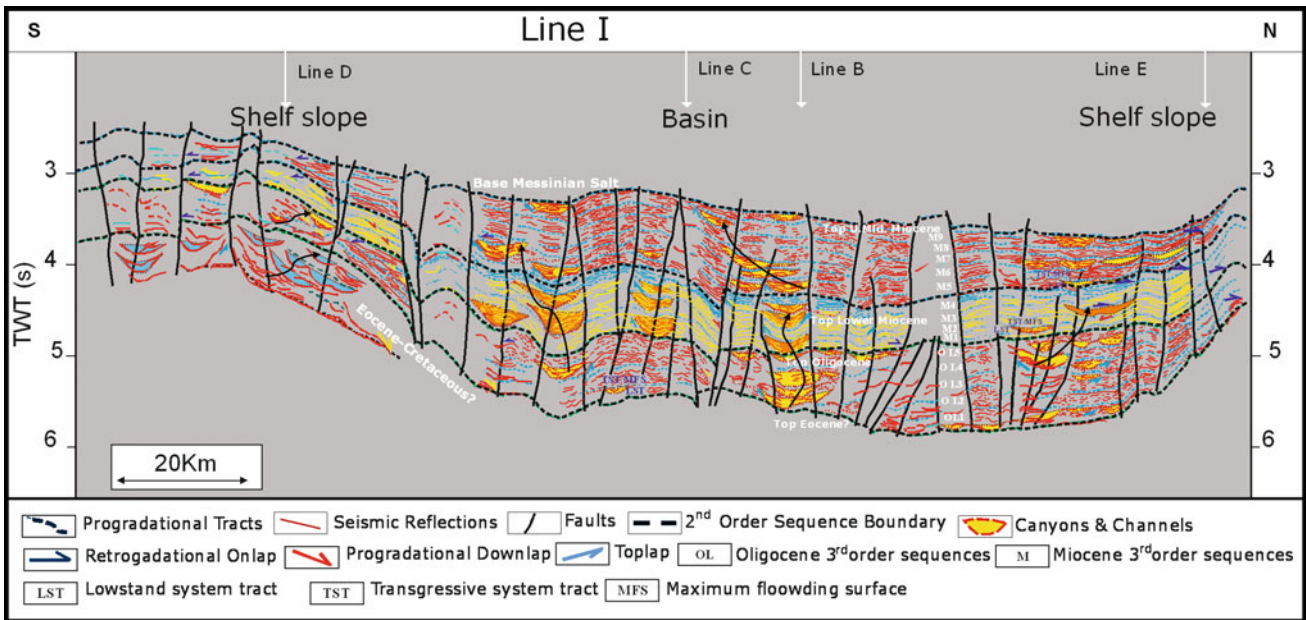
Fig. 3.32 Eastern N-S Geo-Seismic sequence stratigraphic section of Line I showing Eocene, Oligocene and Miocene seismic horizons configurations with Lowstand prograding Downlap, Transgressive retrograding TST/MFS and Highstand aggrading Onlap/Toplap system tracts and storey canyons and channels with space lateral migrations (black arrows)

Despite the intensive tectonics of the area, we succeed to identify general discontinuous reflectors with low to middle variable amplitude and low frequency.

3.11.23 Lower Miocene

Seismic horizons are strongly folded and fractured, they show thickening in the centre of the basin and reductions and pinch outs towards the northern and southern border slopes (Fig. 3.32).

Lower Miocene basal horizons overlay unconformably late Oligocene horizons by an angular surface. They are subdivided in 4 third order seismic sequences M1 to M4, limited at the base by dowlap reflectors and to the top by toplap and onlap terminations (Fig. 3.32).

The base of sequences shows a progradational sigmoidal and oblique patterns situated on the flanks of the northern and southern basin wedges slopes. Patterns are thicker and more developed on the southern lower slope.

Internal sequence horizons present middle continuous configurations with middle to high amplitude and low frequency.

Upper horizons of sequences M1 to M4 present incised channels and stacked and story canyons toplapped by transgressive horizons (Fig. 3.32). They are distributed as well as in the northern and southern low slopes. Their infilling reflectors are from complex type. Their width range from 3 to 10 km whereas the average in axis thickness infill is about 100–300 m.

Seismic horizons are strongly folded and fractured, they show thickening in the centre of the basin and reductions and pinch outs towards the northern and southern border slopes (Fig. 3.32).

3.11.24 Middle-Upper Miocene

Middle-Upper Miocene horizons are subdivided in 5 to 7 third order sequences (M5 to M9); limited by toplap/onlap gradational and retrogradational horizons (Fig. 3.32).

Downlap progradations are located on the flanks of the southern and northern slope basin. They exhibit sigmoid and mounded bodies. Upper sequences show incised channels and storey canyons infill and are distributed according a space-lateral migration. Infilling deposit configurations inside the canyon present onlap and downlap reflectors. The average thickness in axis is about 100–200 m, the width ranges from 2 to 8 km.

Acoustic reflector's parameters exhibit general transparent facies and high frequency in contrast to the underlained Lower Miocene horizons. They are more continuous on the flanks of slope borders and more discontinuous to the centre of the basin. Sequence boundary horizons are more continuous and of higher amplitude.

3.11.25 Seismic Sequence Boundaries— Global-Eustatic Cycle Calibration

As sequence boundary surfaces and systems tracts are controlled by eustatic sea level variations rather than tectonic subsidence for accommodation space of deposits and climate. The previous highlights of sequence deposits limits and lowstand and highstand configurations will permit the comparison and the matching of second and third order sequence boundaries of Oligo-Miocene series of northern Levant basin study area to eustatic global chart (Haq et al. 1987, 1988; Vail et al. 1991).

The purpose and interest is to verify and improve the seismic sequence subdivisions and system tract for characterization and date lowstand reservoir levels. Despite no petroleum well is available in the study area, our seismic horizon calibration from southern Levant basin (Fig. 3.13) had permitted to frame the bases and tops of Oligocene and Miocene packages between Top Eocene, Top Oligocene and Base Messinian. This allows to calibrate the sequence boundaries remarkable surfaces and low and highstand system tracts of second and third order of Oligocene, Lower Miocene and Middle and Upper Miocene to second and third order eustatic global sea level cycle surfaces.

After the identification of third order sequence boundaries and system tracts of Oligocene and Miocene horizons around the northern Levant basin, correlation with second and third eustatic cycles is proposed.

As all the shelf slope borders of the basin present lowstand and highstand systems tracts, we selected for the correlation, a clear seismic sequence subdivisions and systems tracts in the northern shelf slope flank border of Cyprus Arc where coastal onlaps and lowstand horizons are well identified in the N-S lines F and G (Figs. 3.27 and 3.28).

After Haq et al. (1987) cycle dates of second order sequence boundaries of Oligocene and Miocene correspond probably to chronostratigraphic line of 36 MY for Early Oligocene, 25 MY for base Early Miocene, 15,5 MY for Base Middle-Upper Miocene and 6,3 MY for base Messinian salt (Fig. 3.33).
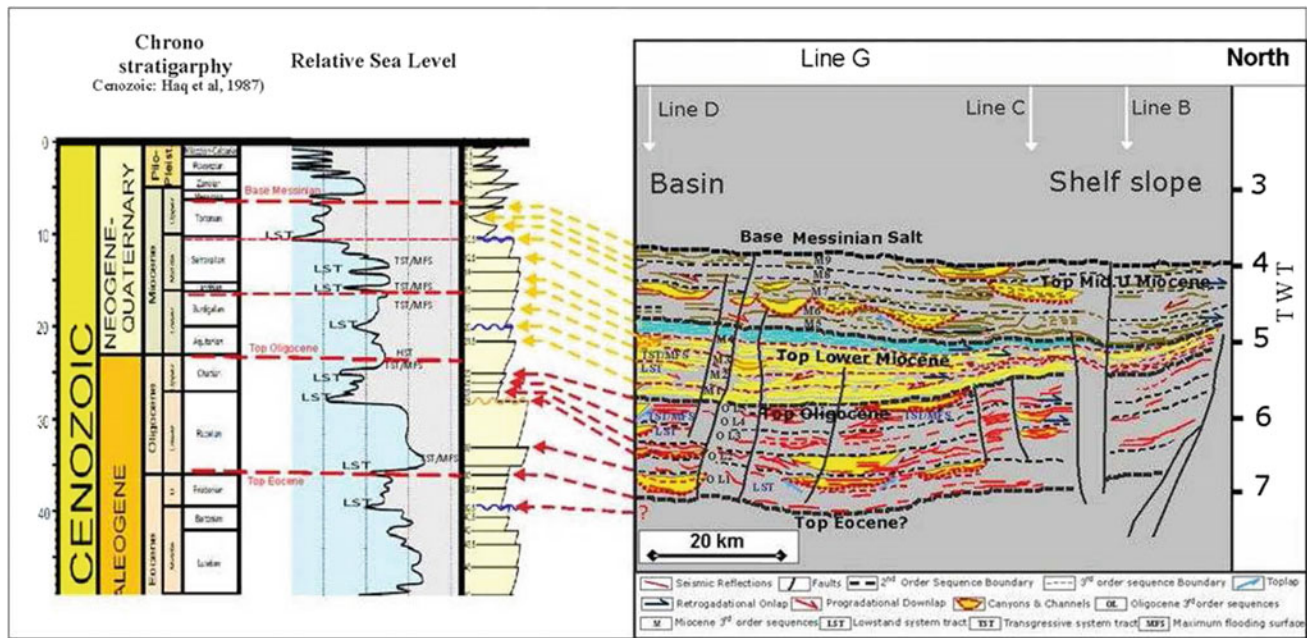
Fig. 3.33 Identified Oligo-Miocene seismic sequence boundaries—global eustatic sea level cycles correlations

Oligocene third order sequence boundaries of OL1 to OL5 are calibrated at the base by the Top Eocene-Early Oligocene second order erosive unconformity of 39,5 Millions years (Fig. 3.33).

Oligocene sequence boundaries are calibrated to eustatic global cycle chart as below:

- OL1: Early Rupelian (36-33 Million years)
- OL2: Middle-Upper Rupelian (33-30 MY)
- OL3: Late Rupelian-Early Chattian (30-28,4 MY)
- OL4: Early Chattian (28,4-26,5 MY)
- OL5: Middle Chattian (26,5-25,5 MY)

Lower Miocene sequence boundaries are calibrated as follow:

- M1: Late Chattian-Middle Aquitanian (25-21,5 MY)
- M2: Late Aquitanian (21,5-20 MY)
- M3: Late to Middle Burdigalian (20-18 MY)
- M4: Late Burdigalian-Langhian (18-15,5 MY)

Middle-Upper Miocene sequence boundaries from Top Langhian to Base Messinian are correlated to eustatic global chart as:

- M5: Early Serravallian (15,5-14 MY)
- M6: Middle Serravallian (14-12,5 MY)
- M7: Late Serravallian (12,5-10,5)
- M8: Early Tortonian (10,5-8,2 MY)
- M9: Late Tortonian (8,2-6;3 MY)

This proposed second and third order sequence boundaries correlation with chronostratigraphic eustatic sea level global chart from basin to coastal onlap scale and levels seem to be matching with the remarkable unconformity surfaces and seismic reflection configuration system tracts of Oligocene and Miocene horizons in the study area.

These sequences are similar and equivalent to those that had been highlighted in the central Mediterranean North African onshore and offshore margin (Bédir et al. 1996; Houatmia et al. 2015; Bédir et al. 2016)

3.11.26 Results and Discussions

3.11.26.1 Tectono-Sedimentary and Reservoir Distribution Modelling

According the mapping of the interpreted lowstand depositional systems, siliciclastic reservoir system tracts present three Oligo-Miocene superposed systems from shelf domain to the basin floor one. They can be divided to three domains limited by deep seated faults.

3.11.26.2 Oligocene

After previous seismic stratigraphic analyses along E-W and N-S lines of Oligocene horizons around the study area and geologic data from outcrops and petroleum wells of the region, depositional system seems to be marked by progradational slope fan to deep sea fan lobe turbidites with incised channels and canyons.

System tract and paleogeographic synthetic mapping of third order Oligocene sequences OL1, OL2, OL3, OL4 and OL5 highlights a distribution of Oligocene early and late lowstand progradational slope fans from eastern, western and northern shelf edges of the basin and southern ridges and deep sea fan basin floor lobes (Fig. 3.34).

Lowstand incised canyons with levee overbank channels follow to the progradational slope fans and lobes through a strong erosive incision surfaces that cut the previous early system tracts and often the highstand horizons of lower sequences. They are distributed from eastern, western, northern and southern slopes basin borders to the central basin area. They present stacked, storey and multistorey canyons.

Space–temporal migrations of canyons are documented along E-W and N-S directions. Foot walls of deep-seated WNW-ESE faults in the central basin, NE-SW ones in the eastern and western shelf borders and some N-S faults to the northern area of the basin constitute a privileged pathways for the channels and canyons locations. This figure is well recorded in the continental shelf margin of Lebanon and Palestine (Fig. 3.35), where present day canyons follow NW-SE (Carmel fault) and Messinian salt NE-SW Tyre Rosh Hniqra fault (Ben-Avraham and Hall 1977; Carton et al. 2009).

Proximal positions of the canyons are located along the upper slope domain characterized by complex, prograded and some chaotic infill, whereas distal canyons are distributed from lower slope to the central basin marked by onlap infilling (Fig. 3.35). This distribution can be verified by their size. All the integrated seismic parameters and regional data conduct to define depositional environments of variable middle to high hydrodynamic energy.

The seismic stratigraphic and seismic tectonic data indicates that we are in presence of mainly forced fall lowstand scenario due to the great sea level fall of early Rupelian and Chattian periods conjugated to the Eocene compressional event that accentuated the reliefs and therefore the erosion through the folds of Syrian Palmyrides and Cyprus Arcs.

Related Sedimentary facies and environments are mostly clastic deep water fan deposits and turbidites composed by
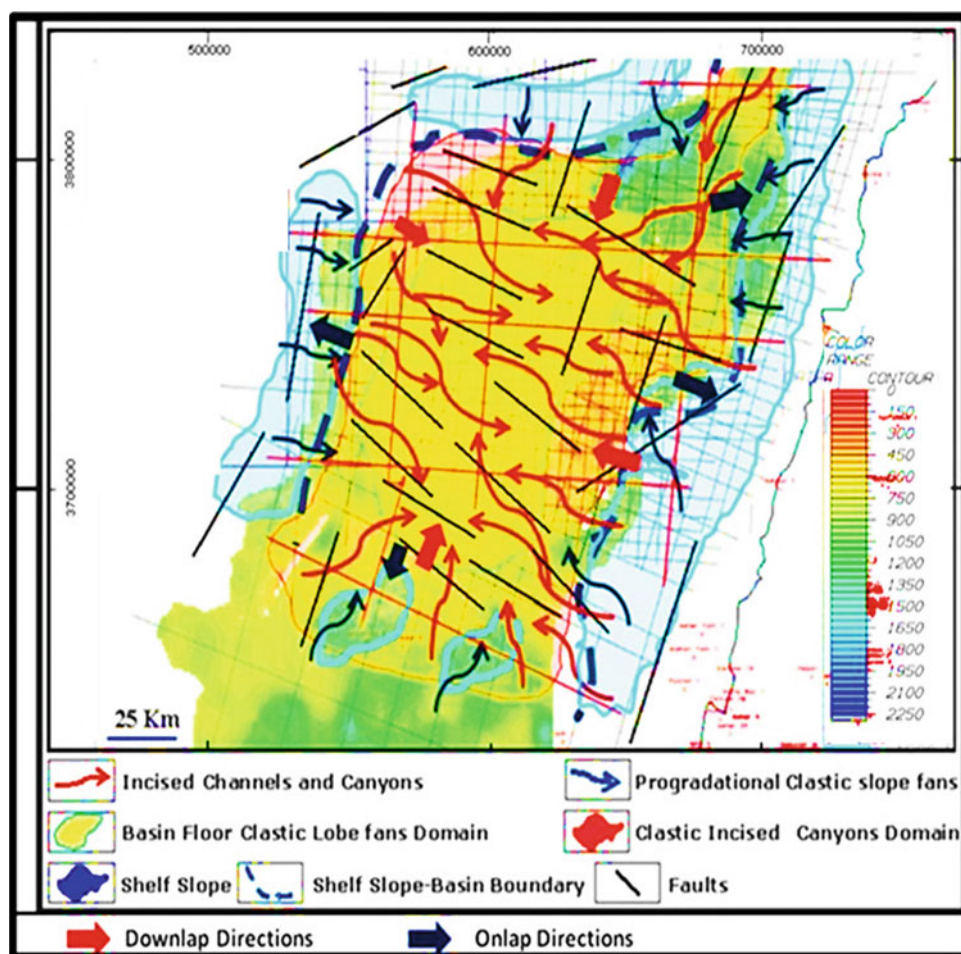
Fig. 3.34 Oligocene Early and Late clastic Lowstand depositional system tracts on time map
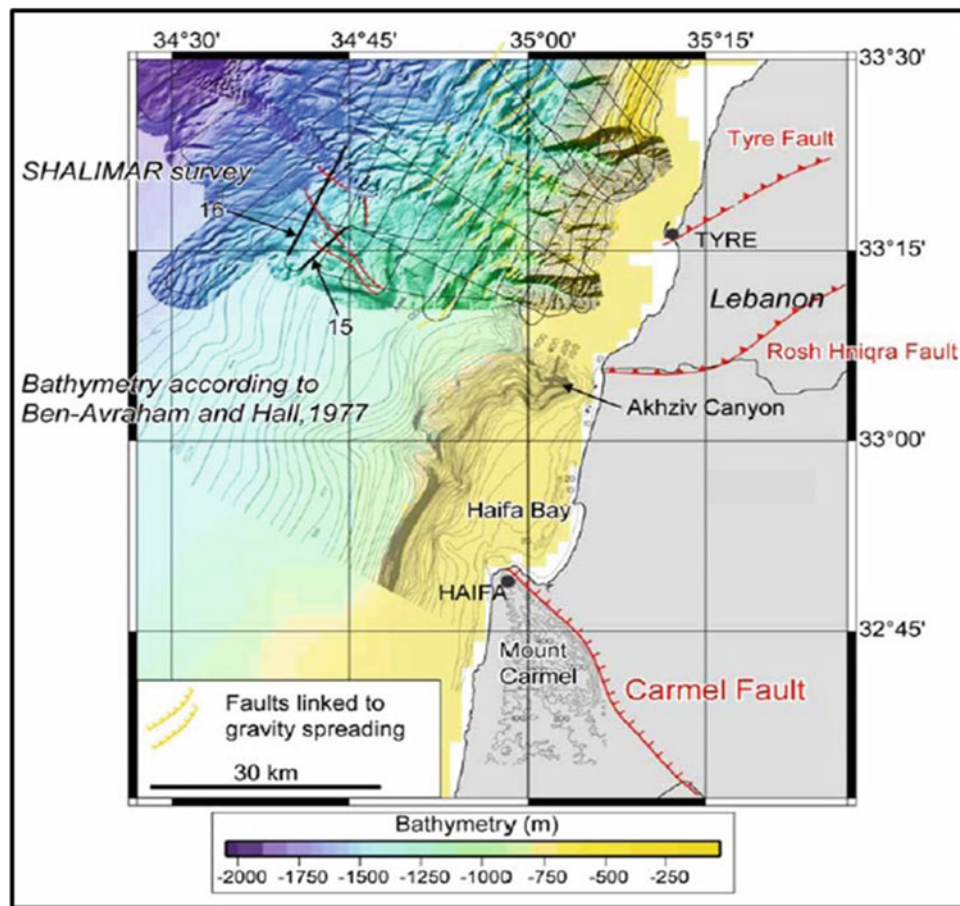
Fig. 3.35 Bathymetric map of Eastern shelf coast of Levant basin showing trace of NW trending Carmel fault on land (in red line), as well as subparallel normal fault scarps. Faults related to gravity spreading (salt tectonics) mapped in southern Lebanese offshore area are marked in yellow. Other active faults are in red lines. After Ben-Avraham and Hall (1977) and Carton et al. (2009), modified

siltstones, sandstones, conglomerates, slumps, debris flows and mass flows intercalated by pelagic and hemipelagic mudstones as it was documented in drilled canyons in the eastern offshore coastline (Gardosh et al. 2008) and in outcrops.

Synthetic depositional model lowstand map of progradational and incised canyons system tracts from multi-source continental feeders (Fig. 3.35) seems to highlights principal eastern, southeastern and northeastern sediment supply origin along the continental shelf from Egypt and Leviathan high to the south to Syria and Turkey to the North. This proposed model is supported by presented previous geotectonic setting and depositional environment and stratigraphic data from outcrop and wells.

3.11.26.3 Lower Miocene

Two depositional distribution system tract maps have been established for each lowstand deposits; one for early lowstand and another for late lowstand synthetised in Figs. 3.36 and 3.37.

Lower Miocene depositional sedimentary environment show more lateral extension of progradational slope margin areas around the Levant basin. Early lowstand systems tracts of the four sequences M1, M2, M3 and M4 present upper to lower slope progradational submarine fans and deep sea basin floor lobes and sheets extending to the central basin floor area.

Upper sequences depositional late lowstand tracts are represented by incised channels and canyons infill, smaller and less frequent than those of Oligocene. They are developed preferentially in proximal areas near the margin borders whereas they are less frequent in the central basin area in contrary of Oligocene canyons that are more developed and extended from the upper slope to the central basin area.

These canyons present a single storey type in the central basin and stacked type along N-S eastern line I and southern and northern E-W lines (A and E) near the continental margins (Figs. 3.36 and 3.37).

Lower Miocene canyons are guided by the same deep seated faults affecting the Oligocene horizons as mapped on
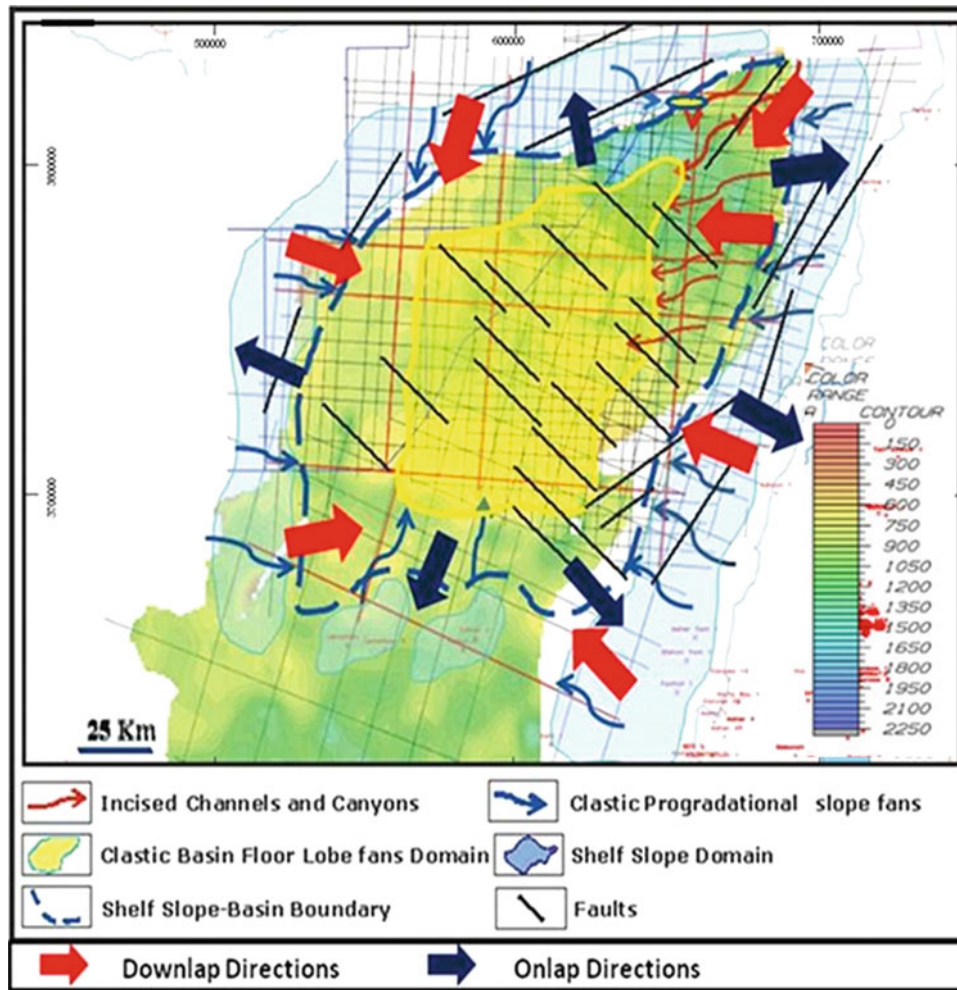
Fig. 3.36 Lower Miocene Early Lowstand depositional clastic system tracts on time structural map
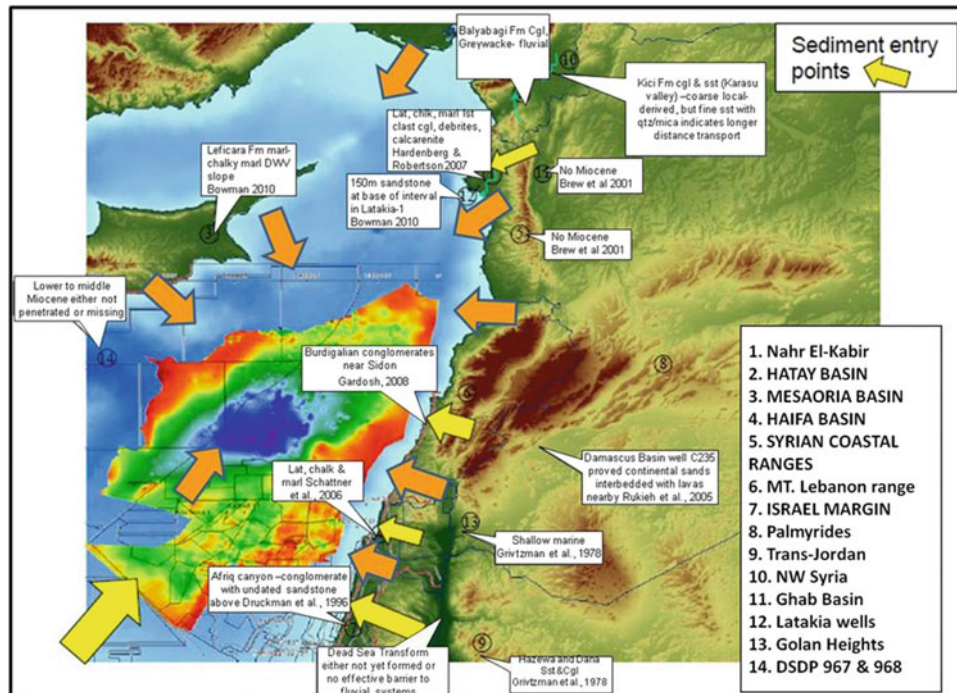
Fig. 3.37 Lower Miocene depositional clastic Late Lowstand system tracts on time structural map

Top structural map of Lower Miocene. They are in general of storey stacked and locally to the northern basin border multistorey types. They exhibit complex, prograded, onlap and chaotic infill.

Sedimentary related facies and environments may be clastic slope fans and deep sea fan deposits of turbidites composed by siltstones, sandstones, debris flows, mass flows and mudflows. The grain size material should be finer than the Oligocene rocks because we are preferentially in normal lowstand stage unless for Tortonian sequences M7 and M8 that could be from forced fall regression.

These maps highlight similarities and changes in comparison to the Oligocene one. Progradational and basin floor deposits are distributed around the same high edge borders of the basin with accentuation of prograding deposits that migrate and expand towards the central area of the basin (Figs. 3.36 and 3.37).

Incised channels and canyons are present in different locations near eastern, northern, western and southern sides of the basin. This is due probably to the erosional supply deficiency according to the Oligocene situation, caused by more or less continental reliefs and erosions and sea level rise after the great Oligocene forced fall period (Fig. 3.33).

To the central basin area, depositional system seems to range from progradational slope fan to deep sea fan lobe turbidites and rare incised distal channels and canyons. Even though, it could change towards the upper slope and shelf to marly and carbonated deposits as it is documented in coastal wells and interior outcrops along the eastern continental margin.

Reconstructed sedimentologic and stratigraphic depositional model from Lebanon outcrops (Hawie 2013) present similar continental shelf to basin floor depositional and system tracts model as presented here by seismic stratigraphic.

Lower Miocene sandstone material sources and feeders reconstructed from outcrops and petroleum wells data (Gardosh et al. 2008; Hawie 2013; Plummer et al. 2013) had been presented as from southern Nile delta, northern and eastern continental coastal provenance (Fig. 3.38).

In our study, we highlighted a western and northwestern Oligocene and Miocene source feeder from the Cyprus-Lattakia arc high for the first time in the northern Levant basin.

3.11.27 Middle-Upper Miocene

Middle-Upper Miocene sequence systems tracts have been divided into two maps of early stage lowstand and late lowstand distributions.

Early lowstand system tracts are characterized by progradational slope deposits along the shelf slope margin borders of the basin. They present general expansion towards the basin (Fig. 3.39). Submarine slope fans deposits of debris flow and turbidites could constitute these system tracts. Deep sea basin floor lobes fans and sheets occupy the central part of the basin as it was highlighted by seismic line's amplitude analysis in the same basin (Hawie 2013).

This model join the paleogeographic framework of Upper Miocene deposits reconstructed along the Lebanon eastern border outcrops which present a continent, shelf, slope and basin floor profile system tracts (Hawie 2013).

Late lowstand system tracts of incised channels and canyons infill become more frequent and developed than the Lower Miocene ones. They are distributed along the margin slope basin and extended to the central part of the basin (Fig. 3.39). The latter is due to the sea level progressive fall since the Serravallian to Tortonian times (Fig. 3.33), which induced important erosions of the continental outcrops and improved supply material for the slope and the basin accommodation.

These data seem to correspond to a forced fall lowstand type and thus they are near the Oligocene situation particularly for Tortonian deposits.

The synthesis of Oligocene and Miocene depositional lowstand systems tracts around the study area of northern Levant basin (Fig. 3.40) highlights three main superposed and shifted domains of reservoir systems related to the Upper slope, lower slope and basin floor zones.

3.12 Conclusions

Seismic stratigraphic study of Oligo-Miocene horizons of the northern Levant basin based on the analysis of eight selected E-W and N-S selected lines, lithostratigraphic outcrops analogues and wells data highlights the basin configuration around the study area.

Oligo-Miocene horizons are generally thicken in the central subsiding area of the basin with subsidence migrations along borders and thinner towards eastern, western, northern and southern slope flanks with angular discontinuities and pinch outs of Lower Miocene horizons, indicating more uplifted and resistant domains during this time.

Basin borders are bounded by NE-SW and N-S deep-seated sub vertical strike slip normal and reverse faults and NW-SE ones in the central basin. These faults are inherited from the Mesozoic rifting stage and reactivated during Tertiary compressive orogeny events inducing the formation of surrounding Syrian and Cyprus Arcs fold belts and folding of the Oligo-Miocene section in the basin. These movements had induced basin inversions and subsidence lateral migrations between Eocene-Oligocene and
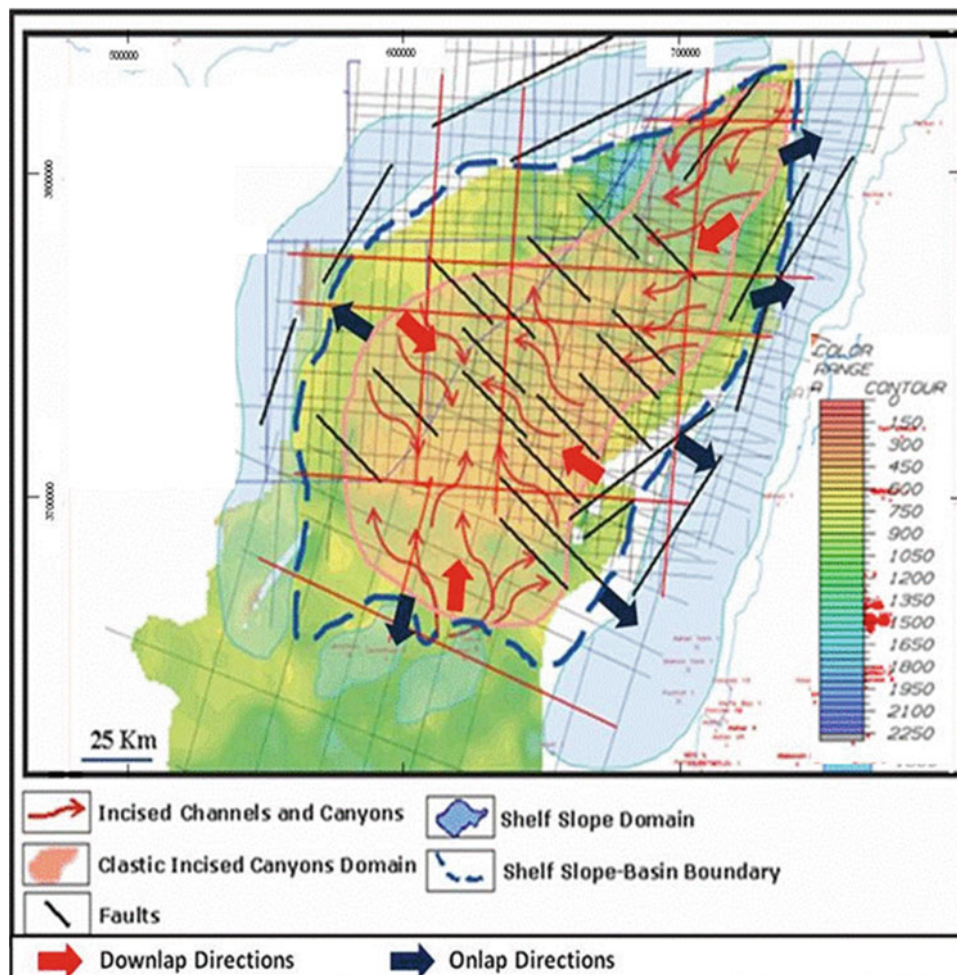
Fig. 3.38 Lower Miocene reservoir provenance from surrounding outcrops of Northern Levant basin (yellow arrows) from Plummer et al. (2013), modified by adding subsurface reconstructed provenance from present seismic analysis of this work (orange arrows)

Lower-Middle-Upper Miocene horizons according west to east and south to north directions.

Tectonic events and deformations from Mesozoic heritage to Neogene played an important role for the basin configuration and subsidence migrations on the system deposits distribution between slopes and basin, in addition to the eustatic sea level control.

Oligo-Miocene infilling of the basin show 3 s order and 5 Oligocene, 4 Lower Miocene, and 5 to 7 Middle-Upper Miocene third order seismic sequences, limited by regional erosive unconformity surfaces and by remarkable chronostratigraphic surfaces of alternated forced and normal erosive lowstand and highstand systems tracts separated by transgressive and maximum flooding surfaces correlabal to the global eustatic sea level cycles.

The sequence boundary and LST, TST/MFS and HST surface horizons and their systems tracts has been tentatively correlated to the global eustatic cycle chart which permitted to define the second and third order sequence age.

Early Lowstand seismic reflectors characteristics highlight a downlap prograding sigmoid, oblique shingled and mounded slope fans configurations and basin floor mounds and sheets large turbidites lobes, overlain and cut by late lowstand incised channels, canyons and levees infill. Horizontal toplap and onlap transgressive horizons and maximum flooding surface cover lowstand horizons and are extended from the central basin to the upper slope edges.

According the basin configuration of Oligocene and Miocene lowstand systems tracts distribution, principal source feeders seems to be from eastern, northeastern continental shelf slopes, in addition to southern and new highlighted western areas.

The three age sequence systems tracts present superposed and shifted progradational shelf, slope and basin fan deposits reservoirs with space lateral migrations along E-W and N-S directions of storey to multistory channels and canyons.

Incised Canyons and channels pathways seem to follow NE-SW and N-S footwall faults of shelf slope and central
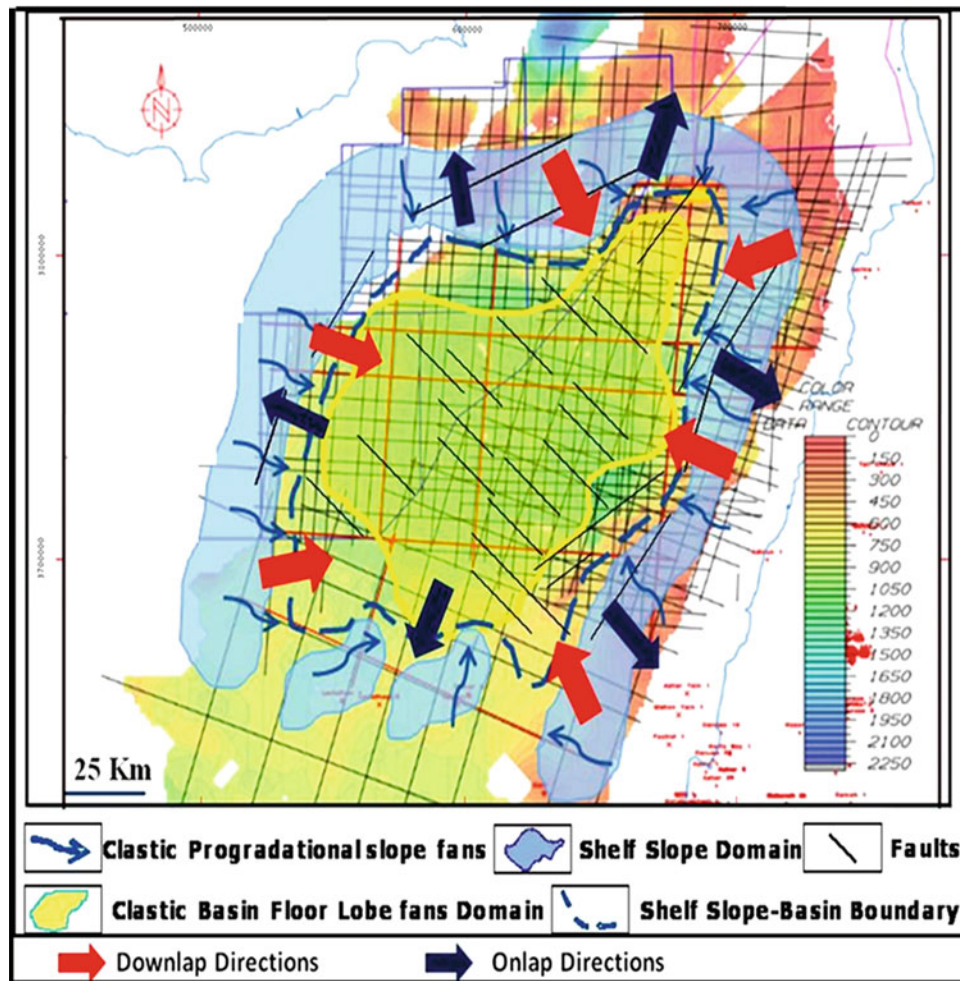
Fig. 3.39 Middle-Upper Miocene Early Lowstand depositional clastic system tracts on time structural map

basin NW-SE ones. Canyons and channels migrations indicates their important sinuous pathways geometries that seem to be obliquely directed to E-W and N-S seismic lines which is an additional argument for the WNW-ESE to NW-SE and NE-SW fault conduit role.

The infilling of channels and canyons is marked by complex, prograded, chaotic and onlap deposits indicating low to high hydrodynamic energy of the cut- fill-built and spill mechanisms that could be an argument to differentiate proximal to distal position from Oligocene to Middle-Upper Miocene.

The size of channels and canyons of Oligocene ranges from 3 to 5, 10 and 15 km width with an average thickness between 100 and 350 m, sometimes reaching 1500 m whereas size of channels and canyons of Miocene ranges from 3 to 10 km width and 100–300 m infill thickness. Locally, near proximal feeders to the northeastern Turkish shelf of the basin, canyons are bigger and stacked as multistory extending from Oligocene to Lower Miocene showing in axis infill from 500 to 800 m. Lower Miocene

deep-sea mound lobes can reach 3 km width and 100–150 m in axis thickness.

Highlighted Oligo-Miocene reservoir depositional environment distribution of horizontal and vertical succession framework and tectonic structuring allow to have a variety of Hydrocarbon stratigraphic and structural traps as it was proven by several gas and oil fields discoveries in the southern Levant basin and Cyprus offshore. Structural traps are assured by folds and normal and reverse faults closures whereas stratigraphic ones present several traps of onlap/toplap transgressive sandstone and marl pinch outs, unconformity surfaces, downlap slope fan sandstone channels, lobes, sheets and mound deep sea fan turbidites reservoirs closures. Oligocene and Miocene petroleum system is charged by Mesozoic thermogenic source rocks and also Oligo-Miocene biogenic ones and sealed by the Messinian evaporites. Based on seismic tectonic reconstructions, deep-seated Faults represent the main hydrocarbon migrations pathways (Fig. 3.41).

Fig. 3.40 Middle-Upper Miocene Late Lowstand depositional clastic system tracts on structural time map
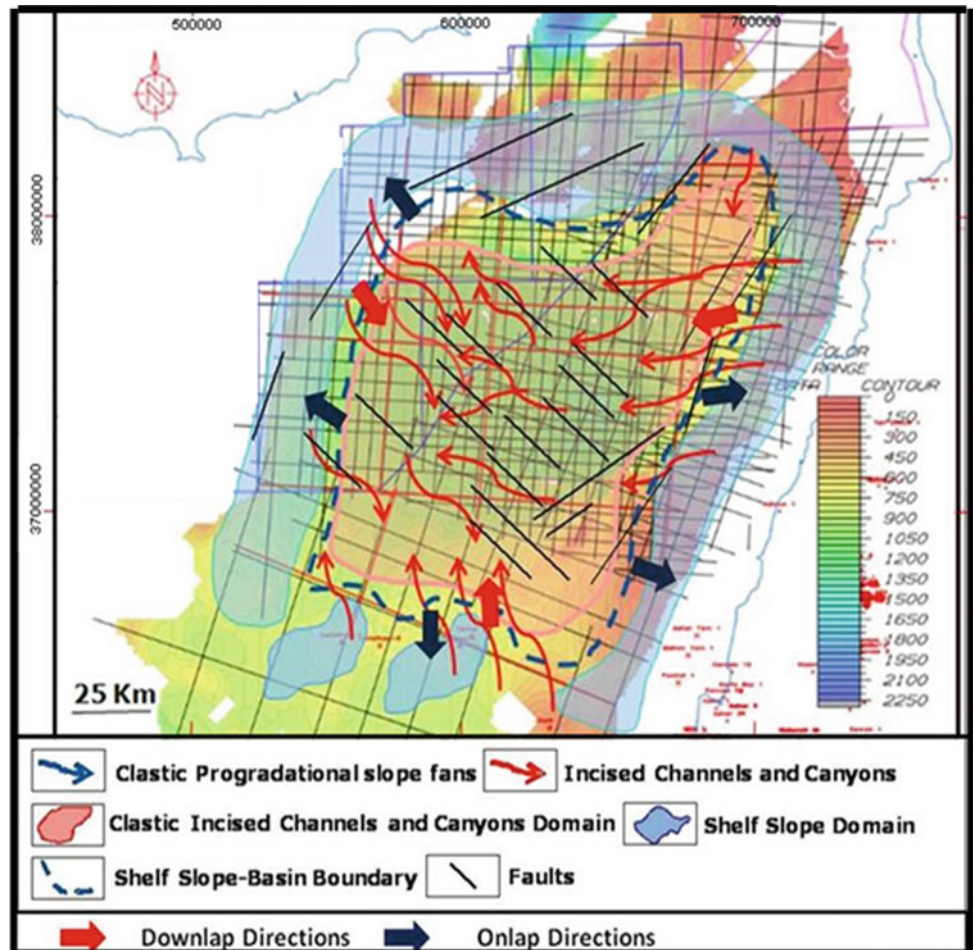
Fig. 3.41 Reconstructed synthetic reservoir fair map of the study area showing the main Oligocene and Miocene Lowstand potential clastic reservoir system paleogeographic domains
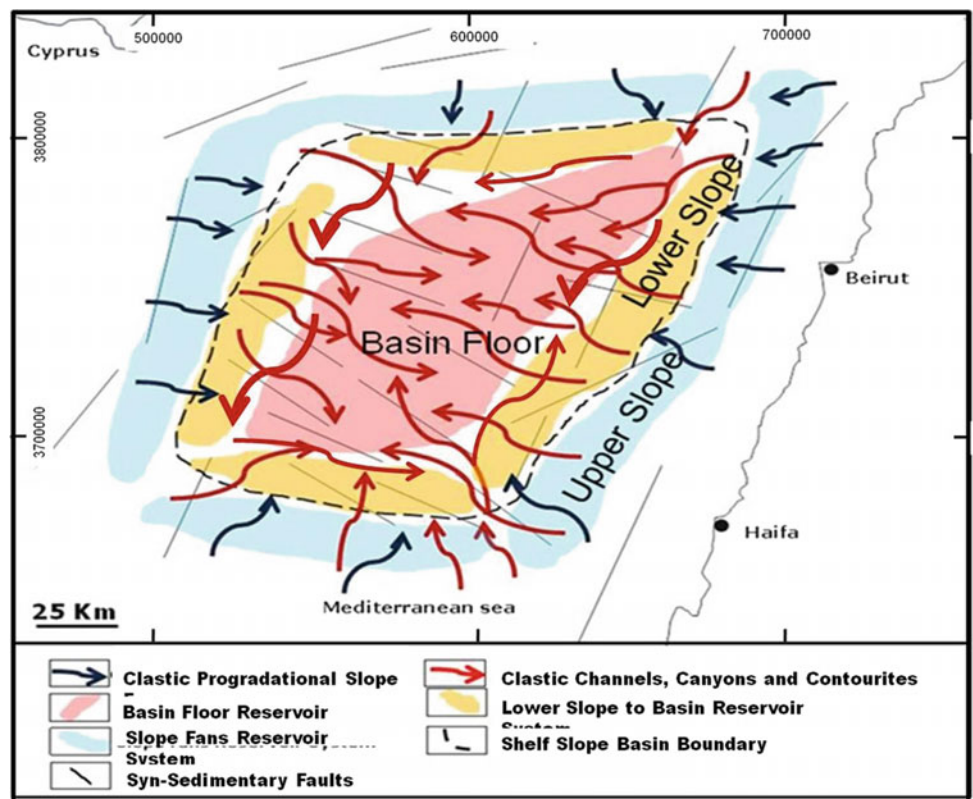
References

Ball MW, Ball D (1953) Oil prospects of Israel. Am Assoc Petrol Geol Bull 37:1–113

Bar O, Gvirtzman Z, Zilberman E, Feinstein S (2008) The development of the continental margin of central and Southern Israel from early Mesozoic formation to Late Tertiary reshaping: the role of tectonic and sedimentary processes in structural and morphological evolution of a continental shelf. GSI report GSI/31/2008, 68

Bédir M, Bobier Cl (1987) Les grabens de Mahdia et Sidi Chérif (Tunisie orientale). Dynamique des fossés oligo-miocènes induits au toit d'anticlinaux crétacés-éocènes par les jeux au Néogène de décrochement Est-Ouest et Nord-Sud. Bull Soc Géol France 3 (6):1143–1151

Bédir M, Zargouni F, Tlig S, Bobier CL (1992) Subsurface geodynamics and petroleum geology of the transform margin basins in the Sahel of El Jem and Mahdia (Eastern Tunisia). Am Assoc Petrol Geol Bull (AAPG) 76(9):1417–1442

Bédir M (1995) Mécanismes géodynamiques des bassins associés aux couloirs de coulissement de la marge atlasique de la Tunisie: sismo-stratigraphie, sismo-structurale et implications pétrolières. State Thesis of Science, Université de Tunis II El Manar, 420

Bédir M, Tlig S, Bobier C, Aissaoui N (1996) Sequence stratigraphy, basin dynamics and petroleum geology of the Miocene from eastern Tunisia. Am Assoc Petrol Geol Bull (AAPG) 80(1):63–81

Bédir M, Zitouni L, Boukadi N, Tlig S, Alouani R, Cl Bobier (2000) Rifting, halocinèse et structuration des bassins péri-téthysiens jurassiques et Crétacé inférieur de subsurface sur la marge atlasique centre-ouest de la Tunisie (Région de Gafsa-Sidi Ali Ben Oun). Afr Geosci Rev 7(3):289–306

Bédir M, Boukadi N, Tlig S, Ben Timzal F, Zitouni L, Alouani R, Slimane F, Bobier CL, Zargouni F (2001) Subsurface mesozoic basins in the central Atlas of Tunisia: tectonics, sequence deposit distribution and hydrocarbon potential. Am Assoc Petrol Geol Bull (AAPG) 85(5):885–907

Bédir M, Arbi A, Khomsi S, Houatmia F (2016) Aissaoui N 2016 Seismic tectono- stratigraphy of fluvio-deltaic to deep marine Miocene silicoclastic hydrocarbon reservoirs systems in the Gulf of Hammamet, Northeastern Tunisia. Arab J Geosci 9(19):1–33. https://doi.org/10.1007/s12517-016-2745-7

Bédir M, Aissaoui MN (2017) Seismic tectono-stratigraphy modeling of deep marine Oligo-Miocene siliciclastic reservoirs in Levant-Cyprus basin frontier zone. In: AAPG Annual Convention & Exhibition, Houston, Texas, USA, pp 1–5 (Datapages © 2017. Search and Discovery Article #10940)

Bein A, Gvirtzman G (1977) A mesozoic fossil edge of the Arabian plate along the Levant coastline and its bearing on the evolution of the Eastern Mediterranean. In: Biju-Duval B, Montadert L (eds) Structural history of the Mediterranean basins: Editions Technip, Paris, pp 95–110

Ben-Avraham Z, Hall JK (1977) Geophysical survey of Mount Carmel structure and its extension into the Eastern Mediterranean. J Geophys Res 82(5):793–802

Ben-Gai Y, Druckman Y (2013) Mega-Scale Swells and diapirs in the deep Levant Basin, Eastern Mediterranean, and their Association with Recent World-Class Gas Discoveries. AAPG Search and Discovery Article #90161©2013 AAPG European Regional Conference, Barcelona, Spain, 8–10 April 2013

Ben Ismail-Lattrache K, Bobier C (1984) Sur l'évolution des paléoenvironnements marins paléogènes des bordures occidentales du détroit Siculo-Tunisien et leurs rapports avec les fluctuations du paléo-océan mondial. Mar Geol 55:195–217

Benjamini C (1993) Paleobathymetry of the Eocene of Israel. Geol Soc Annu Meet Arad Abstr, Isr, p 17

Bertoni C, Cartwright JA (2007) Major erosion at the end of the Messinian Salinity Crisis: evidence from the Levant Basin, Eastern Mediterranean. Basin Res 19:1–18

Bismuth H (1984) Les unités stratigraphiques du Miocène de Tunisie orientale: Réunion de la Société des Sciences de la Terre de Tunisie, Tunis, 2 planches, 1 tableau

Bouaziz S, Barrier E, Soussi M, Turki MM, Zouari H (2002) Tectonic evolution of the northern African margin in Tunisia from paleostress data and sedimentary record. Tectonophysics 357:227–253

Bowman SA (2011) Regional seismic interpretation of the hydrocarbon prospectivity of offshore Syria. GeoArabia 16(3):95–124 (Gulf PetroLink, Bahrain)

Brew G, Barazangi M, Al-Maleh AK, Sawaf T (2001) Tectonic and geologic evolution of Syria. Geoarabia 6:4–573

Buchbinder B, Sneh A, Dimant E (1986) The Neogene Bet Nir Formation, a study of alluvial aggradation along the toe of the Judean monoclines. Isr J Earth Sci 35:183–191

Buchbinder B, Benjamini C, Mimran Y, Gvirtzman G (1988) Mass transport in Eocene pelagic chalk on the northwestern edge of the Arabian platform, Shefela area, Israel. Sedimentology 35:257–274

Buchbinder B, Martinotti GM, Siman-Tov R, Zilberman E (1993) Temporal and spatial relationships in Miocene reef carbonates in Israel. Paleogeogr Palaeoclimatol Palaeoecol 101:97–116

Buchbinder B, Zilberman E (1997) Sequence stratigraphy of Miocene-Pliocene carbonate-siliciclastic shelf deposits in the eastern Mediterranean margin (Israel): effects of eustasy and tectonics. Sed Geol 112:7–32

Buchbinder B, Calvo R, Siman-Tov R (2005) The Oligocene in Israel: a marine realm with intermittent denudation accompanied by mass-flow deposition. Isr J Earth Sci 54:63–85

Butler RWH, McClelland EM, Jones RE (1999) Calibrating the duration and timing of the Messinian salinity crisis in the Mediterranean: linked tectono-climatic signals in thrust-top basins in Sicily. J Geol Soc Lond 156:827–835

Carton H, Singh C, Tapponnier P, Elias A, Briais A, Sursock A, Jomaa A, King R, Daeron GCP, Jacques M, Barrier EL (2009) Seismic evidence for Neogene and active shortening offshore of Lebanon (Shalimar cruise). J Geophys Res 114:B07407, 1–26 https://doi.org/10.1029/2007JB005391

Catuneanu O (2002) Sequence stratigraphy of clastic systems: concepts, merits, and pitfalls. J Afr Earth Sci 35(1):1–43

Catuneanu O (2003) Sequence stratigraphy of clastic systems. Geol Assoc Can Short Course Notes 16:248

Catuneanu O (2006) Principles of sequence stratigraphy, 1st ed. Elsevier, The Netherlands (Copyright © 2006 Elsevier B.V. 375)

Chapin MA, Davies P, Gibson JL, Pettingill HS (1994) Reservoir architecture of turbidite sheet sandstones in laterally extensive outcrops, Ross formation, western Ireland. In Weimer P, Bouma AH, Perkins BF (eds) Submarine fans and turbidite systems: Gulf Coast Section SEPM Foundation 15th annual research conference, pp 53–68

Cohen A (1988) Stratification of the Messinian evaporites in Israel. Isr J Earth Sci 37:193–203

Dolson JC, Shann MV, Matbouly S, Harwood C, Rashed R, Hammouda H (2001) The petroleum potential of Egypt, in

petroleum provinces of the twenty-first century. AAPG Memoir 74:453–482

Dolson JC, Shann MV, Hammouda H, Rashed R, Matbouly S (2000) The petroleum potential of Egypt: AAPG. California, Memorial Conference, p 28

Druckman Y, Buchbinder B, Martinotti GM, Siman-Tov R, Aharon P (1995) The buried Afiq Canyon (eastern Mediterranean, Israel): a case study of a tertiary submarine canyon exposed in Late Messinian times. Mar Geol 123:167–185

Eppelbaum L, Katz Y (2011) Tectonic-geophysical mapping of Israel and the Eastern Mediterranean: implications for hydrocarbon prospecting. Positioning 2:36–54

Flexer A, Rosenfeld A, Lipson-Benitah S, Honigstein A (1986) Relative sea level changes during the Cretaceous in Israel. Am Assoc Petrol Geol Bull 70:1685–1699

Freund R, Goldberg M, Weissbrod T, Druckman Y, Derin B (1975) The Triassic-Jurassic structure of Israel and its relation to the origin of the Eastern Mediterranean. Isr Geol Surv Bull 65:26

Galloway WE (1989) Genetic stratigraphic sequences in basin analysis II: application to Northwest Gulf of Mexico Cenozoic Basin. AAPG Bull. 73(2):143–154

Gardner MH, Sonnenfeld MD (1999) Stratigraphic changes in facies architecture of the Permian Brushy Canyon Formation in Guadalupe Mountain National Park, West Texas, vol 96, issue no 38. Permian Basin Section-SEPM Publication, pp 17–40

Gardner MH, Borera JM, Melickb JJ, Mavillac N, Dechesnea M, Wagerled RN (2003) Stratigraphic process-response model for submarine channels and related features from studies of Permian Brushy Canyon outcrops, West Texas. Mar Petrol Geol 20 (2003):757–787

Gardosh M (2002) The sequence stratigraphy and petroleum systems of the Mesozoic, Southeastern Mediterranean continental margin. Ph. D. thesis, Tel Aviv University, p 159

Gardosh M, Druckman Y (2006) Seismic stratigraphy, structure and tectonic evolution of the Levantine Basin, offshore Israel. In: Robertson AHF, Mountrakis D (eds) Tectonic development of the Eastern Mediterranean region, vol 260. Geological Society, London, Special Publications, pp 201–227

Gardosh M, Druckman Y, Buchbinder B, Rybakov M (2008) The Levant Basin Offshore Israel: stratigraphy, structure, tectonic evolution and implications for hydrocarbon exploration, revised edn. GII Rep. 429/328/08, GSI Rep. GSI/4/2008, 119

Garfunkel Z, Derin B (1984) Permian-early Mesozoic tectonism and continental margin formation in Israel and its implications to the history of the eastern Mediterranean. In: Dixon JE, Robertson AHF (eds) The geological evolution of the Eastern Mediterranean, vol 17. Geological Society, London, Special Publications, pp 18–201

Garfunkel Z, Horowitz A (1966) The upper tertiary and quaternary morphology of the Negev. Isr. Isr. J. Earth Sci. 15:101–117

Garfunkel Z (1998) Constraints on the origin and history of the eastern Mediterranean basin. Tectonophysics 298:5–35

Gorini C, Montadert l, Rabineau M (2015) New imaging of the salinity crisis: dual messinian lowstand megasequences recorded in the deep basin of both the eastern and western mediterranean. Mar Pet Geol 66(Part 1):278–294

Gradmann S, Hubscher C, Ben-Avraham Z, Gajewski D, Netzeband G (2015) Salt tectonics off northern Israel. Mar Pet Geol 22:597–611

Gvirtzman G, Buchbinder B (1978) The tertiary history of the coastal plain and continental shelf of Israel and its bearing on the history of the Eastern Mediterranean. Init Rep Deep Sea Drilling Proj 42B:1195–1222

Hardenberg MF, Robertson AHF (2007) Sedimentology of the NW margin of the Arabian plate and the SW–NE trending Nahr El-Kabir half-graben in northern Syria during the latest Cretaceous and

Cenozoic. Sed Geol 201(3–4):231–266 (Geological Society, London, Special Publications, 372:447–471)

Hawie N, Gorini Ch, Deschamps R, Nader FH, Montadert L, Grangeon D, Baudin F (2013) Tectono-stratigraphic evolution of the northern Levant Basin (offshore Lebanon). Mar Petrol Geol 48:392–410

Hawie N, Deschamps R, Nader FH, Gorini C, Müller C, Desmares D, Hoteit A, Granjeon D, Montadert L, Baudin F (2014) Sedimentological and stratigraphic evolution of northern Lebanon since the Late Cretaceous: implications for the Levant margin and basin. Arab J Geosci. https://doi.org/10.1007/s12517-013-0914-5. (Hay, W.W. 1998. Detrital sediment fluxes)

Haq BU, Hardenbol J, Vail PR (1987) The chronology of the fluctuating sea level since the Triassic. Science 235:1156–1167

Haq BU, Hardenbol LJ, Vail PR (1988) Mesozoic and Cenozoic chronostratigraphy and cycles of sea-level change. In: Wilgus CK, Hastings BS, Kendall CGSC. St, Posamentier HW, Ross CA, Van Wagoner JC (eds) Sea-level changes: an integrated approach, vol 42. Society of Economic Paleontologists and Mineralogists, SEPM, Special Publication, pp 71–108

Homewood PW, Mauriaud P, Lafont P (2002) Best practices in sequence stratigraphy for explorationists and reservoir engineers. Total Fina Elf Publications. Pau, p 81

Houatmia F, Khomsi S, Bédir M (2015) Oligo-Miocene reservoir sequence characterization and structuring in the Sisseb El Alem-Kalaa Kebira regions (Northeastern Tunisia). J Afr Earth Sci 111(2015):434–450

Hsu KJ, Cita MB, Ryan WBF (1973a) The origin of the Mediterranean evaporites. Init Rep Deep Sea Drilling Proj 42:1203–1232

Hsu K, Ryan WBF, Cita MB (1973b) Late Miocene desiccation of the Mediterranean. Nature 242:240–244

Hsu KJ, Montadert L, Bernoulli D, Cita MB, Erickson A, Garrison RG, Kid RB, Melieres F, Mulle C, Wright R (1978) History of the Mediterranean salinity crisis. Init Rep Deep Sea Drilling Proj 42A:1053–1078

Khomsi S, Bédir M, Soussi M, Ben Jemia MG, Ben Ismail K (2006) Mise en Evidence des Compressions Eocène moyen et supérieur en Tunisie orientale. C R Acad Sci Géosciences 2006(338):41–49

Khomsi S, Ben Jemia MG, Frizon De Lamotte D, Maherssi C, Echihi O, Mezni R (2009) An overview of the Late Cretaceous-Eocene positive inversions and Oligo-Miocene subsidence events in the foreland of the Tunisian Atlas: Structural style and implications for the tectonic agenda of the Maghrebian Atlas system. Tectonophysics 475(2009):38–58

Khomsi S, De Frizon Lamotte D, Bédir M, Echihi O (2016) The Late Eocene and Late Miocene fronts of the Atlas Belt in eastern Maghreb: integration in the geodynamic evolution of the Mediterranean Domain. Arab J Geosci 9:650. https://doi.org/10.1007/s12517-016-2609-1

Krenkel E (1924) Der Syrische Bogen. Zentralbl Mineral 9:274–281 and 10:301–313

Lofi J, Deverchère, J, Gaullier V, Gillet H, Gorini C, Guennoc P, Loncke L, Maillard A, Sage F, Thinon I, Capron A, Obone Zue Obame E (2008) The Messinian Salinity Crisis in the offshore domain: an overview of our knowledge through seismic profile interpretation and multi-site approach, vol 33. The Messinian salinity crisis from mega-deposits to microbiology—a consensus report—Almeria, 7–10 November 2000. CIESM workshop monographs issue, pp 83–90

Lofi J, Sage F, Déverchère J, Loncke L, Maillard A, Virginie G, Thinon I, Gillet H, Guennoc P, Gorini C (2011) Refining our knowledge of the Messinian salinity crisis records in the offshore domain through multi-site seismic analysis. Bull Soc Géol Fr 182 (2):163–180

Mahaffie MJ (1994) Reservoir classification for turbidite intervals at the Mars discovery, Mississippi Canyon 807, Gulf of Mexico. In: Weimer P, Bouma AH, Perkins BF (eds) Submarine fans and turbidite systems, sequence stratigraphy, reservoir architecture and production characteristics: Gulf Coast Section SEPM 15th annual research conference, pp 233–244

Martinotti GM (1973) Miogypsina in the Gaza-1 well, coastal plain. Isr Isr Geol Surv Bull 57:1–6

Melki F, Zouaghi T, Ben Chelbi M, Bédir M, Zargouni F (2010) Tectono-sedimentary events and geodynamic evolution of the Mesozoic and Cenozoic basins of the Alpine Margin, Gulf of Tunis, northeastern Tunisia offshore. C R Geosci 342:741–753

Micro-Strat Inc (2003) High resolution biostratigraphy of Mediterranean sea Hannah 1 well, offshore Israel. Report prepared for Samedan Mediterranean Sea, p 40

Mitchum RM Jr., Vail PR, Sangree JB (1977) Seismic stratigraphy and global changes of sea level 6: stratigraphic interpretation of seismic reflection patterns in depositional sequences. Seismic stratigraphy—application exploration. AAPG Mém 26:117–132

Montadert L, Nicolaides S, Semb PH, Lie Ø (2014) Petroleum systems offshore Cyprus. In: Marlow L, Kendall C, Yose (eds) Petroleum systems of the Tethyan region, vol 106. AAPG Special Publications, Memoir, pp 301–334

Nader FH (2011) The petroleum prospectivity of Lebanon: an overview. J Pet Geol 34:135–156

Neev D, Almagor G, Arad A, Ginzburg A, Hall JK (1976) The geology of the southeastern Mediterranean. Isr Geol Surv Bull 68:52

Plummer M, Belopolsky Fish AP, Norton M (2013) Tectonostratigraphic evolution and exploration potential of the Northern Levant Basin. Search and discovery. In: AAPG european regional conference & exhibition, Barcelona, Spain, April 8–10, article #10516

Picard L (1951) Geomorphology of Israel, Part I—the Negev. Isr Geol Surv Bull 1:28

Picard L (1959) Geology and oil exploration of Israel. Bull Res Council Isr G8:1–30

Richards M, Bowman M, Reading H (1998) Submarine-fan systems I: characterization and stratigraphic prediction. Mar Pet Geol 15:687–717

Roberts G, David (2007) Hydrocarbon plays and prospectivity of the Levantine Basin, offshore Lebanon and Syria from modern seismic data. GeoArabia 12(3):99–124

Robertson AHF (1998a) Mesozoic-Tertiary tectonic evolution of the easternmost Mediterranean area: integration of marine and land evidence. In: Robertson AHF, Emeis KC, Richter C, Camerlenghi A (eds) Proceedings of the Ocean Drilling Program, Scientific Results, vol 160, pp 723–782

Robertson AHF (1998b) Tectonic significance of the Eratosthenes Seamount: a continental fragment in the process of collision with a subduction zone in the eastern Mediterranean Ocean Drilling Program (Leg 160). Tectonophysics 298:63–82

Robertson AHF, Mountrakis D (2006) Tectonic development of the Eastern Mediterranean region: an introduction. In: Robertson AHF, Mountrakis D (eds) Tectonic development of the Eastern Mediterranean region, vol 260. Geological Society, London, Special Publications, pp 1–9

Rybakov M, Segev A (2004) Characterization of top of the crystalline basement in the Levant. Geochem Geophys Geosyst 5(9). (Published by AGU and the Geochemical Society an Electronic Journal of the Earth Sciences)

Ryan WBF (1978) Messinian badlands on the southeastern margins of the Mediterranean Sea. Mar Geol 27:349–363

Satur N, Hurst A., Kelling G., Cronin BT, Gurbuz K (2007) Controlling factors on the character of feeder systems to a deep-water fan, Cingoz Formation, Turkey. In Nilsen THT, Studlick J, Steffens G (eds) Atlas of Deepwater Outcrops, Studies in Geology, 56. American Association of Petroleum Geologists, Tulsa

Sharnugam G (2003) Deep-marine tidal bottom currents and their reworked sands in modern and ancient submarine canyons. Mar Pet Geol 20(2003):471–491

Steinberg J, Gvirtzman Z, Folkman Y, Garfunkel Z (2011) The origin and nature of the rapid Late Tertiary filling of the Levant Basin. Geology 39(4):355–358

Tibor G, Ben-Avraham Z, Steckler M, Fligelman H (1992) Late Tertiary subsidence history of the southern Levant Margin, eastern Mediterranean Sea, and its implications to the understanding of the Messinian Event 1992. J Geophys Res: Solid Earth 97(B12):17593–17610

Walley CD (2001) The Lebanon passive margin and the evolution of the Levantine Neotethys. In: Ziegler PA, Cavazza W, Robertson AHF, Crasquin-Soleau S (eds) Peri-Tethys Memoir 6: Peri-Tethyan Rift/wrench basins and passive margins, vol 86. Mémoire du Muséum national d'Histoire naturelle, Paris, pp 407–439

Vail PR, Mitchum RMJ, Todd RG, Widmier JW, Thomson S, Sangree JB, Bubb JM, Hatelid WG (1977) Seismic stratigraphy and global changes of sea level. In: seismic stratigraphy, application to hydrocarbon exploration. A.A.P.G., Memory 26, 49:49–212

Vail PR (1987) Seismic Stratigraphy Interpretation Using stratigraphy, Part 1, Seismic stratigraphy interpretation procedure. Atlas of Seismic Stratigraphy, A.A.P.G. studies in Geology, Memory 27(1) 1–10

Vail PR, Audemard E, Bowman S., Eisner PN, Pers-Cruz C (1991) The stratigraphic signatures of tectonics, eustacy and sedimentology. An over view. In: Einsel G, Ricken W, Seilacher A (eds) Cycles and events in stratigraphy. Spinger, Berlin: 617–659

Van Wagoner JC, Posamentier HW, Mitchum RM, Vail PR, Sarg JF, Loutit TS, Hardedenbol J (1988) An overview on the fundamentals of sequence stratigraphy and key definitions. In: Wilgus CK et al (eds) Sea level changes an integrated approach, SEPM Spec. Pub., vol 42, pp 39–45

Paul W, Pettingill HS (2007) Deep-water exploration and production: a global overview. In Nilsen TH, Shew RD, Steffens GS, Studlick JRJ (eds) Atlas of deep-water outcrops: AAPG Studies in Geology, vol 56, CD-ROM, 29 p

Worral DM, Bourque MW, Steele DR (2001) Exploration in deep water basins…where next? In Fillon RH, Rosen NC, Weimer P, Lowrie A, Pettingill HW, Phair RL, Roberts HH, Van Hoorn B eds., Petroleum systems of deepwater basins: global and Gulf and Mexico experience: Gulf Coast Section SEPM Bob F. Perkins 21st Annual Research Conference: 273

Zilberman E (2000) Formation of "makhteshim" - Unique erosion cirques in the Negev, southern Israel. Israel J Earth Sci 49(3):127–141

Zilberman E (1997) Sequence stratigraphy of Miocene-Pliocene carbonate-siliciclastic shelf deposits in the eastern Mediterranean margin (Israel): effects of eustasy and tectonics. Sediment Geol 112 (1–2):7–32

Source-to-Sink Analysis of the Plio-Pleistocene Deposits in the Suez Rift (Egypt)

Sébastien Rohais and Delphine Rouby

4

Abstract

We present a source-to-sink (S2S) study of the Plio-Pleistocene deposits in the Suez rift (Egypt). We used stratigraphic record and quantitative geomorphology to constrain relief evolution in a rift setting from a high-resolution database at basin-scale (~ 300 km $\times$ 100 km) including, digital elevation model, outcrop and subsurface data. The stratigraphic architecture shows five main stages ranging from rift initiation to tectonic quiescence (Oligo-Miocene) plus a post-rift stage (Plio-Pleistocene). We quantified sediment accumulation history and analysed the relationship between catchment and sediment supply for the Plio-Pleistocene (post-rift stage). The results of the source-to-sink study for the post-rift stage were then compared to previous estimations for the main rifting stages. We show that the sediment supply dynamics of the Plio-Pleistocene deposits of the Suez rift records a renewed uplift ca. 5 Myr ago. However, we also show that a major climate shift related to the Pliocene revolution was most probably coeval to reach the magnitude of accumulation observed.

Keywords

Suez rift • Syn-rift • Post-rift • Catchment • Sediment supply • Source-to-sink • Pliocene • Pleistocene

4.1 Introduction

Source-to-sink (S2S) approaches integrate the domains in erosion, transport and deposition of sediment routing systems as a single dynamically linked system. These approaches are fundamental to understand the controls of each of the three sub-systems and their feedbacks (e.g. Einsele et al. 1996; Allen 2008; Sømme et al. 2009; Pechlivanidou et al. 2017). However gathering the data necessary to constrain the three domains for a single sedimentary system can be very challenging as it requires the characterization of the entire sedimentary basin that is to say isopach and paleogeographic maps, timelines calibrated in absolute ages, timing of deformation and, ideally, constraints on evolution of reliefs and drainage systems through time. These data allow for the quantification of the sedimentary budget of the basin, that have been implemented in various types of basins (e.g. Einsele et al. 1996; Rouby et al. 2009; Guillocheau et al. 2012). Paleo-relief and erosion dynamic models have also been successfully applied (Kennan et al. 1997; Babault et al. 2005; Barnes and Heins 2009). Nevertheless, as ancient reliefs and drainage systems are not usually preserved, their characterization remains very challenging at geological time scales. The joint characterization of the catchments and the deposits resulting from their erosion is more often possible for the present-day systems (e.g. Syvitski et al. 2003; Eide et al. 2017). Using these relationships and the associated sedimentary budget, we can somewhat infer the dynamic of erosion and paleo-reliefs. Nevertheless, the down-system grain size fining is usually poorly known and still limits the determination of the proper relationship between sediment supply and erosional processes in the catchments (Whitakker et al. 2010; Hampson et al. 2014). Consequently, breakthroughs in source-to-sink approaches of sediment routing systems can only happen once the three domains, erosion, transport and deposition are well characterized at basin-scale.

S. Rohais (✉)
IFPEN, Direction Géosciences, 1 et 4 Avenue de Bois-Préau, 92852 Rueil-Malmaison Cedex, France
e-mail: sebastien.rohais@ifpen.fr

D. Rouby
Géosciences Environnement Toulouse, UMR CNRS 5563, 31400 Toulouse, France

Well-constrained S2S case study are extremely rare but the Suez rift is a good candidate because it is a "closed system" where the material eroded in the catchments has been entirely trapped in the sedimentary basin. We expanded the detailed database established by Rohais et al. (2016) for the Plio-Pleistocene to characterize the evolution of the sediment routing system since the Miocene. The description of the sediment supply dynamic and high-resolution accumulation history at basin-scale have been used to discuss the associated paleo-reliefs evolution.

4.2 The Suez Rift

The Suez rift is the NW–SE-trending branch of the Red Sea rift system (Fig. 4.1), resulting from the late Oligocene to early Miocene rifting of the African and Arabian plates (Garfunkel and Bartov 1977). It is bounded by large-scale normal fault zones (ca. 40–80 km long and ca. 2–6 km offset, Fig. 4.1b). The polarity of the major faults varies along the rift axis, dividing the rift into three 50–100 km long sub-basins (Colletta et al. 1988; Patton et al. 1994; Moustafa 1996): (i) the northern Darag basin with northeast dipping major faults (Fig. 4.1b), (ii) the Central basin (Belayim province) with southwest dipping major faults, and, (ii) the Southern basin (Amal-Zeit province) with northeast dipping major faults (Figs. 4.1 and 4.2). The sub-basins are separated by two major accommodation zones ca. 20-km wide (Colletta et al. 1988): the Zaafarana and the Morgan accommodation zones (Fig. 4.2).

The stratigraphic succession of the Gulf of Suez includes (i) pre-rift, (ii) syn-rift and (iii) post-rift deposits (Fig. 4.3). (i) The pre-rift comprises a Precambrian Pan-African crystalline basement unconformably overlain by a 1-km thick succession of Cambrian to Eocene sedimentary rocks progressively thinning southward. They are sub divided into three units (e.g. Moustafa 1976; Garfunkel and Bartov 1977): (1) the "Nubia Sandstones" mostly consist of fluvial sandstones (Cambrian to Early Cretaceous), (2) the Late Cretaceous mixed carbonate-siliciclastic succession and (3) the Paleocene-Eocene carbonate-dominated succession (Fig. 4.3). (ii) Red-bed deposits record the transition from pre-rift to syn-rift (Tayiba and Abu Zenima Formations) and are usually attributed to the Oligo-Miocene (Fig. 4.3). The overlying Miocene syn-rift succession is subdivided into the Gharandal Group (Nukhul, Rudeis and Kareem Formations) of mixed depositional environments, and the RasMalaab Group (Belayim, South Gharib and Zeit Formations) dominated by evaporites (Egyptian General Petroleum Corporation (EGPC) 1964; Fig. 4.3). (iii) Catchments feeding post-rift depositional systems developed on both pre-rift and syn-rift deposits. The post-Zeit, post-rift succession (Wardan and Zaafarana Formations; Figs. 4.3 and 4.4) is attributed to

the Plio-Pleistocene (e.g. Abd El Shafy 1990). The mean tectonic subsidence was estimated ca. 31 mm/kyrat that time (Bosworth et al. 1998).

4.3 Data and Method

We expanded the database of Rohais et al. (2016) for the Plio-Pleistocene deposits taking into account previous findings for this time interval (e.g. Said 1962, 1990; Abdel Salam and El-Tablawy 1970; Fawzy and Abdel Aal 1984; Abd El Shafy 1990; Gheith and El-Sherbini 1993; Alsharhan and Salah 1995, 1998; Rioual 1996; Orszag-Sperber et al. 1998). It includes high resolution digital topographic data, aerial maps, 279 subsurface wells, 31 sedimentological outcrop sections and published geological, structural, isopach and paleogeographicmaps and cross-sections (see Rohais et al. 2016 and references herein).

We followed a seven steps workflow: five steps analyse the "sink" domain and two addresses the "source".

(i) From outcrop analysis, geological mapping, bibliographic review, seismic interpretation and well correlation we build structural maps of the basin (Fig. 4.2).

(ii) We then correlated key stratigraphic surfaces across the basin using a sequence stratigraphy analysis (Figs. 4.4 and 4.5).

(iii) From control wells, outcrop sections and published 3D geological models (Barrois et al. 2010; Barrois 2011), we build isopach and lithological maps using the present day structural framework (Fig. 4.6).

(iv) We estimated the relative proportion of siliciclastics (shales, sandstones, conglomerates), carbonates (carbonates and offshore mudstones) and evaporites (anhydrite and halite) deposits using an automatic image analysis on both the lithological maps and the cross sections (Table 4.1). We differentiated two end-members (maximum and minimum) and a mean scenarios to estimate the uncertainties associated with each lithologic component. From this, we estimated, for each time step, the volumes of each lithology and corrected them from remaining porosity using the method of Poag and Sevon (1989).

(v) To allow for the computation of accumulation rates and sediment supply (Table 4.1), we then calibrated the main stratigraphic surfaces into absolute ages. We used the few biostratigraphic constrains available and assumed that the major sequence boundaries were correlated to the ones of the International Commission on Stratigraphy (ICS) stratigraphic chart that includes the synthesis by Hardenbol et al. (1998), Haq and Al-Qahtani (2005) and Gradstein et al. (2012).

Fig. 4.1 a Geodynamic setting of the Gulf of Suez. Major elements including the Aqaba–Levant intra-continental transform boundary, the Bitlis-Zagros convergence zone and the Red Sea—Gulf of Aden are highlighted. The red rectangle shows the Gulf of Suez that corresponds to the NW termination of the Red Sea. Light blue corresponds to present day marine setting (modified after Rohais et al. 2016 and references herein). **b** Structural cross-section of the Suez rift illustrating the large scale tilted block structure of the Darag Basin (modified after Colletta et al. 1988). Blue arrows indicate the present day shoreline
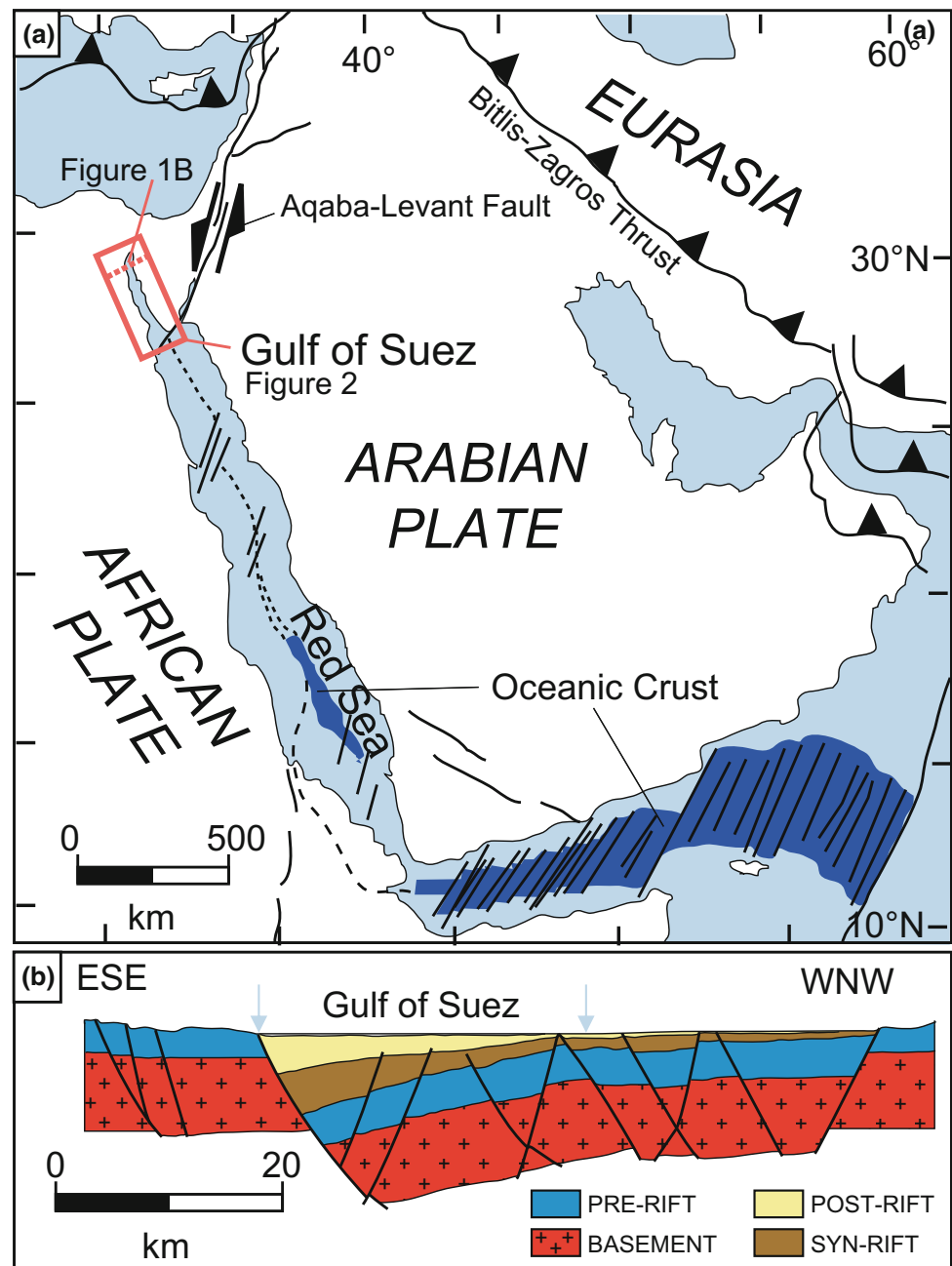
(vi) For the source areas, we quantified the drainage catchments characteristics (relief, area, length, slope, bedrock lithology). To do this, we used the Hydrology toolset from the Spatial Analyst toolbox available in ArcGIS on the 30 m resolution digital topographic data from ASTER GDEM (http://reverb.echo.nasa.gov/reverb/), as well as aerial maps (WGS 1984 UTM Zone 36 N, https://www.microsoft.com/maps/).

(vii) From the present day climatic setting and catchment morphological parameters, we used the method of Syvitski et al. (2003) to predict a theoretical sediment supply (Qs) for each catchment from its relief (R, m) and catchment area (A, km^2) according to the empiric law:

$$Qs = \alpha R^{3/2} A^{1/2} \qquad (4.1)$$

where $\alpha = \beta \, \varrho \, g^{1/2} = 2 \times 10^{-5}$ (M L$^{-2.5}$ T^{-1}) with β a constant of proportionality depending on the climate (Syvitski and Morehead 1999), ϱ the grain density (2650 kg/m^3); g the acceleration due to gravity (9.8 m/s^2). Using these catchment characteristics, we then estimated the
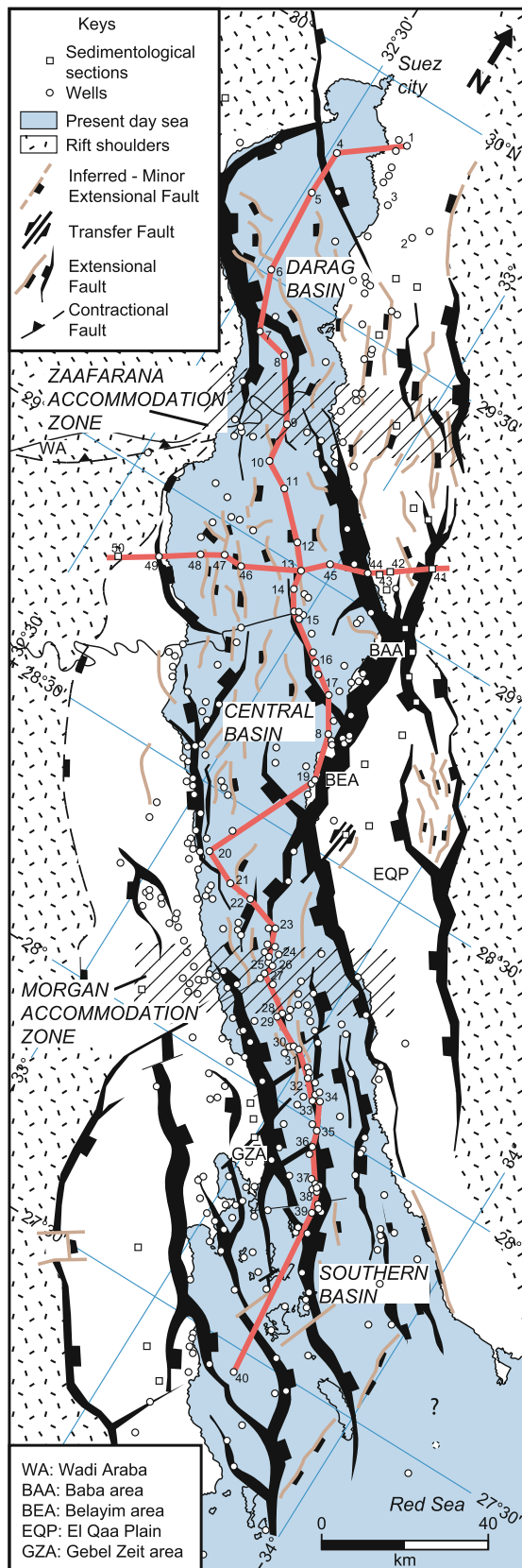
Fig. 4.2 Structural map of the Suez rift and location of the dataset used in this study. Hatched areas indicate major accommodation zones separating from north to south: the Darag basin, the Central Basin and the Southern Basin. Red lines show the cross-sections presented in Fig. 4.5

water discharge (Q) from the empirical relationship between discharge (Q) and catchment area (A) of Syvitski et al. 2003):

$$Q = \alpha_1 A^{\alpha 2} \qquad (4.2)$$

where α1, and α2 are constants determined using a regression analysis of a large river database. We used α1 = 0.51, and α2 = 0.7 defined for the north tropics (Syvitski et al. 2003). We verified these estimations with the present day river sediment supply in the Suez rift.

Assuming the drainage system remained constant throughout the Gulf of Suez history, we extrapolated the estimation of the theoretical Qs since the Miocene, using similar parameters.

4.4 Sink: Sedimentary Budget for the Plio-Pleistocene

4.4.1 Stratigraphic Architecture and Age Model

For the sedimentology and lithostratigraphy of the Plio-Pleistocene sequence of the Suez rift, we used previous works by Said (1962, 1990), Abdel Salam and El-Tablawy (1970), Fawzy and Abdel Aal (1984), Abd El Shafy (1990), Gheith and El-Sherbini (1993), Alsharhan and Salah (1995, 1998), Bosworth and Taviani (1996), Rioual (1996), Orszag-Sperber et al. (1998) and Ali et al. (2010). However, the calibration in absolute ages within the Plio-Pleistocene succession remains poorly constrained, especially for the offshore domain (e.g. Ali et al. 2010). The base of the WardanFm is interpreted as the base Pliocene (ca. 5.3 Ma) overlying the ZeitFm attributed to the Messinian (Abd El Shafy 1990). Above, the boundary between the Wardan and Zaafarana Formations is commonly attributed to the Plio-Pleistocene boundary (ca. 2.5 Ma) based on very limited biostratigraphical constrains (Abd El Shafy 1990; Gheith and El-Sherbini 1993; Orszag-Sperber et al. 1998; Ali et al. 2010).

Using stacking pattern analysis, we identified correlated at rift scale seven units: from PQ1 for the earliest Pliocene to PQ7 for the most recent Quaternary (Figs. 4.4 and 4.5). We defined the stratigraphic architecture using six lithologies: carbonates (including reef and platform s.l. deposits), shales (silty-rich from protected to restricted deposits and mud-rich for offshore deposits), sandstones (including fan delta, shallow marine, and turdiditic deposits), conglomerates (including alluvial fan and proximal fan delta deposits), anhydrite, and halite (mainly from lagoon and saline to sabkha depositional settings). The PQ1 unit comprises deep basinal facies preserved along the basin axis organized in aggrading to backstepping trend (Fig. 4.5). It corresponds to a starved

Fig. 4.3 Simplified stratigraphic column of the Suez rift (modified after Rohais et al. 2016 and references herein). The present study is focused on the post-rift series including the Wardan and Zaafarana Formations. See Fig. 4.5 for lithology colour code

Stratigraphy			Groups and Formations		Litho.	Rifting Phases
CENOZOIC		Quaternary	El Tor	Zaafarana		POST-RIFT
				Post-Zeit		
		Pliocene		Wardan		
	Miocene	Late	Ras Malaab Gr.	Zeit		SYN-RIFT
				South Gharib		
		Middle		Belayim		
			Gharandal Group	Kareem		
		Early		Rudeis		
				Nukhul		
		Oligocene		Abu Zenima		
	Eocene	Late	El Egma Group	Darat		PRE-RIFT
		Early		Thebes		
		Paleocene		Esna Shale		
MESOZOIC	Late Cretaceous	Senonian		Sudr Chalk		
				Brown Lm - Duwi		
			Nezzazat Group	Matulla		
		Turonian		Wata		
		Ceno-manian		Abu Qada		
				Raha		
	Jurassic - Lower Cretaceous			Nubia "A"		
PALEOZOIC	Carboniferous			Nubia "B"		
	Cambrian to Devonian			Nubia "C and D"		
	PRE-CAMBRIAN			Basement		

Fig. 4.4 Synthetic stratigraphic framework of the Plio-Pleistocene of the Suez rift. Lithologies are constrained from calibration wells. Silty rich for restricted deposits in green versus mud rich for offshore deposits in light blue. Transgressive system tracts are shown in blue, highstand and falling stage system tracts are shown in red, lowstand system tracts are shown in orange. The age model is derived from the Hardenbol et al. (1998), Haq and Al-Qahtani (2005) and Gradstein et al. (2012) stratigraphic charts
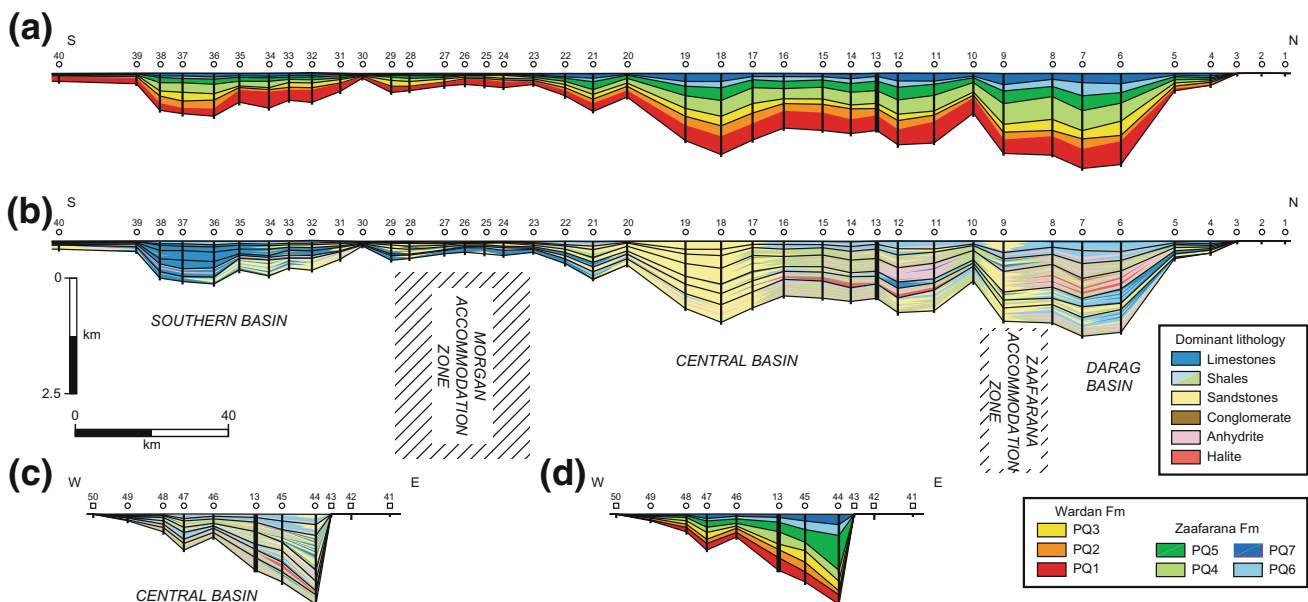
Fig. 4.5 Transversal cross-section of the rift flattened on the present day topography showing **a** the main depositional units and **b** the main lithology. E-W cross section of the Central Basin flattened on the present day topography showing **c** the main depositional units and **d** the main lithology within the. Sections cross-cut at well 13. See Fig. 4.2 for location

carbonate platform along the basin margins and a shallow siliciclastic deposits along the main accommodation zones. It records a progressive northward flooding of the Suez rift. The base of PQ2 is a major sequence boundary (Fig. 4.4). The PQ2 unit is characterized by thick halite deposits, associated to anhydrite-rich and restricted deposits, and is preserved in the Central basin (Fig. 4.5). These deposits were interpreted as marginal, semi-restricted lagoonal

settings (Alsharhan and Salah 1998). As a difference, shallow platform deposits are preserved in the Southern basin, isolating the restricted Central Suez rift from the Red Sea whereas siliciclastics deposits prevailed in the northern Darag basin (Fig. 4.5). The PQ3 unit is characterized by basinal to marginal facies organized in a prograding trend (Fig. 4.4). It recorded a single pulse of carbonates: a widening of the patch reef and carbonate platform in the

Fig. 4.6 a Maps of the Plio-Quaternary deposits and the main depocenters (>1700 m) and dominant lithologies for the highstand (**b** present day) and lowstand settings (**c** PQ4, ca. 1.8 Ma). Silty rich shales for restricted deposits are shown in green. Mud rich shales for offshore deposits in light blue. See Fig. 4.5 for further keys information
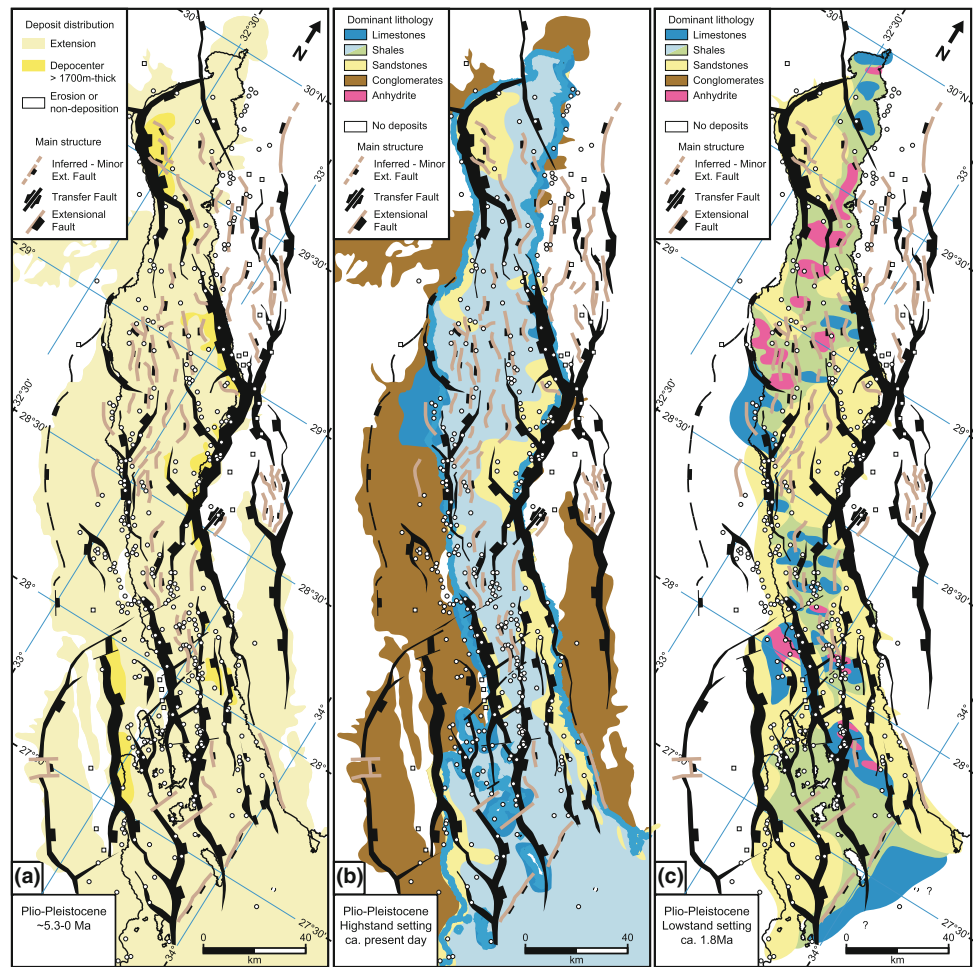
Table 4.1 Results of the sedimentary budget characterization for the Plio-Pleistocene deposits of the Suez rift. The preferred scenario is highlighted in grey. See text for further explanation

Formation	Unit	Estimated duration (Myr)		Preserved Volume at rift scale	Carbonate accummulation rate (m/Myr)Porosity corrected			Evaporite accummulation rate (m/Myr)			Mean Sediment supply at rift scale (km3/Myr) Porosity corrected		
		Age (Ma)	Duration (Myr)	Km3	Preferred	*Max.*	*Min.*	Preferred	*Max.*	*Min.*	Preferred	*Max.*	*Min.*
Zaafarana	PQ7	0-0.4	0.4	1164	55.0	56.5	44.8	83.2	260.7	18.7	942.9	1005.6	848.9
	PQ6	0.4-0.8	0.4	994	55.8	60.3	43.8	82.9	235.0	15.9	820.4	859.1	751.4
	PQ5	0.8-1.65	0.85	1938	78.2	80.9	76.6	86.9	124.3	38.8	738.7	781.2	702.0
	PQ4	1.65-2.5	0.85	2497	59.4	66.1	46.8	112.0	243.8	72.3	881.4	1042.6	724.0
Wardan	PQ3	2.5-3.2	0.7	1565	64.4	74.3	62.0	42.6	48.7	5.8	798.0	879.2	681.0
	PQ2	3.2-4	0.8	1614	97.7	116.7	50.6	57.7	191.3	23.3	678.1	871.2	605.6
	PQ1	4-5.3	1.3	3033	84.4	86.5	61.0	44.5	184.9	16.7	898.3	922.4	878.2

Darag basin (Fig. 4.5). The PQ4 unit is characterized by m-thick halite intervals associated to anhydrite-rich and restricted deposits preserved in the Darag basin (Fig. 4.5). As a difference with the PQ2 interval, there is no evidence for halite occurrence in the Central basin at that time. The

PQ4 unit records the maximum backstep of the most restricted and evaporative depositional environment of the Plio-Pleistocene. The PQ5, PQ6 and PQ7 units correspond to basinal facies alternating with thin (m-scale) anhydrite layers organized in an overall prograding trend (Figs. 4.4

and 4.5). Over this period, siliciclastics including turbidites dominates the deposition in the Central basin and the western Darag basin whereas, in the Southern basin, a shallow platform facing an open marine environment to the south (Red Sea) developed, including evaporite, reefs and lagoonal deposits during lowstand periods. A longitudinal N-S depositional gradient then prevailed along the basin axis (Fig. 4.5).

To calibrate stratigraphic surfaces bounding these units in absolute ages, we used the ICS stratigraphic chart based on the synthesis by Gradstein et al. (2012; Fig. 4.4). We interpreted the high evaporite contents of PQ2 and PQ4 units as lowstand system tracts. Using ICS stratigraphic chart, we attributed the base of PQ2 unit to the 4 Ma sea-level drop (Za2), the top of PQ2 unit to the 3.2 Ma sea-level drop (Pia 1), the base of PQ4 unit to the 2.5 Ma sea-level drop (Wardan to Zaafarana boundary, Ge1) and the top the PQ4 unit to the 1.65 Ma sea-level drop (Cala 1). The PQ5, PQ6 and PQ7 unit calibration in absolute ages is poorly constrained and remains speculative. Nonetheless, as MIS22 and MIS12 are the two major sequence boundaries of this time interval, we attributed the base of the PQ6 unit to the 0.8 Ma sea-level drop and the top of the PQ6 unit to the 0.4 Masea-level drop. Our calibration is consistent with the recent work of Jackson and Rotevatn (2013) in the Central basin of the Suez rift.

4.4.2 Lithology and Paleogeography Evolution

As the Miocene, the Plio-Pleistocene shows alternating (i) overfilled phases with a transversal E-W depositional gradient from the rift margins to the basin axis (mainly highstands, Fig. 4.6b), and (ii) underfilled phases with a longitudinal N-S depositional gradient along the basin axis (mainly lowstands, Fig. 4.6c).

During highstands, the Darag basin shows a simple tilted block configuration, with a single alluvial to fan delta system fed by large catchment areas on the western (high-relief) footwall, and a starved shorelines with small isolated fan deltas, small patch reefs and isolated carbonate platforms on the eastern (low-relief) hanging wall (Fig. 4.6b). As a difference, during lowstands, the Darag basin was subaerially exposed with lagoonal to restricted depositional environments along the basin axis. Evaporites were locally preserved in small depocenters (Fig. 4.6c).

The Central basin had a similar configuration than the Darag basin with an inverse polarity: hanging wall to the west and footwall to the east (Fig. 4.6). During highstands, a 10–20 km wide bajada to alluvial fan system developed on the first tilted blocks of the western margin (low-relief hanging wall; Fig. 4.6). Small patch reefs and isolated platforms formed along starved shoreline as well. Large

alluvial to fan delta systems (Wadi Baba, Feiran, Belayim) formed along the eastern margin (high-relief footwall) and fed turbidite systems preserved in the basin axis. As a difference, during lowstands, the Central basin was partially subaerially exposed. The basin axis showed lagoonal to restricted environments with large alluvial to fan delta system derived from the eastern margin (Fig. 4.6c).

In the Southern basin, during highstands, 10–20 km wide bajada to alluvial fan systems formed along the rift shoulder and on the first set of tilted blocks (Zeit, Esh El Mellaha and El Qaa plains, Fig. 4.6b). They evolved into fan delta and starved shorelines prograding into lagoonal to open sea environments. Reefs and isolated carbonate platforms developed on tilted block crests and along starved shorelines, preferentially along the western margin where sediment supply from the catchments are stored and controlled by the tilted block crest (Zeit, Esh El Mellaha, Fig. 4.6). The basin axis preserved moderately deep deposits (50–80 m water depth). As a difference, during lowstands, the Southern basin was partially subaerially exposed with lagoonal to restricted environments in the basin axis. Evaporites were locally preserved in small depocenters (Fig. 4.6c). As suggested by seismic data, a carbonate platform is suspected to the south (towards the Red Sea; Rioual 1996).

4.4.3 Isopach Maps and Sediment Supply

The main Plio-Pleistocene depocenters are fairly similar to the Late Miocene ones (Rohais et al. 2016) with nonetheless (i) an additional major depocenter in the Darag basin (Fig. 4.6a) and (ii) an overall tilt of the basin axis northward during the Plio-Pleistocene (Fig. 4.5). The Darag and Central basins preserved most of the sediments and the Southern basin subsided at a lower rate, probably in response to the Aqaba transform fault activity.

We estimated the total volume of Plio-Pleistocene sediments ca. 12,800 km^3 and the incremental accumulated volumes of PQ1 to PQ7 units for each lithology are shown in Table 4.1 (the remaining porosity correction was estimated between 30% at the base Pliocene and 40% at the top Quaternary for siliciclastics).

The carbonate accumulation rate is relatively constant over the Plio-Pleistocene (ca. 60–70 m/Myr, Fig. 4.7) and similar to the Miocene (Rohais et al. 2016). It is consistent with previous estimations that also suggested stable type of carbonates in the Suez rift over the whole the Plio-Pleistocene (Burchette 1988; Bosence et al. 1994). The carbonate accumulation rate also ranges in worldwide values published for the 0.5–2 Myrtime interval (Davies 1988; Enos 1991).

The evaporite accumulation rate is relatively low during the Plio-Pleistocene (70–80 m/Myr) with nonetheless an
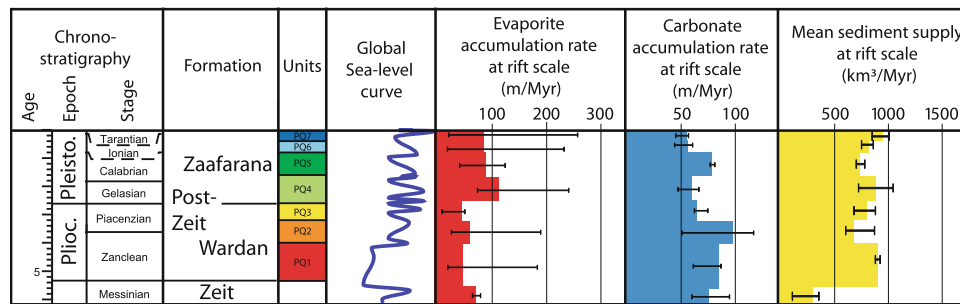
Fig. 4.7 Accumulation rates of evaporates and carbonates (km^3/Myr) and mean sediment supply from siliciclastics (km^3/Myr) for the Plio-Pleistocene deposits. The chronostratigraphy and sea-level curve are derived from Gradstein et al. (2012). Relative proportions of lithologies for each map have been combined with thickness map to estimate the accumulation rate. See text for further information

acceleration during PQ4 (112 m/Myr; Table 4.1). The values are consistent with Miocene accumulation rates (Rohais et al. 2016) as well as previous estimations for the 0.5–2 Myr time interval (Decima and Wezel 1973; Enos 1991).

The sediment supply (Qs) ranges from 650 to 950 km^3/Myr during the Plio-Pleistocene (Fig. 4.7, Table 4.1). Taking into account the uncertainties, rates increased during the early Pliocene (PQ1) and decreased slightly during PQ2. They increased again progressively back to the previous rate during the late Pliocene (PQ3 and PQ4), decreased slightly during the early Pleistocene (PQ5) before increasing to the maximum rate at the end of the Pleistocene (PQ6 and PQ7).

4.5 Source: Geomorphological Characteristics

We analyzed the present day catchment areas on aerials photos and a Digital Elevation Model (DEM) from which we extracted the catchments characteristics using the Hydrology toolset of ArcGIS with a 20 km^2 cut-off for merging smallest catchment areas. We identified 68 catchments with an outlet feeding the Suez rift (Fig. 4.8) for which we measured (i) the relief (R) between the outlet and the maximum elevation in the catchment, (ii) the catchment area (A), (iii) the dominant lithology of the catchment bedrock (basement, siliciclastics or carbonates) using the geological map (EGSMA 1981), (iv) the location of the outlet (Darag, Central or Southern basins) and (v) its tectonic setting (footwall or hanging wall). For catchments larger than 20 km^2, and if occurring, we also measured the mean slope of the alluvial fans and/or bajadas (Gf, m/m), their areas (Af) and their bedrock lithology. Results are shown in Table 4.2 and Fig. 4.9. Out of the 68 catchments, 13 do not have fan at the outlet and deliver sediments directly to the sea.

At rift scale, the mean catchment relief is about 850 m (from 124 to 2511 m), the mean area about 450 km^2 (from 21 to 3290 km^2), the mean fan slope about 0.02 m/m (from 0.005 to 0.05 m/m) and the mean fan area about 210 km^2 (from 2.5 to 1455 km^2). This mean fan area is very large because most of the alluvial to fan delta system correspond to bajada in the Suez rift. Indeed, the Baba, Rudeis, and Sidri fan deltas, that could be considered as typical fan deltas, have an mean area of ca. 70 km^2. Hereafter, we use the term fan for both alluvial and fan delta.

4.5.1 Alluvial to Fan Delta Systems

The fans located on the footwalls of the three sub-basins (Darag, Central and Southern) show a similar fan gradient/area relationship (triangles on Fig. 4.9a), different than the fans located on the hanging walls (squares on Fig. 4.9a), excluding the fans located in the Central basin. The steepest fan systems are located in the hanging wall of the Southern basin whereas the gentlest are located in the hanging wall of the Darag basin. Steeper systems develop from crystalline basement, and gentlest from siliciclastic-dominated catchments (Fig. 4.9b). For crystalline basement catchment, fans are steeper on the hanging wall (e.g. Southern basin) whereas, for a more erodible bedrock (e.g. siliciclastics) fan are steeper in the footwall (e.g. the Miocene, the recent alluvial and/or the poorly consolidated Paleozoic siliciclastic rocks of the Darag basin). The extracted dataset indicates that the fan slope depends on the catchment area by a negative power law, in agreement with the results of Bull (1964), Hooke (1968) and Saito and Oguchi (2005) (Figs. 4.9c, d; Table 4.3).

4.5.2 Catchment Areas

The catchment relief (R, m) relates to the catchment area (A, km^2) by a positive power law (Table 4.3) that does not seem impacted by the tectonic setting or the bedrock lithology (Fig. 4.9e, f). The hanging wall of the Southern basin does however show a specific behavior, that is out of the dataset

Fig. 4.8 Simplified geological and structural map showing the dominant lithology, size and shape of present day catchments. See Table 4.2 for the quantified parameters
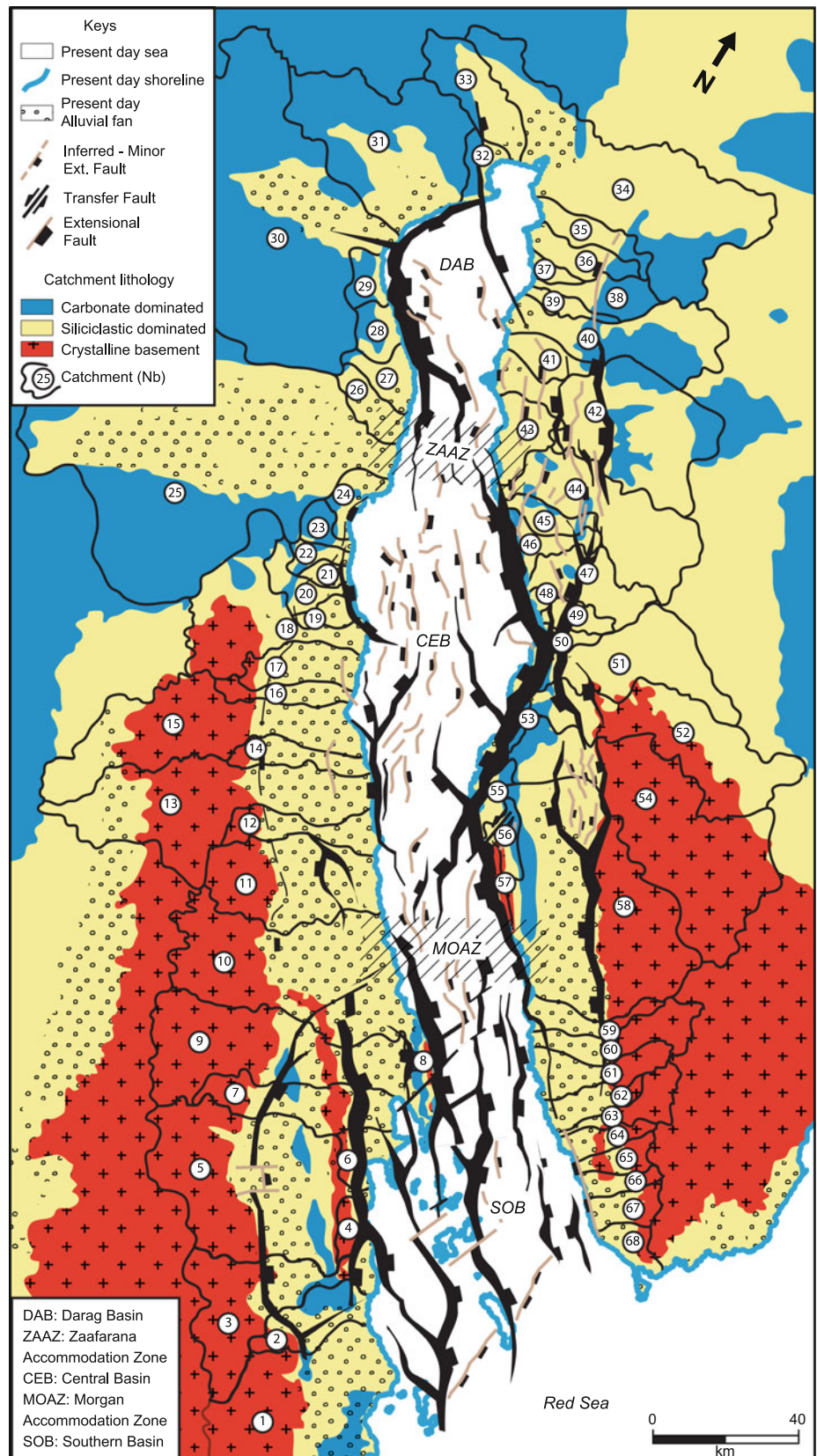
Table 4.2 Database extracted using the Hydrology toolset from the Spatial Analyst toolbox developed in ArcGIS for the Suez rift. The relief (R, m) corresponds to the maximum altitude in the catchment minus the altitude of the outlet

Catchment				Fan			Setting
N°	Relief (m)	Area (km2)	Dominant lithology in the catchment	Fan gradient (m/m)	Fan area (km2)	Type	Tectonic domain
1	1569	694.9	Crystalline basement	0.0115	721.3	Bajada	SOB-FW
2	748	102.9	Crystalline basement	0.0156	265.5	Bajada	SOB-FW
3	1304	594.5	Crystalline basement	0.0110	336.9	Isolated	SOB-FW
4	168	87.1	Crystalline basement	0.0180	17.7	Bajada	SOB-FW
5	956	1055.2	Crystalline basement	0.0100	845.6	Bajada	SOB-FW
6	124	78.2	Crystalline basement	0.0154	125.1	Bajada	SOB-FW
7	709	226.4	Crystalline basement	0.0095	333.1	Bajada	SOB-FW
8	318	50.4	Crystalline basement	0.0384	68.1	Bajada	SOB-FW
9	691	905.5	Crystalline basement	0.0088	455.0	Bajada	SOB-FW
10	650	787.4	Crystalline basement	0.0117	1021.0	Bajada	SOB-FW
11	934	375.8	Crystalline basement	0.0168	598.9	Bajada	SOB-FW
12	298	82.0	Crystalline basement	0.0135	230.2	Bajada	CEB-HW
13	533	1081.0	Crystalline basement	0.0156	451.0	Bajada	CEB-HW
14	361	29.7	Crystalline basement	0.0132	197.6	Bajada	CEB-HW
15	485	1015.0	Crystalline basement	0.0206	331.0	Bajada	CEB-HW
16	362	63.6	Crystalline basement	0.0205	129.1	Bajada	CEB-HW
17	455	81.0	Crystalline basement	0.0170	249.2	Bajada	CEB-HW
18	1216	807.0	Crystalline basement	0.0129	127.3	Bajada	CEB-HW
19	174	21.2	Carbonate dominated	0.0163	85.7	Bajada	CEB-HW
20	1069	173.0	Carbonate dominated	0.0191	19.3	Bajada	CEB-HW
21	442	45.5	Carbonate dominated	0.0204	26.2	Bajada	CEB-HW
22	1114	86.8	Carbonate dominated	0.0173	9.9	Bajada	CEB-HW
23	903	111.1	Carbonate dominated	0.0291	2.5	Bajada	CEB-HW
24	524	87.3	Carbonate dominated	0.0350	77.4	Bajada	DAB-FW
25	964	3289.7	Carbonate dominated	0.0120	1455.0	Bajada	DAB-FW
26	929	44.9	Carbonate dominated	0.0171	159.1	Bajada	DAB-FW
27	1083	146.1	Carbonate dominated	0.0163	47.3	Bajada	DAB-FW
28	1241	169.2	Carbonate dominated				DAB-FW
29	1180	140.1	Carbonate dominated				DAB-FW
30	1011	3035.0	Carbonate dominated	0.0153	378.0	Bajada	DAB-FW
31	756	1338.1	Carbonate dominated	0.0111	140.4	Bajada	DAB-FW
32	765	136.6	Carbonate dominated	0.0263	15.0	Bajada	DAB-FW
33	588	175.7	Carbonate dominated	0.0180	47.3	Bajada	DAB-FW
34	683	1791.6	Siliciclastic dominated	0.0057	253.1	Bajada	DAB-HW
35	625	223.0	Carbonate dominated				DAB-HW
36	590	204.8	Carbonate dominated	0.0057	28.1	Bajada	DAB-HW
37	236	64.1	Carbonate dominated				DAB-HW
38	690	226.2	Carbonate dominated	0.0091	15.2	Bajada	DAB-HW
39	262	97.3	Carbonate dominated				DAB-HW
40	822	728.7	Carbonate dominated	0.0046	62.1	Bajada	DAB-HW
41	267	190.1	Carbonate dominated				DAB-HW

Table 4.2 (continued)

Catchment				Fan			Setting
42	1024	1351.2	Siliciclastic dominated	0.0052	58.0	Isolated	DAB-HW
43	374	259.3	Carbonate dominated	0.0114	17.3	Bajada	DAB-HW
44	1145	956.1	Siliciclastic dominated	0.0144	11.2	Isolated	DAB-HW
45	630	154.1	Carbonate dominated				DAB-HW
46	845	171.0	Carbonate dominated				CEB-FW
47	1021	406.1	Siliciclastic dominated				CEB-FW
48	211	43.5	Siliciclastic dominated				CEB-FW
49	644	130.0	Siliciclastic dominated				CEB-FW
50	596	78.2	Siliciclastic dominated				CEB-FW
51	1282	767.2	Siliciclastic dominated	0.0137	55.8	Isolated	CEB-FW
52	1517	1163.7	Siliciclastic dominated	0.0193	68.1	Isolated	CEB-FW
53	476	70.1	Carbonate dominated				CEB-FW
54	2511	1951.4	Crystalline basement	0.0125	78.4	Isolated	CEB-FW
55	486	125.8	Carbonate dominated	0.0226	9.6	Bajada	CEB-FW
56	418	126.5	Carbonate dominated	0.0243	11.5	Bajada	CEB-FW
57	469	52.9	Crystalline basement	0.0522	15.0	Bajada	CEB-FW
58	2360	1499.7	Crystalline basement	0.0153	833.4	Bajada	CEB-FW
59	1963	52.9	Crystalline basement	0.0165	153.5	Bajada	SOB-HW
60	1928	224.8	Crystalline basement	0.0233	148.8	Bajada	SOB-HW
61	1959	122.5	Crystalline basement	0.0223	201.6	Bajada	SOB-HW
62	1051	32.6	Crystalline basement	0.0326	167.6	Bajada	SOB-HW
63	1776	177.2	Crystalline basement	0.0288	40.9	Bajada	SOB-HW
64	973	58.4	Crystalline basement	0.0253	93.9	Bajada	SOB-HW
65	1074	86.6	Crystalline basement	0.0285	55.9	Bajada	SOB-HW
66	861	34.0	Crystalline basement	0.034	85.7	Bajada	SOB-HW
67	818	74.6	Crystalline basement	0.0236	105.6	Bajada	SOB-HW
68	397	55.2	Crystalline basement	0.0366	103.4	Bajada	SOB-HW

cluster and characterized by high catchment reliefs and relatively low catchment areas (Fig. 4.9e). This may be related to the combined effects of the crystalline bedrock, the tectonic setting and the vicinity of the Sinai Peninsula where important uplift occurred. Indeed, uplift along the Gulf of Suez increased southward on the Sinai Peninsula but remained more stable on the Egyptian side (Garfunkel 1988).

4.5.3 Predicting the Sediment Supply and Discharge

Using Eq. (4.1), we estimated the predicted total sediment supply produced by the Suez rift catchments at about 970 km³/Myr which is remarkably similar to the value determined from the PQ7 (0–0.4 Ma) unit volume (about 940 km³/Myr; ranging from 850 to 1000 km³/Myr).

Using Eq. (4.2), we estimated the mean water discharge at rift scale between 1500 and 1800 m³/s during the

Plio-Pleistocene (variations are small with respect to uncertainties; Fig. 4.10, Table 4.4). These values are consistent with present-day hydrographic study of Geriesh et al. (2004) for the Suez rift.

4.5.4 Estimating the Plio-Pleistocene Relief, Catchment Size and Uplift Rate

We used the relative proportion of each catchment area to the total sediment supply (Qs) at present day to (i) estimate the past sizes of catchments (during time intervals PQ1 to PQ7) assuming they had the present-day relief. (ii) Alternatively, we estimate past reliefs of catchments assuming they had the present-day area (Fig. 4.10, Table 4.4). We estimated uncertainties in our calculation from the uncertainties associated to the sediment supply quantification.

Assuming the catchment areas remained constant throughout Plio-Pleistocene, the estimated mean relief of
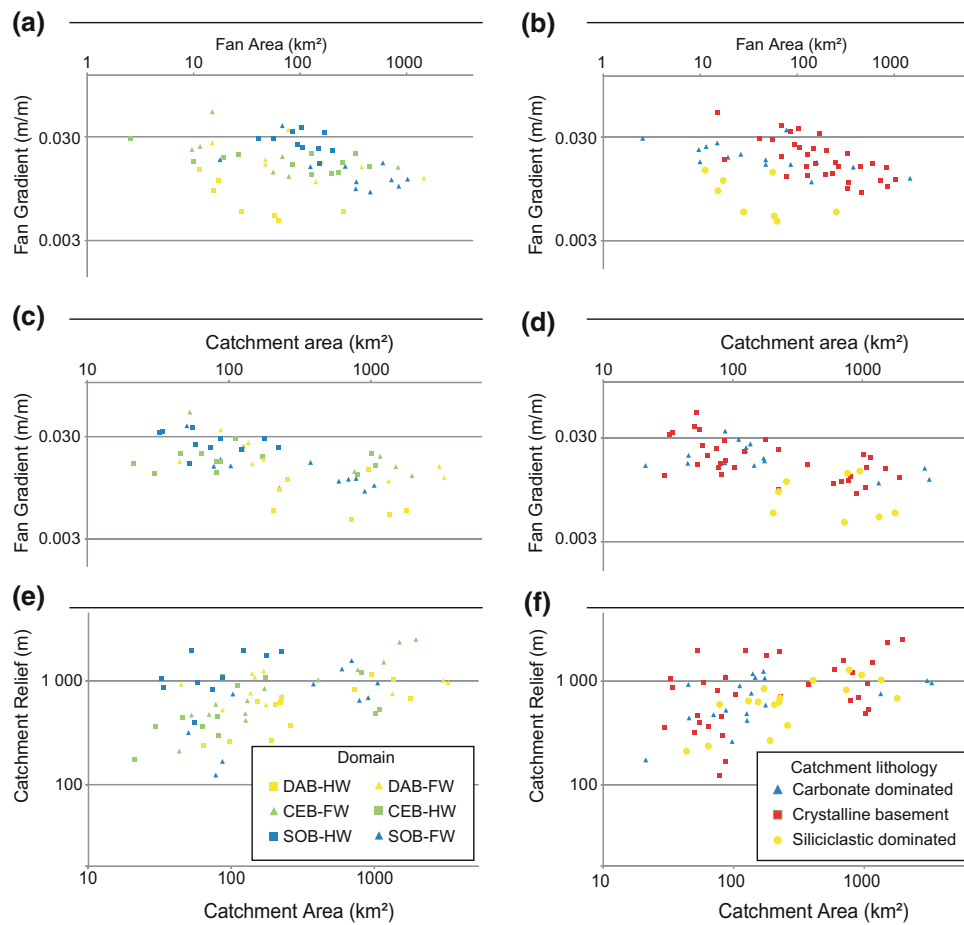
Fig. 4.9 Characterization of the catchment areas (Source) in the Suez rift. **a** Relationship between the fan gradient (m/m) to the fan area (km^2) of the fans according to the sub-basin and the tectonic setting (hanging wall—HW or footwall—FW). Blue: Southern Basin—SOB, Green: Central Basin—CEB, Yellow: Darag Basin—DAB. Square forhanging wall and triangle for footwall. **b** Relationship between the fan gradient (m/m) to the fan area (km^2) of the fans according to the dominant lithology in the catchments. Blue for carbonate, red for basement and yellow for siliciclastic from the geological map in Fig. 4.8. **c**, **d**: Relationship between the fan gradient (m/m) to the catchment area (km^2). **e**, **f**: Relationship between the catchment relief (m) to the catchment area (km^2)

Table 4.3 Regression coefficients established in Figure 9; Gf = $\alpha_3 Af^{\alpha4}$; Gf = $\alpha_5 A^{\alpha6}$; R = $\alpha_7 A^{\alpha8}$

a. Fan gradient (Gf, m/m) versus Fan area (Af, km2)

	α3	α4	r2
Southern Basin - SOB			
Footwall - FW	0.046	-0.214	0.3924
Hangingwall - HW	0.0626	-0.185	0.1518
Central Basin - CEB			
Footwall - FW	0.041	-0.184	0.3461
Hangingwall - HW	0.0262	-0.094	0.408
Darag Basin - DAB			
Footwall - FW	0.0386	-0.165	0.3678
Hangingwall - HW	0.0218	-0.304	0.5648
Carbonate basement	0.0307	-0.125	0.4256

(continued)

Table 4.3 (continued)

a. Fan gradient (Gf, m/m) versus Fan area (Af, km2)			
Crystalline basement	0.0799	-0.286	0.4511
Siliciclastic basement	0.0207	-0.263	0.3347

b. Fan gradient (Gf, m/m) versus Catchment area (A, km2)			
	α5	α6	r2
Southern Basin - SOB			
Footwall - FW	0.0701	-0.288	0.6032
Hangingwall - HW	0.0434	-0.114	0.0974
Central Basin - CEB			
Footwall - FW	0.1202	-0.94	0.7723
Hangingwall - HW	0.018	-0.006	0.0012
Darag Basin - DAB			
Footwall - FW	0.0429	-0.152	0.4483
Hangingwall - HW	0.0169	-0.0169	0.0727

c. Catchment relief (R, m) versus Catchment area (A, km2)			
	α7	α8	r2
Southern Basin - SOB			
Footwall - FW	28.502	0.536	0.5558
Hangingwall - HW	170.21	0.4419	0.3098
Central Basin - CEB			
Footwall - FW	46.426	0.5182	0.9016
Hangingwall - HW	173.43	0.2294	0.2645
Darag Basin - DAB			
Footwall - FW	740.07	0.029	0.0233
Hangingwall - HW	55.696	0.3966	0.6081
Carbonate basement	82.309	0.358	0.5026
Crystalline basement	220.29	0.239	0.1798
Siliciclastic basement	257.05	0.1896	0.2129

catchment remained similar to the present-day (about 850 m) over that period (variations are small with respect to uncertainties; Fig. 4.10). Assuming the catchment relief remained constant throughout Plio-Pleistocene, the estimated mean catchment remained similar to the present-day (450 km^2) over that period (variations are small with respect to uncertainties; Fig. 4.10).

These estimations suggest relief remained at equilibrium throughout the Plio-Pleistocene, (uplift rate balanced by erosion rate). We can therefore estimate the mean uplift rate at about 0.03 km/Myr (+/− 0.0025) during the last 0.4 Myr from the present-day total catchment area (about 31,000 km^2) and the most recent sedimentary supply (PQ7, 0–0.4 Ma, about 940 km^3/Myr). This rate is three times lower than the maximum uplift estimated on tilted block crest of the southern Suez rift for the Pleistocene (about 0.1 km/Myr in the Gebel Zeit area; Bosworth and Taviani 1996; Plaziat et al. 1998). It is however consistent with the mean uplift values estimated at basin-scale ca. 0.01–0.06 km/Myr by Plaziat et al. (1998) for the Pleistocene.

4.6 Discussion

4.6.1 The Pliocene Revolution?

We bring here our estimations of accumulation rates for the Plio-Pleistocene in perspective with the estimations for the Oligo-Miocene of the Suez rift by Rohais et al. (2016; Fig. 4.10). Over that period, the sediment supply followed an expected trend during a rifting. From the rift initiation to the rift climax phases, sediment supply increased rapidly (up to almost 1400 km^3/Myr at the end of the RudeisFm deposition). It then decreased down to ca. 50 km^3/Myr during the late to latest syn-rift phases that corresponds to a subdued tectonic (Kareem, Belayim and South GharibFms;
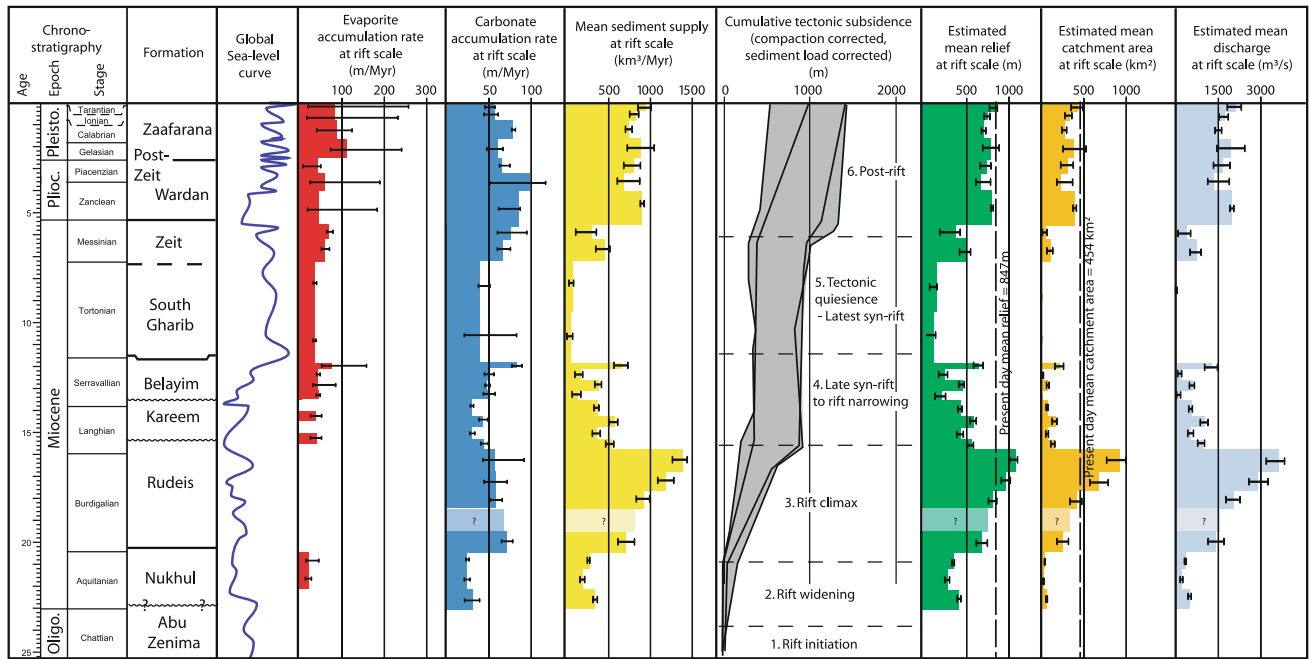
Fig. 4.10 Mean accumulation rates of evaporites, carbonates and siliciclastics sediment supply (km³/Myr) and cumulative tectonic subsidence. The grey area includes all the wells analyzed for estimating the cumulative tectonic subsidence (modified from the wells analyzed by Moretti and Colletta 1987; Richardson and Arthur 1988). The chronostratigraphy and global sea-level curve are after Gradstein et al. (2012). The present day values for the mean relief (847 m) and mean catchment area (454 km²) are represented with dash lines. See text for further information

Table 4.4 Results for the estimated mean relief (m), mean catchment area (km²) and mean discharge (km³/Myr) at rift scale based on the sediment supply (Qs) quantification and using the relationships of Syvitski et al. (2003). See text for further explanation

Formation	Interval	Estimated duration (Myr)		Mean discharge at rift scale (m3/s)			Mean catchment size at rift scale (km2)			Mean Relief at rift scale (m)		
		Age (Ma)	Duration (Myr)	Preferred	Max.	Min.	Preferred	Max.	Min.	Preferred	Max.	Min.
Zaafarana	PQ7	0-0.4	0.4	2136	2337	1844	432	491	350	833	870	777
	PQ6	0.4-0.8	0.4	1758	1875	1554	327	358	274	759	783	716
	PQ5	0.8-1.65	0.85	1518	1641	1413	265	296	239	708	735	684
	PQ4	1.65-2.5	0.85	1943	2459	1476	377	528	254	796	891	699
Wardan	PQ3	2.5-3.2	0.7	1691	1937	1354	308	375	225	745	795	671
	PQ2	3.2-4	0.8	1346	1912	1149	223	368	178	669	790	620
	PQ1	4-5.3	1.3	1996	2071	1933	392	413	374	807	821	794
Zeit	Zeit Upper	5.3-6.2	0.9	423	546	104	43	61	6	385	435	197
	Zeit Lower	6.2-7.2	1	764	918	527	99	129	59	511	557	428
South Gharib	South Gharib Upper	7.2-9.5	2.3	67	71	15	3	3	0	161	165	79
	South Gharib Lower	9.5-11.8	2.3	37	57	2	1	2	0	120	149	27
Belayim	Belayim-B1 Hammam Faraun	11.8-12.1	0.3	1289	1495	1042	210	259	155	655	703	592
	Belayim-B2 Feiran	12.1-12.6	0.5	181	229	89	13	18	5	257	288	184
	Belayim-B3 Sidri	12.6-13.1	0.5	612	680	504	72	84	55	459	483	419
	Belayim-B4 Baba	13.1-13.6	0.5	133	192	52	8	14	2	222	265	142

(continued)

Table 4.4 (continued)

Formation	Interval	Estimated duration (Myr)		Mean discharge at rift scale (m3/s)			Mean catchment size at rift scale (km2)			Mean Relief at rift scale (m)		
		Age (Ma)	Duration (Myr)	Preferred	*Max.*	*Min.*	Preferred	*Max.*	*Min.*	Preferred	*Max.*	*Min.*
Kareem	Kareem-K1 top Shagar	13.6-14.3	0.7	568	*608*	*480*	65	*72*	*51*	443	*458*	*409*
	Kareem-K2/K1 Markha/Shagar	14.3-14.8	0.5	1058	*1161*	*888*	158	*181*	*123*	596	*623*	*549*
	Kareem-K2 middle Markha	14.8-15.3	0.7	559	*647*	*445*	64	*78*	*46*	440	*472*	*395*
	Kareem-K2 base Markha	15.3-15.8	0.5	959	*1036*	*797*	138	*154*	*106*	569	*590*	*521*
Rudeis	Rudeis-R1	15.8-16.7	0.9	3671	*3863*	*3219*	936	*1006*	*776*	1078	*1105*	*1013*
	Rudeis-R2	16.7-17.6	0.9	2924	*3276*	*2609*	676	*795*	*575*	967	*1021*	*916*
	Rudeis-R3	17.6-18.5	0.9	2061	*2293*	*1792*	410	*478*	*336*	819	*862*	*766*
	Rudeis-R5	19.6-20.4	0.8	1439	*1726*	*1166*	245	*318*	*182*	690	*753*	*624*
Nukhul	Nukhul-Nu1	20.4-21.2	0.8	372	*383*	*328*	36	*37*	*30*	362	*367*	*341*
	Nukhul-Nu2	21.2-22.1	0.9	236	*270*	*179*	19	*23*	*13*	292	*311*	*256*
	Nukhul-Nu3 top Shoab Ali Mb.	22.1-23	0.9	507	*568*	*459*	55	*65*	*48*	420	*443*	*401*

Langhian-Serravalilan-Tortonian). However afterwards, during the post-rift, sediment supply unexpectedly peaked up again up to almost 900 km³/My in the lower Pliocene (PQ1) and remained between 650 and 850 km³/Myr throughout the Plio-Pleistocene, i.e. within values similar to the rifting climax. Experimental and numerical modeling (e.g. Bonnet and Crave 2003; Rohais et al. 2012) suggest that the increase of the uplift rate in the catchment areas could produce this increase in sediment supply. This increase in uplift rate is also consistent with the post-rift renewal of tectonic subsidence documented in the sedimentary basin from backstripping methods (Fig. 4.10).

The similar amplitude of sediment supply during rift climax (Burdighalian) and post-rift (Plio-Pleistocene) phases could suggest similar uplift rates assuming similar catchment areas and reliefs. However, the Pleistocene uplift rate estimated at basin-scale or along the crest of tilted block in the Southern basin (ca. 0.01–0.1 km/Myr; Bosworth and Taviani 1996; Plaziat et al. 1998) is 2–80 times lower than the uplift rate estimated during the rift climax (Steckler 1985; Garfunkel 1988; Steckler et al. 1988; Steckler and Omar 1994). We therefore suggest an additional control on the Plio-Pleistocene increase of the sediment supply.

Peihzen et al. (2001) suggested a global-scale increase in accumulation of coarser sediments 2–4 Myr ago triggered by the "Pliocene revolution", i.e. a shift from a relatively stable climate during the Miocene to a high frequency glacial/interglacial oscillating one in the Plio-Pleistocene. This interpretation should be moderated because it is based on sediment thicknesses not corrected from remaining porosity that could introduce up to 50% uncertainties in volume estimation in the recent deposits because they undergo major porosity changes in the first 500–1000 m of burial. Nonetheless, our estimations in the Suez rift are corrected from remaining porosity and their increase is coeval with the occurrence of this global climate shift. The amplitude and magnitude of the phenomenon remain nevertheless to be determined.

Evaporites accumulation rates at rift scale are a proxy for the long-term aridification in the Suez rift during the Late Miocene and of the Plio-Pleistocene high frequency climatic changes (Fig. 4.10). However, the stratigraphic resolution is no sufficient to identify high frequency trends in accumulation rates as expected between glacial/interglacial periods. These trends have been however documented in the Corinth rift with accumulation values for the lowstand glacial periods 60% higher than during interglacial highstand periods (Collier et al. 2000). These high frequency sediment supply oscillations produced an overall increase of the mean sediment supply over the Plio-Pleistocene. This suggests that the increase in sediment supply in the Suez rift at that time is consistent with the transition to glacial/interglacial oscillations during the "Pliocene revolution".

4.6.2 Additional Feedbacks

The accumulation history during the rift evolution could also be used to discuss and refine the calibration in absolute age

of some poorly constrained of the stratigraphic horizons. Indeed, the accumulation peak at the end of the BelayimFm deposition may be related to an underestimation of the duration of that time interval rather than to an actual increase in siliciclastic sediment supply. It is in fact coeval of a peak in in situ carbonate accumulation, that is peculiar and unexpected as both types of accumulation should evolve in opposite phase. Assigning an 11.5 Ma to the transition between Belayim and South GharibFm (instead of 11.8 Ma) would divide the estimated accumulation rate by two. These updated siliciclastic and carbonate accumulation rates would be more consistent with the estimations for the previous and following periods and their geodynamic context (tectonic quiescence). This would however not alter significantly the accumulation rates for the following South GharibFm deposition period since the duration of that interval would be reduced by only 13.5%. Avoiding any circular reasoning, this illustrates how S2S analyses may also provide additional constraints and feedbacks on the age model by highlighting accumulation rate anomalies in the frame of a well-known basin evolution.

4.6.3 Limits of the Approach

This study illustrates a workflow allowing quantification of the sediment supply dynamics in a sedimentary basin and its discussion in term of sediment production from the catchment areas (erosion). We estimated the relief and the catchment area over the rift evolution (from the rift initiation to the post-rift) assuming stable catchments at rift scale both in terms of size and erodability. For erodability, we assumed a constant lithology value during the rift evolution. Many studies however demonstrated rapid catchment area growth and variations in similar tectonic contexts (Bishop 1995; Attal 2009; Bonnet 2009; Willett et al. 2014). Surface process modeling (SPM) would provide a tool to integrate the catchment variability in the evaluation of the sediment production through time. Also, to constrain paleo-climate modeling, the runoff, precipitations and temperatures evolution during the rift history could be estimated using the approach of Syvitski et al. (2003), that has been recently updated by Eide et al. (2017).

To fully discuss the sediment supply dynamics during the basin history, we showed that sediment budget should be quantified at high resolution, at least in the same order of duration than response time of the system to a given control (glacial/interglacial climate oscillations for example). Otherwise, sediment supply dynamics might be misinterpreted (climate versus tectonic). For example, in this study, the increase in sediment supply at the Miocene/Plio-Pleistocene transition may be interpret just in terms of tectonic change (non-transient uplift increase), missing the

climatic signal ("Pliocene revolution"). Also, estimating sediment supply for even duration time step throughout the basin evolution would avoid trends related only to scaling and allow a discussion of the response times between the areas of sediment production and accumulation. In that respect, a major limit to this work is lack of biostratigraphic constraints within the Plio-Pleistocene. Concluding remarks of this paper should therefore be updated by future works on biostratigraphy or absolute dating.

4.7 Conclusion

We studied the Plio-Pleistocene evolution of the Suez rift using an integrated S2S approach from the sedimentary basin ("sink") to the upstream catchment area ("source").

(1) The quality of the dataset is critical to undertake this type of studies: the geometries, facies and lithologies of deposits, their calibration in absolute ages as well as the type and timing of deformation need to be addressed to allow for the sedimentary budget quantification. Also, the sediment routing system needs to be as closed as possible to avoid loss (or gain) of sediments between the sources and the sinks. In situ production and remaining porosity must be properly corrected to extract the siliciclastic sediment supply that is the only one relevant to discuss the catchment dynamics. First-order constraints on the location and size of sediment sources and on the sediment routing systems can be derived from geological mapping. A quantification of the siliciclastic sedimentary budget can then provide first order constraints on paleo-reliefs. Nevertheless, deformation or climate driven changes in regional drainage patterns requires numerical experimentation using surface-process models to be integrated in the analysis.

(2) Quantitative geomorphology analysis of the most recent systems allowed determining the relationships between sediment supply and catchment properties (area, relief, gradient, lithology). Assuming the present day configuration is representative of the past basin evolution in the Suez rift, those relationships were used to assess the first order relief dynamics at geological time-scale. It also provided first-order estimations of temperature, runoff and precipitations very useful in past climate modeling.

(3) The sediment supply dynamics of the Plio-Pleistocene deposits of the Suez rift shows a renewed uplift ca. 5 Myr ago. Nonetheless, a major climate shift related to the Pliocene revolution was most probably coeval to reach the magnitude of accumulation observed. To decipher the relative contribution of uplift or climate, the sediment budget should be quantified at higher

resolution (time steps lower than the system response time), although surface process modeling (SPM) might also help address this question.

References

Abd El Shafy A (1990) Miocene-Pliocene boundary in the Gulf of Suez region, Egypt, vol 1. In: 10th EGPC Exploration Seminar, Cairo, Egypt, pp 213–233

Abdel Salam H, El-Tablawy M (1970) Pliocene diatom assemblage from EastBakr and EastGharib exploratory wells in Gulf of Suez, vol 57, issue no (B-3). Seventh Arab Petroleum Congress, Kuwait

Ali DM, El-Awamri AA, Badawi AA, Hamed AF (2010) Fossil diatoms in Zaafarana Formation, Gulf of Suez, Egypt. Int J Acad Res 2(6):91–100 (Part I)

Allen PA (2008) From landscapes into geological history. Nature 451:274–276

Alsharhan AS, Salah MG (1995) Geology and hydrocarbon habitat in rift setting: northern and central Gulf of Suez, Egypt. Bull Can Petrol Geol 43(2):156–176

Alsharhan AS, Salah MG (1998) Sedimentological aspects and hydrocarbon potential of the Quaternary in the Gulf of Suez rifted basin. In: Alsharhan AS, Glennie KW, Whittle GL, St. Kendall CG (eds) Quaternary deserts and climate changes: Rotterdam, Balkema, pp 531–538

Attal M (2009) Rivers split as mountains grow. Nat Geosci 2:747–748. https://doi.org/10.1038/ngeo675

Babault J, van den Driessche J, Bonnet S, Castelltort S, Crave A (2005) Origin of the highly elevated Pyrenean peneplain. Tectonics 24. https://doi.org/10.1029/2004tc001697

Barnes JB, Heins WA (2009) Plio-quaternary sediment budget between thrust belt erosion and foreland deposition in the central Andes, southern Bolivia. Basin Res 21:91–109. https://doi.org/10.1111/j.1365-2117.2008.00372.x

Barrois A (2011) Couplage d'un modèle structural 3D restauré (Kiné3D-3) avec un modèle de remplissage stratigraphique (Dionisos) en contexte extensif, cas du rift de Suez (Égypte). I.F.P. report 62044

Barrois A, Rohais S, Granjeon D, Rudkiewicz JL, Cacas MC (2010) Coupling 3D structural restoration with stratigraphic modelling in rifted margins, Suez Rift, Egypt. In: International conference "Modelling sedimentary basins and their petroleum systems", June 3–4th 2010, Geological Society of London

Bishop P (1995) Drainage rearrangement by river capture, beheading and diversion. Prog Phys Geogr 19:449–473. https://doi.org/10.1177/030913339501900402

Bonnet S (2009) Shrinking and splitting of drainage basins in orogenic landscapes from the migration of the main drainage divide. Nat Geosci 2:766–771. https://doi.org/10.1038/ngeo666

Bonnet S, Crave A (2003) Landscape response to climate change: insights from experimental modeling and implications for tectonic vs. climatic uplift of topography. Geology 31:123–126

Bosence DWJ, Pomar L, Waltham D, Lankester TG (1994) Computer modelling a Miocene carbonate platform, Spain. Am Assoc Petrol Geol Bull 78:247–266

Bosworth W, Crevello P, Winn RD Jr, Steinmetz J (1998) Structure, sedimentation, and basin dynamics during rifting of the Gulf of Suez and north-western Red Sea. In: Purser BH, Bosence DWJ (eds) Sedimentation and Tectonics in Rift Basins: RedSea—Gulf of Aden. Chapman Hall, London, pp 77–96

Bosworth W, Taviani M (1996) Late Quaternary reorientation of stress field and extension direction in the southern Gulf of Suez, Egypt: evidence from uplifted coral terraces, mesoscopic fault arrays, and borehole breakouts. Tectonics 15:791–802

Bull WB (1964) Relation of alluvial fan size and slope to drainage basin size and lithology in western Fresno County, California. U.S. Geological Survey Professional Paper 450-B, pp 51–53

Burchette TP (1988) Tectonic control on carbonate platform facies distribution and sequence development: Miocene, Gulf of Suez. Sed Geol 59:179–204

Colletta B, LeQuellec P, Letouzey J, Moretti I (1988) Longitudinal evolution of the Suez rift structure (Egypt). Tectonophysics 153:221–233

Collier REL, Leeder MR, Trout M, FerentinosG Lyberis E, Papatheodorous G (2000) High sediment yields and cool, wet winters: rest of past glacial paleoclimates in the northern Mediterranean. Geology 28(11):999–1002

Davies PJ (1988) Evolution of the Great Barrier Reef: reductionist dream or expansionist vision, vol 1. In: Proceedings of 6th International Coral Reef Symposium, Townsville, pp 9–17

Decima A, Wezel FC (1973) Late Miocene evaporites of the Central Sicilian Basin. In: Ryan WBF, Hsü KJ (eds) Initial reports of the Deep Sea Drilling Project, vol 13, Part2. U.S. Government Printing Office, Washington D.C, pp 1234–1240

EGSMA (1981) Egyptian geological survey and mining authority, Geological map of Egypt, 1981. Ministry of Industry and Mineral Resources

Egyptian General Petroleum Corporation (EGPC) (1964) Oligocene and Miocene rock-stratigraphy of the Gulf of Suez region, report of the Stratigraphic Committee: Egyptian General Petroleum Corporation, 142 pp

Eide CH, Muller R, Helland-Hansen W (2017) Using climate to relate water-discharge and area in modern and ancient catchments. Sedimentology. https://doi.org/10.1111/sed.12426

Einsele G, Ratschbacher L, Wetzel A (1996) The Himalaya-Bengal Fan denudation-accumulation system during the past 20Ma. J Geol 104:163–184

Enos P (1991) Sedimentary Parameters for computer modeling, sedimentary modeling: computer simulation and methods for improved parameter definition, vol 233. In: Franseen EK, Watney WL, St. CG Kendall, Ross W (eds) Kansas Geological Survey, pp 63–98

Fawzy H, Abdel Aal A (1984) Regional study of Miocene evaporates and Pliocene–recent sediments in the Gulf of Suez. In: 7th EGPC Exploration Seminar, Egyptian General Petroleum Corporation, Cairo, Egypt, pp 49–74

Garfunkel Z (1988) Relation between continental rifting and uplifting: evidence from the Suez rift and northern Red Sea. Tectonophysics 150:33–49

Garfunkel Z, Bartov Y (1977) The tectonics of the Suez rift. Geol Surv Isr Bull 71:45

Geriesh MH, El-Rayes AE, Fouad A (2004) Runoff control and water management in WadiGhweabae hydrographic basin, Northwest of Gule of Suez region, Egypt. In: Proceedings of 7th conference on Geology of Sinai for Development, Ismailia, pp 53–67

Gheith AM, El-Sherbini ME (1993) Post-Miocene Sedimentation in the Gulf of Suez, Egypt. JKA U Mar Sci 4:73–92

Gradstein FM, Ogg JG, Schmitz MD, Ogg GM (2012) The geologic time scale. Elsevier. https://doi.org/10.1016/b978-0-444-59425-9.10003-4

Guillocheau F, Rouby D, Robin C, Helm C, Rolland N, Carlier Le, de Veslud C, Braun J (2012) Quantification and causes of the terrigeneous sediment budget at the scale of a continental margin: a new method applied to the Namibia-South Africa margin. Basin Res 24:3–30. https://doi.org/10.1111/j.1365-2117.2011.00511.x

Hampson GJ, Duller RA, Petter AL, Robinson RAJ, Allen PA (2014) Mass-balance constraints on stratigraphic interpretation of linked alluvial-coastal-shelfal deposits from source to sink: example from Cretaceous Western Interior Basin, Utah and Colorado, U.S.A. J Sed Res 84:935–960

Haq BU, Al-Qahtani AM (2005) Phanerozoic cycles of sea-level change on the Arabian Platform. GeoArabia 10(2):127–160

Hardenbol J, Thierry J, Farley MB, Jacquin T, de Graciansky PC, Vail P (1998) Mesozoic and Cenozoic sequence chronostratigraphic framework of European basins. In: Gracianski PC et al (eds) Mesozoic and cenozoic sequence stratigraphy of European Basins: SEPM special publication, vol 60, pp 3–13, charts 1–8

Hooke RL (1968) Steady-state relationships onarid-region alluvial fans in closed basins. Am J Sci 266:609–629

Jackson CA-L, Rotevatn A (2013) 3-D seismic analysis of the structure and evolution of a salt-influenced normal fault zone: a test of competing fault growth models. J Struct Geol 54(2013):215–234

Kennan L, Lamb SH, Hoke L (1997) High-altitude palaeo surfaces in the Bolivian Andes; evidence for late Cenozoic surface uplift. In: Widdowson M (eds) Palaeo surfaces; recognition, reconstruction and palaeo environmental interpretation, special publication, The Geological Society in London, vol 120, pp 307–323

Moretti I, Colletta B (1987) Spatial and temporal evolution of the Suez Rift subsidence. J Geodyn 7:151–168

Moustafa AR (1996) Internal structure and deformation of an accommodation zone in the northern part of the Suez rift. J Struct Geol 18:93–107

Moustafa AG (1976) Block faulting in the Gulf of Suez. In: Proceedings of the 5th petroleum exploration and production seminar, Egypt, vol 1, 19p

Orszag-Sperber F, Purser BH, Rioual M, Plaziat JC (1998) Post Miocene sedimentation and rift dynamics in the southern Gulf of Suez and northern Red Sea. In: Purser BH, Bosence DWJ (eds) Sedimentation and tectonics of rift basins: Red Sea-Gulf of Aden. Chapman and Hall, London, pp 427–447

Patton TL, Moustafa AR, Nelson RA, Abdine SA (1994) Tectonic evolution and structural setting of the Suez Rift. In: London SM (ed) Interior rift basins, vol 59. American Association of Petroleum Geologists Memoir, pp 7–55

Pechlivanidou S, Cowie PA, Hannisdal B, Whittaker AC, Gawthorpe RL, Pennos C, Riiser OS (2017) Source-to-sink analysis in an active extensional setting: Holocene erosion and deposition in the Sperchios rift, central Greece. Basin Res. https://doi.org/10.1111/bre.12263

Peihzen Z, Molnar P, Downs WR (2001) Increase sedimentation rates and grain sizes 2-4 Myr agodue to the influence of climate change on erosion rates. Nature 410:891–897

Plaziat J-C, Baltzer F, Choukri A, Conchon O, Freytet P, Orszag-Sperber F, Raguideau A, Reyss J-L (1998) Quaternary marine and continental sedimentation in the northern Red Sea and Gulf of Suez (Egyptian coast): influences of rift tectonics, climatic changes and sea-level fluctuations. In: Purser BH, Bosence DWJ (eds) Sedimentation and Tectonics in Rift Basins Red Sea: Gulf of Aden. Springer, Dordrecht

Poag CW, Sevon WD (1989) A record of Appalachian denudation in post-Rift Mesozoic and Cenozoic sedimentary deposits of the U.S. Middle Atlantic Continental margin. Geomorphology 2:119–157

Richardson M, Arthur MA (1988) The Gulf of Suez-northern Red Sea Neogene rift: a quantitative basin analysis. Marine Pet Geol 5:247–270

Rioual M (1996) Sedimentation et tectonique post-Miocene dans Ie rift du Golfe de Suez et Ie NW de la Mer Rouge (Egypte). Doctoral Thesis, Universite de Paris Sud, 240 pp

Rohais S, Barrois A, Colletta B, Moretti I (2016) Pre-salt to salt stratigraphic architecture in a rift basin: insights from a basin-scale study of the Gulf of Suez (Egypt). Arab J Geosci 9:317. https://doi.org/10.1007/s12517-016-2327-8

Rohais S, Bonnet S, Eschard R (2012) Sedimentary record of tectonic and climatic erosional perturbations in an experimental coupled catchment-fan system. Basin Res 24:198–212. https://doi.org/10.1111/j.1365-2117.2011.00520.x

Rouby D, Bonnet S, Guillocheau F, Gallagher K, Robin C, Biancotto F, Dauteuil O, Braun J (2009) Sediment supply to the Orange sedimentary system over the last 150 My: an evaluation from sedimentation/denudation balance. Mar Petrol Geol 26:782–794

Said R (1990) Cenozoic. In: Said R (ed) The geology of Egypt. Balkema, Rotterdam, pp 451–486

Said R (1962) The Geology of Egypt. Elsevier Pub!. Co., Amsterdam, New York, 377 p

Saito K, Oguchi T (2005) Slope of alluvial fans in humid regions of Japan, Taiwan, and Philippines. Geomorphology 70:147–162

Steckler MS (1985) Uplift and extension at the Gulf of Suez: indications of induced mantle convection. Nature 317:135–139

Steckler MS, Bertholot F, Lyberis N, Le Pichon X (1988) Subsidence in the Gulf of Suez: implications for rifting and plate kinematics. Tectonophysics 153:249–270

Steckler MS, Omar GI (1994) Controls on erosional retreat of the uplifted rift flanks at the Gulf of Suez and Northern Red Sea. J Geophys Res 99:12159–12173

Syvitski JPM, Morehead MD (1999) Estimating river—sediment discharge to the ocean: application to the Eel Margin, northern California. Mar Geol 154:13–28

Syvitski JPM, Peckham SD, Hilberman RD, Mulder T (2003) Predicting the terrestrial flux of sediment to the global ocean: a planetary perspective. Sed Geol 162:5–24. https://doi.org/10.1016/j.sedgeo.2003.11.001

Sømme TO, Helland-Hansen W, Martinsen OJ, Thurmond JB (2009) Relationships between morphological and sedimentological parameters in source-to-sink systems: a basis for predicting semi-quantitative characteristics in subsurface systems. Basin Res 21:361–387

Whitakker AC, Attal M, Allen PA (2010) Characterising the origin, nature and fate of sediment exported from catchments perturbed by active tectonics. Basin Res 22:809–828

Willett SD, McCoy SW, Perron JT, Goren L, Chen C-Y (2014) Dynamic reorganization of river basins. Science 343:1248765. https://doi.org/10.1126/science.1248765

The Southern Atlas Front in Tunisia: Regional-Scale Geometry and Structural Evolution

Mohamed Gharbi, Amara Masrouhi, Olivier Bellier, and Mohamed Ben Youssef

Abstract

This chapter provides an overview of data-compilation, recently published, as well as newly collected data on the structure and evolution of Southern Atlas front in Tunisia. The Northern Chotts Range, one of most geologic features in southern Atlas, separates a dominantly deformed area of Gafsa to the north, from a relatively undeformed area of Chotts basin and Saharan platform to the south. The Cenozoic contractional period shapes a chain with mixed thick- and thin-skinned tectonic style, controlled by deep-seated basement faults with shallower décollement within the sedimentary cover. The present-day general "en echelon" fold distribution of the overall Northern Chotts Range, the age and the geometry of units, are likely the surface expression of the "en echelon" WNW- to- NW-trending faulting, which controls the fold's emplacement and style. These systems usually exhibit a fault kinematics, with striation showing a multiphase history. During Mesozoic times, the extensional activity of WNW- to- NW-trending normal faults is associated with significant thickness and/or facies variations comprising abundant syntectonic sequences. The growth of major synsedimentary typical normal fault systems, which produce a general framework delivering tilted blocks basin geometry, displays well-developed half-graben fill and large rollover structures along the southern Atlas. The Northern Chotts Range is, therefore, considered as the results of the Mesozoic inherited faults reverse–reactivation. The Chotts basin was previously considered as a large anticline related to the Cenozoic compressional events to explain the gentle deep observed "antiform structure". It was, therefore, marked as the far-foreland of the southern Tunisian Atlas. Like many other inverted margin, extensional inherited structures are still preserved in the southern Tunisian Atlas. The Chotts preserves Mesozoic extensional structures, of which the so-called Chotts anticline is defined in this study as large inherited rollover structure. The subsequent tertiary compressional front will be, therefore, repositioned in the Northern Chotts Range Front.

5.1 Introduction

The relative motions between Africa and Europe have recorded, in Tunisian Atlas, a kinematic evolution of a long-living Alpine foreland structure. In northwestern Africa, the Maghrebian fold-and-thrust belt extends about 2000 km from Morocco to Tunisia. This chain, which define the Atlas orogen, is acknowledged as one of some type-example of intercontinental chain (Ziegler et al. 1995; Guiraud 1998; Beauchamp et al. 1999; Frizon de Lamotte et al. 2000; Laville et al. 2004; Roure et al. 2012; Gharbi et al. 2015). This belt result from polyphase tectonic history related to the collision between Africa and Eurasia started at about 70 Ma (Roure and Colletta 1996; Bracène and Frizon de Lamotte 2002; Guiraud et al. 2005; Said et al. 2011b; Frizon de Lamotte et al. 2011; Masrouhi and Koyi 2012; Roure et al. 2012; Masrouhi et al. 2014a, b; Van Hinsbergen et al. 2014; Gharbi et al. 2015; El Amari et al. 2016). The complex geodynamic history shaped this belt, records mainly two major periods. The first one of Mesozoic rifting

M. Gharbi (✉) · M. Ben Youssef
Water Research and Technologies Center, Geo-Resources Laboratory, Borj-Cedria, Soliman, Tunisia
e-mail: gharbim.mohamed@gmail.com;
mohamed.gharbi@certe.rnrt.tn

A. Masrouhi
King Abdulaziz University, Faculty of Earth Sciences,
Geo-exploration Techniques Department, Jeddah, Saudi Arabia

O. Bellier
Aix Marseille Univ, CNRS, IRD, Coll France, CEREGE,
Aix-en-Provence, France

occurred after the late Paleozoic collision with Laurasia, is followed by passive margin stage defined the Tethyan Mesozoic evolution. A second Cenozoic period during which active compressional tectonic prevailed from Late Cretaceous to present-day (Ziegler et al. 1995; Piqué et al. 2002; Laville et al. 2004; Guiraud et al. 2005; Said et al. 2011b; Roure et al. 2012; Gharbi et al. 2013, 2015; El Amari et al. 2016). This period is responsible for the major uplift in the evolution of the belt overprinting the inherited Tethyan structures during successive stages. The overprinting of two different large-scale system is expressed in the Southern Atlas of Tunisia by multidirectional structures.

Different tectonics reconstructions and/or models were made to explain the multidirectional structures along the Southern Atlas of Tunisia. Previous studies of the structural styles in southern Atlas of Tunisia distinguish four different models and can be summarized as follows: (i) "en echelon folds related mainly to the NW-trending dominant strike slip faults (Zargouni 1984; Zargouni et al. 1985; Abbès and Zargouni 1986; Burollet 1991; Abbès et al. 1994; Bédir et al. 2001) (ii) recent thrust systems deformed the sedimentary cover with a preferential decollement level localized in the Triassic evaporites themselves separate the sedimentary cover from the rigid ante-Mesozoic basement (Outtani et al. 1995; Ahmadi et al. 2006, 2013) (iii) active Mesozoic salt diapirism nucleated the subsequent fold location (Hlaiem 1999; Zouaghi et al. 2011) (iv) reactivation of preexisting Mesozoic inherited faults coupled to variable distribution of sequences led to identify a shallow decollement levels and recorded deep basement fault inversion at depth (Gharbi et al. 2013, 2015; El Amari et al. 2016).

This paper summarizes the tectono-sedimentary data acquired during the last decade in the South Atlas front of Tunisia. Data are coupled to new seismic interpretation to reconstruct the tectonic style and deformation history of the far-foreland of Tunisia. Sequential restoration has been developed to consider the style of extension during the Mesozoic times. The extension amount is calculated (amount of extension/Time) for keys-periods to precise the rift stage expansion of the southern Tethyan margin in Tunisia.

5.2 Geological Setting

5.2.1 Structural Pattern

The Atlas Mountains, that extends from Morocco to Tunisia, is a fold-and-thrust belt (named by authors the Maghrebides belt) formed during the alpine orogeny. The eastern part of this belt (Fig. 5.1a) lies the Tunisian domain including: (i) the Tellian domain in the north which corresponds to the Alpine Tellian thrust range. This orogen consists, in its Tunisian portion, of thrust sheets transported southeastward during Middle Miocene paroxysmal compressional event. (ii) In the south, the Tunisian Atlas is divided into three domains, so-called by authors as the Northern, the Central, and the Southern Tunisian Atlas.

Major NW-trending lateral strike-slip faults (Gafsa and Negrine-Tozeur, Fig. 5.1b) are recognized in the southern Tunisian Atlas fold-and-thrust belt. They were structurally connected to the present-day distribution of folds during the 70s and 80s reconstructions. The 100-km-long Gafsa's dextral strike-slip fault is a NW-trending system, which cuts the Bou Ramli, Ben Younes and Orbata anticlines in the north and the Zemlet el Beidha and Koudiat Hammamet anticlines in the south (Zargouni 1984; Zargouni et al. 1985; Abbès and Zargouni 1986; Burollet 1991; Abbès et al. 1994; Hlaiem 1999). Westward, the Gafsa–Metlaoui basin is recognized by previous work as delineated by a second dextral strike-slip fault system named Negrine–Tozeur fault (Zargouni 1984; Zargouni et al. 1985). In the eastern part, and from north to south, the Sehib, Berda, Chemsi and Belkheir folds separate the Gafsa–Metlaoui basin from the northern Chotts range (Fig. 5.1b). The Northern Chotts range lies the southernmost folded segment in the Southern Atlas Front of Tunisia, which is composed of the Askar, Bir Oum Ali, Hachichina, Beidha, and Zemlet el Beidha anticlines. These aforementioned east-trending anticlines, separate the Metlaoui–Gafsa Basin from the Chotts Basin in the south. The gentle south-dipping series observed at the southern Chotts Range, were used to interpret the Chotts basin as a large anticline bounded by the curved Tebaga de Kebili ridge at the southern edge of the Chotts El-Fejej (Zargouni and Abbes 1987; Fakraoui 1990; Bouaziz et al. 1994; Swezey 1996). Otherwise, the Chotts basin is a foredeep depozone of the Atlassic foreland system (DeCelles and Giles 1996; Said et al. 2011b; Gharbi et al. 2013, 2015). This basin is considered as a Mesozoic graben bordered, to the northern and southern sides, by contemporaneous normal fault systems (Fig. 5.1b). More recently, Gharbi et al. (2015) published a ~120 km-long-balanced cross-section of region. Authors were interpreted for the first time that this large anticline is likely a wide Mesozoic rollover limited to the south by the preserved Tebaga Kebili normal fault system.

The present-day southern Tunisian Atlas fold-and-thrust belt shape is the result of the positive inversion of the southern Tunisian Tethyan margin mini-basins of compressional tectonic that prevailed during Cenozoic times, shows two main contractional stages. The first stage corresponds to the rifting stage, highlighted for Late Permian (?) to the Early Cretaceous (Guiraud 1998; Piqué et al. 2002). An extensional tectonic regime dominates this period which is contemporaneous with the Tethyan and Atlantic opening. Early Triassic salt basins were formed, during the earlier stage of this evolution (Soussi et al. 2017) covered all of

Fig. 5.1 a Structural sketch map of the Atlas belt within its geodynamics context. Gray arrows represent the present-day NW to N oriented horizontal compression related to the convergence between Africa and Europe (after Michard et al. 2002; Faccenna et al. 2004; Serpelloni et al. 2007; Billi et al. 2011). Black square indicates the location of the study area. **b** Simplified geological map of the southern Atlas foreland of Tunisia. Using the geographic Coordinate system (modified Gharbi et al. 2015). Locations of seismic lines (with blue colors) and wells are shown (with red colors). Detailed geological map of the Zelmet el Beidha of Fig. 5.3 and the Bir Oum Ali–Hachichina structure of Fig. 5.9 are shown by the black frame
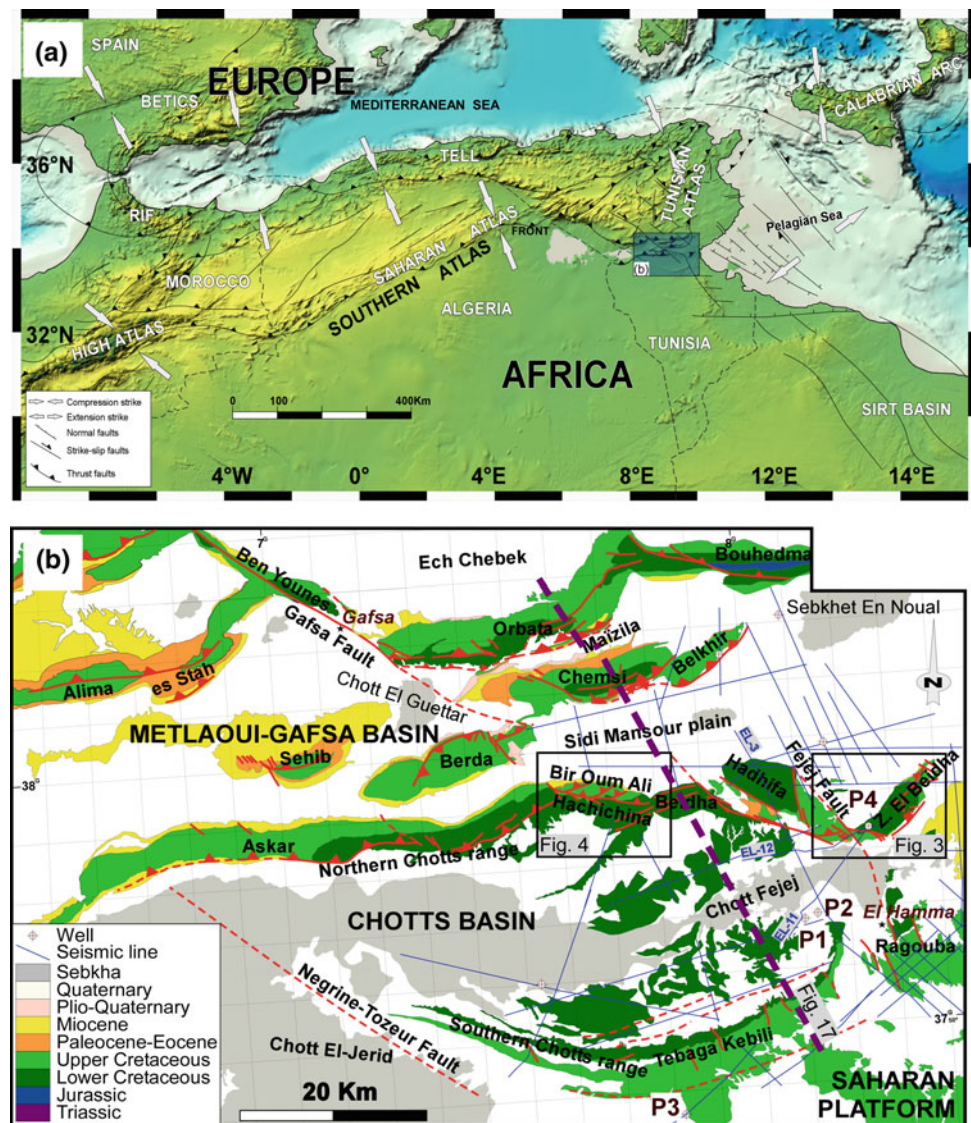
what is now Tunisia. The extensional setting prevailed during Jurassic and Early Cretaceous (Boughdiri et al. 2007; Souquet et al. 1997; Masrouhi and Koyi 2012; Masrouhi et al. 2014a) is related to the opening of Tethyan and the Central Atlantic. This extensional tectonic regime was also accompanied, in several regions of the Atlas, by volcanic and halokinetic activity testifying to the extensional nature of these periods (Laaridhi-Ouazaa 1994; Guiraud et al. 2005; Mattoussi Kort et al. 2009; Masrouhi et al. 2014a, b). During Aptian–Albian times, the extensional activity is associated with WNW- to- NW-trending normal faults that are associated with significant thickness and/or facies variations comprising abundant syntectonic sequences (Gharbi et al. 2013), in addition to active salt tectonic. The Aptian–Albian times are identified as time of maximum extension in the Tunisian southern Tethyan margin basins, which are especially well documented for the Early Cretaceous rifting stage

(Souquet et al. 1997; Bouaziz et al. 1999; Gharbi et al. 2013; Masrouhi et al. 2014b; El Amari et al. 2016). During Cenomanian to Santonian times, the Tethyan extensional basin in Tunisia has received mostly pelagic to hemi-pelagic sediments, typifying a slow deposition product of a post-rift subsidence-related sequences (Morgan et al. 1998; Gharbi et al. 2015).

The second main stage, started since Late Cretaceous, corresponds to compressive events that had caused the inversion along the inherited normal fault and the initiation of folding and trigger a positive tectonic inversion related to the Africa and Eurasia plate convergence (Guiraud and Bosworth 1997). The southern foreland fold-and-thrust belt of Tunisia results from two main superimposed compressional events: Mid-to-late Eocene defining the Atlassic contractional event (Frizon De Lamotte et al. 2000; Masrouhi et al. 2008; Khomsi et al. 2009; Gharbi et al. 2015)

and Middle–Late Miocene to present-day compression corresponding to the Alpine compression event (Zargouni and Ruhland 1981; Zargouni and Termoliéres 1981; Zouari et al. 1990; Chihi 1992; Dlala 1992; Said et al. 2011a; Gharbi et al. 2014; El Amari et al. 2016).

5.2.2 Generalized Lithostratigraphy of the Southern Atlas Domain

The lithostratigraphy of the southern Atlas of Tunisia domain is derived from outcrops around the Chotts Basin and exploration well data. The Mesozoic–Cenozoic lithostratigraphy of units that are exposed in study area is illustrated in the log of Fig. 5.2.

The oldest rocks exposed in the field belong to Trias and are known in the Hadifa diapir. Triassic series consist of evaporites, red claystones, sandstones, anhydrites, halite, carbonates and gypsum deposited with a continental origin during the pre-rifting in relation to the crustal extensional movement of the Tethyan passive margin are started along the African plate (Stampfli et al. 1991; Ben Ismaïl 1982; Kamoun et al. 2001; Bouaziz et al. 2002). The Triassic Formation show important variations that can reach thicknesses of more than 800 m in petroleum wells. During the Jurassic stage, the rifting continuous by a shallow water

Fig. 5.2 Synthetic stratigraphic and lithotectonic sedimentary columns Northern Chotts Range. Major unconformities are enhanced by a wavy line
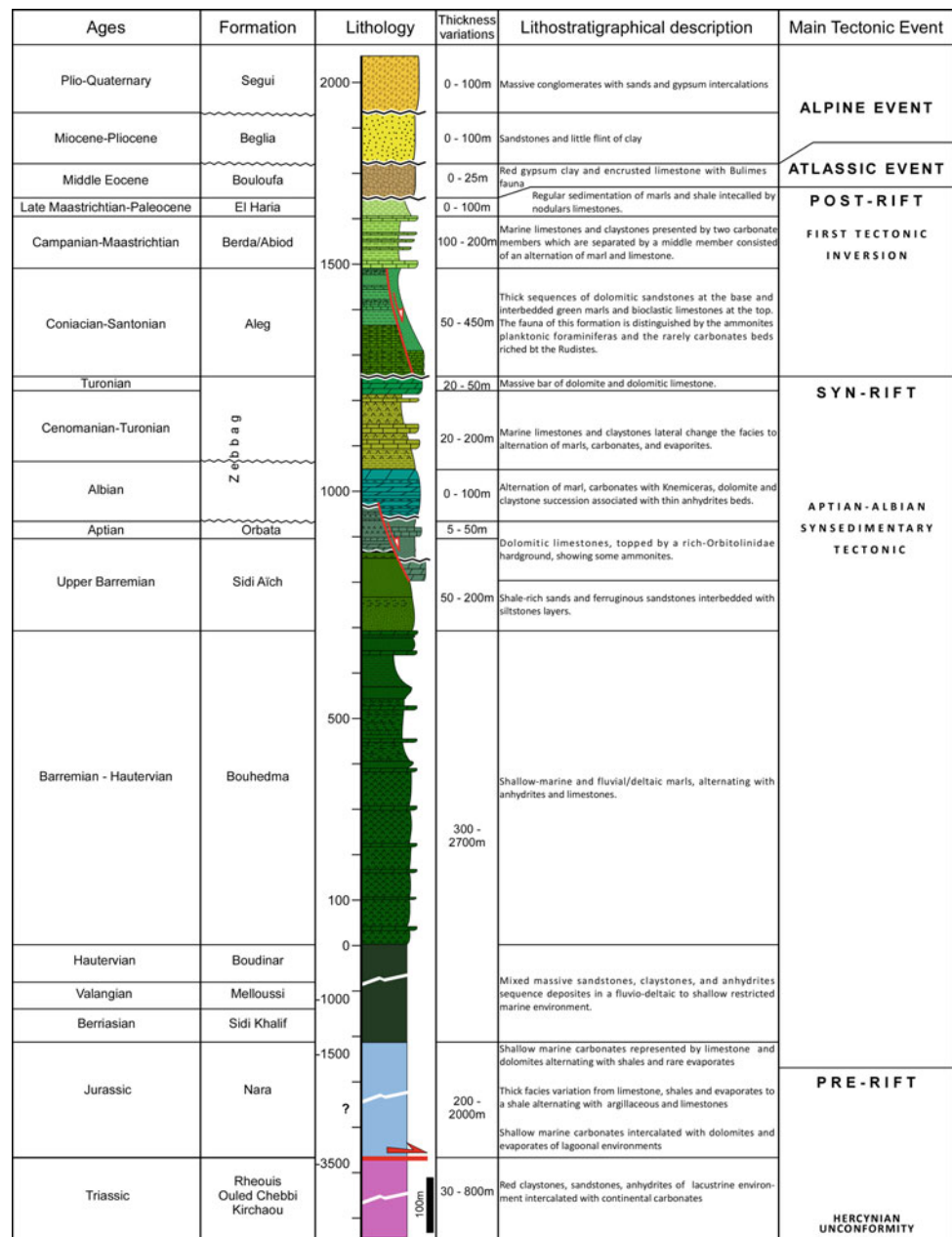
marine deposits at the Lias (Faure and Peybernes 1986; Soussi 2002; Sekatni et al. 2008) followed by the lagoon to marine deposits of the Middle and late Jurassic series which mainly consist of thick limestones intercalated with dolomites, claystones and anhydrites (Tlig 2015). Thicknesses range from ∼200 m in the Kebili to 2000 m in the exploration wells along the Chotts Fejej. This extensional tectonic regime accompanied with highly subsidence, continued during the early Cretaceous. The Early Cretaceous transgression is accompanied by shallow marine conditions invaded the Southern Atlas. Sequences have started with the deposition of Berriasian–Hauterivian continental deposits of the Sidi Khalif, Melloussi and Boudinar Formation. At the base, these deposits typify a shallow restricted marine environment to fluvio-deltaic sequences consisting of mixed sandstones, anhydrites and claystones (Marie et al. 1984; M'Rabet 1987; Boukhalfa et al. 2015). The above-described sequences are overlain by shallow-marine and fluvial/deltaic marls, alternating with anhydrites and limestones Hauterivian–Barremian Bouhedma Formation (Damotte 1990). Thickness of Hauterivian–Barremian continental deposits varies from 300 m in the Metlaoui–Gafsa basins (Riley et al. 2011; Gharbi et al. 2015) to 2000 m in the LMG-1 well in

the southern part (El Amari et al. 2016). The Hauterivian–Barremian Bouhedma Formation crops out mainly in the core of the Northern Chotts Range anticlines (e.g., the Koudiat Hammamet, Zemlet el Beidha and Beidha anticlines; Figs. 5.1b and 5.3). The Bouhedma Formation is overlain by shale-rich sands and ferruginous sandstone of Sidi Aïch Formation recently dated by Boukhalfa et al. (2015) as Late Barremian. In the southern Tunisian Atlas, the Sid Aïch Formation's thicknesses range between from ∼50 to 200 m. During the Aptian times, the deposition of the Orbata Formation characterized by the syn-rift sediment (Ben Youssef et al. 1985; Ben Youssef and Peybernes 1986; Lazzez and Ben Youssef 2008) was generally related to a transgression that invaded all of is what now the Northern Chotts range. The Orbata Formation conformably overlies the Sidi Aich Formation, in all sections described in this belt (Ben Youssef and Peybernes 1986; Louhaichi and Tlig 1993; Gharbi et al. 2013, 2015). The Orbata Aptian-aged is commonly described as composed at the base by the Bedoulian dolomitic bar that is capped by the marly and sandy carbonates. The top of this Formation consists of Gargasian sandy unit. In the Chotts basin, during the hiatus from the upper Aptian (Clansaysian) to the lower–Middle
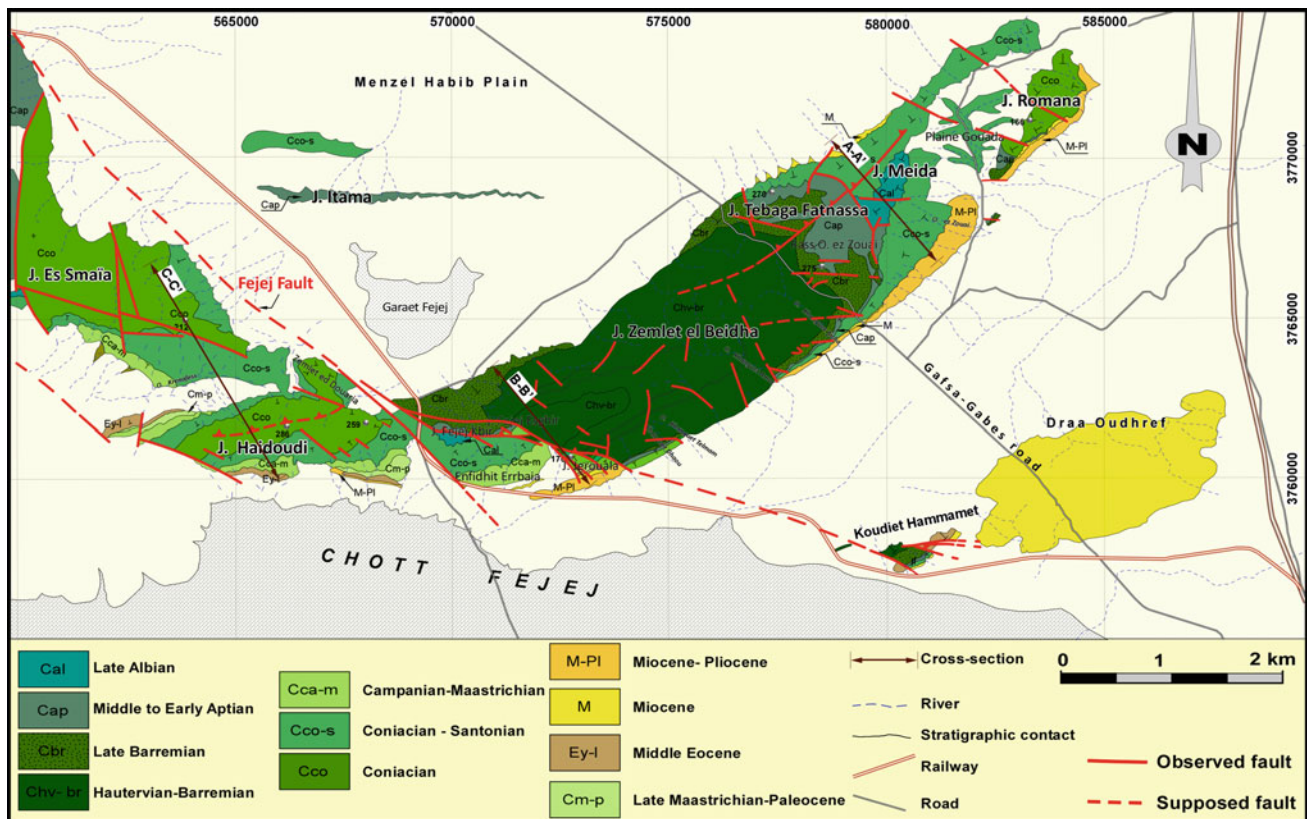
Fig. 5.3 Detailed geological and structural map of Zemlet el Beidha-Jebel Haidoudi structure (ZBHS). See location on Fig. 5.1b (Gharbi et al. 2013). Coordinate system is UTM zone 32, WGS 84 system (metres). Location of the cross section of Fig. 5.4 is shown

Albian which is named Aptian–Albian crisis is probably related to tilted blocks geometry prevailed during the Aptian–Albian rifting (Ben Youssef and Peybernes 1986; Guiraud and Maurin 1992; Souquet et al. 1997). During this period, of significant tectonic extension, thicknesses range from few meters in the East to ~50 m in the Bir Oum Ali structure (central part of the Northern Chotts Range (Fig. 5.1b)). Following this period, an Albian transgression invaded (Ben Youssef 1999; Guiraud et al. 2005) the Southern Tunisian Atlas, leading to the deposition of dolomite and claystone sequences interbedded with thin anhydrites beds. In the southern part (Tebaga Kebili; Figs. 5.1b and 5.2), the Zebbag Formation thick sequences of massive dolomite covers the Albian series. The Albian marine deposits range from a few meters in eastward of the Northern Chotts Range to a maximum observed thickness of ~100 m in the Jebel Berrani (South Bir Oum Ali, Figs. 5.1b and 5.2) to. During Late Cretaceous, a general regional transgression is recorded during the Cenomanian–Turonian times. This later is accompanied by the deposition of marine limestones and claystones ranged by authors as the upper member of the Zebbag Formation. Significant thickness variations exist also in these marine series, which are from ~20 m in Northern Chotts Range to ~200 m in the Tebaga Kebili.

The above-described Zebbag Formation is usually capped by massive bar of dolomite and dolomitic limestone of the Guettar member dated as Uppermost Cenomanian–Early Turonian (Abdallah et al. 1995; Abdallah and Meister 1997). The Coniacian–Santonian-aged Aleg Formation, is composed by thick sequences of the post-rift sediments (Gharbi et al. 2013, 2015; El Amari et al. 2016). These sequences are made of dolomitic sandstones at the base and interbedded green marls and bioclastic limestones at the top. Campanian–late Maastrichtian series consist of marine limestones and claystones of the Abiod Formation (locally named Berda Formation) and characterized by significant thickness and facies variations. Thicknesses range from ~80 m in Northern Chotts Range to ~400 in the Tebaga Kebili (Figs. 5.1b and 5.2). The late Cretaceous sequences are overlain by the marine dark marls of El Haria Formation dated as Maastrichtian–Paleocene. The Paleocene series show a lateral variation of thickness which are ranged from few meters in the East to ~80 m in the Bir Oum Ali structure. This previously mentioned sequences are normally overlain by the Eocene Limestone of Metlaoui Formation in western part of the Northern Chotts Range and by the Eocene continental carbonate of Bouloufa Formation in the Eastern part. The Miocene sandstones of the Beglia Formation unconformably overlie the Eocene series. The continental Mio-Pliocene Segui Formation, considered as syntectonic sequences, is the result of the reliefs erosion that were uplifted during contemporaneous compressional event. This Formation unconformably overlie all the above-mentioned series along the chain.

5.3 The Northern Chotts Range Structure

The structural arrangement of the Northern Chotts Range shows E- to NE-trending folds as shown in Fig. 5.1b, and regional NW- to WNW-trending oblique faults systems (e.g., El Fejej and Negrine–Tozeur faults; Zargouni 1985; Zargouni et al. 1985; Zargouni and Abbes 1987; Gharbi et al. 2013, 2015; El Amari et al. 2016).

Most of previous studies, propose a scenario in which the Northern Chotts range results from the NW-trending lateral strike-slip faulting (Zargouni 1985; Zargouni et al. 1985; Rabiaa 1985; Fakraoui 1990; Fakraoui et al. 1991; Abbès et al. 1994; Bédir 1995) associated with asymmetric "en echelon" fold with steeper southern limbs than gentle northern limbs. A second interpretation was presented with fault-propagation model generated folding during the Cenozoic thin-skinned tectonics (Creuzot et al. 1993; Outtani et al. 1995; Ahmadi et al. 2006, 2013). Based on a geologic mapping, lithotectonic sedimentary sections identification together with seismic reflection data, a recent study of Gharbi et al. (2015) concluded that the Northern Chotts Range, separates two sedimentary basins in which tectonic style is different. The northern one corresponds to the Metloui–Gafsa basin where the deformation is mainly controlled by deep thick-skinned and shallow thin-skinned thrusting. The southern part, including the Chotts basin, illustrates mainly a deformation governed by the deep thick-skinned tectonics.

The following sections address the structural analysis of the Northern Chotts Range, which is based on field observations across the Eastern and the central parts of the Range, and interpretation of seismic reflection profiles across the Chotts Fejej Basin.

5.3.1 Geologic Field Data and Structural Analysis

Data used are derived from the preexisting 1/25000 geologic map published by Gharbi (2013) and El Amari et al. (2016), of the Zemlet el Beidha-Jebel Haidoudi (ZBHS) and Bir-Oum Ali–Hachichina structure (BOAHS), and controlled by six surface geological cross-section. Fault kinematics analysis, provides an idea on the Cretaceous tectonic regime in the Northern Chotts Range. Seismic interpretation coupled to surface data is exploited as a part of this work to
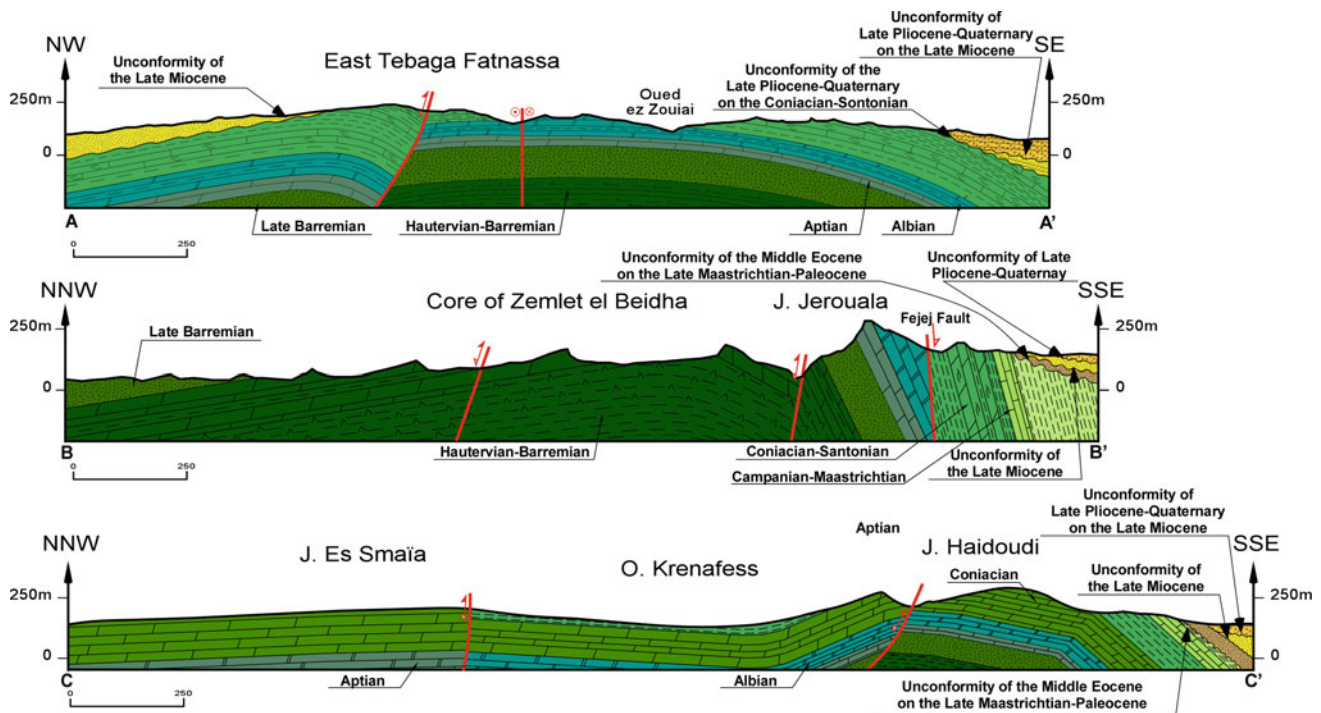
Fig. 5.4 Geological cross sections showing the tectonic style of Zemlet el Beidha-Jebel Haidoudi structures (ZBHS). For location, see Fig. 5.3

dissect the local style and the development of the Northern Chotts Range in its ZBHS and BOAS portions (Fig. 5.1b, 5.3, 5.4 and 5.5).

5.3.1.1 Zemlet El Beidha-Jebel Haidoudi Structure

The ZBHS is located in the eastern part of the Northern Chotts range. This structure, of about 24 km long, have a curve-shaped geometry (Fig. 5.1b and 5.3) with two main anticlines separated by the NW-trending Fejej fault.

The Zemlet el Beidha is a south-to-south-east verging asymmetric anticline with only an east closure and shows, from west to east, a curved axis that changes from E strike to NE strike (Fig. 5.3). This 16 km long and 3–5 km wide structure, is located between the Menzel Habib plain to the north and the Chotts Fejej and Draa Oudhref respectively southwest and southeast (Fig. 5.3). The Zemlet el Beidha anticline is respectively cored by the Hauterivian–Barremian in the central part, the Albian in the Jebel Meida and the Coniacian–Santonian in the Jebel Romana and Gouada plain (Fig. 5.3). This structural arrangement, simple at surface, is illustrated by two geological cross sections presented in Fig. 5.4. The north-eastern segment of the ZBHS, as shown by the cross-section A–A', is a gentle deformed Cretaceous sequences covered unconformably by Late Miocene–Pliocene to Quaternary series. Along this cross section A–A', the surface geometry of the ZBHS shows a $\sim 20°$ N-dipping

backlimb made of Coniancian–Santonian green marls alternated with bioclastic limestones unconformably overlain by Miocene continental sandstones. The forelimb is formed by the Aleg 45° S-dipping Formation, itself unconformably overlain by the Segui late Plio-Quaternary Formation. Eastward of the Djebel Tebaga Fatnassa a disturbance of dips is recorded in the limestones of the Aleg Formation possibly associated with N-dipping reverse faulting (Figs. 5.3 and 5.4). Westward at the central part of the ZBHS, numerous N100–110°E apparent trending strike-slip faults, along Khanguet Aïcha and Khanguet Amor, regions affect the 45° S-dipping limb (Fig. 5.3).

Along the second surface elaborated B–B' cross-section (Figs. 5.3 and 5.4; the western part of the ZBHS), at the Jebel Fejej and Jebel Jerouala, shows a northern limb formed by late Barremian sequences that dips $\sim 5°–10°$ northward while the southern limb dips about 70°–80° southward. The ZBHS shows a highly deformed forelimb geometry usually affected by the NW to WNW-trending Fejej strike-slip systems (Figs. 5.3 and 5.4; Abdeljaouad and Zargouni 1981; Zargouni et al. 1985; Abbès and Zargouni 1986; Abbès et al. 1994). The striae measured on the fault planes of the Jebel Jerouala and Jebel Fejej (see sites c and d in Fig. 5.5) are rotated to reestablish their bedding to its initial horizontal orientation. Using the fault diagram, the back-tilting of these NW-trending apparent strike-slip fault give a result of SW-dipping normal faults. The structural
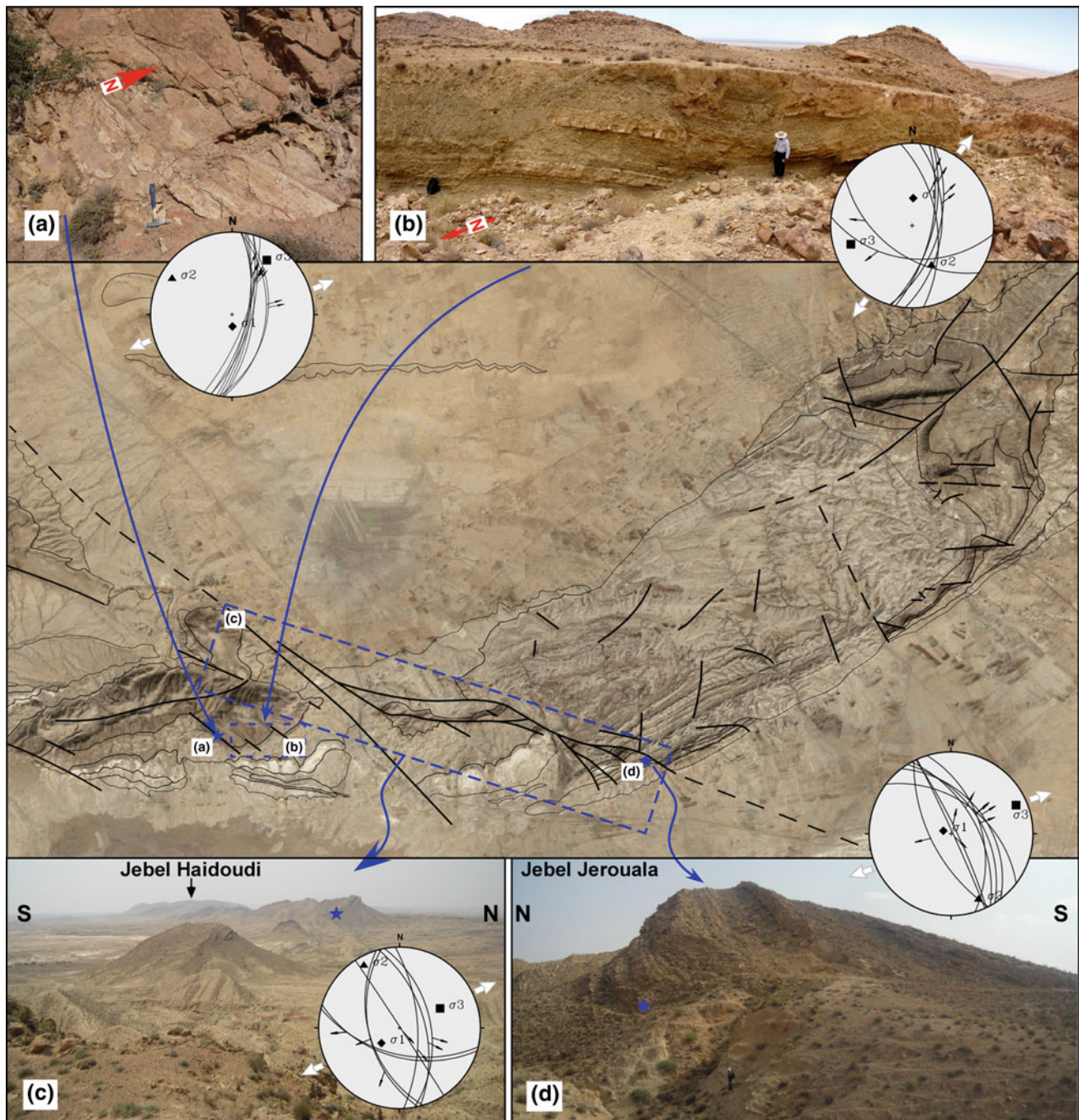
Fig. 5.5 Based on Google Earth satellite images, the structural mapping of Zemlet el Beidha-Jebel Haidoudi structure (ZBHS) shows the Cretaceous extensional (normal faulting) tectonic regime resulting from the back-tilting diagram. **a** Striations recorded on fault plane indicates a Coniacian normal faulting characterized by NE-trending extension. **b** Coniacian–Santonian normal faulting (recorded on south flank of the Jebel Haidoudi anticline) associated with NE-trending extensional tectonic regime. **c** West-looking panoramic view of the tilted bloc structures from the Jebel Khaguet Telmam to Jebel Fejej through Jebel Jerouala related to a regional NE-trending extension regime. **d** Synsedimentary normal fault with lower hemisphere stereograms of fault slip data and shown the NNE-trending direction of extension. Red dashed plane corresponds to the bedding plane

analysis portrays a Cretaceous extensional tectonic regime characterized by NE-trending state of minimum stress axis (Fig. 5.5c, d).

The fault kinematic analysis carried out by Gharbi et al. (2013) shows that restoration of the back-tilted of all ZBHS present-day apparent strike-slip faults, testifies to the

occurrence of normal faults activity developed during a NE-trending Cretaceous extensional tectonic regime. The geologic map and the fault kinematics analysis, of this work, portray an ancient normal faulting reactivated as strike-slip ones well observed in the Khanguet Aïcha as well as the Khanguet Amor (see Fig. 5.3) is. The Cretaceous inherited faults affect the Hauterivian to Albian series and are regularly sealed by the Coniacian–Santonian Formation (Gharbi et al. 2013). Along the ZBHS area, the normal faulting is usually associated with thickness and facies variations, which explicitly concerns the Aptian–Albian sequences. The normal faulting activity is associated in the ZBHS with syntectonic conglomerates that were deposited in the half-grabens structures (a, b, c in Fig. 5.6; Gharbi et al. 2013). The extensional tectonic movement forms the growth strata into some hanging-walls like the preserved listric normal fault in Jebel Tebaga Fatnassa (Fig. 5.7). The Late

Barremian–Aptian dolomite strata is cut by the NE-trending preserved normal. The tilted block geometry records the Aptian growth strata and indicates their normal activity during the Aptian stage. The normal faulting continues during the Albian times and creates the growth-strata geometry into hanging-walls. The E-dipping normal fault cuts the Albian sequences of the Jebel Es Smaïa (Figs. 5.3 and 5.8) and generates growth strata.

Along the 2.5 km-long NNW–SSE surface C–C' cross section, across Jebel Es Smaïa at the north and the Jebel Haidoudi anticline at the south (Figs. 5.3 and 5.4). Here, the fold Jebel Haidoudi is an asymmetric fold with a core occupied by Coniacian dolomites showing a $\sim 15°$ to $\sim 20°$ N-dipping northern backlimb and $\sim 40°$ S-dipping southern forelimb. In this south limb, the Late Cretaceous strata unconformably overlain by Plio-Quaternary continental deposits (Fig. 5.4). The north limb is affected by

Fig. 5.6 Syntectonic index of extensional regime. **a** The Aptian conglomerate. **b** The metric bed of Aptian conglomerates located in the Khanguet Amor. **c** Small Aptian conglomerates resedimented in the Jebel Jerouala. **d** Rudist fossils (arrows) within the Aleg Formation (Coniacian–Santonian)
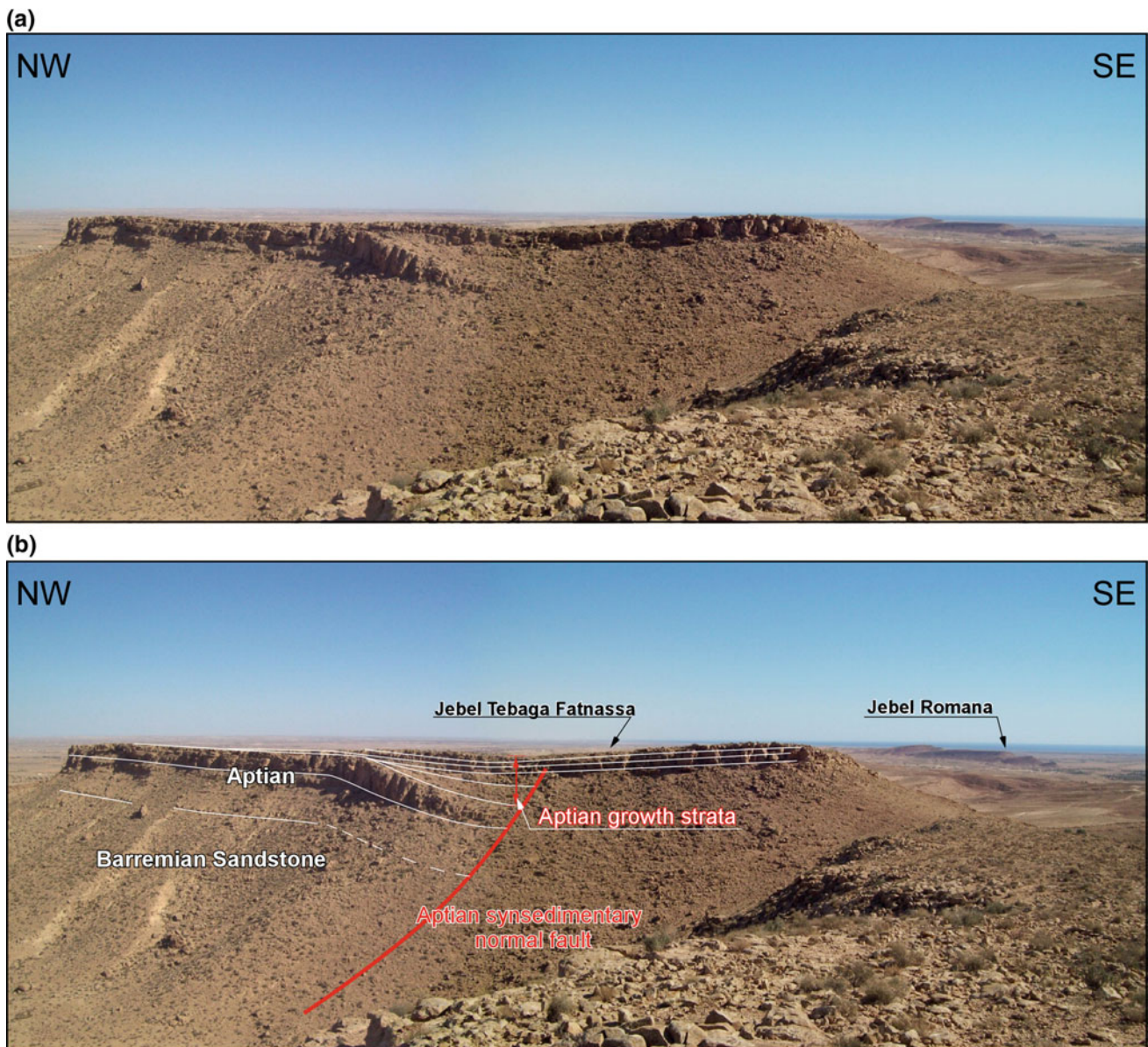
Fig. 5.7 Preserved Aptian normal fault associated with growth strata in the Jebel Tebaga Fatnassa indicating that these Aptian series was deposited during the extensional tectonic regime

ENE-trending reverse fault that separates the Jebel Haidoudi anticline from the Oued Krenafess syncline in the south. This later syncline forms the footwall of the NW-trending strike-slip fault that delimits the Jebel Es Smaïa monocline at the north (Figs. 5.3 and 5.4).

In the southern limb of Jebel Haidoudi anticline, a main ∼45° to 70°–NE-dipping normal faults are observed, most of them are a preserved synsedimentary sealed normal faults. This normal faulting is usually sealed by the Santonian marls (Figs. 5.3 and 5.4) attesting an ante-Santonian synsedimentary activity. The Coniacian dolomitic sequence thickness increases toward the NE hanging wall and are characteristic of synsedimentary faults activity. The numerical analysis of

data, consisting of bedding rotation data to restore the horizontal bedding planes, highlights a ∼N30 to 65°–E-trending tectonic extension that prevailed during the Coniacian–Santonian times (see a and b in Fig. 5.5).

5.3.1.2 Bir Oum Ali–Hachichina Structure

The general structure of BOAHS comprises two major anticlines separated by the Bir Oum Ali–Hachichina fault systems (BOAHFS). Deformation of this area exposed two different styles with a northern highly deformed anticline and a southern gentle deformed one (Fig. 5.9). Anticline of the BOAHS shows a curved-axis which changes which change from West to East (El Amari et al. 2016). As shown
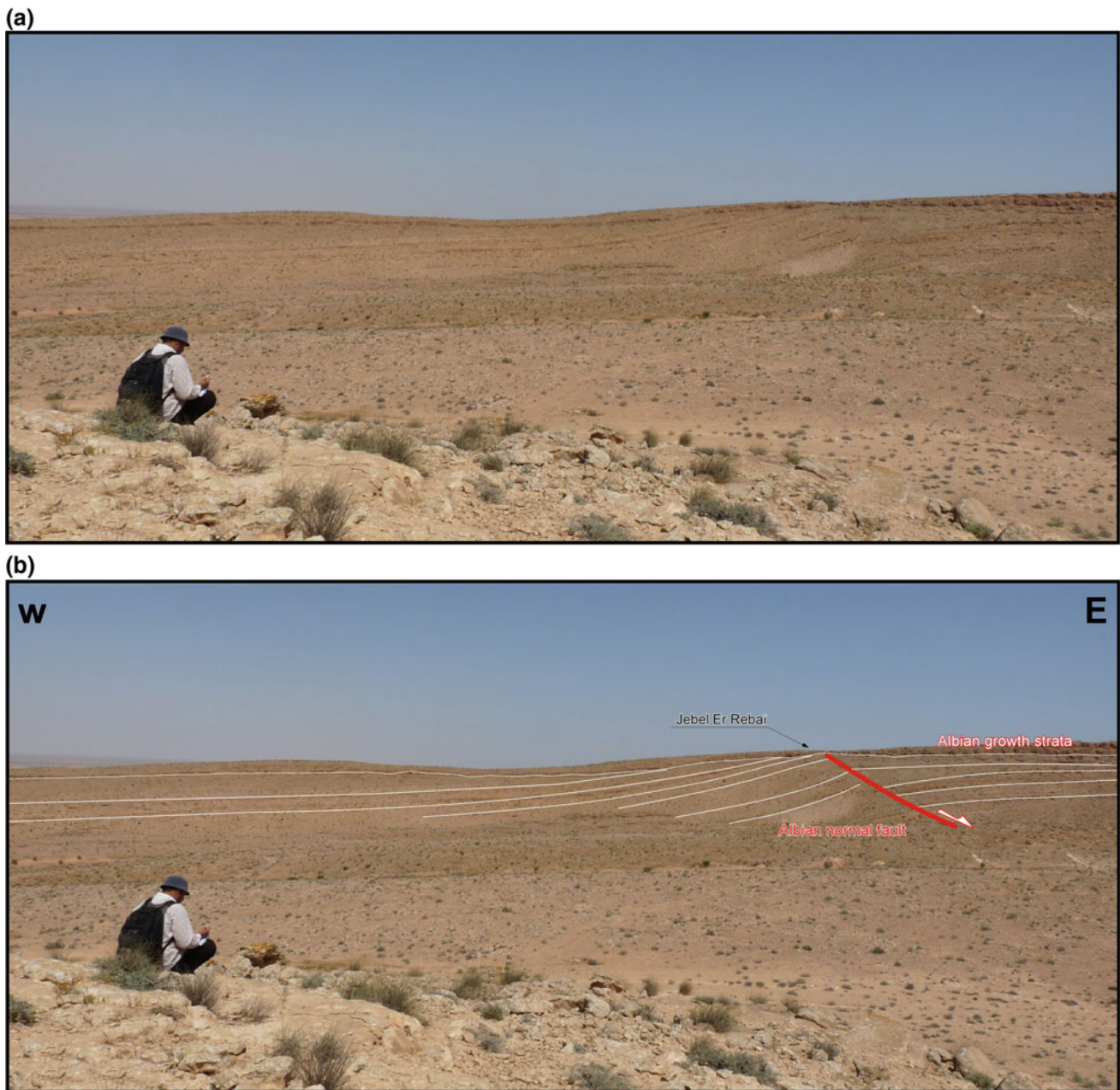
Fig. 5.8 Preserved Albian synsedimentary "growth faults" in the Jebel Es Smaïa related to the extensional tectonic regime

on the geologic map, the BOAHS have a NE-trending axis in the Jebel Bir Oum Ali, a NW-trending one in the Jebel Hachichina and an ESE-trending axis in the Jebel Naimia (Figs. 5.9 and 5.10 D–D'). Three surface constructed cross-sections (Figs. 5.9 and 5.10), along the BOAS anticline, highlight that the southern part is only formed by the Early Cretaceous series showing a long southern limb and a short northern one characterized by $\sim 10°$–$15°$ S-dipping southern forelimb and $\sim 45°$–$65°$ N-dipping northern backlimb (El Amari et al. 2016). While the southern side is simple and shows a little deformed side of the BOAHS, the

northern part shows a complex pattern. This part is characterized by the anticlines succession with curved hinge line and showing a right stepping "en echelon" arrangement. These two different sides are separated by the BOAHFS and does show a syncline in-between (Figs. 5.9 and 5.10). The curved secondary (in respect to general structure) anticline succession is well observed along O. El Araguib, O. Sania, O. Karma, east of O. Karma, the O. Batoum, and the O. Saoudi, at the northeastward. Furthermore, from west to east geometric complexity increase in O. Karma, O. Batoum, and the O. Saoudi anticline with usually south overturned
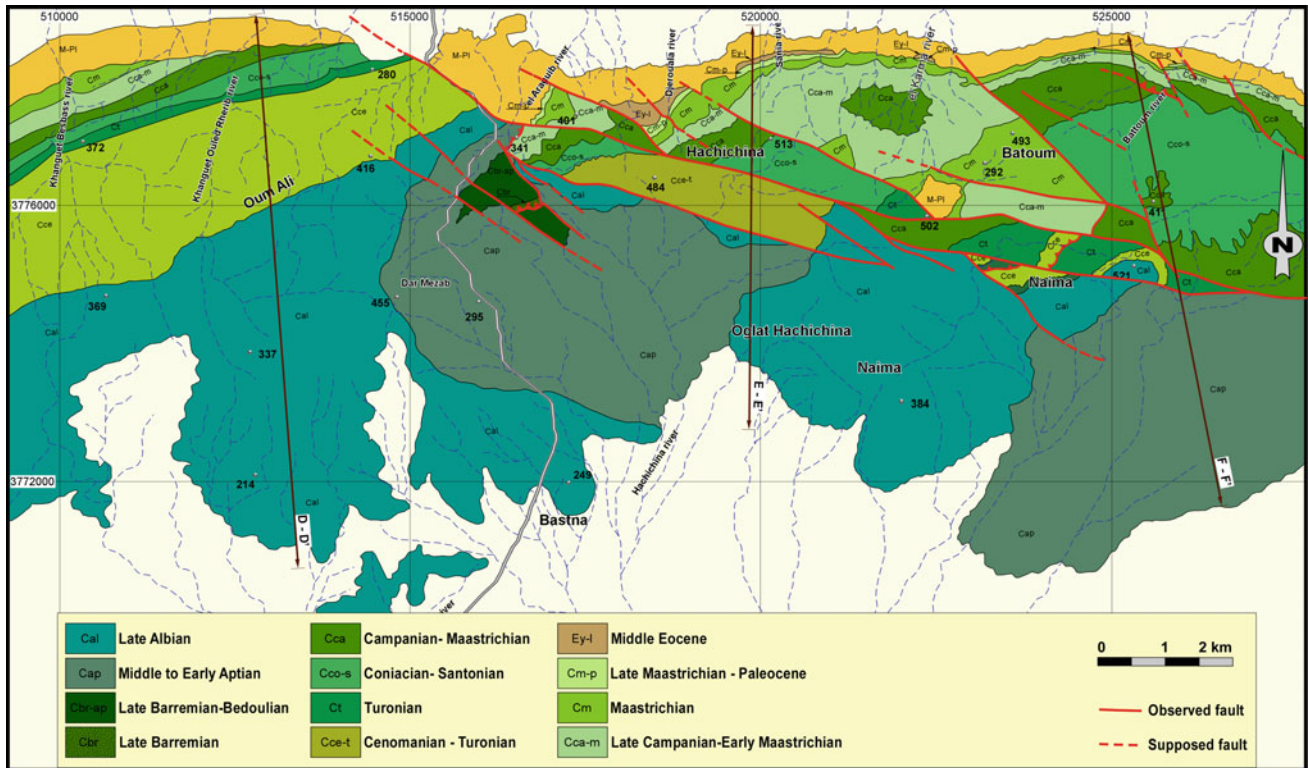
Fig. 5.9 Detailed geological and structural map of Bir-Oum-Ali–Hachichina structures (BOAHS) See location on Fig. 5.1b (El Amari et al. 2016). Coordinate system is UTM zone 32, WGS 84 system (metres). Location of the cross section of Fig. 5.10 is shown
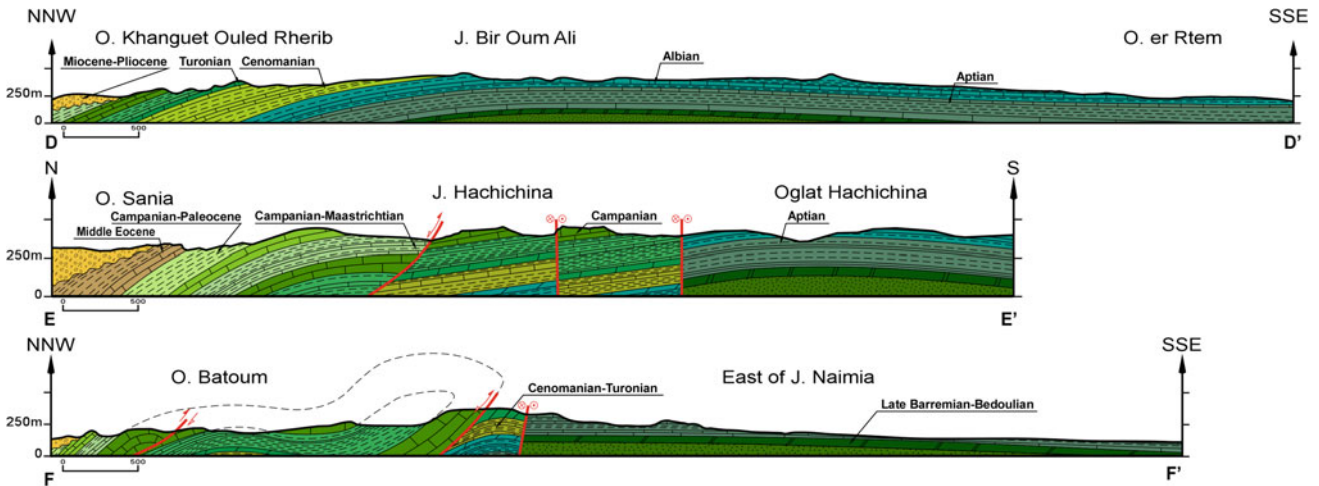
Fig. 5.10 Geological cross sections showing the tectonic style of Bir-Oum-Ali–Hachichina structures (BOAS). For location, see Fig. 5.9

limbs (Figs. 5.9 and 5.10, El Amari et al. 2016). This area offers a well outcropping ~15°–20° angular unconformity between the aforementioned Cretaceous series and Miocene–Pliocene sequences. Eastward, this angular unconformity is localized between Paleocene–Eocene and Miocene–Pliocene series in the Oued Sania and Oued el Karma (Figs. 5.9 and 5.10, El Amari et al. 2016).

Several previous works (Abdeljaouad and Zargouni 1981; Rabiaa 1985, Zargouni 1985; Fakraoui 1990; Abbès et al. 1994) have usually interpreted the BOAHFS as strike-slip fault systems, mainly active during Cenozoic times. The examination of all adjacent areas limited by this fault systems, based on new geologic mapping (El Amari et al. 2016), the surface geologic cross-sections (Fig. 5.10) and

the fault kinematics analysis does not reflect this old interpretation. The first of evidences, is that north-dipping BOAHFS separate a north hanging wall filling by the Late Cretaceous–Paleogene series and a south footwall that consists of Early Cretaceous strata. These data confirm an inverted fault system in which the second contractional throw does not compensate the first extensional one. In addition, secondary anticlines are in close relationship with the BOAHFS (Fig. 5.10). Furthermore, the majority of measurements carried out along all this system fault revels that this N100°–110° E-trending BOAHFS exhibits usually striation with a first normal movement generation cut by second dextral strike-slip one (Fig. 5.11a–d). The fault kinematics analysis of the back tilted fault surfaces carried out along the BOAHFS shows that the Aptian is characterized by the N40°E-trending minimum stress axis (σ3) (Fig. 5.11c). This extensional regime is associated with graben and half-graben structures (Fig. 5.11a, c, and d). During Coniacian–Santonian, BOAS domain is also controlled by the same faults reactivated by normal faulting with a tectonic regime characterized by a NNE (∼N15° to 20°E)-trending tectonic extension (Fig. 5.11d) responsible also for half-graben structure. During Campanian, BOAS is controlled again by normal faulting with tectonic regime characterized by a NNW (∼N170°E)-trending tectonic extension (Fig. 5.11a). In addition, the Campanian normal faulting generates syntectonic conglomerates and the growth strata in the hanging-walls these normal faults (Fig. 5.12).
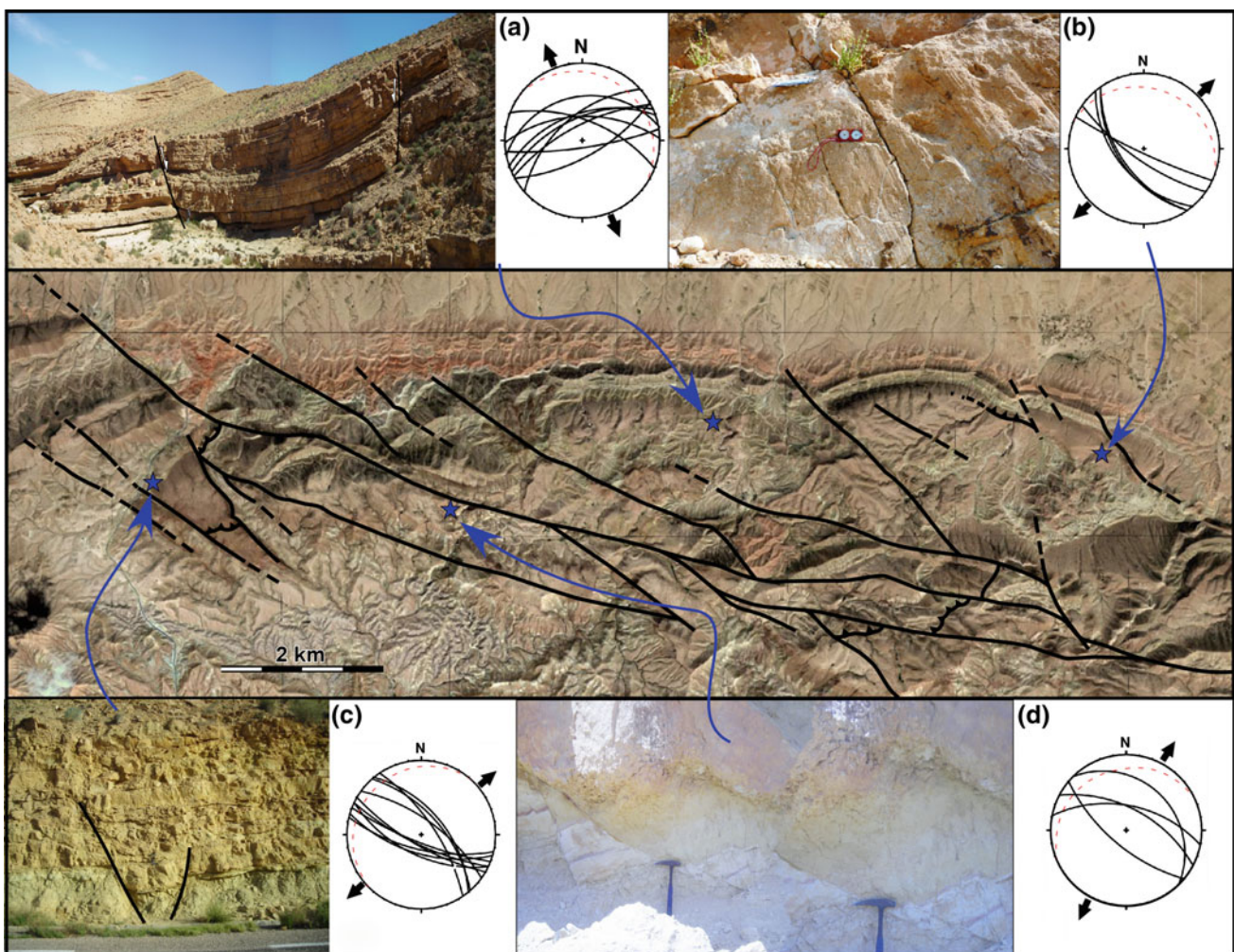
Fig. 5.11 Based on Google Earth satellite images, the structural mapping of Bir-Oum-Ali–Hachichina structures (BOAS) shows the Cretaceous extensional (normal faulting) tectonic regime resulting from the back-tilting diagram. **a** Campanian normal fault results from an extensional tectonic regime characterized by NNW (∼N170°E)-trending; **b** striations recorded on fault plane indicates a Coniacian– Santonian normal faulting characterized by NE-trending extension; **c** NW-trending graben related to a NE-trending extension; **d** half-graben structure recorded in the Coniacian–Santonian deposits related to a regional NNE-trending extension regime. Red dashed plane corresponds to the bedding plane (El Amari et al. 2016)
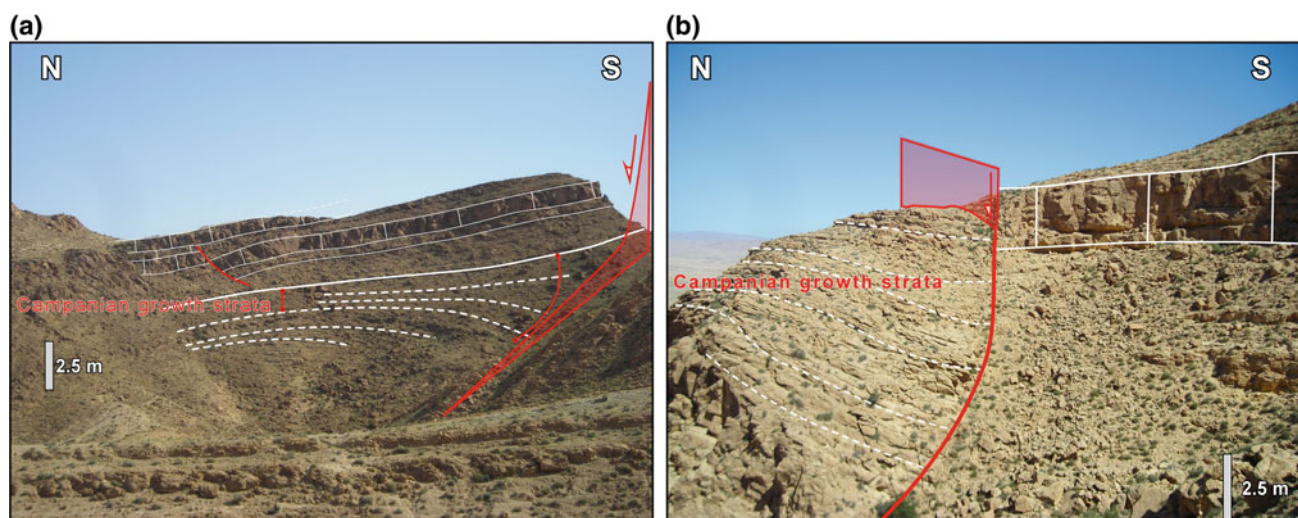
Fig. 5.12 Panoramic view, looking NE, of a preserved Late Cretaceous normal fault showing growth strata located in the hanging wall that indicate a normal faulting active during Campanian time (El Amari et al. 2016)

5.3.2 Subsurface Structural Data

Three seismic profiles EL03, EL11 and EL12 (Figs. 5.13 and 5.14) are used in this work to illustrate the southern Atlas of Tunisia deep geometry. Data presented are based on the conversion of the travel times to depth and calibrated by the exploration wells (P1, P2, P4, Figs. 5.1b, 5.13 and 5.14) and present work surface data.

The interpreted seismic profiles EL11 (Fig. 5.13a) highlights that Mesozoic sequences vary considerably in both facies and thicknesses along the southern Atlas of Tunisia. The thickness of Mesozoic sequences increases toward the Chotts Fejej compared to thin series in the Northern Chotts Range. This profile highlights also that the thick sequences are expanded on listric southwest-verging growth normal fault. In the eastern part of the ZBHS, the Early Cretaceous series thickness exceeds ∼1800 m. The same thickness is recorded for the Jurassic. These series of the Cretaceous and Jurassic reach the 2000–2300 m beneath Chotts Fejej basin. These significant and rapid variations attest a main episode of subsidence in the Chotts Fejej basin, associated with deep normal faulting during the Mesozoic times. These southwest-facing normal faults recorded especially in the Jurassic and Cretaceous Formations were recently interpreted as synsedimentary "growth faults" by Gharbi et al. (2015) and associated with large rollover anticline. Growth faults are mainly developed in what is now the Chotts Fejej basin. The Maximum throw is recorded at the Triassic–Jurassic sedimentary interface, suggesting a rapid subsidence and active growth faults during this period. Furthermore, high throw gradients were detected near the upper tips of these faults in the Early Cretaceous qualified to be characteristic of syn-sedimentary growth normal faults.

Diachronous Early Cretaceous lithostratigraphic successions led to a reactivation of the preexisting normal faults during the sedimentation during this period. This fact is testified by the sedimentary package associated with normal dragging of the strata in the hanging-wall of the faults (Fig. 5.13a). The geometry of the growth strata in the Early Cretaceous series are well defined on the EL11 seismic profile. High thickness triggers differential overloading along the growth faults. Into these hanging-walls of normal fault, Early Cretaceous filling draws an onlapping structure (Fig. 5.13a). A detailed analysis of these profiles has been carried out to predominant role of inherited extensional structures in evolution of the southern Tethyan margin, and their influence on the geometry of the Atlassic thrust belt.

The ENE–WSW seismic line of EL12 (Fig. 5.13b) offers well-imaged structures of the buried Chotts Fejej basin that occur over a listric fault geometry confirming the above-mentioned configuration in the seismic Line EL11. This line EL12 highlights a main graben structure beneath the Chott Fejej Basin likely resulting from a local intensive extensional tectonic located beneath a major regional listric normal fault. The sedimentary pile, that shows a thickness variation recorded at least since Jurassic and Early Cretaceous, has deeply controlled by these faults systems. The rapid accumulation of the Jurassic and Early Cretaceous sediments in the Chotts Fejej graben announce a high subsidence related to the diachronic activity of the normal fault. Analysis of the seismic profiles EL11 and EL12 crossing the Chotts Fejej Basin (Fig. 5.1b) permits to identify faults with normal components bounding the subsiding domains (Fig. 5.13). These faults are associated with other synthetic faults that have contributed to the formation of a Fejej graben. The study area is characterized by thick Jurassic and

Fig. 5.13 Subsurface data showing the preserved extensional structures reflected the structural architecture of the ancient southern Tethyan margin. EL11a and EL12a are the uninterpreted, migrated, depth-converted seismic reflection data from the Chotts Fejej basin. For location, see Fig. 5.1b. Horizons were calibrated using projected data from the P1 and P4 wells and surface data. Interpreted seismic section of the EL11b showing the half grabens systems of the Chotts Fejej basin connected to an intrabasement detachment and associated with syn-rift growth strata. Interpreted seismic section of the EL12b showing the deep Jurassic-Early Cretaceous graben beneath the Chotts Fejej basin connected to the same intrabasement detachment mentioned in the EL11b
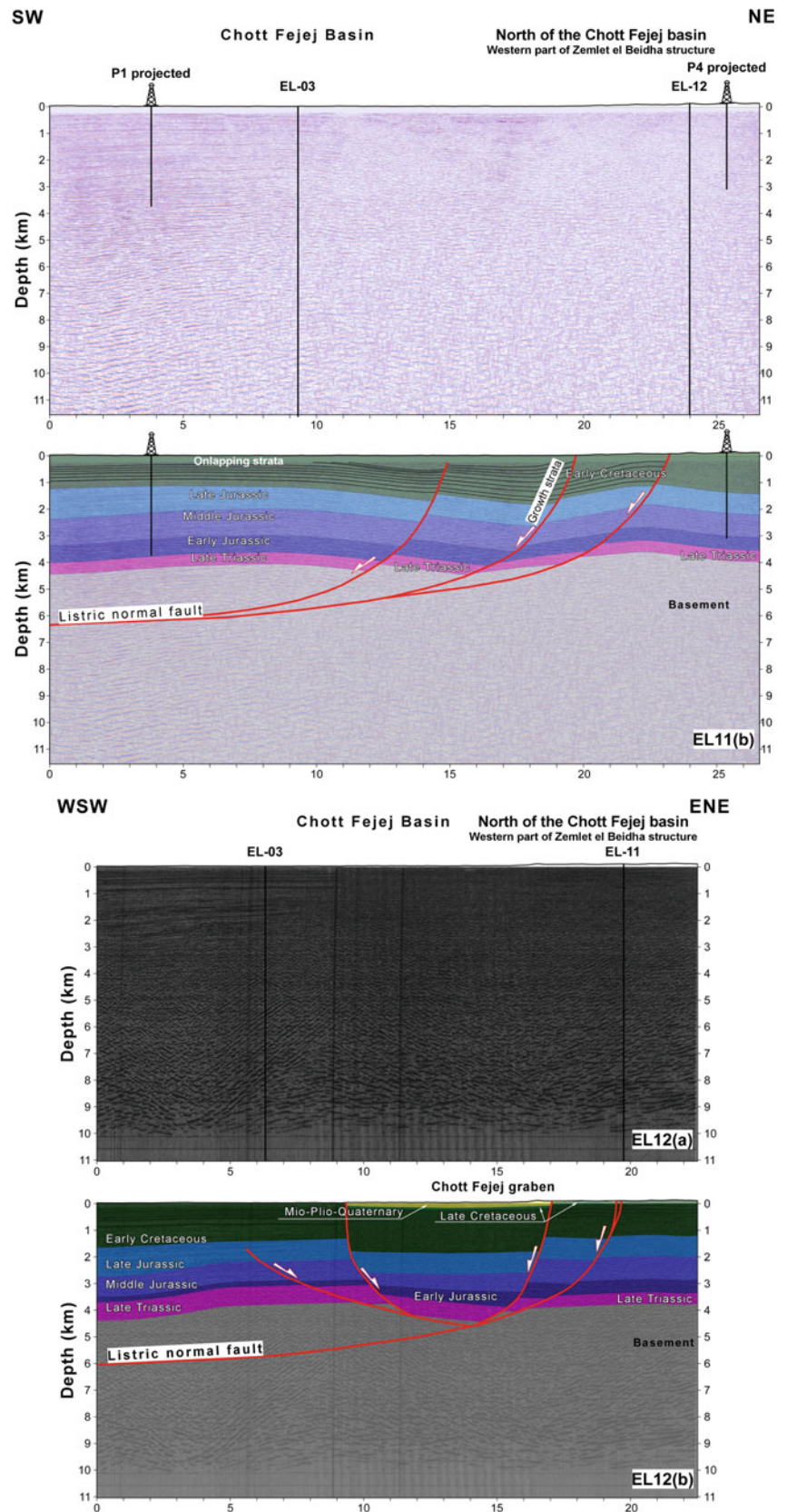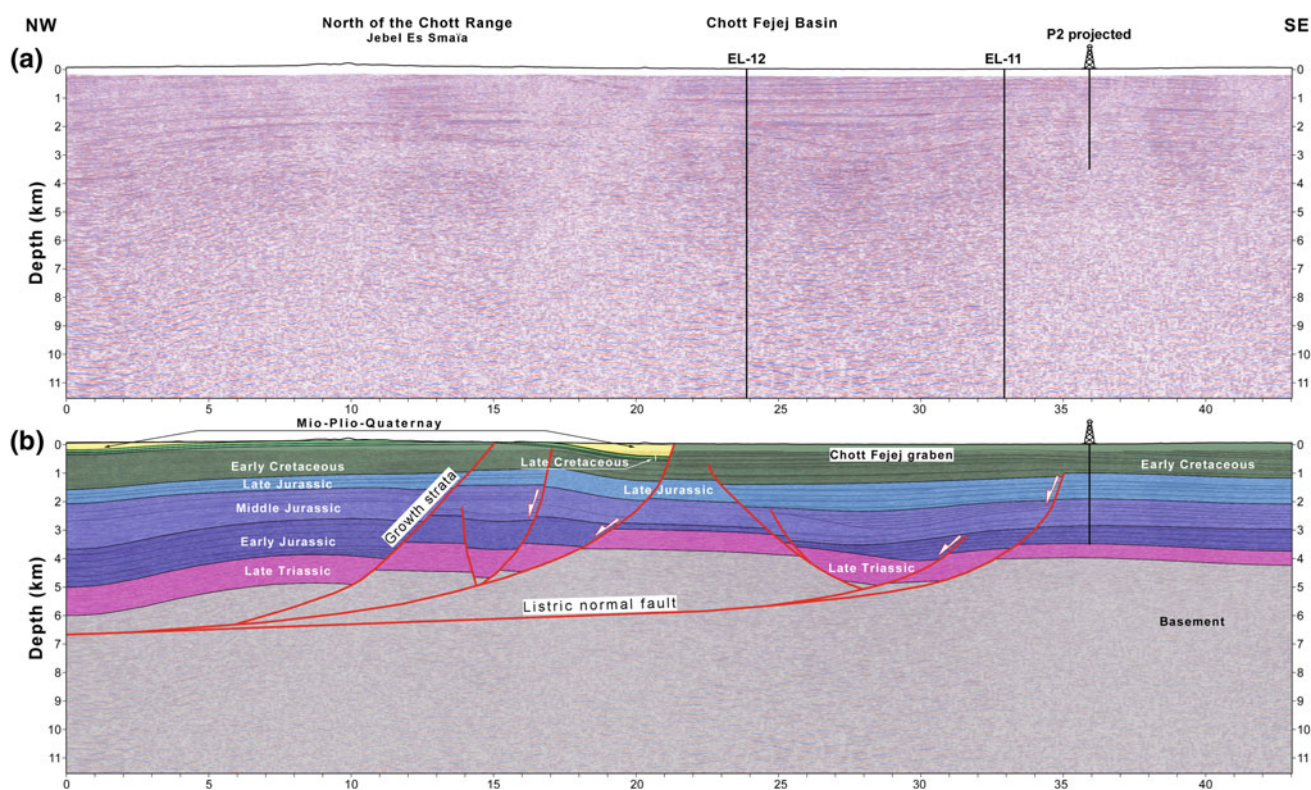
Fig. 5.14 **a** Uninterpreted, migrated, depth-converted seismic reflection data from the Chotts Fejej basin. **b** Interpreted seismic line of EL03 showing the preserved extensional structures associated with the preserved Chotts Fejej graben, and horst and rollover anticline limited by the listric normal fault connected to the intrabasement detachment. For location, see Fig. 5.1b

Early Cretaceous deposits, which are progressively thickening, associated with listric faults (Fig. 5.13). The geometry and the thickness variations are related to the regional extensional tectonics during the synrift period.

The deep structure of the Northern Chotts Range is well illustrated by the NNW–SSE trending seismic reflection line EL03 (Fig. 5.14). Reflectors have been calibrated using projected data of P2 well onto the section and present seismic interpreted of EL11 and EL12. To the south, the Chotts Fejej basin is formed above a normal movement of the fault systems which delimited a deep graben beneath Chotts Fejej and associated with rapid subsidence during Jurassic and Early Cretaceous. To the north, a similar extensional structure created by listric normal faulting delimits a tilted blocks geometry with north-verging beneath the Jebel Es Smaïa (Fig. 5.14).

Deep structural inheritance indicated by seismic interpretation is well illustrated by the synsedimentary normal faulting associated with the growth strata and the thickness and facies variation of Jurassic and Early Cretaceous. This structural architecture presented in the study area reflects the geometry of the south Tunisian basin as part of the southern Tethyan margin.

5.4 Sequential Restorations of the Southern Tethyan Rift Margin of Tunisia

The sequential restoration of balanced cross sections is viewed today as a sound way calculate the extension and/or shortening amount and to estimate the slip rate, and the depth of the décollement surface in both contractional and extensional tectonics (Castelluccio et al. 2015). This method is considered today as the only way to decipher the tectonic evolution of deformed structures in the time. Our sequential restoration published in previous works by Gharbi et al. 2015 quantify for the first time the extension amount of Mesozoic period of the Tethyan margin rifting stage of in South Tunisia (Fig. 5.15). We expose hereinafter the role of the rift-related structures in the structuration of the southern Atlas domain of Tunisia.

The calculated amount of extension, along the southern Atlas domain of Tunisia, shows a total horizontal extension of about 9.4 km during the Tethyan rifting. This amount is calculated for four stages of rift i.e. Permian, upper Barremian, Aptian–Albian, and Coniacian–Santonian (Fig. 5.16). The Tethyan margin rifting in southern Tunisian
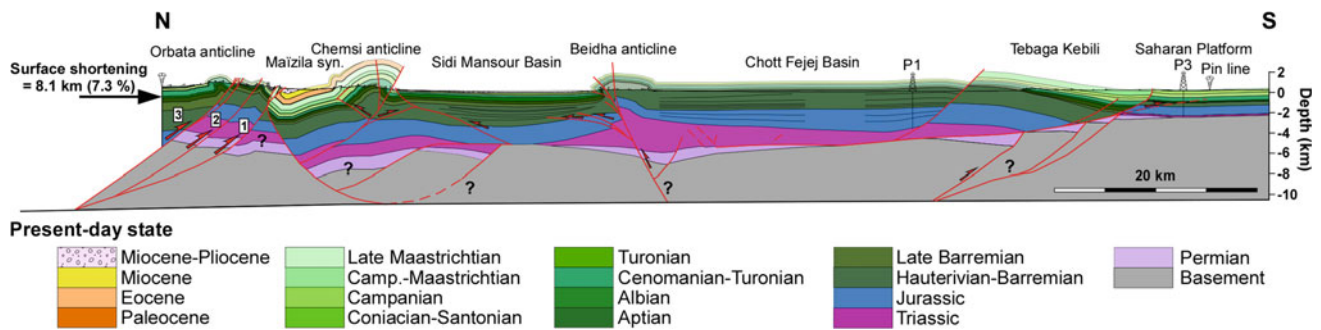
Fig. 5.15 Balanced cross sections across southern Atlas foreland of Tunisia. For location, see Fig. 5.1b shows that the structural architecture of the Tunisian foreland consists in a by mixed thick- and thin-skinned tectonic style, controlled by deep-seated basement faults (corresponding to inherited Permian (?) to Cretaceous normal faults) and shallower décollement within the sedimentary cover (Gharbi et al. 2015)

domain is started by the Permian–Triassic pre-rift stage where its sedimentary platforms are governed by extensional tectonic regime. The structural style was designed by normal faults associated with tilted blocs, grabens and horsts (Fig. 5.16a). A Triassic basin formed in the beginning of this rifting stage were filled by evaporitic massive salt layers (mainly halite and gypsum) with clays and dolomites reflecting an epicontinental environment (Kamoun et al. 2001). Following, a rapid subsidence typifies the rifting event during the Jurassic–Early Cretaceous stage. This period is characterized by extensional tectonic episodes linked to the opening of the Central Atlantic Ocean. Structures developed during this period were infilled by Early Cretaceous fluvio-deltaic to shallow marine environment sequences (Louhaïchi and Tlig 1993; Gharbi et al. 2013). The Early Cretaceous period is synchronous with the growth of major synsedimentary typical normal fault systems which produce a general framework delivering tilted blocks basin geometry responsible of the dislocation of the continental platform in the southern Atlassic domain of Tunisia. The sequential restoration proposed by this work shows a wide-ranging extension that reach ∼6.5 km at the Upper Barremian showing high subsidence rate and flexure of the south Tunisia margin in what is now the Chotts basin (Fig. 5.16b). The Chotts Fejej basin is dissected by listric normal faults branched on the Triassic intra-basement. Accumulation of Jurassic–Early Cretaceous thick sediments in the Chotts Fejej basin allows the lateral migration of the evaporitic Triassic salts towards the north associated to the development of the salt pillow beneath the Northern Chotts Range (Fig. 5.16b). Northward, the sequential restoration permits to define an ancient southern Tethyan margin in Tunisia likely controlled by the extensional structures. The extensional deformation was accommodated by basement normal faults bounding horsts and grabens structures patterned on tilted blocks major's ones. Normal faults controlled the sedimentation where the deposits were thicker

and showed growth strata architectures in the hanging wall. Furthermore, this tectonic event induced variation in thickness and facies of the sedimentary pile (Hlaiem, 1999; Bédir et al. 2001; Bouaziz et al. 2002; Patriat et al. 2003; Gharbi et al. 2013, 2015; El Amari et al. 2016). The calculated amount of stretching that occurred between upper Barremian and Aptian–Albian is of about ∼2.5 km (Fig. 5.16c). The southern Atlassic basin was affected by growth syndepositional strata well integrated in the extensional tectonics leading to the deposition of a syn-rift sequence controlled by alternating horsts and grabens structures. The synsedimentary normal faulting delivering a general tilted blocks geometry, for which the Aptian–Albian ages are perceived to have the most extreme extensional related-structures time of the south Tethyan edge in southern Atlas of Tunisia (Gharbi et al. 2013, 2015; El Amari et al. 2016). In addition, Aptian–Albian sequences display abundant conglomeratic horizons and slumping, in addition to significant thickness changes (Gharbi et al. 2013; Masrouhi et al. 2014a; Naji et al. in press). This period shows in south Tunisia sedimentary gap of Upper Aptian–Lower Albian sequences. Detailed investigations portray an unconformity, reordered in the study area, as a consequence of rift derived tilted blocks. This configuration is well known today in this structural setting and qualified to be an "Atlantic type passive margin setting". This setting is recently well elaborated in central and northern Tunisia (Jaillard et al. 2017; Naji et al. in press) particularly for the Aptian–Albian times. During this time, data are agreeable with the intraplate extensional deformation which is linked to the opening of South Atlantic central segment. The northward motion of the African Plate has been accompanied by N trending extension registered in the central and north African basins (Martinez et al. 1991; Guiraud and Maurin 1991; Guiraud et al. 2005). In addition, the syn-rift structures of the southern Tethyan margin in Tunisia are accompanied by episodes of volcanism that is testified by basalt flows observed in the pelagian blocks of
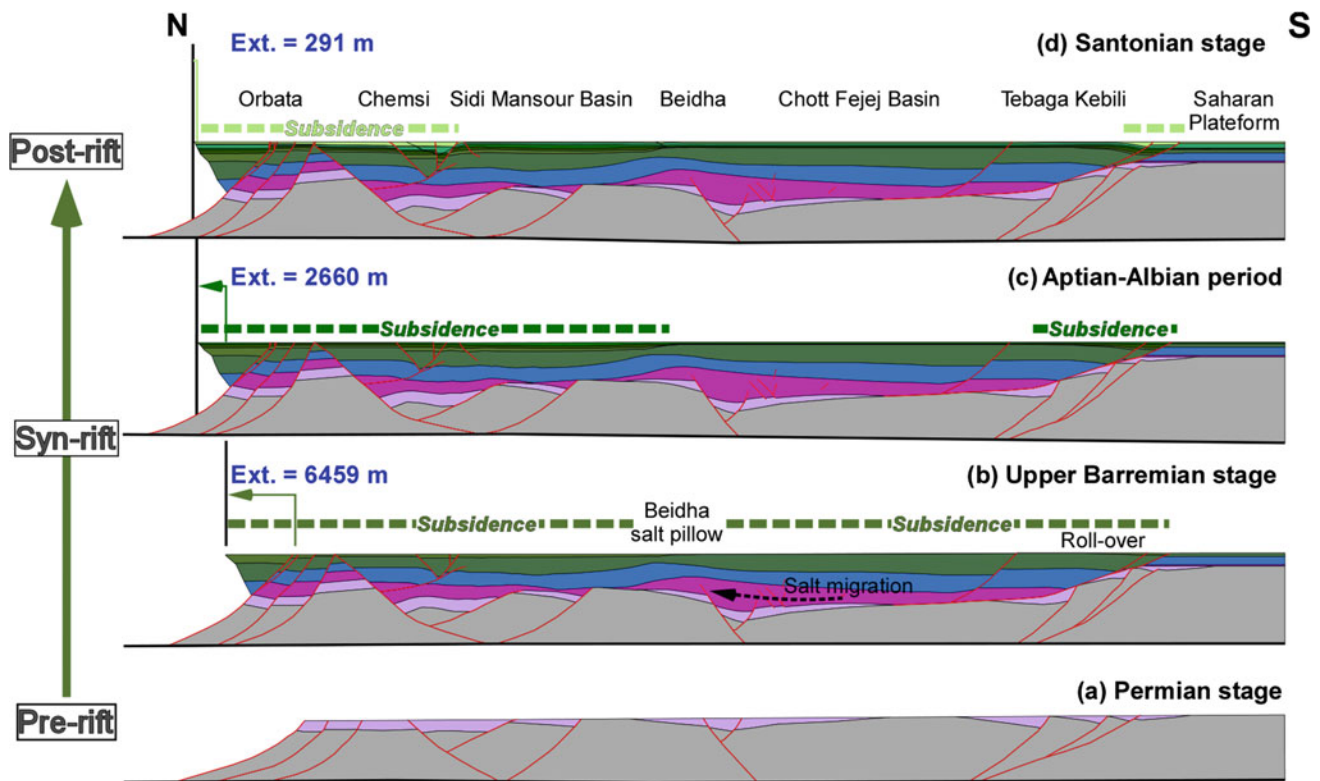
Fig. 5.16 Sequential restorations of the southern Tethyan rift margin of Tunisia (**a–d**). **e** Extensional amount versus time. Ext.: Extension (Gharbi et al. 2015)

eastern Tunisia (Laaridhi-Ouazaa 1994; Ellouz et al. 2003; Patriat et al. 2003). This extensional geometry is well exposed in a deep through at the northern region, i.e., Tunisian through (Boltenhagen 1985; Burollet 1991; Martinez et al. 1991; Soua 2016; Masrouhi et al. 2014a; Naji et al. in press) and in northern Algeria (Vila 1980; Herkat and Guiraud 2006; Marmi and Guiraud 2006).

During the Cenomanian–Santonian post-rift stage, a 300-m extension is perceived in south Tunisian basin (Fig. 5.16d). This small amount of extension is associated with thick sequences deposition rate of pelagic and benthic facies (Soua et al. 2009; Naji et al. in press). These characteristics are indicative of post rift stage sediment accumulation. Furthermore, this period was described as associated to an important transgression in the southern Atlassic domain of Tunisia. The Ancient normal faults, inherited from Jurassic to Early Cretaceous rifting stage, have controlled the distribution of the Cenomanian–Santonian deposits. Regionally, these extensional structures are usually sealed by the Coniacian–Santonian post-rift sequences, which themselves testifies for a post-rift stage with major transgression (Abdallah and Rat 1987; Herkat and Guiraud 2006).

5.5 Amount of Mesozoic Extension Rate in the Chotts Basin

In this work, we provide new detailed sequential restorations of the southern Tethyan rift margin in Tunisia. We quantify the long-term extension mainly accommodated by the Cretaceous normal faulting structures. With this procedure described above by the section-time restoration, it is possible to decipher three mainly stages characterized this ancient passive margin. As shown the Fig. 5.16, the amount of Mesozoic extension rate varies during the time. After the Permian–Triassic pre-rift stage, we calculate an extension rates averaged ∼6.5 km with a velocity of opening about ∼550 m/Ma during the Upper Barremian (Fig. 5.17). The velocity of extension increases and reached more than 1000 m/Ma. This extensional deformation occurred during the Aptian–Albian stage indicates the maximum of opening of the southern Tethyan margin and reached 2.5 km of extension rate (Gharbi et al. 2015). During the Cenomanian–Santonian post-rift stage, the velocity of extensional decreases for reach 6.5 m/Ma with 300 m of extensional rates.
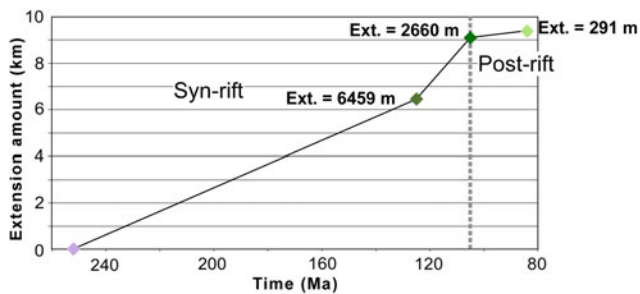
Fig. 5.17 Amount of Mesozoic extension rate recorded in the southern Tethyan margin in Tunisia versus time. Ext.: Extension (Gharbi et al. 2015)

5.6 Discussion and Conclusions

During the past 65 years, various interpretations of the geologic results pending from the Southern Atlassic front of Tunisia have been proposed. The reviewing of the geological data highlights four different eras in term of structural interpretation i.e. between 1952 and 1994 geologic interpretation was dominated by the view that the present fold distribution is the result of (i) strike-slip faulting, (ii) between 1997 and 2002 geoscientists featured an interpretation is the consequence of salt tectonic activity (1997–2002) or the result of both aforementioned processes, (iii) in parallel, for the same period from 1995 to 2006, geologists highlighted a model of anticline structures that were interpreted as developed and the result of ramp-related folding, deformed the sedimentary cover (thin-skinned model) over the rigid basement during a single tectonic event, (iv) between 2011 and 2017, geoscientists working in the area, lead to the inversion of inherited major fault in the development of tertiary structures. The inherited Triassic–Jurassic–Early Cretaceous normal faults are actively involved in the far-foreland tertiary deformation of the Southern Atlassic Front in Tunisia.

The first era, from 1952 to 1994, featured a general hypothesis of strike-slip faulting generating the fold distribution of the Southern Atlas (Castany 1954; Abdeljaouad and Zargouni 1981; Rabiaa 1985; Zargouni 1985; Abbès and Zargouni 1986; Fakraoui 1990; Abbès et al. 1994, among others). During the 70s and 80s, many detailed mapping by many geologists has begun to elucidate the southern Tunisia structural complexities. Two major NW-trending lateral strike-slip faults (i.e. Gafsa and Negrine-Tozeur) were recognized in the southern Tunisian Atlas fold-and-thrust belt. They were structurally connected to the present-day distribution of folds, which was widely accepted by the 70s and 80s geologic reconstructions. In this way, ZBHS and BOAHS were interpreted previously as curved, right-stepping "en echelon" geometry folds (Abdeljaouad

and Zargouni 1981; Rabiaa 1985; Zargouni 1985; Abbès and Zargouni 1986; Fakraoui 1990; Abbès et al. 1994) a model which was generalized for all the Northern Chotts Range. However, the case of ZBHS and BOAS does not show in any point the classical relationship between folds and strike-slip faults. Indeed, the deformation must be relatively comparable along the two adjacent blocks moving sideways for which these anticlines are much different, and these structure does not correspond to a doubly plunging and relatively short with steeply dipping axial planes that must exist if it was the case of strike-slip fault controlling the folding.

The second period from 1997 to 2002, a salt tectonics developed model (Hlaiem et al. 1997; Hlaiem 1999) featured an evolution in which a significant diapirs began to rise-up during Early Jurassic. This tectonic model highlights a structural configuration in which the subsequent tertiary folding is preferentially nucleated on the preexistent diapir apex. In the same period, composite model of strike-slip faulting and salt diapir generated in response to shearing faulting (Bédir et al. 2001; Zouaghi et al. 2011). However, this is in pure contradiction to the diapiric structure itself, in which structure must be circular and associated with radial faulting. Our interpreted seismic reflection shows the absence of salts structure beneath these anticlines. Excluding the Jebel Beida to the East of the BOAHS, this geometry is not found anywhere in this belt and does not show significance of salt tectonics activity (Masrouhi et al. 2013; Masrouhi et al. 2014a, b).

The third period, from 1995 to 2006, was dominated by south verging thrust system on which folds are located (Outtani et al. 1995; Ahmadi et al. 2006). This model, interprets the anticline structures in this zone as developed and the result of ramp-related folding, deformed the sedimentary cover (thin-skinned model). Ramps were presented as usually connected in the Triassic evaporites over the rigid basement during a single tectonic event. Field data collected in these works highlight usually "en echelon" geometry folds underlain by steeply dipping faults. In this model, the previously syn-rift strata thicken toward the border-fault zone are omitted. Unconformities and Mesozoic growth strata refute this interpretation.

The fourth period (2011–2017), which was characterized by the rise of inherited role of the pre-existent faults systems, featured a structural evolution controlled by deep-seated basement faults (corresponding to inherited Permian (?) to Cretaceous normal faults) and shallower décollement within the sedimentary cover (Riley et al. 2011; Gharbi et al. 2013, 2015; El Amari et al. 2016).

This chapter provides an overview of data-compilation recently published by Gharbi et al. (2013, 2015), El Amari et al. (2016) in addition to newly collected data. Detailed

geological mapping, local structural analyses, interpretation of seismic reflection profiles and the sequential restoration of balanced cross section along the southern Tunisian Atlas front, together with recent published data reveal a structural similarity between the ZBHS and BOAHS, which likely link to a general tectonic style of the all Northern Chotts Range structures. The age, the geometry of the units, and the present distribution of several secondary thrust-related anticlines give evidences of the reactivation of the pre-existing normal faults acting now as thrust ramps generating an associated folding (Fig. 5.15). Most of this shortening is accommodated by mixed thick- and thin-skinned tectonic style, controlled by deep-seated basement faults (corresponding to inherited Permian (?) to Cretaceous normal faults) and shallower décollement within the sedimentary cover. Field relationships between units and the present distribution of faults and folds clearly involve two different times of shortening evolution, i.e., Eocene and Miocene–Quaternary events. The most recent study of stress state in southern Tunisia (Gharbi et al. 2014) highlighted a stress state characterized for the Miocene time by NW-trending regional compressional tectonic regime. This NW-trending compression was possibly responsible for the right-lateral strike-slip reactivation of the E-trending BOAHFS. This major fault system was probably accompanied by minor, to the respect of the main strike-slip ones, reverse movement along the E-trending BOAHFS (El Amari et al. 2016). During the Quaternary to present-day period, a modern N-trending state of stress was also considered by recent studies as a compressional tectonic regime (Gharbi et al. 2014). During this phase, the N-trending compression is responsible for thrust tectonics, which as well typified as reverse–reactivation of the Mesozoic inherited faults (El Amari et al. 2016).

The new interpretation of the preserved extensional structures using the surface and deep-subsurface data sets refined by the sequential restorations of the balanced cross section allow us to highlight the role of pre-existing rift basin architecture on the evolution of the southern Atlas fold-and-thrust belt of Tunisia. Cretaceous sedimentary cover of BOAHS is more deformed than the ZBHS. These structures are cut by N100–110° E-trending fault systems. These systems usually exhibit a fault kinematics, with striation showing a multiphase history with a first generation indicating normal movement and a second as dextral strike-slip (Figs. 5.5 and 5.11). The second-order fault systems associated to the main trend of these anticlines are usually apparent strike- slip faults. Unfolding of the structure easily shows an inherited normal faulting. In addition, the normal faulting generates growth strata (surface see Figs. 5.7, 5.8, 5.12 and subsurface Figs. 5.13a and 5.14) filled by a syntectonic sequences associated to typical syntectonics conglomerates (Fig. 5.6) and abundant

soft-sediment sequences associated to the first normal faulting activity. Like many other extensional areas, the Mesozoic history of this margin was dominated by growth of listric normal faults, which are associated with well-developed half-graben fill and large rollover structures. The subsurface data provides a well image in the Chotts Fejej basin as governed by deep listric normal faults. Seismic profiles well featured this geometry with listric fault system vertical at surface and rapidly decreases becoming planar at depth. These growth normal faults, controlling the genesis of the ZBHS and BOAHS, are symptomatic of this evolution with up-thrown side largely more thicker and characteristic of growth related-normal faults strata (Figs. 5.13 and 5.14). These E-trending listric extensional growth faults draws the structural architecture of the south Tethyan margin in south Tunisia. A preserved Jurassic–Early Cretaceous graben is identified beneath the Chotts Fejej range, which is associated to the listric normal fault connected to an intra-basement detachment. The Chotts Fejej basin was usually considered as a large anticline (Zargouni and Abbes 1987; Fakraoui 1990; Bouaziz et al. 1994; Swezey 1996; Bédir et al. 2001) marked the far-foreland of the southern Tunisian Atlas. Lithostratigraphic data provided by petroleum well, presented above, reveal that the depth of the top Triassic salt horizons is reaches more than ∼3 km. In addition, the surface and subsurface interpretation allow to identify a southwest-verging listric normal fault. In the footwall of this later, the top of the Triassic level is reaches more than ∼3.2 km in the P4 well while in the hanging wall this horizon is reaches more than ∼3.5 km in the P2 well. These results are concordant with the regional calculated tectonic subsidence rates in the Chotts basin (Patriat et al. 2003).

Many authors believe that the E-trending fault systems are inherited from the southern Tethyan rifting growth periods (Souquet et al. 1997; Patriat et al. 2003; Raulin et al. 2011; Dhaoui and Gabtni 2013; Gabtni et al. 2011; Masrouhi et al. 2014a, b; Gharbi et al. 2015; El Amari et al. 2016; Naji et al. in press). The basement normal faults recorded in this domain were likely responsible for development of the evaporites basins during the Late Triassic–Jurassic synrift times (Kamoun et al. 2001). The continued synrift tectonic process generates an extension of about ∼6.5 km and associated to high subsidence rates during Jurassic–Early Cretaceous times (Gharbi et al. 2015). This extensional tectonic context is naturally related to the opening of the Central Atlantic Ocean. The rifting period seems to be synchronous with the dislocation of the continental platform and the development of major synsedimentary normal fault systems producing tilted block basin geometry in the southern Atlassic domain of Tunisia (Abbès and Tlig 1991; Louhaïchi and Tlig 1993; Gharbi et al. 2013, 2015; El Amari et al. 2016). This setting is recognized in Tunisia, which is

synchronous with segmentation between platforms in central-southern Tunisia (Gharbi et al. 2013) and the deep Tunisian trough in northern Tunisia. During upper Barremian and Aptian–Albian times, the Chotts basin was probably extended about ∼2.5 km showing typical geometry of a rollover related structure (Gharbi et al. 2013, 2015). This Barremian and Aptian–Albian original situation was accompanied in some segments by progressive unconformities. The Upper Aptian–Lower Albian regional unconformity is the well-known, which was identified in this area as mainly related to growth normal faulting. This geometry was possibly the raison misleading the previous interpretation of compressional "Austrian event" as responsible for the observed sedimentary gap and progressive unconformities. In addition, the rifting has been accompanied by an episode of volcanism, which is testified by basalt flows observed in the pelagian blocks of eastern Tunisia (Ellouz et al. 2003; Patriat et al. 2003) and southern Tethyan margin in the southern Atlas of Tunisia (Gharbi et al. 2015). During this period, extensional normal faulting has produced space for the salt to rise (Masrouhi et al. 2014b) and caused different salt geometry. In this evolution, the Albian is recognized to have been the time of the maximum regional extension occurring during the Early Cretaceous rifting stage (Masrouhi et al. 2014b). During Cenomanian–Santonian post-rift period, the margin records a low extension associated with an important transgression in the southern Atlassic domain of Tunisia and thick deposits of pelagic and benthic facies (Abdallah and Meister 1997; Soua et al. 2009).

Based on the above-presented results, the following conclusions can be drawn:

1. The present-day "en echelon" fold distribution is conceivably the surface expression of the "en echelon" faulting, which controls the fold's emplacement and style. The present-day general tectonic style of the all Northern Chotts Range structures, the age and the geometry of units, and, the distribution of thrust-related anticlines, all of them are significant of a pre-existing normal faults reactivation, acting now as thrust ramps generating an associated folding. The Northern Chotts Range is well typified as the results of reverse–reactivation of the Mesozoic inherited faults. Toward the end, this multiphase evolution shapes a chain with mixed thick- and thin-skinned tectonic style, controlled by deep-seated basement faults (inherited Permian (?) to Cretaceous normal faults) and shallower décollement within the sedimentary cover.

2. The Chotts basin was previously considered as a large anticline related to the Cenozoic compressional events to explain the gentle deep observed "antiform structure". It was, therefore, marked as the far-foreland of the southern Tunisian Atlas. Like many other inverted margin, extensional inherited structures are still preserved in the southern Tunisian Atlas. The Chotts basin appears to well preserve the Mesozoic history of this margin, which was dominated by growth of listric normal faults, themselves associated with well-developed half-graben fill and large rollover structures. The subsequent tertiary compressional front will be, therefore, repositioned in the Northern Chotts Range Front.

References

Abbès C, Zargouni F (1986) Anatomie d'un couloir de décrochements: le couloir de Hadifa (Chaîne Nord des Chotts-Tunisie). In: Rev Sc de la Terre, vol 4. Tunisie

Abbès A, Tlig S (1991) Tectonique précoce et sédimentation de la série Crétacée dans le bassin des Chotts (Tunisie du sud). Géologie Méditerranéenne XVIII(3), 149–161

Abbès C, Abdeljaoaud S, Ben Ouezdou H (1994) Carte Geologique d'El Hamma au 1/100.000, feuille n°74. Institut National de recherche Scientifique de Tunisie et Service Géologique Nationale d'Office Nationale de Mines, Tunisie

Abdallah H, Meister C (1997) The Cenomanian—Turonian boundary in the Gafsa-Chott area (southern part of Central Tunisia): biostratigraphy, paleoenvironments. Cretac Res 18:197–236

Abdallah H, Rat P (1987) Le rôle de la faille de Gafsa dans le jeu transgressif et régressif au Crétacé supérieur de la chaîne nord des Chotts (Tunisie). In: Saloman J (ed) Colloque: Transgressions et régressions au Crétacé (France et régions voisines), vol 11, 1985. Mémoires Géologiques de l'Université de Dijon, Dijon, pp 232–242

Abdallah H, Memmi L, Damotte R, Rat P, Magniez JF (1995) Le Crétacésupérieur de la chaîne Nord des Chotts (Tunisie du centre-sud): biostratigraphie et comparaison avec les régions voisines. Cretac Res 16:487–538

Abdeljaoaud S, Zargouni F (1981) Mise en évidence d'une tectonique intra crétacé dans le secteur de J. Zemlet El Beïda (chaîne des Chotts). In: Acte de 1er Congr. Nat. Sc. Terre, Tunis, t. I, p 285

Ahmadi R, Mercier E, Ouali J (2013) Growth-strata geometry in fault-propagation folds: a case study from the Gafsa basin, southern Tunisian Atlas. Swiss J Geosci 106:91–107

Ahmadi R, Ouali J, Mercier E, Mansy JL, Van-Vliet Lanoe B, Launeau P, Rhekhiss F, Rafini S (2006) The geomorphologic imprints of hinge migration in the fault-related folds. A case study in Southern Tunisian Atlas. J Struct Geol 28:721–728

Beauchamp W, Allmendinger RW, Barazangi M, Demnati A, El Alji M, Dahmani M (1999) Inversion tectonics and the evolution of the High Atlas Mountains, Morocco, based on a geological-geophysical transect. Tectonics 18:163–184

Bédir M (1995) Mécanismes géodynamiques des bassins associés aux couloirs de coulissements de la marge atlasique de la Tunisie, séismo-stratigraphie, séismo-tectonique et implications pétrolières. (Thèse d'Etat), Université de Tunis-II, Tunis, Tunisie, 412 p

Bédir M, Boukadi N, Tlig S, Ben Timzal F, Zitouni L, Alouani R, Slimane F, Bobier C, Zargouni F (2001) Subsurface Mesozoïc Basins in the Central Atlas of Tunisia, tectonics, sequence deposit distribution and hydrocarbon potential. AAPG Bull 85:885–907

Ben Ismaïl MH (1982) Le Trias et le Jurassique inférieur et moyen évaporitiques de l'extrême Sud tunisien: étude de sondages profonds et de terrain, synthèses paléogéographiques, p 180. Unpublished thesis, 3éme cycle, Université Paris VI

Ben Youssef M (1999) Stratigraphie génétique du Crétacé de Tunisie, Micropaléontologie, stratigraphie séquentielle et géodynamique des bassins de la marge sud et péri-téthysienne, p 420. D.Sc. Thesis. Univ. de Tunis II

Ben Youssef M, Peybernes B (1986) Données micropaléontologiques et biostratigraphiques nouvelles sur le Crétacée inférieur marin du Sud tunisien. J Afr Earth Sci 5:217–231

Ben Youssef M, Biely A, Memmi L (1985) La Formation Orbata (Aptien) en Tunisie méridionale. In: Précisions biostratigraphiques nouvelles, no 51, pp 105–120

Billi A, Faccenna C, Bellier O, Minelli L, Neri G, Piromallo C, Presti D, Scrocca D, Serpelloni E (2011) Recent tectonic reorganization of the Nubia–Eurasia convergent boundary heading for the closure of the western Mediterranean. Bull Soc Geol Fr 182:279–303

Boltenhagen C (1985) Paléogéographie du crétacé moyen de la Tunisie centrale. In: 1ercongr. Nat Sci Terre (Tunis 1981), pp 97–114

Bouaziz S, Barrier E, Angelier J, Turki MM (1994) Paleostress in the Southern Tunisian platform. In: Roure F (ed) Peri-tethyan platforms. Technip Editions, France, pp 179–196

Bouaziz S, Barrier E, Turki MM, Tricart P (1999) La tectonique permo-mésozoïque (anté-Vraconien) dans la marge sud téthysienne en Tunisie méridionale. Bull Soc Géol Fr 170:45–56

Bouaziz S, Barrier E, Soussi MM, Turki MM, Zouari H (2002) Tectonic evolution of the northern African margin in Tunisia from paleostress data and sedimentary record. Tectonophysics 357:227–253

Boughdiri M, Cordey F, Sallouhi H, Maalaoui K, Masrouhi A, Soussi M (2007) Jurassic radiolarian-bearing series of Tunisia: biostratigraphy and significance to western Tethys correlations. Swiss J Geosci 100:431–441

Boukhalfa K, Li G, Ben Ali W, Soussi M (2015) Early Cretaceous spinicaudatans ("conchostracans") from lacustrine strata of the Sidi Aïch Formation in the northern Chotts range, southern Tunisia: taxonomy, biostratigraphy and stratigraphic implication. Cretac Res 56:482–490

Bracène R, Frizon de Lamotte D (2002) Origin of intraplate deformation in the Atlas system of western and central Algeria: from Jurassic rifting to Cenozoic-Quaternary inversion. Tectonophysics 357:207–226

Burollet PF (1991) Structures and tectonics of Tunisia. Tectonophysics 195:359–369

Castany G (1954) Les grands traits structuraux de la Tunisie Bull. Soc Géol France 6:151–173

Castelluccio A, Andreucci B, Zattin M, Ketcham RA, Jankowski L, Mazzoli S, Szaniawski R (2015) Coupling sequential restoration of balanced cross sections and low-temperature thermochronometry: the case study of the Western Carpathians. Lithosphere 7:367–378

Chihi L (1992) Seismotectonic study in Central and southern Tunisia. Tectonophysics 209:175–178

Creuzot G, Mercier E, Ouali J, Tricart P (1993) La tectogenèse atlasique en Tunisie centrale: Apport de la modélisation géométrique. Eclogae Geol Helv 86:609–627

Damotte R (1990) Early Cretaceous ostracodes from Tethyan regions. Cretac Res 11:307–311

DeCelles PG, Giles KN (1996) Foreland basin systems. Basin Res 8:105–123

Dhaoui M, Gabtni H (2013) Fault pattern delineation and structural interpretation of the Gafsa trough (onshore central Tunisia) using gravity data. Arab J Geosci 6(5):1559–1568

Dlala M (1992) Seismotectonic study in northern Tunisia. Tectonophysics 209:171–174

El Amari EA, Gharbi M, Youssef MB, Masrouhi A (2016) The structural style of the Southern Atlassic foreland in Northern Chotts Range in Tunisia: field data from Bir Oum Ali Structure. Arab J Geosci 9:389

Ellouz N, Patriat M, Gaulier JM, Bouatmani R, Sabounji S (2003a) From rifting to Alpine inversion: Mesozoic and Cenozoic subsidence history of some Moroccan basins. Sediment Geol 156:185–212

Ellouz N, Patriat M, Dey Z, Gaulier JM, Ben KH (2003b) The Hammamet, Gabes and Chotts basins (Tunisia) a review of the subsidence history. Sediment Geol 156:241–262

Faccenna C, Piromallo C, Crespo-Blanc A, Jolivet L, Rossetti F (2004) Lateral slab deformation and the origin of the westernMediterranean arcs. Tectonics 23:TC1012

Fakraoui M (1990) Etude stratigraphique et structurale des chaînes de Chotts: Evolution géométrique et cinématique liée à l'accident Sud-Atlasique. Thèse 3ième cycle

Fakraoui M, Rabiaa C, Abbès C, Zargouni F, Bensalem H (1991) Carte géologique de Bir Rakeb, au 1/100.000, feuille n°73. Service Géologique Nationale d'Office Nationale de Mines, Tunisie

Faure P, Peybernes B (1986) Biozonation par Ammonites et essai de corrélation des séries réduites liasiques de la "Dorsale Tunisienne". Bull Soc Hist Nat Toulouse 22:4149

Frizon de Lamotte D, Saint-Bezar B, Bracene R, Mercier E (2000) The two main steps of the Atlas building and geodynamics of the western Mediterranean. Tectonics 19:740–761

Frizon de Lamotte D, Raulin C, Mouchot N, Wrobel-Daveau JC, Blanpied C, Ringenbach JC (2011) The southernmost margin of the Tethys realm during the Mesozoic and Cenozoic: initial geometry and timing of the inversion processes. Tectonics 30:TC3002

Gharbi M (2013) Relationship between the southern Atlas foreland and the eastern margin of Tunisia (Chotts-Gulf of Gabes): Tectono-sedimentary, fault kinematics and balanced cross sections. Ph.D, Marseille University

Gabtni H, Jallouli C, Mickus KL, Bédir M (2011) Geodynamics of the Southern Tethyan Margin in Tunisia and Maghrebian domain: new constraints from integrated geophysical study. Arab J Geosci 6:271–286

Gharbi M, Masrouhi A, Espurt N, Bellier O, Amari EA, Ben Youssef M, Ghanmi M (2013) New tectono-sedimentary evidences for Aptian to Santonian extension of the Cretaceous rifting in the Northern Chotts range (Southern Tunisia). J Afr Earth Sci 79:58–73

Gharbi M, Bellier O, Masrouhi A, Espurt N (2014) Recent spatial and temporal changes in the stress regime along the southern Tunisian Atlas front and the Gulf of Gabes: new insights from fault kinematics analysis and seismic profiles. Tectonophysics 626:120–136

Gharbi M, Espurt N, Masrouhi A, Bellier O, Amari EA (2015) Style of Atlassic tectonic deformation and geodynamic evolution of the southern Tethyan margin, Tunisia. Mar Pet Geol 66:801–816

Guiraud R (1998) Mesozoic rifting and basin inversion along the northern African Tethyan margin: an overview. In: MacGregor DS, Moody RTJ, Clark-Lowes DD (eds) Petroleum geology of North Africa, vol 133. Geological Society, London, Special Publication, pp 217–229

Guiraud R, Bosworth W (1997) Senonian basin inversion and rejuvenation of rifting in Africa and Arabia: synthesis and implications to plate-scale tectonics. Tectonophysics 282:39–82

Guiraud R, Bosworth W, Thierry J, Delplanque A (2005) Phanerozoic geological evolution of Northern and Central Africa: an overview. J Afr Earth Sci 43:83–143

Guiraud R, Maurin JC (1991) Le rifting en Afrique au Crétacé inférieur: synthèse structurale, mise en évidence de deux étapes dans la genèse des bassins, relations avec les ouvertures océaniques périafricaines. Bull Soc Géol Fr 162:811–823

Guiraud R, Maurin JC (1992) Early Cretaceous rifts of Western and Central Africa: an overview. Tectonophysics 213:153–168

Herkat M, Guiraud R (2006) The relationships between tectonics and sedimentation in the Late Cretaceous series of the Eastern Atlasic Domain (Algeria). J Afr Earth Sci 46:346–370

Hlaiem A (1999) Halokinisis and structural evolution of the major features in eastern and southern Tunisian Atlas. Tectonophysics 306:79–95

Hlaiem A, Biju-Duval B, Laatar E, Rolland V, M'Rabet A (1997) The Gafsa-Metlaoui foreland basin (Southern Tunisia): quantitative modeling of the burial and thermal histories. Implications on the petroleum exploration. J Pet Geol 20:403–426

Jaillard E, Bouillin JP, Ouali J, Dumont T, Latil JL, Chihaoui A (2017) Albian salt-tectonics in Central Tunisia: evidences for an Atlantic-type passive margin. J Afr Earth Sci 135:220–234

Kamoun F, Peybernes B, Ciszak R, Calzada S (2001) Triassic paleogeography of Tunisia. Paleogeogr Paleoclimatol Paleoecol 175:223–242

Khomsi S, Ben Jemia MG, Frizon de Lamotte D, Maherssi C, Echihi O, Mezni R (2009) An overview of the Late Cretaceous–Eocene positive inversions and Oligo–Miocene subsidence events in the foreland of the Tunisian Atlas: structural style and implications for the tectonic agenda of the Maghrebian Atlas system. Tectonophysics 475:38–58

Laaridhi-Ouazaa N (1994) Etude minéralogique et géochimique des épisodes magmatiques mésozoïques et miocènes de la Tunisie, p 466. Univ. Tunis II, Tunisia. Thèse Doc. Etat

Laville E, Pique A, Amrhar M, Charroud M (2004) A restatement of the Mesozoic Atlasic rifting (Morocco). J Afr Earth Sci 38:145–153

Lazzez M, Ben Youssef M (2008) Relative sea level changes of the Lower Cretaceous deposits in the Chotts area of Southern Tunisia. Turk J Earth Sci 17:835–845

Louhaïchi MA, Tlig S (1993) Tectonique synsédimentaire des séries post-Barrémiennes au Nord-Est de la chaîne Nord des Chotts (Tunisie méridionale). Géologie Méditerranéenne XX(1), 53–74

M'Rabet A (1987) Stratigraphie, sédimentation, et diagenèse carbonatée des séries du Crétacé inférieur de Tunisie centrale. Ann Mines Géol (Tunis) 18:412

Marie J, Trouve P, Desforges G, Dufaure P (1984) Nouveaux éléments de paléogéographie du Crétacée de Tunisie. In: Notes Mém. Comp. Franc. Pétrol, vol 19

Marmi R, Guiraud R (2006) End Cretaceous to recent polyphased compressive tectonics along the "Mole Constantinois" and foreland (NE Algeria). J Afr Earth Sci 45:123–136

Martinez C, Chikhaoui M, Truillet R, Ouali J, Creuzot G (1991) Le contexte géodynamique de la distension albo-aptienne en Tunisie septentrionale et centrale: structuration éocrétacée de l'Atlas tunisien. Eclogae Geol Helv 84:61–82

Masrouhi A, Bellier O, Koyi H, Vila JM, Ghanmi M (2013) The evolution of Lansarine-Baouala salt canopy in North African Cretaceous passive margin in Tunisia. Geol Mag 150(5):835–861

Masrouhi A, Bellier O, Koyi H (2014a) Geometry and structural evolution of Lorbeus diapir, northwestern Tunisia: polyphase diapirism of the North African inverted passive margin. Int J Earth Sci (Geol Rundsch) 103:881–900

Masrouhi A, Bellier O, Youssef MB, Koyi H (2014b) Submarine allochthonous salt sheets: gravity-driven deformation of North African Cretaceous passive margin in Tunisia e Bled Dogra case study and nearby salt structures. J Afr Earth Sci 97:125–142

Masrouhi A, Ghanmi M, Ben Slama M-M, Ben Youssef M, Vila J-M, Zargouni F (2008) New tectono-sedimentary evidence constraining the timing of the positive tectonic inversion and the Eocene Atlasic phase in northern Tunisia: implication for the North African paleo-margin evolution. C R Geosci 340:771–778

Masrouhi A, Koyi H (2012) Submarine "salt glacier" kinematics of Northern Tunisia, a case of Triassic salt mobility in North African Cretaceous passive margin. In: Alsop GI, Archer SG, Hartley A, Grant NT, Hodgkinson R (eds) J. Geol. R. Salt tectonics, sediments and prospectivity, vol 363. Geological Society, London, Special Publications, pp 579–593

Mattoussi Kort H, Gasquet D, Ikenne M, Laridhi Ouazaa N (2009) Cretaceous crustal thinning in North Africa: Implications for magmatic and thermal events in the Eastern Tunisian margin and the Pelagic Sea. J Afr Earth Sci 55:257–264

Michard A, Chalouan A, Feinberg H, Goffé B, Montigny R (2002) How does the Alpine belt end between Spain and Morocco? Bull Soc Géol Fr 173:3–15

Morgan MA, Grocott J, Moody RTJ, (1998) The structural evolution of the Zaghouan-Ressas Structural Belt, northern Tunisia. In: MacGregor DS, Moody RTJ, Clark-Lowes DD (eds) Petroleum Geology of North Africa, vol 132. Special Publications of the Geological Society, London, Special Publication, pp 405–422

Naji Ch, Gharbi M, Amri Z, Masrouhi A, Bellier O (In press) Temporal and spatial changes of the submarine Cretaceous paleoslope in Northern Tunisia, inferred from slump folds analysis. In: Proceedings of the Geologists' Association

Outtani F, Addoum B, Mercier E, de Frizon Lamotte D, Andrieux J (1995) Geometry and kinematics of the south Atlas front, Algeria and Tunisia. Tectonophysics 249:233–248

Piqué A, Tricart P, Guiraud R, Laville E, Bouaziz S, Amrhar M, Ait Ouali R (2002) The Mesozoic–Cenozoic Atlas belt (North Africa): an overview. Geodin Acta 15:185–208

Rabiaa MC (1985) Etude géologique de la région des Chotts (Sud tunisien) par télédétection spatiale, détection de la radioactivité naturelle et analyse hydrogéochimique. Thèse 5ème cycle. Bordeaux, p 201

Raulin C, Frizon de Lamotte D, Bouaziz S, Khomsi S, Mouchot N, Ruiz G, Guillocheau F (2011) Late Triassic–early Jurassic block tilting along E-W faults, in southern Tunisia: New interpretation of the Tebaga of Medenine. J Afr Earth Sci 61:94–104

Riley P, Gordon C, Simo JA, Tikoff B, Soussi M (2011) Structure of the Alima and associated anticlines in the foreland basin of the southern Atlas Mountains, Tunisia. Lithosphere 3(1):76–91

Roure F, Casero P, Addoum B (2012) Alpine inversion of the North African margin and delamination of its continental lithosphere. Tectonics 31:TC3006

Roure F, Colletta B (1996) Cenozoic inversion structures in the foreland of the Pyrenees and Alps. In: Ziegler PA (ed) Peri-TethysMemoir 2: structure and prospects of Alpine Basins and forelands. Memoirs of the National Museum of Natural History, vol 170, pp 173–209

Said A, Dominique C, Baby P, Ouali J (2011a) Active oblique ramp faulting in the Southern Tunisian Atlas. Tectonophysics 499:178–189

Said A, Baby P, Dominique C, Ouali J (2011b) Structure, paleogeographic inheritance, and deformation history of the southern Atlas foreland fold and thrust belt of Tunisia. Tectonics 30:TC6004

Sekatni N, Fauré P, Alouani R, Zargouni F (2008) Le passage Lias–Dogger de la Dorsale de Tunisie septentrionale. Nouveaux apports biostratigraphiques. Âge Toarcien supérieur de la distension téthysienne C. R. Palevol. 7185–7194

Serpelloni E, Vannucci G, Pondrelli S, Argnani A, Casula G, Anzidei M, Baldi P, Gasperini P (2007) Kinematics of the western Africa-Eurasia plate boundary from focal mechanisms and GPS data. Geophys J Int 169:1180–1200

Soua M (2016) Cretaceous oceanic anoxic events (OAEs) recorded in the northern margin of Africa as possible oil and gas shale potential in Tunisia: an overview. Int Geol Rev 58(3):277–320

Soua M, Echihi O, Herkat M, Zaghbib-Turki D, Smaoui J, Jemia HFB, Belghaji H (2009) Structural context of the paleogeography of the Cenomanian–Turonian anoxic event in the eastern Atlas basins of the Maghreb. C R Geosci 341(12):1029–1037

Souquet P, Peybernès B, Saadi J, BenYoussef M, Ghanmi M, Zarbout M, Chikhaoui M, Kamoun F (1997) Séquences et cycles d'ordre 2 en régime extensif et transtensif: exemple du Crétacé inférieur de l'Atlas tunisien. Bull Soc Geol Fr 168:373–386

Soussi M (2002) Le Jurassique de la Tunisie atlasique : Stratigraphie, dynamique sédimentaire, Paléogéographie et intérêt pétrolier, vol 157. Documents des Laboratoires de Géologie de Lyon, p 363

Soussi M, Niedźwiedzki G, Tałanda M, Drożdż D, Sulej T, Boukhalfa K, Mermer J, Błażejowski B (2017) Middle Triassic (Anisian-Ladinian) Tejra red beds and Late Triassic (Carnian) carbonate sedimentary records of southern Tunisia, Saharan Platform: biostratigraphy, sedimentology and implication on regional stratigraphic correlations. Mar Pet Geol 79:222–256

Stampfli GM, Marcoux J, Baud A (1991) Tethyan margins in space and time. Palaeogeogr Palaeoclimatol Palaeoecol 87:373–410

Swezey CS (1996) Structural controls on Quaternary depocentres within the Chotts Trough region of southern Tunisia. J Afr Earth Sci 22:335–347

Tlig S (2015) The Upper Jurassic and Lower Cretaceous series of southern Tunisia and northwestern Libya revisited. J Afr Earth Sci 110:100–115

van Hinsbergen D, Vissers R, Spakman W (2014) Origin and consequences of western Mediterranean subduction, rollback, and slab segmentation. Tectonics 33(4):393–419

Vila JM (1980) La chaine alpine d'Algérie orientale et des couffins Algéro-tunisiens, Thèse Es-sciences, Paris

Zargouni F (1984) Style et chronologie des déformations des structures de l'Atlas tunisien méridional. Evolution récente de l'accident Sud-atlasique. C R Acad Sci Paris 299:179–196

Zargouni F (1985) Tectonique de l'Atlas méridional de Tunisie, évolution géométrique et cinématique des structures en zone de cisaillement. Univ. Louis Pasteur, Strasbourg-Paris. Thèse d'Etat

Zargouni F, Abbes C (1987) Zonation structurale de la Tunisie. In: Rev Sc De la terre, vol 6, pp 63–69. Tunisie, 1987

Zargouni F, Ruhland M (1981) Style des déformations du quaternaire récent liée au coulissement de la faille de Gafsa et chronologie des phases tectoniques de l'Atlas méridional de Tunisie. C R Acad Sc Paris T 292:913–915

Zargouni F, Termoliéres JC (1981) Déformations tectoniques postérieures au dépôt de la série du Segui (Plio-Villafranchien) dans l'Atlas méridional tunisien. In: Actes 1er Cong. Nation. Sci. Terre, Tunis

Zargouni F, Rabiaa MC, Abbés C (1985) Rôle des couloirs de cisaillement de Gafsa et de Négrine-Tozeur dans la structuration du faisceau des plis des Chotts, éléments de l'accident sud-atlasique. C R Acad Sci Paris 301(11):831–883

Ziegler PA, Cloetingh S, van Wees JD (1995) Dynamics of intra-plate compressional deformation: the alpine foreland and other examples. Tectonophysics 252:7–59

Zouaghi T, Guellala R, Lazzez M, Bédir M, Ben Youssef M, Inoubli MH, Zargouni F (2011) The Chott Fold Belt of Southern Tunisia, North African Margin: structural pattern, tectono-sedimentary, and regional geodynamic implications. New frontiers in tectonic research—at the midst of plate convergence. Intech-Book, Vienna, Austria, pp 49–72. ISBN 978-953-307-594-5

Zouari H, Turki MM, Delteil J (1990) Nouvelles données sur l'évolution tectonique de la chaîne de Gafsa. Bull Soc Géol Fr 8:621–628

U–Pb Zircon Geochronology and Geochemistry of Some Plutonic Rocks from the Afif Terrane of Saudi Arabia, Arabian Shield: Implications for Crustal Evolution

Hesham M. Harbi

Abstract

The study areas (Bulghah and Hamimuah) are located in the Afif terrane between the Halaban–Zarghat fault zone and Ar Rika fault zone. They consist of many gabbroic to granitic I-type intrusions emplaced into Neoproterozoic volcanosedimentary rocks and are intruded by Neoproterozoic A-type granites. The studied plutonic rocks are I-type magmatic rocks, calk-alkaline, metaluminous to slightly peraluminous (A/CNK > 1.2), formed in a volcanic arc setting. On a primitive mantle-normalized spider diagrams, almost all rocks show a significant Nb–Ta–Ti depletions relative to K and La, which is typical of magmatism from a subduction zone tectonic setting. Geochemical features of the mafic intrusion (gabbro and diorite) are comparable to those of the arc-metavolcanic calc-alkaline rocks of the Arabian Shield, which were produced by partial melting of plagioclase- or spinel-peridotite in the upper most mantle <80 km deep in an intra-oceanic island arc. This suggests that the mafic intrusive rocks of Bulghah and Humaymah represent the plutonic equivalents of the Arabian Shield arc metavolcanic calc-alkaline rocks. The compositional variations from granodiorite to monzogranite of Bulghah and Humaymah suggest various degree of fractional crystallization of feldspar, biotite and amphibole. Y/Nb with Th/Nb, Th/Ta and Ce/Pb relationships indicate that the granodiorite and monzogranite were generated by a mafic parental magma contaminated with crustal materials, and controlled by fractional crystallization. Zircon U–Pb dating indicates that the mafic intrusive rocks from Bulghah and Humaymah, Saudi Arabia were formed at ∼670 Ma, whereas the granitoid I-type intrusions were formed between 661 ± 5 and 643 ± 4 Ma, confirming the importance of the 640–700 Ma crust forming event in Saudi Arabia.

6.1 Introduction

The Arabian Shield (AS, Fig. 6.1) consists of Neoproterozoic juvenile tectonostratigraphic island-arc terranes formed by subduction within and around the Mozambique Ocean between 850 and 550 Ma in the framework of the Gondwana supercontinent assembly (Stern 1994; Nehlig et al. 2002; Stern and Johnson 2010). These terranes are joined by ophiolite-decorated sutures (Stoeser and Camp 1985; Johnson and Woldehaimanot 2003). The AS is divided into at least five tectonostratigraphic terranes (Fig. 6.1; Stoeser and Camp 1985): Midyan, Hijaz, Asir, Ar Ryan and Afif with some workers (e.g., Johnson and Woldehaimanot 2003) discussed the possibility of three more terranes (Jiddah, Ad Dawadimi and Khida). All terranes (except Khida; Stacey and Agar 1985; Stoeser and Frost 2006) are regarded as Neoproterozoic oceanic arcs, including fore-arc and/or backarc crust and ophiolites (Dilek and Ahmed 2003; Stoeser and Frost 2006).

The evolution of the AS terranes records three main tectonic stages of intra-oceanic subduction (850–700 Ma), collision and terrain amalgamation (700–635 Ma), and tectonic escape, strike-slip faulting and extension (635–550 Ma) of the newly formed continental crust (Genna et al. 2002; Johnson and Woldehaimanot 2003; Be'eri-Shlevin et al. 2009; Eyal et al. 2010; Stern and Johnson 2010; Johnson et al. 2011). The volcanic arc crust range in composition from tholeiitic, through calc-alkaline to late high-K suites (Robool et al. 1983). Syn-to Post-collisional

H. M. Harbi (✉)
Department of Mineral Resources and Rocks, Faculty of Earth Sciences, King Abdulaziz University, P.O. Box 80206 Jeddah, 21589, Saudi Arabia
e-mail: harbihesham@hotmail.com
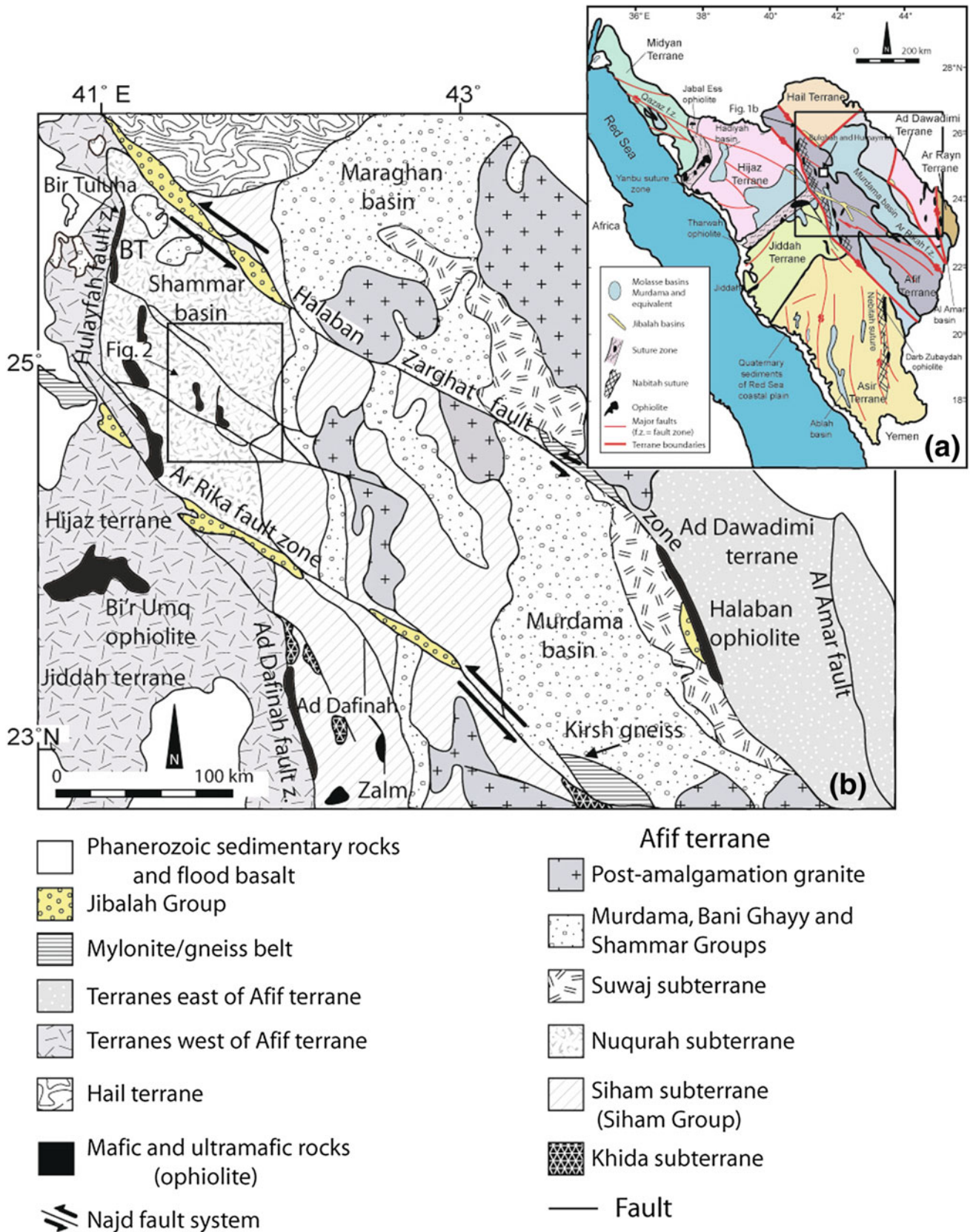
Fig. 6.1 a General geologic map of the Arabian Shield showing major tectonostratigraphic terranes, ophiolite belts, sutures, fault zones and post-accretionary basins in the Arabian Shield of western Saudi Arabia (modified after Nehlig et al. 2002; Johnson and Woldenhaimanot 2003; Stern and Johnson 2010). Numbers are locations of the I-type intrusive rocks represented in geochemical Figures as follows: (1) Bulghah and Humaymah, (2) Sukhaybarat, (3) Jabal Ghadarah, and (4) Makkah Suite. b Geological sketch map of the Afif Terrane and adjacent parts of the Arabian Shield showing location of the study area (modified after Johnson and Kattan 1999)

calc-alkaline to alkaline I-type granites intruded by Post-collisional K-rich alkaline to peralkaline A-type granites (e.g., Ali et al. 2009, 2012; Be'eri-Shlevin et al. 2009; Eyal et al. 2010; Moreno et al. 2014; Moghazi et al. 2012).

I-type granitoids (Cryogenian and Early Ediacaran) are major components of the ANS (Moussa et al. 2008; Johnson et al. 2011). Geochemical studies reveal that they are met-aluminous to slightly peraluminous, calc-alkaline, subduction-related intrusives (Pearce et al. 1984; Maniar and Piccoli 1989; Jarrar et al. 2003; Moussa et al. 2008; Be'er-i-Shlevin et al. 2009; Ali et al. 2015; Robinson et al. 2015), formed synchronously with the formation of large molasse basins (Genna et al. 2002; Johnson 1998; Nehlig et al. 2002; Stern and Johnson 2010). The orogenic phase was then followed by continued convergence and the development of regionally extensive strike-slip fault (escape tectonics) from 610 to 525 Ma (Greiling et al. 1994; Stern 1994; Genna et al. 2002; Johnson et al. 2011; Robinson et al. 2014).

Intrusion of post-collisional alkaline to peralkaline rocks (A-type granites) and development of extensive pull-apart basins during the final suturing of the Arabian-Nubian Shield and the formation of subsequent extensional basins (Greiling et al. 1994; Johnson 1998, 2003; Wilde and Youssef 2000; Nehlig et al. 2002; Johnson et al. 2011). The alkaline granites constitute about 2% of the Arabian–Nubian Shield and represent one of the largest fields of alkaline granites on Earth (Stoeser 1986; Liégeois and Stern 2010; Johnson et al. 2011). Petrogenetic models for the generation of A-type alkaline granites range from partial melting of the lower crust to extreme differentiation of mantle-derived tholeiitic or alkaline basaltic magma (Bonin and Giret 1990; Turner et al. 1992; Collins et al. 1992; Frost and Frost 1997; Patiño Douce 1997; Mushkin et al. 2003; Huang et al, 2011). Assimilation of older crustal material into mantle derived granitic magma is plausible model to account for the petrogenesis of such rocks (Eby 1990, 1992; Kemp et al. 2006; Zhang et al. 2012).

This paper will present results of U–Pb zircon geochronology and whole-rock geochemical data of some plutonic rocks from Bulghah and Humaymah areas (west of the Afif terrane) of Saudi Arabia. While gold is mined from Bulghah area since 2001, it is still under evaluation and development by Ma'aden Co. in the Humaymah area. In these areas, gold is spatially associated with some intrusive rocks intruding the layered volanosedimentary the Hulayfah/Siham and Murdamah group rocks. These intrusive rocks can be grouped into two groups; older mafic to intermediate gabbro-diorite and younger intermediate to felsic tonalite-granodiorite intrusive bodies. These data will be used to clarify the magma sources for these rocks, and to assess fractional crystallization as a possible petrogenetic mechanism for the formation of these rocks (Miller 1985; Secchi et al. 1991; Teixeira et al. 2012; Wang et al. 2014).

6.2 Geology Background and Petrography

The two selected areas (Bulghah and Humaymah) for the present study are located in the Afif terrane (Figs. 6.1 and 6.2). The Afif terrane is one of the largest terranes in the Arabian Shield. Much of the recent researches on the shield in the last 15 years, Johnson and Kattan (1999) addressed the composite nature of the Afif terrane in age and provenance, mainly based on detailed mapping, Pb-isotope systematics and U–Pb zircon geochronology (e.g., Stacey and Hedge 1984; Stacey and Agar 1985; Agar 1985, 1988; Agar et al. 1992). Based on these studies, the Afif terrane was divided into four possible subterranes including the Khida, Nuqrah, Siham, and Suwaj (Fig. 6.2). While the Khida subterrane represents remnants of the Archean to Paleoproterozoic continental rocks, the Nuqrah, Siham, and Suwaj subterranes and the post-amalgamation assemblages (Murdama and Bani Ghayy groups) represent the Neoproterozoic volcanic/magmatic arc-subterranes (Johnson and Kattan 1999). Agar et al. (1992) reported 1.7 Ga zircon ages for pre-Neoproterozoic sources in the Khida subterrane. The ophiolite assemblages (mafic/ultramafic rocks) represent the oldest Neoproterozoic rocks in the study areas. A plagiogranite dyke in serpentinized peridotites from a near vicinity to the study area in the Bir Tuluha ophiolite (Fig. 6.2) yielded U–Pb zircon ages from 843 to 821 Ma (Pallister et al. 1988). The mafic-ultramafic rocks are represented by gabbro, metabasalt, serpentinites, listvenites and amphibolites. The Siham group (Fig. 6.2) is unconformably overlain by the volcanosedimentary rocks of the Bani Ghayy group (Stacey and Agar 1985). The Siham group is metamorphosed to greenschist facies and composed mainly of volcanosedimentary assemblages. It is composed mainly of basaltic lava range from tholeiitic to calc-alkaline and has affinity with lavas in active continental margins (Agar 1986). The sedimentary rocks of Siham group are represented by lithic sandstone, shale and conglomerate. The age of the Siham group is constrained at ~746 ± 10 Ma (Agar et al. 1992) from a granodiorite sample from Naim complex which intruded the Siham group. The Bani Ghayy group in the study area consists of unmetamorphosed sandstone, conglomerate, limestone, basalt and rhyolite. In the western part of the study area (Fig. 6.2), the Bani Ghayy and Murdama groups are separated by a thrust fault. Some workers considered the two groups to be equivalent because they are similar in age and lithology (Brown et al. 1989). The two groups suggested to be deposited during and soon after the Nabitah orogeny (680–640 Ma, Johnson et al. 2011). Stacey and Agar (1985) reported a U–Pb zircon age of 620 ± 5 Ma for a rhyolite sample from the Bani Ghayy group and a volcanic sample from Murdama group yielded a U–Pb zircon age of 625 ± 4 (Kusky and Matsah 2003)..
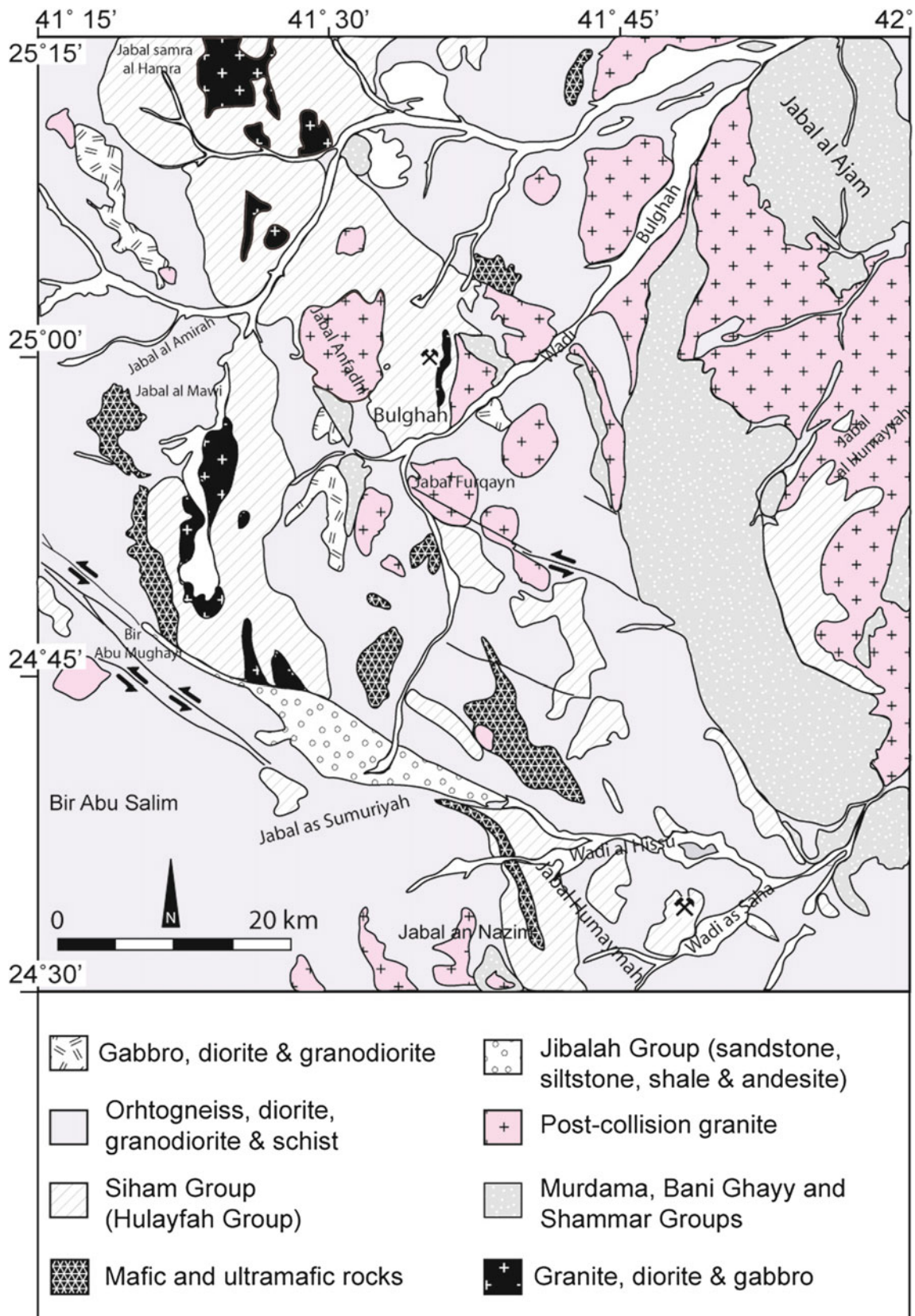
Fig. 6.2 Geological map showing the study areas (Bulghah and Humaymah) modified from the Geological maps 1:250000 of the Al Hissu quadrangle, sheet 24 E (Delfour 1981) and the Nuqrah quadrangle, sheet 25 E (Delfour 1977)

Table 6.1 SHRIMP Th-U-Pb zircon data for samples from Saudi Arabia

Spot No.	U ppm	Th ppm	Th/U	204Pb/206Pb	208Pb/232Th	% error	f206 %	207Pb*/206Pb*	% error	206Pb*/238U	% error	207Pb*/235U	% error	208Pb/232Th	% error	err corr	AGE 204 correction 208Pb/232Th	1σ error	207Pb*/206Pb*	1σ error	206Pb*/238U	1σ error
Sample B139 (Bulgah diorite)																						
B139.1	115	39	0.34	0.00019	0.0356	2.76	0.33	0.0597	0.001	0.113	0.002	0.930	0.028	0.033	3.71	0.57	663	25	591	53	691	11
B139.2	78	21	0.27	0.00021	0.0361	3.33	0.37	0.0592	0.001	0.111	0.002	0.910	0.027	0.033	3.85	0.56	655	25	575	53	681	10
B139.3**	102	51	0.50	0.00005	0.0359	2.48	0.08	0.0632	0.001	0.116	0.002	1.010	0.025	0.035	2.54	0.63	704	18	715	40	707	10
B139.4	69	24	0.35	0.00056	0.0355	3.32	0.99	0.0564	0.003	0.110	0.002	0.858	0.052	0.029	8.63	0.29	578	50	468	129	675	11
B139.5	114	31	0.27	0.00033	0.0371	2.85	0.58	0.0583	0.001	0.111	0.002	0.896	0.022	0.032	2.93	0.62	640	19	543	42	681	10
B139.6	138	38	0.28	0.00027	0.0378	2.79	0.47	0.0609	0.002	0.112	0.002	0.938	0.041	0.034	7.17	0.35	674	48	634	88	683	10
B139.7	133	41	0.30	0.00004	0.0348	2.82	0.07	0.0630	0.001	0.108	0.002	0.941	0.024	0.035	3.18	0.61	702	22	708	42	663	10
B139.8	95	30	0.31	0.00010	0.0343	3.27	0.17	0.0647	0.001	0.112	0.002	0.997	0.028	0.036	3.65	0.61	705	26	764	47	683	11
B139.9**	136	70	0.52	0.00001	0.0344	2.37	0.02	0.0658	0.001	0.111	0.002	1.003	0.022	0.035	2.34	0.67	686	16	800	35	676	10
B139.10	113	54	0.48	0.00032	0.0361	2.54	0.56	0.0591	0.003	0.113	0.002	0.921	0.045	0.033	5.05	0.32	664	33	573	101	690	10
B139.11	118	37	0.31	0.00011	0.0349	2.89	0.20	0.0637	0.001	0.108	0.002	0.948	0.024	0.033	3.14	0.61	664	21	731	42	661	10
B139.12	161	43	0.27	0.00007	0.0359	2.71	0.13	0.0634	0.001	0.110	0.002	0.961	0.022	0.035	3.04	0.64	692	21	722	37	672	9
B139.13	134	52	0.39	0.00038	0.0344	2.62	0.68	0.0591	0.001	0.111	0.002	0.904	0.025	0.030	3.21	0.55	606	19	571	51	678	10
B139.14	120	59	0.49	0.00016	0.0354	2.49	0.28	0.0622	0.002	0.109	0.002	0.937	0.030	0.034	3.22	0.49	677	22	681	59	668	10
B139.15	65	18	0.28	0.00032	0.0342	3.94	0.56	0.0591	0.002	0.112	0.002	0.912	0.040	0.029	7.19	0.41	588	42	571	87	684	12
B139.16	100	31	0.31	0.00044	0.0355	3.10	0.77	0.0564	0.002	0.112	0.002	0.869	0.038	0.030	6.49	0.37	594	39	470	90	682	10
B139.17**	98	45	0.45	0.00123	0.0355	3.11	2.17	0.0582	0.006	0.101	0.002	0.812	0.080	0.025	11.34	0.17	507	57	537	212	622	10
B139.18	156	41	0.27	0.00000	0.0371	2.69	0.00	0.0645	0.001	0.113	0.002	1.005	0.022	0.037	2.65	0.67	737	20	757	33	691	9
B139.19**	72	24	0.34	0.00014	0.0386	4.61	0.25	0.063	0.004	0.112	0.002	0.973	0.072	0.037	9.80	0.25	732	72	709	151	684	12
B139.20	69	22	0.32	0.00048	0.0355	3.60	0.85	0.0603	0.002	0.109	0.002	0.903	0.029	0.030	3.68	0.55	588	22	614	58	665	11
B139.21	130	64	0.49	0.00043	0.0323	2.47	0.77	0.0582	0.003	0.107	0.002	0.857	0.044	0.029	5.46	0.30	576	31	536	107	654	10
Sample B-mine (Bulgah quartz diorite)																						
B-mine.1	58	16	0.28	0.00046	0.0374	3.68	0.54	0.0598	3.888	0.111	1.539	0.911	4.182	0.031	6.61	0.37	610	40	596	84	676	10
B-mine.2**	60	16	0.27	0.00059	0.0460	7.80	0.46	0.0595	7.185	0.123	2.005	1.006	7.460	0.036	10.10	0.27	719	73	586	156	746	14
B-mine.3	75	32	0.43	0.00028	0.0343	2.96	0.48	0.0615	2.817	0.108	1.453	0.919	3.169	0.032	3.52	0.46	631	22	657	60	663	9
B-mine.4	69	22	0.32	0.00033	0.0386	3.22	0.68	0.0627	6.80	0.110	1.537	0.951	6.968	0.034	10.36	0.22	685	71	700	145	673	10
B-mine.5	102	35	0.35	0.00035	0.0352	3.03	0.39	0.0603	4.30	0.111	1.346	0.921	4.506	0.031	6.55	0.30	620	41	615	93	677	9
B-mine.6	70	21	0.30	0.00041	0.0349	3.33	0.67	0.0610	5.03	0.107	1.484	0.899	5.243	0.030	8.79	0.28	588	52	638	108	655	9
B-mine.7	76	21	0.28	0.00047	0.0349	3.32	0.46	0.0584	5.42	0.107	1.462	0.861	5.617	0.028	10.00	0.26	565	57	546	118	655	9
B-mine.8	74	28	0.37	0.00027	0.0351	3.29	0.31	0.0605	3.23	0.109	1.433	0.909	3.532	0.032	4.50	0.41	641	29	620	70	667	9
B-mine.9	163	58	0.36	0.00019	0.0338	2.25	0.04	0.0592	2.66	0.108	1.190	0.879	2.916	0.032	3.75	0.41	629	24	573	58	660	7

(continued)

Table 6.1 (continued)

Spot No.	U ppm	Th ppm	Th/U	$^{204}Pb/$ ^{206}Pb	$^{208}Pb/$ ^{232}Th	% error	$f206$ %	$^{207}Pb*/$ $^{206}Pb*$	% error	$^{206}Pb*/$ ^{238}U	% error	$^{207}Pb*/$ ^{235}U	% error	$^{208}Pb/$ ^{232}Th	% error	err corr	AGE 204 correction $^{208}Pb/$ ^{232}Th	1σ error	$^{207}Pb*/$ $^{206}Pb*$	1σ error	$^{206}Pb*/$ ^{238}U	1σ error
B-mine.10	150	61.1	0.41	0.00019	0.0346	2.20	0.07	0.0597	2.84	0.109	1.213	0.902	3.088	0.033	3.58	0.39	651	23	594	62	670	8
Sample Hm19 (Humaymah diorite)																						
Hm19.1	76	27	0.36	0.00157	0.0467	2.26	2.77	0.0576	0.006	0.108	0.002	0.856	0.084	0.029	13.08	0.14	581	76	515	212	659	9
HM19.2	150	36	0.24	0.00008	0.0339	2.10	0.15	0.0638	0.001	0.112	0.001	0.986	0.021	0.035	3.144	0.52	702	22	736	38	685	7
Hm19.3*	188	67	0.36	0.00002	0.0333	1.75	0.04	0.0630	0.001	0.106	0.001	0.920	0.014	0.034	1.752	0.69	667	12	707	24	649	6
Hm19.4	106	29	0.28	0.00010	0.0362	2.33	0.18	0.0620	0.002	0.111	0.001	0.953	0.027	0.035	4.515	0.42	690	31	673	55	681	8
Hm19.5	325	124	0.38	0.00023	0.0366	1.39	0.41	0.0621	0.001	0.112	0.001	0.956	0.024	0.034	2.192	0.38	677	15	677	50	683	6
Hm19.6	232	113	0.49	0.00014	0.0338	1.49	0.25	0.0615	0.001	0.109	0.001	0.926	0.016	0.033	1.839	0.57	650	12	657	31	668	6
Hm19.7	100	30	0.30	0.00015	0.0366	2.28	0.27	0.0591	0.002	0.113	0.001	0.917	0.030	0.034	4.848	0.36	685	33	570	67	688	8
Hm19.8	138	57	0.41	0.00033	0.0356	1.86	0.57	0.0590	0.001	0.111	0.001	0.905	0.024	0.032	3.013	0.42	644	19	568	51	679	7
Hm19.9	149	44	0.30	0.00005	0.0344	2.12	0.10	0.0607	0.001	0.108	0.001	0.906	0.024	0.034	3.857	0.41	669	26	629	52	662	7
Hm19.10	86	23	0.27	0.00035	0.0354	2.55	0.62	0.0596	0.002	0.113	0.001	0.926	0.037	0.03	7.503	0.31	596	45	589	81	688	8
Hm19.11	96	34	0.36	0.00070	0.0363	2.63	1.23	0.0556	0.003	0.107	0.001	0.821	0.046	0.029	7.342	0.23	569	42	437	121	656	8
Hm19.12	139	38	0.27	0.00140	0.0465	2.80	2.47	0.0562	0.005	0.109	0.001	0.841	0.082	0.026	18.6	0.13	516	96	459	215	664	8
Hm19.13	104	36	0.35	0.00001	0.0365	3.15	0.02	0.0644	0.001	0.112	0.001	0.994	0.019	0.037	2.165	0.63	727	16	753	31	685	8
Hm19.14	138	57	0.42	0.00005	0.0354	2.01	0.09	0.0616	0.001	0.113	0.001	0.956	0.021	0.035	2.61	0.51	693	18	660	40	688	7
Hm19.15	101	36	0.36	0.00020	0.0357	2.16	0.35	0.0617	0.002	0.112	0.001	0.954	0.031	0.034	4.419	0.37	666	29	665	66	685	8
Hm19.16*	240	75	0.31	0.00003	0.0361	1.67	0.05	0.0634	0.001	0.109	0.001	0.949	0.015	0.036	2.104	0.61	711	15	721	27	664	6
Hm19.17	177	86	0.49	0.00001	0.0355	1.68	0.01	0.0638	0.001	0.112	0.001	0.985	0.019	0.035	1.731	0.61	704	12	736	33	684	8
Hm19.18*	112	24	0.22	0.00247	0.0617	12.82	4.34	0.0437	0.019	0.115	0.003	0.69	0.297	0.000	0.000	0.05	0	0	-129	1064	699	16
Hm19.19	76	23	0.31	0.00025	0.0356	2.79	0.45	0.0679	0.003	0.112	0.002	1.047	0.043	0.039	6.067	0.42	772	47	865	77	683	11
Hm19.20	110	33	0.30	0.00011	0.0370	2.24	0.19	0.0628	0.002	0.112	0.001	0.972	0.032	0.036	4.054	0.36	707	29	702	65	686	8
Hm19.21	95	28	0.29	0.00014	0.0354	2.33	0.25	0.0656	0.001	0.108	0.001	0.978	0.024	0.037	3.448	0.47	740	26	794	46	662	7

*Common lead corrected using the measured ^{204}Pb
**Indicates data excluded from calculated age

Table 6.2 LA-ICP-MS isotopic data for zircons from Saudi Arabia

Spot	U	^{206}Pb	Isotope ratios								Disc.	Min. rim	Ages					
	ppm	ppm	^{206}Pb/^{204}Pb	^{207}Pb/^{206}Pb*	1σ	^{207}Pb/^{235}U*	1σ	^{206}Pb/^{238}U*	1σ	Rhô	(%)**	(%)***	^{207}Pb/^{206}Pb	1σ	^{207}Pb/^{235}U	1σ	^{206}Pb/^{238}U	1σ
Humaymah tonalite (HC196, n = 14)																		
HC196-01	238	23	7960	0.061600	0.000480	0.870350	0.012180	0.102467	0.001189	0.83	2.5	0	653	17	641	7	638	8
HC196-02*	149	14	3585	0.061060	0.000480	0.877320	0.012320	0.104203	0.001211	0.83	5	0	660	16	636	7	629	7
HC196-03	169	16	3553	0.060760	0.000490	0.878010	0.012490	0.104802	0.001223	0.82	0.4	0	641	15	640	7	639	7
HC196-05	179	17	5076	0.061530	0.000500	0.895960	0.012740	0.105612	0.001235	0.82	1.9	0	631	16	640	7	642	7
HC196-06	149	14	4985	0.061080	0.000500	0.889420	0.012840	0.105618	0.001257	0.83	1.7	0	658	16	650	7	647	7
HC196-07	230	22	6911	0.061430	0.000520	0.887330	0.013220	0.104755	0.001278	0.82	0.9	0	642	17	646	7	647	7
HC196-08*	236	21	5802	0.062440	0.000500	0.840990	0.012380	0.097679	0.001211	0.84	13.5	8.2	689	16	620	7	601	7
HC196-09	154	15	4620	0.061470	0.000560	0.879320	0.013230	0.103747	0.001236	0.79	2	0.0	654	17	645	7	642	7
HC196-11	128	12	3809	0.062260	0.000560	0.897630	0.013480	0.104570	0.001261	0.80	3.1	0.0	656	19	641	7	636	7
HC196-12	101	10	3249	0.060700	0.000490	0.884230	0.012800	0.105650	0.001271	0.83	6.4	0.1	683	18	650	7	641	7
HC196-13	210	20	4786	0.061350	0.000510	0.891900	0.013010	0.105438	0.001267	0.82	3.1	0	629	17	643	7	647	7
HC196-14	163	16	5591	0.061100	0.000490	0.884830	0.012920	0.105026	0.001283	0.84	0.9	0	652	17	647	7	646	7
HC196-17	256	24	9562	0.061430	0.000520	0.884190	0.013160	0.104383	0.001272	0.82	0.2	0	643	17	644	7	644	7
HC196-18	135	13	4827	0.061400	0.000500	0.880050	0.012990	0.103955	0.001285	0.84	2.3	0	655	18	643	7	640	7

*Indicated data excluded from calculated age
**Discordance from the centre of an error ellipse
***Minimum discordance from the rim of an error ellipse

Table 6.3 Major and trace elements of the intrusive rocks from Saudi Arabia

Sample	DL	B20	B21	B22	B24	B26	B27	B28	B29	B30	B31	B32	B39	B40
SiO_2	0.01	51.4	54.7	54.1	56.0	68.1	69.3	68.2	67.4	66.9	68.0	66.4	64.6	65.4
TiO_2	0.01	0.74	0.78	0.77	0.79	0.36	0.33	0.37	0.35	0.35	0.31	0.51	0.5	0.4
Al_2O_3	0.01	17.4	16.2	17.95	16.55	15.15	14.95	15.1	15	14.95	14.65	15.25	14.15	13.7
Fe_2O_3	0.04	7.28	7.21	7.41	6.55	2.8	2.63	2.69	2.73	2.82	2.52	4.03	3.96	3.28
MnO	0.01	0.14	0.14	0.13	0.13	0.04	0.03	0.04	0.04	0.05	0.05	0.04	0.05	0.05
MgO	0.01	1.7	1.87	2.28	1.41	1.41	1.37	1.5	1.57	1.53	1.35	2.23	2.08	1.98
CaO	0.01	7.31	6.81	6.35	6.3	2.83	2.21	3.04	2.99	3.76	3.33	1.99	4.81	4.56
Na_2O	0.01	4.79	3.23	4.41	5.19	4.26	4.71	4.9	4.24	4.31	4.69	4.97	3.1	3.98
K_2O	0.01	2.61	3.51	1.94	2.94	3.12	3.07	2.6	2.52	2.41	2.83	2.39	2.98	2.81
P_2O_5	0.01	0.42	0.43	0.42	0.5	0.11	0.12	0.12	0.11	0.12	0.1	0.14	0.14	0.15
LOI	0.1	4.6	4.5	4.6	4.5	3.2	2.6	3.1	3.6	3.8	3.3	2.8	4.4	4.2
Total		98.5	99.5	100.5	101.0	101.5	101.4	101.8	100.6	101.1	101.3	101.0	100.9	100.7
Ni	20	5	9	7	4	15	14	14	14	14	12	20	19	36
Cr	2	20	30	20	20	80	70	70	70	70	60	70	70	130
Co	20	16	17	19	15	6	7	7	7	9	6	11	12	10
Sc	1	14	13	12	9	2	2	2	1	1	1	4	4	3
V	8	197	165	192	151	53	49	54	55	52	51	83	89	65
Cu	5	195	166	205	163	25	28	23	16	12	24	24	31	26
Ag	0.1	0.2	bdl	bdl	bdl	bdl	bdl	bdl	0.4	0.5	0.3	bdl	0.3	bdl
Pb	1	19	10	10	13	9	6	7	131	294	34	10	5	7
Zn	5	141	91	114	95	27	24	24	27	57	23	32	33	30
Sn	1	1	1	1	1	1	1	1	1	1	1	1	1	1
Ba	1	10	20	30	10	40	30	30	30	30	100	650	40	40
Rb	0.1	46.1	70.1	39.7	47.3	85.5	73.7	63.4	81.4	76.4	72.8	55.8	88.9	64.7
Cs	0.1	1.4	2.3	2.5	1.2	1.5	1.1	1.1	1.2	1.0	1.2	1.0	1.8	1.1
Sr	0.5	618	430	636	422	499	495	549	421	420	430	464	424	468
Ga	0.5	21.2	18.3	20	17.7	18	17.9	18	18.1	18.1	17.8	18.4	17.2	17
Hf	0.1	3.2	3.5	3.3	3.7	3.2	3.7	3.3	3	2.9	3.2	3	3.2	3.3
Nb	0.1	6.9	7.7	6.9	8.1	4.3	7.3	4.8	4.3	4.3	4.1	4	3.4	4.4
Zr	5	117	129	119	141	133	139	135	123	122	131	116	114	117
Y	3	26	26	25	28	11	11	9	9	9	11	14	11	14
Ta	0.1	0.5	0.5	0.5	0.5	0.3	0.4	0.3	0.3	0.4	0.3	0.3	0.2	0.4
Th	0.2	2.5	2.7	2.4	2.9	5.5	9.0	6.6	5.0	4.7	7.2	8.1	5.5	9.6
U	0.1	0.8	0.9	0.8	1.0	3.3	4.2	3.6	3.1	3.0	4.0	3.9	3.3	5.0

(continued)

Table 6.3 (continued)

Sample	DL	B20	B21	B22	B24	B26	B27	B28	B29	B30	B31	B32	B39	B40
La	0.1	15.7	14.2	12.9	15.5	13.4	17.8	15.2	12	13.9	15.7	17.3	13.5	14.8
Ce	0.1	33.0	31.9	29.5	35.5	26.1	33.3	28.6	23.7	25.8	28.0	31.1	26.7	28.2
Pr	0.02	4.33	4.24	3.93	4.76	3.08	3.82	3.28	2.82	2.89	3.13	3.6	3.22	3.25
Nd	0.3	19.7	18.6	17.9	20.7	11.6	14.1	12.6	10.2	10.7	12.1	14.9	12.0	12.1
Sm	0.05	4.62	5.15	4.59	5.25	2.13	2.88	2.39	2.19	1.99	2.37	3.25	2.57	2.51
Eu	0.02	1.47	1.26	1.20	1.27	0.56	0.71	0.65	0.57	0.52	0.59	0.67	0.87	0.91
Gd	0.05	4.50	4.60	4.63	5.12	1.89	2.36	1.98	1.70	1.81	2.14	2.97	2.50	2.66
Tb	0.01	0.72	0.74	0.74	0.83	0.31	0.35	0.28	0.28	0.29	0.34	0.46	0.39	0.4
Dy	0.05	4.40	4.37	4.46	4.98	1.66	2.09	1.61	1.60	1.62	1.94	2.67	2.17	2.52
Ho	0.02	0.96	0.94	0.94	1.05	0.33	0.40	0.34	0.33	0.30	0.39	0.51	0.43	0.52
Er	0.03	2.79	2.77	2.76	3.07	0.93	1.09	0.86	0.84	0.86	1.17	1.33	1.22	1.44
Tm	0.01	0.40	0.40	0.43	0.47	0.15	0.17	0.12	0.15	0.13	0.15	0.21	0.17	0.21
Yb	0.05	2.68	2.85	2.53	2.87	0.93	0.85	0.81	0.84	0.84	0.98	1.16	1.09	1.36
Lu	0.01	0.43	0.45	0.42	0.52	0.14	0.17	0.14	0.14	0.12	0.16	0.17	0.18	0.18
Eu/Eu*		0.98	0.79	0.79	0.75	0.85	0.83	0.91	0.90	0.84	0.80	0.66	1.05	1.08
K/Rb		0.001	0.001	0.001	0.001	0.001	0.001	0.001	0.001	0.001	0.001	0.001	0.001	0.001
Mg#		45.3	46.9	45.0	44.0	26.8	25.8	26.1	26.5	27.2	25.4	34.4	35.7	32.2
Al		0.62	0.56	0.52	0.71	0.69	0.74	0.72	0.65	0.65	0.74	0.71	0.59	0.70
La/Nb		2.3	1.8	1.9	1.9	3.1	2.4	3.2	2.8	3.2	3.8	4.3	4.0	3.4
(La/Yb)N		3.98	3.38	3.46	3.67	9.79	14.23	12.75	9.70	11.24	10.88	10.13	8.41	7.39
(Dy/Yb)N		1.07	1.00	1.15	1.14	1.17	1.61	1.30	1.25	1.26	1.30	1.51	1.30	1.21
(Y/Nb)N		0.58	0.53	0.56	0.55	0.39	0.23	0.30	0.33	0.33	0.43	0.54	0.51	0.48
(Th/Nb)N		3.01	2.92	3.00	3.05	10.79	10.42	11.66	9.90	9.29	14.86	17.26	13.70	18.43
(Th/Ta)N		2.37	2.56	2.36	2.81	8.80	10.83	10.62	8.08	5.68	11.55	13.10	13.25	11.54
(Ce/Pb)N		0.07	0.13	0.12	0.11	0.12	0.22	0.16	0.01	0.00	0.03	0.12	0.21	0.16

(continued)

Table 6.3 (continued)

Sample	B41	B42	B43	B44	B45	B46	B48	B49	B50	B53	B54	B11	B14
Sample	B41	B42	B43	B44	B45	B46	B48	B49	B50	B53	B54	B11	B14
SiO_2	67.4	69.2	67.9	67.1	67.1	74.7	72.5	74.3	74.5	70.5	72.7	55.1	57.5
TiO_2	0.38	0.3	0.33	0.35	0.31	0.19	0.24	0.18	0.19	0.23	0.24	0.98	0.99
Al_2O_3	14.4	14.25	14.25	14.35	13.8	13.00	13.95	12.95	13.00	13.60	13.95	14.63	16.74
Fe_2O_3	2.94	2.39	2.46	2.69	2.26	2.34	2.7	2.32	2.32	2.6	2.55	7.16	6.28
MnO	0.05	0.03	0.03	0.04	0.04	0.05	0.06	0.05	0.05	0.05	0.06	0.1	0.09
MgO	1.78	1.32	1.32	1.18	1.06	0.30	0.63	0.30	0.30	0.61	0.62	6.5	3.59
CaO	3.5	2.69	2.63	3.07	3.7	1.06	1.73	1.05	1.06	1.68	1.72	6.83	4.53
Na_2O	4.57	4.2	4.17	5.33	5.31	4.53	4.10	4.51	4.55	4.02	4.12	3.85	4.31
K_2O	2.27	2.88	2.79	2.45	2.33	4.11	3.51	4.08	4.11	3.43	3.52	2.49	3.16
P_2O_5	0.12	0.11	0.11	0.12	0.13	0.05	0.09	0.04	0.06	0.08	0.09	0.27	0.29
LOI	3.4	2.7	2.8	2.9	3.4	0.93	1.14	0.91	0.87	1.13	1.13	1.7	2.3
Total	101.0	100.2	98.9	99.7	99.5	101.4	100.8	100.8	101.1	98.1	100.9	99.65	99.73
Ni	24	13	15	14	13	1	3	1	2	3	3	123	57
Cr	100	70	70	60	60	20	20	20	10	30	40		
Co	8	5	6	7	6	2	3	2	1	3	3	29.9	18.9
Sc	3	2	2	3	2	3	2	3	3	2	2	20	14
V	58	52	52	47	47	13	24	15	12	23	23	147	120
Cu	16	16	24	27	23	7	5	7	7	5	5	42.1	19.6
Ag	bdl	bdl	bdl	bdl	bdl	bdl	bdl	bdl	bdl	bdl	bdl	0.1	0.1
Pb	4	5	8	6	7	24	4	24	23	4	3	5	4.7
Zn	32	23	23	22	20	68	45	66	67	43	41	27	35
Sn	1	1	1	1	1	4	3	4	4	3	3	2	1
Ba	30	20	20	40	30	110	120	110	110	120	110	538	592
Rb	54.7	82.8	78.8	57.9	58.9	101.0	93.8	106.5	105.0	90.6	94.8	53.5	66.5
Cs	1.0	1.2	1.3	0.7	0.7	1.1	0.8	1.1	1.2	0.9	0.9	1.7	0.9
Sr	620	549	477	377	300	110.5	431	119.5	115	405	423	640	931
Ga	17.4	18.6	17.1	16.7	16.4	19.6	18.2	21.6	20.5	16.8	16.8	16.6	18.2
Hf	3	3.2	3.4	3.5	4	7.6	3.9	8.1	7.6	3.5	4.1	4.1	4.5
Nb	3.9	3.9	3.6	3.8	3.8	9.5	6.7	10	9.7	6.5	6.8	7.5	7.7
Zr	118	125	129	130	147	272	166	280	258	134	153	159	159
Y	8	8	7	19	24	36	8	39	37	7	7	16	15
Ta	0.3	0.3	0.2	0.2	0.3	0.7	0.5	0.7	0.7	0.5	0.5	0.4	0.5
Th	4.8	5.9	4.8	14.7	20.0	10.6	7.5	11.3	10.7	7.4	7.6	3.3	3.8
U	3.2	3.9	3.2	5.7	9.6	3.4	3.7	3.7	3.6	3.7	3.7	1.8	2.0

(continued)

Table 6.3 (continued)

Sample	B41	B42	B43	B44	B45	B46	B48	B49	B50	B53	B54	B11	B14
La	13.6	15.2	13	13.7	16.2	39.2	22.8	43.9	39	23	24.1	15.3	18.3
Ce	25.6	28.1	24.8	27.0	30.8	81.6	40.6	91.2	81.4	40.6	42.7	33.6	37.1
Pr	3.07	3.08	2.82	3.34	3.84	9.64	4.27	10.75	9.64	4.21	4.41	4.57	4.85
Nd	11.2	11.5	10.8	13.5	15.8	37.1	14.8	41.0	36.8	14.3	14.9	18.5	18.4
Sm	1.91	2.21	1.75	3.35	4.30	6.96	2.23	7.97	7.45	2.26	2.49	3.77	3.64
Eu	0.75	0.58	0.62	0.88	1.02	0.85	0.54	0.87	0.83	0.49	0.57	1.18	1.15
Gd	1.75	2.03	1.73	3.84	5.15	6.47	1.71	7.26	6.25	1.68	1.74	3.55	3.37
Tb	0.26	0.25	0.26	0.66	0.84	1.05	0.23	1.09	1.06	0.23	0.26	0.55	0.54
Dy	1.31	1.27	1.37	3.87	5.01	6.4	1.4	7.2	6.7	1.2	1.4	2.82	2.73
Ho	0.27	0.26	0.24	0.79	0.94	1.42	0.26	1.45	1.31	0.27	0.26	0.56	0.54
Er	0.74	0.74	0.66	1.97	2.33	4.05	0.74	4.5	4.17	0.72	0.77	1.7	1.57
Tm	0.11	0.12	0.11	0.23	0.30	0.6	0.11	0.68	0.61	0.1	0.1	0.24	0.25
Yb	0.82	0.65	0.70	1.52	1.54	4.18	0.78	4.33	4.15	0.72	0.82	1.43	1.43
Lu	0.12	0.12	0.11	0.18	0.21	0.65	0.12	0.66	0.66	0.12	0.1	0.22	0.21
Eu/Eu*	1.25	0.84	1.09	0.75	0.66	0.39	0.84	0.35	0.37	0.77	0.84	0.98	1.00
K/Rb	0.001	0.001	0.001	0.001	0.001	0.001	0.001	0.001	0.001	0.001	0.001	0.001	0.001
Mg#	28.8	24.9	25.5	27.1	24.5	26.3	27.7	26.2	26.1	27.5	26.6	49.2	42.6
Al	0.69	0.70	0.69	0.80	0.82	0.92	0.76	0.91	0.92	0.76	0.76	0.62	0.63
La/Nb	3.5	3.9	3.6	3.6	4.3	4.1	3.4	4.4	4.0	3.5	3.5	2.0	2.4
(La/Yb)N	11.27	15.89	12.62	6.12	7.15	6.37	19.86	6.89	6.38	21.70	19.97	7.27	8.69
(Dy/Yb)N	1.05	1.28	1.28	1.67	2.13	1.00	1.16	1.09	1.05	1.13	1.13	1.29	1.25
(Y/Nb)N	0.31	0.31	0.31	0.80	0.99	0.60	0.18	0.62	0.59	0.17	0.17	0.33	0.31
(Th/Nb)N	10.48	12.85	11.38	32.81	44.65	9.46	9.46	9.59	9.31	9.66	9.43	3.73	4.19
(Th/Ta)N	7.76	9.51	11.66	35.48	32.18	7.31	7.21	7.79	7.34	7.14	7.30	3.98	3.67
(Ce/Pb)N	0.26	0.22	0.12	0.18	0.18	0.14	0.41	0.15	0.14	0.41	0.57	0.27	0.32

(continued)

Table 6.3 (continued)

Sample	B139	C57	C58	B12	B13	Bulc	Bul	C55	HUM1	HUM2	HUM3	HUM4	HUM1A
Sample	B139	C57	C58	B12	B13	Bulc	Bul	C55	HUM1	HUM2	HUM3	HUM4	HUM1A
SiO_2	54.6	58.4	58.5	65.9	69.3	66.5	73.5	71.1	49.9	52.4	55.0	54.7	49.4
TiO_2	0.9	1.02	0.99	0.47	0.37	0.41	0.21	0.28	1.3	0.82	1.17	1.12	1.3
Al_2O_3	19.95	16.07	16.67	14.83	15.4	15.88	12.39	13.57	15.4	14.0	16.5	16.3	15.6
Fe_2O_3	2.22	5.83	5.89	3.59	2.72	3.08	1.06	2.39	9.89	9.63	8.66	9.19	9.71
MnO	0.05	0.08	0.09	0.04	0.04	0.04	0.03	0.06	0.17	0.17	0.15	0.15	0.17
MgO	2.16	3.34	3.6	2.33	1.42	1.91	0.3	1.05	7.85	8.91	4.89	5.28	7.78
CaO	9.95	4.28	4.78	2.67	1.17	2.9	2.66	2.2	10.30	10.00	8.04	8.47	10.15
Na_2O	5.85	5.43	4.18	3.91	4.84	5.19	3.91	3.8	2.30	1.80	3.09	2.82	2.32
K_2O	1.07	2.92	2.7	2.89	2.57	1.49	2.79	4.03	0.39	0.40	1.07	0.78	0.39
P_2O_5	0.25	0.29	0.27	0.15	0.14	0.14	0.04	0.06	0.16	0.14	0.30	0.20	0.16
LOI	2.8	2.1	2	3	1.9	2.2	2.9	1.2	0.99	1.23	1.34	1.23	1.03
Total	99.75	99.77	99.68	99.8	99.88	99.72	99.82	99.75	98.8	99.6	100.3	100.3	98.1
Ni	20	30	26	28	20	26	20	20	19	30	12	19	16
Cr									370	610	140	140	320
Co	5	20.6	23.6	9.8	6.5	9.1	8.6	15.6	15	16	13	19	14
Sc	10	14	14	7	5	6	3	5	3	3	2	3	3
V	83	140	132	57	38	51	11	30	301	267	181	232	252
Cu	35.8	23.8	16.8	17	14.2	12.3	5.6	4.9	9	11	14	16	9
Ag	0.1	0.1	0.1	0.1	0.1	0.1	0.1	0.1	bdl	bdl	bdl	bdl	bdl
Pb	6.8	9	6	5.6	10.6	3.6	7	11	2	bdl	2	bdl	2
Zn	28	47	40	39	54	45	31	41	21	17	36	28	19
Sn	4	1	2	1	1	1	2	1	<1	1	1	1	<1
Ba	92	329	584	570	576	482	502	1015	30	20	50	30	30
Rb	42.5	61	62	75.8	67.3	40	60	63	6.6	8.2	24.5	18.2	5.7
Cs	1.5	1.4	1.3	2.8	1.4	1.2	1.0	0.5	0.4	0.7	0.8	1.0	0.4
Sr	868	290	987	483	502	887	204	250	415	371	451	443	409
Ga	14.5	17.1	18.3	16.1	14.7	17.1	12.9	13.4	16.8	15.1	19.1	18.3	16.5
Hf	6.7	5	4.2	3.5	3.5	3.4	4.9	4.2	1.3	0.8	2.4	2.8	1.1
Nb	10.2	7.8	7.9	4.9	4.2	4.5	6.1	5.7	6.9	3.9	13.5	7.4	8.3
Zr	268	171	161	128	120	131	175	138	43	29	104	114	38
Y	18	15	15	8	7	7	16	13	14	11	17	17	14
Ta	0.7	0.6	0.6	0.3	0.2	0.3	0.8	0.5	0.4	0.2	0.8	0.5	0.2
Th	6.5	4.2	3.9	4.8	4.8	3.3	9.4	10.4	0.2	0.2	2.3	1.1	0.2
U	3.2	2.0	2.0	2.6	2.3	2.2	5.0	3.0	0.2	0.1	1.0	0.6	0.1
La	16	19.3	19.2	14.2	16.5	12.6	24.1	21.4	6.1	4.3	15.6	9.1	6.2

(continued)

Table 6.3 (continued)

Sample	B139	C57	C58	B12	B13	Bulc	Bul	C55	HUM1	HUM2	HUM3	HUM4	HUM1A
Ce	36.3	39.4	40.3	28.5	28.5	25.8	50.5	42.9	13.6	9.5	30.5	20.4	13.2
Pr	5.02	5.1	5	3.51	3.38	3.07	5.1	4.3	1.89	1.32	3.73	2.78	1.86
Nd	19.5	19.4	18.9	13.4	12.7	11.3	18.8	16.0	8.8	6.6	15.6	12.1	9.2
Sm	4.3	3.79	3.7	2.25	2.22	2.17	3.36	2.8	2.36	1.70	3.50	2.99	2.72
Eu	1.34	1.14	1.16	0.67	0.68	0.71	0.62	0.47	0.98	0.91	1.25	1.11	1
Gd	3.95	3.55	3.41	2.04	1.94	1.82	2.89	2.36	2.87	2.21	3.47	3.27	2.84
Tb	0.61	0.53	0.53	0.29	0.27	0.26	0.44	0.36	0.45	0.36	0.56	0.51	0.46
Dy	3.11	2.81	2.79	1.37	1.29	1.35	2.56	2.13	2.8	2.1	3.1	3.4	2.5
Ho	0.66	0.57	0.56	0.3	0.25	0.26	0.51	0.45	0.59	0.41	0.66	0.67	0.53
Er	1.85	1.58	1.6	0.8	0.72	0.76	1.67	1.29	1.61	1.18	1.73	1.95	1.35
Tm	0.28	0.23	0.23	0.13	0.11	0.12	0.28	0.23	0.22	0.17	0.25	0.27	0.2
Yb	1.68	1.45	1.37	0.8	0.71	0.71	1.77	1.5	1.46	1.11	1.54	1.94	1.33
Lu	0.24	0.21	0.19	0.13	0.11	0.11	0.3	0.25	0.22	0.17	0.26	0.26	0.2
Eu/Eu*	0.99	0.95	1.00	0.95	1.00	1.09	0.61	0.56	1.15	1.43	1.10	1.08	1.10
K/Rb	0.001	0.001	0.001	0.001	0.001	0.001	0.001	0.001	0.001	0.001	0.001	0.001	0.001
Mg#	18.1	41.8	41.2	32.4	25.9	27.8	14.5	25.9	56.0	57.7	51.0	52.8	55.3
Al	0.54	0.75	0.59	0.64	0.70	0.64	0.76	0.78	0.27	0.24	0.38	0.34	0.27
La/Nb	1.6	2.5	2.4	2.9	3.9	2.8	4.0	3.8	0.9	1.1	1.2	1.2	0.7
(La/Yb)N	6.47	9.04	9.52	12.06	15.79	12.06	9.25	9.69	2.84	2.63	6.88	3.19	3.17
(Dy/Yb)N	1.21	1.27	1.33	1.12	1.19	1.24	0.95	0.93	1.24	1.25	1.31	1.14	1.24
(Y/Nb)N	0.27	0.31	0.30	0.26	0.26	0.26	0.42	0.34	0.33	0.44	0.19	0.36	0.25
(Th/Nb)N	5.41	4.57	4.19	8.31	9.69	6.22	13.07	15.48	0.26	0.52	1.43	1.28	0.17
(Th/Ta)N	4.48	3.38	3.14	7.72	11.59	5.31	5.67	10.04	0.25	0.58	1.37	1.08	0.41
(Ce/Pb)N	0.21	0.18	0.27	0.20	0.11	0.29	0.29	0.16	0.27	0.19	0.61	0.41	0.26

(continued)

Table 6.3 (continued)

Sample	HUM1B	HUM2A	HUM2B	HUM3A	HUM3B	HUM4A	HUM4B	Hm2	HM20	HM18	HM19	C47	C48
Sample	HUM1B	HUM2A	HUM2B	HUM3A	HUM3B	HUM4A	HUM4B	Hm2	HM20	HM18	HM19	C47	C48
SiO_2	50.1	52.6	52.6	54.6	54.5	53.9	54.4	50.3	49.3	49.0	64.3	52.4	54.5
TiO_2	1.32	0.83	0.84	1.15	1.16	1.14	1.14	1.59	1.6	0.45	0.65	0.77	1.48
Al_2O_3	15.7	14.3	14.4	16.8	16.8	16.4	16.5	19.33	18.2	15.37	15.78	15.55	15.86
Fe_2O_3	9.88	9.63	9.61	8.52	8.47	9.00	9.12	9.12	9.62	8.57	5.35	9.09	8.7
MnO	0.17	0.17	0.17	0.15	0.15	0.15	0.15	0.11	0.16	0.15	0.05	0.15	0.13
MgO	7.88	8.99	8.98	4.86	4.83	5.22	5.27	3.95	6.36	10.64	1.78	7.2	4.11
CaO	10.25	9.96	9.96	7.92	7.86	8.25	8.32	9.71	10.04	12.22	4.26	7.27	5.82
Na_2O	2.35	1.85	1.86	3.16	3.14	2.85	2.87	3.97	2.7	1.05	4.09	3.27	3.54
K_2O	0.39	0.41	0.41	1.07	1.07	0.77	0.77	0.29	0.44	0.43	0.89	1.53	2.5
P_2O_5	0.16	0.13	0.14	0.30	0.30	0.20	0.21	0.62	0.39	0.04	0.16	0.23	0.38
LOI	0.96	1.17	1.42	1.35	1.29	1.24	1.22	0.7	0.9	1.7	2.5	2.1	2.6
Total	99.3	100.2	100.5	99.9	99.6	99.2	100.0	99.7	99.8	99.7	99.9	99.5	99.6
Ni	17	30	29	12	10	19	19	53	21	62	20	123	28
Cr	330	530	530	120	130	120	120						
Co	13	16	15	12	12	18	19	48	32.7	38.3	11.1	36.1	30.3
Sc	3	2	2	2	2	3	3	20	26	39	9	21	16
V	259	228	224	154	158	194	200	165	243	296	64	201	158
Cu	9	10	10	14	13	15	16	151.3	19.4	4.7	34.9	39.7	16.2
Ag	bdl	bdl	bdl	bdl	bdl	bdl	bdl	0.1	0.1	0.1	0.1	0.1	0.1
Pb	3	2	bdl	bdl	bdl	2	2	1	3	11	4	7	4
Zn	19	16	16	33	32	27	28	29	22	14	46	44	85
Sn	<1	1	1	1	1	1	1	<1	1	1	1	1	2
Ba	30	20	20	50	50	30	30	118	127	58	338	757	484
Rb	6.0	7.8	7.9	22.6	22.7	16.8	17.2	5.4	8.5	9.2	19.3	35	64.2
Cs	0.4	0.7	0.7	0.8	0.8	1.0	1.1	0.7	0.7	0.6	0.3	1.5	2.1
Sr	418	383	381	453	455	433	444	735	545	390	409	753	637
Ga	16.4	14.5	14.7	18.2	18.6	17.3	17.9	18.2	17.8	13.3	17.8	19.6	20
Hf	1.3	0.7	0.8	2.7	3.2	2.4	2.4	1.2	1.1	0.5	6.9	2.1	4.4
Nb	7.3	3.8	3.7	13.2	13.7	7.2	7.3	17	9.4	1.2	17.2	2.8	11.6
Zr	40	24	28	102	127	97	89	51	34	16	240	64	157
Y	14	10	10	16	16	16	17	14	13	9	20	10	25
Ta	0.2	<0.1	<0.1	0.6	0.6	0.3	0.3	1	0.5	0.1	0.9	0.3	0.9
Th	0.2	0.2	0.2	2.4	2.3	1.0	1.1	0.5	0.4	0.2	8.1	3.5	4.8
U	0.1	0.1	0.1	0.9	1.0	0.5	0.5	0.5	0.2	0.1	3.1	1.0	2.8

(continued)

Table 6.3 (continued)

Sample	HUM1B	HUM2A	HUM2B	HUM3A	HUM3B	HUM4A	HUM4B	Hm2	HM20	HM18	HM19	C47	C48
La	6.3	4.4	4.2	16	16.1	9.4	9.4	12.1	8.6	2.7	33.2	14.4	20.8
Ce	13.5	9.1	9.4	29.7	30.3	19.6	19.7	27.0	18.0	6.2	58.8	30.3	48.8
Pr	1.99	1.33	1.35	3.67	3.76	2.78	2.74	3.48	2.52	0.95	6.58	3.7	6.44
Nd	9.3	6.9	6.7	16.0	15.7	11.8	12.2	16.2	11.7	4.6	23.1	15.6	26.2
Sm	2.52	1.83	1.83	3.42	3.69	3.24	3.15	3.3	2.48	1.46	4.27	3.2	5.95
Eu	1.01	0.83	0.83	1.16	1.14	1.03	1.12	1.43	1.22	0.72	1.05	1.04	1.61
Gd	2.75	2.17	2.15	3.55	3.68	3.27	3.49	3.47	2.84	1.68	3.97	2.48	5.41
Tb	0.45	0.35	0.33	0.49	0.5	0.52	0.54	0.53	0.46	0.3	0.63	0.37	0.89
Dy	2.6	2.0	1.9	3.1	3.0	2.9	3.0	2.84	2.4	1.65	3.41	2	4.84
Ho	0.57	0.45	0.4	0.63	0.65	0.63	0.65	0.5	0.49	0.34	0.69	0.36	0.89
Er	1.34	1.04	1.08	1.62	1.66	1.63	1.62	1.42	1.33	0.94	2.02	1.02	2.5
Tm	0.2	0.17	0.18	0.25	0.24	0.24	0.26	0.19	0.2	0.16	0.29	0.14	0.36
Yb	1.44	1.04	1.08	1.65	1.49	1.63	1.69	1.14	1.25	0.89	1.83	0.87	2.19
Lu	0.21	0.16	0.16	0.23	0.23	0.26	0.25	0.17	0.18	0.14	0.29	0.14	0.33
Eu/Eu*	1.17	1.27	1.28	1.02	0.94	0.97	1.03	1.29	1.40	1.40	0.78	1.13	0.87
K/Rb	0.001	0.001	0.001	0.001	0.001	0.001	0.001	0.001	0.001	0.001	0.001	0.001	0.001
Mg#	55.5	57.2	57.0	50.2	50.0	52.2	52.3	48.3	51.2	52.5	40.2	53.7	52.1
Al	0.27	0.24	0.24	0.38	0.38	0.34	0.34	0.35	0.27	0.14	0.49	0.45	0.54
La/Nb	0.9	1.2	1.1	1.2	1.2	1.3	1.3	0.7	0.9	2.3	1.9	5.1	1.8
(La/Yb)N	2.97	2.87	2.64	6.59	7.34	3.92	3.78	7.21	4.67	2.06	12.32	11.24	6.45
(Dy/Yb)N	1.18	1.28	1.14	1.22	1.30	1.16	1.16	1.63	1.26	1.21	1.22	1.50	1.45
(Y/Nb)N	0.30	0.43	0.44	0.19	0.19	0.35	0.36	0.13	0.22	1.19	0.18	0.54	0.34
(Th/Nb)N	0.22	0.54	0.48	1.52	1.43	1.18	1.22	0.25	0.36	1.41	3.99	10.60	3.51
(Th/Ta)N	0.46	1.16	1.01	1.91	1.86	1.61	1.69	0.24	0.39	0.97	4.34	5.63	2.57
(Ce/Pb)N	0.18	0.18	0.19	0.59	0.61	0.39	0.39	1.08	0.29	0.02	0.60	0.17	0.48

Major (wt.%), trace and REE (ppm) elements were determined by ICP-AES (major elements) and ICP-MS (trace and REEs) at ACME Labs, Canada. Eu/Eu* = Eu$_N$/SQRT(Sm$_N$ × Gd$_N$)
Lithium borate fusion technique is used for all elements to completely decompose even most refractory matrices to provide total element concentrations. DL = detection limit and bdl = below detection limit. Major oxides detection limits in % and elements concentration detection limits in ppm

The volcanosedimentary rocks and intermediate to felsic intrusions of the Afif terrane were intruded by gabbros to highly evolved granites between ∼750 and 570 Ma. Based on their composition, textures and/or absolute ages, these rocks are classified from the oldest to the youngest as the Jidh, Suwaj, Fahud, Khishaybi, Humaymah, Haml and syn- to post-Shammar intrusions of the Idah and Abanat suites. The post-collision monzogranite rocks of Haml batholith were dated at 609 ± 8 Ma (Robinson et al. 2014).

6.3 Analytical Techniques

Four representative samples of the intrusive rocks were selected for dating using U–Pb zircon geochronology. Bulk samples of these rocks (each weight ≈ 3 kg) were crushed and pulverised to a fine fraction and sieved. The fractions of these samples that fall between 250 and +75 μm were washed by distilled water and dried. These initial sample preparations were carried out in the laboratory facilities at the department of Mineral Resources and Rocks at the Faculty of Earth Sciences, King Abdulaziz University (KAU) in Jeddah (Saudi Arabia). Heavy liquids were used to separate the heavy fraction from these samples using Methylene Iodide (specific gravity 3.3 gm/ml). The non-magnetic fraction of these samples which may contain the zircon grains were separated using a Franz Isodynamic separator. Finally, zircon grains were collected by hand-picking under a binocular stereoscopic microscope. Zircons were analysed for their U–Pb age at John de Laeter Centre, Curtin University of Technology (Australia) and at the University of Oslo (Norway).

Prior to analysis, zircon grains were imaged on the polished puck by cathodoluminecence (CL) to examine the growth structure of individual grains using a scanning electron microscope. U–Pb isotope data on zircons were obtained by laser-ablation inductively coupled plasma source mass spectrometry (LA-ICP-MS) using a Nu Plasma HR mass spectrometer and a New Wave LUV213 laser microprobe at University of Oslo (Norway) and by sensitive high resolution ion microprobe (SHRIMP II) at Curtin University (Australia). The analytical protocols of the LA-ICP-MS are described in detail by Rosa et al. (2009), and SHRIMP analytical procedure is described by Compston et al. (1984) and Kennedy and de Laeter (1994). The 1065 ± 0.6 Ma (2σ) Geostandards zircon 91500 (Wiedenbeck et al. 1995) and 600 ± 4.5 Ma (2σ) Geostandards GJ-1 (Jackson et al. 2004) were both used for Pb/U calibration and U concentration estimates and were analysed on a regular basis during the analytical sessions by LA-ICP-MS, and BR266 (559 Ma; 903 ppm U) was used for SHRIMP. Calculations used the routines of Isoplot

(Ludwig 2001a, b). U–Th–Pb concentrations and isotopic compositions are listed in Table 6.1 (SHRIMP II) and Table 6.2 (LA-ICP-MS), and plotted as two-sigma error ellipses on Concordia diagrams (Wetherill 1956).

A total of 53 intrusive samples were selected for major, trace and rare earth elements analyses. Major element compositions and Sc, Ba, and Ni abundances were determined by inductively coupled plasma-atomic emission spectrometry (ICP-AES). All the others trace and rare earth elements (REE) were determined by inductively coupled plasma-mass spectrometry (ICP-MS). All the analyses were carried out at the ACME Analytical Laboratories Ltd., Canada. Analytical precision, as calculated from replicate analyses, is 0.5% for major elements and varies from 2 to 20% for trace elements. Analytical results are listed in the Table 6.3.

6.4 Results

6.4.1 U–Pb Geochronology

Sample B139 (N25° 01′ 37.0″, E41° 36′ 32.9″) is a dark grey, coarse-grained diorite collected from Bulghah area. Zircons separated from this sample are euhedral, acicular, and yellowish brown in color. A total of 21 measurements were made on the twenty one zircon crystals (Table 6.1). The U content varies from 65 to 161 ppm and Th from 18 to 70 ppm. One zircon analysis produced a concordant data point with $^{206}Pb/^{238}U$ age of 707 ± 10 Ma, interpreted as that as xenocryst derived from older source material. Omitting three analyses with high common Pb and/or discordant leaves seventeen tightly grouped and concordant analyses that define a concordia age of 677 ± 8 Ma (95% conf.; MSWD = 0.91; Fig. 6.3a). We interpret this as the age of intrusion and crystallization of the diorite.

Sample B-mine (N24° 59′ 21.5″, E41° 35′ 51.6″) is a quartz-diorite collected from Bulghah mine area (Fig. 6.2). Zircon extracted from this sample is mostly euhedral, clear to yellow-brown, prismatic (∼200 μm × 50 μm) and show well-developed oscillatory zoning consistent with a magmatic origin. One analysis was made on each of 10 zircons (Table 6.1) and these are presented on a concordia plot (Fig. 6.3b). Zircon U contents are low (58–163 ppm) and Th/U is low (0.3–0.4; Table 6.1). One analysis is concordant and has low Th content (16 ppm) and yields a $^{206}Pb/^{238}U$ age of 746 ± 14 Ma, higher than the 9 analyses, interpreted to represent an inherited grain from the older rocks in the area. The remaining nine analyses are concordant, defining a concordia age of 667 ± 6 Ma (2σ; MSWD = 2.3; Fig. 6.3 b). This age is identical to the age of the previous diorite sample (B139) and is interpreted as the crystallization age of the quartz-diorite.
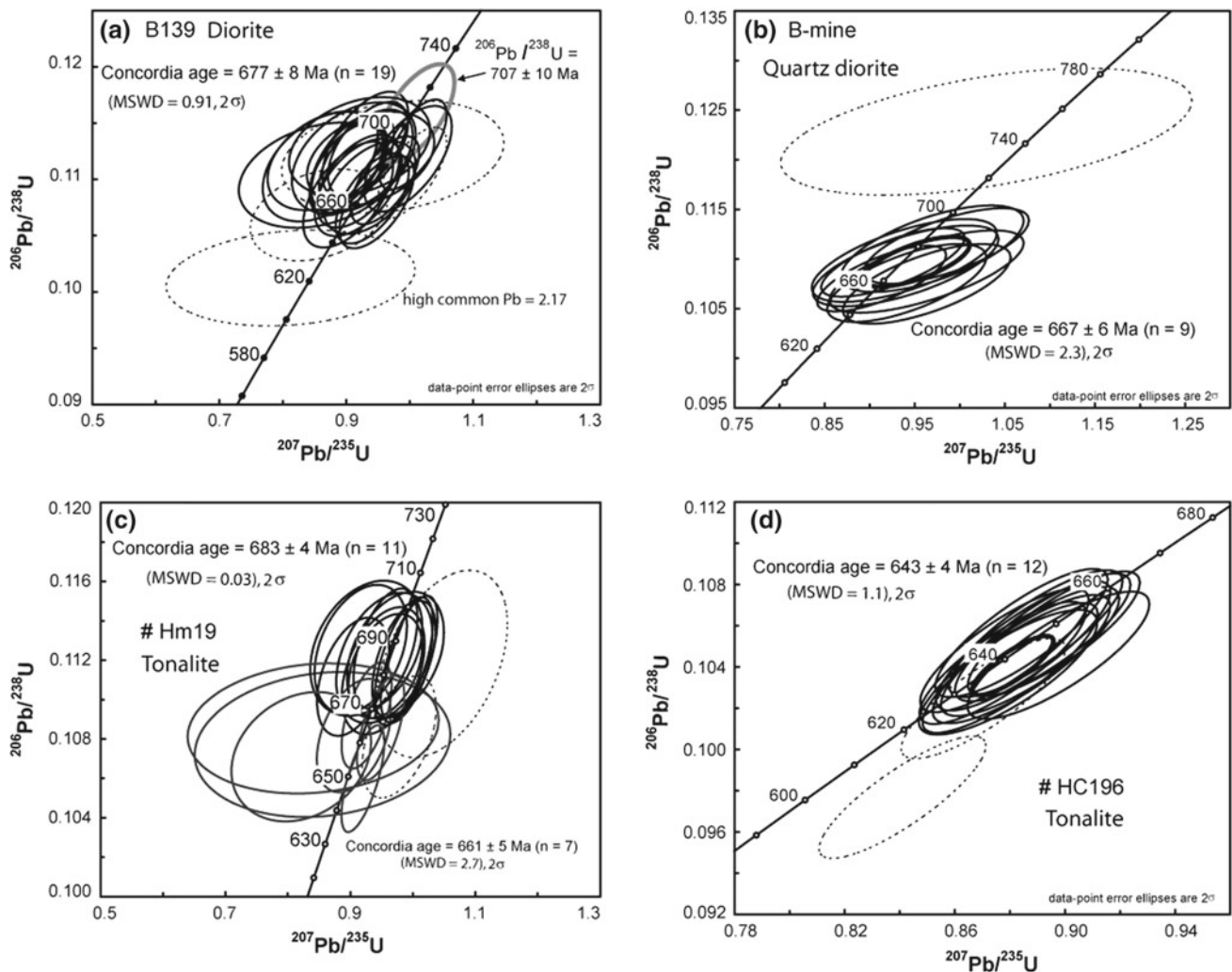
Fig. 6.3 U–Pb concordia diagrams of ion microprobe (SHRIMP) and laser-ablation inductively coupled plasma source mass spectrometry (LA-ICP-MS) data for zircons studied from the Bulghah and Humaymah areas. Dashed ellipses indicate zircon analyses that were excluded from age calculations. Errors for data ellipses are 2σ. Analytical data are given in Tables 6.1 and 6.2

Sample Hm19 (N24° 42′ 11.3″, E41° 42′ 57.8″) is medium to coarse-grained tonalite from Humaymah area (Fig. 6.2). Zircon recovered from this sample is subhedral to euhedral and yellow to pale brown. Zircon grains are idiomorphic, slender, and needle shaped, and exhibit well-preserved oscillatory growth zoning. These zircons contain moderate U contents (76–325 ppm) and have Th/U in the range expected for igneous zircons (0.2–0.5). Out of twenty-one zircon grains analyzed (Table 6.1), eleven analyses yield a concordia age of 683 ± 4 Ma (2σ, MSWD = 0.03), interpreted to represent inheritance from older rocks in the area. Three analyses are discordant and excluded from age calculation (Fig. 6.3c). Seven analyses were done on the rims of the same zircon grains produced a concordant data points and yield a concordia age of 661 ± 5 Ma (2σ, MSWD = 2.7; Fig. 6.3c), interpreted

to represent the crystallization age of the tonalite intrusion.

Sample HC196 (N24° 43′ 01.5″, E41° 43′ 2.5″) is coarse-grained tonalite from Humaymah (Fig. 6.2). Zircon recovered from this sample is subhedral to euhedral and yellow to pale brown. Zircon grains are idiomorph, slender, and needle shaped, and exhibit well-preserved oscillatory growth zoning. Out of fourteen zircon grains analyzed (Table 6.2), twelve analyses yielded a concordia age of 643 ± 4 Ma (2σ, MSWD = 1.1), interpreted to represent the age of the tonalite. Two analyses are discordant and excluded from age calculation (Fig. 6.3d). This age is indistinguishable from the age of a quartz diorite sample (629 ± 6 Ma; Harbi et al. 2018) in the Sukhaybarat area (70 km north of the study area) and the age of a monzogranite sample (631 ± 1 Ma) from Bulghah area (Bakhsh, unpublished data).

6.4.2 Whole-Rock Geochemistry

The results of chemical composition of 53 whole-rock samples from Bulghah and Humaymah areas are listed in Table 6.3. We compared our results with previous geochemical data of the I-type intrusive rocks (Figs. 6.5, 6.6, 6.7, 6.8, 6.9, 6.10, 6.11, 6.12 and 6.13) from Harbi et al. (2016, 2018) and Robinson et al. (2015). The intrusive samples from Bulghah show wide variations (in wt%) of SiO_2 (51.4–74.7), Al_2O_3 (12.39–19.95), CaO (1.05–9.95), Na_2O (3.10–5.85), MgO (0.30–6.50), Fe_2O_3t (1.06–7.41), and TiO_2 (0.18–1.02) (Table 6.3, Fig. 6.4). The K_2O content
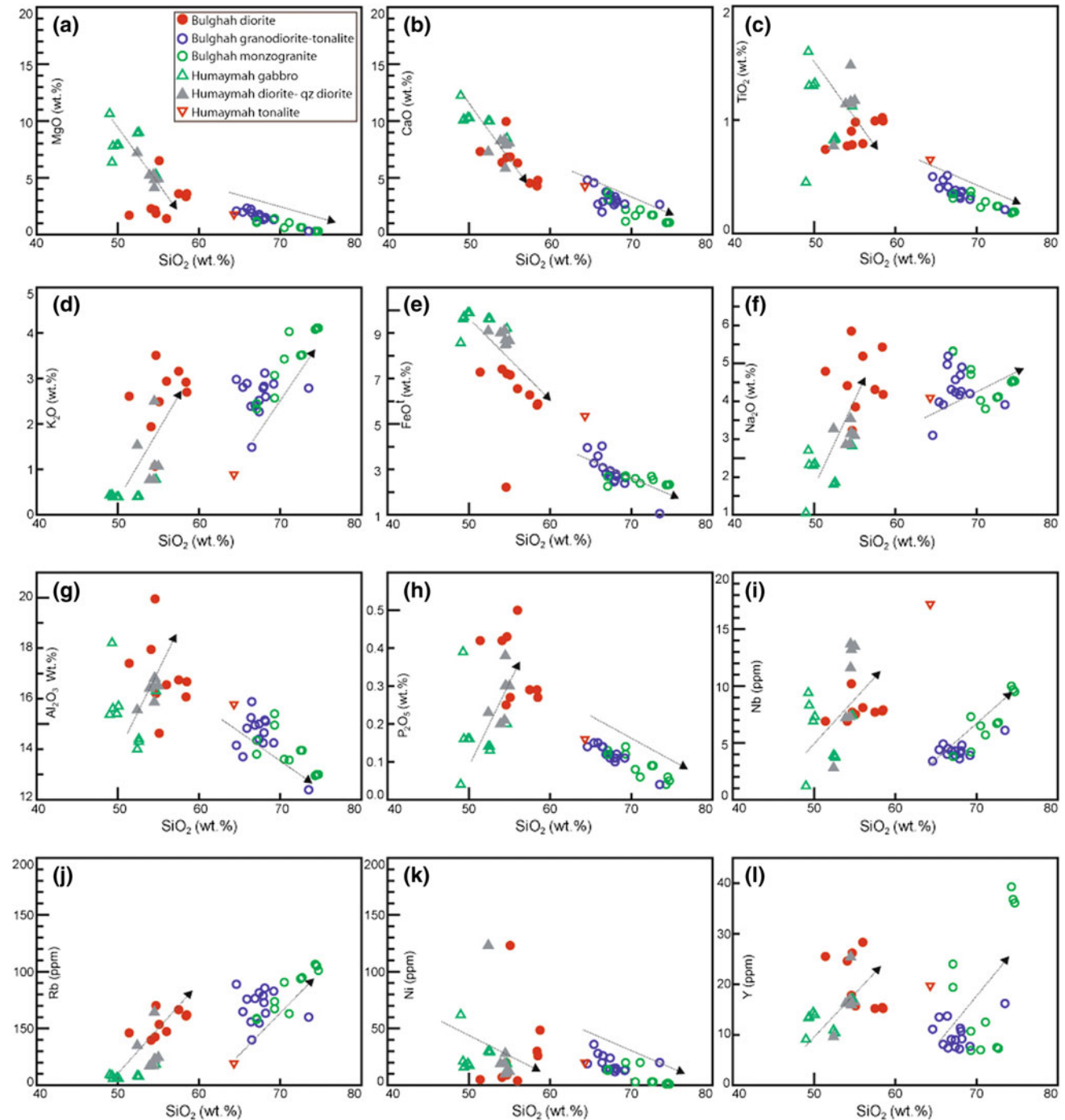
Fig. 6.4 Major and trace element variations diagrams (Harker diagrams) for the gabbro, diorite, tonalite, granodiorite and monzogranites define two different trends and showing compositional gap between the mafic intrusive rocks (gabbro and diorite) and granitoids (granodiorite-tonalite and monzogranite)
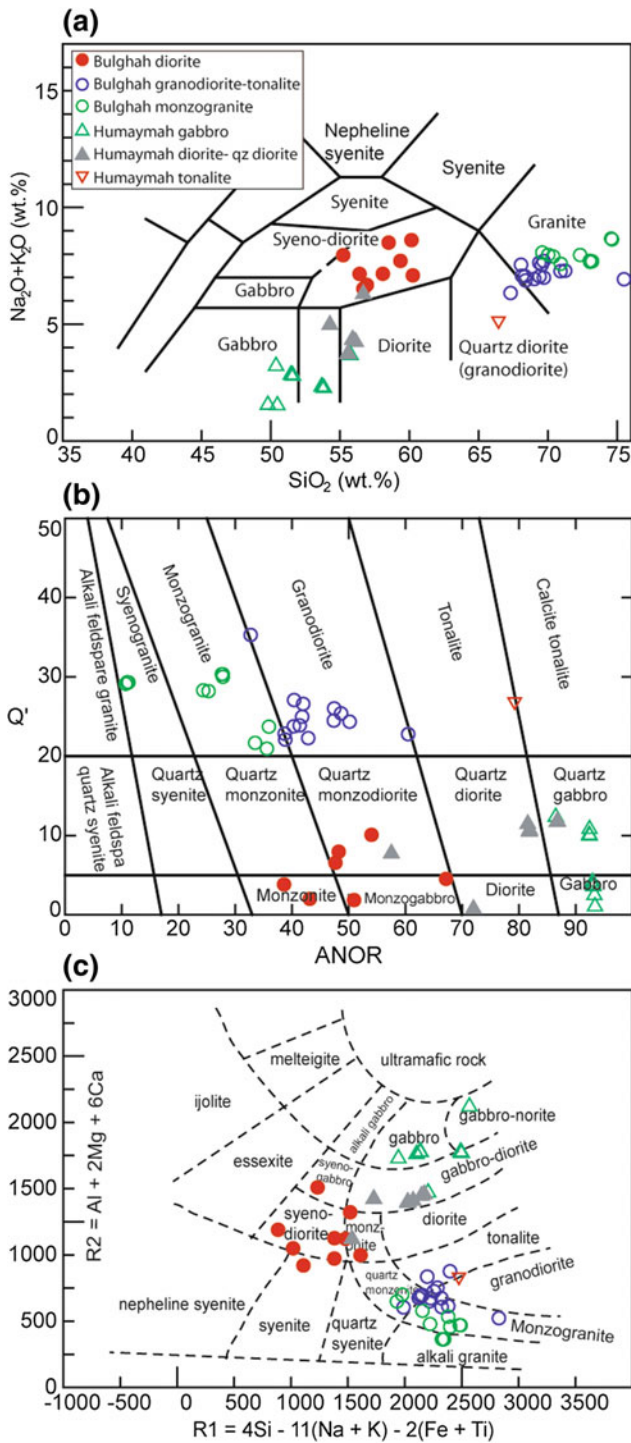
Fig. 6.5 Major and trace elements chemical classification diagrams. **a** Total alkalis ($Na_2O + K_2O$) versus SiO_2 (Cox et al. 1979), **b** The Q'–ANOR plutonic rocks classification diagram using their molecular normative compositions (after Streckeisen and Le Maitre 1979), **c** R1-R2 diagram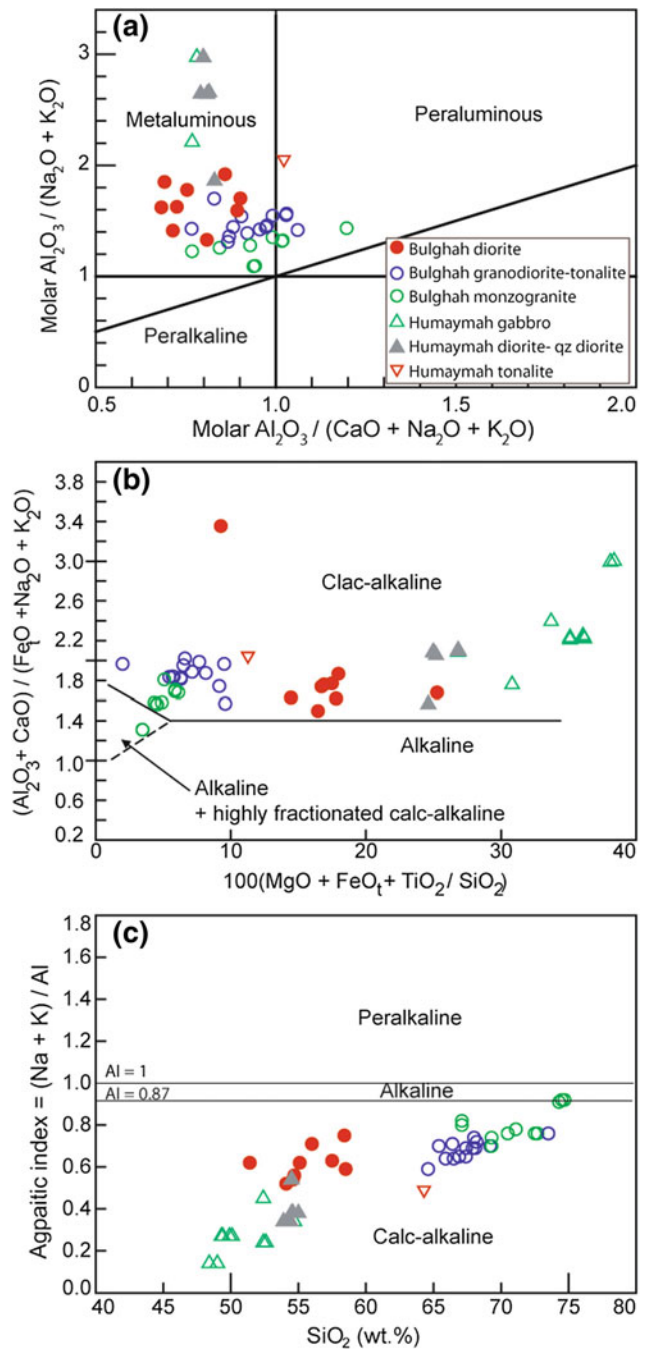 (de la Roche et al. 1980). The field of Sukhaybarat I-type granitoids from Harbi et al. (2018) and the field of Jabal Ghadarah I-type granitoids from Harbi et al. (2016). Analytical data are given in Table 6.2

Fig. 6.6 a Shand's index (Maniar and Piccoli 1989) classification diagram, showing the intrusive studied samples exhibit metaluminous to slightly peraluminous geochemical features. **b** ($Al_2O_3 + CaO/FeO_t + Na_2O + K_2O$) versus $100(MgO + FeO_t + TiO_2 + SiO_2)$ discrimination diagram (Sylvester 1998) showing the predominantly calc-alkaline to highly fractionated calc-alkaline characteristics of the studied samples. **c** Agpaitic index (AI = Na + K/Al) versus SiO_2 diagram showing the calc-alkaline characters of the studied intrusive samples, the line with AI = 0.87 (Liégeois and Black 1987) separates alkaline and calc-alkaline granite series. The field of Sukhaybarat I-type granitoids from Harbi et al. (2018) and the field of Jabal Ghadarah I-type granitoids from Harbi et al. (2016)
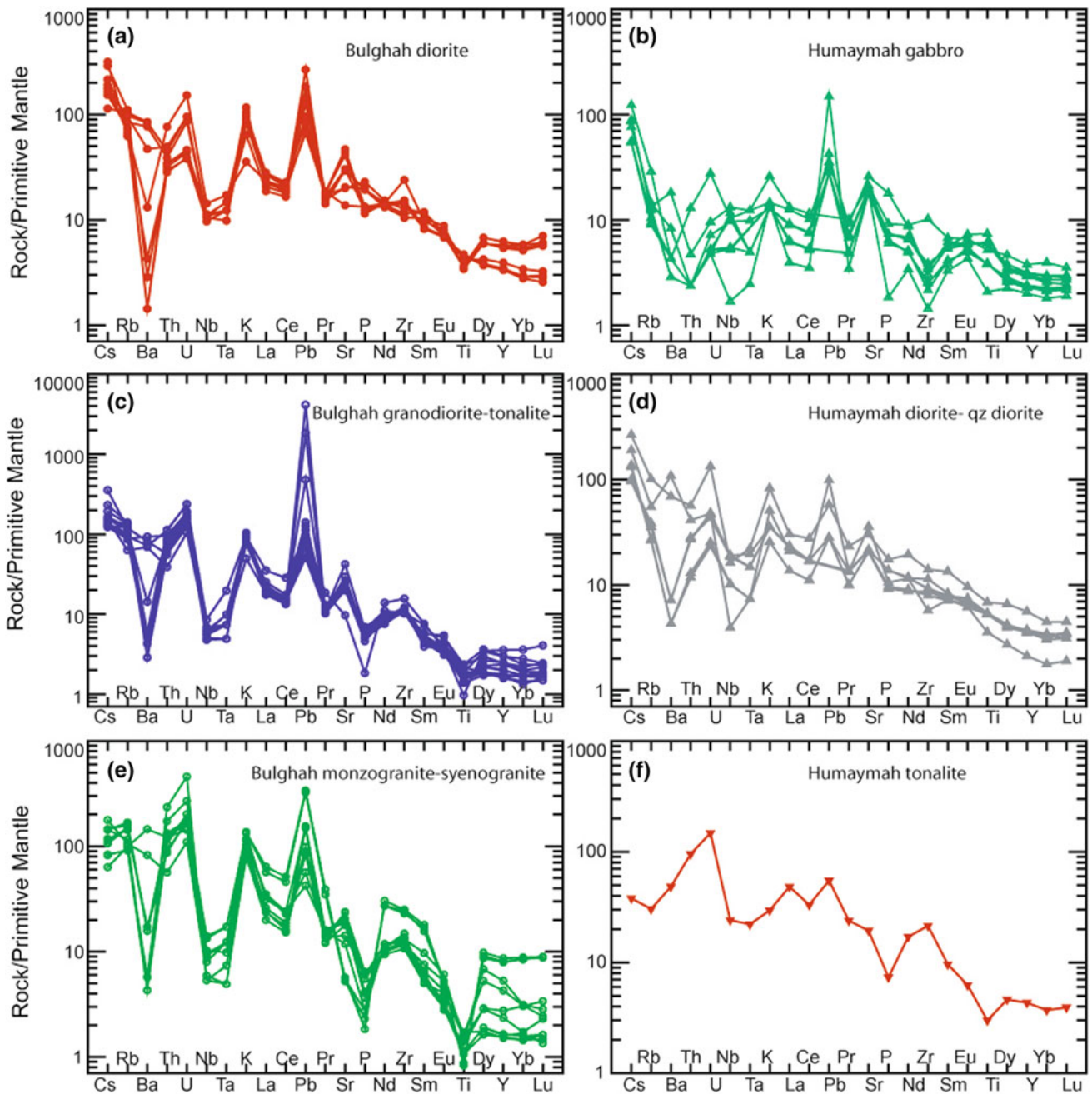
Fig. 6.7 Primitive mantle-normalized trace element diagrams for the studied Bulghah and Humaymah samples. Normalizing values from Sun and McDonough (1989)

indicates that the studied samples are high-K calc-alkaline (1.07–4.11 wt%; Fig. 6.4d). The intrusive rocks from Humaymah are more mafic than samples from Bulghah area. They exhibit variable variations (in wt%) of SiO_2 (48.4–64.3), Al_2O_3 (14.0–19.33), CaO (4.26–12.22), Na_2O (1.05–4.09), and high TiO_2 (0.45–1.60), MgO (1.78–10.64) and Fe_2O_3t (5.35–9.89) (Table 6.3, Fig. 6.4). The intrusive rocks have been classified using the total alkalis versus silica (Cox et al. 1979), Q′–ANOR diagram of Streckeisen and Le

Maitre (1979) and R1-R2 diagram of de la Roche et al. (1980). The intrusive samples of Bulghah plot in the monzogranite–synogranite, granodiorite-tonalite and syenodiorite fields (Fig. 6.5), whereas the Humaymah intrusive samples fall in the diorite, quartz diorite, gabbro and quartz gabbro fields, and one sample (Hm 19) plots in the tonalite field (Fig. 6.5).

According to Shand's index (Maniar and Piccoli 1989) classification diagram, the studied mafic intrusive samples

(gabbro and diorite-quartz diorite) from Bulghah and Humaymah are strongly metaluminous, whereas the granitoid rocks (granodiorite, tonalite and monzogranite) are strongly metaluminous to slightly peraluminous (Fig. 6.6a). On the major element discrimination diagram of Sylvester (1998), the studied intrusive rocks are calk-alkaline (Fig. 6.6b). They also fall in the calc-alkaline field (AI <

0.87; Fig. 6.6c) according to Liégeois and Black (1987). Three monzogranite samples (B46, B49 and B50) fall in the alkaline and highly fractionated calc alkaline field in both diagrams (Fig. 6.6b, c).

Primitive mantle normalized trace-element patterns for all intrusive samples from Bulghah and Humaymah are enriched in incompatible elements, showing negative anomalies
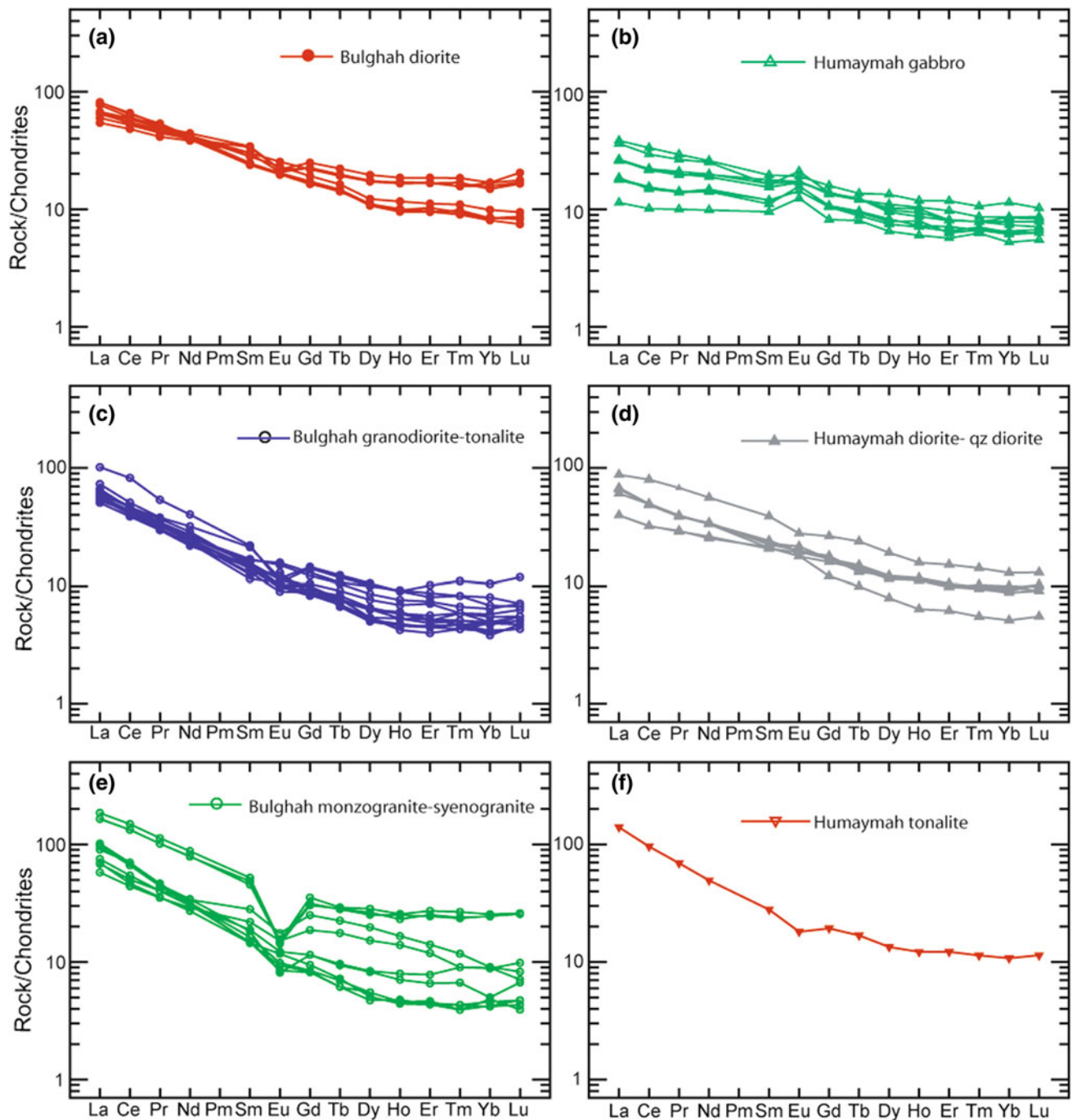
Fig. 6.8 Chondrite normalized REE patterns for the studied Bulghah and Humaymah samples. Normalizing values from Sun and McDonough (1989)

in Nb–Ta, Ti and P and a positive Pb anomaly (Fig. 6.7). The mafic and granitoid rocks in the studied areas have variable $Al_2O_3/(CaO + Na_2O + K_2O)$ molar ratios (A/CNK), mostly less than 1.1 (Fig. 6.6a), which is typical of I-type magmatism (Chappell 1999). The trace element

Fig. 6.9 a Th versus U, b Ta versus Nb, and c Hf versus Zr variation diagrams of the studied intrusive samples from the Bulghah and Humaymah areas, showing geochemical positive correlation between the different granitic types, suggesting that the behavior of these trace elements are largely controlled by magmatic processes. The field of Sukhaybarat I-type granitoids from Harbi et al. (2018)

patterns (Fig. 6.7) are typical of those developed in island arc settings (Elliott 2003; Ali et al. 2015).

The granodiorite-tonalite and monzogranite samples are both LREE and MREE enriched [(La/Yb)$_N$ = 6.12 − 21.70], with slightly fractionated HREE patterns [(Dy/Yb)$_N$ = 0.93 − 2.13] and minor negative to slightly positive Eu (E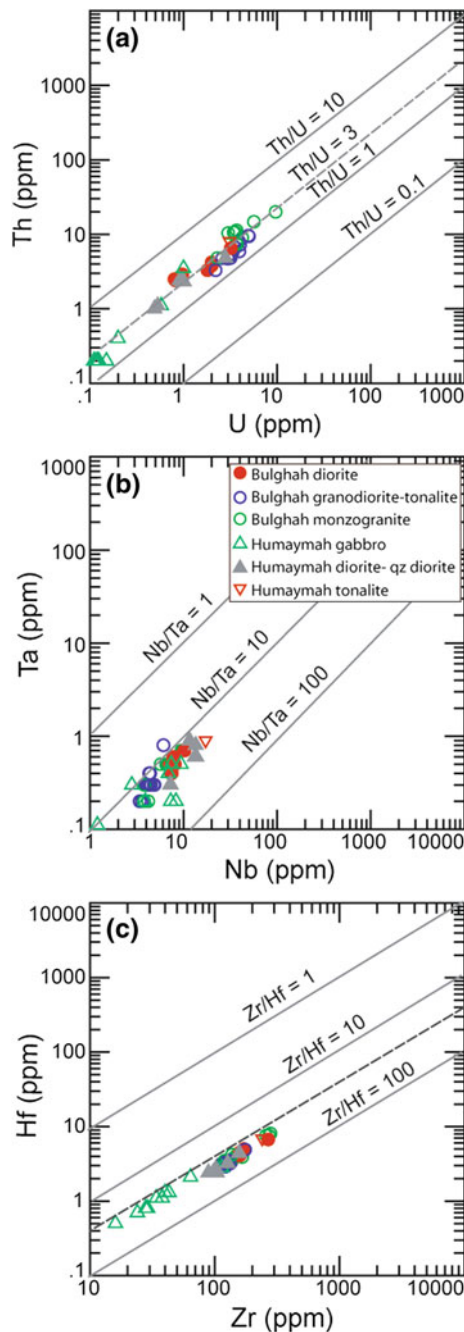u/Eu* = 0.35 − 1.25) and positive Sr anomalies (Figs. 6.7 and 6.8) which are indicative of feldspar fractionation. The diorite-quartz diorite samples are LREE and MREE enriched [(La/Yb)$_N$ = 3.38 − 11.24], with flat to slightly fractionated HREE patterns [(Dy/Yb)$_N$ = 1.00 − 1.63] and minor negative to slightly positive Eu (Eu/Eu* = 0.75 − 1.29) and positive Sr anomalies (Figs. 6.7 and 6.8). However, the Humaymah gabbro samples show almost flat REE patterns [(La/Yb)$_N$ = 2.06 − 4.67 and (Dy/Yb)$_N$ = 1.14 − 1.28], indicating that garnet did not control elemental partitioning during melting or fractionation, with positive Eu (Eu/Eu* = 1.08 − 1.43) and Sr anomalies (Figs. 6.7 and 6.8), and overall REE abundance is lower.

The variation of Th and U show strong positive correlations (Fig. 6.9a) which indicates magmatic behavior of Th and U during magmatic differentiation (Moghazi et al. 2011). Moreover, the variation of Ta versus Nb, and Hf versus Zr (Fig. 6.9b, c) show positive correlation, suggesting that the behavior and enrichment of Nb and Ta are largely controlled by magmatic process (Lehmann and Mahawat 1989; Charoy and Nornoha 1991).

6.5 Discussion

New U–Pb zircon ages and geochemical data that characterize the Bulghah and Humaymah areas, when combined with available geochemical data from previous studies (Harbi et al. 2016, 2018; Robinson et al. 2015), allow us to discuss their tectonic setting and their petrogenesis.

6.5.1 Tectonic Stetting

Granitic rocks are divided into I-, S- and A-types (Whalen et al. 1987; Chappell and White 1992, 2001). A-type granites contain high temperature hydrous phases such as pyroxene and fayalite, and late crystallization biotite and alkali amphibole (Wormald and Price 1988; King et al. 1997). However, petrographic investigation indicates that Bulghah and Humaymah granites show no pyroxene or fayalite, and contain hornblende which is inconsistent with alkali amphibole in typical A-type granites. Moreover, the slight enrichment in high field strength element (HFSE) and REE concentrations, in combination with the petrographic characteristics and the slight low Zr, Nb, Ce and Y

concentrations in most granitic samples, suggest that the studied samples are not A-type granites. The studied granitoids are not also S-type granites because they are metaluminous to slightly peraluminous, and have A/CNK < 1.1 and A/NK > 1 (Fig. 6.6a). It show also that P_2O_5 decreases with increasing SiO_2 (Fig. 6.4h). Additionally, the studied samples contain no Al-rich minerals such as cordierite, muscovite or garnet which are considered the common features of S-type granites (Chappell and White 1992; Huang et al. 2013).

Except for three samples, the granitoid rocks of Bulghah and Humaymah fall in the magnesian field on FeO^t/FeO^t + MgO versus SiO_2 diagram (Frost et al. 2001) (Figure not shown). They are classified as I-type granites on the 10,000 × Ga/Al versus Zr diagram (Whalen et al. 1987) (Fig. 6.10a). Rb, Ta, Nb and Y, among other trace elements, have been used to discriminate the different tectonic setting of granitoid rocks (Pearce et al. 1984). The studied granitoids fall in the volcanic-arc/syn-collisional fields (VAG + syn-COLG) in the Y + Nb versus Rb, Y versus Nb, and Yb versus Ta diagrams (Fig. 6.10b–c) of Pearce et al. (1984).

Mafic intrusive rocks (gabbro and diorite) have been classified using the Cr versus Y diagram (Fig. 6.10a; Pearce et al. 1984) and Cr versus Ce/Sr diagram (Fig. 6.10b; Pearce 1982), they plot in the island arc tholeiites (IAT) field. However, V versus Ti/1000 discrimination diagram ((Fig. 6.7c; Shervais 1982) classify the gabbro and diorite samples as mid-ocean ridge (MORB)/back-arc basin (BAB) mafic components. In summary, variation in multi-elements diagrams (Fig. 6.7) and REE discrimination diagram (Figs. 6.10 and 6.11) indicates that the studied rocks are related to calc-alkaline I-type magmatism formed in an island-arc setting.

6.5.2 Petrogenetic Evaluation

The main compositional trends of the studied intrusive rocks are shown on Harker variation diagrams (Fig. 6.4). The figure shows that many elements do not have straight-line variations (e.g., Al_2O_3, MgO, CaO, TiO_2, Na_2O, P_2O_5, Nb, Ni and Y) but exhibiting compositional gap between different intrusive types. This suggest two different

Fig. 6.10 Major and trace elements tectonic discrimination diagrams. **a** Rb versus Y + Nb, **b** Nb versus Y and **c** Ta versus Yb diagrams (after Pearce et al. 1984), showing the studied granitoids plot in the VAG field. **d** Zr versus 10,000 Ga/Al diagram (Whalen et al. 1987), showing the studied intrusive fall in the I-type granite field. However, few monzogranite samples fall in the A-type field, perhaps due to the mobility of Al (major element). Note diorite intrusive samples are also plotted to highlight the compositional range within these suites, but are classified in Fig. 6.11. VAG = volcanic arc granite, syn-COLG = syn-collision granite, ORG = ocean ridge granite, WPG = within plate granite and post-COLG = post-collisional granite. The field of Sukhaybarat I-type granitoids from Harbi et al. (2018) and the field of Jabal Ghadarah I-type granitoids from Harbi et al. (2016)
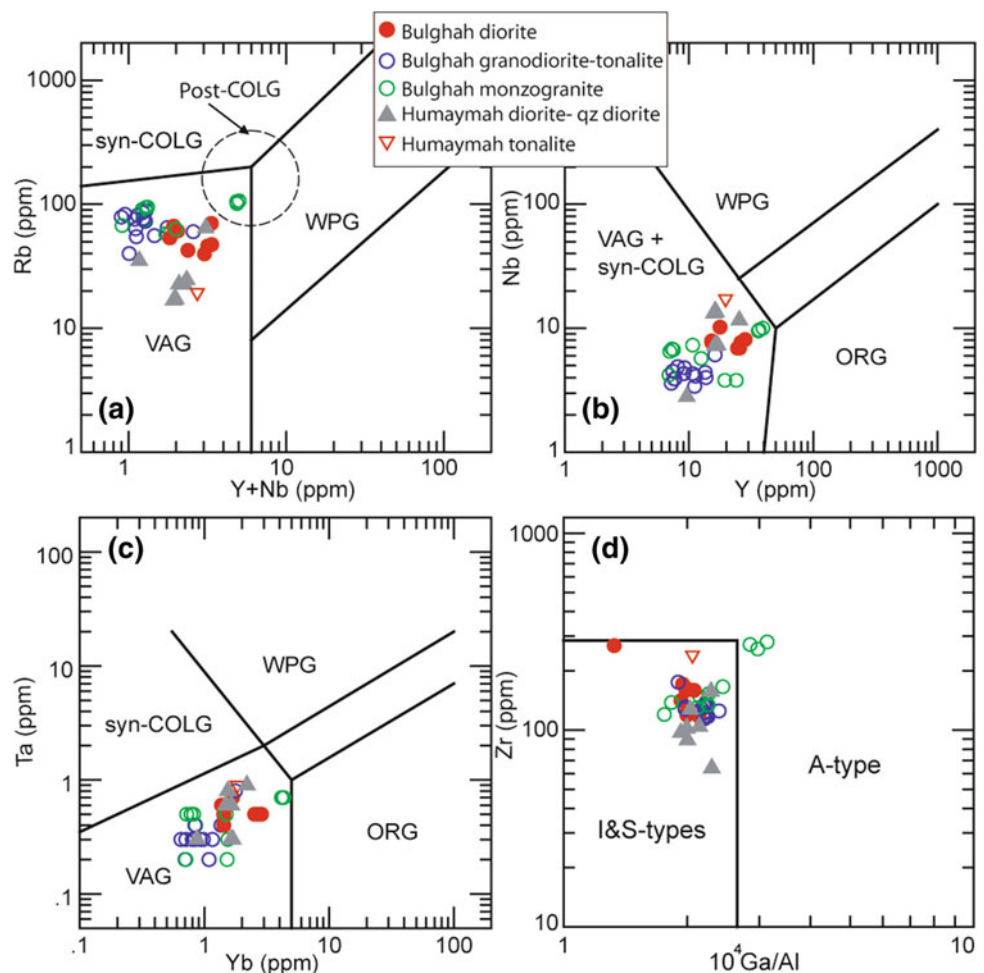
Fig. 6.11 Mafic intrusive classification schemes applied to gabbroic and dioritic samples from Bulghah and Humaymah areas. **a** Cr versus Y and **b** Cr versus Ce/Sr (after Pearce et al. 1984), showing the studied samples fall in the IAT field. **c** V versus Ti/1000 (after Shervais 1982), showing the studied samples plot in the IAT, MORB and BAB fields. The field of Makkah Suite mafic intrusive rocks (Jeddah terrane) from Robinson et al. (2015). Results are discussed in text. MORB = mid-ocean ridge basalt, BAB = back-arc basalt, and IAT = island-arc tholeiitic
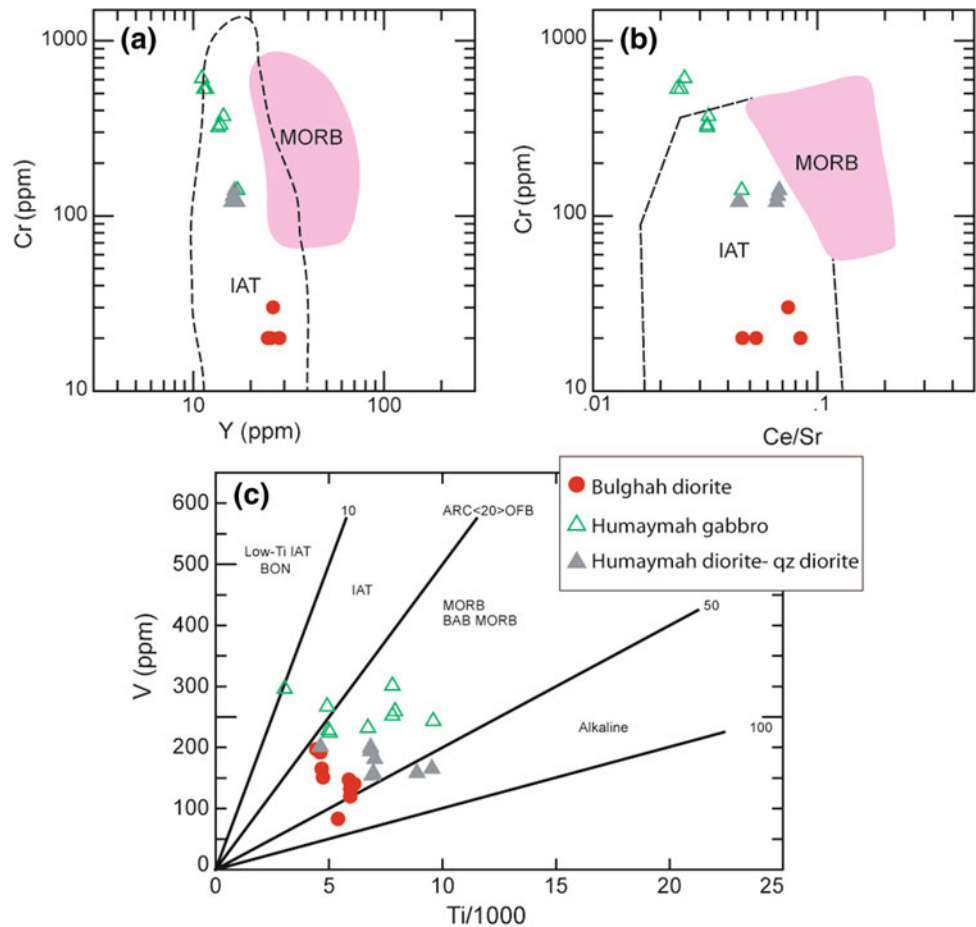
compositional trends in Bulghah and Humaymah intrusive rocks; one for gabbro and diorite and the other for granodiorite-tonalite and monzogranite. Overall, the mafic intrusive rocks are characterized by slightly LREE enriched patterns and relatively flat HREE patterns $[(Dy/Yb)_N = 1.00 - 1.33$, except for three diorite samples show higher values $[(Dy/Yb)_N = 1.45 - 1.63)$ (Fig. 6.8a, d, e). Most samples show Cs, Sr, Rb and K enrichments and Nb, Ta and Ti depletions. The gabbroic samples have La/Nb ratios range from 0.9 to 2.3 and slightly LREE enriched $[(La/Yb)_N = 2.06 - 4.67]$ (Fig. 6.8), although all mafic samples (gabbro and diorite) are outside this range $[(La/Yb)_N = 2.06 - 11.24]$. All mafic intrusive samples show negative Ce and positive or slightly negative Eu anomalies (Eu/Eu* = 0.75 - 1.43) (Figs. 6.7 and 6.8). These geochemical features are comparable to those of the arc-metavolcanic calc-alkaline rocks of the Arabian Shield (Ali et al. 2010), which were produced by partial melting of plagioclase- or spinel-peridotite in the upper most mantle <80 km deep in an intra-oceanic island arc, as indicated from the flat HREE patterns (Rudnick et al. 2004) and other trace element characteristics (Ali et al. 2010). This suggests that the mafic intrusive rocks of Bulghah and Humaymah

represent the plutonic equivalents of the Arabian Shield arc metavolcanic calc-alkaline rocks.

I-type granitoids can be formed through number of magmatic processes (e.g., Miller 1985; Jiang et al. 2007; Hassanen et al. 1996; Best and Christiansen 2001; Roberts and Clements 1993; Skjerlie and Johnston 1992; Frost and Frost 1997; Clemens et al. 2011; Chappell et al. 2012; Huang et al. 2013; Zhang et al. 2015), including Derivation from magmas generated by partial melting of mafic and intermediate igneous rocks has been proposed for some I-type granitoids (see Best and Christiansen 2001). Others have suggested that the I-type granitoids derived from partial melting of ancient lower crust (e.g., Jiang et al. 2007) or hydrous, calc-alkaline to high-K calk-alkaline old metamorphic rocks (Roberts and Clemens 1993). Several studies proposed fractional crystallization of mafic/intermediate magmas as an important process to generate felsic magmas (e.g., Miller and Mittlefehlt 1984; Miller 1985; Secchi et al. 1991; Teixeira et al. 2012). Partial melting of eclogite or garnet amphibolite at mantle depth (Hassanen et al. 1996) and dehydration melting of amphibole-bearing tonalite (Creaser et al. 1991; Skjerlie and Johnston 1992; Frost and Frost 1997) are other potential sources to generate I-type

granites. Differentiation (i.e. partial melting and/or fractional crystallization) of crust and then the magma may have been modified to a degree by fractional crystallization (Miller 1985; Turpin et al. 1990; Barbarin 1996; Champion and Chappell 1992; Chappell et al. 2012; Zhang et al. 2015) could be another source for the I-type granites.

The I-type granitoids (granodiorite-tonalite to monzogranite) of the current study cannot account as a product of mafic magma fractionation since Harker diagrams exhibiting compositional gap between different intrusive types (Fig. 6.4). This exclude the possibility that the granitoids were produced from magmas generated by partial melting of mafic igneous rocks. This is further supported by the U–Pb geochronology data, the dioritic rocks yielded U–Pb ages of 677 ± 8 Ma and 667 ± 6 Ma (Fig. 6.3), whereas the U–Pb zircon age of the monzogranite intrusion is 631 ± 1 Ma

(Bakhsh, unpublished data). A large span in U–Pb ages from 677 (mafic rocks) to 631 (intermediate and felsic rocks) implies that the granodiorite and monzogranite originated from a different magma source than that of the mafic magma (gabbro and diorite).

The compositional variations from granodiorite-tonalite to monzogranite of Bulghah and Humaymah perhaps caused by varying degree of partial melting suggest various degree of fractional crystallization. Varying degree of partial melting of a source could effectively produce melts that have diverse concentration of both major and trace elements (Huang et al. 2013). The most felsic rocks (monzogranite) representative of the lowest degree of partial melting of a source should have the highest La/Yb but lowest Dy/Yb (Huang et al. 2013). However, monzogranite and granodiorite samples show scattered ratios (Fig. 6.12a), inconsistent
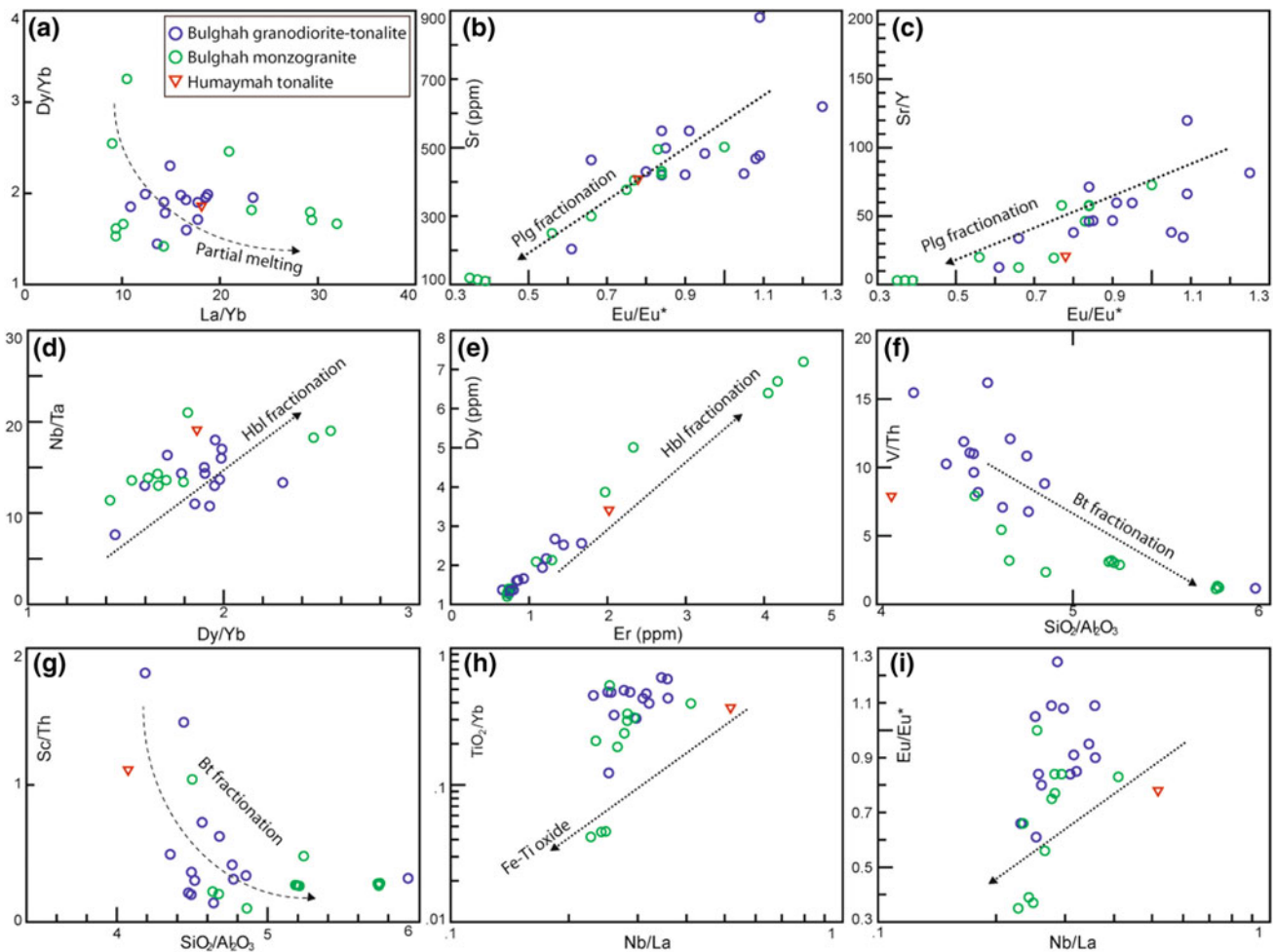
Fig. 6.12 a Dy/Yb versus La/Yb compositional variation diagram, indicating that the studied granitoid samples inconsistent with the partial melting trend. b Sr versus Eu/Eu* and c Sr/Y versus Eu/Eu* variation diagrams, showing that fractionation of plagioclase played an important role in the differentiation of the studied I-type granitoids. d Nb/Ta versus Dy/Yb and e Dy versus Er variation diagrams, showing that fractionation of hornblende played an important role in the differentiation of the studied I-type granitoids. f V/Th versus SiO₂/Al₂O₃ and g Sc/Th versus SiO₂/Al₂O₃ variation diagrams, suggesting biotite fractionation between granodiorite and monzogranite samples. h TiO₂/Yb versus Nb/La and i Eu/Eu* versus Nb/La diagrams for the granitoid samples, showing no correlation indicate a minor role of Fe–Ti oxides fractionation in the genesis of the granodiorites and monzogranites

with the partial melting trend. Thus, it is unlikely that varying degree of partial melting is responsible for the diverse elemental concentrations in Bulghah grantoid rocks. Partial melting model of garnet amphibolite at mantle depth (Hassanen et al. 1996) generates a peraluminous melt (Beaard and Lofgen 1991). However, the studied granitoid samples are metaluminous to weakly peraluminous, indicating water undersaturated partial melting (Huang et al. 2013). Garnet with plagioclase and orthopyroxene would be major residual phases at high pressure (Wolf and Wyllie 1994). If garnet is a residual phase in the source, the HREE patterns will show strong depletion, but the studied granitoid samples show flat to slightly depleted HREE (Fig. 6.8b, c, f). Therefore, the possibility of a high pressure magma source can be excluded as a source for the studied granitoid samples. Contrasting REE patterns between the granodiorite-tonalite and monzogranite samples may have resulted from various degree of fractional crystallization. K-feldspar separation is responsible for the depletion of Ba (Wu et al. 2002; Fig. 6.7c, e), whereas Plagioclase fractionation depleted Eu and Sr in the melts (Figs. 6.7 and 6.8). As shown by Sr, Sr/Y versus Eu/Eu* (Fig. 6.12b and c), the correlations observed in Bulghah granite samples are indicative of plagioclase fractionation. Fractionation of amphibole will lower the Nb/Ta and Dy/Yb ratios in the remaining melt because of its $D(Nb)/D(Ta) > 1$ (Tiepolo et al. 2001) and $D(Dy)/D(Yb) > 1$ (Sisson 1994). A positive correlation between Nb/Ta and Dy/Yb in the Bulghah I-type granitoids strongly suggests amphibole fractionation (Fig. 6.12d). This is further confirmed by the positive correlation between Er and Dy corresponds to the fractionation of hornblende from the parental magma (Drummond et al. 1996; Fig. 6.12e). Biotite have a low value for Th, but high partition coefficients for Sc and V (Bea et al. 1994), therefore biotite fractionation will increase SiO_2/Al_2O_3 but decrease Sc/Th and V/Th ratios in residual melts (Huang et al. 2013). Thus, negative correlations between V/Th and Sc/Th and SiO_2/Al_2O_3 (Fig. 6.12f, g), perhaps indicate biotite fractionation between granodiorite and monzogranite samples of Bulghah. Ti-bearing minerals, such as titanite and ilmenite, might be other fractionated phases as suggested by increasing TiO_2 with decreasing SiO_2 (Huang et al. 2008; Table 6.3, Fig. 6.4c). The fractional crystallization of titanium-rich minerals commonly generates negative Nb–Ta and Ti anomalies in basalts (Xiong et al. 2005; Huang et al. 2008). However, this cannot be the reason for low Nb–Ta (Fig. 6.8b) in the studied granitoids because there are lack of correlations between TiO_2/Yb, Eu/Eu* and Nb/La (Fig. 6.12h, i), indicating a minor role of Fe–Ti oxide fractionation in the genesis of the studied granitoids. Therefore, various degrees of plagioclase, hornblende and biotite fractional crystallization would be important mechanism for variations in chemical composition of the studied granitoids (Fig. 6.12a–

i). The wide range of Mg# (14.5–40.2), Ni (<1–36 ppm) and V (11–89 ppm) contents of the studied granitoids (Table 6.3), perhaps suggest that two or more different
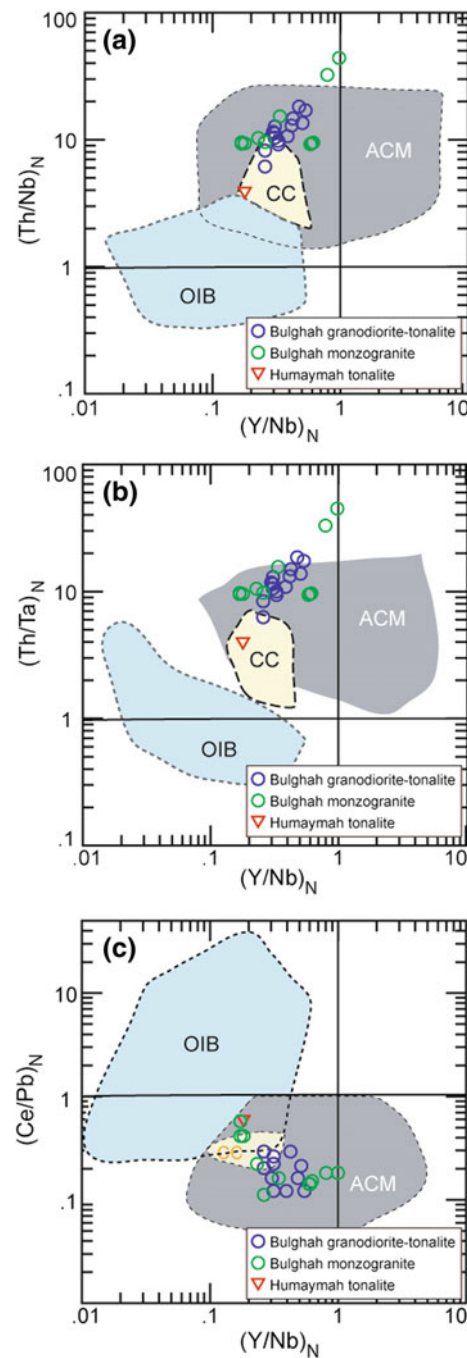
Fig. 6.13 Relationships of $(Th/Nb)_N$, $(Th/Ta)_N$, and $(Ce/Pb)_N$ versus $(Y/Nb)_N$ for the studied granitoid samples from the Bulghah and Humaymah areas with compositional fields of active continental margin (ACM), ocean island basalt (OIB) and continental crust (CC) from Moreno et al. (2014). The field of Sukhaybarat I-type granitoids from Harbi et al. (2018) and the field of Jabal Ghadarah I-type granitoids from Harbi et al. (2016). Normalization values are from McDonough and Sun (1995)

magma sources are likely for the granodiorites and monzogranites (Kelemen 1995; Taylor and Mclennan 1985; Wang et al. 2014). This is supported by the relationships between Y/Nb with Th/Nb, Th/Ta and Ce/Pb (Fig. 6.13) which are sensitive to mantle and continental crust magma sources (Hofmann et al. 1986; Miller et al. 1994; Montero et al. 2009; Rudnick and Gao 2003; Rudnick et al. 2004; Moreno et al. 2014). The relationships of the Y/Nb with Th/Nb and Th/Ta (Fig. 6.13a, b) provide an efficient discrimination between oceanic island (OIB) and convergent margin (ACM) rock types. This is because that any change in incompatible trace-element ratios resulting from magmatic differentiation (e.g., crystal fractionation or partial melting) should be small in comparison to that which may result from two magma sources. The studied samples lie within the field of convergent margin magmatism and inside, or close to, the continental crust field (Fig. 6.13a and b). The $(Y/Nb)_N$ versus $(Ce/Pb)_N$ diagram also show that the granodiorite and the monzogranite samples have the features of a convergent margin and continental crust component (Fig. 6.13c). Therefore, these relationships (Fig. 6.13) suggest the significant involvement of a continental crust component in the granodiorites and monzogranites.

These rocks also show crustal-like trace-element patterns with negative Nb, Ta and Ti, and positive Pb anomalies (Fig. 6.7c, e, f). This is supported by Nb/Ta ratios ranging from (7.6 to 21.0, average of 14.5) that are close to the composition of magmas derived from crust and mantle (17.5; Green 1995). However, mixing model between mafic and felsic magmas needs to be confirmed by whole-rock Sr-Nd isotopes.

6.6 Conclusions

The following are the conclusions from our study:

1. Zircon U–Pb dating indicates that the mafic intrusive rocks from Bulghah and Humaymah, Saudi Arabia were formed at ∼670 Ma, whereas the granitoid I-type intrusions were formed between 661 ± 5 and 643 ± 4 Ma, confirming the importance of the 700–640 Ma crustal forming event in Saudi Arabia.
2. Our analyses of the intrusive samples revealed no evidence of pre-Neoproterozoic zircons, further indicating that ANS crust in this region is mostly juvenile.
3. The studied intrusive rocks range in composition from gabbro-diorite to monzogranite. The gabbro-diorites and granodiorite-tonalite rocks are calk-alkaline, metaluminous to slightly peraluminous, whereas the monzogranite samples are classified as calc-alkaline to highly fractionated calc-alkaline.

4. The granodiorite-tonalite and monzogranite samples are I-type granites and classified as magnesian formed in a volcanic arc setting.
5. The mafic intrusive rocks (gabbro and diorite) formed in island arc setting, perhaps represent the plutonic equivalents of the Arabian Shield arc metavolcanic calc-alkaline rocks which were produced by partial melting of plagioclase- or spinel-peridotite in the upper most mantle <80 km deep in an intra-oceanic island arc.
6. Y/Nb with Th/Ta, Th/Nb Nb and Ce/Pb relationships indicated that the granodiorites-tonalies and monzogranites generated by a combination of mafic parental magma contaminated with crustal materials and controlled by fractional crystallization.

References

Agar RA (1985) Stratigraphy and paleogeography of the Siham group: direct evidence for a late Proterozoic continental microplate and active continental margin in the Saudi Arabian shield. J Geol Soc London 142:1205–1220

Agar RA (1986) The Bani Ghayy group; sedimentation and volcanism in "pullapart" grabens of the Najd strike-slip orogen, Saudi Arabian Shield. Precambrian Res 31:259–274

Agar RA (1988) Geologic map of the Zalm quadrangle, sheet 22 F, Kingdom of Saudi Arabia: Saudi Arabian Deputy Ministry for Mineral Resources Geologic Map Number GM 89, scale 1:250,000, 41 p

Agar RA, Stacey JS, Whitehouse MJ (1992) Evolution of the southern Afif terrane—a geochronologic study. Saudi Arabian Deputy Ministry for Mineral Resource, Open File Report DGMR-OF-10-15, 41 p

Ali KA, Andresen A, Stern RJ, Manton WI, Omar SA, Maurice AE (2012) U–Pb zircon and Sr-Nd–Hf isotopic evidence for a juvenile origin of the c 634 Ma El-Shalul Granite, Central Eastern Desert, Egypt. Geol Mag 149:783–797

Ali KA, Kröner A, Hegner E, Wong J, Li S-Q, Gahlan HA, Abu El Ela AA (2015) U–Pb zircon geochronology and Hf–Nd isotopic systematics of Wadi Beitan granitoid gneisses, South Eastern Desert, Egypt. Gondwana Res 27:811–824

Ali KA, Stern RJ, Manton WI, Kimura J-I, Khamees HA (2009) Geochemistry, Nd isotopes and U–Pb SHRIMP dating of Neoproterozoic volcanic rocks from the Central Eastern Desert of Egypt: New Insights into the ∼750 Ma Crust-Forming Event. Precambrian Res 171:1–22

Ali KA, Stern RJ, Manton WI, Kimura J-I, Whitehouse MJ, Mukherjee SK, Johnson PR, Griffin WR (2010) Geochemical, U–Pb zircon, and Nd isotope investigations of the Neoproterozoic Ghawjah Metavolcanic rocks, Northwestern Saudi Arabia. Lithos 120: 379–393

Barbarin B (1996) Genesis of the two main types of peraluminous granitoids. Geology 24:295–298

Bea F, Pereira MG, Stroh A (1994) Mineral/leucosome trace-element partitioning in a peraluminous migmatite (a laser ablation-ICP-MS study). Chem Geol 117:291–312

Beard JS, Lofgren GE (1991) Dehydration melting and water-saturated melting of basaltic and andesitic greenstones and amphibolites at 1, 3, and 6.9 kbar. J Petrol 32:365–401

Be'eri-Shlevin Y, Katzir Y, Whitehouse M (2009) Post-collisional tectono-magmatic evolution in the northern Arabian-Nubian Shield (ANS): time constraints from ionprobe U–Pb dating of zircon. J Geol Soc London 166:71–85

Best MG, Christiansen EH (2001) Igneous Petrology. Blackwell Science Inc. 458 pp

Bonin B, Giret A (1990) Plutonic alkaline series: Daly gap and intermediate compositions for liquids filling up crustal magma chambers. Schweiz Mineral Petrogr Mitt 70:175–187

Brown FB, Schmidt DL, Huffman AC (1989) Geology of the Arabian Peninsula: shield area of Western Saudi Arabia. US Geological Survey Professional Paper 560-A, 188 p

Champion DC, Chappell BW (1992) Petrogenesis of felsic I-type granites: an example from northern Queensland. Trans R Soc Edinb Earth Sci 83:115–126

Chappel BW (1999) Aluminum saturation in I- and S-type granites and the characterization of fractionated haplogranites. Lithos 46:535–551

Chappell BW, White AJR (1992) I- and S-type granites in the Lachlan Fold Belt. Trans R Soc Edinb Earth Sci 83:1–26

Chappell BW, White AJR (2001) Two contrasting granite types: 25 years later. Aust J Earth Sci 48:489–499

Chappell BW, Bryant CJ, Wyborn D (2012) Peraluminous I-type granites. Lithos 153:142–153

Charoy B, Nornoha F (1991) The Argemella granite-porphyry (central Portugal): the subvolcanic expression of a high fluorine, rare-element pegmatite magma. In: Pagel M, Leroy JL (eds) Source, transport and deposition of metals. A.A. Balkema, Rotterdam, pp 741–744

Clemens JD, Stevens G, Farina F (2011) The enigmatic sources of I-type granites: the peritectic connexion. Lithos 126:174–181

Collins WJ, Beams SD, White AJR, Chappell BW (1992) Nature and origin of A-type granites with particular reference to southeastern Australia. Contrib Miner Petrol 80:189–200

Compston W, Williams IS, Meyer C (1984) U–Pb geochronology of zircons from lunar breccia 73217 using a sensitive high-resolution ion microprobe. J Geophys Res 89:B525–B534

Cox KG, Bell JD, Pankhurst RJ (1979) The interpretation of data for plutonic rocks, The interpretation of igneous rocks. Springer, Netherlands, pp 308–331

Creaser RA, Price RC, Wormald RJ (1991) A-type granites revisited: assessment of a residual source model. Geology 19:163–166

Delfour J (1977) Geological map of the Nuqrah quadrangle, 25E, Kingdom of Saudi Arabia. Saudi Arabian Dir. Gen. Miner. Resour. Geological Map GM 28, scale 1:250,000, 32 p

Delfour J (1981) Geological map of the Al Hissu quadrangle sheet 24 E, Kingdom of Saudi Arabia. Saudi Arabian Dir. Gen. Miner. Resour. Geological Map GM 58, scale 1:250,000, 47 p

de la Roche H, Leterrier J, Grandclaude P, Marchal M (1980) A classification of volcanic and plutonic rocks using R1R2 diagram and major-element analyses—its relationships with current nomenclature. Chem Geol 29:183–210

Dilek Y, Ahmed Z (2003) Proterozoic ophiolites of the Arabian Shield and their significance in Precambrian tectonics. Ophiolites Earth Hist Geol Soc Lond, Special Publications 218:685–701

Drummond MS, Defant MJ, Kepezhinskas PK (1996) Petrogenesis of slab derived trondhjemite-tonalite-dacite/adakite magmas. Trans R Soc Edinb Earth Sci 87:205–215

Eby GN (1990) The A-type granitoids: a review of their occurrence and chemical characteristics and speculations on their petrogenesis. Lithos 26:115–134

Eby GN (1992) Chemical subdivision of the A-type granitoids; petrogenetic and tectonic implications. Geology 20:641–644

Elliott T (2003) Tracers of the slab. In: Eiler J (ed) Inside the subduction Factory. Geophysical Monograph Series, vol 138. American Geophysical Union, Washington, pp 23–45

Eyal M, Litvinovsky B, Jahn B, Zanvilevich A, Katzir Y (2010) Origin and evolution of post-collisional magmatism: coeval Neoproterozoic calc-alkaline and alkaline suites of the Sinai Peninsula. Chem Geol 269:153–179

Frost CD, Frost BR (1997) Reduced rapakivi-type granites: the tholeiite connection. Geology 25:647–650

Frost BR, Barnes CG, Collins WJ, Arculus RJ, Ellis DJ, Frost CD (2001) A Geochemical classification for granitic rocks. J Petrol 42:2033–2048

Genna A, Nehlig P, Le Goff E, Gguerrot C, Shanti M (2002) Proterozoic tectonism of the Arabian Shield. Precambrian Res 117:21–40

Green TH (1995) Significance of Nb/Ta as an indicator of geochemical processes in the crust–mantle system. Chem Geol 120:347–359

Greiling RO, Abdeen MM, Dardir AA, El Akhal H, El Ramly MF, Kamal El Din GM, Osman AF, Rashwan AA, Rice AHN, Sadek MF (1994) A structural synthesis of the Proterozoic Arabian–Nubian Shield in Egypt. Geol Rundschau 83:484–501

Harbi HM, Ali KA, Eldougdoug AA, Al Jahdali NS (2016) [40]Ar/[39]Ar and U–Pb zircon dating constraints along Bir Tawilah shear zone, central Saudi Arabia: implication for age of gold mineralization. Chem Erde 76:309–324

Harbi HM, Ali KA, McNaughton NJ, Andresen A (2018) U–Pb zircon and [40]Ar/[39]Ar geochronology of sericite from hydrothermal alteration zones: new constraints for the timing of Ediacaran gold mineralisation in the Sukhaybarat area, western Afif terrane, Saudi Arabia. Miner Deposita 53:459–476

Hassanen M, El-Nisr S, Mohamed FH (1996) Geochemistry and petrogenesis of Pan-African granitoids at Gabal Igla Ahmar, Easter Desert, Egypt. J Afr Earth Sci 22:29–42

Hofmann AW, Jochum KP, Seufert M, White WM (1986) Nb and Pb in oceanic basalts: new constraints on mantle evolution. Earth Planet Sci Lett 79:33–45

Huang HQ, Li XH, Li WX, Li ZX (2011) Formation of high $\delta 18O$ fayalite-bearing A-type granite by high-temperature melting of granulitic metasedimentary rocks, Southern China. Geology 39:903–906

Huang X-L, Xu Y-G, Li X-H, Li W-X, Lan J-B, Zhang H-H, Liu Y-S, Wang Y-B, Li H-Y, Luo Z-Y, Yang Q-J (2008) Petrogenesis and tectonic implications of Neoproterozoic, highly fractionated A-type granites from Mianning, South China. Precambrian Res 165: 190–204

Huang X-L, Yu Y, Li J, Tong L-X, Chen LL (2013) Geochronology and petrogenesis of the early Paleozoic I-type granite in the Taishan area, South China: middle-lower crustal melting during orogenic collapse. Lithos 117:268–284

Jackson SE, Pearson NJ, Griffin WL, Belousova EA (2004) The application of laser ablation-inductively coupled plasma-mass spectrometry to in-situ U–Pb zircon geochronology. Chem Geol 211:47–69

Jarrar G, Stern RJ, Saffarini G, Al-Zubi H (2003) Late- and post-orogenic Neoproterozoic intrusions of Jordan: implications for crustal growth in the northernmost segment of the East African Orogen. Precambrian Res 123:295–319

Jiang N, Liu Y, Zhou W, Yang J, Zhang S (2007) Derivation of Mesozoic adakitic magmas from ancient lower crust in the North China Craton. Geochim Cosmochim Acta 71:2591–2608

Johnson PR (1998) Tectonic map of Saudi Arabia and adjacent areas. Saudi Arabian Deputy Ministry for Mineral Resource, Technical Report USGS-TR-98-3, scale 1:40,000,000

Johnson PR (2003) Post-amalgamation basins of the NE Arabian shield and implications for Neoproterozoic III tectonism in the northern East African orogen. Precambr Res 123:321–338

Johnson PR, Andresen A, Collins AS, Fowler AR, Fritz H, Ghebreab W, Kusky T, Stern RJ (2011) Late Cryogenian–Ediacaran history of the Arabian-Nubian Shield: a review of depositional, plutonic, structural, and tectonic events in the closing stages of the northern East African Orogen. J Afr Earth Sci 61: 167–232

Johnson PR, Kattan F (1999) The timing and kinematics of a suturing event in the northeastern part of the Arabian shield, Kingdom of Saudi Arabia: Saudi Arabian Deputy Ministry for Mineral Resources Open File Report USGS-OF-99-3, 29 p

Johnson PR, Woldehaimanot B (2003) Development of the Arabian-Nubian Shield: Perspectives on accretion and deformation in the northern East African Orogen and the assembly of Gondwana. In: Yoshida M, Dasgupta S, Windley B (eds) Proterozoic East Gondwana: supercontinent assembly and breakup. Geol Soc Lond, Special Publications 206:289–325

Kelemen PB (1995) Genesis of high Mg # andesites and the continental crust. Contrib Miner Petrol 120:1–19

Kemp AIS, Hawkesworth CJ, Paterson BA, Kinny PD (2006) Episodic growth of the Gondwana supercontinent from hafnium and oxygen isotopes in zircon. Nature 439:580–583

Kennedy AK, De Laeter JR (1994) The performance characteristics of the WA SHRIMP II ion microprobe. U.S. Geological Survey Circular 166:1107

King PL, White AJR, Chappell BW, Allen CM (1997) Characterization and origin of aluminous A-type granites from Lachlan Fold Belt, Southeastern Australia. J Petrol 38:371–391

Kusky T, Matsah MI (2003) Neoproterozoic dextral faulting on the Najd Fault System, Saudi Arabia, preceded sinistral tectonics related to the closure of the Mozambique Ocean. J Geol Soc, Lond 206:327–361 (Special Publications)

Lehmann B, Mahawat C (1989) Metallogeny of tin in central Thailand: a genetic concept. Geology 17:426–429

Liégeois JP, Black R (1987) Alkaline magmatism subsequent to collision in the Pan-African belt of the Adrar des Iforas (Mali). In: Fitton JG, Upton BJG (eds) Alkaline igneous rocks. Geol Soc Lond, Spec Publ 30:381–401

Liégeois JP, Stern RJ (2010) Sr-Nd isotopes and the geochemistry of granite-gneiss complexes from the Meatiq and Hafafit domes, Eastern, Desert, Egypt: No evidence for pre-Neoproterozoic crust. J Afr Earth Sci 57:31–40

Ludwig KR (2001a) SQUID 1.02: a user's manual. Berkeley Geochronology Center, Special Publication No 2, Berkeley, CA, p 19

Ludwig KR (2001b) Users manual for Isoplot/Ex version 2.05. Berkeley Geochronology Center, Special Publication No 1a, Berkeley, CA, p 48

Maniar PD, Piccoli PM (1989) Tectonic discrimination of granitoids. Geol Soc Am Bull 101:636–643

McDonough WF, Sun SS (1995) The composition of the Earth. Chem Geol 120:223–253

Miller CF (1985) Are strongly peraluminous magmas derived from politic sedimentary sources? J Geol 93:673–689

Miller CF, Mittlefehlt DW (1984) Extreme fractionation in felsic magma chambers: a product of liquid-state diffusion or fractional crystallization? Earth Planet Sci Lett 68:151–158

Miller DM, Goldstein SL, Langmuir CH (1994) Cerium/lead and lead isotope ratios in arc magmas and the enrichment of lead in the continents. Nature 368:514–520

Moghazi A-KM, Ali KA, Wilde SA, Zhou Q, Andersen T, Andresen A, Abu El-Enen MM, Stern RJ (2012) Geochemistry, geochronology, and Sr–Nd isotopes of the Late Neoproterozoic Wadi Kid volcano-sedimentary rocks, Southern Sinai, Egypt. Lithos 154:147–165

Moghazi AM, Harbi HM, Ali KA (2011) Geochemistry of the Late Neoproterozoic Hadb adh Dayaheen ring complex, Central Arabian Shield: implications for the origin of rare-metal-bearing post-orogenic A-type granites. J Asian Earth Sci 42:1324–1340

Montero P, Bea F, Corretge LG, Floor P, Whitehouse MJ (2009) U–Pb ion microprobe dating and Sr–Nd isotope geology of the Galiñeiro Igneous Complex. A model for the peraluminous/peralkaline duality of the Cambro-Ordovician magmatism of Iberia. Lithos 107:227–238

Moreno JA, Molina JF, Montero P, Abu Anbar M, Scarrow JH, Cambeses A, Bea F (2014) Unraveling sources of A-type magmas in juvenile continental crust: constraints from compositionally diverse Ediacaran post-collisional granitoids in the Katerina Ring Complex, southern Sinai, Egypt. Lithos 192–195:56–85

Moussa EMM, Stern RJ, Manton WI, Ali KA (2008) SHRIMP zircon dating and Sm/Nd isotopic investigations of Neoproterozoic granitoids, Eastern Desert, Egypt. Precamb Res 160:341–356

Mushkin A, Navon O, Halicz L, Hartmann G, Stein M (2003) The petrogenesis of A-type magmas from the Amram Massif, Southern Israel. J Petrol 44:815–832

Nehlig P, Genna A, Asirfane F (2002) A review of the Pan-African evolution of the Arabian Shield. GeoArabia 7:103–124

Pallister JS, Stacey JS, Fischer LB, Premo WR (1988) Precambrian ophiolites of Arabia; geologic setting, U–Pb geochronology, Pb-isotope characteristics, and implications for continental accretion. Precambr Res 38:1–54

Patiño Douce AE (1997) Generation of metaluminous A-type granitoids by low-pressure melting of calc-alkaline granitoids. Geology 25:743–746

Pearce J (1982) Trace element characteristics of lavas from destructive plate boundaries. In: Thorpe RS (ed) Andesites: orogenic andesites and related rocks. Wiley, pp 525–548

Pearce J, Harris NB, Tindle AG (1984) Trace element discrimination diagrams for the tectonic interpretation of granitic rocks. J Petrol 25:956–983

Roberts MP, Clemens JD (1993) Origin of high potassium, calc-alkaline, I-type granitoids. Geology 21:825–828

Robinson FA, Foden JD, Collins AS, Payne JL (2014) Arabian Shield magmatic cycles and their relationship with Gondwana assembly: Insights from zircon U–Pb and Hf isotopes. Earth Planet Sci Lett 408:207–225

Robinson FA, Foden JD, Collins AS (2015) Geochemical and isotopic constraints on island arc, synorogenic, post-orogenic and anorogenic granitoids in the Arabian Shield, Saudi Arabia. Lithos 220–223:97–115

Roobol MJ, Ramsay CR, Jackson NJ, Darbyshire DPF (1983) Late Proterozoic lavas of the Central Arabian Shield—evolution of an ancient volcanic arc system. J Geol Soc London 140:185–202

Rosa DRN, Finch AA, Andersen T, Inverno CMC (2009) U–Pb geochronology and Hf isotope ratios of magmatic zircons from the Iberian Pyrite Belt. Mineral Petrol 95:47–69

Rudnick R, Gao S (2003) Composition of the continental crust. Treatise Geochem 3:1–64

Rudnick RL, Gao S, Ling W-L, Liu Y-S, McDonough WF (2004) Petrology and geochemistry of spinel peridotite xenoliths from Hannuoba and Qixia, North China craton. Lithos 77:609–637

Secchi FA, Brotzu P, Callegari E (1991) The Arburese igneous complex (SW Sardinia, Italy)—an example of dominant igneous fractionation leading to peraluminous cordierite-bearing leucogranites as residual melts. Chem Geol 92:213–249

Shervais JW (1982) Ti-V plots and the petrogenesis of modern and ophiolitic lavas. Earth Planet Sci Lett 59:101–118

Sisson TW (1994) Gornblende-melt trace-element partitioning measured by ion microprobe. Chem Geol 117:331–344

Skjerlie KP, Johnston AD (1992) Vapor-absent melting at 10 kbar of a biotite- and amphibole-bearing tonalitic gneiss: implication for the generation of A-type granites. Geology 20:263–266

Stacey JS, Agar RA (1985) U–Pb isotopic direct evidence for the accretion of a continental microplate in the Zalm region of the Saudi Arabian shield. J Geol Soc London 142:1189–1203

Stacey JS, Hedge CE (1984) Geochronologic and isotopic evidence for early Proterozoic crust in the eastern Arabian shield. Geology 12:310–313

Stern RJ (1994) Arc assembly and continental collision in the Neoproterozoic East African Orogen: implications for the consolidation of Gondwanaland. Ann Rev Earth Planet Sci 22:319–351

Stern RJ, Johnson PR (2010) Continental lithosphere pf the Arabian Plate: a geologic, petrologic, and geophysical synthesis. Earth-Sci Rev 101:29–67

Stoeser DB (1986) Distribution and tectonic setting of plutonic rocks of the Arabian Shield. J Afr Earth Sc 4:21–46

Stoeser D, Camp E (1985) Pan-African microplate accretion of the Arabian Shield. Geol Soc Am Bull 96:817–826

Stoeser D, Frost C (2006) Nd, Pb, Sr, and O isotopic characterization of Saudi Arabian Shield terranes. Chem Geol 226:163–188

Streckeisen A, Le Maitre RW (1979) A chemical approximation to the modal QAPF classification of the igneous rocks. N Jb Miner Abh 136:169–206

Sun SS, McDonough WF (1989) Chemical and isotopic systematics of oceanic basalts: implications for mantle composition and processes. In: Saunders AD, Norry MJ (eds) Magmatism in Ocean Basins. Geological Society of London, Special Publications 42:313–345

Sylvester PJ (1998) Post-collisional strongly peraluminous granites. Lithos 45:29–44

Taylor SR, McLennan SM (1985) The continental crust: its composition and evolution. Blackwell Scientific Publishers, Oxford, p 312

Teixeira RJS, Neiva AMR, Gomes MEP, Corfu F, Cuesta A, Croudace IW (2012) The role of fractional crystallization in the genesis of early syn-D3, tin mineralized Variscan two-mica granites from the Carrazeda de Ansiães area, Northern Portugal. Lithos 153:177–191

Tiepolo M, Bottazzi P, Foley SF, Oberti R, Vannucci R, Zanetti A (2001) Fractionation of Nb and Ta from Zr and Hf at mantle depths: the role of titanian pargasite and kaersutite. J Petrol 42:221–232

Turner SP, Foden JD, Morrison RS (1992) Derivation of some Atype magmas by fractionation of basaltic magma: an example from the listvenites Ridge, South Australia. Lithos 28:151–179

Turpin L, Cuney M, Friedrich M, Bouchez JL, Aubertin M (1990) Metaigneous origin of Hercynian peraluminous granites in N.W. French Massif Central: implications for crustal history reconstructions. Contrib Miner Petrol 104:163–172

Wang L-X, Ma C-Q, Zhang C, Zhang J-Y, Marks MAW (2014) Genesis of leucogranite by prolonged fractional crystallization: a case study of the Mufushan complex, South China. Lithos 206–207:147–163

Wetherill GW (1956) Discordant uranium–lead ages I. Trans Am Geophys Union 37:320–326

Whalen JB, Currie KL, Chappell BW (1987) A-type granites: geochemical characteristics, discrimination and petrogenesis. Contrib Miner Petrol 95:407–419

Wiedenbeck M, Allé P, Corfu F, Griffin WL, Meier M, Oberli F, Von Quadt A, Roddick JC, Spiegel W (1995) Three natural zircon standards for U–Th–Pb, Lu–Hf, trace element and REE analyses. Geostand Newsl 19:1–23

Wilde SA, Youssef K (2000) Significance of SHRIMP U–Pb dating of the Imperial Porphyry and associated Dokhan Volcanics, Gebel Dokhan, North Eastern Desert, Egypt. J Afr Earth Sci 31:403–410

Wolf MB, Wyllie PJ (1994) Dehydration-melting of amphibolite at 10 kbar: the effects of temperature and time. Contrib Mineral Petrol 115:369–383

Wormald RJ, Price RC (1988) Peralkaline granites near Temora, Southern New South Wales: tectonic and petrological implications. Aust J Earth Sci 35:209–221

Wu FY, Sun DY, Li H, Jahn BM, Wilde S (2002) A-type granites in northern China: age and geochemical constraints on their petrogenesis. Chem Geol 187:143–173

Xiong XL, Adam J, Green TH (2005) Rutile stability and rutile/melt HFSE partitioning during partial melting of hydrous basalt: implications for TTG genesis. Chem Geol 234:105–126

Zhang Y, Yang J-H, Sun J-F, Zhang J-H, Chen J-Y, Li X-H (2015) Pterogenesis of Jurassic fractionated I-type granites in Southeast China: constraints from whole-rock geochemical and zircon U–Pb and Hf-O isotopes. J Asian Earth Sci 111:268–283

Zhang XH, Yuan LL, Xue FH, Zhang Y (2012) Contrasting Triassic ferroan granitoids from northwestern Liaoning, North China: magmatic monitor of Mesozoic decratonization and craton-orogen. Lithos 144–145:12–23

Aeromagnetic Data Investigation of Al-Shamiyya Area, North East of Makkah Quadrangle, Saudi Arabia

Mansour A. Al-Garni, El-Sawy K. El-Sawy, and Sami Khomsi

Abstract

The study area lies within the Arabian Shield which includes Al-Shamiyya area. The aeromagnetic data are utilized to investigate the magnetic features of the study area. Several techniques have been used in order to enhance the interpretation of the aeromagnetic data where each technique implements a task towards the purpose of the study. The aeromagnetic data have been subjected to 3D Euler deconvolution, magnitude magnetic transforms, edge enhancement using standard deviation, and pseudo gravity techniques. 3D Euler deconvolution is used to estimate the depth to magnetic sources and the structural indices which estimates the structural types that may exist within the study area. The results of this technique show that the depth of causative targets varies between 1.37 and 5.29 km with average depth of about 3.6 km. Furthermore, the estimated structural indices varies between 0.08 and 0.27 with average of about 0.16, indicating that the common structure types is a contact (fault) model. Magnitude magnetic transforms is used it demonstrate the subsurface features where it is compared with the conventional reduce to pole technique to extra the zones if any. Also, this technique used to demonstrate the deepest and shallowest causative targets within the study area using E and L transforms. Furthermore, total horizontal and vertical derivatives have been implemented using the magnitude magnetic transform showing the major structural contacts and the enhancing shallow magnetic sources, respectively. Edge enhancement technique is mainly used to demonstrate the possible contacts within the study area. Several windows have been chosen in order to enhance the detail and the fine edges where larger windows are used to demonstrate the possible major contacts within the study area. The pseudogravity technique is used to constraint and better depict the nature of subsurface causative targets which are essentially dominated by structures. This technique shows that the area mainly consists of three domains varies from low to high.

7.1 Introduction

The area of study is located within the Arabian Shield between latitudes 21° 32′ 30″N and 21° 52′ 29″N and longitudes 40° 03′ 44″E and 40° 30′ 17″ (Fig. 7.1), where the Arabian Shield represents the eastern part of Arabian-Nubian Shield. The tectonic evolution of the Arabian Shield has been a matter of debate (Al-Garni 2007). The evolution was discussed in terms of Wilson Cycle dynamic in 1970s; however, the terrane concept has become the main accepted since in mid-1980s. Wider views have been taken place in the mid-1990s in which the whole Arabian-Nubian Shield is located at the northern edge of the East African orogeny and viewed geodynamically in terms of fragmentation of Rodina with subsequent, collision between east and west Gondwana, leading through tome to arc accretion,

M. A. Al-Garni (✉)
Geophysics Department, Faculty of Earth Sciences, King Abdulaziz University (KAU), Jeddah, Saudi Arabia
e-mail: maalgarni@kau.edu.sa; ; malgarni@mewa.gov.sa

National Center for Water Research and Studies (NCWRS), Ministry of Environment, Water and Agriculture (MEWA), Riyadh, Saudi Arabia

E.-S. K. El-Sawy · S. Khomsi
Geoexploration Technique Department, Faculty of Earth Sciences, King Abdulaziz University, P.O. 80206 Jeddah, 21589, Saudi Arabia

E.-S. K. El-Sawy
Geology Department, Faculty of Science, Al-Azhar University (Assiut Branch), Assiut, Egypt

S. Khomsi
Laboratory Georesources, CERTE/University of Carthage, Tunis, Tunisia

Fig. 7.1 ETM images showing the location of the study area

orogeny, extension and orogenic collapse (Johnson and Woldehaimanot 2003). However, the final collision between east and west Gondwana has been still a matter of argument where the geodynamics-process played an important role in the control of the structural styles of the Arabian-Nubian Shield (Shackleton 1996; Abdelsalam et al. 1998; Johnson and Woldehaimanot 2003). Johnson and Woldehaimanot (2003) stated that the shield itself forms the suture zone between east and west Gondwana. Furthermore, the most important fabrics in the shield have been categorized into sutures and shear zones, thrusts, thrust duplex and thrust-related folds, successive phases of folding, domes and fractures (Hamimi 2006). In the present study, the aeromagnetic data are used to investigate the subsurface features as well as the estimation the depth to the causative targets. The subsurface features will be investigated using different techniques which are mainly pseudogravity, magnitude

magnetic transforms (MMTs) and normalized standard deviations (NSTD). The depth determination will be using an automatic algorithm based on the Euler deconvolution with unprescribed structural index.

In this study, aeromagnetic data are used to delineate the subsurface features and approximating the depth to magnetic sources. In order to implement that goals, several techniques are utilized such as edge enhancement, and magnitude magnetic transforms (MMTs). The proposed techniques have been applied on the reduced-to-pole data deduced from the total magnetic intensity map. The aeromagnetic data have been subjected to filters based on using normalized statistics (normalized standard deviation, NSTD), which are mainly used as edge detectors in different ways. Magnitude magnetic transform (MMTs) have been utilized in order to enhance the aeromagnetic data interpretation.

7.2 Geology of the Study Area

7.2.1 Syn-Tectonic Intrusions

Precambrian layered rocks are largely confined to the northwest and southeast of the quadrangle (Fig. 7.2a). In the northwest they occupy less than 20% of the outcrop area and their occurrence is widespread but discontinuous because of intruding Plutons and a cover of Cenozoic sedimentary rocks and lavas. The layered rocks are predominantly metamorphosed lavas and associated volcaniclastic rocks ranging in composition from basalt to rhyolite, but quartz-, feldspar-, and carbonate-rich meta sedimentary rocks are also quite common, especially in the Zibarah and Fatima groups (Fig. 7.2a). The Zibarah group is an aggregate of the Madiq, Jumum, and Wuhayt formations. The characteristics of this group are comprised of the association of quartz-rich schists and metaquartzites with intruded banded of amphibolites, a metamorphic grade in the almandine-amphibolite facies, and the presence of structures thought to be related to the earliest tectonic event in the study area. The group is faulted and thrusted against formations of the Samran group and is overlain unconformably by the Fatima and Rahat groups (Fig. 7.2a, Moore and Al-Rehaili 1989).

The Samran group occurs as rafts within and screens between plutons, and as envelopes of country rock around intrusions, except for a northeast-trending belt of Samran rocks in the east central part of the study area (Fig. 7.2a). The dominant structural trend is northeast. The group is consisted originally of mafic to felsic lavas and volcaniclastic rocks with subordinate sedimentary rocks. In many places the original volcanic, volcaniclastic, and sedimentary textures are preserved, but elsewhere deformation and metamorphism have caused the development of chlorite chlorite-sericite quartz-sericite, and quartz-feldspar schists (Schmidt et al. 1973). The Milh complex occurs as large to small masses enclosed by younger plutons within a broad zone of rugged, in places mountainous that extends northeastward from the south-central boundary to the northeastern corner of the study area (Fig. 7.2a, b). The complex comprises about half of the Makkah batholith, and consists predominantly of diorite and quartz diorite. It is metamorphosed in the greenschist facies, and is generally weakly foliated except in zones of more intense deformation such as in the south and on the northwestern flank of the Al Sayl al Kabir pluton. In the southwest, the complex is preserved as roof pendants within the Nu'man batholith (Moore and Al-Rehaili 1989). The diorite to gabbro unit consists mainly of diorite, grading locally to gabbro. The diorite is fine to medium grained and is composed of an hypidiomorphic intergrowth of andesine and poikilitic hornblende, a few phenocrysts of zoned but untwinned feldspar (? oligoclase),

and minor accessory iron oxide. In places, the plagioclase laths have heavily sericitized cores and clear albitic rims, the hornblende crystals have developed fibrous blue-green amphibole at their margins, and minor amounts of brown biotite, muscovite, and chlorite are present.

Diorite to quartz diorite is developed principally in two large intrusions, each elongated in a northeasterly direction and measuring about 30 km long and from 10 to 15 km wide, in the Red Sea escarpment zone northeast of the Makkah al Mukarramah At Ta'if highway and in the drainage area of wadi Malakan in the south. Quartz diorite predominates in both intrusions.

7.2.2 Post-tectonic Precambrian Intrusive Rocks

The Bahitah granite forms a single pluton that is located close to the east-central edge of the study area at the town of As Sayl Al Kabir. The pluton has a roughly circular outline about 12 km in diameter. It intrudes the Milh and Shamiyah complexes, contains large rafts of the Madiq formation, and is cut by numerous andesitic, rhyolitic, and granitic dikes, and quartz veins. The dikes are arranged tangentially to the circumference of the pluton and are possibly associated with ring fracturing (Smith 1980). Contacts of the Bahitah granite with its country rocks are sharp, and fine grained granite intrudes the country rocks in the contact zone (Fig. 7.2a). The Bahitah granite was described briefly by Nejaim. It is typically pink, leucocratic and fine- to medium grained and is composed of pink potassium feldspar, white plagioclase, and clear quartz. Modal analysis of a sample of microgranite collected during the present compilation from the granite at its contact with the Milh complex in wadi Harad (Sharq) indicated that the margin of the pluton is syenogranitic.

7.2.3 Late-Tectonic Precambrian Intrusive Rocks

The Nu'man complex (ngm, ngd) is well exposed in rugged country in the southeast of the quadrangle where it forms a large batholith, continuous into the Al Lith quadrangle (Pallister 1986). The complex is compiled from: most of the Na'man monzogranite of Smith (1980); the Al-Asayriah granite of monzogranite and biotite monzogranite at Az Ziyamah and northwest of Wadi as Sadr in the east-central part of the study area; the small granodiorite plutons of Wadi al Khaniq, Jabal al Laban and Jabal al Laban al Aswad in the south of the study area (Skiba and Gilboy 1975; Tayeb 1983); and, in the same area, granite and granodiorite of the Abyad lobe of the batholith (Skiba and Gilboy 1975). Most of the Nu'man complex consists of light-pink, coarse-grained biotite monzogranite potassium feldspar
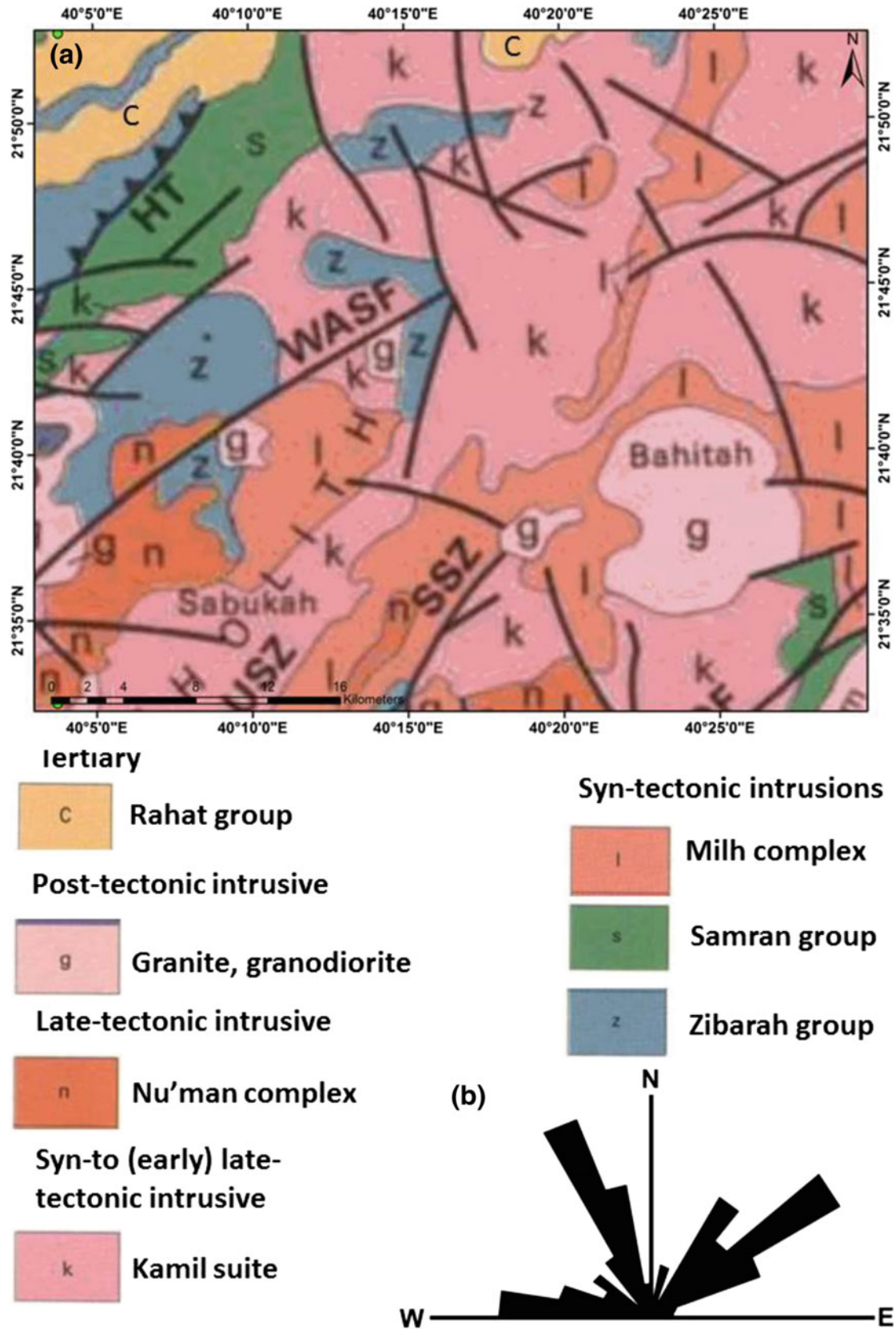
Fig. 7.2 a Geology map of the study area (after Moore and Al-Rehaili 1989) and **b** rose diagram showing the trends of fault

phenocrysts. A detailed description of the monzogranite is provided by Marzouki (1977). Graded layering in monzogranite at the top of the batholith in the escarpment southwest of Al Hada was studied by Hadley and Greenwood (1982), who demonstrated that individual layers are differentiated from base to top, from quartz diorite, tonalite and granodiorite, to monzogranite and syenogranite. On the flanks of the Abyad lobe, monzogranite grades outward to granodiorite (ngd). In the contact zone with tonalites country rocks, coarse-grained porphyritic biotite-hornblende granodiorite of the Nu'man complex is interlayered with, and contains abundant xenoliths of, diorite to gabbro of the Milh complex. Massive green-flecked pinkish-gray biotite-hornblende granodiorite forms a small pluton centered 12 km southwest of As Sayl al Kabir, and off-white, medium-grained granodiorite occurs as small bodies within the batholith in the Wadi Rahjan-Jabal Zahran area.

7.2.4 Syn to (Early) Late-Tectonic Intrusive Rocks

The Qattanah complex forms a large elliptical pluton 19 by 10 km elongated northeast in the south of the Hafnah batholith, and some smaller plutons in the northern and southwestern parts. The plutons represent about 10% by area of the batholith. The main Qattanah pluton is composed of biotite monzogranite at the center grading outward into hornblende granodiorite. There are minor amounts of biotite leucogranite and granophyre. Contacts with the country rocks (Samran-group meta-volcanics and quartz diorite of the Dighbij complex) are sharp and irregular, with numerous tongues of the Qattanah complex extending into the country rocks. At the contacts, the intrusive and country rocks are brecciated and very friable, and the country rocks are affected by contact metamorphism. The marginal zones of plutons are characterized by a planar fabric, and an abundance of xenoliths and roof pendants that decrease in size and number away from the contract. Granodiorite of the Qattanah pluton consists of altered oligoclase-andesine, quartz, poikilitic microcline/microperthite, and minor amounts of hornblende, and brown biotite altered to chlorite in places.

7.2.5 Tertiary Rocks

The Cenozoic lava field of Harrat Rahat, one of the largest in Saudi Arabia, extends south for about 310 km from Al Madinah al Munawwarah into the northeastern part of the Makkah quadrangle (Camp and Roobol 1987, Fig. 7.2a). The Harrat has a total surface area of about 20,000 km^2 Lava tongues and erosional remnants form large and small Harrats that extend westward almost to the Red Sea coast north of Sharm Ubhur. The Harrats are composed of flat-lying, un deformed alkali basalt surmounted by a few pyroclastic cinder cones. The lavas rest on a peneplain, or have infilled ancient Wadis, as indicated by the Khulaysiyah formation and the sinuous curve of Al Harrat and harrats flanking Wadi Fayd. The volcanic rocks of Harrat Rahat were mapped as the Shawahit basalt and Hammah basalt and assigned to the Rahat group by Smith (1981, 1982). The reader is referred to the work of Smith (1981, 1982), Ramsay (1983), and Camp and Roobol (1987) for detailed descriptions of the volcanic rocks.

7.3 Structural Setting

The structural zones have three principal trends: (1) northeast (Fatima, Al Abar, Hubaytah, Liyah, As Sadr, and Al Bujaydi zones); (2) east-northeast (Nu'man and Makkah zones); and (3) north-northwest (Zahran, Aydiyah, Yaj, and Samd zones). Lineaments are defined as mappable linear surface features, which differ distinctly from the patterns of adjacent features and presumably reflect subsurface phenomena. Earth surface linear features have been study theme for geologists through many years. Figure 7.3 showing the different lineament in the study area contain (faults, mafic dike and felsic dike Fig. 7.3a).

The Nu'man and Makah structural zones may be of different ages; the Nu'man zone is younger than the intrusion of the post tectonic Nu'man complex, whereas the Makkah zone is older, at least in part, than the Ju'ranah complex of the Kamil suite. Thus, the Nu'man zone involves foliated rocks of the Nu'man complex and cuts across, and is therefore possibly younger than, the northeast-trending (Fig. 7.3a, c, e) Hubaytah and As Sadr zones. In contrast, the Makkah zone runs between plutons of the Ju'ranah complex and involves foliated unassigned amphibolite, and the Milh and Ju'ranah complexes. It is intruded by small, post-tectonic granite and granodiorite plutons. The amphibolites, and possibly the Milh complex, were foliated prior to the emplacement of the Ju'ranah complex. Thus, the Makkah zone is in part older than the Ju'ranah complex, but is also partly the result of shearing between, and at the margins of, the Ju'ranah complex. The Nu'man zone is at least 55 km long and is paralleled for much of its length by a thick dike of pegmatite to spherulitic rhyolite. At its western end the zone is cut off by the later north northwest-trending Aydiyah structural zone. The Makkah zone is defined by parallel foliation, faults, and granitic dikes in the Milh and Ju'ranah complexes. In the east, the zone merges into the Wadi Ya'ruj fault that bisects the arc of dikes dragged parallel to the Ad Damm fault (Smith 1980).

The Ad Damm fault is the dominant structural feature in the southeast of the quadrangle. It extends from the Red Sea
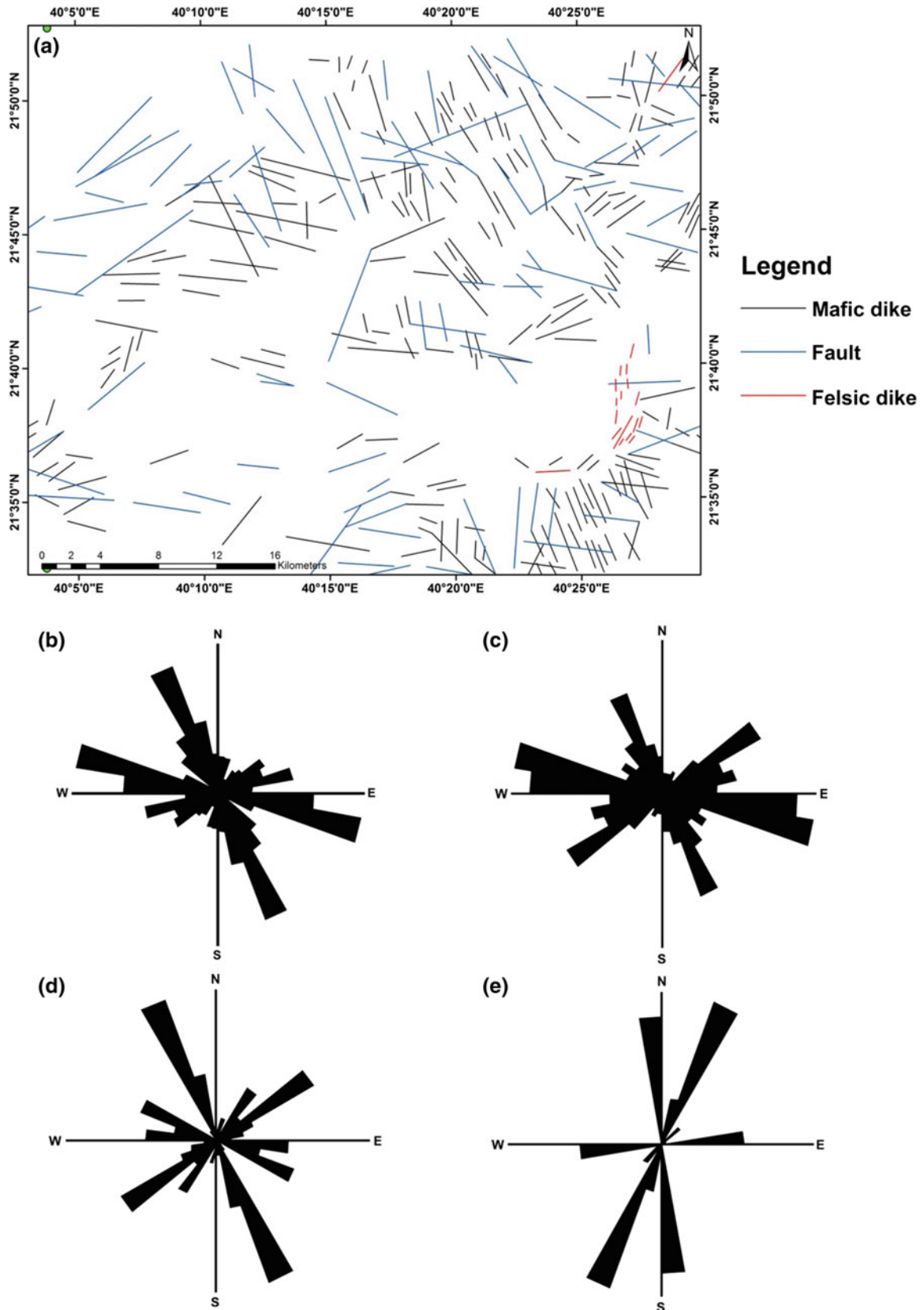
Fig. 7.3 a Lineament map of the study area (after Moore and Al-Rehaili 1989) and rose diagrams showing the trends of **b** mafic dike, **c** fault, **d** felsic dike **e** total lineament

coast, in the Al Lith quadrangle, into the adjacent Turabah quadrangle. The fault was named by Brown (cited in Falcon et al. 1970) and has been described by Smith (1980). Within then Makkah quadrangle, the fault strikes northeast to north northeast (Fig. 7.3e) and can be traced for about 85 km. It is divisible into two sections—a northern section that anastomoses and becomes less distinct south of Ad Duhayyah, and a southerly continuation that is about 10 km to the west and is mostly coincident with wadi Ad Damm. The fault has a steep dip (65–80°) to the east and consists of several phyllonitic shear zones in a belt as much as 1 km wide. It is thought to be a right-lateral fault but the amount of displacement has not been determined (Goldsmith 1971; Smith 1980). Evidence for right-lateral displacement in the Makkah quadrangle is based largely on drag, and arcuate fractures infilled by felsic and mafic dikes, on the western side of the fault. In the southerly adjacent Al Lithe quadrangle, the displacement is also right lateral. The relationship between the fault and the parallel structural zones to the west is not known.

7.4 Aeromagnetic Data Analysis

The aeromagnetic data have been digitized to 184×150 data points from the original data (sheet 135) (Fig. 7.4). The data have been subjected to reduced-to-pole (RTP) where $D = D_0 = 1.37°$, $I = I_0 = 30.55°$, assuming induced-only magnetization (Fig. 7.5). The aeromagnetic maps (Figs. 7.4

and 7.5) show various magnetic features characterized by relatively high, intermediate, and low magnetic values. A relatively high magnetic values is shown at the eastern and south western parts of the study area attributing to massive monzogranite to syenogranite and massive hornblende, interlayered gabbro, norite diorite and pyroxinite. The circular feature in the satellite image and geology maps (Figs. 7.1 and 7.2a) are attributed to the Bahitah granite (syenogranite), which we believe it associated with magnetite in composition (Figs. 7.4 and 7.5). Furthermore, the relatively high magnetic values all over the magnetic map are attributed to either exposed/buried mafic and ultramafic rocks. The relatively quiet magnetic features are attributed mostly to felsic rocks such as granite.

7.4.1 3D Euler Deconvolution with Unprescribed Structural Index

The equation of Euler homogeneity has been utilized for the development of Euler deconvolution method (Thompson 1982). In this particular method the anomaly is assumed as homogeneous function in the spatial coordinates. The method is mainly used to estimate the depths and the structural indices of the causative target Gerovska and Araúzo-Bravo (2003). The present technique has been used in the interpretation of aeromagnetic data (Abuelnaga and Al-Garni 2015; Al-Garni 2007, 2016; Al-Garni and Hassanein 2012; Saad et al. 2012). Following the method of

Fig. 7.4 A total intensity aeromagnetic map of Shamiyya area, north east of Makkah Quadrangle, Saudi Arabia
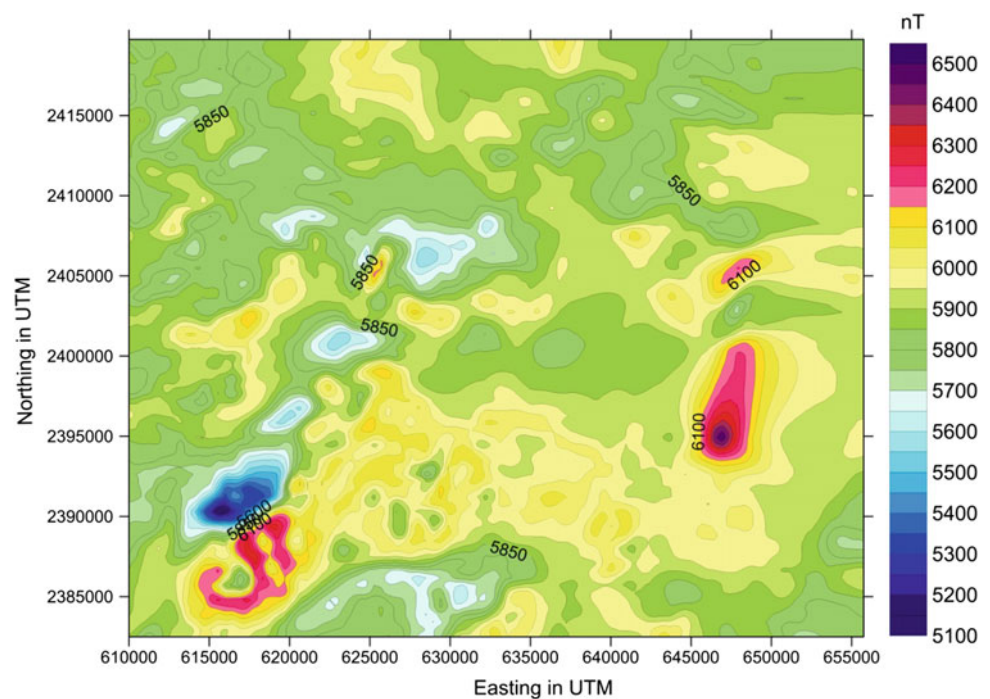
Gerovska and Araúzo-Bravo (2003), the total magnetic intensity map has been subjected to the application of this technique, using window 6 × 6. In order to avoid many interfering singular points in one window, the size of the window has been kept appropriate. The grid spacing that are chosen here is 0.25 km in both x and y directions. The parameters that are used to implement the deconvolution as follow:

Acceptance Level: It shows the maximum value which is allowed for the relative standard deviation that is weighted by the computed structural index. It is given the value 0.05 where it is an empirical criterion as recommended by Thompson (1982), corresponding to a threshold value, $\tau = 0.009$ for the second cluster stage in order to avoid highly dispersed solutions.

ρmic   It is the function of grid spacing, providing the maximum horizontal distance permitting two solutions to the same cluster when multiplied by the grid spacing. It is given a value of 1 as a scale unit

ρmac   It is used in the cluster fusion after multiplication by the maximum horizontal radius of confidence of all the clusters. It gives the maximum distance to permit two clusters to be fused where it is given a value of 1.

ρz   It is the scaling factor that is used to convert the depth to circles with radii proportional to the depths. It is given a value of 0.5 units.

The total magnetic field map has been subjected to the 3D Euler technique where the solutions have been extracted automatically using the method of Gerovska and Bravo (2003). The results have been demonstrated in 3D and 2D for the structural elements of the subsurface (Figs. 7.6, 7.7, 7.8, 7.9, 7.10 and 7.11).

The depth to the magnetic causative targets is shown in Fig. 7.6. The accepted structural indices are shown in Fig. 7.7. The second cluster stage can be shown in Figs. 7.8 and 7.9 where the data have been nicely clustered after rejection the dispersed solutions. Hence, the level of confidence of the clustered solutions is commonly accepted (Fig. 7.10). There are 46 groups of final cluster indices of the accepted solutions (Fig. 7.11). The computed depths from these final clustering solutions varied between 0.5 and 1.17 km with average depth of about 0.76 km, and structural indices range between 0.29 and 1.1 with average structural index of about 0.59, indicating a magnetic contact model, see Table 7.1.

7.5 Magnitude Magnetic Transforms

A total of three main groups of magnitude magnetic transforms (MMTs) has been constituted by Stavrev and Gerovska (2000). These transformed based on the field derivative order. The first group contains the T_a transform which is considered as the derivative of the magnetic potential of the same order as the measured magnetic field, corresponding to the same magnetic anomalies as the measured magnetic field. However, the T_a transform have a better centered anomalies over the magnetic sources. The second group contains R, E, and Q transform as defined by

Fig. 7.5 Reduced-to-pole map of total magnetic intensity map of Shamiyya area, north east of Makkah Quadrangle, Saudi Arabia
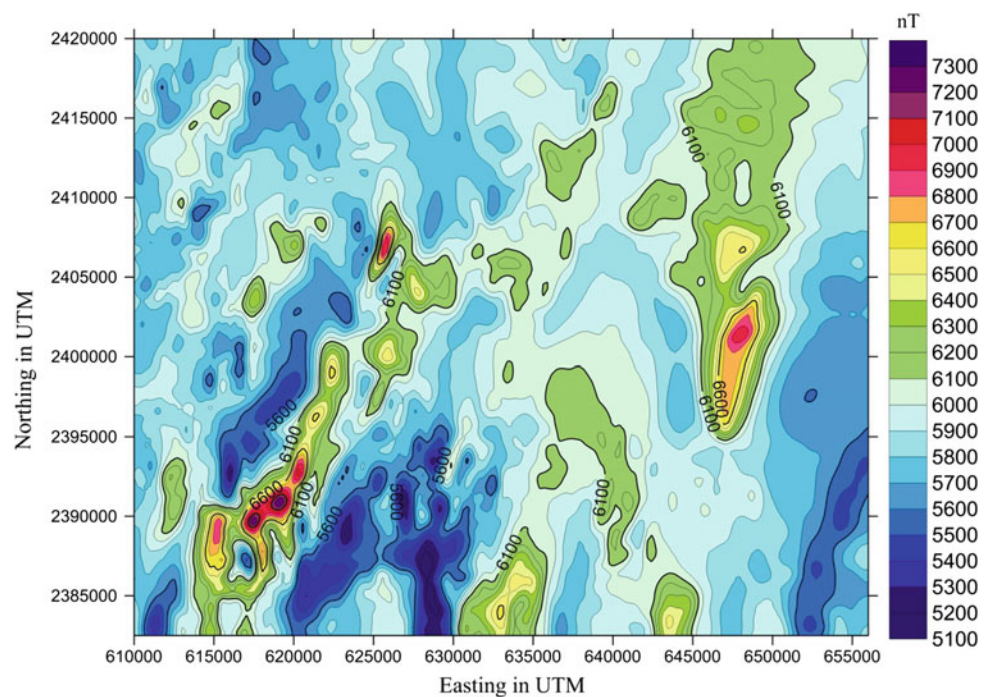
Fig. 7.6 A 3D graph of the estimated depths of sources singular points of Shamiyya area, north east of Makkah Quadrangle, Saudi Arabia, after second clustering stage
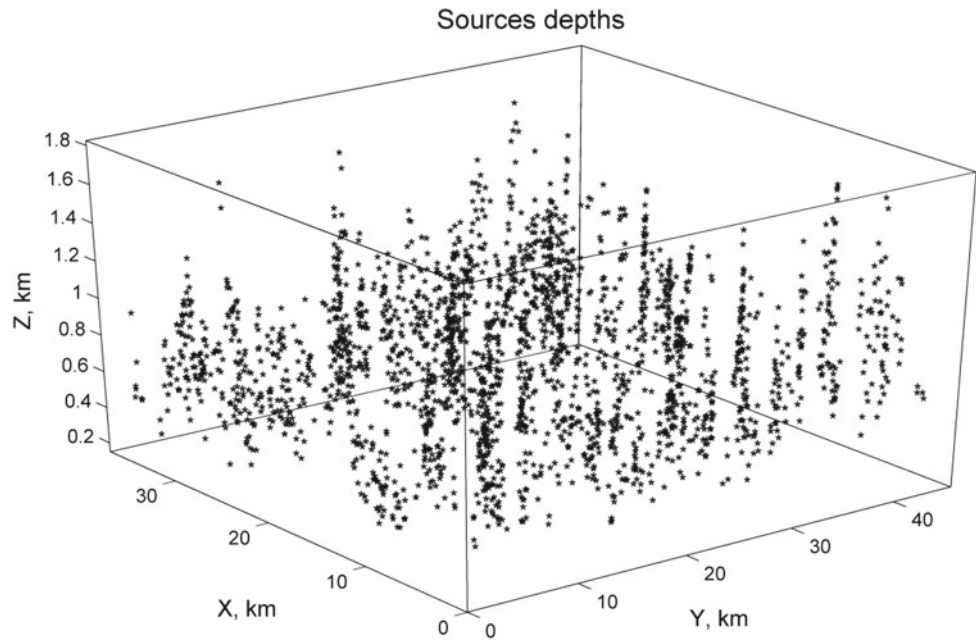
Fig. 7.7 A 3D graph of the estimated structural indices of sources singular points of Shamiyya area, north east of Makkah Quadrangle, Saudi Arabia, after second clustering stage
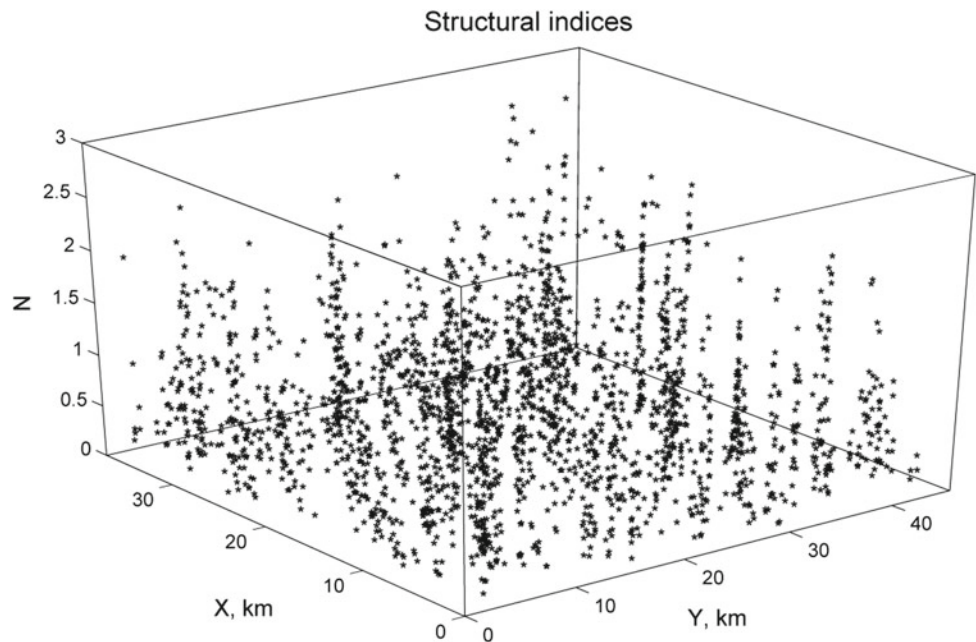
Stavrev and Gerovska (2000) where this group involves the first order derivative of the measured magnetic field. Thus, this group is particularly used to present relatively shallow magnetic sources. Al-Garni (2016) used this technique for the subsurface magnetic features of the southeast of Al-Muwayh quadrangle. The second group, the group contains R, E, and Q transform, is related to each other by the following expression (Stavrev and Gerovska 2000):

$$E^2 = (Q^2 + R^2)/2 \qquad (1)$$

In this study, the E transform is computed and used as a representative for the second group. The third group is the L transform which involves the second derivative of the measured magnetic field. Thus, it can be considered as the most sensitive transform among the others for the shallowest magnetic causative targets.

There are five expressions of the MMTs have been provided by Stavrev and Gerovska (2000) where the total magnetic anomaly ΔT,

Fig. 7.8 Solutions of deconvolution algorithm for the southeast of Shamiyya area, north east of Makkah Quadrangle, Saudi Arabia, after second clustering stage
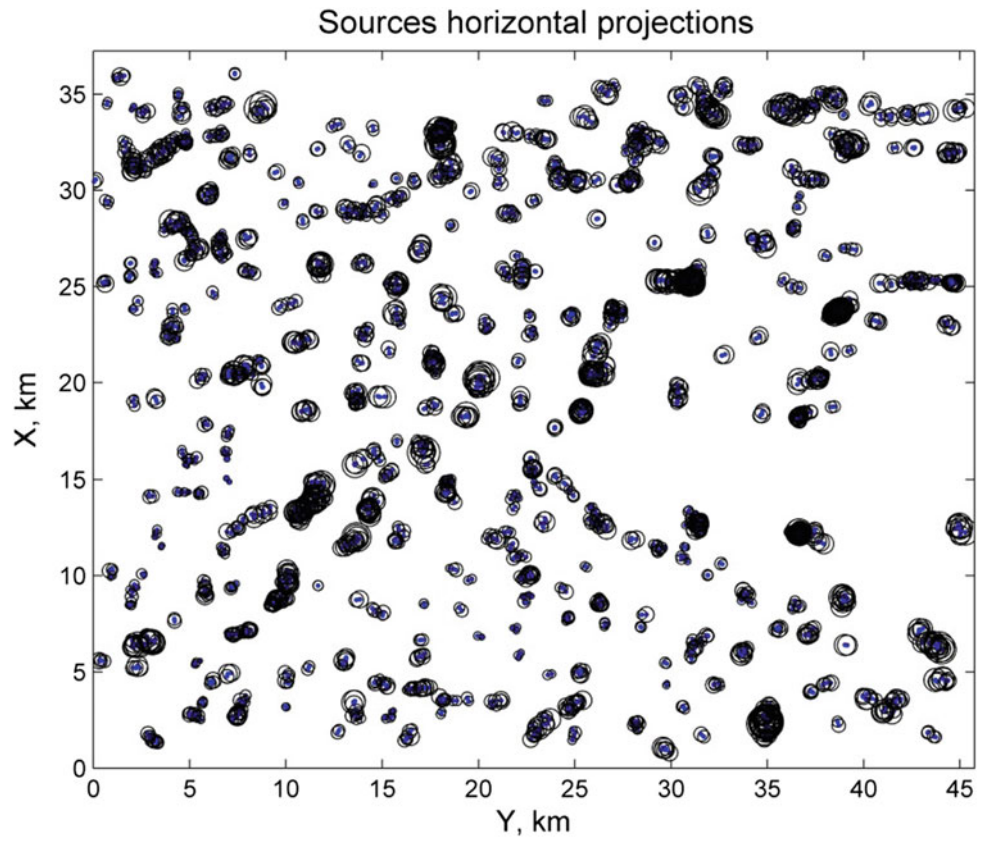
Fig. 7.9 Indices of clusters solutions for the southeast of Shamiyya area, north east of Makkah Quadrangle, Saudi Arabia, after second clustering stage
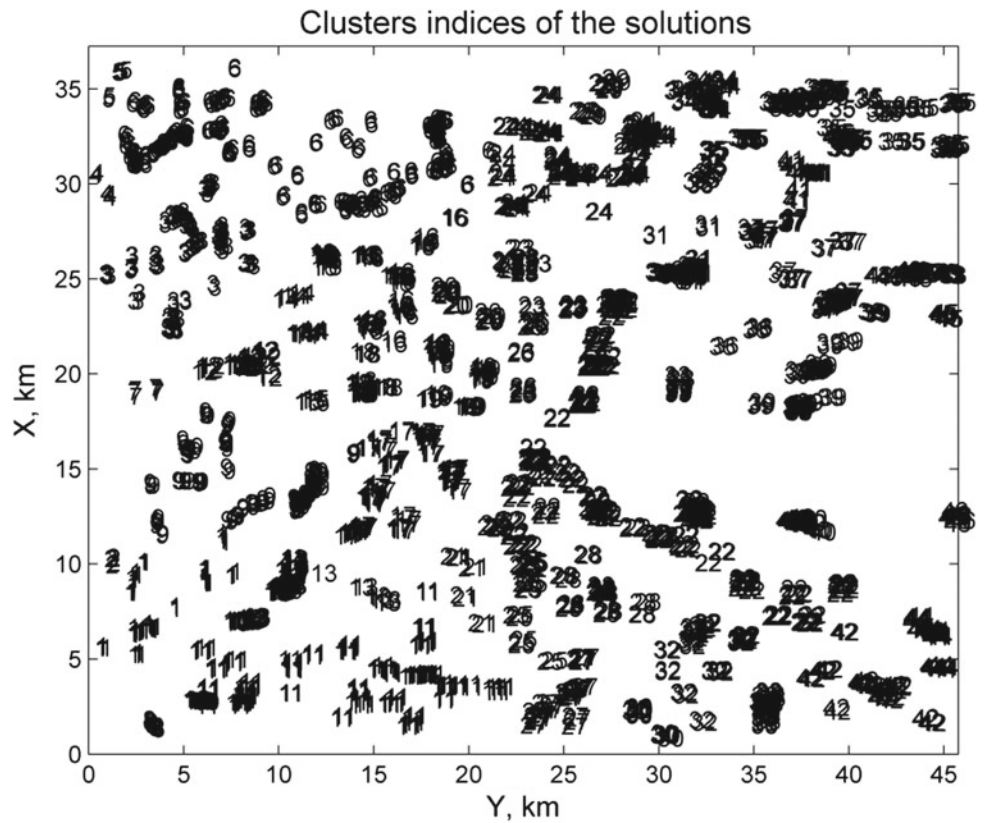
Fig. 7.10 Confidence intervals of horizontal positions of the center of gravity of clusters with their depths, obtained by deconvolution algorithm of Shamiyya area, north east of Makkah Quadrangle, Saudi Arabia, after second clustering stage, for $\tau = 0.009$ after second clustering stage, applied for $\rho_{mic} = 1$ and $\rho_{mac} = 1$. Depth scaling parameter is $\rho_z = 0.5$
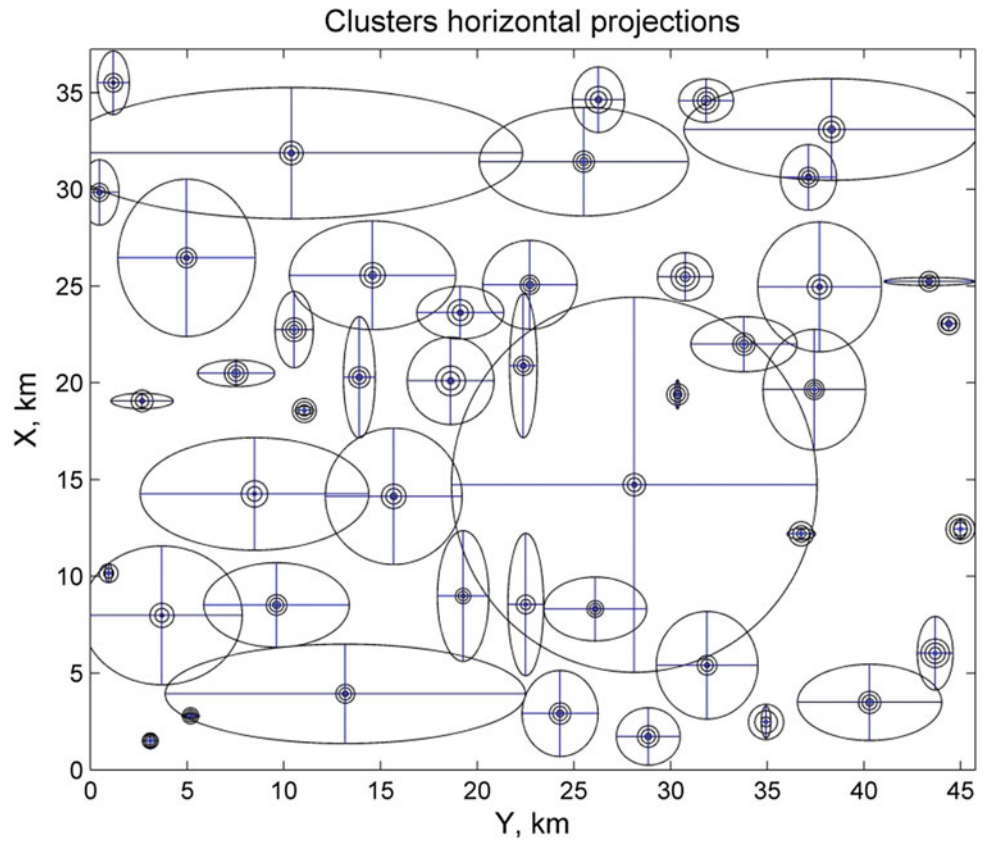
Fig. 7.11 Indices of final clusters of clusters with their depths, obtained by deconvolution algorithm of Shamiyya area, north east of Makkah Quadrangle, Saudi Arabia, after second clustering stage
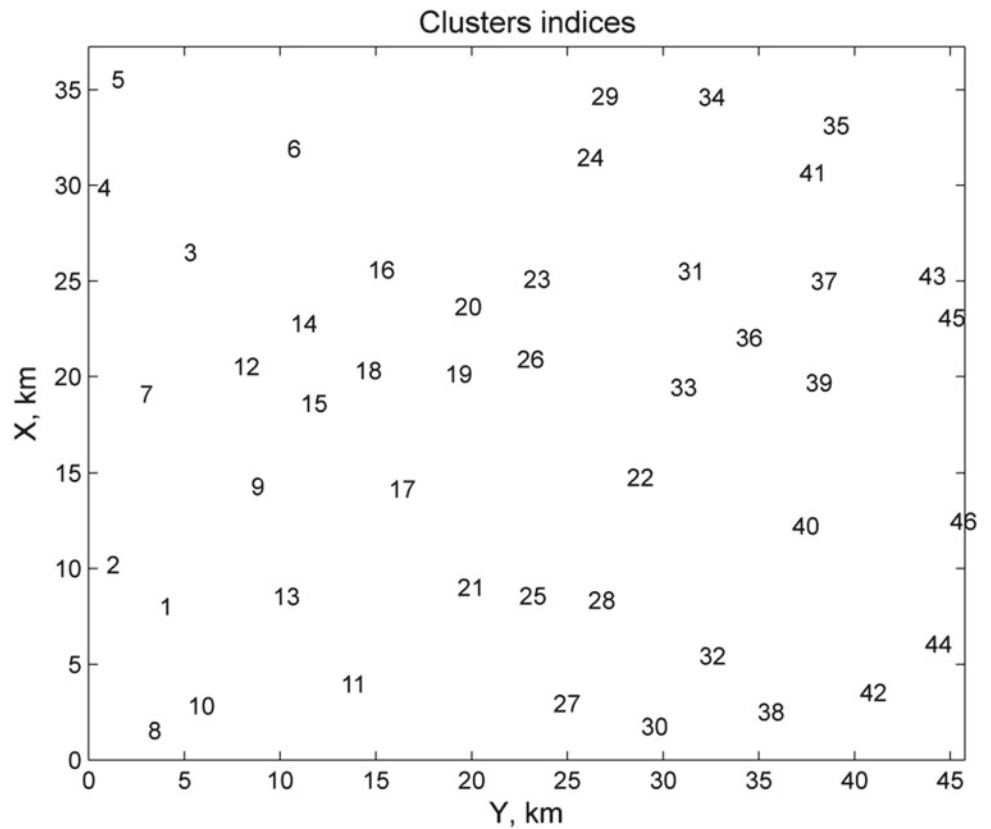
Table 7.1 Summarizes the numerical results of 3D Euler deconvolution method for the aeromagnetic data

C. I.	N. P.	Xave	Xcon	Yave	Ycon	Zave	Zcon	Nave	Vcon
1.00	64.00	7.99	3.59	3.69	4.15	0.71	0.54	0.71	1.21
2.00	5.00	10.17	0.49	0.93	0.19	0.51	0.46	0.50	1.02
3.00	122.00	26.47	4.07	4.96	3.55	0.65	0.38	0.64	1.03
4.00	5.00	29.85	1.69	0.46	1.01	0.61	0.33	0.43	0.56
5.00	7.00	35.51	1.64	1.17	0.83	0.56	0.40	0.60	1.54
6.00	239.00	31.88	3.40	10.38	11.96	0.75	0.46	0.69	1.03
7.00	6.00	19.07	0.40	2.66	1.61	0.68	0.44	0.31	0.63
8.00	10.00	1.50	0.37	3.08	0.42	0.63	0.19	0.29	0.41
9.00	117.00	14.26	2.91	8.47	5.91	0.75	0.61	0.51	0.74
10.00	8.00	2.80	0.11	5.17	0.46	0.62	0.21	0.73	0.64
11.00	126.00	3.93	2.57	13.17	9.32	0.63	0.34	0.53	0.84
12.00	35.00	20.50	0.69	7.52	1.99	0.81	0.39	0.73	1.14
13.00	79.00	8.52	2.19	9.61	3.77	0.72	0.34	0.47	0.80
14.00	16.00	22.76	1.97	10.53	0.99	0.85	0.37	0.36	0.39
15.00	7.00	18.58	0.21	11.05	0.48	0.92	0.32	0.32	0.37
16.00	58.00	25.57	2.81	14.58	4.30	0.84	0.46	0.94	1.32
17.00	99.00	14.14	3.53	15.67	3.54	0.81	0.46	0.90	1.20
18.00	33.00	20.29	3.14	13.89	0.82	0.71	0.38	0.54	0.95
19.00	46.00	20.11	2.26	18.62	2.24	0.93	0.60	0.90	1.26
20.00	16.00	23.63	1.36	19.12	2.25	0.82	0.53	0.73	0.81
21.00	9.00	8.99	3.38	19.26	1.33	0.50	0.30	0.46	0.70
22.00	259.00	14.74	9.70	28.11	9.45	0.71	0.45	0.67	0.98
23.00	32.00	25.07	2.30	22.71	2.44	0.68	0.31	0.41	0.73
24.00	114.00	31.44	2.81	25.50	5.41	0.76	0.33	0.57	0.79
25.00	26.00	8.55	3.68	22.50	0.93	0.53	0.45	0.48	0.80
26.00	12.00	20.89	3.72	22.38	0.72	0.65	0.34	0.31	0.41
27.00	39.00	2.92	2.23	24.28	1.97	0.74	0.37	0.53	0.86
28.00	33.00	8.32	1.65	26.10	2.66	0.58	0.28	0.53	0.81
29.00	13.00	34.64	1.69	26.27	1.35	0.85	0.52	0.59	0.84
30.00	14.00	1.73	1.48	28.84	1.65	0.73	0.39	0.30	0.60
31.00	68.00	25.49	1.25	30.74	1.44	0.98	0.49	0.91	1.33
32.00	39.00	5.41	2.78	31.88	2.63	0.64	0.38	0.54	1.13
33.00	11.00	19.41	0.74	30.35	0.14	0.78	0.33	0.44	0.66
34.00	39.00	34.59	1.12	31.83	1.41	0.91	0.43	0.59	0.81
35.00	141.00	33.10	2.63	38.32	7.64	0.86	0.49	0.74	1.30
36.00	5.00	22.00	1.43	33.79	2.74	0.80	0.34	0.48	0.96
37.00	86.00	24.97	3.36	37.70	3.20	0.77	0.50	0.63	1.17
38.00	40.00	2.48	0.82	34.93	0.25	1.17	0.66	0.97	1.34
39.00	58.00	19.65	3.12	37.42	2.66	0.75	0.27	0.49	0.84
40.00	54.00	12.20	0.29	36.75	0.73	0.86	0.40	0.53	0.91
41.00	22.00	30.62	1.70	37.12	1.45	0.69	0.35	0.48	0.68
42.00	43.00	3.49	1.97	40.28	3.73	0.77	0.37	0.49	0.85

(continued)

Table 7.1 (continued)

C. I.	N. P.	Xave	Xcon	Yave	Ycon	Zave	Zcon	Nave	Vcon
43.00	48.00	25.25	0.21	43.36	2.32	0.69	0.34	0.92	1.25
44.00	31.00	6.03	1.90	43.68	0.93	1.05	0.43	0.45	0.79
45.00	6.00	23.06	0.37	44.38	0.41	0.72	0.39	0.74	1.15
46.00	9.00	12.45	0.47	44.98	0.35	1.10	0.39	1.10	0.91

NumPoi: Number of points
Xcon: Confidence interval for variable X
Ycon: Confidence interval for variable Y
Zcon: Confidence interval for variable Z
Ncon: Confidence interval for estimated structural indices N
Xave: Average X value
Yave: Average Y value
Zave: Average Z value (depth)
Nave: Average estimated structural indices for each cluster

$$\Delta T = |T_a + T_0| - |T_0| = T_m - T_0, \tag{2}$$

where T_0 is the vector of the normal geomagnetic field and T_m is the magnitude of the measured magnetic field. The five expression of the MMTs have the following expressions:

$$T_a = \left(X_a^2 + Y_a^2 + Z_a^2\right)^{1/2}, \tag{3}$$

$$R = |\nabla T_a| = |X_a \nabla X_a + Y_a \nabla Y_a + Z_a \nabla Z_a|/T_a \tag{4}$$

$$E = (\nabla^2 T_a^2)^{1/2}/2 = \left(|\nabla X_a|^2 + |\nabla Y_a|^2 + |\nabla Z_a|^2/2\right)^{1/2} \tag{5}$$

$$L = \nabla^2 T_a = \left(|\nabla X_a|^2 + |\nabla Y_a|^2 + |\nabla Z_a|^2 - |\nabla T_a|^2\right)/T_a \tag{6}$$

and

$$Q = \left(T_a \nabla^2 T_a\right)^{1/2} = \left(|\nabla X_a|^2 + |\nabla Y_a|^2 + |\nabla Z_a|^2 - |\nabla T_a|^2\right)^{1/2}, \tag{7}$$

where 'a' stands for anomalous, X_a, Y_a and Z_a are the magnetic field components in the north, east, and vertically down direction, respectively. The reader can be referred to the work of Gerovska and Araúzo-Bravo (2006) for more detailed information. In case of 2-D, the three gradients R, E and Q are equivalent where the Laplacian $L = R^2/T_a$.

The computation of non-negative transform T_a does not depend on the direction of the vector magnetization (D, I) where in 2D and 3D cases this influence is weak unlike the RTP filter which requires the calculation of the direction of vector of magnetization (D, I) and the direction of geomagnetic field (D_0, I_0). The correlation between the results of the conventional RTP filer and the high centricity of the TMA, T_a, has been carried out by Gerovska et al. (2009) to investigate the presence of remnant magnetization.

In this study, the MMTs have been computed for the study area where the total magnetic field intensity map has been utilized in all computations. The aeromagnetic map of the study area has been digitized to 184×150 units (1 unit = 0.25 km) in both x and y directions, respectively. The computation of T_a transform map (Fig. 7.12) requires a knowledge about the normal geomagnetic field (D_0, I_0) (Stavrev and Gerovska 2000). Figures 7.12, 7.13, 7.14, 7.15, and 7.16 show the computation of the MMTs where they have a pattern similar to the shapes of the field causative targets anomalies which are centered over the magnetic causative targets. Stavrev and Gerovska (2000) studied the sensitivity integral coefficient where they found that the transformed T_a has 10 times less dependence on the direction of magnetization compared to the measured field ΔT. They also found that T_a transform has high centricity than the measured field ΔT, using the relative derivative of the extremum principle of the anomaly from the epicenter of causative target.

The correlation between the T_a and the RTP maps (Fig. 7.17) have been carried out where they shows almost the same pattern, revealing that the magnetic field causative targets have a direction of magnetization vector that is close to the present Earth's magnetic field. However, there are at least two zones A and B (Fig. 7.17) show that there are causative targets causing these anomalies, having remnant magnetization with different directions which could be opposite to the inducting field during the survey time. The positive values of the T_a transform (Fig. 7.12) make the comparison between the magnetic anomalies with the horizontal position of the causative targets easier. The E transform map (Fig. 7.13) shows high dense of magnetic anomalies in the same manner as in T_a transform. These magnetic anomalies are related to the shallower parts of the magnetic sources whereas the L transform map (Fig. 7.14) shows the shallowest parts of the magnetic sources.

The horizontal gradient of T_a (T_h) (Fig. 7.15) shows the horizontal derivative along line normal to the T_a transform

Fig. 7.12 T_a transform map of Shamiyya area, north east of Makkah Quadrangle, Saudi Arabia
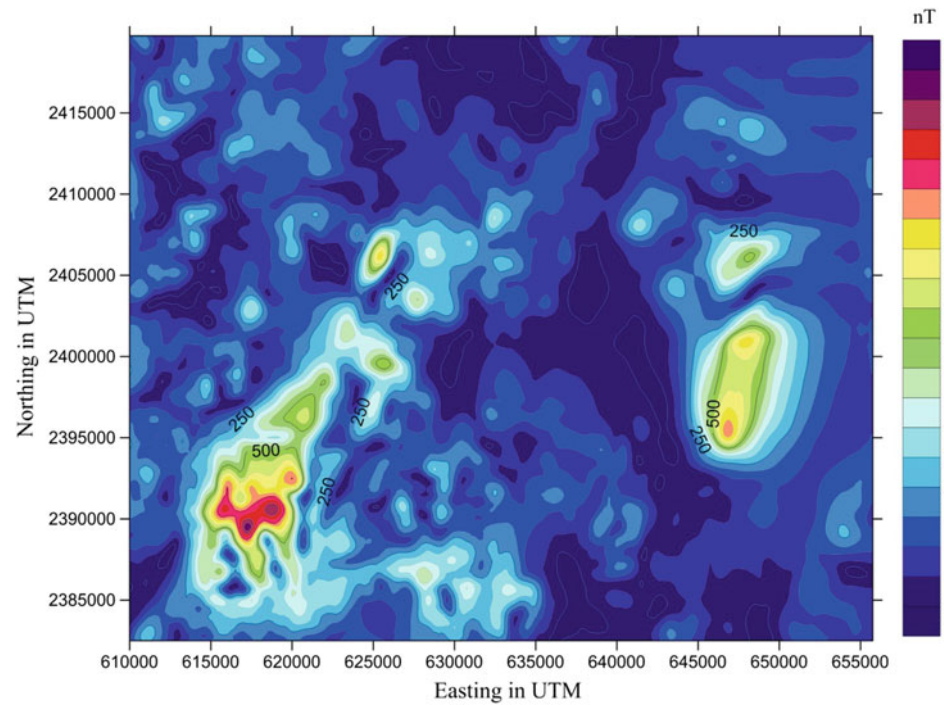
Fig. 7.13 E transform map of Shamiyya area, north east of Makkah Quadrangle, Saudi Arabia
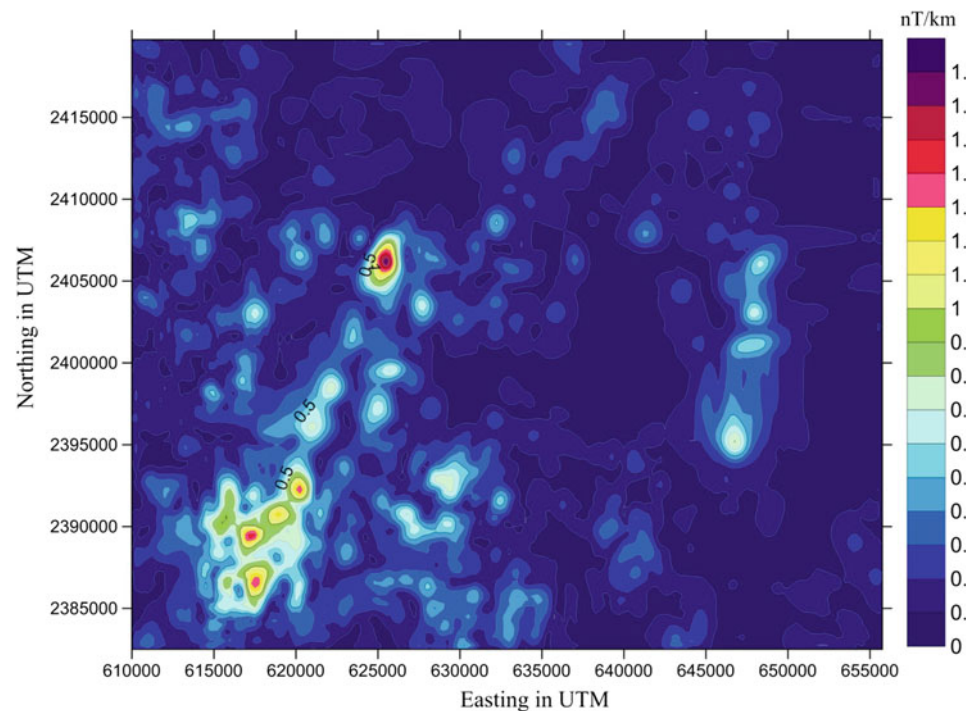
axis. The maxima of map anomaly represent the causative targets' edges where they have mainly NNW–SSE, NW–SE, NNE–SSW, N–S, E–W to ENE–WSW directions, corresponding to the inferred structures from the surface structural geology. The vertical derivative map of T_a (T_z) (Fig. 7.16) enhances and emphasizes the near surface features which shows similar features as in the E and L transforms together.

Fig. 7.14 L transform map of Shamiyya area, north east of Makkah Quadrangle, Saudi Arabia
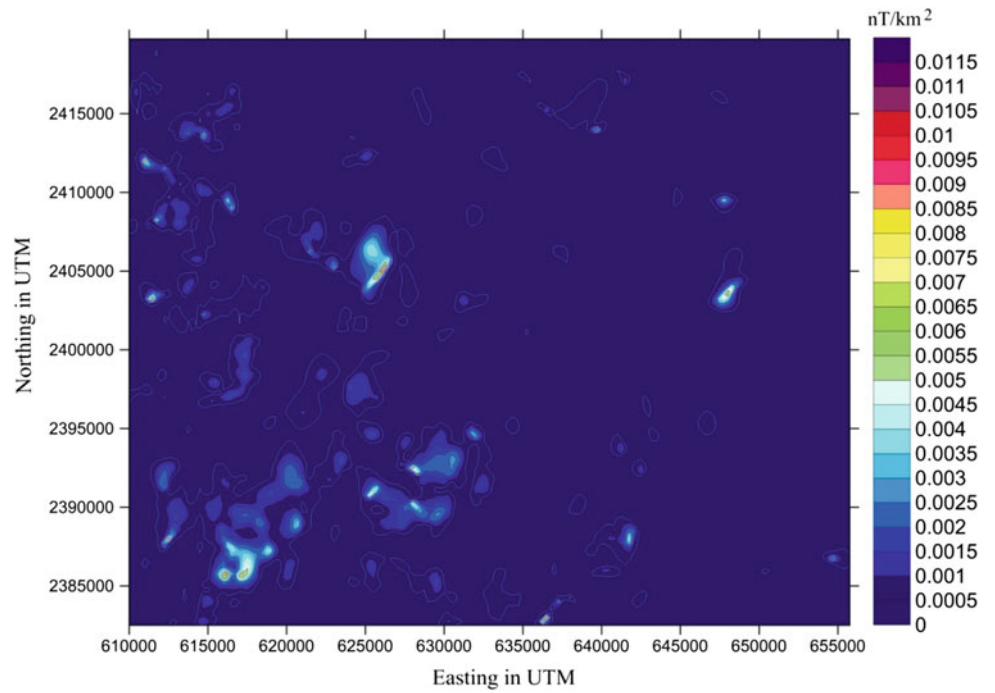
Fig. 7.15 Horizontal gradient of T_a transform map of Shamiyya area, north east of Makkah Quadrangle, Saudi Arabia
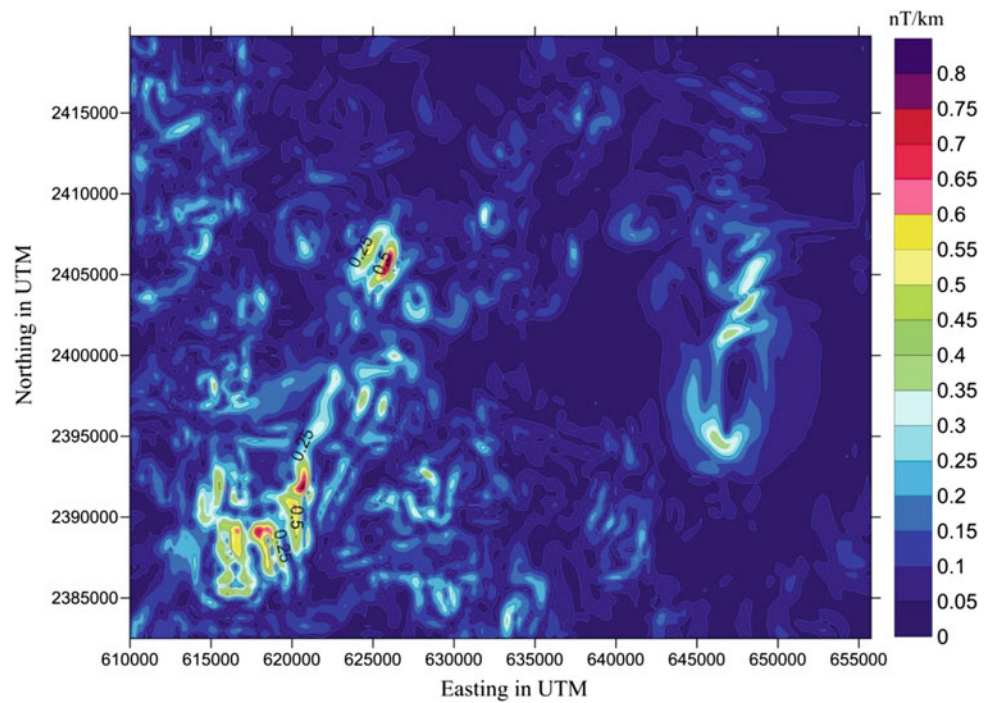
Fig. 7.16 Vertical gradient of T_a transform map of Shamiyya area, north east of Makkah Quadrangle, Saudi Arabia
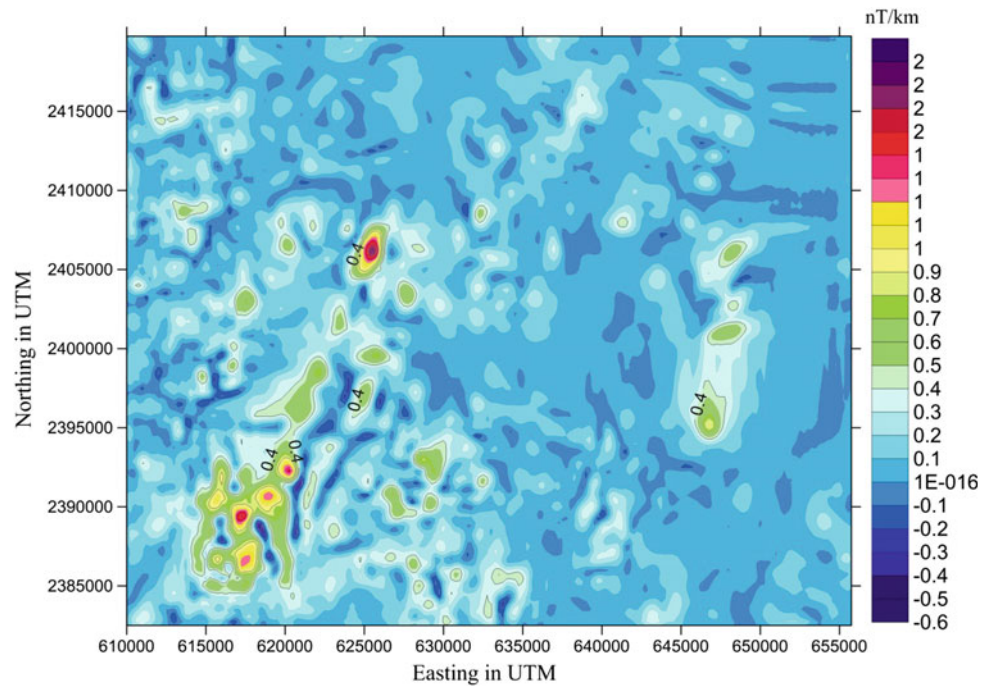
7.6 Edge Enhancement Using Normalized Standard Deviation

A local variability can be evaluated using windowed computation of the standard deviation of an image (Cooper and Cowan 2008). If the data are smooth, it is small; however, it is relatively large elsewhere. It works exactly as the same as the other filters of edge detectors such as horizontal gradient. In fact, the filter is basically based on the ratio of normalized standard deviations (NSTD) where large and small amplitudes edges can be observed all together and can be given as Cooper and Cowan (2008):

$$NSTD = \frac{\sigma \frac{\partial f}{\partial z}}{\sigma\left(\frac{\partial f}{\partial x}\right) + \sigma\left(\frac{\partial f}{\partial y}\right) + \sigma\left(\frac{\partial f}{\partial z}\right)} \quad (8)$$

where

f is the total magnetic intensity field
σ is the standard deviations.

The standard deviations (σ) can be computed using a moving square window of the data points. Further more, it can be computed for any given direction to enhance edges that normal to it. The filter is lesser sensitive to noise if a larger windows are used in the computation process whereas distort edges smaller than the window size. The algorithm has been widely used as an edge detector for the interpretation of aeromagnetic data (Abuelnaga and Al-Garni 2015; Al-Garni 2007, 2016; Al-Garni and Hassanein 2012; Saad

et al. 2012). The filter is used for different window sizes (W) 3, 5, 7, 9, 11 and 13 units (1 unit = 250 m) as edges enhancement where it provides better resolution of edges of deeper sources (Figs. 7.18, 7.19, 7.20, 7.21, 7.22, 7.23 and 7.24). It has been observed that there are larger number of edges using W = 3, 5, 7, 9, 11, 13, and 15 units. However, these fine detail edges can be suppressed using larger window (W = 9, 11, 13 and 15 units) where there will be the major basement features shown (Figs. 7.21, 7.22, 7.23, and 7.24). The analysis of the results of this filter shows that the edges are trending in NNW–SSE, N–S, and E–W to ENE–WSW directions as in the case of horizontal gradient techniques (Fig. 7.15).

7.7 Pseudogravity

It is known that the gravity anomalies are simpler than the magnetic anomalies, which is attributed mostly to the interaction between the earth's magnetic field and the geological features where the magnetic field is generally at an angle to the surface. The magnetic and gravitational fields are linked via a well-known equation which is Poisson's relation. The assumptions behind that are the boundaries of magnetic and gravity causative targets should be the same and the magnetization intensity and density are proportional through the study area. Thus, the gravity field, which is known as pseudogravity in this transformation, can be derived from magnetic field via the following Poisson's relation (Fig. 7.25):

Fig. 7.17 Comparison between T_a transform and RTP maps showing different zones
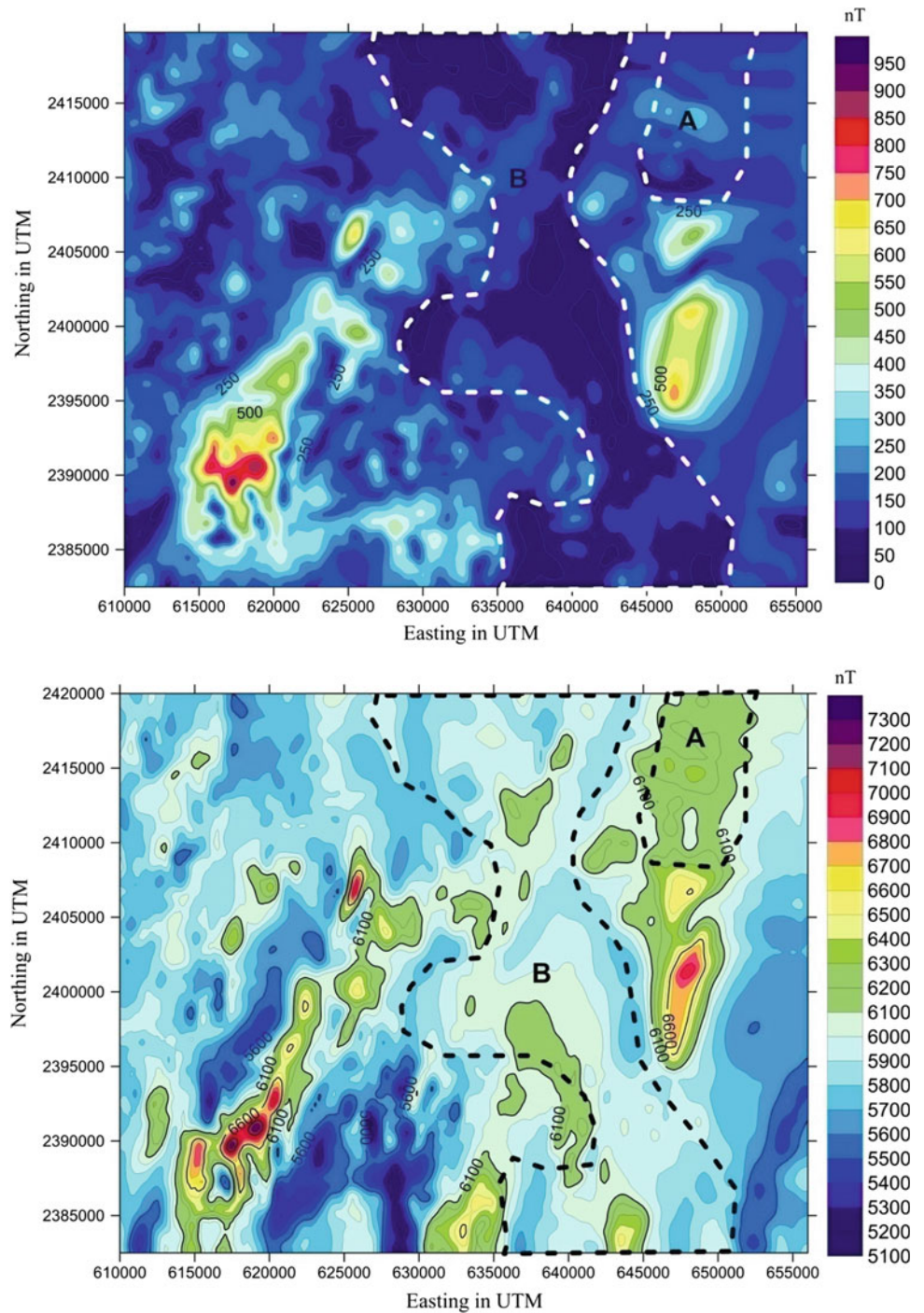
$$M_{(x,y,z)} = \frac{I}{G\rho} \frac{\partial G_{(x,y,z)}}{\partial \alpha}$$

where

$M_{(x,y,z)}$	is the magnetic field potential
$G_{(x,y,z)}$	is the gravitational field potential
I	is the uniform magnetization intensity in direction
α, and ρ	is the uniform density.

Baranov (1957) used the Poisson's relation where he introduced a linear filter that is usually mentioned to as the pseudogravity transformation where the output from the pseudogravity transformation is a unipolar field. This transformation has similar proprieties to a gravity anomaly which would be observed should the magnetization be complemented with an accurately proportional density distribution (Cheyney et al. 2011). The result of this transformation can simplify the interpretation of shape and location

Fig. 7.18 Calculated normalized standard deviation (NSTD) filter using window = 3 units (1 unit = 0.250 km)
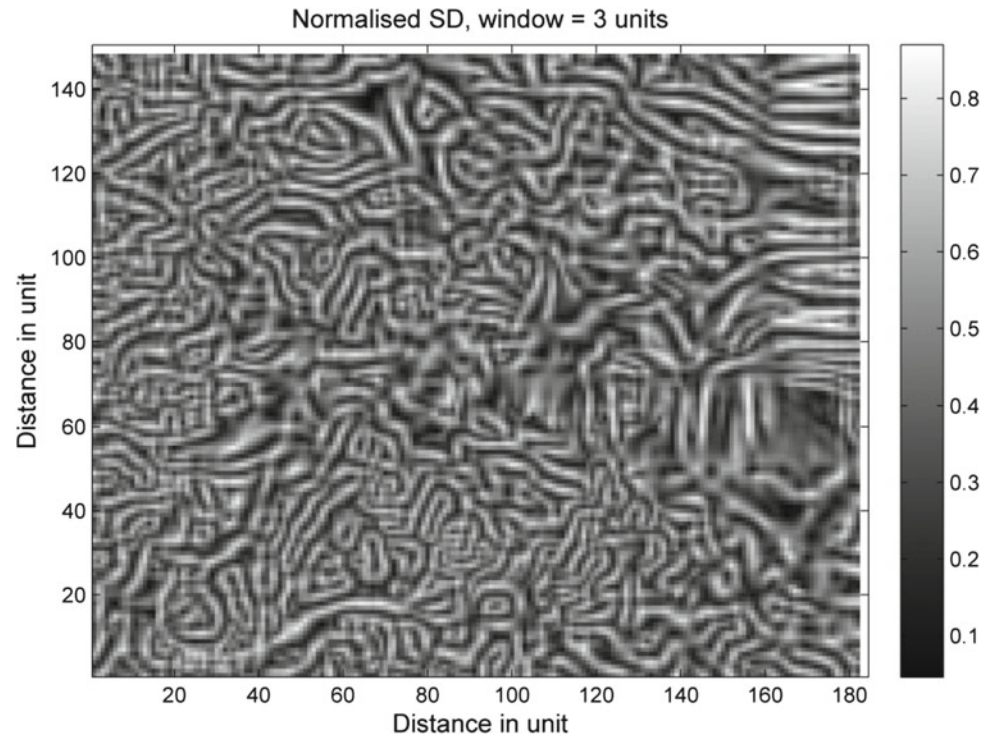
Fig. 7.19 Calculated normalized standard deviation (NSTD) filter using window = 5 units (1 unit = 0.250 km)
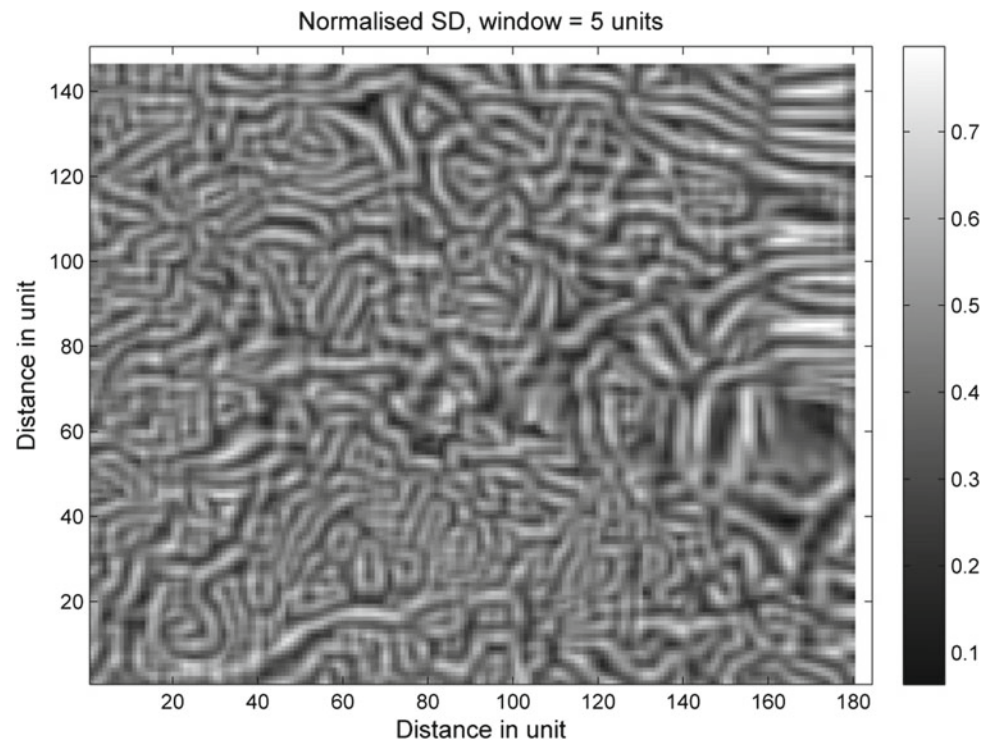
Normalised SD, window = 7 units
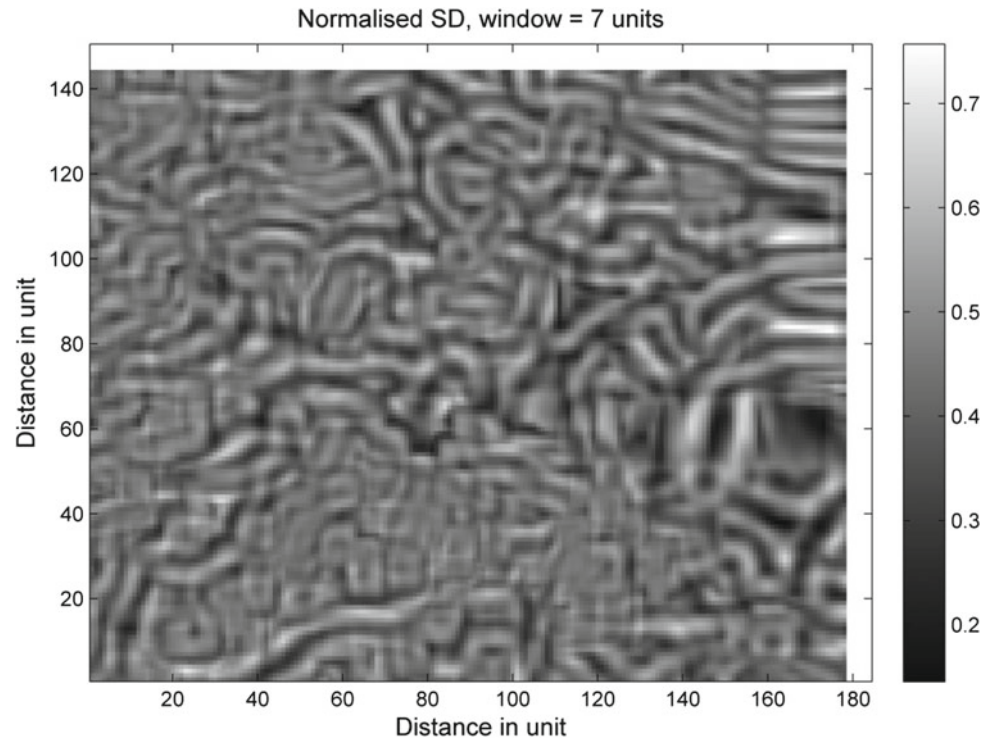
Normalised SD, window = 9 units
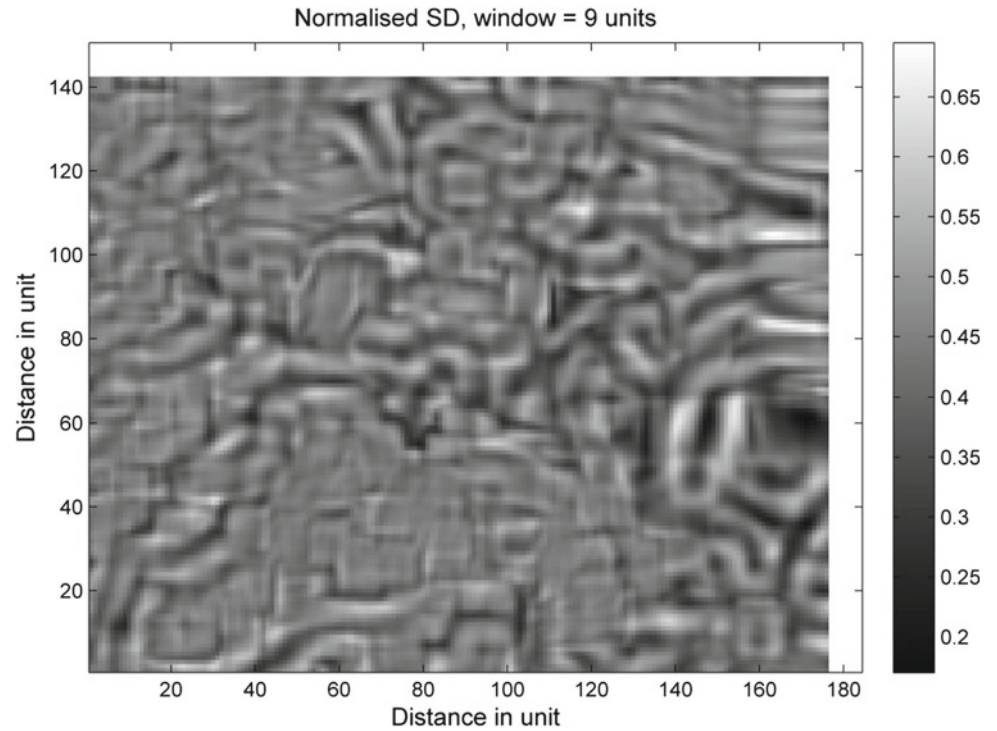
Fig. 7.22 Calculated normalized standard deviation (NSTD) filter using window = 11 units (1 unit = 0.250 km)
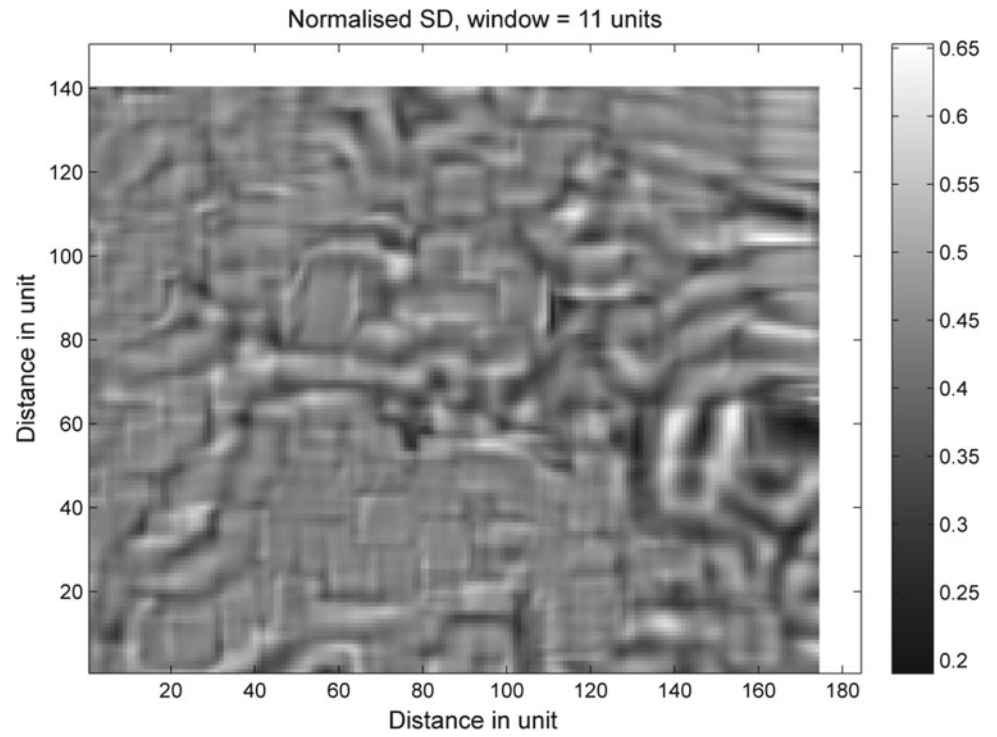
Fig. 7.23 Calculated normalized standard deviation (NSTD) filter using window = 13 units (1 unit = 0.250 km)
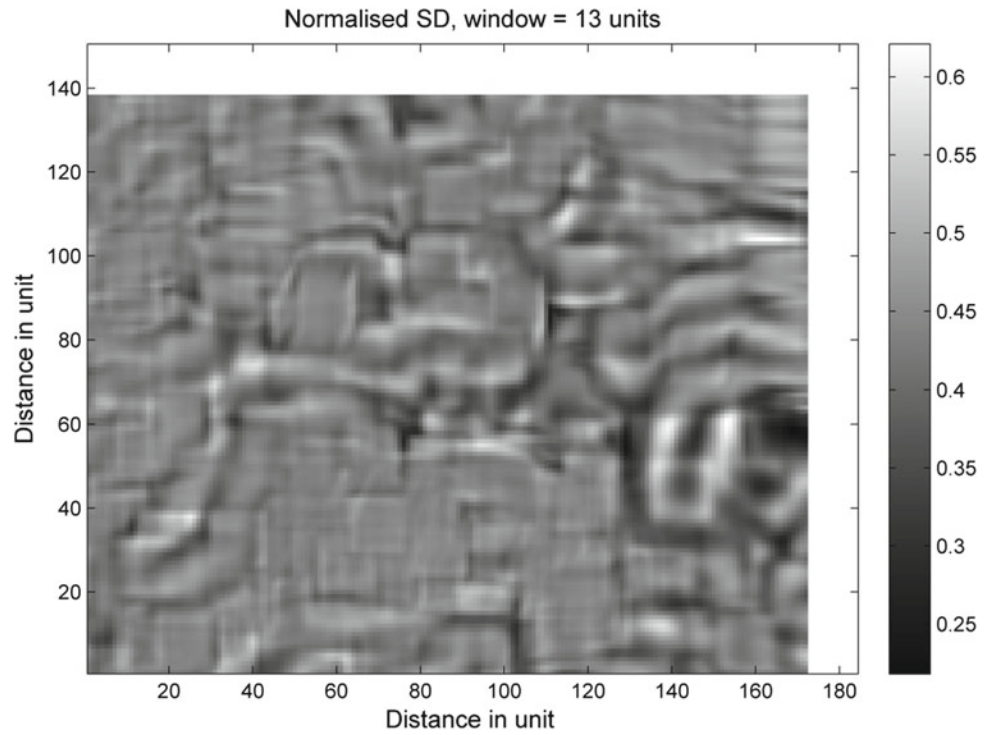
Fig. 7.24 Calculated normalized standard deviation (NSTD) filter using window = 15 units (1 unit = 0.250 km)
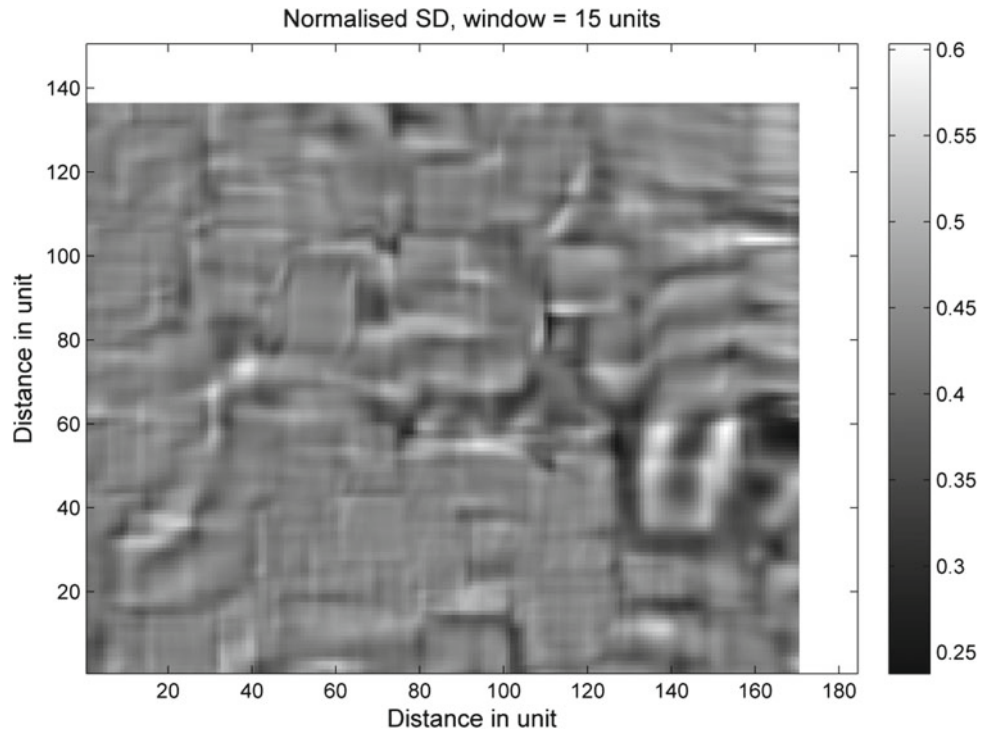
Fig. 7.25 Pseudogravity map of Shamiyya area, north east of Makkah Quadrangle, Saudi Arabia
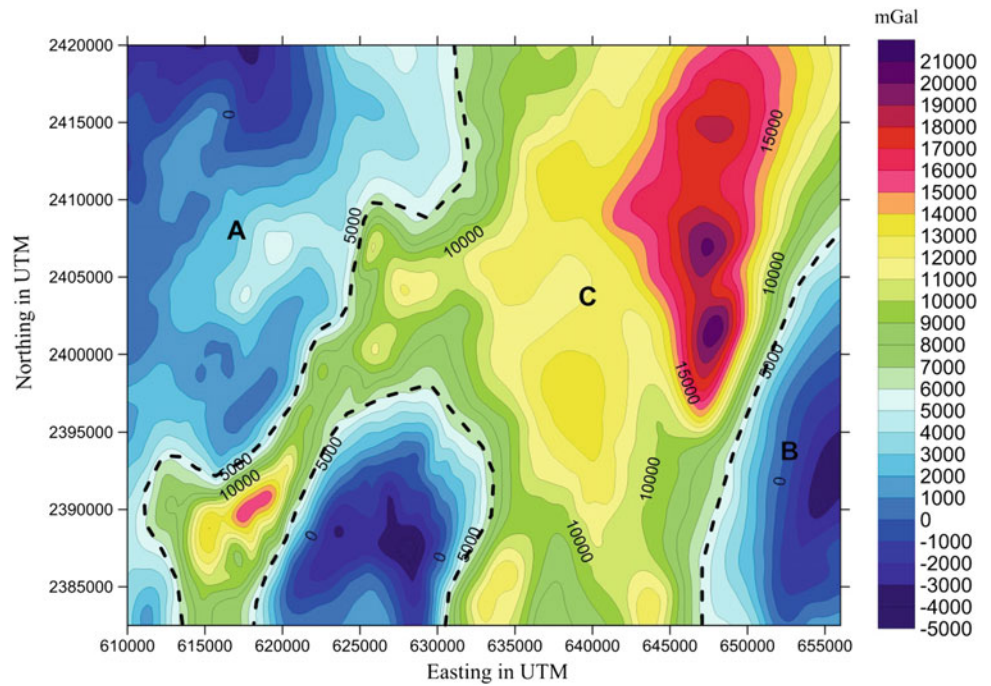
of causative targets. Computing the pseudogravity transformation of the total magnetic intensity field data has the effect of suppressing the high-wavenumber component of the data which causes that the pseudogravity transformation map (Fig. 7.25) appears much smoother than the total magnetic intensity map (Fig. 7.4).

In certain cases where gravity and magnetic data arise from the same sources, transforming magnetic field into their equivalent pseudogravity field can be a useful tool to investigate the relationship between the two fields where this process has the effect of centering sources at their causative bodies as well as enhancing broad features of the data. Figure 7.9 shows the pseudogravity map which has been derived from the total magnetic field intensity map (Fig. 7.4). It shows, in general, three major identified domains: the western domain may correspond to a broad low, separated by a high in the middle. The second pseudo–gravimetric domain corresponds to low where it is located at the southwest of the study area. The third pseudo–gravimetric domain is located at the middle of the study area and on the flanks of the broad two low domains. Within this pseudo–gravimetric configuration, the main lineaments are observed striking NNW–SSE and NNE–SSW.

7.8 Conclusions

The aeromagnetic data have been processed and analyzed using different techniques such as 3D Euler deconvolution, magnitude magnetic transforms, edge enhancement using standard deviation and pseudogravity. Each of which has been utilized to demonstrate and enhance the magnetic features of Al-Shamiyya area. 3D Euler deconvolution used as a depth estimator technique and structural indices estimator. It shows that the depths range between 1.37 and 5.29 km with average depth of about 3.6 km. The estimated structural indices from 3D Euler deconvolution varies between 0.08 and 0.27 with average of about 0.16, showing that the common structure types is a contact (fault) model. The magnetic magnitude transforms are used to implement the so-called T_a, E and L transforms. The T_a transform is used as the RTP technique where it less depend on the inclination and declination unlike the RTP technique. The E and L transforms show the shallow and the shallowed magnetic causative targets, respectively. In order to study the possible contacts within the study area, edge enhancement using standard deviation is applied to the aeromagnetic data where small windows are used to show the small fine details contacts and larger windows for the possible major contacts. Three domains are recognized within the study area using pseudogravity technique. Utilizing different techniques is very helpful in enhancing and demonstrating the aeromagnetic data where they provide us a nice view of the subsurface structures.

References

Abdelsalam MG, Stern RJ, Copeland P, Elfaki EM, Elhur B, Ibrahim FM (1998) The Neoproterozoic Keraf Suture in NE Sudan: sinistral transpression along the eastern margin of West Gondwana. J Geol 106:133–147

Abuelnaga HSO, Al-Garni MA (2015) Airborne gamma-ray spectrometric and magnetic studies of Wadi Um Geheig-Wadi Abu Eligam area, central east desert, Egypt. Arab J Geosci 8:8811–8833

Al-Garni MA (2007) Aeromagnetic data analysis of the southeastern quarter of Al-Muwayh quadrangle, Saudi Arabia. J Appl Geophys 6:487–512

Al-Garni MA (2016) Analysis of subsurface magnetic features of the southeast of Al-Muwayh quadrangle, Saudi Arabia. Arab J Geosci 9:155

Al-Garni MA, Hassanein HIE (2012) Aeromagnetic data analysis to enhance the demonstration of the subsurface mineralized zone occurrences, As-Safra prospect area, Saudi Arabia. Arab J Geosci 5:313–326

Baranov V (1957) A new method for interpretation of aeromagnetic maps: pseudo-gravimetric anomalies. Geophysics 22:359–383

Camp VE, Roobol MJ (1987) The geologic map of the Cenozoic lava field of Harrat Rahat. Saudi Arabian Deputy Ministry for Mineral Resources Open-File Report DGMR-OF-07-9, scale 1:250,000, with text, 91p

Cheyney S, Hill I, Linford N (2011) Advantages to using the pseudogravity transformation to aid edge detection of total field archaeomagnetic datasets. Archaeol Prospect 18:81–93

Cooper GRJ, Cowan DR (2008) Edge enhancement of potential-field data using normalized statistics. Geophysics 73:H1–H4

Falcon NL, Gass IG, Girdler RW, Laughton AS (1970) A discussion on the structure and evolution of the Red Sea and the nature of the Red Sea, Gulf of Aden and Ethiopia rift junction. Philos Trans Royal Soc London A 267:417p

Gerovska D, Araúzo-Bravo MJ (2006) Calculation of magnitude magnetic transforms with high centricity and low dependence on the magnetization vector direction. Geophysics 71:I21–I30

Gerovska D, Araúzo-Bravo MJ, Stavrev P (2009) Estimating the magnetization direction of sources from southeast Bulgaria through correlation between reduced-to-the-pole and total magnitude anomalies. Geophys Prospect 57:491–505

Gerovska D, Araúzo-Bravo MJ (2003) Automatic interpretation of magnetic data based on Euler deconvolution with unprescribed structural index. Comput Geosci 29:949–960

Goldsmith R (1971) Mineral resources of the southern Hijaz quadrangle, Kingdom of Saudi Arabia. Saudi Arabian Directorate General of Mineral Resources Bulletin 5:62p

Hadley DG, Greenwood WR (1982) Graded layering in the Al Hadapluton near At Ta'if, Kingdom of Saudi Arabia. Saudi Arabian Deputy Ministry for Mineral Resources Professional Papers PP-l, pp 3–38

Hamimi Z (2006) Atlas of geologic structures in the Arabian-Nubian shield. Hebet El nil Al Arabiya, Cairo, 97p

Johnson PR, Woldehaimanot B (2003) Development of the Arabian-Nubian shield: perspectives on accretion and deformation in the northern East Africa Orogen and the assembly of Gondwana, Geol Soc London (Special Publication) 2006:289–325

Marzouki FMH (1977) Petrogenesis of Al Hada plutonic rocks, Kingdom of Saudi Arabia. Unpublished Ph.D. thesis, University of Western Ontario, Canada

Moore TA, Al-Rehaili MH (1989) Geological map of the Makkah quadrangle, Sheet 21D, Kingdom of Saudi Arabia. Map GM107. Saudi Arabian Directorate General of Mineral Resources

Pallister, (1986): Geologic map of the Al Lith quadrangle, sheet 20D, Kingdom of Saudi Arabia. Saudi Arabian Deputy Ministry for Mineral Resources Geoscience Map GM-95, 1:250,000 scale

Ramsay CR (1983) Geology of the Rabigh quadrangle, sheet 22D, Kingdom of Saudi Arabia. Saudi Arabian Deputy Ministry for Mineral Resources Open-File Report DGMR-OF-03-l5, 90p

Saad MH, Al-Garni MA, Hassanein HIE (2012) Interpretation of aeromagnetic and gravity data in East Qattara Depression North Western Desert, Egypt. Arab J Geosci 5:747–756

Schmidt DL, Hadley DG, Greenwood WR, Gonzalez L, Coleman RG, Brown GF (1973) Stratigraphy and tectonism of the southern part of the Precambrian shield of Saudi Arabia. Saudi Arabian Directorate General of Mineral Resources Bulletin 8:13p

Shackleton RM (1996) The final collision zone between East and West Gondwana: where is it? J Afr Earth Sci 23:271–287

Skiba WJ, Gilboy CF (1975) Geology of the Rabigh-Khulay squad range, 22/39, Kingdom of Saudi Arabia. Saudi Arabian Directorate General of Mineral Resources unpublished manuscript, 2 volumes, 597p

Smith JW (1980) Reconnaissance geology of the At Ta'if quadrangle, sheet 21140C, Kingdom of Saudi Arabia. Saudi Arabian Directorate General of Mineral Resources Geologic Map GM-56, 1:100,000 scale, with text, 33p

Smith JW (1981) Reconnaissance geologic map of the Wadi Mahani quadrangle, sheet 22/40A, Kingdom of Saudi Arabia. Saudi Arabian Deputy Ministry for Mineral Resources Geologic Map GM-35, 1:100,000 scale, with text, 18p

Smith JW (1982) Reconnaissance geologic map of the Wadi Hammah quadrangle, sheet 22/40C, Kingdom of Saudi Arabia. Saudi Arabian Deputy Ministry for Mineral Resources Geologic Map GM-65, 1:100,000 scale, with text, 19p

Stavrev P, Gerovska D (2000) Magnetic field transforms with low sensitivity to the direction of source magnetization and high centricity: geo-physical prospecting 48:317–340

Tayeb GMS (1983) Reconnaissance geologic map of the Makkah quadrangle, sheet 21/39D, Kingdom of Saudi Arabia. Saudi Arabian Deputy Ministry for Mineral Resources Open-File Report DGMR-OF-03-3, 1:100,000 scale, no text

Thompson DT (1982) EULDPH: a new technique for making computer assisted depth estimates from magnetic data. Geophysics 47(1):31–37

Groundwater Contamination of Wadi Haliy Area, Southwestern Arabian Shield, Saudi Arabia

8

Saleh A. Bajabaa

Abstract

Contamination of surface water, groundwater, sediment, and atmosphere by heavy metals and radionuclide is among the most significant issues facing the Kingdom. Wadi Haliy is considered as important source of water to the Red Sea coastal plain. Copper, zinc and other base-metals mineralization occur in the Precambrian Arabian shield rocks that dominate the water catchments area of this wadi. The water samples were analyzed for major, trace elements and heavy metals using collaborative techniques. The groundwaters in Wadi Haliy are of Cl–SO–Na–Ca type. The variation in water type indicates variation in natural processes such as evaporation, differences in rock units and mineralization, water rock interactions and water residence time. The data analyses showed some samples are of high heavy metals and uranium contents. Pollution by heavy metals and uranium arises mainly from neighboring rocks and also from emissions from mining activities. Generally, the uranium and heavy metal contents are higher in samples collected from the upstream area of the wadi where the crystalline rocks are exposed and in direct contact with the runoff. The Elevated heavy metal and uranium contents suggests that these mining areas are considered as potential sources for these natural pollutants and likely affecting the water quality in these wadis. The attenuation of heavy metals and uranium is reported in this study along the flow path, from the mining area to downstream. The processes governing the evolution of the leachates plume and its heavy metals budget are modeled in two steps: (1) Neutralization of acidic mine drainage water; (2) Heavy metal attenuation by adsorption, evaporation and co-precipitation with Fe oxides.

8.1 Introduction

Groundwater quality mainly depends on the geological formation of underlying rocks. i.e. the aquifer's size and the sampling position (Hussain et al. 2010). This is controlled by the variation in local and regional geology, water/rock interactions, and dilution due to precipitation (Zaidi et al. 2015). The groundwater quality in most regions of Saudi Arabia does not show serious problems, but there are some of problems in the water quality. This appear in the work published about Hail area by Al-Turki (2010) where the microbial and chemical contamination of groundwater is caused by many different sources that include intensive usage of fertilizers, pesticides and animal waste. Generally, the quality of groundwater in Saudi Arabia is scarcely tested before wells are put into production.

The problem of contamination of groundwater by heavy metals has received much attention in recent years. In particular, lead which is a heavy metal of serious environmental concern. One of the physiological effects of lead is its detrimental to the neurological development of children. Major sources for heavy metals in groundwater are the areas where there has been significant mining activity. Drainage flowing from mine tailings can enter surface water, irrigate soils and groundwater, and causing harm to human beings and animals.

An understanding of the movement of heavy metals in soils, and its interaction with the soil minerals is important. Heidmann (2004) investigated the influence of a natural organic substance on Cu and Pb binding to a clay mineral in a model system, and determined the effects of Pb, Cu, and Ca on particle aggregation in these clay-organic substance suspensions. The types of reactions that are likely to control

S. A. Bajabaa (✉)
Faculty of Earth Sciences, Hydrogeology Department, King Abdulaziz University, P.O. Box 80206 Jeddah, 21589, Saudi Arabia
e-mail: Saleh_Bajabaa@Yahoo.com

the distribution of heavy metals in soils are mineral precipitation and dissolution, ion exchange, adsorption and desorption, aqueous complication, biological immobilization and mobilization, and plant uptake (Pierzynski et al. 1994; Levy et al. 1992). Generally, levels of more than 4 ppb uranium are considered to be anomalous. However, in arid continental conditions contents of several hundred ppb U have been recorded (Thornton 1983). The reason for selecting Wadi Haliy is the occurrence of copper, zinc and other base-metals at eastern parts of these quadrangles close to the water divide (Al-Hageri 1977; Prinz 1983).

8.1.1 Objective and Scope of the Present Study

The overall goal of this research is to provide a new information concerning the distribution and concentrations of different kinds of heavy metals and radio-elements in the groundwater of the study area, their fate and source rocks.

8.1.2 Materials and Methods

Thirty one groundwater samples were collected from surface and groundwater wells of Wadi Haliy area. The majority of these samples were collected in spring and early summer while the rest were collected in fall after rainy season and floods.

The collected water samples were analyzed for their heavy and trace elements contents (72 elements) at the Acme Analytical Laboratories (Acmi Labs). High precision Inductively Coupled Plasma-Atomic Emission Spectroscopy (ICP-AES) was used in these analyses. Sulfates were determined spectrophotometrically using Spectronic 20D. The standard used was sodium sulfate, Merick and the measurements were done at wave length 420 nm. Sodium and Potassium were determined using Flame photometer (Jenway). The used standards are Nentech NaCl and Merick KCl. Chlorine, carbonate, bicarbonate, calcium and magnesium were determined using titration method. Chlorine was measured against silver nitrate using potassium dichromate as indicator; carbonate and bicarbonate were measured against sulfuric acid using methyl orange and ph.ph. as indicators. Calcium and magnesium were measured against EDTA using eriochrome black-T and murexide as indicators.

Trace and heavy metals were determined using the Ultra-sonic Nebulizer equipped ICP-ES. This technique involves pouring 10 ml aliquots into acid-treated test tubes and a duplicate aliquot is taken from one sample for monitoring precision. Control standards STD-W and STD-WO2 were used to monitor accuracy. Immediately prior to analysis, calibration standards are used in the beginning and at the end of the analysis. Water blanks are randomly inserted into the sample sequence. Samples are aspirated using an Ultrasonic Nebulizer into a Jarrel Ash AtomComp 950 Inductively Coupled Plasma optical Emission. Spectrograph (ICP-ES). The data were corrected for instrument and element interference using a computer soft ware connected with the ICP-ES.

8.1.3 Climate Conditions and Air Masses

The climatic conditions at the catchment areas are influenced by the topography of the region and its proximity to the Red Sea on the western side and its nearness to the Empty Quarter Desert on the east side. The meteorological data that include information on temperature, solar radiation, sunshine, air humidity, wind speed and evaporation were reported in the data manual known as the Climatic Water Balance in Saudi Arabia (Al-Jarash 1989). Taha et al. (1981) indicated that the south-west of Arabia can be divided into three main climatic types: 1—The warm, rainy climatic type with a dry winter which prevails in the Asir Mountains. 2—The hot steppe climatic type which prevails on the plateau. 3—The hot desert climatic type which prevails in the Red Sea coast area.

8.1.4 Geologic Setting

The southwestern part of the Kingdom of Saudi Arabia consists of a wide coastal plain stretching eastward to the summits of Asir escarpment. The escarpment consists mainly of highly deformed and metamorphosed Neoproterozoic (850–550 Ma) volcanic and sedimentary rocks with vast amounts of granitic, dioritic and other igneous rocks of the Arabian Shield developed in an oceanic island arc environment. Wadi Haliy quadrangle were mapped at a scale of 1:100,000 and explanatory notes to the geological map of Wadi Haliy quadrangle at 1:250,000 were prepared by Prinz (1983). Prospecting and stream sediment sampling in the western part of the study area were carried out by Dames and Moore (1978).

The Arabian Shield is thought to have formed by accretion of intra-oceanic island arcs, back-arc basin complexes, and allochthonous continental blocks or microplates mainly during Pan-African time (about 680–640 Ma) (Camp 1984; Stoeser and Camp 1985; Johnson 2000; Stoeser et al. 2001). This complex tectonic history formed the Neoproterozoic (about 900–570) Arabian Shield crystalline basement, composed of: (1) deformed and metamorphosed volcano—sedimentary assemblages of oceanic plateau, mid-oceanic-ridge, intraoceanic and continental-margin tholeiitic and calc-alkaline volcanic arcs, epicontinental volcano-sedimentary rocks, and back-arc, pull-apart and graben assemblages; (2) vast amount of orogenic plutonic rocks such as gabbro, diorite, quartz diorite, tonalite, trondhjemite and

granodiorite; and (3) synorogenic, post-orogenic and anorogenic granites such as tonalite, trondhjemite, granodiorite, gabbro, granite and syenite (Johnson 2000; Stoeser 1986). The latest tectonic model divides the Arabian Shield into eight distinct geological terrains separated mostly by ophiolite-decorated suture zones. The four ensimatic terrains: Asir composite, Jeddah, Hijaz, and Midyan, occur in the west, whereas the four continental affinity terrains: Afif composite, Ad Dawadimi, Ar Rayn and Hail, crop out in the east.

Wadi Haliy area is bounded between latitudes 18° 30′–19° 00′N and longitudes 41° 15′–42° 00′E (Figs. 8.1 and 8.2a). It comprises mainly metamorphosed volcanic, sedimentary and plutonic rocks of late Proterozoic in age. Four principle units were identified in this area, namely: Baish, Bahah, Jeddah and Ablah groups. The first three groups represent an island-arc complex, whereas the latter (Ablah group) originated early in the formation of Andean-type arc system (Prinz 1983). The Baish group consists predominantly of mafic metavolcanics rocks, whereas, Bahah group consists of schists and Jeddah group consists mainly of amphibolites.

According to the geologic map (Fig. 8.3, Johnson 2006) the following rock units are described in the study area and described from the older to the younger as follows:

1. *Bidah-belt volcanic and sedimentary rocks (bb)* which is named after the Bidah structural belt, consists of metamorphosed volcanic, volcaniclastic, and sedimentary rocks in the western part of the Asir terrane, located on either side of Wadi Bidah and extending south as far as Ad Darb.

2. *Shwas belt volcanic and sedimentary rocks (sh)* which forms a narrow structural domain along the west side of the An Nimas batholith in the Asir terrane. It contains an assemblage of greenschist-facies moderately deformed volcanic and sedimentary rocks. The rocks include flows and pyroclastic rocks of andesitic, dacitic, and basaltic compositions, green and red, feldspathic to lithic graywacke, tuff, flat-pebble-to-boulder conglomerate, and thin gray marble. They are metallogenically significant as the host rocks for VMS base metal and gold deposits, one of which (Al Hajar) is currently exploited.

3. *Hali group (ho)* which forms a narrow belt of metasedimentary and subordinate metavolcanic rocks in the southern part of the Ablah belt in the western part of the Asir terrane. It consists of sequence of high-grade quartz-biotite-garnet schist, interlayered with
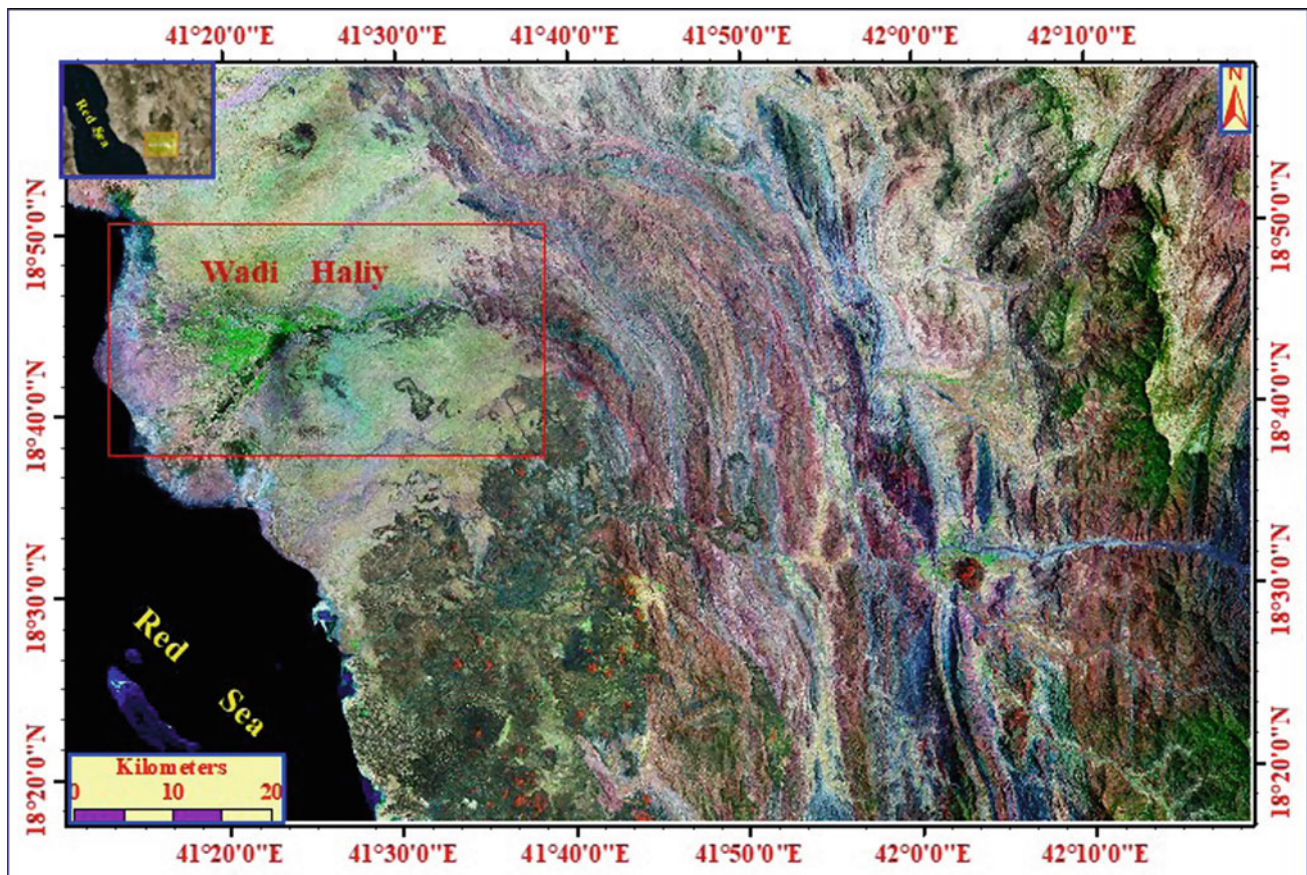
Fig. 8.1 Satellite image of Wadi Halyi district showing the Arabian Shield rocks in the upstream part

Fig. 8.2 a Drainage basins in the southwestern part of Saudi Arabia showing Wadi Halyi Basin; **b** Stations and Location numbers of the studied water samples
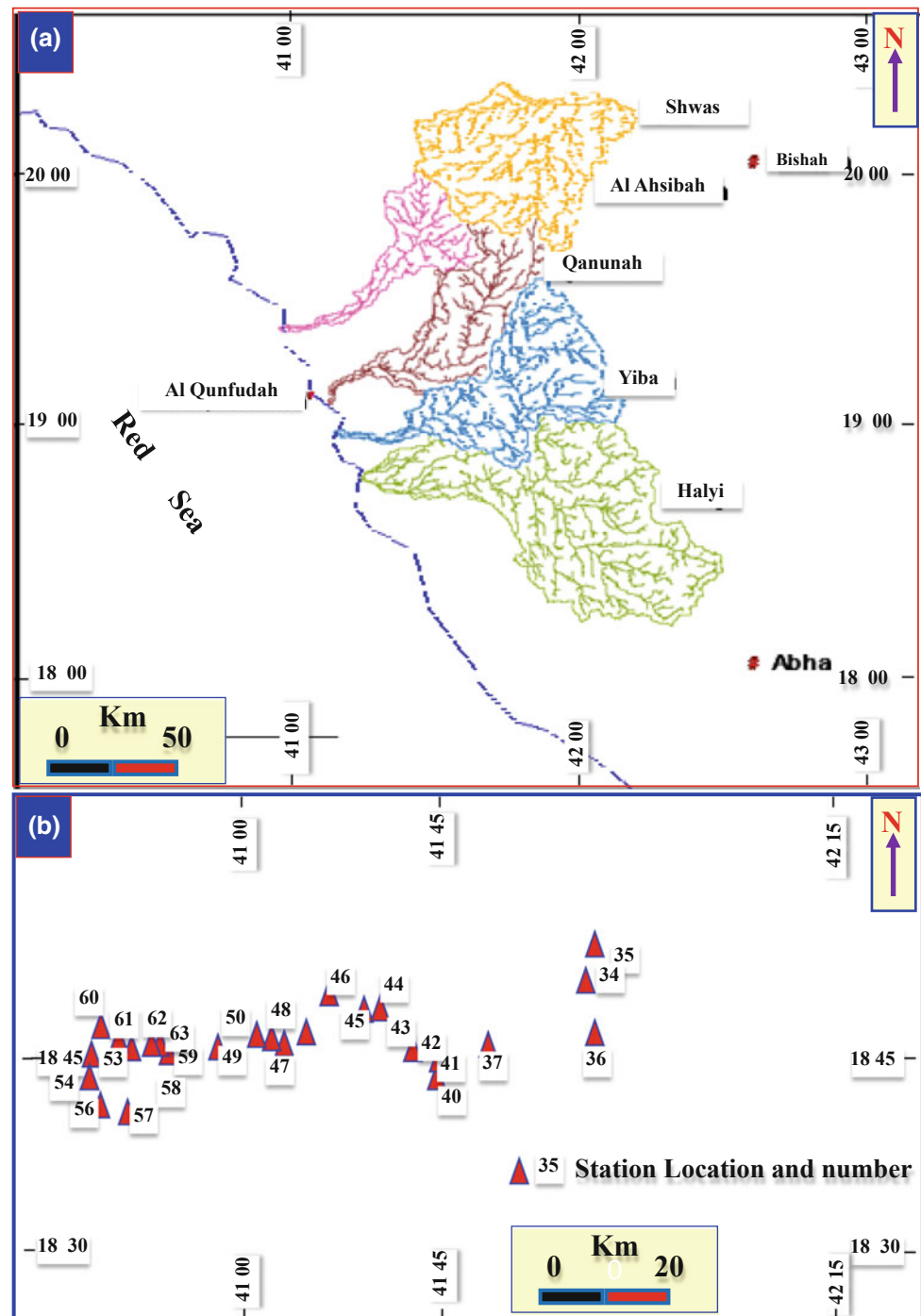
amphibolite and subordinate layers of marble, pebble-conglomerate schist, and rhyolitic schist, phyllite, and sandstone.

4. *Nimas complex (an)* consists of pretectonic mafic to intermediate plutonic rocks that intrude the layered rocks of the Tayyah and Shwas belts in the Asir terrane.

5. *Qiya complex (qg)* consists of bodies of deformed tonalite, granodiorite, and granite in the western part of the

Asir terrane. The complex forms a large batholith of orthogneiss at Qiya village, 75 km southeast of At Ta'if. Other antiforms or domes of massive to foliated granitoids assigned to the complex extend as far south as the Baqarah dome at about 18°50′N, 42°10′E, and together make up the Afaf gneiss belt.

6. Cenozoic Rocks which are consist of Tertiary basic volcanics (Harrat) and quaternary wadi deposits.

Fig. 8.3 Geologic map of the study area (modified after Johnson 2006)

Cryogenian intrusive rocks

qg Qiya complex

an An Nimas complex

bw Buwwah suite

Cryogenian layered rocks

ho Hali group

sh Shwas belt volcanic and sedimentary rocks

bb Bidah belt volcanic and sedimentary rocks

CENOZOIC

Qu Cenozoic surficial cover

Cb Cenozoic basalt
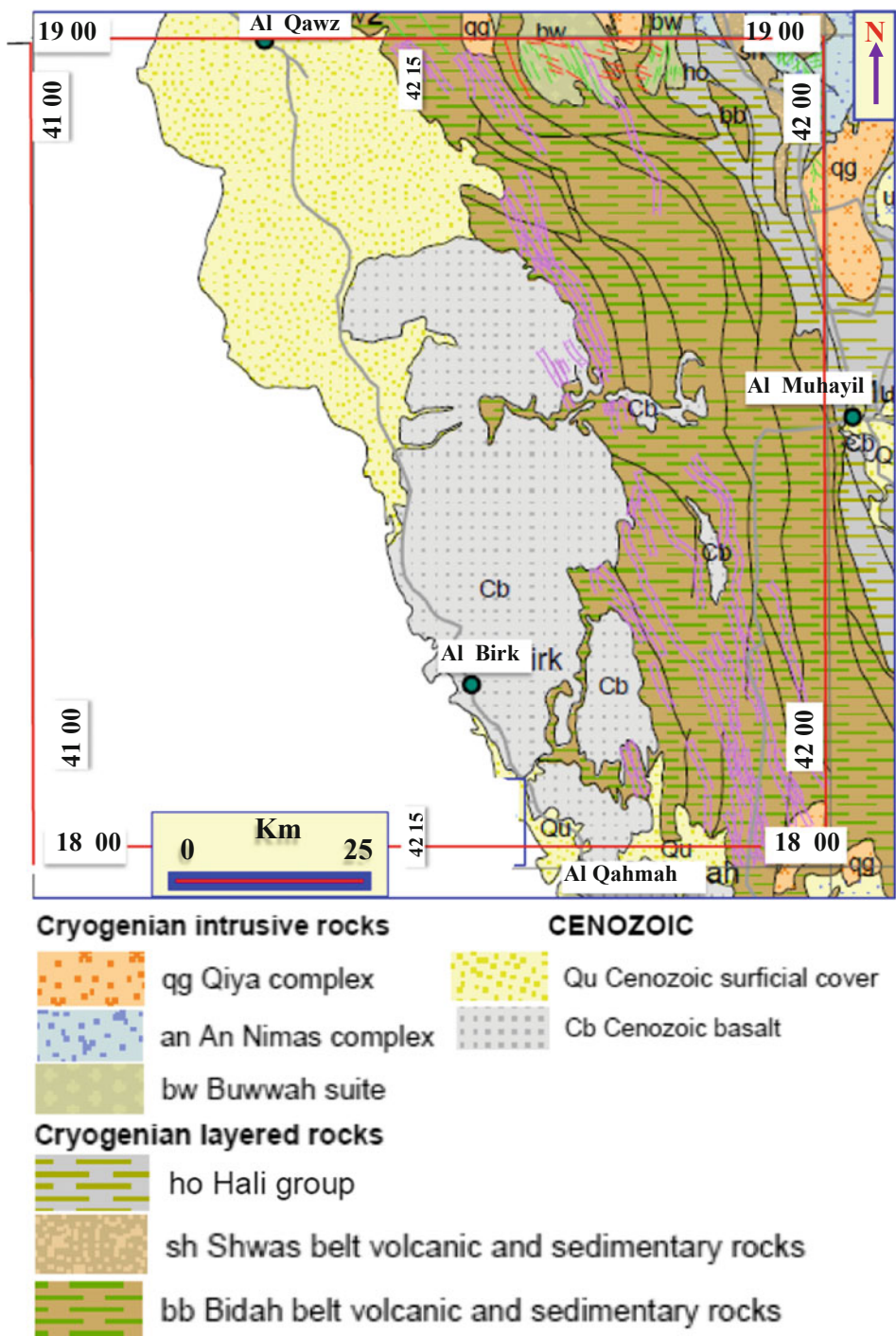
8.2   Groundwater Chemistry

8.2.1   Groundwater Aquifer

The only known significant aquifer systems in the basin are contained within the wadi infill alluvium. Pediment and outwash deposits surrounding igneous and metamorphic intrusions contain aquifers, which are locally important to individual farms and small communities, but the most significant groundwater systems are contained in what has been termed the Principal Wadis Alluvium. The Principal wadi Alluvium is contained within the drainage line of the main wadi and some of its largest tributaries. The Principal Wadi Alluvium system has been defined as main channel alluvium and is generally limited to those areas where the mean wadi

alluvium range between 20 and 500 m approximately meters in width.

Secondary alluvium, which is made up of the alluvial deposits flanking the main channels, plus other alluvial deposits are also occur. These deposits are generally of much lower permeability than the Principal Wadi Alluvium, and generally cannot maintain widespread groundwater development.

The meteoric water recharge in the study area depends upon the intensity of rainfall rather than the value of the mean annual precipitation because the evaporation rate may exceed the infiltration capacity after the low intensity rainfalls. On the other hand, the intensive floods have quantities of water responsible for the groundwater recharges through the alluvial sediments and the weathered and fractured hard rocks of Asir Escarpment Mountain chain. Because of the steep gradient and low permeability of the hard rocks, runoff plays a significant role in the hydrological balance as a source for the recharge to alluvial and fractured rocks in the studied wadis. The water levels and salinity are expected to be varies seasonally where the minimum of salinity and the maximum of water levels are attained at the end of floods.

The composition of natural waters is determined by a number of processes, which include wet and dry deposition of atmospheric salts, evapotranspiration and water-rock interaction. In any hard rock, trace and minor elements are distributed between rock-forming minerals, accessory minerals and intergranular space. The latter includes phenomena such as surface ion exchange, ion adsorption at mineral surfaces and easily soluble phases. The portion of individual elements in the intergranular space is particularly accessible to fluids. The mobility of metal ions in any rock, therefore depends on the amount of elements hosted in these spaces (Giese et al. 1991). On the other hand, the breaking down of some rock-forming minerals such as feldspars is considered to be one of the most important elements contributors to surface and groundwater.

8.2.2 Major Ions of Groundwaters

The data of the major ion content of the groundwater of Wadi Haliy (Fig. 8.2b; Table 8.1) shows that, in Wadi Haliy, the dominant anions are sulfate and chloride, but bicarbonate is also found in some samples. The typical proportions for major anions are 50:35:15 (SO_4:Cl:HCO_3). The dominant cations are sodium and calcium but magnesium is also prevailing in some samples.

The major elements of the groundwater of the study area are plotted on the Trilinear and Durv diagrams (Figs. 8.4 and 8.5), the cations plotted in the diagram are showing the typical proportions of the major cations are 50:39:11 (Na:Ca:Mg). The ground waters in wadi Haliy can also be classified as secondary salinity where (SO^4 + Cl > Na + K). The variation diagrams show nearly the same values of Ca in most of the wells (Fig. 8.6a). Also, Na shows the same values where it reaches not more than 400 ppm except three wells (Fig. 8.6b). Mg shows also the same values (Fig. 8.6c) except one well (well No. WH34). Which have a high Mg values (323.55 ppm). Also, Cl shows normal distribution without well no. WH 34, WH 60 (Fig. 8.6d).

Figure 8.7a also shows nearly the same values of SO_4 in the studied wells. Figure 8.7b also shows a very strong positive correlation between Ca and SO_4 which indicate gypsum dissolution. There is a very strong positive correlation between SO_4 and Mg which indicate sulphate mineral dissolution (Fig. 8.7c). Figure 8.7d also shows a positive correlation between Na and Cl which indicate halite dissolution.

8.2.3 Heavy Metals Contents of Groundwater

Pollution by heavy metals arises mainly from neighboring rocks enriched in heavy metals and from point source emissions from mining activities and a wide variety of industries. These heavy metals contaminants represent a threat both to aquatic ecosystems and to human health, since they tend to accumulate in all living organisms. The threat is increasing because of the enormous number of new compounds constantly being produced and released into the environment. Heavy metals in surface water can damage plants and affect humans through the food chain or exposure to contaminated drinking water. The fate and effects of pollutants discharged into a particular water body will depend not only on the amount of polluting substances emitted, but also on the hydrological, physical, chemical and biological conditions characterizing the concerned water body.

The trace elements content of the studied groundwater samples are shown in Table 8.2. The variation diagram of these trace elements (Figs. 8.8 and 8.9). Figure 8.8a shows the distribution of Ag where most of the wells are nearly of the same of the Ag contents. Wells no. 1 and 15 are of relatively high Ag content. The distribution of Cu (Fig. 8.8b) show nearly the same values (1–3 ppm). Wells no. 1–10 are of relatively of high Ag content. Figure 8.8c shows the Fe distribution and it is clear that well no. 1 and 32, 33, 34 are also of relatively higher Fe content. The distribution of Pb is clear in Fig. 8.8d where the values are nearly similar to Ag which reflects the releasing of these metals from sulphide ore deposits. The Pb values are within three levels. The

Table 8.1 Trilinear (piper) diagram of Wadi Halyi groundwater

No.	Ca	K	Mg	Na	CI	SO^{4-}	HCO$_3$
HW 34	588.99	15.46	323.55	469.13	1651	1354.16	238.95
HW 35	142.97	6.71	42.94	77.17	92	241.2	292.71
HW 36	164.52	1.38	46.63	181.81	313	355.62	249.7
HW 37	174.6	4.66	68.52	218.35	441	545.78	121.86
HW 38	181.61	5.35	70.54	221.27	466	563.89	121.86
HW 39	183.07	4.83	70.27	223.83	470	559.78	119.48
HW 40	76.05	1.89	21.81	58.32	71	122.66	191.16
HW 41	149.53	4.62	50.17	146.63	315	429.71	112.31
HAY 42	98.09	3.85	29.89	75.82	152	232.97	112.31
HW 43	109.1	4.66	34.5	87.07	178	264.25	121.86
HW 44	287.89	1.16	85.49	474.29	602	947.5	232.98
HW 45 A	133.05	5.48	39.41	105.5	201	299.64	107.53
HW 45 B	86.96	4.51	23.63	67.12	131	186.87	103.94
HW 46	77.56	4.49	22.98	69.7	131	190.16	87.22
HW 47	123.61	5.48	37.93	101.38	206	288.94	119.48
HW 4S	179.24	7.13	60.67	131.57	297	460.17	119.48
HW 49	186.51	6.44	88.52	243.84	630	488.98	103.94
HW 50	171.31	6.89	61.98	153.39	362	435.47	95.58
HW 51	145.32	3.97	68.39	155.6	282	423.12	107.53
HW 52	148.36	5.18	50.52	119.8	248	372.91	95.58
HW 53	133.88	4.8	48.84	120.72	227	351.51	103.94
HW 54	161.84	5.87	85.51	206.94	407	549.9	123.06
HW 55	210.3	5.95	94.08	191.24	377	693.96	103.94
HW 56	108.68	4.83	52	147.88	209	370.44	181.6
HW 57	178.4	5.02	84.31	286.56	445	694.78	152.93
HW 58	100.53	2.23	74.08	102.74	206	303.76	156.51
HWY 59	112.45	2.95	84.1	125	290	355.62	139.79
HW 60	220.66	2.3	151.43	647.65	1063	977.14	114.7
HW 61	171.55	3.59	101.84	247.74	616	533.43	89.61
HW 62	159.31	4.49	66.23	154.57	310	419.01	114.7
HW 63	123.06	4.63	41.1	84.36	188	279.06	95.58

distribution of S (Fig. 8.9a) shows irregular distribution and the wells are present in some clusters which reflect the passing of the groundwater along sulphide deposits of patchy distribution during the flowing from up to down stream. Figure 8.9b shows the Si distribution which is nearly similar to the irregular distribution of S. The plotting of U against Sr reflects a very positive correlation (Fig. 8.9c) and it also reflect the localization of Sr values between 0 and 200 ppm. The plotting of Fe against Cu (Fig. 8.9d) show weak positive correlation which indicate the derivation of the cations from sulphides deposits.

8.2.3.1 Lead (Pb)

Because of size and charge similarities, lead can substitute for calcium and included in bone. Children are especially susceptible to lead because developing skeletal systems require high calcium levels. Lead that is stored in bone is not harmful, but if high levels of calcium are ingested later, the lead in the bone may be replaced by calcium and mobilized. Once free in the system, lead may cause nephrotoxicity, neurotoxicity, and hypertension. Areas of particular risk are places where the drinking water is obtained from geologic strata with significant lead content. Areas which have
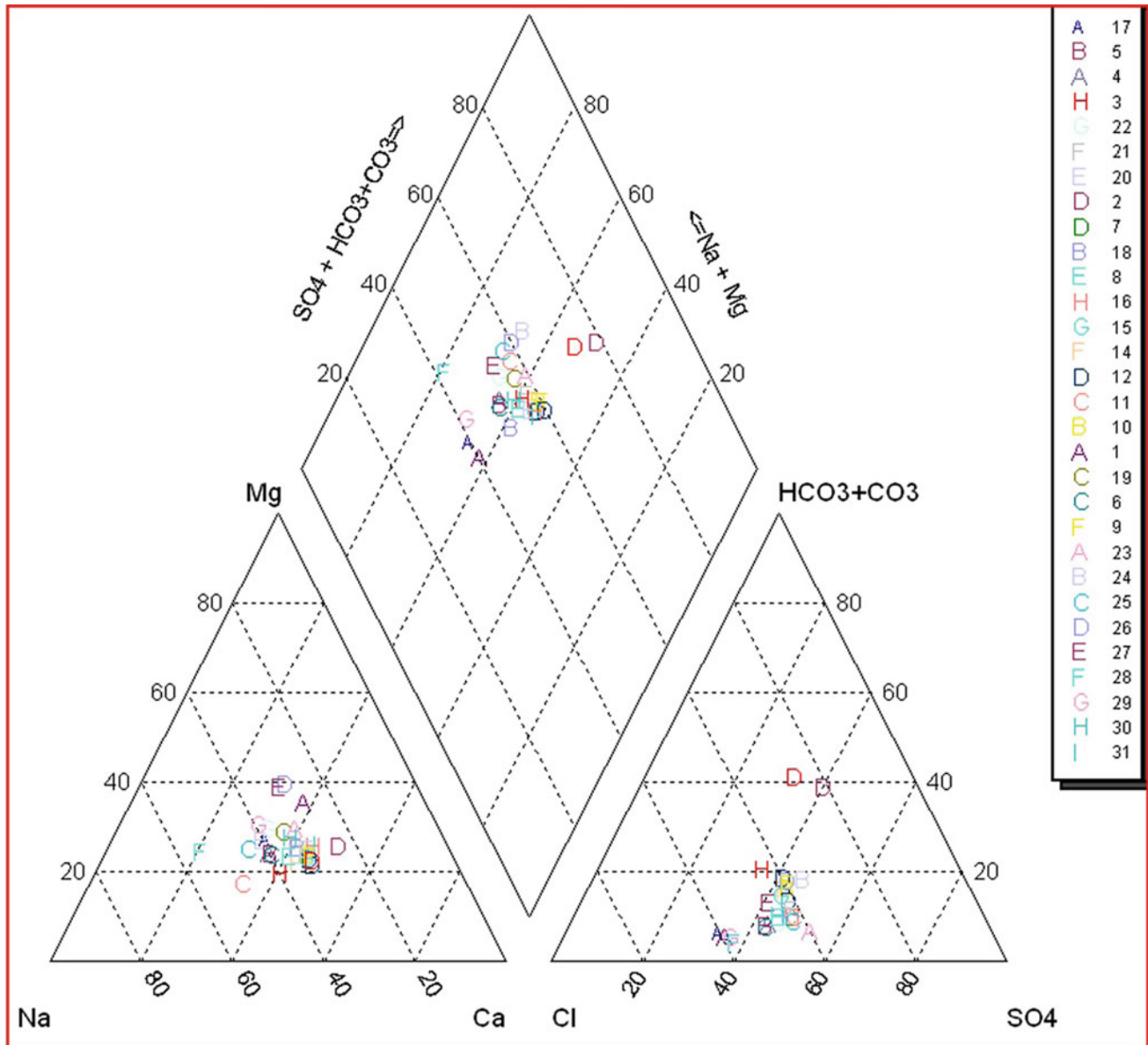
Fig. 8.4 Trilinear (piper) diagram of Wadi Halyi groundwater

deposits of gold, zinc, and other economically useful metals, also have lead as an ore contaminant and the "tailings" of the mining and purification of the ore often have a very high lead content. The current concentrations of lead in the groundwater and surface runoff in most of Wadi Haliy (Table 8.2) are within safe values (average less than 0.1 µg/l).

Toxicity

Following ingestion of a large amount of lead, there will be direct tissue interaction. This includes tissue desiccation, mucosal tissue damage in the GI tract, and convulsion possibly resulting in death. The most sensitive system is the hematopoietic (blood forming) system, with hypochromic microcytic anemia common (Nwankwo and Ibrahim 2006). The biosynthesis of hemes in general is deranged by the presence of lead.

8.2.3.2 Arsenic (As)

Arsenic (As) is another heavy metal that could become a problem with respect to polluting groundwaters, impairing their use for domestic water supply purposes. The current US EPA drinking water MCL for As is 50 µg/l, the US EPA is in the process of lowering this MCL to 20, 2 or 0.2 µg/l, based on the projected cancer risk to humans through
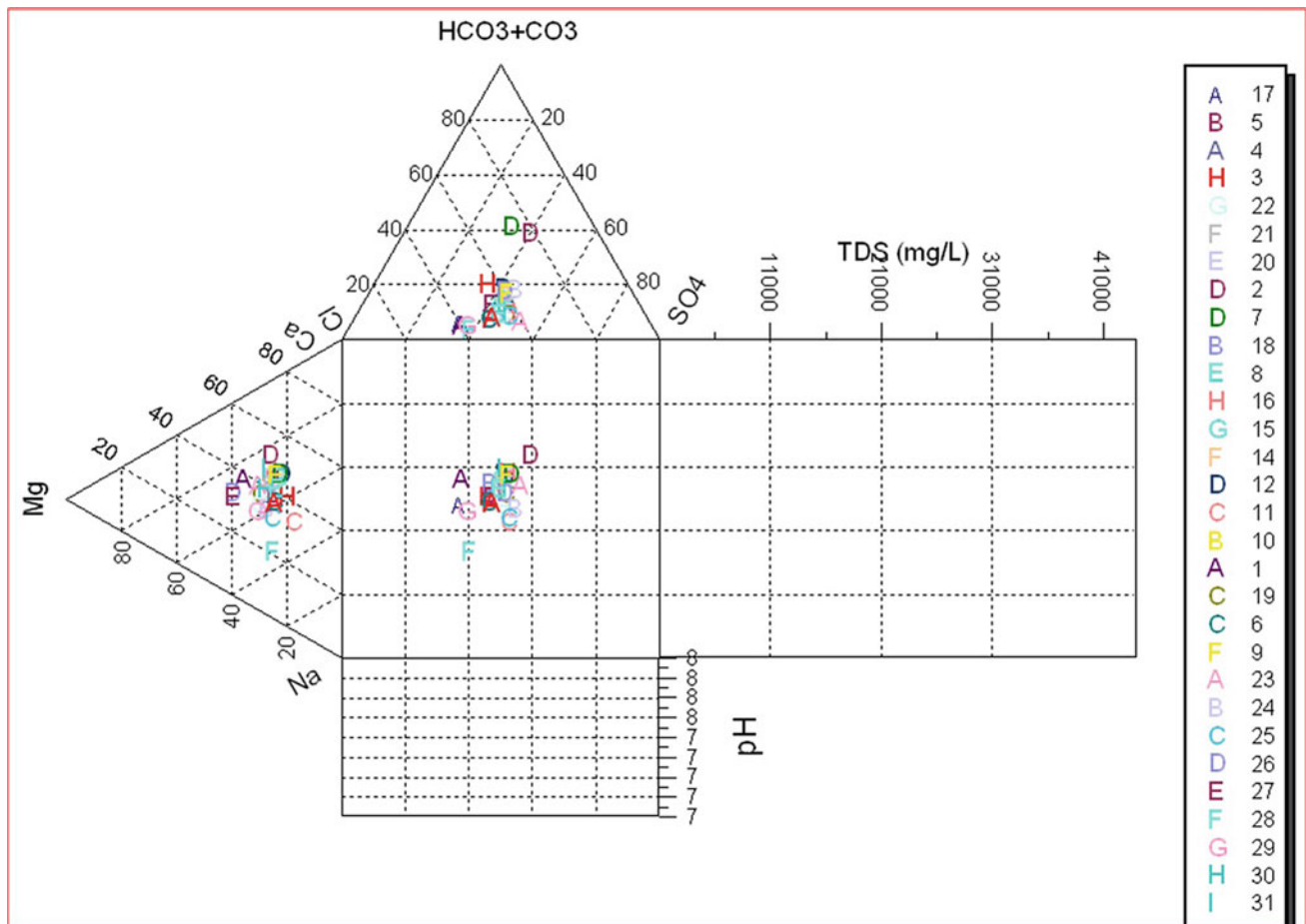
Fig. 8.5 Durov diagram of Wadi Halyi groundwater

consumption of drinking water. If 2 µg/l or less is selected as the new As MCL, then there could be significant problems in most of the studied area (Table 8.2) where groundwater system is used for domestic water supply purposes.

Toxicity

Arsenic ingestion can cause severe toxicity through ingestion of contaminated food and water. Ingestion causes vomiting, diarrhea, and cardiac abnormalities (Huet et al. 1975). Arsenic sprays or gases were used during World War I trench warfare, the one favored by the British was known as Lewisite. Arsenic can produce all three types of toxicity at difference dosages, acute, sub-acute, and chronic. One sign of acute exposure is edema of the eyelids, and gastrointestinal irritation, and both central and peripheral neuropathies frequently occur.

The first rational antidote to heavy metal intoxication was developed during World War II in anticipation of a re-initiation of gas warfare by the Germans. It was developed specifically for the British Lewisite gas and was thus known as British Anti-Lewisite, or BAL. The chemical compound is DIMERCAPROL. The rationale for its use was based on the fact that arsenic binds quite specifically to sulfur groups in the affected tissues. Dimercaprol has very active and relatively non-toxic sulfhydryl groups that interact with the arsenic to inactivate it. This phenomenon is known as chelation. Chelators are the class of compounds which are used in the treatment of heavy metal intoxication.

8.2.3.3 Mercury (Hg)

Mercury is a highly toxic heavy metal; it frequently combines with a methyl group to become methyl mercury. This form of mercury is found in a variety of environmental pollution situations and can produce a range of toxicities. Elemental mercury is less labile but produces a similar set of toxic manifestations. When mercury enters water it is often transformed by microorganisms into the toxic methyl mercury form which causes a great risk to humans. The National Drinking Water Standard (NPDWS) for mercury is 2 µg/l (Rechcigl 1995). The measured Hg values in the
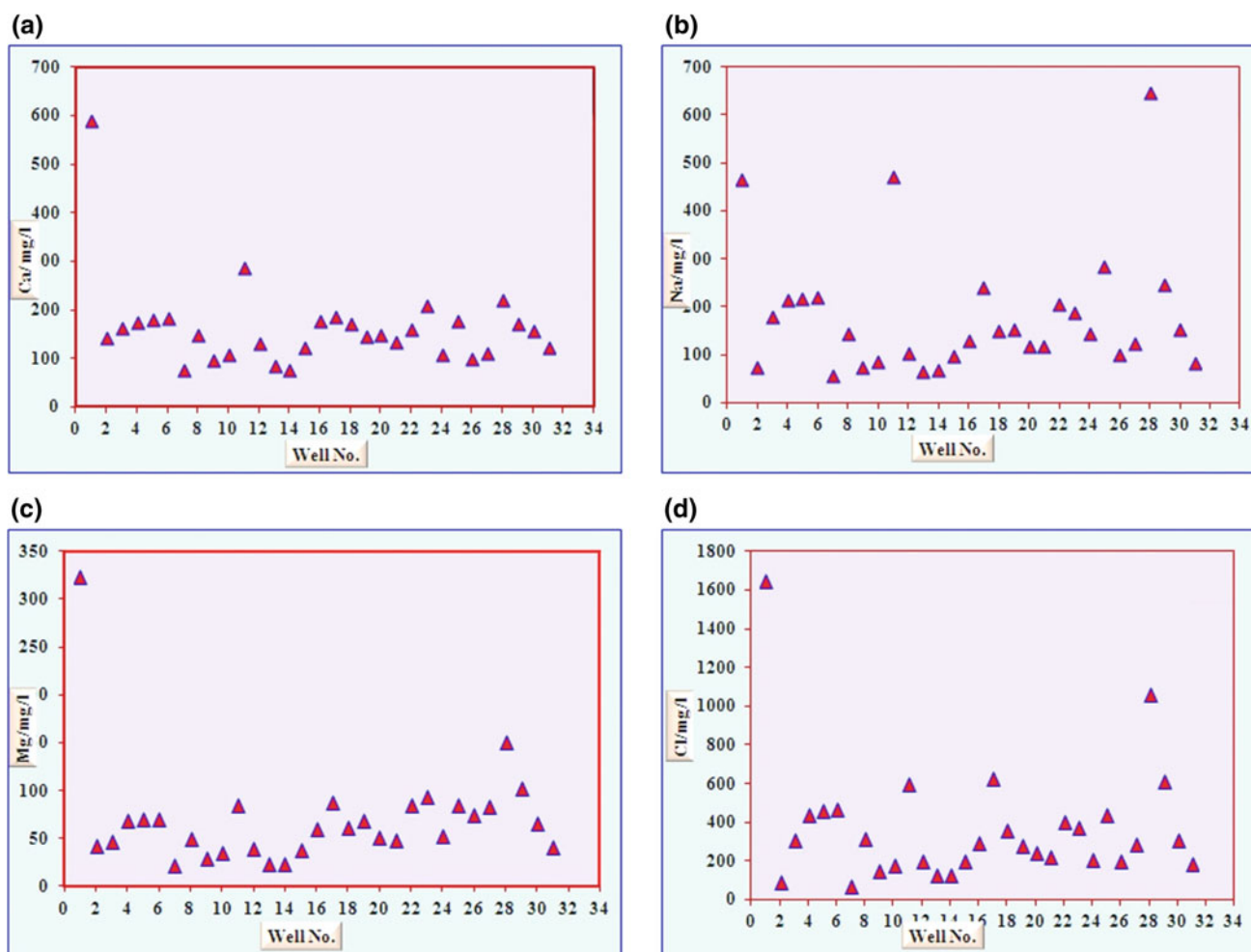
Fig. 8.6 Distribution of the major cations and anions of Wadi Halyi area. **a** Ca; **b** Na; **c** Mg; **d** Ca

groundwaters from the studied wadis fortunately indicate safe levels where the averages in all wadis are less than 0.1 µg/l.

Toxicity

Organic or inorganic mercury can both precipitate protein in a local reaction. In the GI tract, acute poisoning produces a sloughing away of the mucosa to an extent where pieces of the intestinal mucosa can be found in the stools. This produces a large loss of fluids and electrolytes. Mercury also breaks down barriers in the capillaries. This results in edema throughout the body (Hua et al. 1996). A range of neurological toxicities are also common. These include lethargy (at low doses), excitement, hyper-reflexia, and tremor. Often a psychotic state resulting in hyper-excitability. The expression 'Mad as a Hatter' originates from the hat-makers of the 19th century who were chronically exposed to mercury compounds used in making felt hats. The CNS effects are slowing or incompletely reversible. In chronic

intoxication there is mercury line at the gingival border similar to the "lead line". Mercury is especially poisonous to rapidly growing tissue. A common effect is deterioration of alveolar bone in the jaw, with a subsequent loosening of the teeth.

8.2.3.4 Cadmium (Cd)

Cadmium is an element that occurs naturally in the earth's crust. Pure cadmium is a soft, silver-white metal; however cadmium is not usually found in the environment as a metal. It is usually found as a mineral combined with other elements such as oxygen, chlorine, or sulfur (cadmium sulfate, cadmium sulfide). These compounds are solids that may dissolve in water but do not evaporate or disappear from the environment. All soils and rocks have some cadmium in them. It is extracted during the production of other metals such as zinc, lead, or copper. Cadmium is often found as part of small particles present in air. You cannot tell by smell or taste that cadmium is present in air or water, because it does not have any definite odor or taste.
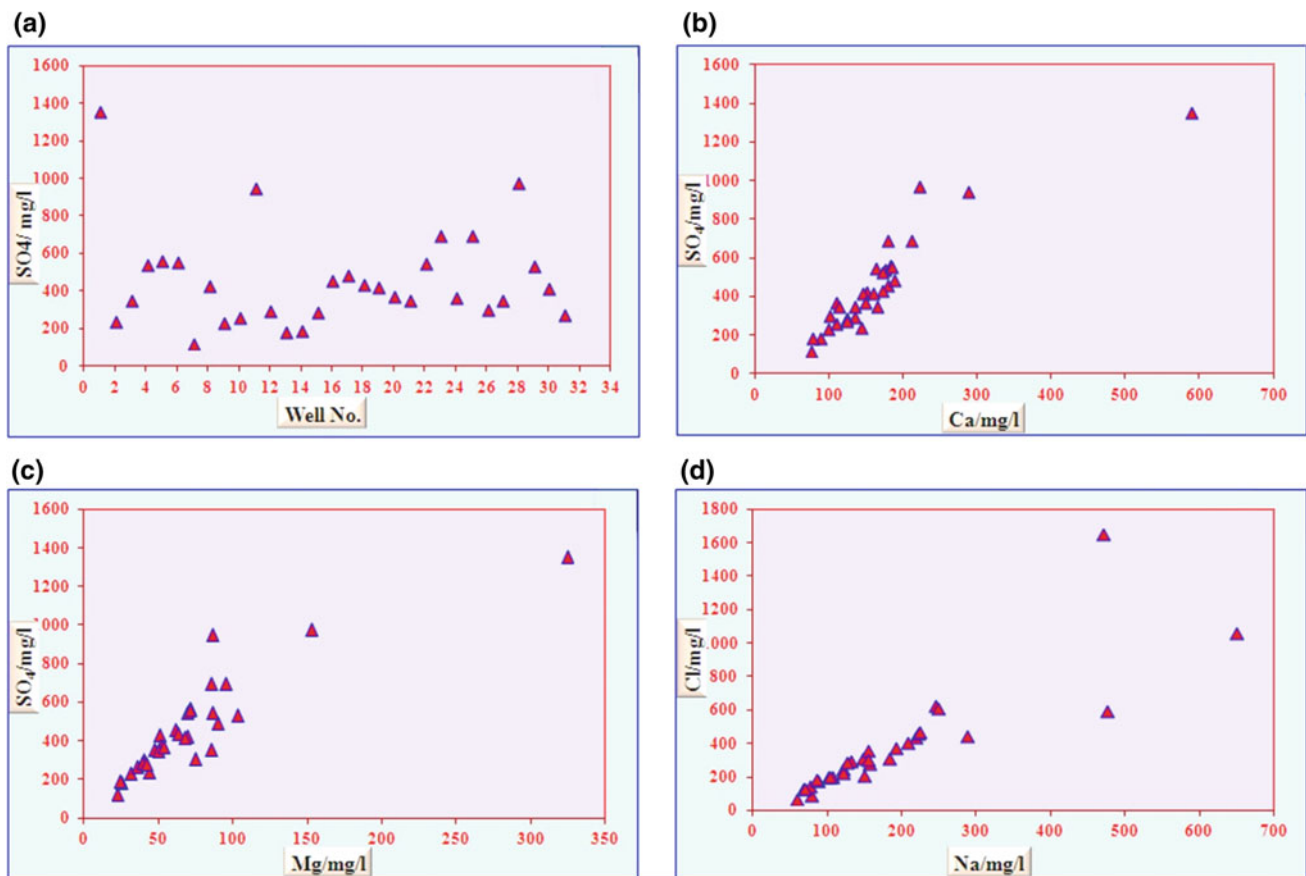
Fig. 8.7 Distribution of the major cations and anions of Wadi Halyi area. **a** SO$_4$; variation diagram: **b** SO$_4$ versus Ca; **c** SO$_4$ versus Mg; **d** Cl versus Na

Cadmium can enter the environment in several ways. It can enter the air from the burning of coal and household waste, and metal mining and refining processes. It can enter water from disposal of waste water from households or industries. Fertilizers often have some cadmium in them and fertilizer use causes cadmium to enter the soil. Spills and leaks from hazardous waste sites can also cause cadmium to enter soil or water. Cadmium attached to small particles may get into the air and travel a long way before coming down to earth as dust or in rain or snow. Cadmium does not break down in the environment but can change into different forms. Most cadmium stays where it enters the environment for a long time. Some of the cadmium that enters water will bind to soil but some will remain in the water. Cadmium in soil can enter water or be taken up by plants. Fish, plants, and animals take up cadmium from the environment.

The National Drinking Water Standard (NPDWS) for cadmium is 10 µg/l (Rechcigl 1995). In the study areas, cadmium could be present in sulfide mineralization associated with volcanic rocks. Table 8.2 shows the analyzed values of cadmium from groundwater of the studied wadis.

Toxicity

Symptoms of excess cadmium in human body appear as Anemia, dry and scaly skin, emphysema, fatigue, hair loss, heart disease, depressed immune system response, hypertension, joint pain, kidney stones or damage, liver dysfunction or damage, loss of appetite, loss of sense of smell, lung cancer, pain in the back and legs, and yellow teeth (Koçak and Akçil 2006). Eating food or drinking water with very high cadmium levels severely irritates the stomach, leading to vomiting and diarrhea. Eating lower levels of cadmium over a long period of time leads to a build-up of cadmium in the kidneys. This cadmium build-up causes kidney damage, and also causes bones to become fragile and break easily. Animals eating or drinking cadmium sometimes get high blood pressure, iron poor blood, liver disease, and nerve or brain damage.

8.2.3.5 Copper (Cu)

Copper is a reddish metal that occurs naturally in rock, soil, water, sediment, and air. Its unique chemical and physical

Table 8.2 Continue: chemical analyses of trace elements of Wadi Halyi groundwater

No.	Ag	Al	As	B	Ba	Be	Br	Ca	Cd	Cl	Co	Cr	Cs
34	0.5>	10>	6.6	1347	27.32	5>	10,351	588,981	0.53	1,651,000	0.2	13.2	0.1
35	0.5>	1	0.7	365	67.84	0.5	783	142,970	0.5	92,000	0.2	14	0.01
36	0.5	1	32.2	675	2.84	0.5	1769	164,518	0.5	313,000	0.2	11.3	0.08
37	0.05	1	4.3	371	80. 47	0.05	2378	174,602	0.07	441,000	0.15	4.9	0.02
38	0.05	2	5.5	366	93.72	0.05	2557	181,613	0.05	466,000	0.04	5.2	0.02
39	0.05	6	5.8	361	90.68	0.06	2593	183,069	0.05	47,000	0.02	5.3	0.02
40	0.05	2	1.5	155	22.83	0.06	330	76,053	0.05	71,000	0.06	7.7	0.01
41	0.05	1	4.8	295	98.62	0.08	1763	149,530	0.05	315,000	0.02	4.6	0.01
42	0.05	3	3.3	196	60.31	0.5	923	98,190	0.5	152000	0.03	4.3	0.01
43	0.05	6	4	217	71.85	0.05	1098	109,097	0.05	179,000	0.02	4.7	0.01
44	0.05	10	5	624	58.99	0.77	2363	287,830	0.5	602,000	0.2	11	0.1
45a	0.05	2	3.1	256	44.67	0.05	1158	133,051	0.05	201,000	0.02	7.3	0.02
45b	0.05	4	3.4	168	59.27	0.08	787	86,956	0.05	131,000	0.02	4.2	0.01
46	0.05	6	2.9	175	52.14	0.05	778	77,560	0.05	131,000	0.02	3.1	0.01
47	0.05	1	3.4	234	36.48	0.16	1178	123,606	0.05	206,000	0.02	6.4	0.01
48	0.05	5	3.7	319	32.73	0.08	1647	179,238	0.05	297,000	0.02	8.6	0.01
49	0.17	2	6.3	313	25.49	0.05	3741	186,508	0.05	630,000	0.02	6.5	0.01
50	0.05	1	5.4	242	109.1	0.08	1987	171,311	0.05	362,000	0.08	7.1	0.01
51	0.05	1	1.8	372	15.25	0.08	1811	145,319	0.05	282,000	0.02	6.8	0.02
52	0.05	1	3	287	28.09	0.05	1503	148,356	0.05	248,000	0.02	7.5	0.01
53	0.05	1	3.1	282	39.35	0.09	1482	133,876	0.05	227,000	0.02	12.9	0.01
54	0.05	1	5.2	38.5	37.59	0.5	2598	161,843	0.05	407,000	0.02	13.1	0.01
55	0.05	1	4.7	367	36.4	0.05	2620	210,296	0.05	377,000	0.02	10.2	0.01
56	0.05	1	3.3	197	24.58	0.05	1466	108,682	0.05	209,000	0.02	8.8	0.01
57	0.05	1	5.7	391	36.53	0.05	2818	148,401	0.05	445,000	0.02	12.8	0.01
58	0.05	1	2.3	201	12.98	0.05	1203	100,534	0.05	206,000	0.02	9.9	0.01
59a	0.05	1	3.4	207	23.4	0.09	1704	112,453	0.05	290,000	0.02	8.8	0.01
59b	0.05	1	3.5	208	24.16	0.05	1718	111,309	0.05	286,000	0.02	8.6	0.01
60	0.05	10	5	1463	28.07	5	6357	220,663	0.5	1,063,000	0.2	6.7	0.1
61	0.05	1	6.4	475	33.19	0.18	3720	171,553	0.05	616,000	0.02	5.9	0.01
62	0.05	1	4.2	304	35.88	0.05	1967	159,314	0.05	31,000	0.02	8.4	0.01
63	0.05	1	2.8	222	20.14	0.09	1172	123,063	0.05	185,000	0.02	6.9	0.01

(continued)

Table 8.2 (continued)

No.	Cu	Fe	Hg	K	Li	Mg	Mn	Mo	Na	Nb	Ni	P	Pb	Rb	Re	S	Sb	Sc	Se	Si	Sr	Th	Tl	Ti	U	V	W	Y	Zn
34	4.5	100	1	154,560	18.2	323,541	6.92	3.6	469,127	0.1	2	669	1	3.14	0.27	612,000	0.5	10	61.8	20,081	7375.6	0.5	100	0.1	2.91	2	0.2	0.1	1402.6
35	1	10	0.1	6713	2.3	4039	167.53	0.2	77,172	0.02	2	745	1	2.08	0.03	99,000	0.12	6	4	24,855	729.25	0.07	10	0.01	1.16	3.4	0.06	0.02	92.3
36	1.2	10	1	1376	18.5	46,631	0.5	2.5	181,809	0.02	2	20	1	0.82	0.05	144,000	0.05	5	21.9	20,706	1260.68	0.5	10	0.01	1.73	4	0.02	0.02	539.3
37	3	31	0.1	466	2.1	68,521	35.79	2.9	2,118,346	0.01	0.5	20	0.3	0.42	0.08	232,000	0.13	2	13	8376	1292.82	0.05	10	0.03	0.44	6.7	0.02	0.02	1207.3
38	2.1	41	0.1	5347	1.9	70,537	0.05	2.9	221,271	0.01	0.6	20	0.1	0.65	0.1	238,000	0.18	2	14	8338	1340.39	0.05	10	0.01	0.4	9	0.02	0.01	2.8
39	2.7	38	0.1	4829	1.9	70,268	0.25	3	223,826	0.01	0.3	20	0.1	0.51	0.09	238,100	0.15	2	14.2	8666	1407.93	0.05	10	0.01	0.43	10.1	0.03	0.02	2.2
40	0.7	10	0.1	1891	4.6	21,837	7.17	4	58,324	0.01	0.2	20	0.1	0.5	0.03	52,000	0.15	4	6.3	14,857	550.96	0.05	10	0.01	0.21	5.3	0.02	0.02	674.6
41	1.9	10	0.1	4616	1.3	50,166	0.21	2.8	146,630	0.01	0.2	20	0.1	0.44	0.06	179,000	0.16	2	8	7344	1092.5	0.05	10	0.01	0.42	7.7	0.02	0.02	3.6
42	2.3	10	1	3854	0.8	29,591	2.48	2.3	75,823	0.01	0.2	20	0.1	0.38	0.04	101,000	0.13	2	4.2	6283	649.84	0.05	10	0.01	0.31	6.7	0.03	0.01	32.3
43	1.9	10	0.1	4655	0.8	345,000	0.12	2.7	87,067	0.01	0.5	20	0.1	0.47	0.04	115,000	0.14	2	4.5	7175	756.06	0.05	10	0.01	0.42	8	0.03	0.01	8
44	2.7	10.1	1	1157	6.9	85,484	0.5	4.7	474,290	0.1	2	201	1	0.75	0.12	418,000	5	10	20.5	22,940	2694.46	0.5	100	1	2.98	17.6	0.2	0.1	326
45a	1.1	17	0.1	5481	1.9	39,413	25.83	1.7	105,497	0.01	0.2	20	0.1	0.68	0.04	129,000	0.07	3	6.4	10,701	969.41	0.05	10	0.01	0.42	4.4	0.02	0.01	1.1
45b	2.1	10	0.1	4509	0.6	23,628	0.05	2.5	67,117	0.01	0.5	20	0.1	0.41	0.02	83,000	0.14	2	3	6236	583.76	0.05	10	0.01	0.36	8.3	0.03	0.01	14.5
46	2.2	10	0.1	4491	1	22,981	0.07	2.5	69,697	0.01	0.5	20	0.1	0.37	0.03	8100	0.14	1	3.4	6018	549.58	0.05	10	0.01	0.31	8	0.03	0.01	2.2
47	1	10	0.1	5484	1.4	37,929	1.8	3.8	101,382	0.01	0.2	28	0.1	0.5	0.04	120,000	0.09	3	6.2	12,082	820.97	0.05	10	0.01	0.44	7.7	0.02	0.01	81.5
48	1.5	27	0.1	7131	2.5	60,666	0.05	4.5	131,573	0.01	2	20	0.1	0.46	0.07	185,000	0.07	3	10.9	14,939	1452.67	0.5	10	0.01	1.04	9.7	0.02	0.01	77.8
49	1.8	10	0.1	6439	12.6	88,518	0.78	6	243,833	0.01	0.4	20	0.1	0.41	0.11	199,000	0.05	4	15.4	17,145	2016.26	0.05	10	0.01	0.8	11.6	0.02	0.01	1.3
50	2.2	30	0.1	6592	2.2	61,984	113.5	4.3	153,392	0.01	0.7	20	0.1	0.54	0.96	177,000	0.12	3	8.3	12,207	1310.12	0.05	10	0.01	0.8	7.4	0.02	0.01	44
51	1.2	17	0.1	3965	5.1	68,385	0.05	4.5	155,601	0.01	2	20	0.1	0.43	0.07	177,000	0.5	4	15.8	19,370	1703.09	0.5	10	0.1	1.39	5.9	0.02	0.01	1.4
52	1.3	10	0.1	5182	3.4	50,521	0.05	3.7	119,801	0.01	0.2	20	0.1	0.2	0.06	147,000	0.05	4	13.3	19,036	1206.61	0.05	10	0.01	1.37	10.5	0.02	0.01	0.09
53	1.3	10	0.1	4799	2.7	48,835	0.05	3.8	120,721	0.01	0.2	20	0.1	0.21	0.05	141,000	0.05	5	15.7	21,255	1288.89	0.05	10	0.01	1.85	11.1	0.02	0.01	0.9
54	1.3	10	0.1	5868	3.8	85,509	0.05	3.5	206,943	0.01	0.2	20	0.1	0.41	0.08	21,000	0.05	5	32.3	23,492	1838.61	0.05	10	0.01	3.57	14.4	0.02	0.01	1.4
55	2.4	12	0.1	5945	3	94,076	0.16	10.8	191,237	0.01	0.3	20	0.1	0.48	0.08	281,000	0.05	6	28.7	26,700	2423.9	0.05	10	0.01	3.46	12.9	0.02	0.01	2
56	1.4	10	0.1	4827	3	51,998	0.05	9.5	147,875	0.01	0.2	20	0.1	0.22	0.06	142,000	0.05	5	16.6	23,947	1422.22	0.05	10	0.01	2.05	15.3	0.02	0.01	1
57	2.4	14	0.1	5020	4.6	84,308	0.19	9.9	286,562	0.01	0.2	20	0.1	0.36	0.1	262,000	0.05	6	32.7	27,290	1871.19	0.05	10	0.01	1.64	17.1	0.02	0.01	1.7
58	1.4	19	0.1	2228	1.9	74,050	0.05	7.5	102,744	0.01	2	20	0.1	0.28	0.05	120,000	0.05	5	13.7	24,397	1048.29	0.05	10	0.01	1.44	18.5	0.02	0.01	0.8
59a	1.2	17	0.1	2949	2.8	84,103	0.05	8.7	124,999	0.01	0.2	20	0.1	0.38	0.06	142,000	0.05	6	11.3	26,510	1972.1	0.05	10	0.01	1.8	19.6	0.02	0.01	0.9
59b	1.2	10	0.1	2884	2.7	84,201	0.05	9	122,406	0.01	0.2	20	0.1	0.35	0.07	140,000	0.05	6	11.5	26,351	1879.88	0.05	10	0.01	1.72	19.5	0.02	0.01	0.9
60	2.3	100	1	2296	13	151,433	0.5	15.5	647,646	0.1	2	22	1	0.12	0.14	414,000	0.5	10	37.5	36,494	4589.49	0.5	100	0.1	2.15	3.5	0.2	0.1	5
61	1.8	23	0.01	3592	4.9	101,839	4.55	9.4	247,735	0.01	2	20	1	0.13	0.1	214,000	0.05	5	23.5	24,086	2444.81	0.05	10	0.01	1.76	8.9	0.02	0.01	1.2
62	1.7	37	0.1	4491	3.8	66,228	0.05	4.4	154,566	0.01	2	20	1	0.33	0.08	178,000	0.05	5	16.7	21,489	1683.63	0.05	10	0.01	1.67	12.8	0.02	0.01	1.1
63	1	62	0.1	4625	2	41,102	0.05	3.7	84,355	0.01	2	20	1	0.17	0.04	110,000	0.05	4	11	18,693	949.56	0.05	10	0.01	0.83	10	0.02	0.01	0.6

Fig. 8.8 Distribution of trace elements of Wadi Halyi area. **a** Ag; variation diagram: **b** Cu; **c** Fe; **d** Pb

properties have made it one of the most commercially important metals. Since copper is easily shaped or molded, it is commonly used to make pennies, electrical wiring, and water pipes. Copper compounds are also used as an agricultural pesticide, and to control algae in lakes and reservoirs. Copper also occurs naturally in plants and animals. It is an essential element for all known living organisms, including humans. However, very large single or long-term intakes of copper may harm human health.

Dissolved copper in water is more likely to affect human health. Levels of copper found naturally in groundwater and surface water are generally very low; about 4 μg of copper in one liter of water (4 μg/1) or less. Cupric ion (Cu^{+2}) is considered as the primary form of copper in natural surface waters. High levels of copper occur if corrosive water comes in contact with Cu-bearing mineralization. If corrosive water remains motionless in contact with this mineralization, copper levels may exceed the allowed maximum contaminant level for human use. The U.S. Environmental Protection Agency (U.S. EPA) has determined that copper levels in drinking water should not exceed 1.3 mg/l. No adverse

health effects would be expected if this level is not exceeded. Measures should be taken to reduce exposure to copper if this level is exceeded. The average of Cu values in the groundwaters of Wadi Haliy is 1.84 μg/l. These values are considered safe according to the U.S. EPA maximum copper level in drinking water.

Toxicity

Copper is one of a relatively small group of metallic elements which are essential to human health. These elements are required for normal metabolic processes. However, as the body cannot synthesize copper, the human diet must supply regular amounts for absorption. The adult body contains between 1.4 and 2.1 mg of copper per kilogram of body weight. Hence a healthy human weighing 60 kg contains approximately a tenth of one gram of copper. However, this small amount is essential to the overall human well-being. Drinking water normally contributes approximately 150 μg/day. Immediate effects from drinking water which contains elevated levels of copper include vomiting,
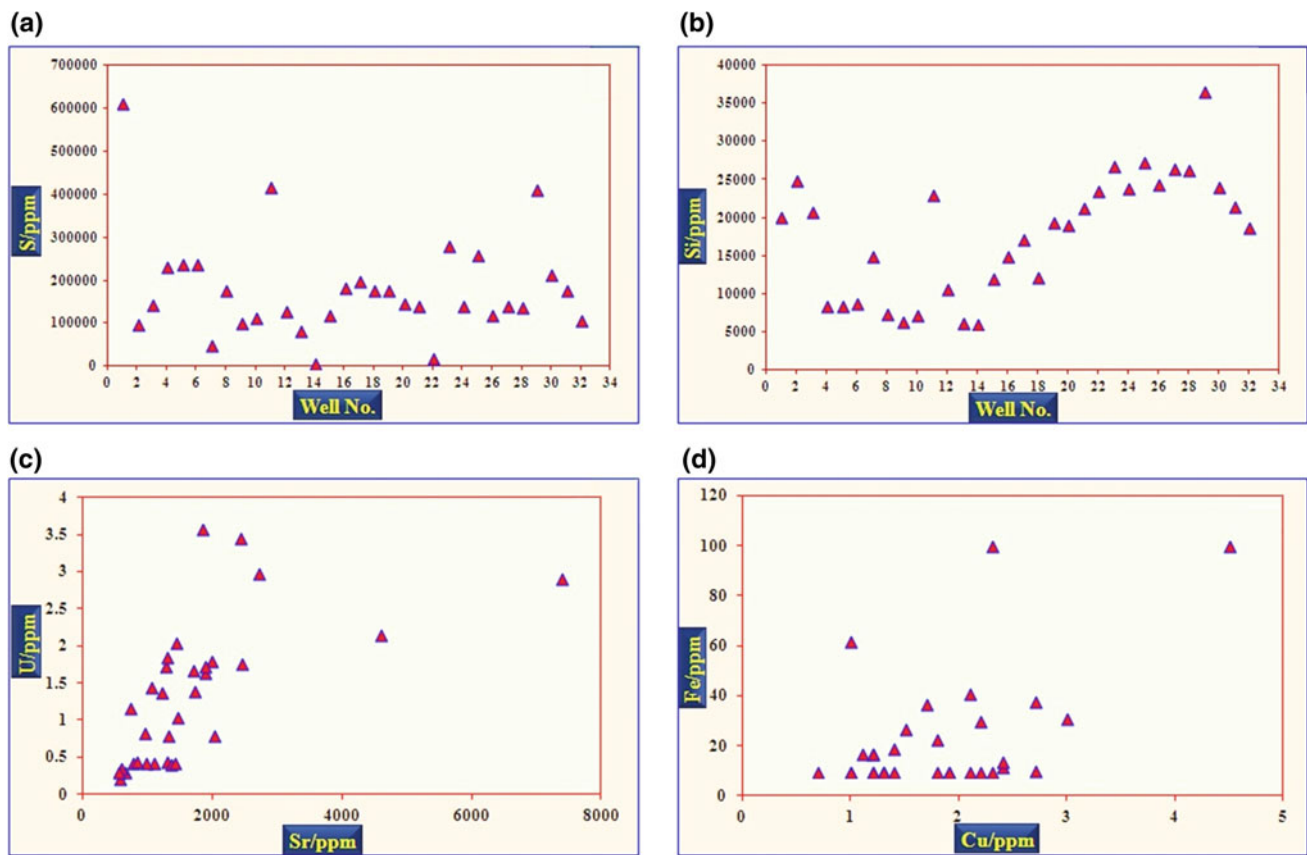
Fig. 8.9 Distribution of trace elements of Wadi Halyi area. **a** S; variation diagram: **b** Si; **c** U versus Sr; **d** Fe versus Cu

diarrhea, stomach cramps, nausea. The seriousness of these effects can be expected to increase with increased copper levels or length of exposure. Children under one year of age are more sensitive to copper than adults. Long-term exposure to copper in drinking water which is much higher than 1000 µg/l has been found to cause kidney and liver damage in infants. Other persons who are highly susceptible to copper toxicity include people with liver damage or Wilson's disease.

8.2.3.6 Uranium (U)

Generally, the U content of all the studies groundwater samples are within the acceptable limit (Table 8.2). The uranium and heavy metal contents are higher in samples collected from the upstream area of the wadi where the crystalline rocks are exposed and in direct contact with the runoff. The Elevated heavy metal and uranium contents suggests that these mining areas are considered as potential sources for these natural pollutants and likely affecting the water quality in these wadis. The attenuation of heavy metals and uranium is reported in this study along the flow path, from the mining area to downstream.

8.3 Summary and Conclusions

The present field investigations and analytical procedures support the contamination of the Wadi Halyi groundwater with some metals. These metals are mostly derived by chemical dissolution and mechanical destruction of the sulphides-bearing gold deposits of the eastern (upstream) Arabian Shield Precambrian rocks. These elements are still not higher than required Saudi standards. The comparison of the chemical analyses with those of the WHO Guidelines (2017) and the Saudi Arabian Standards Organization (SASO) of Un-bottled groundwater (Table 8.3) revealed that, the groundwater of Wadi Halyi Area is within the limit of the groundwater of Saudi Arabia except the U.

Pollution by heavy metals and uranium arises mainly from neighboring rocks and also from emissions from mining activities. Generally, the uranium and heavy metal contents are higher in samples collected from the upstream area of the wadi where the crystalline rocks are exposed and in direct contact with the runoff. The Elevated heavy metal and uranium contents suggests that these mining areas are

Table 8.3 The comparison of the chemical analyses with those of the WHO Guidelines (2017) and the Saudi Arabian Standards Organization (SASO) of un-bottled

Element	WHO guidelines (2017)	Saudi Arabian Standards Organization (SASO) of un-bottled groundwater (1985) (mg/l)	W. Halyi (mg/l)
A1	0.2 mg/l		
Sb	0.02 mg/l		
Ba	1.3 mg/l	1.0	0.1091
B	0.3 mg/l		
Cd	0.003 mg/l		
CN	No guideline		
Mn	0.5 mg/l	0.5	0.1675
Hg	0.006 mg/l	0.001	0.001
Na	50 mg/l		647.65
Zn	3 mg/l	15	1.4026
Bi	No guideline		
Cl	5 mg/l	600	1651
TDS	No guideline	1500	
Cu	2 mg/l	1.5	0.0045
Fe	0.3 mg/l		
Pb	0.01 mg/l		
SO_4	No guideline	400	1354.16
Ca	No guideline	200	588.99
Ag	No guideline	0.05	
AS	0.01		0.0322

considered as potential sources for these natural pollutants and likely affecting the water quality in these wadis. The attenuation of heavy metals and uranium is reported in this study along the flow path, from the mining area to downstream. The processes governing the evolution of the leachates plume and its heavy metals budget are modeled in two steps: (1) Neutralization of acidic mine drainage water; (2) Heavy metal attenuation by adsorption, evaporation and co-precipitation with Fe oxides.

References

Al-Hageri FY (1977) Groundwater studies of Wadi Qudaid. Institute of Applied Geology, King Abdulaziz University, Jeddah, Saudi Arabia. Research series no. 2. 132–178

Al-Jarash MA (1989) The climatic water balance in Saudi Arabia 1970–1986. Scientific Publishing Centre, King Abdulaziz University, Jeddah, Saudi Arabia, 441 pp

Al-Turki AL (2010) Assessment of well drinking water quality in Hail Region of North Central Saudi Arabia. J Agric Vet Sci 2(2):101–110

Camp VE (1984) Island arcs and their role in the evolution of the western Arabian Shield. Geol Soc Am Bull 95:913–921

Dames and Moore (1978) Representative basin study for wadis. Yiba, Habonah, Tabalah, Liyyah and Lith, Saudi Arabia 52

Giese U, Moller P, Munzberg S (1991) Mobilization of metals in granitoids. In: Pagel M, Leory JL (eds) Source, transport and deposition of metals. Balkema, Rotterdam, pp 49–52

Heidmann I (2004) Influence of fulvic acid on ion binding and colloidal stability of kaolinite particles, Ph.D. thesis unpublished, University of Kiel, Germany, 117 pp

Hua MS, Huang CC, Yang YJ (1996) Chronic elemental mercury intoxication: neuropsychological follow-up case study. Brain Inj 10:377–384

Huet PM, Guillaume E, Cote J, Légaré A, Lavoie P, Noncirrhotic Viallet A (1975) Presinusoidal portal hypertension associated with chronic arsenical intoxication. Gastroenterology 68(5):1270–1277

Hussain G, Alquwaizany A, Al-Zarah A (2010) Guidelines for irrigation water quality and water management in the Kingdom of Saudi Arabia: an overview. J Appl Sci 10(2):79–96

Johnson PR (2000) Proterozoic geology of Saudi Arabia: current concepts and issues. In: Contribution to a workshop on the geology of the Arabian Peninsula, 6th meeting of the Saudi Society for earth science, King Abdulaziz City for Science and Technology, Riyadh, Saudi Arabia, 32 pp

Johnson PR (2006) Explanatory notes to the map of proterozoic geology of western Saudi Arabia. Technical report SGS-Tr-2006-4

Koçak M, Akçil E (2006) The effects of chronic cadmium toxicity on the hemostatic system. Pathophysiol Haemost Thromb 35(6):411–416

Levy DB, Barbarick KA, Siemer EG, Sommers LE (1992) Distribution and partitioning of trace metals in contaminated soils near Leadville, Colorado. J Environ Qual 21:185–195

Nwankwo EA, Ibrahim U (2006) Environmental lead intoxication and chronic kidney disease: a review. Internet J Nephrol 3(1)

Pierzynski GM, Schnoor JL, Banks MK, Tracy JC, Licht LA, Erickson LE (1994) Vegetative remediation at superfund sites, mining and its environmental impact. In: Hester RE, Harrison RM (eds) Issues in environmental science and technology. Royal Society of Chemistry, vol 1, pp 49–69

Prinz WC (1983) Geologic map of the Al Qunfudhah quadrangle, sheet 19E, Kingdom of Saudi Arabia: Saudi Arabian Deputy Ministry of Mineral Resources Geoscience Map GM-70 A, C, scale 1:250,000; text, 19p

Rechcigl JE (1995) Soil amendments and environmental quality. Soil and Water Science Department, Research and Education Center, Ona, Florida

Stoeser DB (1986) Distribution and tectonic setting of plutonic rocks of the Arabian Shield. J Afr Earth Sci 4:21–46

Stoeser DB, Camp VE (1985) Pan-African microplate accretion of the Arabian Shield. Bull Geol Soc Am 6:817–826

Stoeser DB, Whitehouse MJ, Stacey JS (2001) The Khida terrane-geology of Paleoproterozoic rocks in the Muhayil area, Eastern Arabian Shield, Saudi Arabia (Abstract). Int Geosci J Gondwana Res 4(2):192–194

Thornton I (1983) Applied environmental geochemistry. Academic Press, London, 501p. Research volume 2, no 7, pp 1–17, July 2011

Taha M, Harb S, Nagib M, Tantawy A (1981) The climate of the Near East. In: Climates of southern and western Asia, vol 9. Elsevier, New York, pp 183–229

Zaidi FK, Nazzal Y, Jafri MK, Naeem M, Ahmed I (2015) Reverse ion exchange as a major process controlling the ground-water chemistry in an arid environment: a case study from northwestern Saudi Arabia. Environ Monit Assess 187:607

Analysis of Rainfall, Missing Data, Frequency and PMP in Al-Madinah Area, Western Saudi Arabia

Nassir S. Al-Amri and Ali M. Subyani

Abstract

The estimation of rainfall variability, especially in arid regions, represents a major element for flood prediction and water resources development design works. Such a task presents a major challenge to water resources engineers and hydrologists in arid regions due to the extreme random and erratic nature of rainfall events, which is further compounded by climate change impact. In arid region that covers major portion of Saudi Arabia, the length of rainfall and runoff records is usually short and sometime with information gaps for undertaking proper design work. Such constraints present a difficulty in the application of rainfall and runoff frequencies. In this study the application of different frequency for stations with missing rainfall record in Al-Madinah region, located in western Saudi Arabia was addressed. The analysis first used the record of 10 rainfall stations over the period of 1970–2015 (46-years), to fill the missing information through the application of Inverse Distance Weighted and Kriging techniques and later applied Gamma and GEV probability density distributions. The two distributions parameters were estimated and tested by the K-S and Chi square tests. The two distributions predication estimated the maximum annual rainfall depths for 100, 200, 300, 500 and 1000 years return periods. The Gamma distribution provided a better fits for 3 stations with values ranging from 64 to 92 mm depths for the 100 year return period while GEV for the remaining 7 stations ranging from 55 to 107 mm depth. In addition, the Probable Maximum Precipitation (PMP) technique was applied to estimate the different return periods based on 24-h maximum annual amounts. The proposed approach may provide a mean to estimate the design rainfall depth for stations with missing records, however, it may require further evaluation for other regions of Saudi Arabia or other areas of similar characteristics.

9.1 Introduction

Arid regions of the world which cover most area of Saudi Arabia are usually characterized by rainfall scarcity and frequent drought cycles. Evaluation and prediction of the space-time variability of rainfall in these regions are essential requirements for flood protection works and water engineering projects. The erratic and random rainfall characteristics present a challenge to hydrologists and water resources engineers to apply most of the analytical, statistical and numerical techniques for reasonable accuracy of the rainfall and runoff depth and volume. The design of major water structures such as water supply, storage dams and flood protection and urban drainage works in arid regions through the improved rainfall-runoff predictions can contribute towards reducing the failure probability risks regarding losses of live and infrastructural damages as well as enhance adequate water supply availability (Hershfield 1961; Hosking and Wallis 1997; Şen 2008; Filho 2012).

All types of analysis require the availability of rainfall and runoff records with adequate length, coverage and reliable accuracy especially for the application of statistically techniques such as frequency distributions. However, the collection of daily or events based data from a given rainfall and runoff network represents an essential component to undertake hydrological analysis to develop such as; the

N. S. Al-Amri (✉)
Department of Hydrology and Water Resources Management, King Abdulaziz University, P.O. BOX 80208, Jeddah 21589, Saudi Arabia
e-mail: nalemari@kau.edu.sa

A. M. Subyani
Water Research Center, King Abdulaziz University, P.O. BOX 80200, Jeddah 21589, Saudi Arabia
e-mail: asubyani@kau.edu.sa

intensity-duration-frequency (IDF) curves, design hydrographs and frequency distributions, including probable maximum precipitation (PMP) needed for water related projects (Abdulrazzak et al. 1995; Millington et al. 2011).

To overcome data constraints, various estimation techniques have been applied in different arid regions including many regions of Saudi Arabia. Using the collected information from the established 1960 hydrological network in Saudi Arabia, several flood protection and water supply assessment studies were carried out at the national level by Sogreah (1968), German Consult (1979), Saudi Arabian Dames and Moore (1988) and most recently the Schlumberger Water Services (2012). On the regional level, various researches have been carried out in the western region including Al-Madinah area by Şen (1983), Şorman et al. (1991), Subyani et al. (2009) and Subyani and Al-Ahmadi (2011). Most of the recent hydrological analysis have focused on the application of statistical techniques to overcome data constraints. Different frequency distributions such as the Cumulative Density Function (CDF), Probability Density Function (PDF) and distribution parameter estimation were applied in Saudi Arabia included Al-Madinah area. Many researchers (Nouh 2006; Şen 2009; Subyani and Al-Amri 2013) have carried out the probability of future maximum rainfall frequency.

In regard to the focus of this research, Subyani and Al-Ahmadi (2011) applied a rainfall-runoff model for five ungagged catchments in Al-Madinah area. Data for daily annual maximum rainfall were analyzed to derive the Generalized Extreme Value (GEV) distribution for different return periods. In addition, hydrographs, regional probable maximum precipitation maps and maximum flood estimation are also produced for this area. Al-Ahmadi (2014) applied rainfall partial duration series (PDS) using different statistical distributions and different selection criteria models. He concluded that GEV distribution with the partial duration daily rainfall series provided the best fit for Al-Madinah rainfall.

The issue of filling missing rainfall information to improve the prediction process can be addressed through the application of approximation techniques such as Inverse Distance Weighted (IDW) and Kriging that have been used in different part of the world (De Silva et al. 2007; WMO 2008). However, the Kriging cannot be applied only to spatial interpolation, but also to identify the best location for new measurement points as well as in the optimization network design coverage (Isaaks and Srivastava 1989). Tabios III and Salas (1985) discuss the problem of estimating missing or ungagged sites for rainfall data using different spatial interpolation techniques, which have varies degrees of complexity. Based on the error of estimate, their study indicated that the Kriging technique and optimal interpolation are superior to other techniques.

In this study, the analysis focused initially on using some interpolation method to fill some missing daily rainfall records. The main objective of the present study is to identify appropriate rainfall frequency approaches which will be applied to predict the maximum rainfall depth for different return periods up to 1000 years. In addition, Probable Maximum Precipitation (PMP) is provided that may pose risk to Al-Medinah region.

9.2 Study Area and Available Data

Al-Madinah region, located in the western part of the Kingdom of Saudi Arabia, lies between latitude 23° 00′ to 26° 00′N and longitude 39° 00′ to 44° 00′E (Fig. 9.1). The climate is affected by the tropical Atlantic Ocean air mass as well as the Mediterranean Sea maritime polar air mass in addition to the influence of the local topography. Both regional and local circulation patterns have a dominant influence on the climate of the region (El-Khatib 1980; Şen 1983; Al-Jerash 1989; Subyani and Al-Ahmadi 2011; Subyani and Al-Amri 2013). The region has a moderate elevation and characterized by random rainfall pattern with large seasonal variations due to its location within the subtropical zone. The rainfall regime is generally characterized by the occurrence of sporadic rains in winter and spring and meager amount in summer and fall seasons, also with high evaporation rate. Mean monthly temperature ranges between 16 and 33 °C, the highest temperature record in July is 49 °C and the lowest temperature record in January is 1 °C. Relative humidity ranges below 20% in summer and more than 40% in winter.

Geologically, Al-Madinah region is covered by part of the Arabian Shield that extended over one-third of the Arabian Peninsula. The Shield is composed of sequences of volcanic and sedimentary rocks and a great variety of intrusive sub-volcanic and plutonic rocks. Lava (i.e., Harrats) and sediments from Tertiary and Quaternary ages overlay many parts of the shield. Wadis underneath alluvial deposits filled with sand, gravel and silt deposits (Kemp et al. 1982; Brown et al. 1989).

The data of the 10 rainfall stations was collected for this study from the Hydrology division of the Ministry of Water and Electricity (2016). These 10 rainfall stations (M001, M004, M103, M110, M113, M205, J109, U002, U205, and R202) shown in Fig. 9.1. These rainfall stations were selected based on the following criteria: (1) provide a good spatial coverage; (2) have maximize daily rainfall records; (3) have continuous daily records; and (4) represent different climatic regimes and topographic conditions. The station characteristics are listed in Table 9.1. The maximum 1970–2015 daily rainfall for some stations do not cover the same time intervals and also with about 7% of missing records as shown in
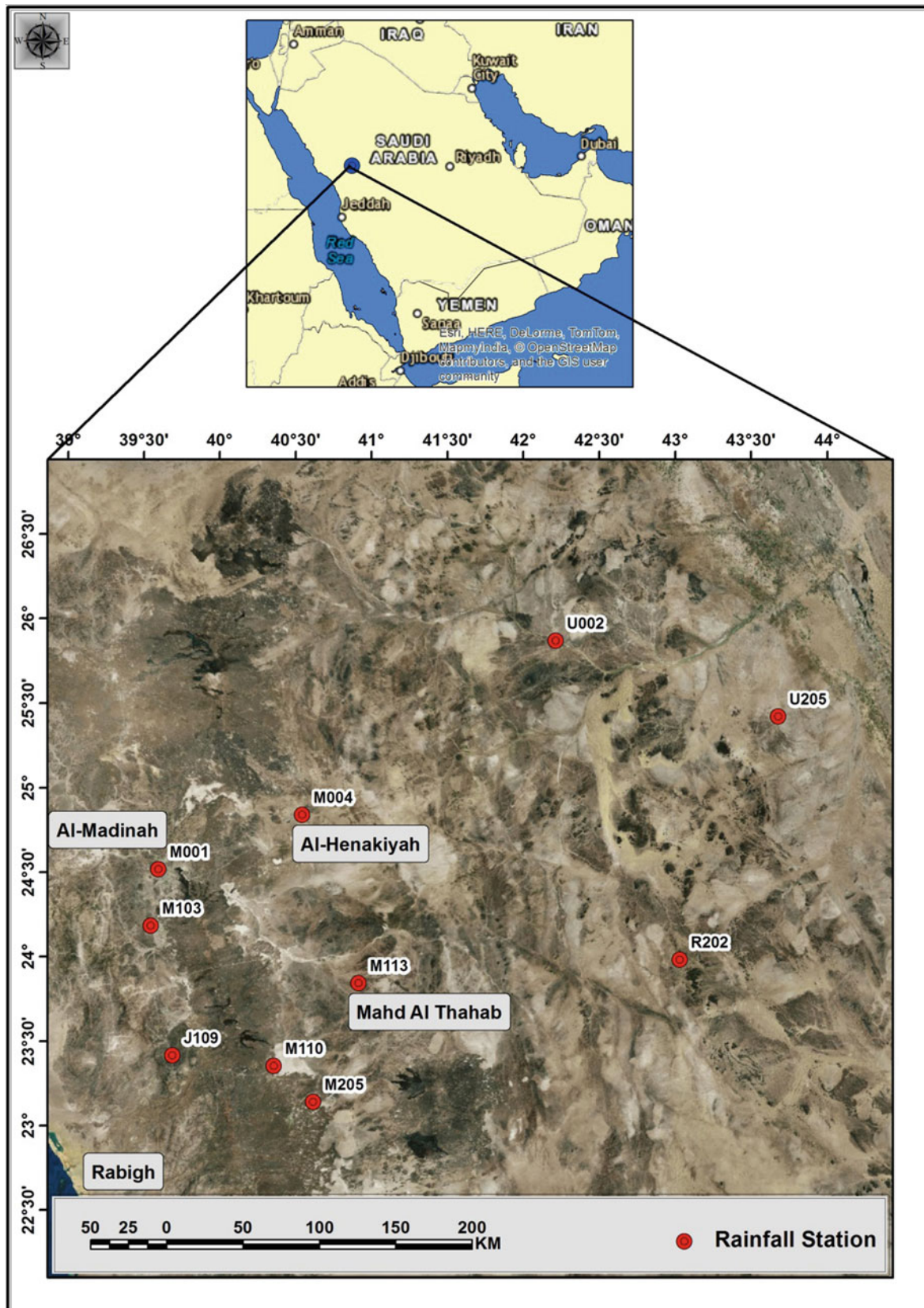
Fig. 9.1 Location map of the study area

Table 9.1 Rainfall stations in Al-Madinah area

| Station name	Station code	Longitude easting	Latitude northing	Altitude (masl)
Al-Madinah	M001	39.58333	24.51667	600
Al-Henakyyah	M004	40.51667	24.83333	855
Abar-Almashi	M103	39.53333	24.18333	660
Swergyah	M110	40.31667	23.34885	900
Mahd-Adahab	M113	40.86667	23.83333	915
Safinah	M205	40.56667	23.13333	930
Al-Faqeer	J109	39.66777	23.41667	690
Uqlat-Alsoqor	U002	42.18333	25.83333	785
Dokhnah	U205	43.61667	25.34925	845
Afif	R202	42.93333	23.93333	1050

**Table 9.2** Annual maximum daily rainfall records with missing periods
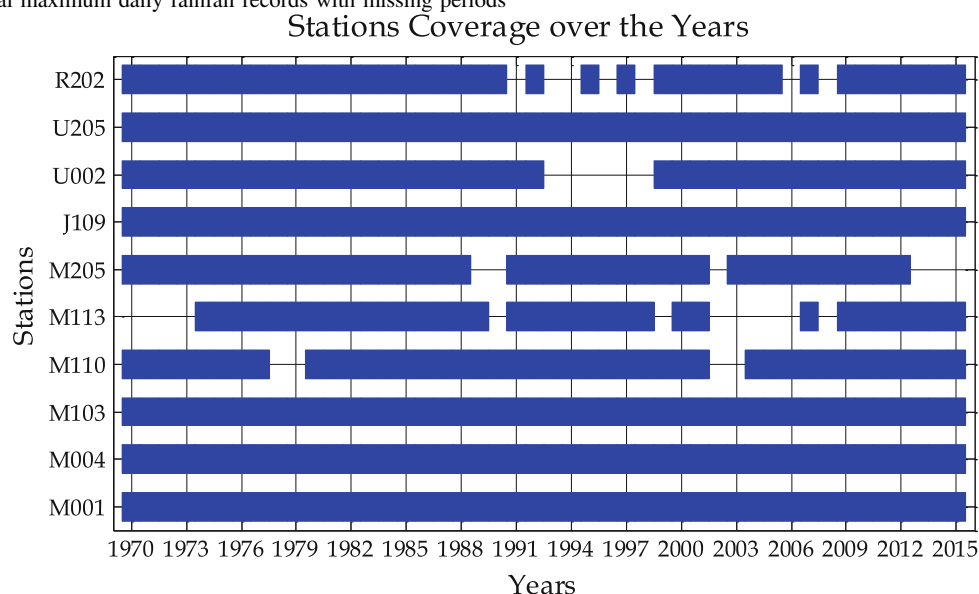
Table 9.2. The stations with missing records are R202, U002, M205, M113 and M110, however the gaps are very short comparing to the total length of records.

The mean monthly rainfall distribution in Al-Madinah area, over the period of 1970–2015, is illustrated in Fig. 9.2. For two stations M001 and M004, rainfall events usually occurs in January, March, April and November in order to give an indication of the large degree of variation reflecting the extreme nature of occurrence and amounts. However, most of extreme events occurred in March and April followed by November. Similar trend was observed for M103 station located at the south with the lowest amount. Stations M110, M113 and M205 located at the southwest of the area received the highest amount of rainfall in April. While station J109 located at the west side received the highest

amount of rainfall in January that may be affected the Red Sea and Mediterranean air mass. The rainfall stations, located in the eastern side of the study area U002, U205 and R202 usually received a considerable amount of rainfall in March and April followed by November.

The mean seasonal spatial and temporal variation of rainfall during winter season (December to February) is associated most of the time with moist cold air of northerly Mediterranean origin, coupled with the local effects of the Red Sea convergence zone and the orographic effect. Figure 9.3a indicates that the amount of 20 mm is exceeded in the southwest of the area due to the relatively high altitude, while the Mahd Adhab area received only 10 mm due to its lactation in shadow area. In spring (March to May), the whole region comes under the influence of air stream the

Fig. 9.2 Mean monthly rainfall in Al-Madinah area

(a) (Winter rainfall, mm)

(b) (Spring rainfall, mm)

(c) (Summer rainfall, mm)

(d) (Fall rainfall, mm)
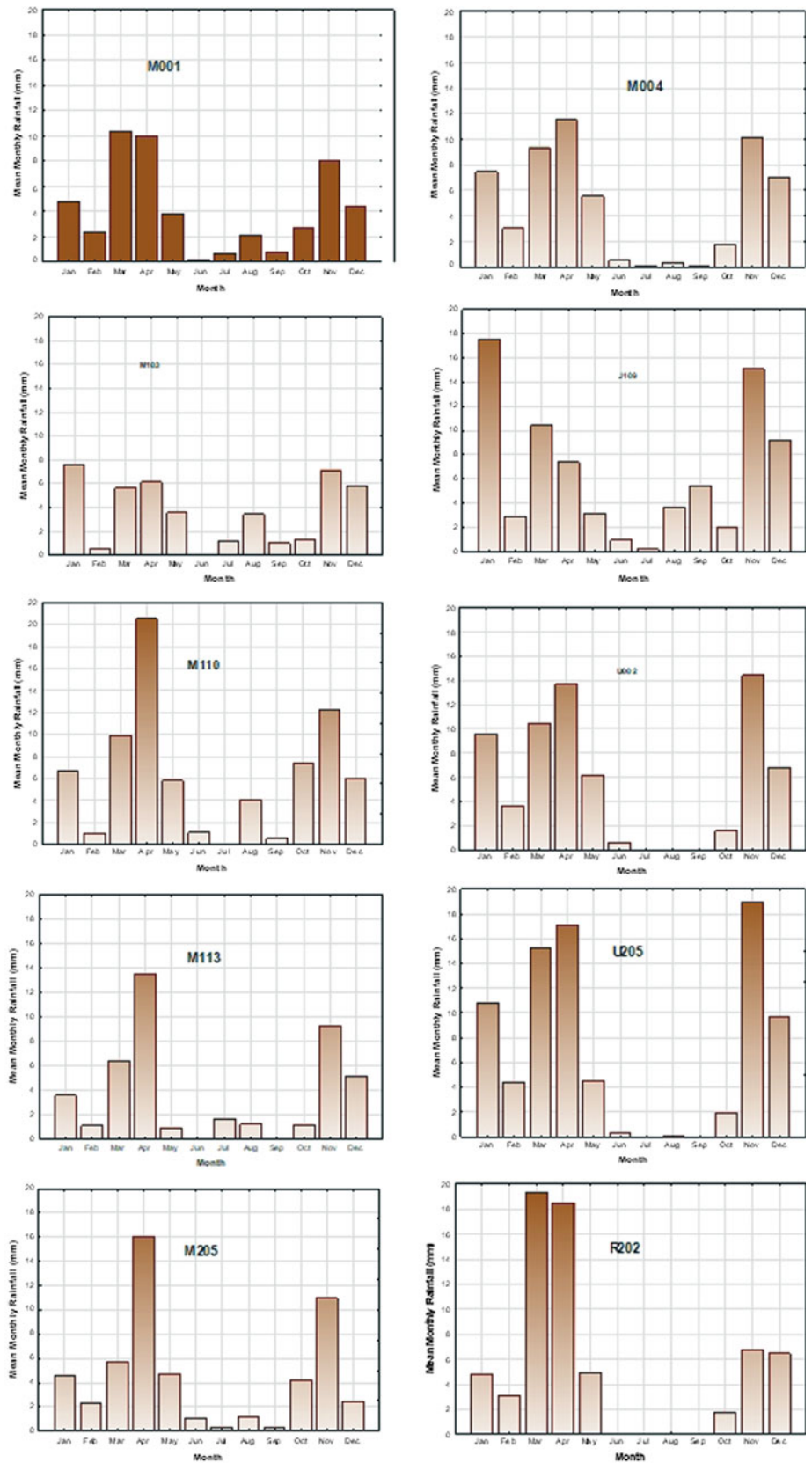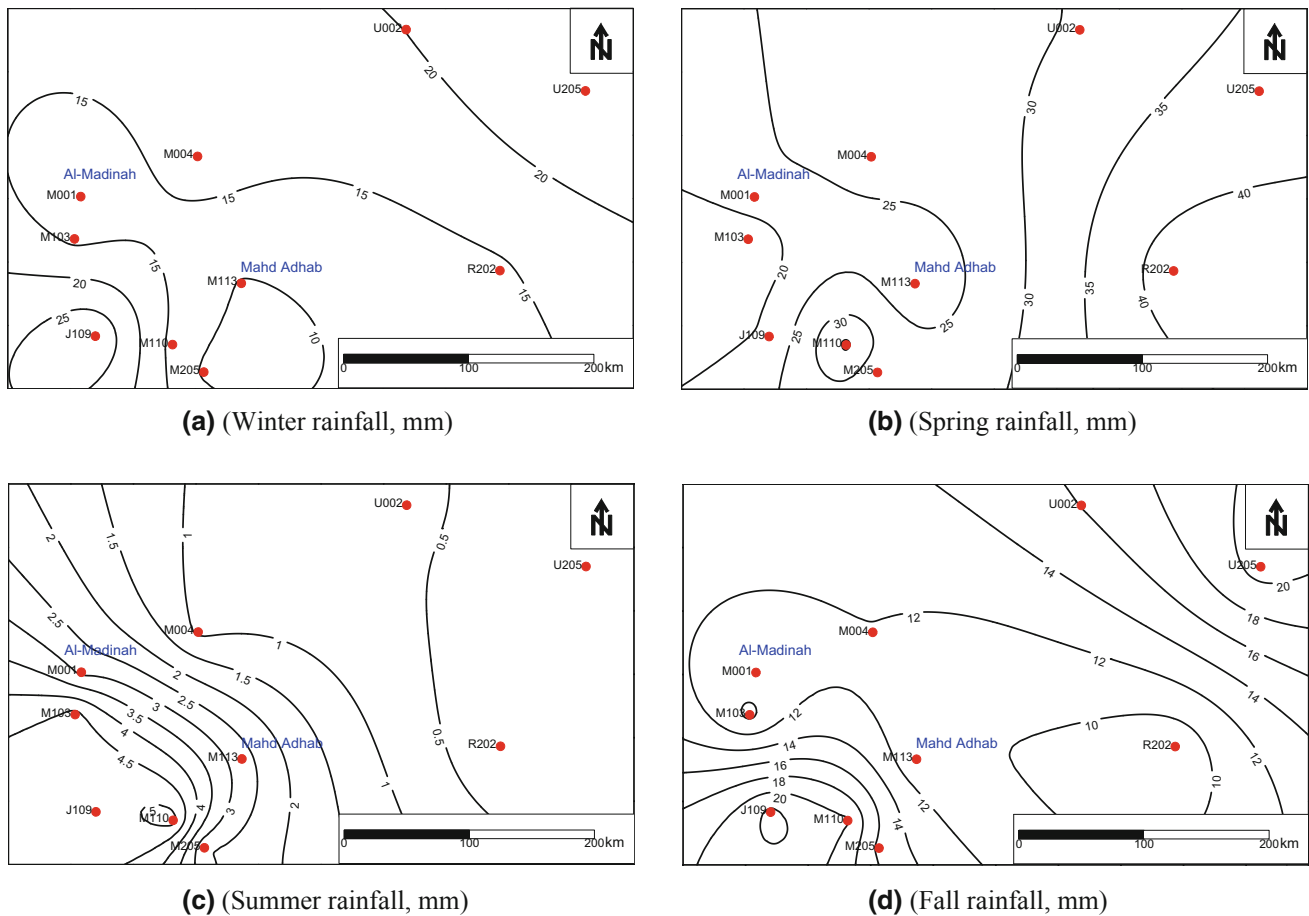
Fig. 9.3 Mean seasonal rainfall variation in Al-Madinah area (mm, 1970–2015)

convergence Red Sea zone and Mediterranean depression as shown in in Fig. 9.3b where the spring rainfall increases gradually from the west (20 mm) to the east (40 mm). Generally, the area received the highest amount of rainfall during spring season compared with other season. The reported high amount of rainfall may be attributed to increasing the effect of African-Mediterranean interaction. In summer (June to August), the rainfall in this dry season is shown in Fig. 9.3c which ranges between 0.5 and 5 mm. Fall season (September to November) represents a dry season associated the transition period from summer to winter except the end of November where the highest amount and extreme events of rain are falling during this month as shown in Fig. 9.3d.

9.3 Methodology

9.3.1 Missing Record Estimation Techniques

According to Şen (2009), the temporal correlation is not clearly defined due to the high variability in the time sequence record. The spatial interpolation dependency can be achieved through the application of two widely used methods, the Inverse Distance Weighted (IDW) and Kriging methods. IDW provide a versatile and easy to understandable technique, and to a certain extend accurate under a wide range of conditions. During spatial interpolation, data are weighted according the influence if distance between points (Davis 2002). Using this method, the property at each unknown location for filling, can be given as follows.

$$x_i = \frac{\sum_{i=1}^{n} \frac{z_i}{d_i^2}}{\sum_i^n \frac{1}{d_i^2}} \tag{1}$$

where x_i is the interpolated value (filling data), z_i is the data value, d_i the distance between x and each data point and n is the number of sample locations. Table 9.3 shows the distances between rainfall stations in decimal degree.

Kriging is an optimal interpolation technique, which is used to estimate the value at an unsampled location. The Kriging is a linear combination estimator for the value of a variable $Z(x_0)$ at a location x_0, where there is no observation (missing value). The expression takes the form

Table 9.3 Distance between stations (decimal degree)

	M001	M004	M103	M110	M113	M205	J109	U002	U205	R202
M001	0.0									
M004	0.99	0.0								
M103	0.34	1.18	0.0							
M110	1.38	1.50	1.14	0.0						
M113	1.45	1.06	1.38	0.73	0.0					
M205	1.70	1.70	1.47	0.33	0.76	0.0				
J109	1.11	1.64	0.78	0.62	1.24	0.91	0.0			
U002	2.91	1.94	3.12	3.11	2.39	3.15	3.47	0.0		
U205	4.12	3.14	4.25	3.86	3.14	3.77	4.37	1.51	0.0	
R202	3.40	2.58	3.41	2.68	2.07	2.50	3.27	2.04	1.57	0.0

$$\hat{Z}(x_0) = \sum_{i=1}^{N} \lambda_i Z(x_i), \quad i = 1, 2, \ldots, N \qquad (2)$$

where λ_i are the Kriging weights which need to be estimated under two conditions, which are unbiasedness and the minimum estimation variance (Subyani 2004; Şen 2009).

To test the validity of the chosen method, cross-validation is used to compare the relative quality of IDW and Kriging gridding methods, root-mean-square error (RMSE) is widely acceptable measure of accuracy and compared between different interpolation methods. In general, best estimation for missing values with minimum RMSE is IDW method. Even if the value of RMSE is minimum in Kriging method, the interpolated values are more or less the same as IDW method. The results of filling missing data will be used for frequency analysis using Gamma and General Extreme Value (GEV) distributions. Figure 9.4 illustrates flowchart of the major steps of the methodology of this study.

9.3.2 Rainfall Frequency Analysis

Based on the scientific and technical experiences in arid regions (Şen 2008; Hassan and Ping 2012), two frequencies, namely, the Gamma and GEV distributions were selected to evaluate the annual maximum daily rainfall for the 10 stations. The suitability of the distributions is evaluated by the application of the goodness of fit tests as Kolmogorov-Smirnov (KS) and the Chi-Square tests. The selected distributions are briefly discussed as followed.

9.3.2.1 Gamma Distribution

Gamma distribution function can take three different types of I, II and III parameters which sometimes are referred to as the family of Pearson Type III distributions. The distribution continuous random variable x of the probability density function takes the forum of:

$$f(x) = \frac{1}{\beta^{\alpha} \Gamma(\alpha)} x^{\alpha - 1} e^{-\frac{x}{\beta}}; \quad x, \alpha, \beta \geq 0 \qquad (3)$$

The variable x has 2-parameters Gamma distribution, with the shape parameter α and β is the scale parameter (Hosking and Wallis 1997). Using 1-parameter gamma distribution in hydrology is limited due to its relative inflexibility in fitting, but 2 or 3 parameters Gamma distributions are commonly used and no significant advantage in the-3-parameter Gamma usage compared to the 2-parameter gamma (Aksoy 2000). It is also found that the Gamma distribution is very suitable for rainfall series in arid regions (Şen and Eljadid 1999; Şen 2008).

9.3.2.2 Generalized Extreme Value (GEV)

The GEV distribution can take the form of three types of distributions the Gumball, Frechet and Weibull distributions depending on selection of the shape parameters. The GEV distribution continuous random variable x of the probability density function takes the form:

$$f(x) = 1/\sigma \exp[-(1 + \kappa((x - \mu)/\sigma)]^{\uparrow}(-1/\kappa)$$
$$\left[\left[[1 + \kappa(x - \mu)/\sigma]^{\uparrow}(-1 - 1/\kappa)\right]\right]; \quad \kappa \neq 0 \qquad (4)$$

where κ is shape, σ is scale and μ is location parameters. According to Cunnane (1988) and Millington et al. (2011), GEV distribution is very appropriate for water resources applications including rainfall time series.

The goodness of fit criteria is usually used to check how well frequency distribution fits a set of observations. The Kolmogorov-Smirnov (KS) and Chai Square (χ^2) tests were selected for the goodness of fit in this study. These tests can describe the differences between observed and expected values from the suggested distribution. In order to use the selected distributions for flood and water resources design projects for extreme rainfall events, further statistical approach such as PMP technique is applied to the study area.
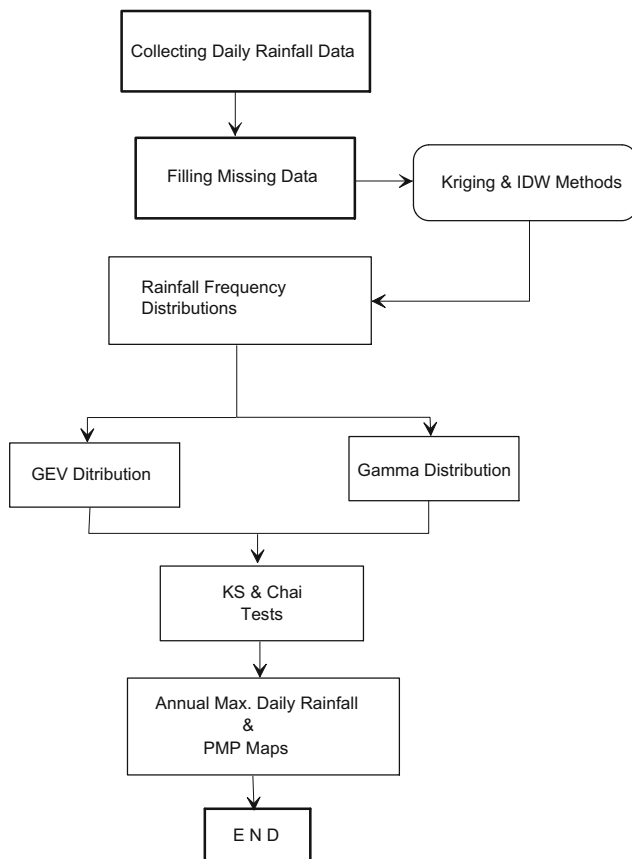
Fig. 9.4 Flowchart for major steps for this study

9.3.3 Probable Maximum Precipitation (PMP-24 h)

In the design and analysis of such water resource structures, Probable Maximum Precipitation (PMP) can used to be the greatest rainfall rates for specific duration at a particular geographic location. Statistically, PMP for specific return period can be estimated as follow:

$$PMP = \bar{p} + K_T \sigma_x \qquad (5)$$

where $\bar{p}$ is the mean annual maximum 24-h rainfall depth, σ_x is standard deviation of the series and K_T is a frequency factor depending on the type of distribution (herein Gamma and GEV distributions), with frequency factor number estimated from readily tables in the literature depending of years of records or the return periods (Aksoy 2000).

9.4 Results and Discussion

The IDW and Kriging techniques were applied to estimate the missing rainfall information for five stations namely R202, U002, M205, M113 and M110 (Table 9.2). These

stations are located in the eastern side of the study area. The application of the two estimation techniques required the establishment of a decimal degree distance grid between stations as shown in Table 9.3. The two estimation techniques were applied to fill the missing information. The completed rainfall data set was used to arrive at the selection of the appropriate probability distribution functions to predict the rainfall depth for different frequencies. Table 9.4 shows the use of IDW and Kriging methods for filling missing of annual maximum daily rainfall for each station with RMSE values. From this table, in general, the best estimation for missing values with minimum RMSE is IDW method. Even if the value of RMSE is minimum in Kriging method, the interpolated values are more or less the same as IDW method as shown in Table 9.4.

The analysis initially focused on the estimation of the statistical parameters of the annual maximum daily rainfall depths for the 10 stations for a 46 years record that included the missing information for five stations. Descriptive statistics for all stations are shown in Table 9.5. The mean daily rainfall depth ranges from 18 to 29 mm with the lowest value for station M205 and the highest for station J109. With positive skew and all stations are approximately log-normally distributed.

The GEV and Gamma distributions frequency analysis was implemented and the station descriptive statistical characteristic in order to fit each of the data series to a probability density function. The distributions are used for the prediction of maximum one day for 100, 200, 300, 400, 500 and 1000-year return periods. According to the goodness of fit (K-S and Chai Square tests), the GEV distribution is suitable for few stations record while others abide by the Gamma distribution. Accordingly, GEV distribution give a better fit the data set of seven stations (M001, M004, M103, M110, M113, M205 and R202), where Gamma distribution for three stations (U205, J109 and U002) as shown in Figs. 9.5 and 9.6, respectively. The two distributions fit the lower values of rainfall depth than the higher values.
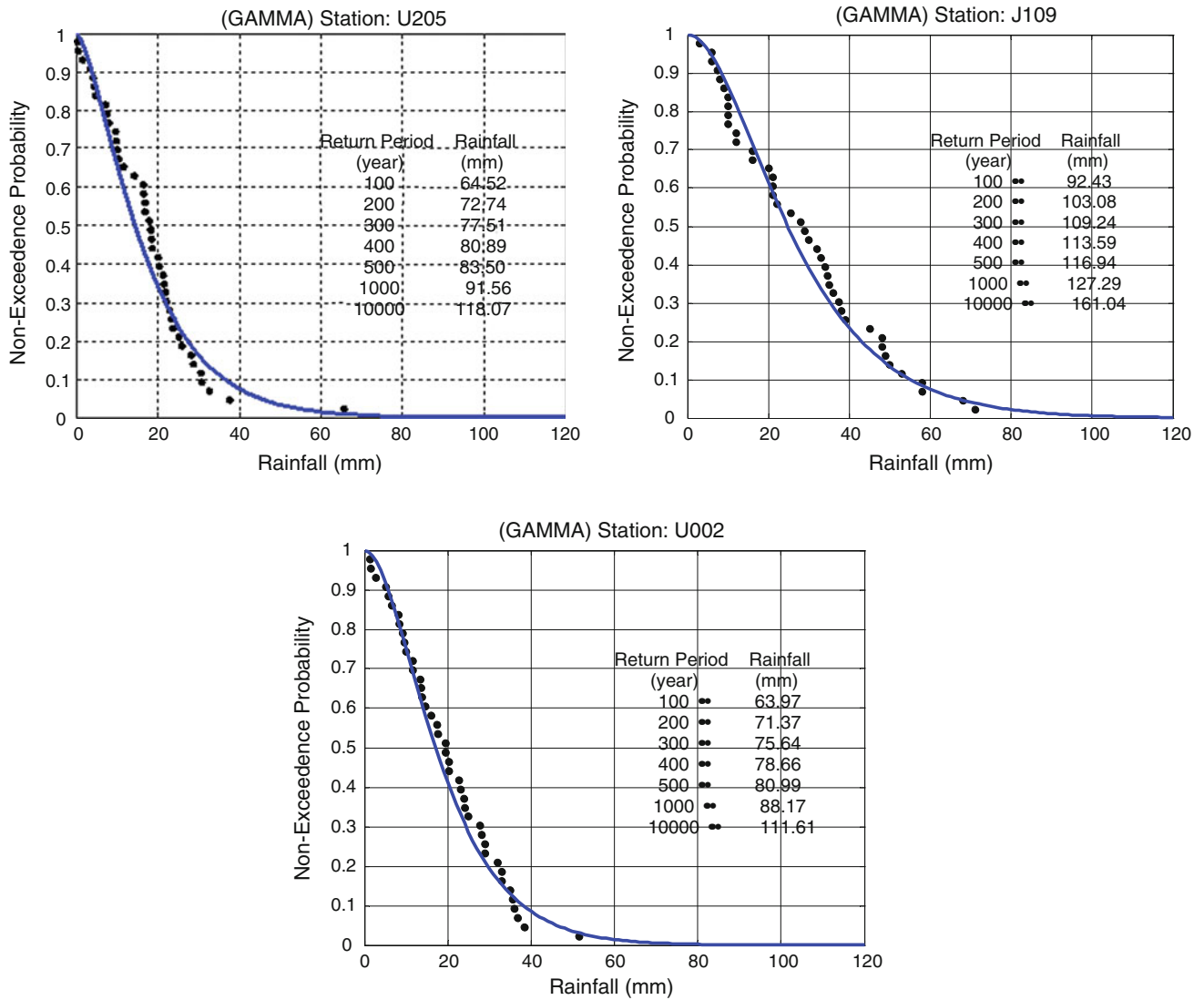
The Gamma distribution degree of fit differs among three stations with the best provide a good best fit for station U002 located at the far east end of the Al-Madinah region and minor deviation for stations U205 at the range 15–21 mm and at the range of 20–40 mm rainfall depths for station J109. The 100 years flood frequencies for stations U205 and U002 reported a similar rainfall depths of about 64.0 mm while for station J109 higher value was estimated at 92.4 mm as shown in Fig. 9.5. The same trend for higher return period is observed for the two stations U205 and U002. Station J109 indicated a high rainfall depth almost 50% higher than the other station and careful consideration should be given to this location which is close to the Red sea coast with major urban development.

Table 9.4 Comparison results between inverse distance and kriging methods for missing data estimation

Year	Inv. dist	RMSE	Kriging	RMSE
M110				
1978	15.9	12.7	25.6	12.8
1979	22.3	22	21	19.6
2002	25.8	32.2	22	34.8
2003	10.1	10.1	9.9	10.2
M113				
1970	15.3	16.6	17	17.3
1971	35	32.5	28	30.9
1972	22.3	27.9	30.7	29
1973	7.1	8.9	7.45	8.5
1990	16.1	13.8	13.25	13.3
1999	20.9	26.6	24.6	26.8
2002	24.9	32.2	20.4	32.3
2003	9.8	10.1	8.3	10.7
2004	20.6	21.2	21.9	21.8
2005	27.8	34.2	27.1	31.2
2005	19.3	18.1	25.5	21.4
2008	16.3	21.8	23.8	24
M205				
1989	21.5	17.2	21.5	17.1
1990	22.3	13.8	17.8	13.4
2002	26	32.2	26.7	30
2014	19	16.1	18	15
2015	15	17.1	17	21
U002				
1993	36	39.3	37.6	39.1
1994	14.7	13.9	25.3	14.2
1995	33	33.7	33	33.5
1996	20.3	23.2	21.4	22.2
1997	35	33	35.5	33.6
1998	23	22.8	22.5	22.7
R202				
1991	16.7	17.3	17	17.4
1993	33	40	38	39.5
1994	13	13.9	13.6	14.6
1996	22	40.3	21.3	41
1998	24.1	22.3	22.1	22.5
2006	15.3	23.5	28	24
2008	31.9	22.4	27	23.4

Table 9.5 Statistical parameters of annual maximum daily rainfall of Al-Madinah area

	M001	M004	M103	M110	M113	M205	J109	U002	U205	R202
Min	1.4	0.0	0.0	2.3	0.0	0.4	3.0	1.4	0.0	0.0
Max	89.6	63.8	57.0	86.3	85.0	65.6	71.0	51.6	85.8	82.0
Mean	22.7	20.3	21.0	23.7	19.4	17.4	28.5	19.4	22.7	19.7
Median	17.8	17.1	20.0	22.0	18.0	16.9	26.8	17.6	20.0	14.2
Std	18.7	13.9	12.7	15.1	13.2	11.7	18.0	11.4	16.9	18.9
CV	0.8	0.7	0.6	0.6	0.7	0.7	0.6	0.6	0.7	1.0
Skew	2.0	1.4	1.0	1.8	2.7	1.5	0.6	0.6	1.6	1.7

Fig. 9.5 Annual maximum daily rainfall with gamma distribution

(GEV) Station: M001

Return Period (year)		Rainfall (mm)
100	•	107.18
200	•	133.70
300	•	151.54
400	•	165.38
500	•	176.84
1000	•	216.96
10000	•	415.82

(GEV) Station: M004

Return Period (year)		Rainfall (mm)
100	•	74.77
200	•	88.17
300	•	96.65
400	•	102.98
500	•	108.07
1000	•	124.99
10000	•	195.26

(GEV) Station: M103

Return Period (year)		Rainfall (mm)
100	•	57.74
200	•	63.58
300	•	66.93
400	•	69.27
500	•	71.07
1000	•	76.58
10000	•	93.97

(GEV) Station: M110

Return Period (year)		Rainfall (mm)
100	•	74.30
200	•	83.98
300	•	89.78
400	•	93.96
500	•	97.23
1000	•	107.63
10000	•	144.62

(GEV) Station: M113

Return Period (year)		Rainfall (mm)
100	•	61.05
200	•	68.61
300	•	73.09
400	•	76.29
500	•	78.79
1000	•	86.66
10000	•	113.84

(GEV) Station: M205

Return Period (year)		Rainfall (mm)
100	•	55.05
200	•	61.41
300	•	65.12
400	•	67.75
500	•	69.78
1000	•	76.09
10000	•	96.92

(GEV) Station: R202

Return Period (year)		Rainfall (mm)
100	•	129.84
200	•	171.74
300	•	201.48
400	•	225.35
500	•	245.62
1000	•	319.94
10000	•	752.35

Fig. 9.6 Annual maximum daily rainfall with GEV distribution

Table 9.6 Maximum observed and predicted of GEV distribution for selected return periods based on 24-h duration

	Max. observed	100 year	200 year	500 year
M001	89.6	107.2	133.7	173.8
M004	63.8	74.8	88.2	108.1
M103	57.0	57.7	63.6	71.0
M110	86.3	74.3	84.0	97.2
M113	85.0	61.0	68.6	78.8
M205	65.6	55.1	61.4	69.8
J109	71.0	85.0	94.1	105.9
U002	51.6	51.3	55.2	59.8
U205	85.8	88.8	106.8	134.4
R202	82.0	129.8	171.7	245.6

The GEV distribution provided a good fit for seven stations namely M001, M004, M103, M110, M113, M205, and R202 (Fig. 9.6). Appropriate fits are achieved for all stations M103 and M113 at the range of 30–40 mm rainfall depths. The return period for the 100 years rainfall is low for three stations M103, M113 and M205 with values ranges of 51.2–57.7 mm depths in comparison to the higher values for two stations M001 and R202 ranging from 107.2 to 129.8 mm, respectively. Similar trend was observed for the remaining high return periods up to 1000 years.

Following the selection of the appropriate distribution the probable maximum precipitation (PMP) depth for 24-h period was estimated for different return periods. The estimates of PMP values for the selected probability distribution function are presented. Table 9.6 shows the values of maximum observed annual daily rainfall and GEV distribution for all stations with 100, 200, and 500-year return periods. Figure 9.7 shows the PMP estimates for 100–200 and 500 year return periods, which indicate increase in the rainfall depth over study area with return period increase. In general, regarding to stations locations, at the east-west direction at 23.5 latitude level, the daily rainfall for 100-year has almost stable level until 41.5 longitude, but towards the east from this point onwards, there is a steadily increasing rainfall trend reaching to 125 mm around the station R202. Such a regional trend reaches slightly over 25.5 latitude. Then, towards the north a reverse but weaker trend appears as decreasing from the west towards the east. On the other hand, along the north-south directions the most daily PMP appears near the eastern part of the study area. For 100-year return period, the area can be ranked into three subareas.

(1) The most risky sub-area is in the south eastern corner,
(2) The second risky region appears at the north western corner,
(3) The south western and north eastern regions have the least risky locations.

With 200-year return period, the area has almost the same three risky locations and trends. The only difference is in the rainfall amounts, which are expected to yield higher rainfall amounts. As for the 500-year return period, the daily rainfall amounts the same pattern of risk sub-areas are existing and the rainfall increases rapidly with the same pattern of previous return periods. Finally, for any engineering or mining activity that might be exposed to rainfall amounts, the south eastern part quantities are recommended for any basic project calculations.

9.5 Conclusion

In this research, the study of the observed daily rainfall series available for Al-Madinah region are investigated over the period of 1970–2015 (46 years) for 10 stations to evaluate the regional monthly and seasonal rainfall variability. Annual maximum daily rainfall has been performed after filling some of the missing data by spatial interpolation techniques such as inverse-distance-weight (IDW) and Kriging methods. The best fitting distribution to all stations for the annual maximum daily rainfall is selected for comparing two distributions, namely, Gamma and GEV distributions. Gamma probability distribution function fits few

Fig. 9.7 PMP 24 h rainfall for 100, 200 and 500 years return period
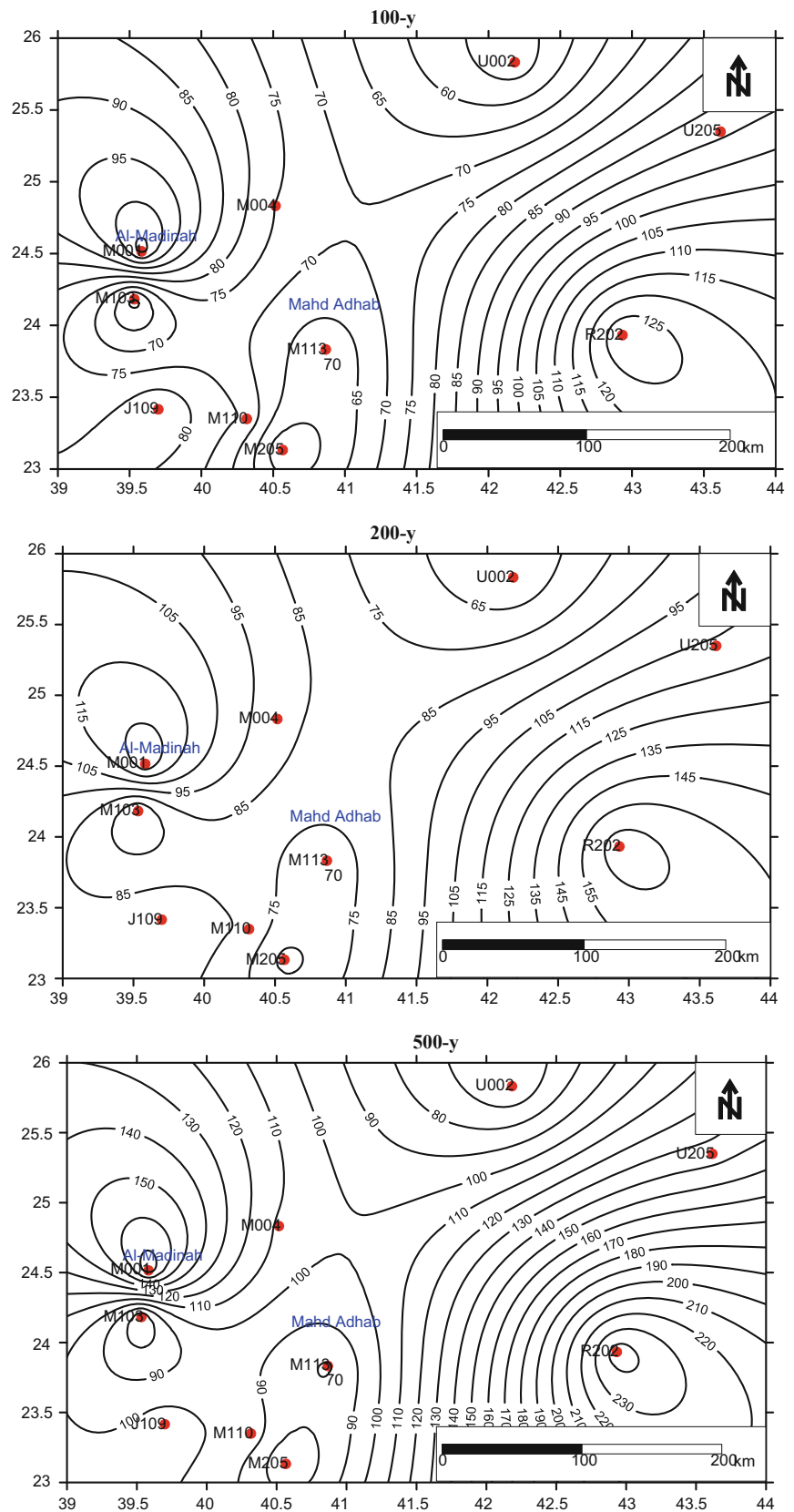
stations and GEV distribution for others. These distributions estimate the maximum rainfall depth for different return periods of 100-year to 10,000-year. Trend in rainfall depth was observed for high return periods. In addition, risky sub-areas have been investigated through different return periods. Probable Maximum Precipitation (PMP) is also performed for different return periods on the basis of 24-h maximum annual amounts. Finally, the proposed approach needs to be further tested in other region of Saudi Arabia with similar characteristics to Al-Madinah region.

References

Abdulrazzak MJ, Sorman A, Onder K, Al-Sari A (1995) Flood estimation and impact: southwestern region of Saudi Arabia. King Abdulaziz City for Science and Technology, Project No. ARP-10-51, Riyadh, Saudi Arabia

Aksoy H (2000) Use of gamma distribution in hydrological analysis. Turk J Eng Environ Sci 24:419–428

Al-Ahmadi FS (2014) Evaluation of the best fit distribution for partial duration series of daily rainfall in Madinah, West of Saudi Arabia. In: Evolving water resources system: understanding, predicting and managing water-society interactions, Proceedings of ICWRS 2014, Bologna, Italy, June 2014 (IAHS Publ. 364, 2014)

Al-Jerash M (1989) Data for climatic water balance. Scientific Publishing Center, King Abdulaziz University, Jeddah, Saudi Arabia

Brown GF, Schmidt DL, Huffman Jr AC (1989) Geology of the Arabian Peninsula, shield area of western Saudi Arabia. USGS professional paper, 560-A

Cunnane C (1988) Methods and merits of regional flood frequency analysis. J Hydrol 100:269–290

Davis J (2002) Statistics and data analysis in geology, 3rd edn. Wiley, New York

De Silva RP, Dayawansa ND, Ratnasiri MD (2007) A comparison of methods used in estimating missing rainfall data. J Agric Sci 3 (2):101–108

El-Khatib A (1980) Seven green spikes. Ministry of Agriculture and Water, Riyadh, Kingdom of Saudi Arabia

Filho WL (2012) Climate change and the sustainable use of water resources. Springer, New York

German Consult (1979) Investigation and detailed studies for the agricultural development of South Tihama. Final report and preliminary design for Ministry of Agriculture and Water, Riyadh, Saudi Arabia

Hassan GB, Ping F (2012) Regional rainfall frequency analysis for the Luanhe Basin—by using L-moments and cluster techniques. APCBEE Proc 1:126–135

Hershfield DM (1961) Rainfall frequency atlas of the United States for durations from 30 minutes to 24 h and return periods from 1 to 100 years. Weather Bureau. Technical paper no. 40. US Weather Bureau, Washington, DC

Hosking JR, Wallis JR (1997) Regional frequency analysis: an approach based on L-moments. Cambridge University Press, Cambridge, UK

Isaaka E, Srivastava R (1989) An introduction to applied geostatistics. Oxford University Press, New York

Kemp J, Gros Y, Prian J (1982) Geologic map of the Mahd Adh Dhahab Quadrangle. Sheet 23 E, Deputy Ministry for Mineral Resources, Kingdom of Saudi Arabia, Jeddah

Millington N, Das S, and Simonovic S (2011) The comparison of GEV, Log-Pearson Type 3 and Gumbe l distributions in the Upper Thames River watershed under global climate models. Report No. 77. The University of Western Ontario, Canada

Ministry of Water and Electricity (2016) Climate data reports. Hydrology Division, Riyadh, Saudi Arabia

Nouh MA (2006) Wadi flow in the Arabian Gulf states. Hydrol Process 20:2393–2413

Saudi Arabian Dames and Moore (1988) Ministry of Agriculture and Water. Water resources development. Al-Lith Basin, Final report, vol E

Schlumberger Water Services (2012) Hydrological assessment report. Detailed water resources studies of western coastal plain of Saudi Arabia. Ministry of Water and Electricity, Riyadh, Saudi Arabia

Şen Z (1983) Hydrology of Saudi Arabia. In: Symposium on water resources in Saudi Arabia. King Saud University, Riyadh, pp A68–A94

Şen Z (2008) Wadi hydrology. CRC Press, New York

Şen Z (2009) Spatial modeling principles in earth sciences. Springer, New York

Şen Z, Eljadid A (1999) Rainfall distribution function for Libya and rainfall prediction. Hydrol Sci J 5(44):665–680

Sogreah (1968) Water and agricultural development survey for area IV. Final report. Ministry of Agriculture and Water, Riyadh, Saudi Arabia

Şorman A, Abdulrazzak MJ, Onder, H (1991) Analysis of maximum flood events and their probability functions under arid climate conditions in Saudi Arabia. In: International hydrology and water resources symposium, Perth

Subyani AM (2004) Geostatistical study of annual and seasonal mean rainfall patterns in southwest Saudi Arabia. Hydrol Sci J 49:803–817

Subyani AM, Qari MH, Matsah ME, Al-Modayan AA, Al-Ahmadi FS (2009) Utilizing remote sensing and GIS techniques to reduce hydrological and environmental hazards in some wadis, Western Saudi Arabia (Jeddah-Yanbu), Project No. APR 25/101. King Abdulaziz City for Sciences and Technology

Subyani AM, Al-Ahmadi FS (2011) Rainfall-runoff modeling in Al-Madinah area of western Saudi Arabia. J Environ Hydrol 19:1

Subyani AM, Al-Amri NS (2013) Hydrological study of Jabal Sayid project. Final Report. Bariq Mining Ltd., Jeddah, Saudi Arabia

Tabios G III, Salas JD (1985) A comparative analysis of techniques for spatial interpolation of precipitation. Water Res Bull 21(3):365–380

WMO (2008) Guide to hydrological practices. In: Volume I: hydrology —from measurement to hydrological information. World Meteorological Organization No. 168, Geneva

Hydrochemical Assessment of Groundwater Within the Lower Wadi Ranyah, Western Saudi Arabia Using Multivariate Statistical Technique

Hassan A. Saleem, Mohammed O. Alharbi, and Ali M. Subyani

Abstract

Wadi Ranyah is located in arid region of Western mountains of Saudi Arabia, which is a highly potential resource of both surface and groundwater. This shallow aquifer is highly demanding and it is subjected to intense exploitation due to the influence of human activities. The lower part of Wadi Ranyah undergoes increasing salinity and significant decline in water level. Therefore, how these processes impact groundwater quality. Multivariate statistical methods, Piper diagram and sodium adsorption ratio employed in this paper. A collection of 18 groundwater samples are analyzed for a total of 26 variables for both major and trace elements for groundwater assessment. Results showed that Piper diagram were used revealing water chemistry is of Calcium-Bicarbonate type. R- and Q-modes of cluster analysis illustrate rock interaction and human activities as two distinctive sources of water quality. Three main principal components influenced the water chemistry in Wadi Ranyah. In addition, salinity increases with HCO_3, SO_4, Cl and Ca for drinking water.

Keyword

Ground water chemistry • Multivariate analysis • Wadi Ranyah • Saudi Arabia

10.1 Introduction

Saudi Arabia is considered to be one of the most arid areas in the Middle East. Therefore, the total reliance is on the groundwater as a fundamental natural source for drinking and various agricultural and industrial activities with the scarcity of rainfall.

Water quality is also very important factor that influences negatively sustainable human life. Researches on groundwater quality assessment have been increased due to the impact of human activities. The early studies of visualized water types started by a graphical representations of the chemistry of water (Piper 1944; Stiff 1951; Hem 1989). These techniques were useful for classifying water quality groups and visually describing the major water constituents. With increasing information about hydrochemical properties of groundwater, statistical techniques were implemented for analyzing and interpreting of hydrochemical data (Suk and Lee 1999; Sanchez-Martos et al. 2001; Woocay and Walton 2008). Cluster analysis (CA) and principal component (PC), are multivariate techniques that used for manipulating, interpreting and presenting water chemistry data, and also reveals a hidden information that cannot be detected from visual observations (Davis 2002; Hussain et al. 2008; Belkhiri et al. 2011).

Several studies have been involved to investigate the groundwater quality in shallow aquifers using multivariate statistical methods. According to a research done by Shihab and Abdul Baqi (2010), which focus on the groundwater quality in Makhmor, Iraq, using multivariate analysis to investigate the relationship among groundwater quality and to classify the wells according their quality. The study found that in deep wells one factor account for more than 50% of the variance among water quality.

Another study done by Yidana et al (2010) found that the groundwater salinity of the shallow unconfined aquifer of Keta, Ghana is largely attributed to minerals and sea water intrusion, the results show that Kaolinite and Na field is stable in groundwater. Also, waste discharge and agriculture are impacting on the water quality. Four clusters analysis are recognized in their study; cluster 1 and 4 are low salinity water type (Ca–HCO_3). Cluster 2 and 3 represent high and intermediate salinity water type (Na–Cl). The investigation done by two types of analysis used to investigate the relationship of the data: Q-mode groups the samples based on their similarities and dissimilarities as a function of the wells location, R-mode classify parameters using the same technique.

H. A. Saleem (✉) · M. O. Alharbi · A. M. Subyani
Department of Hydrogeology, King Abdulaziz University, Jeddah, Saudi Arabia
e-mail: hassansaleem32@gmail.com

A. M. Subyani
e-mail: asubyani@hotmail.com

Yang et al (2016) used major ions ratio and corresponding analysis to investigate the possible sources of pollution in Salawusu aquifer system of Ordos Basin in China. They used the monitored data in 2004 and 2014 before and after coal mining activities. Subyani and Al Ahmadi (2010) focused on the upstream water quality of Wadi Ranyah. R-mode cluster analysis on 22 samples revealed two main sources affecting water quality groundwater-rock interaction, agriculture and anthropogenic sources. In addition, 70% of data variability were explained by three components.

It is very useful to understand the natural and human impacts to environmental by assessment of groundwater quality. The present study attempts to apply multivariate statistical analysis for characterizing the hydrochemical facies of groundwater system in order to differentiate the main processes that affect groundwater chemistry and hydrochemical types in groundwater situated in Wadi Ranyah, Western Saudi Arabia.

10.2 Hydrology and Geology of the Study Area

Western Saudi Arabia receives a good amount of rainfall which formed a valuable sources for groundwater on wadis and streams (Şen 1983; Subyani 2004). Wadi Ranyah is one of the major source of groundwater in Al-Baha region. It starts from Al-Baha high lands and goes to the desert after Ranyah city (Fig. 10.1). It covers approximately 2500 km².
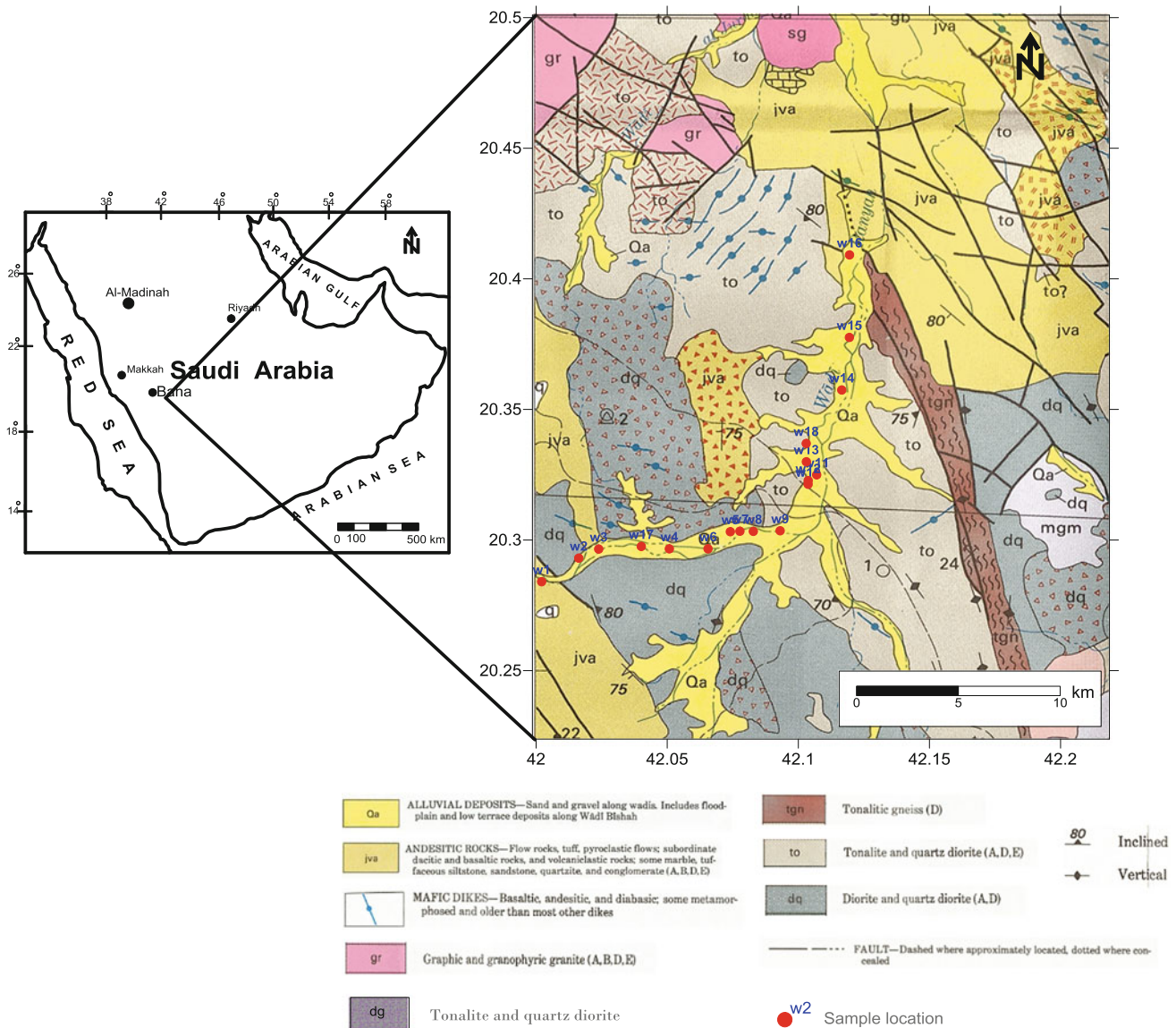

Fig. 10.1 Location map of study area

Climate in the study area is called in winter and warm in summer with obvious seasonal variation of rainfall and temperature with great evaporation. The mean annual rainfall in the upstream of Wadi Ranyah is about 470 mm (Ministry of Water and Electricity 2015). A large part of this amount of rainfall will turn to runoff in the study area. Runoff occurs usually in winter and spring seasons.

Geologically, the study area consists of Precambrian rocks of Baha group, plutonic and hypabyssal intrusive rocks and quaternary alluvial deposits. Jeddah group comprise metavolcanic and metasedimentary such as andesitic rocks (jva) in Fig. 10.1. Plutonic and hypabyssal intrusive rocks consist of mafic dikes, granite (gr), tonalite gneiss (tgn) and diorite (dq). Alluvial deposits consist of sand and gravel (Qa) along wadi tributaries (Simons 1988).

10.3   Materials and Methods

Field investigation for 18 water samples were collected from digging active wells in February 2016. These samples collected from privates and the ministry wells that distributed along the lower part of the wadi. The in situ water parameters include temperature, electrical conductivity (EC), pH and dissolved oxygen. The samples preserved in special bottles for analysis. EC values ranged from 416.0 to 1850 μS/cm and the temperatures between 22 and 32.9 °C. Both majors (Ca, Mg, Na, K, SO_4, HCO_3, Cl and NO_3) and traces (Li, Cr, Mn, Fe, Co, Ni, Cu, Zn, As, Mo, Cd, Ba, Hg, and U) elements were analyzed for each sample in the laboratory of Faculty of Earth Sciences, King Abdul Aziz University. Statistical descriptive, Piper diagram, cluster and PCA analysis techniques are used in this study.

Groundwater facies are identifying using Piper plot (Piper 1944), this diagram is useful for understanding the chemical characters of water in a hydrologic system. This diagram is very useful for isolate the chemical facies of the water (Yang et al, 2016). Gibbs plot is employed in this study to understand the predominant samples fall in the rock–water interaction dominance, evaporation and precipitation dominance field (Kumar et al. 2015).

Cluster analysis is a collection of data that have similarities according to the characteristics found in the data and grouping similar objects (variables or samples) into clusters. These clusters can be visualized as a hierarchical tree as a dendrogram (Woocay and Walton 2008). However, cluster analysis can be visualized in two modes, Q and R-modes. Q-mode is identifying relationships between samples, while R-mode depicts relationships between variables. Euclidean distance and Ward's linkage method (Ward 1963) was used on classification scheme (dendrogram).

Principle component (PCA) is a multivariate statistical visualization method for extracting hidden information from data sets. Theoretically, it is the optimum transform for a given data sets in a least square terms (Usunoff and Guzman 1989; Brown 1998; Ceron et al. 1999). With a new coordinate system, variables were transformed, the first component gets the highest variance, the second component gets the second greatest variance, and so on. In addition, Communality is measuring how well the variance of each variable is described by each factor (Grande et al. 2003; Tabachnick and Fidell 2006).

10.4   Results and Discussion

Tables 10.1 and 10.2 show the statistical summary of the chemical analysis of groundwater for major and trace elements in the study area. The measured parameters compared with water quality standards (WHO 2011; SASO 1984). Most of the water samples parameters are met the standard and the quality of drinking water remains within acceptable national standards. Figure 10.2 shows Piper diagram which illustrate that the groundwater quality is mostly dominated by HCO_3, SO_4, Cl and Ca of maximum concentrations in mg/l of 366, 183, 515 and 176 respectively. These elements are the most constituencies that reflect the salinity of the groundwater.

The sodium adsorption ratio (SAR) is commonly used for sodium hazards associated with an irrigation water supply and refers of Na to Ca and Mg proportion in water. The SAR for the groundwater samples indicating low hazard as shown

Table 10.1 summary of ions of groundwater samples in Wadi Ranyah

Parameter	Ca (mg/l)	Mg (mg/l)	Na (mg/l)	K (mg/l)	SO₄ (mg/l)	HCO₃ (mg/l)	Cl (mg/l)	NO₃ (mg/l)	Temp (°C)	EC (μS/cm)	TDS (mg/l)	TH (mg/l)
Min	24.0	14.6	38.0	1.9	11.5	61.0	53.2	0.0	22.0	416.0	286.3	22.6
Max	176.4	68.1	126.8	6.4	182.5	366.1	514.7	4.2	32.9	1850.0	1122.4	234.7
Mean	67.2	39.4	72.0	4.4	60.3	183.0	186.2	1.7	27.3	1042.2	614.3	103.8
STD	42.5	16.5	26.5	1.2	46.7	75.5	150.4	1.5	3.2	436.5	232.0	58.7
Skew	1.2	0.3	0.6	−0.6	1.2	0.8	1.2	0.6	0.0	0.7	0.8	0.8

Table 10.2 Summary of trace elements of groundwater samples in Wadi Ranyah

Parameter	Li	Cr	Mn	Fe	Co	Ni	Cu	Zn	As	Mo	Cd	Ba	Hg	U
Min	1.06	0.10	0.00	0.00	0.02	0.02	0.45	0.10	0.68	3.99	0.00	21.56	0.00	0.05
Max	2.60	1.17	0.16	9.47	0.15	1.48	3.07	6.05	1.57	10.31	0.12	125.01	0.98	2.16
Mean	1.74	0.73	0.02	4.31	0.05	0.61	1.37	1.34	1.18	6.15	0.01	52.99	0.10	0.71
STD	0.46	0.28	0.04	2.72	0.03	0.43	0.78	1.42	0.27	1.73	0.03	25.46	0.24	0.58
Skew	0.36	−0.3	2.63	−0.2	1.48	0.60	0.90	2.28	−0.3	0.83	3.64	1.48	3.24	1.71

in Fig. 10.3. Two classes have been revealed in this study, C2S1 and C3S1. The C2S1 is very good for irrigation with low alkalinity and medium salinity. The C3S1 is suitable for tolerant crops with high salinity and low alkalinity. In addition, the relationship between electrical conductivity and total dissolved solids is shown in Fig. 10.4, which indicates that the relation is the same for most groundwater samples in the world with a conversion factor (slope) is about 0.58.

To quantify the atmospheric rainfall contribution to groundwater salinity in arid regions, Na/Cl ratio is suggested (Tiwari and Sing 2014). Figure 10.5 shows the relationship between Na/Cl ration and EC, which reveals that only few samples (2, 5, 9, 11, and 18) are within reverse ion exchange, whereas the rest samples are located within ion exchange. However, Na/Cl ratio (avg. 0.8), Higher ratio (Na/Cl > 1.0) indicates silicate rock-weathering dominance as a possible source of Na. Lower ratio (Na/Cl < 1.0) in some samples are probably result from ion exchange of Na for Ca and Mg in clay minerals. Several chemical processes occur through interaction between groundwater and aquifer
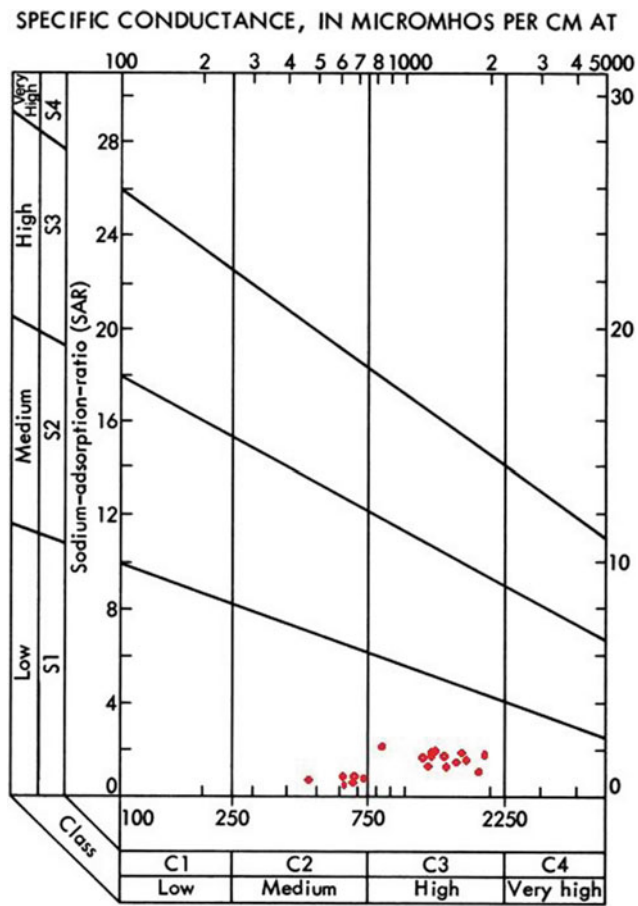
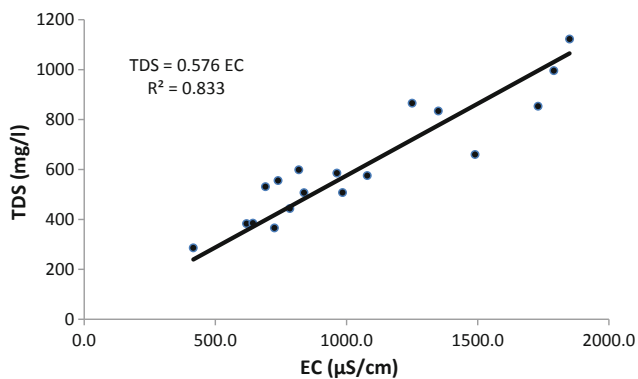**Fig. 10.2** Trilinear diagram
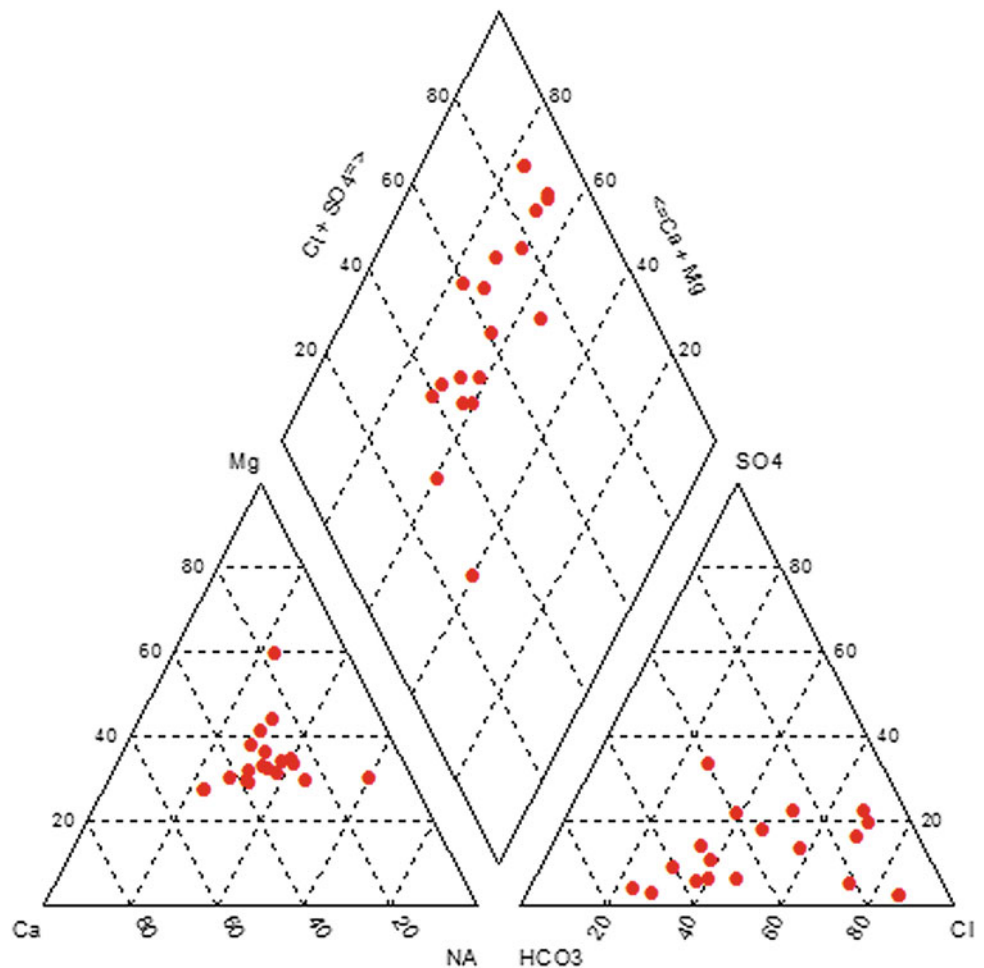
Fig. 10.3 SAR diagram

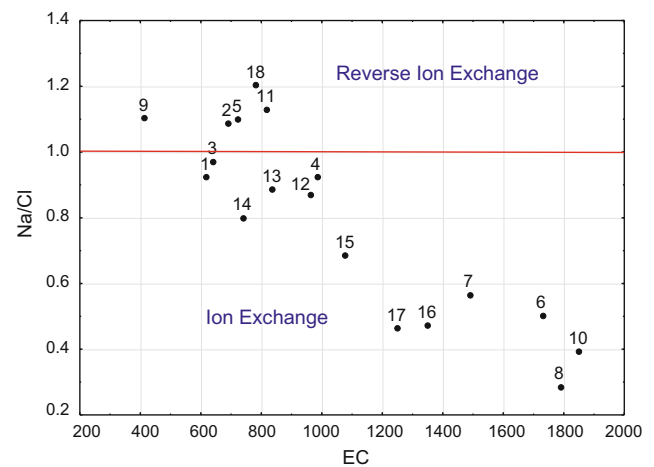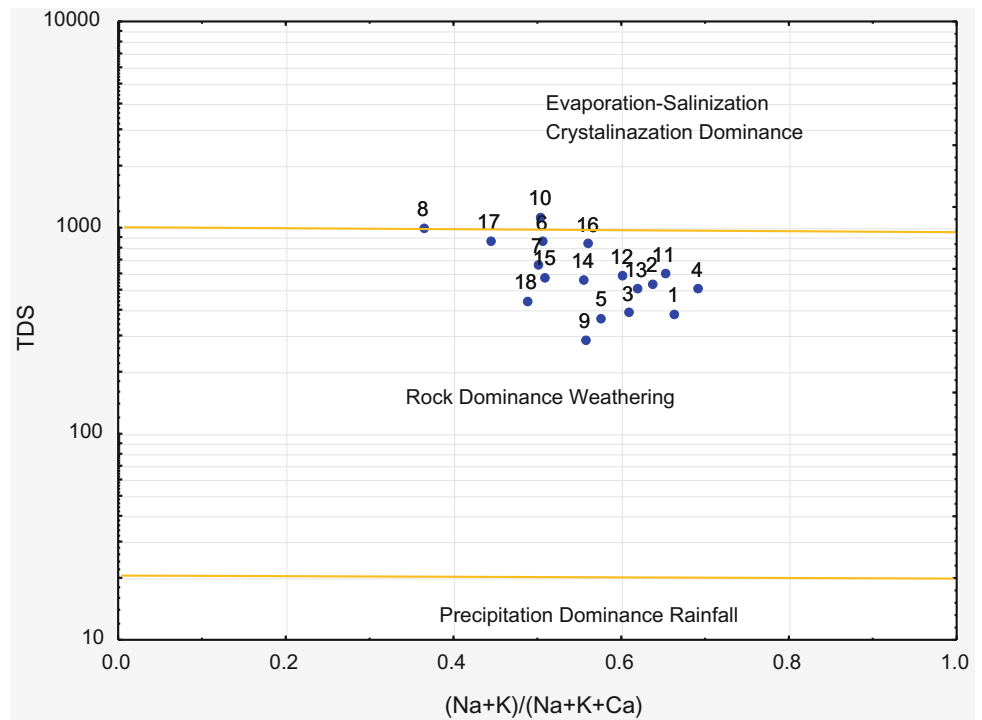Fig. 10.4 Regression analysis of TDS versus EC

Fig. 10.5 Na/Cl versus EC

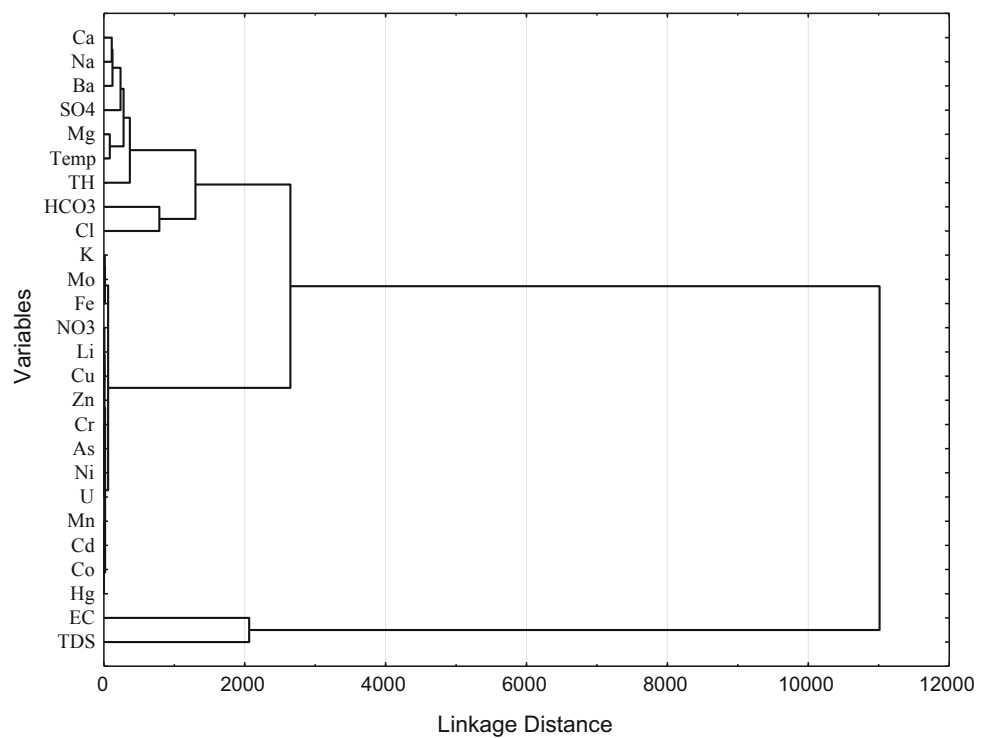weathering rock chemistry and the chemistry of the percolation of groundwater.

Cluster analysis dendrogram (R-mode) of the 26 descriptors. Three major groups is shown in Fig. 10.7. First group indicated recharge zone area with high correlation between major ions (Ca, Mg, Na, HCO_3, SO_4). The second group related to salinity relation with aquifer materials. Nitrate, potassium and manganese and trace elements are as one group in the third cluster, which may be reflects the impact of weathering rocks and agricultural activities.

The correlation reflects the type of rock units interaction and recharge zone in the study area. That is, Igneous and contact metamorphic (high weathering) rocks are the most dominants formations In Wadi Ranyah area. Rocks such as Andesite (pyroxene(augite), plagioclase/amphibole) and Granodiorite have mineral composition of Na–Ca plagioclase, K-feldspar and Quartz. While Mg found in mafic igneous rocks (Pidwirny 2006). It is possible that the condition of the alluvial aquifer in the lower part of the study area since it was not exposed to rainfall for a period of time more than 3 months; due to the fact that the wadi witness rapid cycles of rainfall after sequences of draught, causes to precipitate and increase the concentration of HCO_3 in groundwater. Moreover, a recharge can occur during the time of releasing sufficient amount of the storage water form wadi in order to recharge the aquifer and artificially from agricultural activities in the area. This recharge process can be an additional factor to precipitate bicarbonate from the surface to the groundwater. The presence of trace element occur due to the dissolving of weathering rocks and the agriculture activity in the area. Figure 10.8 shows the similarities in Q-mode, three groups are presented according to the degree of salinity in groundwater. Also well design in alluvial or weathered and fractured hard rocks.

materials. Therefore, Gibbs plot is employed in this study to understand the predominant samples fall in the rock–water interaction dominance, evaporation and precipitation dominance field (Kumar et al. 2015). Figure 10.6 illustrates that all samples fall within rock-interaction interaction dominance field which indicates that there is interaction between

Fig. 10.6 Gibbs diagram

**Fig. 10.7** Dendrogram of 26 variables in R-mode

Principle component (PCA) was done for 26 variables in water samples. Eigenvalues is plotted in Fig. 10.9. Three factors of loading variables with total variance are presented in Table 10.3. 42% of the total variance was explained by the first rotated variance, strong association between Ca, Na, Cl, TH, EC and Li, Fe, Ni, Cu and Ba as the input of
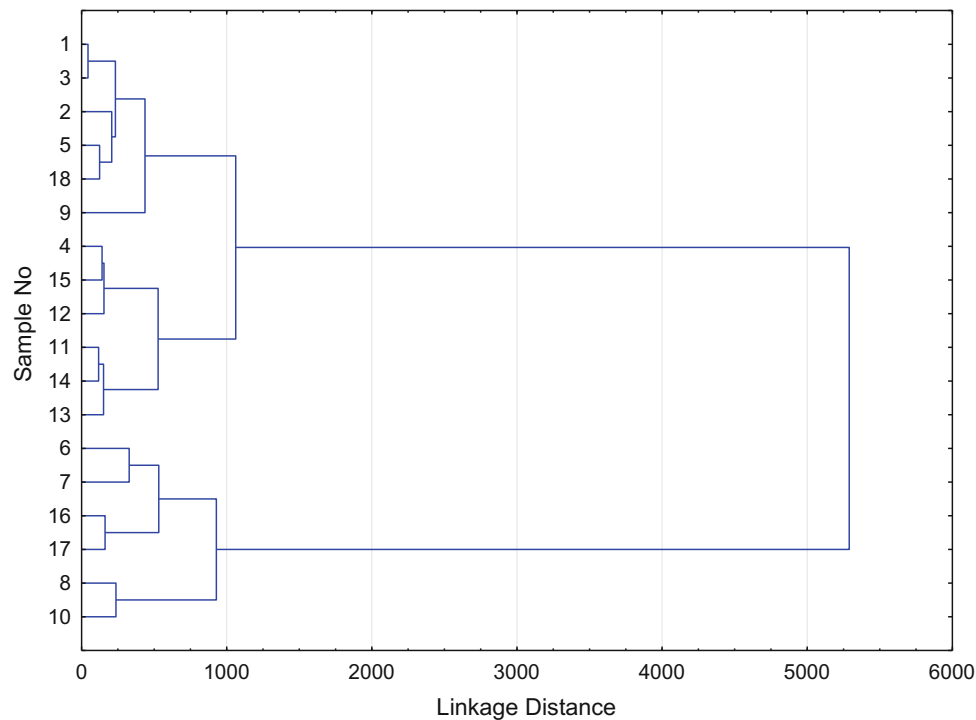
Fig. 10.8 Dendrogram of 18 samples in Q-mode
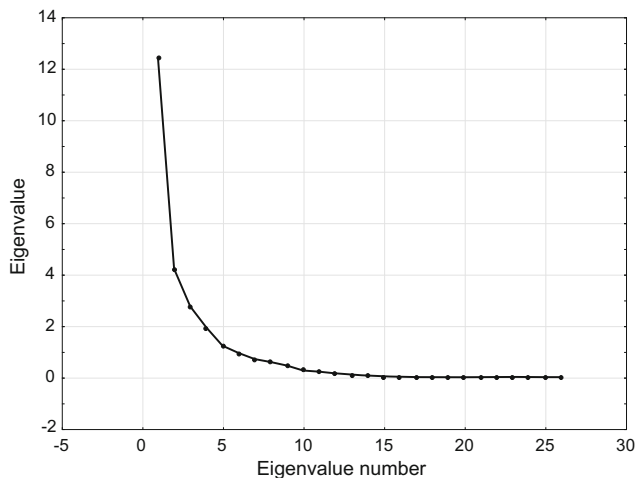
Fig. 10.9 Plot of Eigenvalue

agriculture and anthropogenic influences. 15% of the total variance was explained by the second factor, it represent of Mn and Co loading as input of soil waters, but they are within the save range. The third factor contributes 11% of the total variance, the high loading of Bicarbonate (HCO_3) and Chromium (Cr) are present in this table. Bicarbonte indicates recharge from surface water and Cr could be related to the input of weathered rocks and soil water interaction. Factor 1 distinguishes samples in relation to the enrichment with 47.7% loading in Ca, Mg, Na, TH and SO_4 and trace such as Fe and Coin the positive F1 axis as shown in Fig. 10.10. F2 is also evaluated the quality of water effect (16.2%), and it reflects the impact of HCO_3, Hg, Mn and Cd. No variables in the center of axis. So that indicated no clear facies of water quality.

10.5   Conclusion

Descriptive statistics, Piper diagram and multivariate analysis employed to investigate the groundwater quality in the upper portion of Wadi Ranyah, Western Saudi Arabia. The variation of major ions in the study area reflects the process of aridity and rock-water interaction. Multivariate analysis of cluster and PCA are considered to explore hidden structure for the purpose of interpretation. R- and Q-modes of cluster analysis resulted two distinctive sources of water chemistry, groundwater-rock interaction and human activities.

Factor analysis explained with three rotated factors about 67% of total variance. Despite the rainfall is erratic in Wadi Ranyah area, the renewable recharge from other sources

Table 10.3 Loading factors with communality

Variable	Factor 1	Factor 2	Factor 3	Communality
Ca	**0.8803**	0.1588	0.2327	0.854296
Mg	0.5897	−0.0163	−0.0334	0.349155
Na	**0.9126**	0.1146	0.0732	0.851235
K	0.1953	−0.3434	0.2081	0.199353
SO$_4$	0.3460	−0.0580	0.1473	0.144769
HCO$_3$	−0.2327	0.0957	**−0.8187**	0.733657
Cl	**0.9354**	0.0442	0.1752	0.907698
NO$_3$	0.4825	0.2469	0.4029	0.456118
Temp	0.0977	−0.1128	**0.7539**	0.590554
EC	**0.9082**	0.1160	0.2093	0.882064
TDS	**0.9120**	0.0889	−0.0710	0.844591
TH	**0.8376**	0.0837	0.1498	0.731069
Li	**0.7286**	0.0496	−0.0902	0.541373
Cr	−0.0645	0.2114	**0.7650**	0.634099
Mn	−0.1846	**−0.9450**	−0.0857	0.934524
Fe	**0.7213**	0.4626	−0.3283	0.842106
Co	0.5043	**−0.8258**	0.1785	0.968073
Ni	**0.9321**	0.0302	0.0312	0.870747
Cu	**0.9296**	0.0097	−0.0131	0.864469
Zn	0.6866	0.1689	−0.3758	0.641169
As	−0.6795	−0.1196	0.1685	0.504419
Mo	−0.4027	0.1392	0.2387	0.238568
Cd	−0.1509	**−0.9647**	−0.0250	0.953963
Ba	**0.7505**	−0.0480	0.4401	0.759174
Hg	−0.2950	**−0.9470**	−0.0079	0.983937
U	0.6874	−0.0402	−0.1907	0.51052
% Variance	42	15	11	
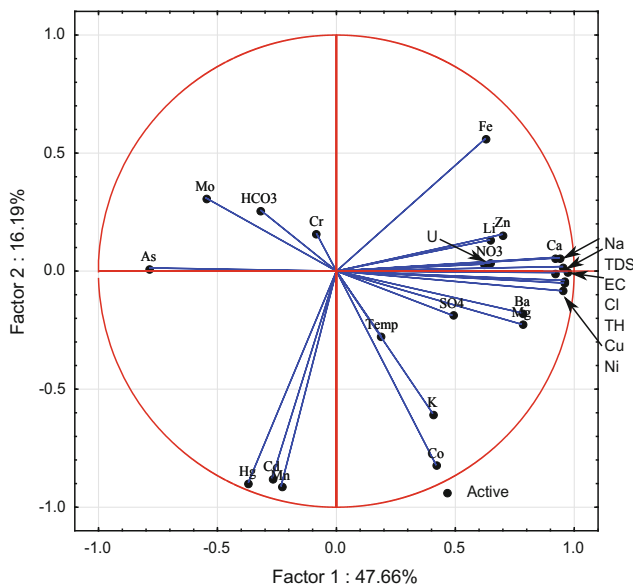
Fig. 10.10 Plots of F1 versus F2

from streams in the study area help to keep water quality within the range of different purposes. Fracture zones, weathering rocks and the agricultures activities in the area are the main sources of the trace elements of the groundwater.

Trace elements, many factors such as highly weathered rocks, complexity and heterogeneity of the rock formations in the study area, well drilling conditions at different depths and the most important the recharge in both surface and groundwater especially in case where the groundwater is flowing from different catchment areas which carrying these trace elements. Accordingly, Results showed that water quality is of Calcium-Bicarbonate type the in Wadi Ranyah and it is subject to the conditions that occur variation in the concentrations of trace elements. This basin and all its branches need sustainable integrated management to develop and maintain its water resources.

References

Belkhiri L, Boudoukha A, Mouni L (2011) A multivariate statistical analysis of groundwater chemistry data. Int J Environ Res 5(2):537–544

Brown C (1998) Applied multivariate statistics in geohydrology and related sciences. Spinger, Berlin

Ceron JC, Pulido-Bosch A, Bakalwicz M (1999) Application of principal components analysis to the study of CO_2-rich thermomineral waters in the aquifer system of Alto Guadalentín (Spain). Hydrol Sci 44(6):929–942

Davis JC (2002) Statistics and data analysis in geology. Wiley

Grande JA, Borrego J, Torre ML, Sainz A (2003) Application of cluster analysis to the geochemistry zonation of the estuary waters in the tinto and odiel rivers (Huelva, Spain). Environ Geochem Health 25:233–246

Hem JD (1989) The study and interpretation of the chemical characteristics of natural water. 3rd edn. USGS Water Supply Paper 2254, US Geological Survey

Hussain M, Ahmad S, Abderrahman W (2008) Cluster analysis and quality assessment of logged water at an irrigation project, eastern Saudi Arabia. J Environ Manag 86:297–307

Kumar SK, Rammohan V, Sahayam JD, Jeevandam M (2015) Assessment of groundwater quality and hydrogeochemistry of Manimuktha River basin, Tamil Nadu, India. Environ Monit Assess 159:341–351

Ministry of Water and Electricity (2015) Climate data reports. Hydrology Division, Riyadh

Pidwirny M (2006) Characteristics of igneous rocks. Fundamentals of physical geography, 2nd edn. Date Viewed

Piper AM (1953) A graphical procedure in the geochemical interpretation of water analysis. USGS. Ground Water: Note 12

Sanchez-Martoz F, Jimenezespinosa R, Pulido-Bosch A (2001) Mapping groundwater quality variables using PCA and geostatistics: a case study of Bajo Andarax, southeastern Spain. Hydrol Sci J 46(2):227–242

SASO (Saudi Arabian Standards Organization) (1984) Bottled and unbottled drinking water. SSA 409/1984, 2nd edn, SASO Information Center, Riyadh, Saudi Arabia, pp 1–8

Şen Z (1983) Hydrology of Saudi Arabia. Symposium on Water Resources in Saudi Arabia, Riyadh, Saudi Arabia, A68-94

Shihab AS, Abdul Baqi YT (2010) Multivariate analysis of groundwater quality of Makhmor Plain/ North Iraq. Damascus Univ J

Simon F (1988) Geologic map of the Wadi Bishah quadrangle, Sheet 20F, Directorate General of Mineral Resources, Kingdom of Saudi Arabia, Scale 1:250,000

Stiff HA (1951) The interpretation of chemical water analysis by means of patterns. J Pet Technol 3:15–17

Subyani A (2004) Geostatistical annual and seasonal mean rainfall pattern in southwest Saudi Arabia. Hydrol Sci J 49:803–817

Subyani AM, Ahmadi M (2010) Multivariate statistical analysis of groundwater quality in Wadi Ranyah, Saudi Arabia. King Abdulaziz University, Earth Sciences 21(2):29–46

Suk HJ, Lee KK (1999) Characterization of a ground water hydrochemical system through multivariate analysis: clustering into ground water zones. G W 37(3):358–366

Tabachnick BG, Fidell L (2006) Using multivariate statistics, 5th edn. Allyn & Bacon, NY

Tiwari AK, Singh AK (2014) Hydrogeochemical investigation and groundwater quality assessment of Pratapgarh District, Uttar Pradesh. J Geol Soc India 83:329–343

Usunoff EJ, Guzman A (1989) Multivariate analysis in hydrochemistry: an example of the use of factor and correspondence analyses. Groundwater 27(1):27–34

Woocay A, Walton J (2008) Multivariate analysis of water chemistry: surface and groundwater interactions. Groundwater 46(3):437–440

Ward JH (1963) Hierarchical grouping to optimize an objective function. J Am Stat Assoc 58(301):236–244

WHO (2011) Guidelines for drinking-water quality, 4th edn. World Health Organization, Geneva, Switzerland

Yang Q, Wang L, Ma H, Yu K, Martin JD (2016) Hydrochemical characterization and pollution sources identification of groundwater in Salawusu aquifer system of Ordos Basin, China. Environ Pollut 216:340–349

Yidana SM, Yakubo BB, Akabzaa TM (2010) Analysis of groundwater quality using multivariate and spatial analysis in the Keta basin, Ghana